PERFORMANCE ACHIEVEMENTS AND CHALLENGES FOR FELS BASED ON ENERGY RECOVERED LINACS*

G. A. Krafft, Jefferson Lab, Newport News, VA 23060, U.S.A.

Abstract

During the past decade several groups have assembled free electron lasers (FELs) based on energy recovered linacs (ERLs). Such devices have been built to obtain high average power electron and photon beams, by using high repetition rate beam pulses driving FEL oscillators. In this paper the performance of many existing and several proposed facilities from around the world are reviewed. Going forward, many questions must be addressed to achieve still better performance including: higher average current injectors, better optimized accelerating cavities, higher energy acceptance and lower loss beam recirculation systems, and better optical cavity designs for dealing with the optical beam power circulating in the ERL FELs. This paper presents some of the current thinking on each of these issues.

INTRODUCTION

The basic idea in same cell beam energy recovery is fairly straightforward to understand and has been discussed in great detail in recent reviews [1,2]. In a front-to-back recirculated linac the recirculation path length is chosen to be approximately an integer plus ½ RF wavelengths, and if the beam current does not change much in the time it takes for a complete circuit of the recirculation loop to be made, then energy can be transferred directly from the decelerating higher-energy beam to the accelerating first-pass beam, without the need for power to be provided by the RF systems attached to the cavities. This opportunity allows one to construct recirculated linacs, particularly those consisting of superconducting cavities, with energy transfer efficiencies approaching those in storage rings. This fact, in turn, allows one to build linacs that can transport and accelerate beam average currents approaching those in storage rings.

The energy transfer efficiency is nicely quantified by the power multiplication factor

$$k = P_{b,ave} / P_{RF} \tag{1}$$

where $P_{b,ave}$ is the average beam power and P_{RF} is the RF power needed to accelerate the beam. For normal conducting recirculators k is much less than 1, for present day ERL FELs k is of order 10, for advanced ERL light sources k is of order 100, and for typical storage rings k is of order 1000. It is straightforward to show that in the limit the optical cavity losses are small compared to the outcoupled radiation power, the transfer efficiency from RF power to photons is equal to ζk, where ζ is the fraction of beam energy converted to photons per pass in an optical cavity oscillator FEL.

The first superconducting linac to demonstrate same cell energy recovery was the Stanford University Superconducting Accelerator as reported at this conference twenty years ago [3]. In an experiment, the recirculation path length was set to allow energy recovery to proceed. Nearly all of the beam energy was recovered as indicated by the absence of RF power being needed to drive the beam load in the superconducting cavities of the accelerator. However, in this early experiment there was no optical cavity inside the recirculation loop.

PRESENT STATUS

Presently, there are three ERL-based free electron lasers in existence and a fourth being rapidly assembled as a prototype project for an advanced fourth generation light source suite. Two of the existing FELs, at Jefferson Lab and the Japan Atomic Energy Agency (JAEA), are based on superconducting RF (SRF) cavities, and the third, at the Budker Institute for Nuclear Physics (BINP), is based on CW normal conducting RF cavities. In all the devices, an optical cavity FEL is placed inside the beam recirculation loop.

Jefferson Lab Free Electron Laser

A group at Jefferson Laboratory has spent the last decade building and improving many increasingly capable free electron lasers based on energy recovery, including the first ERL to have an FEL inside the energy recovery loop [4]. This demonstration device has been upgraded in order to achieve higher average electron beam and optical beam powers. Some recent electron beam parameters are summarized in Table 1. Beam starts from a DC photocathode source, is accelerated to 10 MeV using two standard CEBAF superconducting cavities, injected onto a beamline containing an energy recovered linac that can achieve up to 150 MeV. The beam is recirculated with two Bates bend beam recirculation systems specially designed to contain and transport the large energy spread generated by the FEL in the electron beam.

Recent work at Jefferson Lab has concentrated on extending high power CW operations at the 10 kW level from 6 microns down in wavelength. Over the last year the average power has increased from about 4 kW to 6.7 kW at 2.8 microns, from 1 kW to 5.4 kW at 1.6 microns, and from 1 kW to 2.2 kW at 1 micron. The short wavelength performance of the FEL has improved as low absorption dielectric coatings have been developed for the high power optical systems. The group expects a considerable improvement of the high power performance

*Authored by Jefferson Science Associates, LLC under U.S. DOE Contract No. DE-AC05-06OR23177.

of the FEL when cryogenically cooled optical cavity mirrors are deployed to help deal with mirror distortion in the optical cavities at high power.

Table 1: Electron Beam Parameters for ERL FELs

PROJECT	**JLAB**	**JAEA**	**BINP**
Frequency (MHz)	1500	500	180 NC
Energy (MeV)	130	17	13
Current (mA)	10	8	20
Bunch Charge (pC)	130	400	500
Rep. Rate (MHz)	75	83	11.2
Normalized Emittance (mm mrad)	8	20	30

A user program has developed at the FEL. Because of the short bunch length at the FEL, copious amounts of wideband THz radiation are produced in the bend magnets of the chicanes surrounding the wiggler through the coherent synchrotron radiation emission. The THz radiation has been taken up to a user lab and is now routinely used for electron beam diagnostic purposes. Other experiments are performed with the FEL radiation extending from studies in condensed matter physics, to studies of fundamental optical physics using the FEL light to make far off resonance traps, all the way to fundamental particle physics in dark matter candidate searches.

JAEA Free Electron Laser

The JAEA FEL injector consists of a 230 keV thermionic gun, and 83 MHz subharmonic buncher, and two single-cell 500 MHz superconducting cavities that accelerate the beam to about 2.5 MeV. The injected beam is merged onto the axis of a linac that consists of two 5-cell superconducting cavities that boost the beam energy to 17 MeV. Beam is recirculated with three-bend achromats, and the undulator and optical cavity of the FEL are just upstream of the return achromat. As seen in Table 1, the lower cavity frequency allows higher charge per bunch in the beam to be accelerated efficiently.

Recent work has focused on doubling the electron bunch repetition rate by upgrading the gun grid pulser and the RF power for the non energy recovered 2.5 MeV accelerating cavities, increasing the energy acceptance of the achromats by reworking quad magnets and beam pipes in the achromats, and investigating and optimizing the achromat settings for increasing the FEL efficiency. Recently, the FEL extraction efficiency has been measured and the peak efficiency reaches 2.8%, and the group has achieved 0.7 kW output at 22 micron from an 8 mA beam during a 230 microsecond macropulse. A more complete summary of recent work has been given by N. Nishimori at this conference [5].

BINP THz FEL

The Budker Institute THz FEL is based on a normal conducting CW linear accelerator. Beam originates in a thermionic electron gun, is accelerated to 2 MeV through two 180 MHz cavities, injected on the main linac axis and accelerated up to 13 MeV by 16 180 MHz cavities. The beam drives an FEL oscillator which produces radiation in the THz band, and the beam energy is recovered in the second pass through the linac. This device is the highest average power source of narrowband THz radiation. Because of the low frequency and hence large aperture of the accelerating cavities, this device is able to handle much higher average current than the superconducting ERL FELs, achieving 20 mA average current now and planned to achieve 150 mA average current after an injector upgrade. This device has energy recovered the highest average beam current to date, and is unique in that the recirculation loop is oriented vertically.

There are plans to upgrade this device with two higher energy FELs that will produce radiation at 20-100 μm and 3-20 μm, in optical cavity oscillators. The 20-100 μm optical klystron will sit after a second pass of beam recirculated acceleration for a beam energy greater than 20 MeV, and the shorter wavelength optical klystron will sit after four beam passes up to about 40 MeV. The recirculation loops for this device will be oriented horizontally to the existing linac, which does not need to be upgraded substantially. When completed, the BINP FELs will be unique among energy recovered FELs in that a large number of passes will be accommodated, as the other existing ERL FELs are two pass machines. The multipass “energy recuperator” free electron lasers will be assembled throughout 2007 and commissioning is anticipated to begin towards the end of 2007. A more complete summary of recent work has been given by N. Vinokurov at this conference [6].

4GLS

The British 4GLS project is to produce a suite of three superconducting linac based free electron lasers in addition to an energy recovered high average current recirculated linac light source, to be located at Daresbury Laboratory. The IR FEL and the XUV-FEL in this project are not energy recovered, the IR FEL operating at a MHz-scale repetition rate and the XUV-FEL operating at a repetition rate of 1 kHz, ambitious for a SASE or a seeded source. The UV FEL source, based on a regenerative amplifier, is located in the high average current energy recovered recirculation loop. It is anticipated to operate this FEL simultaneously with the high average current ring.

In order to start the process of building the full 4GLS, which is based on 1.3 GHz superconducting cavities, a 35 MeV energy recovered FEL, ERLP, is being built [7]. Just prior to the conference, beam was extracted from the DC photocathode source of ERLP for the first time. The accelerator consists of two two-cavity cryostats, one inside and one outside the beam recirculation loop. These have now been assembled, as well as the three bend

achromat recirculation optics systems. Cold commissioning of the linac, in its planned location is scheduled for the month of October 2006, with the machine completely installed by the end of 2006. Machine studies, including beam energy recovery, are to be completed in the spring of 2007 and there should be a "first lasing" contribution by ERLP at the next FEL conference. A more complete summary has been given by J. Clarke at this conference [8].

High Average Power X-FELs

Perhaps the ultimate light source, i. e., one that could produce both high peak power and high average power X-ray beams, would consist of an energy recovered X-FEL. A superconducting linac as a driver for such an FEL has many inherent advantages: greater potential efficiency and the possibility of high gradient CW operation, the possibility to achieve repetition rates at the MHz or higher level, and the ability to transport cleanly high bunch charges because of the low transverse impedance of the accelerating structures [9]. Such a scheme has been studied in detail as a follow on project for the TTF FEL [10]. A major concern is achieving a high repetition rate injector. As discussed more thoroughly below, this injector would seem to require an SRF gun electron source.

FUTURE DEVELOPMENTS

In order to achieve another order of magnitude in electron and photon beam power many improvements must be made to the existing devices. The present photocathode injectors must be upgraded to produce higher average current. The accelerator design optics must be stable to the higher average recirculated beam current in the more ambitious designs. The optical cavities must be able to handle the increased recirculating beam power. High order mode (HOM) cooling becomes more problematic at higher average currents. Finally, non-invasive electron beam diagnostics should be developed to help monitor the beam during CW operations.

Electron Photocathode Sources

In order to increase the average beam current in the next generation FELs by an order of magnitude, it seems that the easiest method is to increase the bunch repetition rate until every accelerating (and decelerating!) phase in the RF waves are filled. This can be done with little change to the bunch charge presently obtained. This approach has been adopted by Cornell for the first energy recovered recirculated linac light source, which must achieve beam emittances much smaller than is typical for the long wavelength ERL FELs. Because of the higher average current in the non energy recovered portions of such accelerators, it is expected that the injection energy will be reduced and the number of superconducting cavities increased in order to deal with the increased beam power in the non-recovered portions of the accelerator [11]. Also, larger beam dumps may be needed to dissipate the non-recovered beam energy.

In the further future, one anticipates that SRF photocathode sources will be developed to produce electron beams at high energy and high levels of average current. The group at Rossendorf, who have been leaders in developing SRF guns, hope to achieve 1 mA average current from a 10 MV 3.5 cell gun in construction now, and Brookhaven National Laboratory have been developing guns in the 100 mA-1 A class for electon cooling applications [12]. The main benefit of marrying the SRF and photocathode source technology is the possibility to have high CW accelerating gradient on the photocathodes, which may lead to superior emittance in CW high repetition rate applications.

Drive Lasers

In the high average current applications of photocathode electron sources there is a need to develop drive lasers of sufficient power to extract the needed average current. Roughly an order of magnitude in laser power is needed beyond present experience for the DC photocathode sources presently used. In addition to the power requirement, to get the best beam parameters out of photocathode guns laser pulse shaping is needed. Cornell University is developing a fiber based system with 20 W capabilities untilizing transverse shaping and longitudinal pulse stacking in order to obtain a uniform laser pulse longitudinally. Jefferson Lab is also developing a system that should be able to deliver 32 W [13], about 5 times more than the present drive laser for the Jefferson Lab FEL.

Similar high average power lasers with high repetition rate may be quite useful in seeding applications in high repetition rate X-FELs.

Beam Breakup and Advanced Beam Optics

Recent work at Jefferson Lab has allowed direct quantification of the multipass beam breakup instability, as in some electron beam optical conditions the FEL beam is unstable. A recent review of the subject has been performed [14], including discussions of utilizing special electron beam optics to suppress the instability. The methods studied are likely sufficient for stabilizing the instability in future FELs, but simulation evidence exists indicating that some of the intended solutions may not apply to larger scale accelerators [15]. Significantly, many of the BBU simulation codes have now been properly benchmarked against experimental instability data.

Driven by the desire to operate the ERL FELs at higher energy extraction, advanced beamline designs for beam recirculation with energy spreads of 10% or more have been developed [16]. These designs feature magnet shapes and edges chosen to automatically yield nearly isochronous beam recirculation due to the shape choices. It is anticipated that such designs will become increasingly important as higher average power ERL FELs are built.

High Power Optical Cavities

In designing the next generation of optical cavities the following aspects of the problem must be understood [13]:

- One must minimize the absorptive loss which can quickly lead to mirror distortion and low output.
- Scatter loss should be minimized to control subsequent absorption on components causing pressure rise and drift.
- Mirror coatings and substrates must be chosen to mitigate the effects of any power loading from out-of-band radiation which may be incident on the mirrors.

Optical cavities and beam transport lines must be designed with these effects in mind.

HOM Power

Superconducting RF cavities have been used in storage ring applications for many years at beam average currents of 100 mA and above. Because the power deposited into HOMs can be substantially larger than the heat deposited in the cavity walls when the cavity is operated at gradient, it is particularly important to couple the HOM power out of the cavity volume to be absorbed at locations with higher temperature to reduce cooling requirements on the He refrigerator. Recent storage ring HOM absorbers consist of ferrite absorbers located upstream and downstream of the SRF cavities mounted on the beam pipe wall with a separate cooling loop to deal with the HOM power.

Similar solutions will be needed to absorb the HOM power in 100 mA-scale ERLs, and there is an additional complication. The bunch durations in ERLs can be up to two orders of magnitude smaller than in storage rings and now there is bunch spectrum available to excite HOMs at much higher frequencies than in rings. Thus, the overall power excited increases and the operational range of the HOM absorber must be much broader in frequency to handle the wider range of frequencies excited. This problem afflicts advanced ERL light source designs, and already a group has investigated material which is highly absorbing at frequencies up to 40 GHz at a temperature of 80 K [17]. Also, it is anticipated that advanced HOM absorbers will include several different materials absorbing in different frequency bands [18].

Electron and Photon Beam Diagnostics

Because the average current of next-generation ERLs is approaching that in storage rings, one would expect that the more standard electron beam diagnostics, e.g. beam position monitors, beam profile monitors, and current monitors, would follow the techniques previously developed for storage ring applications. The beam attributes unique to ERLs and ERL FEL sources are the need to diagnose and control short bunches, the need to deal with low average power tune up beam diagnostic modes, and the need to deal with high average beam power. Many longitudinal techniques are being investigated in X-FEL projects. Mainly they are highly disruptive and might not be technically useful in the higher average beam power regimes we are pushing into.

Real time measurements of bunch longitudinal distribution and phase space based on electro-optic methods or based on coherent synchrotron, edge, or undulater radiation, may provide correct approaches for non-invasive monitors. Presently, there seems to be a lack of a universal method yet demonstrated that is unambiguous in the results it reports [19]. Achieving such a universal longitudinal measurement will be at least as important for future ERL development as the development of good profile monitoring was in storage rings.

For photon beams, the key near-term developments need to occur in the shaping, both longitudinally and transversely, of the higher average power drive laser beams for electron production on the photocathodes. The production methods will be need to be diagnosed to some level with techniques suitable for power levels of several tens of W needed in the next generation electron sources. In the further future it will perhaps be required by the users of high average power FELs that the emerging high power optical pulses display customized and controlled characteristics. Very little is known about this subject now.

CONCLUSIONS

- The field of ERL-based FELs continues to grow and the performance of devices continues to improve.
- Upgrade paths for at least an order of magnitude in both electron beam and photon beam power, though not trivial, have been identified.
- Many new ideas are being explored, some in conjunction with recent work on Energy Recovered Linac light sources.
- The field seems to be thriving and there is no shortage of interesting problems to work on.

REFERENCES

[1] L. Merminga, D. R. Douglas, and G. A. Krafft, Ann. Rev. Nucl. Part. Sci., 53 (2003) 387.
[2] G. A. Krafft, “Recirculated and Energy Recovered Linacs”, Joint Accelerator School 2002, Long Beach, CA, USA, p. 301.
[3] T. I. Smith, H. A. Schwettman, R. Rohatgi, Y. Lapierre, and J. Edighoffer, Nucl. Inst. and Methods A 259 (1987) 1.
[4] G. Niel, et al., Phys. Rev. Lett. 84 (2000) 662.
[5] N. Vinokurov, these proceedings.
[6] N. Nishimori, these proceedings.
[7] D. J. Holder, et. al., “Status of the Daresbury Energy Recovery Prototype Project”, EPAC’06, http://www.jacow.org
[8] J. Clarke, these proceedings.
[9] G. A. Krafft, and J. J. Bisognano, “On Using a Superconducting Linac to Drive a Short Wavelength FEL”, PAC’89, Chicago, IL, USA, p. 1256, http://www.jacow.org

[10] J. Sekutowicz, et al., Phys. Rev. ST-AB 8 (2005) 010701.
[11] I. V. Bazarov and C. K. Sinclair, Phys. Rev. ST-AB 8 (2005) 034202.
[12] I. Ben-Zvi, private communication.
[13] M. Shinn, private communication.
[14] E. Pozdeyev, et al., "Multipass Beam Breakup in Energy Recovery Linacs", ERL 2005, Newport News, VA, USA, Nucl. Inst. and Methods A 557 (2005) 176.
[15] G. A. Krafft, and J. J. Bisognano, "Two Dimensional Simulations of Multipass Beam Breakup", PAC'87, Washington,DC,USA, p. 1356, http://www.jacow.org
[16] D. Douglas, private communication.
[17] V. Shemelin, M. Liepe, and H. Padamsee, "Measurements of Epsilon and Mu of Lossy Materials for the Cryogenic HOM Load", PAC'05, Knoxville, TN, USA, p. 3452, http://www.jacow.org
[18] M. Liepe and J. Knobloch, "Superconducting RF for energy-recovery linacs", ERL 2005, Newport News, VA, USA, Nucl. Inst. and Methods A 557 (2005) 354.
[19] G. A. Krafft and J.-C. Denard, "Diagnostics for Recirculated and Energy Recovered Linacs", BIW'02, Upton, NY, USA, AIP Conf. Proc. 648. p. 118.

FUTURE LIGHT SOURCES: INTEGRATION OF LASERS, FELS AND ACCELERATORS AT 4GLS

J. A. Clarke, CCLRC Daresbury Laboratory, Warrington, UK, on behalf of the 4GLS Design Team.

Abstract

4GLS is a novel next generation proposal for a UK national light source to be sited at Daresbury Laboratory, based on a superconducting energy recovery linac (ERL) with both high average flux photon sources (undulators and bending magnets) and three high peak brightness free electron lasers. Key features are a high gain, seeded FEL amplifier to generate XUV radiation and the prospect of advanced research arising from unique combinations of sources with femtosecond pulse structure. The conceptual design is now completed and a CDR recently published [1]. The 4GLS concept will be summarised, highlighting how the significant design challenges have been addressed, and the project status and plans explained.

INTRODUCTION

The 4GLS project design takes advantage of the very latest advances in accelerator science and technology incorporated in a unique scheme to provide state-of-the-art research facilities. This will enable a broad range of outstanding science to be undertaken by the UK and international communities.

4GLS will enable the study of real time molecular processes and reactions on timescales down to tens of femtoseconds in short-lived, nano-structured or ultra-dilute systems. The emphasis is on molecular and device function, rather than the largely 'static' structural focus of work on 3rd generation synchrotron radiation sources and X-ray FELs. Key areas where 4GLS will make unique contributions are in:

- understanding the function of single biomolecules in living systems and membrane transport;
- determining reaction pathways in areas as diverse as enzyme processes, reactions contributing to atmospheric pollution or reactions occurring in the interstellar medium;
- studies of electron motion in atoms/molecules and developing 'coherent control' of reactions and intense laser-matter interaction leading to new physics;
- developing new nano-scale devices through understanding electron charge and spin transport; and
- development of new dynamic imaging techniques to improve early diagnosis of conditions such as cancer and prion based diseases.

The major themes of the science case are time-resolved measurements in the life sciences and nanoscience. Particular areas of strength are high resolution pump-probe spectroscopy of atoms, molecules and clusters, including high field dynamics, dynamics at surfaces and interfaces, many-body problems in condensed matter, and studies of the dynamics of biomolecules in 'real' environments.

The science requirement is for an ultra-high brightness facility that allows the use of short pulsed sources in combination, and where the energy range is optimised to allow the extraction of electronic and vibrational information. The 4GLS suite of synchronised sources, operating from the THz to the soft X-ray range is designed to meet this science need.

The 4GLS facility is planned from the outset to be a multi-source, multi-user facility. This is achieved by superconducting radio-frequency (SCRF) accelerator technology, operating using energy recovery, to provide short pulse spontaneous radiation with pulse length variable from ps to < 100 fs. At long wavelengths this allows the condition for coherent synchrotron radiation (CSR) production to be met, with the result that 4GLS will provide enormously bright THz radiation. The high quality low emittance electron beam provided by the photoinjectors additionally provides an ideal source with which to operate free electron lasers (FELs). In the 4GLS conceptual design these are embedded within the facility, delivering ultra-high brightness short-pulse radiation in the IR, VUV and XUV energy ranges, with pulse lengths as short as 50 fs FWHM. In world terms, this gives a unique suite of synchrotron radiation (SR) and FEL sources covering the THz to the soft X-ray range. Many of the light pulses originate from the same electron bunch, thus offering potential levels of internal synchronization at the tens of femtoseconds level. All the 4GLS sources are offered with variable polarization, while the flexibility of SCRF technology allows the repetition rates of the sources to be varied. The peak brightness of the 4GLS sources is given in Figure 1. There is a typical enhancement of eight orders of magnitude when compared with 3rd generation light sources.

The 4GLS accelerator design concept consists of three inter-related accelerator systems [2, 3]. The high average current loop uses energy recovery as an essential element to deliver a 600 MeV electron beam of 77 pC bunches at repetition rates of up to 1.3 GHz. Distributed bunch compression allows for SR pulse lengths from a few ps to approximately 100 fs (RMS) to be delivered according to user requirements. A low-Q cavity VUV-FEL device is incorporated at the end of this loop. The most challenging area of accelerator design for 4GLS is in transporting and accelerating an extremely high quality high-average current (100 mA) beam to this loop, while simultaneously providing extremely high peak current (1.5 kA) at 750 – 950 MeV for the second accelerator system, the XUV-FEL branch. This beam is derived from 1 nC bunches

produced by a normal conducting RF photoinjector operating at 1 kHz and it is dumped after traversing a final spontaneous undulator source. The XUV-FEL uses an HHG (high harmonic generation) seed, offering considerable advantages in pulse quality over a SASE (self-amplification of spontaneous emission) design. The third accelerator system is required for the IR-FEL. SCRF linac technology is used to accelerate electrons to 25 – 60 MeV to provide a fully integrated and synchronized IR-FEL facility.

Significant aspects of the 4GLS design have been informed by experience gained on the 4GLS Energy Recovery Linac Prototype (ERLP) currently approaching completion at CCLRC Daresbury Laboratory [4, 5]. In considering detailed 4GLS design decisions considerable attention has been given to ensuring that future upgrade options are not designed out at this early stage. These possibilities include various routes to higher energy operation, increased repetition rate for the XUV-FEL and decreased photon pulse lengths.

4GLS is thus the leading energy recovery proposal in Europe and the most comprehensive in terms of utilisation of combined sources. In terms of multi-user capability it is currently the most advanced energy recovery linac (ERL) proposal in the world. 4GLS is complementary to XFEL, to table-top lasers and to 3rd generation sources.

The unique advantages of 4GLS are:

- Combinations of sources. The fully integrated capability to utilize both short pulse SR(ERL) and the FEL sources for pump-probe and two colour dynamics experiments. This results in both experimental flexibility and cost effective delivery.
- Intense, tuneable, variable polarisation FEL sources optimized for spectroscopy and imaging in the frequency ranges of XUV, VUV and IR-THz.
- Energy recovery linac spontaneous light sources available from soft X-ray to THz. This gives short pulse, high repetition rate operation, the capability to 'pulse tailor', and low probability of sample damage.
- Europe's most intense broadband source of coherent THz radiation.

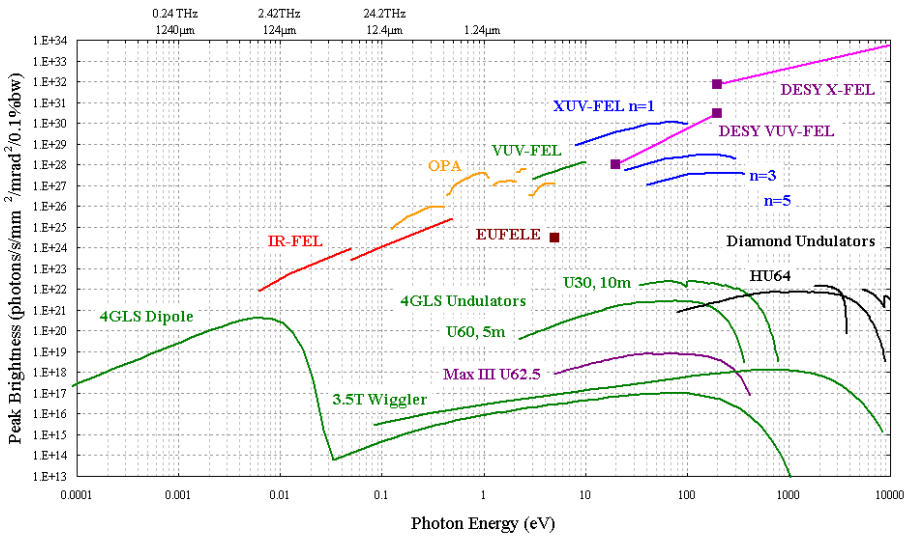

Figure 1. Peak brightness for 4GLS FELs, undulators, wiggler, OPA and dipoles compared with EUFELE, XFEL, Diamond and Max III undulators.

OVERVIEW

The 4GLS project design takes advantage of the very latest advances in accelerator science and technology incorporated in a unique scheme to provide state-of-the-art facilities. This has been made possible by a number of parallel developments at leading international laboratories, including successful demonstrations of technical solutions. The proposed design builds on current world achievements and in some cases extrapolates beyond them. In the most challenging areas an active R&D programme is already underway world-wide and the 4GLS team has augmented this, not least because to do so enhances the necessary skill base for detailed design, construction and operations.

The provision of high intensity electron beams has been revolutionised in the last decade by the successful development of a new variant of accelerator: the Energy Recovery Linac (ERL). Traditionally beam currents in linear accelerators can have high instantaneous values but are restricted to pulses with low repetition rates because the average power dissipation must be kept to manageable levels. For a light source high average flux emission is highly desirable and this output has been possible so far only by the widespread application of the electron storage

ring (e.g. Diamond and other 3rd generation sources) that achieves average currents of hundreds of milliamperes by recirculating the same electrons many times (and for many hours). This solution has serious drawbacks, in particular the ring defines the beam properties and they are dominated by the very emission of synchrotron radiation that the ring is built to deliver. If long-term storage of the electron beam can be avoided then greatly superior properties can be provided and this is one of the principal features of the ERL.

The ERL delivers high average currents without beam storage, since electrons are injected, accelerated and circulated only once before the system recovers their energy, dumps them and replaces them with new electrons. This means that if the beam is injected with superior brightness properties it maintains these during its radiation emission phase. The 4GLS project has an ERL at its heart in a generational leap from storage ring sources. Globally, pioneering work on ERLs has been undertaken at the Jefferson Laboratory in the USA where a low energy proof-of-principle ERL has been successfully demonstrated.

4GLS is best thought of in terms of three inter-related accelerator systems (see Figure 2). The first is the high average current loop. In this a 600 MeV beam of 77 pC bunches is delivered at repetition rates of up to 1.3 GHz and energy recovery is an essential element. Progressive compression of the electron bunches in this loop allows for photon pulse lengths from a few ps to approximately 100 fs (RMS). The VUV-FEL is placed towards the end of the high-average current loop.

The second major accelerator system is the XUV-FEL branch. The XUV-FEL requires a peak current of ~ 1.5 kA at beam energies from 750 to 950 MeV. This beam is derived from 1 nC bunches produced by a normal conducting RF photo injector operating at 1 kHz. At this repetition rate the 1 kW of beam can be safely dumped after traversing a final spontaneous undulator source.

Although the XUV-FEL beam and the high average-current beam discussed above are derived from separate electron sources after suitable low energy acceleration they are merged and accelerated in a single superconducting linac. The two beams are then separated using magnetic, energy dispersion for delivery to their respective devices.

The third accelerator system is that required for the IR-FEL. The same linac technology is used to accelerate electrons to between 25 and 60 MeV to provide a fully integrated and synchronised IR-FEL facility. The main electron beam parameters for 4GLS are given in Table 1.

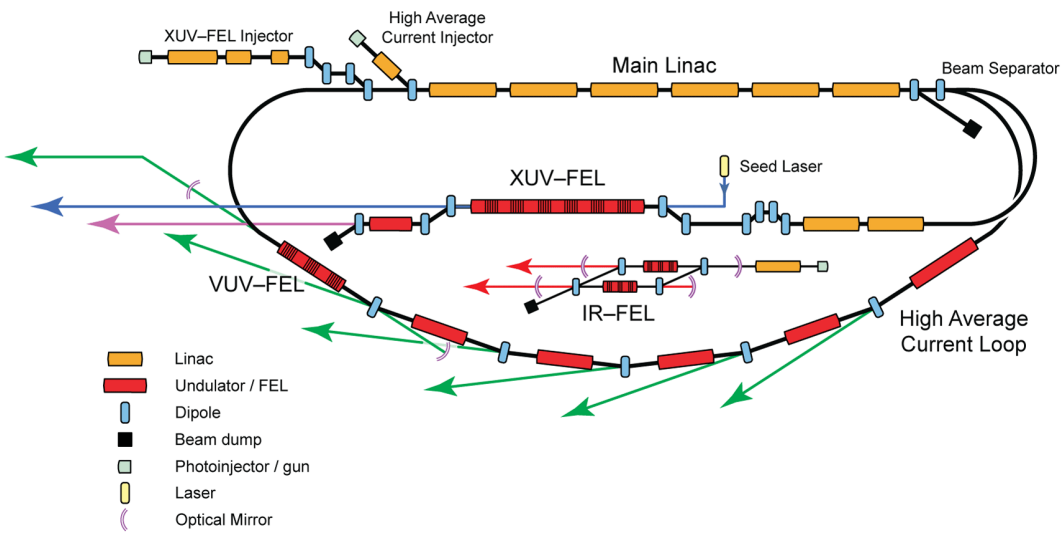

Figure 2. The conceptual layout of 4GLS.

Table 1. Main electron beam parameters of 4GLS

Bunch Parameter	*XUV-FEL*	*100 mA HACL Operation*	*VUV-FEL HACL Operation*	*IR-FEL*
Electron Energy	750 to 950 MeV	600 MeV	600 MeV	25 to 60 MeV
Normalised Emittance	2 mm mrad	2 mm mrad	2 mm mrad	10 mm mrad
RMS Projected Energy Spread	0.1 %	0.1 %	0.1 %	0.1 %
RMS Bunch Length	< 270 fs	100 to 900 fs	100 fs	1 to 10 ps
Bunch Charge	1 nC	77 pC	77 pC	200 pC
Bunch Repetition Rate	1 kHz	1.3 GHz	n x 4.33 MHz	13 MHz
Electron Beam Average Power	1 kW	60 MW	n x 200 kW	156 kW

SUPERCONDUCTING LINACS

The 4GLS design utilises superconducting linacs to accelerate and manipulate the three beams required to drive the photon sources. The accelerating structures are all based on a fundamental RF frequency of 1.3 GHz and a modified TESLA type cavity design operating at 2 K or below [6, 7]. The chosen RF frequency takes advantage of extensive development and operating experience of such systems (including the fact that industrialisation of the production and processing of such cavities is already well underway in preparation for the international linear collider ILC and superconducting XFEL).

Importantly the 4GLS design team at Daresbury are currently close to completing construction of an energy recovery prototype, ERLP, based on commercially procured linac modules incorporating TESLA 9-cell cavities which will provide a valuable test bed for the critical cavity and module developments required to produce linacs capable of operating in CW mode with the high-average beam currents.

For the high average current injector linac the major challenge is the delivery of the beam power required to accelerate a beam of up to 100 mA to 10 MeV without energy recovery. A cavity and coupler scheme similar to the two-cell geometry with symmetric couplers currently being developed at Cornell for the Cornell ERL prototype will be adopted for 4GLS. Two modules consisting of five of these two-cell cavities will suffice to provide the requirements of the ~ 10 MeV high average current injector system.

The main linac will be made up of six cryomodules each containing eight, seven-cell cavities which are currently under development within an international collaboration that includes CCLRC. This development is designed to meet the extreme demands of CW high-average current operation. The choice of six accelerating modules for the main linac is a balance between capital and operating costs which also provides a reasonable overhead in accelerating voltage. Another five similar accelerating modules are required within the accelerator system, two within the XUV-FEL injector system, two for the XUV-FEL linac to take this beam from 750 MeV to 950 MeV and one to give the 60 MeV requirement for the IR-FEL. Development and verification of this challenging module design will be a major activity during the technical design phase of 4GLS. A prototype 2 cavity cryomodule is currently being developed at Daresbury Laboratory [8].

INJECTORS

For linac-based light sources the injectors are an essential element in the delivery of high performance, high quality beams. The requirements for the three injectors proposed for 4GLS come directly from the challenging demands of the FEL and spontaneous sources. Unlike storage rings light sources where the beam properties are essentially decoupled from the properties of the injector beam, the performance of ERL-based sources are directly dependent on the quality of the electron beam as produced by the injector and preserved during transport and acceleration.

The IR-FEL of 4GLS makes relatively modest demands of the injector and the source envisaged requires 200 pC, 1 ps electron bunches with a normalised emittance of around 10 mm mrad. This can be delivered in a cost-effective and reliable way by mature thermionic gun technology. In contrast, the proposed injectors for both the high-average current loop and the high brightness XUV-FEL branch are based on developments of existing injectors.

The XUV-FEL injector source is required to deliver 1.5 kA peak current at 1 kHz repetition rate, the normalised emittance required to drive the device is 2 mm mrad. Normal conducting RF photoinjectors today already exceed the bunch charge (1 nC) and emittance requirements and are a proven mature technology but they are typically low duty-cycle systems operating at a few Hz and require development to meet the 4GLS target repetition rate. Development of the PITZ gun is already underway that would increase the demonstrated 0.9 % duty cycle to 2.5 %, a slightly higher duty cycle than that required for 1 kHz operation of the XUV-FEL. Simulations using well developed particle codes have shown that a normalised emittance of 1.7 mm mrad can still be delivered whilst using relatively modest accelerating gradients, producing acceptable thermal loads in a gun engineered to supply additional cooling. This design is an effective starting point for the technical design of the XUV-FEL gun-cavity.

The photoinjector chosen for the high average current loop is required to deliver an unprecedented 100 mA beam with an emittance of 2 mm mrad. With such a high current demand an optimal choice of cathode material is a high quantum efficiency semiconductor which limits the laser power required to reasonable levels. From the experience of the JLAB DC photo-injector, that has been utilised on the ERLP photo-injector, caesiated gallium arsenide may provide a suitable option for the cathode material. To meet the 4GLS requirements this gun will be driven by a simple stable 160 W, Yb-doped fibre laser operating at 1.3 GHz. Whilst the TJNAF DC and ERLP photo-injectors are already designed to achieve the 77 pC bunch charge required, the emittance of these guns is limited to around 5 – 10 mm mrad and the maximum, average current achieved at JLAB is only 9.1 mA. Further development is clearly required to meet the requirements of 4GLS and verification of such performance goes beyond the scope and capability of the current ERLP. Evolving from JLAB DC photoinjector developments, Cornell University is currently building a prototype injector which will produce a 100 mA beam of 77pC bunches. Extensive simulations of this gun based on the use of particle tracking codes predict that the emittance requirements for 4GLS would be fully met by this design.

BEAM DYNAMICS

The most challenging area of accelerator design for 4GLS is in meeting the requirements of extremely high peak current, (1.5 kA) for the XUV-FEL branch whilst simultaneously transporting and accelerating very high quality high-average current (100 mA) beam to the energy recovery loop. The conceptual solutions to the dynamics challenges for delivering the two most challenging beams are discussed below.

These two beams originate from separate photo-injectors, a high brightness RF photoinjector operating at 1 kHz delivering 2 mm mrad normalised emittance, 1 nC bunches for the XUV-FEL and a low emittance 100 mA, normal conducting DC injector. At relatively low injector energies these high quality beams are susceptible to intense space charge effects. Within the RF gun, the 1 nC beam undergoes rapid acceleration to a few MeV and is then injected into a superconducting linac which quickly boosts the energy to 220 MeV. Rapid acceleration of the 100 mA beam is achieved through the use of a high DC voltage followed closely by two superconducting booster modules delivering the ~1 MW power required to accelerate the beam to 10 MeV.

The bunches within both of these beams have to undergo a significant amount of compression to deliver the required peak currents to drive the XUV- and VUV-FELs and to meet the requirements of the science case for different pulse lengths from undulators in the high-average current loop. An innovative, integrated acceleration and compression scheme is proposed which meets the unique requirements for each of the two beams whilst using the same main superconducting accelerator [9]. By defining appropriate accelerating phases within the linacs, the high compression demands of the XUV-FEL are met using a two-stage compression scheme including a higher harmonic RF system for flexible non-linear correction, whilst progressive compression through the undulator arc delivers the high peak current in the 77pC bunches required to drive the VUV-FEL. An important part of this design is the optimisation of the scheme to maintain a high quality beam throughout the transport. Wakefield effects in the accelerator are reduced by performing the final compression stage at full energy so that the bunches around the arcs are kept relatively long to control the disruptive effects of coherent synchrotron radiation (CSR) emission which if uncontrolled can produce unacceptable energy loss and emittance growth. Acceleration of a 100 mA beam is very challenging; to accelerate and decelerate such a beam requires that the linac transport design is tailored to give a high threshold for the disruptive beam break-up instability. This is achieved through a combination of techniques including substantial damping of HOMs in an advanced design of RF cavity, tight control of beam focussing throughout the linac and optimisation of coupling and overall transport properties in the energy recovery loop [10, 11].

For the 4GLS XUV- and VUV-FELs, very high peak current is demanded simultaneously with narrow magnet gaps. These high peak currents are vulnerable to disruption by associated strong wakefields in nearby metallic chamber walls. This wakefield interaction and its undesirable consequences will be controlled through the use of appropriate vacuum materials and an optimisation of the FEL design which maintains vessel apertures that are compatible with delivering the required high quality beam.

FREE ELECTRON LASERS

The characteristics of 4GLS and its central ERL will be optimally exploited by the inclusion of three FELs, each covering a distinct photon energy range matched to the science needs of the UK and each offering excellent performance levels. The three designs are all state-of-the-art with key advantages over other designs being proposed elsewhere.

XUV-FEL

A simple yet robust seeded design for the XUV-FEL is proposed to ensure that ultra-high quality, reproducible, tunable radiation is available in the 8 to 100 eV photon range [12, 13].

A tunable laser seed pulse from a High Harmonic Generation source, that covers the full photon energy range, is amplified within the FEL. The FEL undulator consists of a lattice of individual undulator modules allowing electron beam focusing elements and diagnostics to be placed in between. The final undulator modules of the FEL will be of APPLE-II design that will enable the generation of variable elliptically polarised radiation. Figure 3 shows a schematic layout for the undulator modules and illustrates that for the low energy photons only the APPLE-II modules are in use whilst at high energy all of the modules are required.

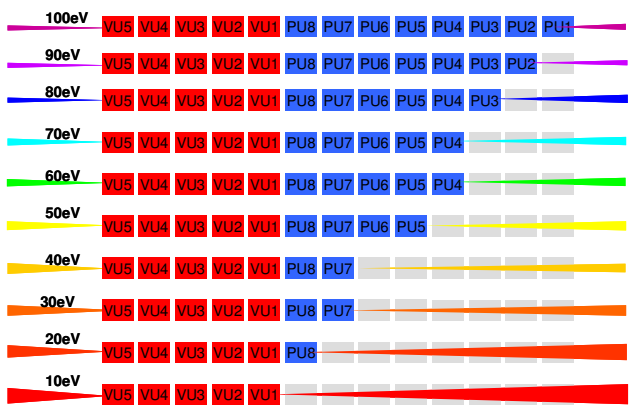

Figure 3. Schematic of the modular undulator system of the XUV-FEL demonstrating the different modes of operation across the photon energy range 10-100 eV. Electron beam transport is right to left. The minimum required undulator gap decreases in gradual steps from 28 mm for PU1 down to 10 mm for PU8 and the variable polarisation modules VU1-VU5.

The output pulses will have selectable polarisation and a pulse repetition rate of 1 kHz is set by the seed laser and the electron beam. Established FEL theory and state-of-the-art simulation codes predict this FEL will generate photon energies at multi giga-watt power levels in pulses of duration 40 - 60 fs FWHM. The pulses will have excellent temporal and spatial coherence with time-bandwidth products close to the Fourier transform limit for a Gaussian pulse. Unlike the self amplified spontaneous emission mode of operation, which effectively self-starts from intrinsic noise, the FEL interaction here is acting as a true amplifier. The high quality spectral properties of the radiation input seed pulses are maintained by the amplified output radiation pulses, as illustrated in Figure 4. Recent advances in High Harmonic Generation seed sources mean that the seed requirements for the XUV-FEL already exist and clearly future advances in conventional lasers can be readily harnessed. Further details on the issues raised by the use of HHG seeding can be found in [14].

The 4GLS design also incorporates an undulator after the XUV-FEL which enables the generation of spontaneous SR light with natural synchronisation to the XUV-FEL radiation

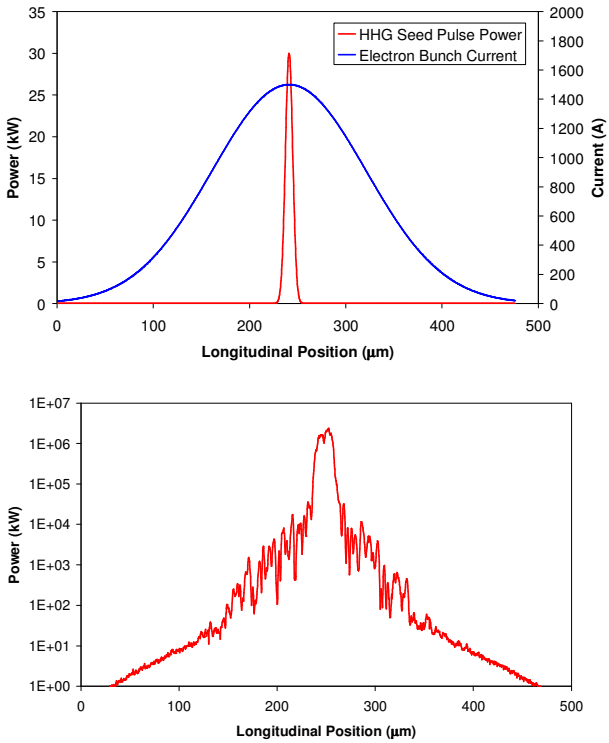

Figure 4. (a) Input HHG seed power (FWHM 30 fs) and electron bunch current as a function of longitudinal position (linear scale) and (b) radiation power (FWHM ~50 fs) at the exit of the XUV-FEL (log scale).

VUV-FEL

The VUV-FEL will be a Regenerative Amplifier FEL (RAFEL) which is a high gain system that is of insufficient length to achieve saturation in SASE mode. A small fraction of the radiation emitted by an electron pulse at the end of the undulator is fed back to the beginning of the undulator to act as a seed field to a subsequent electron pulse. The radiation feedback may readily be achieved by placing the undulator into a low-Q cavity. This self-seeding process rapidly builds up and allows the RAFEL to achieve saturation after only a few electron pulses have propagated through the undulator. Figure 5 shows the intracavity pulse power for a cavity length detuning of ~ 12 μm after the first and eighth pass. After the first pass, the pulse power has a noisy profile characteristic of SASE. However, after only eight passes saturation occurs and the intracavity peak power is 290 MW, equivalent to an output power of 218 MW. The corresponding spectrum, also shown in Figure 5, is seen to be noisy after the first pass. On subsequent passes however the spectrum narrows about a single wavelength. At saturation the spectrum has FWHM bandwidth of 0.26% giving a time-bandwidth product of ~1.0. This is just over a factor two greater than a Fourier transform limited gaussian pulse and indicative of excellent longitudinal coherence.

The FEL will offer high repetition rates (multiples of 4.33 MHz) with giga-watt peak power and > 100 W average power [15]. Here advantage is taken of mirrors (with hole out-coupling) that are able to operate over the photon energy range of 3 to 10 eV. Photon pulse lengths of ~ 170 fs (FWHM) will be obtained in standard mode and simulations suggest that pulses as short as ~ 25 fs will be generated in a super-radiant mode. The output pulses will have selectable polarisation and be fully tunable.

By using a pair of mirrors to reflect light emitted by the FEL back to the entrance of the device it becomes, in effect, self-seeding and no external conventional laser system is required. Hence high quality, stable light is ensured through a rather simple optical feedback loop. A particular feature of this FEL when compared with similar designs covering the same wavelength range is the tolerance to low mirror reflectivity. Extensive simulations have shown that mirror reflectivities in the range 40 to 60 % are acceptable for this design [16].

Detailed modelling has been used to study the effect of timing jitter in the electron bunch arrival time [17]. Figure 6 shows the build up of saturation with no timing jitter and with a jitter of ±80 fs, calculated using the 1D time dependent code FELO [18]. Statistical analysis of the peak output power during saturation suggests that the RMS variation in the peak output power increases from 2.5% for the no jitter case to 8% for a jitter of ±80 fs.

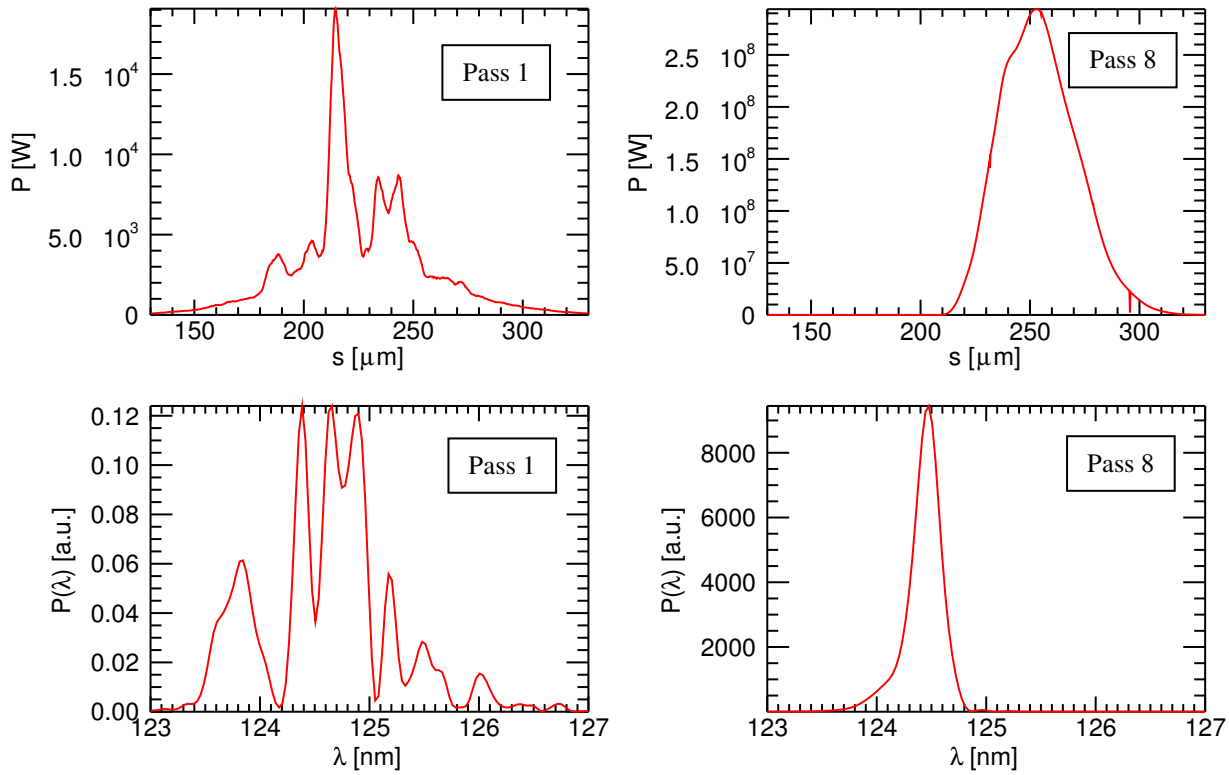

Figure 5. Genesis 1.3 [19] simulation of the radiation pulse power and the radiation spectrum after one and eight passes through the VUV-FEL for a cavity detune of 12μm.

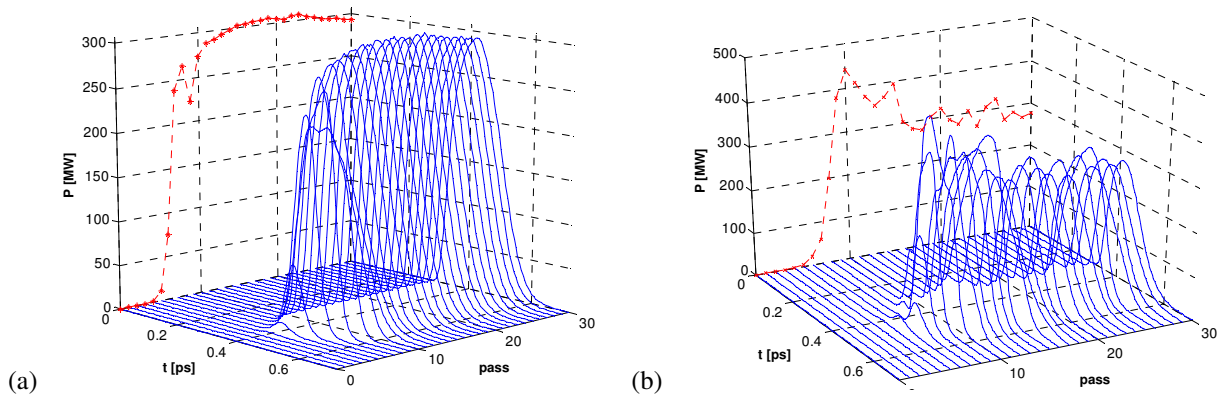

Figure 6. FELO simulation of the VUV-FEL at 10eV and cavity length detuning of 18μm with (a) zero electron bunch arrival time jitter and (b) jitter of ±80 fs. The red points show the peak intensity of the pulse at each pass.

IR-FEL

The IR-FEL has been designed to produce high intensity, spatially and temporally coherent radiation with variable pulse lengths, flexible output pulse patterns and variable polarisation over the wavelength range 2.5 - 200 μm. The high-Q cavity-based design employs two undulators in parallel and hence can serve two user experiments simultaneously. The provision of short electron bunches offers the potential to operate the FEL in super-radiant mode to produce shorter FEL pulses with higher peak intensities than available in normal operation: simulations predict FWHM pulse lengths of only a few optical cycles can be produced in this way. The implementation of a superconducting RF linac with the IR-FEL will offer highly stable operation and also high average powers (> 100 W) though the option of running in modes that reduce the average power for sensitive samples will also be available.

SPONTANEOUS SOURCES

There are six insertion device straights in the high average current loop, one of which is allocated to the VUV-FEL. The remaining five will be used to generate spontaneous radiation. To maximise the potential of the spontaneous sources three different undulator straight

lengths have been chosen; two 14 m straights; two 10 m straights and two 8 m straights. Thus the total space available for undulators is ~ 64 m, which exceeds all other existing low energy 3rd generation light sources. More than one insertion device can be placed in each straight with a small corrector magnet between them so as to angularly separate the photon output. Distributed pulse compression will be employed in the high average current loop in order to deliver to users pulse lengths optimised for their experiments ranging from a few ps down to 100 fs (RMS).

It is well known that electrons in a bunch radiate coherently at wavelengths of the order of, and longer than, the bunch length. Since 4GLS has very short bunch lengths this so-called Coherent Synchrotron Radiation (CSR) is emitted over a broad wavelength range. Calculations indicate that the onset of the CSR for 4GLS is at around 40 μm and hence it will be an extremely intense source THz radiation.

TABLE TOP LASERS

In order to make full use of 4GLS it is important to allow integration of its sources with conventional lasers. Continuous coverage of the visible and near-IR parts of the spectrum is provided by the spontaneous sources as illustrated in Figure 1. However, there are currently no plans to provide FEL radiation in the spectral range from 0.5 – 3 eV, as this is covered more cost-effectively by tabletop laser systems. These wavelengths will be made available by using continuously tuneable mid-infrared laser systems, such as mid-infrared Optical Parametric Oscillator and Optical Parametric Amplifier systems, Difference Frequency Generators and diode lasers. Ability to synchronise the additional lasers to within the temporal profile of the 4GLS sources is required. Current synchronisation is achievable to within < 100 fs, and is the subject of a vigorous worldwide research and development programme.

STATUS

The conceptual design of 4GLS is now complete and reported in [1]. The project is now entering the technical design phase which includes a substantial R & D element. The Energy Recovery Linac Prototype at Daresbury Laboratory is presently being commissioned and the results from this will be fed into the technical design of 4GLS. In addition to this a superconducting RF linac module prototype is under construction that will be capable of operating CW at a high average beam current of 100mA. It is intended that this will be installed into ERLP at a later date for electron beam trials. In addition to this a high current photoinjector project is being initiated at Daresbury Laboratory to ensure that the target current of 100 mA can be delivered with the required electron beam parameters.

REFERENCES

[1] 4GLS Conceptual Design Report 2006, available from www.4gls.ac.uk
[2] M. W. Poole and E. A. Seddon, '4GLS and the Energy Recovery Linac Prototype Project at Daresbury Laboratory', PAC 05, Knoxville, p431.
[3] J. A. Clarke, 'The Conceptual Design of 4GLS at Daresbury Laboratory', EPAC 06, Edinburgh, p181.
[4] D. J. Holder et al, 'The Status of the Daresbury Energy Recovery Prototype Project', EPAC 06, Edinburgh, p187.
[5] S. L. Smith, 'A Review of ERL Prototype Experience and Light Source Design Challenges', EPAC 06, Edinburgh, p39.
[6] P. A. McIntosh et al, 'RF Requirements for the 4GLS LINAC Systems', EPAC 06, Edinburgh, p439.
[7] S. Pattalwar et al, 'Key Cryogenics Challenges in the Development of the 4GLS', EPAC 06, Edinburgh, p499.
[8] P. A. McIntosh et al, 'Development of a Prototype Superconducting CW Cavity and Cryomodule for Energy Recovery', EPAC 06, Edinburgh, p436.
[9] B. D. Muratori et al, 'Lattice Design for the Fourth Generation Light Source at Daresbury Laboratory', EPAC 06, Edinburgh, p184.
[10] E. Wooldridge and B. D. Muratori, 'Linac Focusing and Beam Break Up for 4GLS', EPAC 06, Edinburgh, p2871.
[11] E. Wooldridge, 'Alternate Cavity Designs to Reduce BBU', EPAC 06, Edinburgh, p2874.
[12] B. W. J. McNeil et al, 'Design Considerations for the 4GLS XUV-FEL', FEL 2005, p506.
[13] B. W. J. McNeil et al, 'The Conceptual Design of the 4GLS XUV-FEL', these proc.
[14] B. Sheehy et al, 'Issues in High Harmonic Seeding of the 4GLS XUV-FEL', these proc.
[15] N. Thompson et al, 'A VUV-FEL for 4GLS: Design Concept and Simulation Results', FEL 2005, p79.
[16] N. R. Thompson et al, 'A 3D Model of the 4GLS VUV-FEL Conceptual Design Including Improved Modelling of the Optical Feedback Cavity', these proc.
[17] D. J. Dunning et al, 'First Tolerance Studies for the 4GLS FEL Sources', these proc.
[18] B. W. J. McNeil et al, 'FELO: A One-Dimensional Time-Dependent FEL Oscillator Code', these proc.
[19] S Reiche, Nucl. Instrum. Methods, A 429 (1999) p243.

FEL OSCILLATION WITH A HIGH EXTRACTION EFFICIENCY AT JAEA ERL FEL

N. Nishimori*, R. Hajima, H. Iijima, N. Kikuzawa, E. Minehara, R. Nagai, T. Nishitani, M. Sawamura, JAEA, Ibaraki, Japan.

Abstract

One of challenges that high-power FEL oscillators driven by energy recovery linac (ERL) are facing is to increase the extraction FEL efficiency as high as possible. The high-efficiency oscillation relaxes the total beam current needed for high-power lasing and makes the optical micropulse length shorter, which is useful for various applications. Two triple bend achromatic arcs have been used in a recovery loop for an ERL FEL at Japan Atomic Energy Agency (JAEA). The return arc after an undulator has an energy acceptance of 15%, which is large enough to recover the electron beam used for high-efficiency FEL oscillation. Recently we have achieved the efficiency exceeding 2%, which accompanies large energy spread, by doubling the electron bunch repetition rate. The FEL efficiency has been measured from the horizontal profiles of the exhausted electron beam with a wire scanner installed at a dispersive point in the return arc. The other arc placed upstream of the undulator has been found to work as a bunch compressor for the high-efficiency FEL oscillation.

INTRODUCTION

One of challenges that high-power FEL oscillators driven by energy recovery linac (ERL) are facing is to increase the extraction FEL efficiency as high as possible. The high-efficiency oscillation saves the total beam current needed for high-power lasing, which decreases the beam load to various accelerator components and increases the wall-plug efficiency. The high-efficiency oscillation is also appropriate for producing broadband ultrashort optical pulses, and makes the optical micropulse length shorter, which is useful for various applications [1].

In a high-power ERL FEL at Jefferson Lab, a high-efficiency FEL oscillation has been achieved at near IR wavelength region [2, 3, 4]. The exhausted beam is transported to accelerators through a Bates type recovery loop with energy acceptance of 15%, and full energy recovery has been successfully established [5]. A recovery loop which consists of two triple bend achromatic arcs has been used for an ERL FEL at Japan Atomic Energy Agency (JAEA) [6]. The energy acceptance of the return arc after an undulator was 7% before June 2006 [7, 6]. Recently we have achieved the efficiency exceeding 2%, which accompanies large energy spread beyond the energy acceptance of the arc, by doubling the electron bunch repetition rate [8]. The optical pulse can now interact with a fresh electron bunch every round trip, while it overlapped with an injected electron bunch every two round trips before the doubling.

In this paper, first we give brief description of the configuration and recent upgrade of JAEA ERL for a high-power FEL oscillation with the doubled beam current. Then our recent experimental results on the FEL efficiency and the beam dynamics through the energy recovery loop are reported in details. The FEL efficiency has been measured with a wire scanner installed at a dispersive point in the return arc, which can serve as a monitor of the energy distribution of the exhausted electron beam. The wire scanners have been also installed at other dispersive points for study of the beam dynamics through the triple bend achromatic arcs. A measurement of the energy distributions at the first arc, which is placed upstream of the undulator, as a function of the accelerator phase has revealed that magnetic bunch compression in the first arc is indispensable for a high-power FEL oscillation at the JAEA ERL. Finally, applications planned in JAEA FEL are presented.

CONFIGURATION OF JAEA ERL

The JAEA FEL facility has been developed as a high-power FEL at wavelength in far infrared region around 20 μm. The laser output power exceeded 1 kW within 500 μs macropulse duration without energy-recovery in 2000 [9]. In order to increase the FEL output power higher than 10 kW and demonstrate the technology and commercial profit of high-power FELs for industrial applications, we have developed an ERL FEL as an extension of the original superconducting accelerator [10].

The layout of the JAEA ERL is shown in Fig. 1. An injector, main super-conducting accelerator (SCA) modules, an undulator, and the first arc are from the original FEL. An injection merger, a half chicane before the undulator, and the return arc were installed for the ERL. The injector consists of 230 kV electron gun with a thermionic cathode, 83.3 MHz subharmonic buncher (SHB), and two cryomodules, each of which has a single cell SCA cavity driven at 499.8 MHz. An electron bunch of 0.5 nC with full width half maximum (FWHM) length of 600 ps is generated by a grid pulser at a 10.4 MHz repetition rate, that is 5 mA average current, and compressed by the SHB followed by a 4.5-m drift. The electron bunch is accelerated to 2.5 MeV by two single cells, and further compressed by ballistic bunching through a 9-m drift. A two-step staircase is used for the injection merger, because this configuration fulfills the design requirements, achromaticity and small emittance

* nishimori.nobuyuki@jaea.go.jp

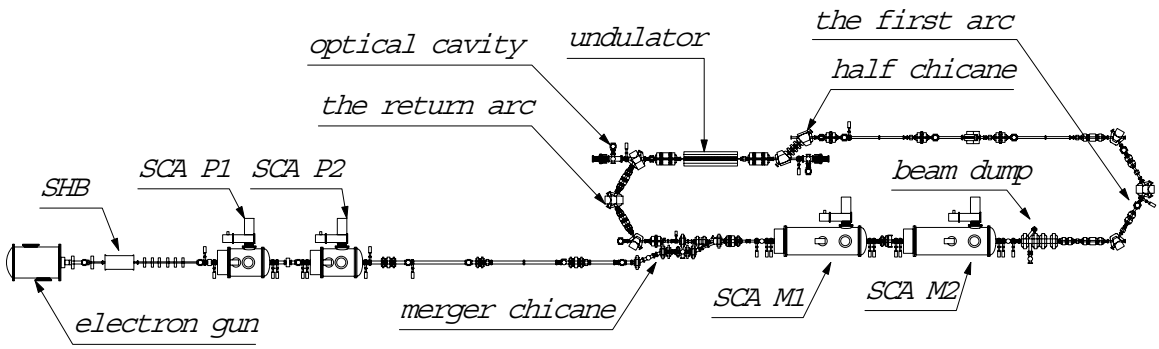

Figure 1: The layout of JAEA Energy-Recovery Linac. An electron bunch generated by 230 kV electron gun is accelerated to 2.5 MeV and injected into the energy-recovery loop. The electron bunch is accelerated to 17 MeV by main superconducting cavities and transported to the FEL undulator. The electron bunch is, then, re-injected to the main cavities and decelerated down to 2.5 MeV and collected by a beam dump.

growth, and fits in the existing space. The achromaticity of the merger is realized by setting three quadrupole magnets to the appropriate strengths. An electron bunch injected to two main cryomodules, each of which has five cell SCA cavities driven at 499.8 MHz, is accelerated up to 17 MeV and transported to the undulator through the first arc and the half chicane. After the FEL interaction, the electron bunch is re-injected into the main cryomodules at a deceleration phase for the energy recovery. The re-injection phase can be controlled by changing the recirculation path length. The return arc has been placed on movable tables for this purpose. Both arcs used in the recirculation loop have two families of quadrupole magnets which enable one to vary M_{56} while maintaining achromaticity. This variable M_{56} can be used for bunch compression in the first arc and for energy compression in the return arc. The return arc also has two families of sextupole magnets to compensate second-order aberrations T_{166}, T_{266}, T_{566} arising from the large energy spread due to the FEL interaction.

The JAEA ERL-FEL has been operated in pulsed mode of 1 ms macropulse length in maximum and 10 Hz repetition rate, because of the following reasons. 1) The cooling power of the refrigerator system for the SCA modules is not sufficient enough to operate in CW mode. 2) The shield of the building for the linac is not thick enough for the radiation protection.

UPGRADE OF JAEA ERL

Gun Grid Pulser and Injector RF sources

Increasing the injector beam current is a straightforward approach to increase the FEL power by taking full advantage of the energy-recovery. The JAEA gun has a thermionic cathode driven by a grid pulser. In the original configuration, the gun was designed to produce 0.5 nC electron bunches at 10.4 MHz repetition. We installed a new grid pulser working at 20.8 MHz, doubled repetition of the original one, and a 10 mA beam is now available [11]. The new grid pulser is designed at Budker Institute of Nuclear Physics and can be operated in CW-mode as well as pulsed mode [12]. The electron beam properties with the new grid pulser keep similar performance to the original one. The pulse width and the normalized rms emittance at the gun are 590 ps (FWHM) and 20 πmm·mrad, respectively [11].

Two single-cell cavities of the injector were driven by 8 kW solid state amplifier for each, enough capacity for 5 mA operation. The solid state amplifier was replaced by an IOT-klystrode of 50 kW, which enables one to inject a 40 mA beam into the ERL [13].

RF low-level controllers

Stable operation of an FEL relies much on the stability of an accelerator. An RF low-level controller for a SCA is one of the key components for achieving good stability. The original JAEA FEL was equipped with a low-level controller, which kept phase flatness at ± 1 degree within a 1 ms macropulse. The low-level controller was replaced by new one, which provides the following functions for the better stability: the feedback gain and bandwidth can be varied during operation to obtain good flatness of RF phase and amplitude, and all the circuits are contained in boxes with temperature stabilization. The new controller is installed in the vicinity of the SCA cavity to make the cable length between the controller and the SCA as short as possible. Furthermore the cables between the controller and the cavities are contained in a temperature-controlled pipe to suppress the temperature drift. After these upgrade, the accuracy and stability of accelerating RF has been improved. The flatness of RF phase and amplitude within a 1 ms macropulse are 0.06 deg. rms and 0.013% rms, respectively, while those for the old system were 0.20 deg. and 0.013% [14]. Phase and amplitude fluctuations for 5 minutes in the new system are measured as 0.15 deg. and

0.015%, respectively.

Increased energy acceptance of the arcs

The doubled beam current has enabled us to operate the JAEA ERL FEL with efficiency higher than 2%. The resulting large energy spread of the exhausted electron beam exceeded the energy acceptance of the return arc, which caused a radiation problem when the FEL was operated for a long time period at a macropulse length longer than 250 μs. We made minor modification of the return arc to increase the beam energy acceptance. The bore of quadrupole magnets of the return arc was enlarged from 64 mm to 102 mm. The beam pipe diameter was enlarged from 55 mm to 100 mm. The energy acceptance of the return arc has been increased from 7% to 15%. The quadrupole magnets in the first arc were also replaced with those used in the return arc. The energy acceptance of the first arc has been increased from 3.5% to 4.3%.

FEL EFFICIENCY

The FEL wavelength at the JAEA FEL is around 20 μm and a holed mirror is used to couple FEL out of the optical cavity. The coupling efficiency of the holed mirror is estimated to be around 30% [15]. It is however difficult to exactly determine the FEL efficiency from the measured FEL power only. The FEL efficiency can be obtained from a measurement of the beam centroid shift of the exhausted beam from the position without lasing at a dispersive point. A non-destructive method is indispensable for the energy analyzer, since the exhausted beam has to be recovered under an ERL operation. A synchrotron radiation (SR) monitor allows for continuous monitoring of the energy spectrum of the beam for an ERL operated even at a full power [16, 5]. The SR wavelength at the JAEA ERL is however longer than 20 μm, where no monitor camera is available. A beam position monitor is also a promising candidate for measuring the shift of the beam centroid [17]. It does not however provide information about the energy distribution of the exhausted beam, which is also important for beam energy recovery. We decided to use a wire scanner, which is appropriate for measuring profiles of pulsed or low-current-CW beams, although it is a partially intercepting device.

Wire Scanners

A wire scanner consists of a thin wire that is moved across the beam path. The local density of the electrons traversing the wire is detected by measuring such secondary particles as secondary electrons and bremsstrahlung photons produced by the interaction of the electron beam with the wire. Detection of the secondary particles allows one to measure the beam profile, and wire scanners are widely used as beam profile monitors. Detecting bremsstrahlung photons with a scintillator and a photomultiplier placed downstream of the wire has enabled one to measure large dynamic range beam profile in an ERL where small beam loss like beam halo represents significant amount of beam power [18]. A wire array based on secondary electron emission current is used to provide time resolved electron spectrum, which is useful to study the evolution of the energy spectrum from a narrow to a broad spectrum as a result of the FEL interaction [19, 20].

The wire scanner used in the present study is based on a linear movement of a copper wire in 0.6 mm diameter through the beam at a speed of 0.39 mm/s by 100 mm-stroke. The copper wire is mounted on an aluminium fork with a gap of 26 mm and electrically floated from the ground. The secondary electron emission current is measured with a current meter (TR8641 electronic picoammeter, ADVANTEST). The wire position is measured with a linear potentiometer and is recorded in an ADC (WE7272 isolated digitizer, YOKOGAWA) together with the secondary electron current.

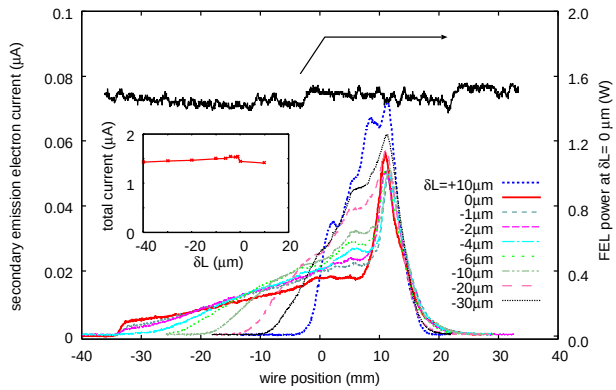

Figure 2: Horizontal beam profiles for various cavity detuning lengths measured with a wire scanner (WIRE #1) placed in the middle of the drift space between two quadrupole magnets just after the first bending magnet in the return arc, where horizontal dispersion is measured to be η = 0.376 m. The vertical axis shows secondary electron emission current and horizontal axis shows wire position. The total secondary emission electron current integrated along the wire position is plotted with respect to optical cavity detuning length in the inset. The FEL power at δL = 0 μm during a wire scan is represented by a black solid line.

Electron energy distributions and FEL efficiency

Figure 2 shows horizontal beam profiles measured for various detuning lengths (δLs) of an optical cavity with the wire scanner, which is installed in the middle between two quadrupole magnets placed just after the first bending magnet in the return arc. This wire is called WIRE #1 in the present paper. The horizontal dispersion at the wire scanner is measured to be η = 0.376 m from the shift of the beam centroid with respect to the magnetic field of the first bending magnet. This is similar to the value of η =

0.41 m calculated from a first-order matrix of beam transport (see Fig. 5). The vertical axis shows secondary emission electron current from the wire scanner and horizontal axis shows wire position. The polarity of the secondary electron current is positive. The inset shows the total secondary emission current integrated along the wire position as a function of δL. The total secondary current is 1.5 μA, which is almost independent of δL. The secondary electron production rate for 17 MeV electron on our wire scanner is estimated to be 8%, since the incident electron beam current during the measurement was 18.5 μA. The production rate is similar to that for for 30 MeV electron on carbon, which is measured to be 3% [21]. The peak secondary electron current measured by the wire is less than 0.07 μA (see Fig. 2), indicating that the beam loss due to the presence of the wire is small (less than 5%). This explains our observation that the FEL power at δL = 0 μm remains unchanged during the wire scan, which is shown by a black solid line in Fig. 2,

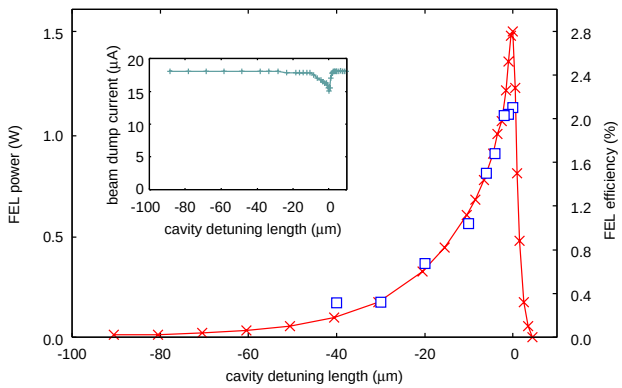

Figure 3: FEL power measured as a function of δL at macropulse length of 230 μs. FEL efficiencies obtained from the energy distributions of the exhausted electron beam are shown by open squares. The efficiencies near zero detuning length cannot be measured with our energy analyzer due to the limited energy acceptance, and they are determined from measured FEL power. The inset shows the beam dump current with respect to δL.

The FEL power changes as a function of δL, as shown in Fig. 3, and the energy distributions of the exhausted electron beam changes as well (see Fig. 2). The shift of the beam centroid from the position without lasing yields the FEL efficiency together with the dispersion η = 0.376 m. The measured FEL efficiencies are plotted as open squares in Fig. 3. The efficiency higher than 2% cannot be measured with our present wire scanner, since the scanner is placed downstream of the focusing quadrupole magnet where the dispersion is maximum of η = 0.6 m. The sharp edge of the beam profiles seen around the wire position of -34 mm in Fig. 2 represents the beam loss in the lower energy side at the first quadrupole. The amount of the beam loss is considered to be small, since the total secondary electron current is almost constant with respect to δL (see inset of Fig. 2). The maximum FEL efficiency is estimated to be 2.8%, as shown in Fig. 3.

Table 1: JAEA ERL FEL parameters

Parameter	Measured
Beam energy at undulator	17 MeV
Average current at undulator	8 mA
Bunch charge at undulator	0.4 nC
Bunch length at undulator	12 ps (FWHM)
Peak current	35 A
Energy spread before undulator	1.5% (FWHM)
after undulator	$>$ 15% (full)
Normalized emittance (rms)	40 mm mr
Bunch repetition	20.8250 MHz
Macropulse	1 ms $\times$ 10 Hz
Undulator period	3.3 cm
Number of undulator periods	52
Undulator parameter (rms)	0.7
Optical cavity length	7.2 m
Rayleigh range	1.00 m
Mirror radii	6 cm
Output wavelength	22 μm
FEL extraction efficiency	$>$ 2.5%

The coupling efficiency of the holed mirror is obtained from the present efficiency measurement. The measured FEL power is 1.5 W for macropulse length of 230 μs. The FEL power during the macropulse is estimated to be 0.75 kW, since the FEL power for the first 30 μs is negligibly small. The FEL is extracted through a KRS5 window, that has the transmittance of 70% in normal incidence. The beam current measured at the beam dump is 18.5 μA corresponding to the average beam current of 8 mA. From those experimental results, the coupling efficiency of the holed mirror is estimated to be 28% and agrees well with the calculated value of 30% [15]. The JAEA ERL FEL parameters are listed in Table 1.

Thermal effect on the wire scanner

Heating of the wire might be a concern when attempting to measure the profile of high average power electron beams [22]. The stopping power for 17 MeV electrons in copper is 2.5 MeV cm^2/g. [23], and the specific gravity of copper is 8.94 g/cm^3. We assume that the copper wire in 0.6 mm diameter is regarded as a foil with width of 0.532 mm and depth of 0.532 mm. The energy loss of 17 MeV electron in the copper wire is estimated to be 1.2 MeV. The total charge struck by the electron beam during a wire scan is measured to be less than 25 μC when macropulse length is 230 μs, and the maximum power deposited on the wire during the scan is 30 J. The specific heat of copper is 0.385 J/g/K at 25°C. Thus the temperature rise of the wire can be estimated to be 15000 K in maximum when we assume that the heat accumulates in the wire within a vertical distance of 2 mm, which is similar to the vertical beam size.

However we need to take thermal radiation power, thermal conductivity of copper, power of secondary emission particles, and others which can alleviate the temperature rise of the wire, into account. Although the wire scanner can be used as an energy analyzer as long as heating is not a problem, we need to study this thermal effect in details.

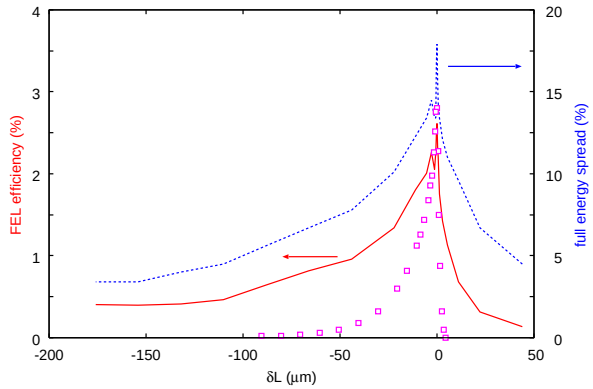

Figure 4: FEL efficiencies as a function of δL obtained from a one-dimensional time-dependent FEL simulation (solid line) and corresponding beam energy spread (dotted line). Measured FEL efficiencies are also plotted as open squares for comparison.

FEL simulation

We have conducted an FEL simulation for comparison with the experimental result. We use one-dimensional time-dependent FEL simulation code, which was used in our previous studies [24] and agrees well with experimental results obtained without energy recovery. The electron bunch length measured at the undulator center is 12 ps (FWHM). The electron bunch shape used in the simulation is assumed to be triangular with the peak Colson's dimensionless beam current of j_0 = 25. A mono energetic electron beam is assumed in the simulation, since the peak FEL efficiency depends little on initial energy spread [24]. The optical cavity loss is measured to be 4.2% from a cavity ring down of the FEL pulse with a Ge:Cu detector. Figure 4 shows calculated FEL efficiency and full energy spread of an electron bunch as a function of δL. The measured FEL efficiencies are much smaller than those obtained in the simulation at large detuning lengths. This may be due to the large energy spread of the incident electron beam.

BEAM TRANSPORT IN THE RETURN ARC

Transverse and longitudinal beam dynamics through the return arc for JAEA ERL has been already studied to find a matched beam envelope from the undulator to the beam dump [7]. In order to roughly estimate dispersion and M_{56} in the return arc, we calculate the beam envelope

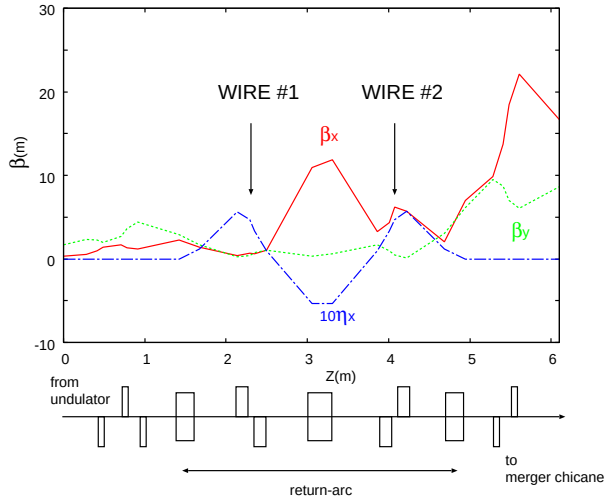

Figure 5: Beam envelopes from the undulator exit through the return arc to the merger chicane calculated from a first-order matrix of beam transport. The positions of wire scanners are indicated by arrows.

from the undulator to the entrance of main SCA modules based on magnet parameters used for actual beam transport. Courant-Snyder parameters at the exit of the undulator are given from the matched beam condition for the undulator, α_x = 0; β_x = 0.33 m; α_y =−1; β_y = 1.7 m. Figure 5 shows obtained betatron functions for the beam envelope, where M_{56} = −0.56 m from the undulator to the entrance of the merger chicane.

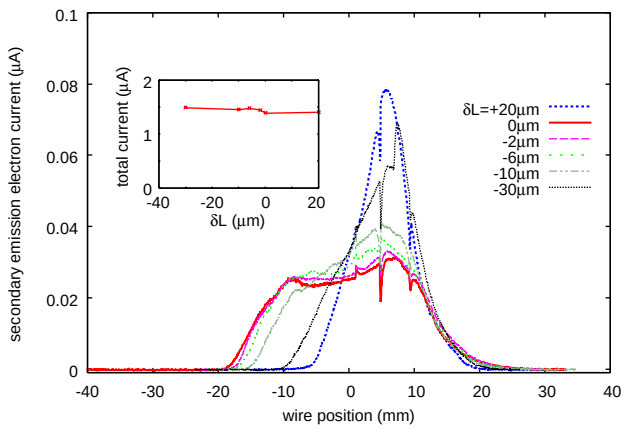

Figure 6: Horizontal beam profiles for various cavity detuning lengths measured with a wire scanner (WIRE #2) placed in the middle of the drift space between two quadrupole magnets just after the second bending magnet in the return arc, where horizontal dispersion should be the same as that of WIRE #1, η = 0.376 m, when the return arc is achromatic. The inset shows the total secondary emission electron current integrated along the wire position with respect to δL.

A drawback of a triple bend achromatic arc is that quadrupole magnets have to be properly set not only to adjust M_{56} for energy compression, but also to establish achromaticity in the arc. This is in contrast to the Bates type end loop where a pair of quadrupole magnets and a pair of sextupole magnets are used just to control M_{56}, T_{566}, respectively, since the end loop is intrinsically achromatic [5]. Therefore achromaticity has to be carefully checked in a triple bend achromatic arc. We have measured horizontal beam profiles downstream of the second bending magnet in the return arc with a wire scanner (see Fig. 6). This wire scanner is called WIRE #2 in the present paper and has been installed in the middle of the drift space between two quadrupole magnets after the second bending magnet and should have the same dispersion function as WIRE #1 when the return arc is achromatic. However, the beam profiles shown in Fig. 6 are similar to those in Fig. 2 only when the FEL efficiency is less than 1%, and they are quite different from each other when the efficiency is higher than 1%, requiring chromaticity correction. The total secondary electron current measured with WIRE #2, which is shown in the inset of Fig. 6, is almost the same as that with WIRE #1. The beam loss is thus expected to be small in the return arc. In the measurement shown in Fig. 6, sextupole magnets are not used to compensate second order aberrations T_{166}, T_{266}, T_{566} arising from the large energy spread due to the FEL interaction. We will perform a systematic measurement of the horizontal beam profiles with various parameter sets of sextupole magents soon.

A current transformer placed downstream of the return arc, which picks up an induction current, is also used as a beam loss monitor for the return arc. The current transformer signal remains almost the same when the FEL efficiency is low, but some beam loss is observed for the efficiency higher than 2%. The beam dump current with respect to δL should be constant when the full energy recovery is established. However the beam current gradually drops as the efficiency increases over 2%, as shown in the inset of Fig. 3. One possible reason is that the energy spread of the recovered beam is beyond the energy acceptance of the beam dump. Although the dump can collect the beam with four times different momentum, the energy spread of the recovered beam can exceed the acceptance under high-efficiency FEL oscillation. Without sufficient energy spread compression, the energy spread can remain 2.5 MeV, which corresponds to 15% of 17 MeV beam, while the mean energy of the recovered beam is lower than 2.5 MeV. We need to study carefully how much beam is recovered through the main SCA modules and how much of the recovered beam is collected by the beam dump.

MAGNETIC BUNCH COMPRESSION IN THE FIRST ARC

A high peak current electron beam, which can be accomplished by means of magnetic, ballistic, or velocity bunch compression, is indispensable to realize a high-efficiency

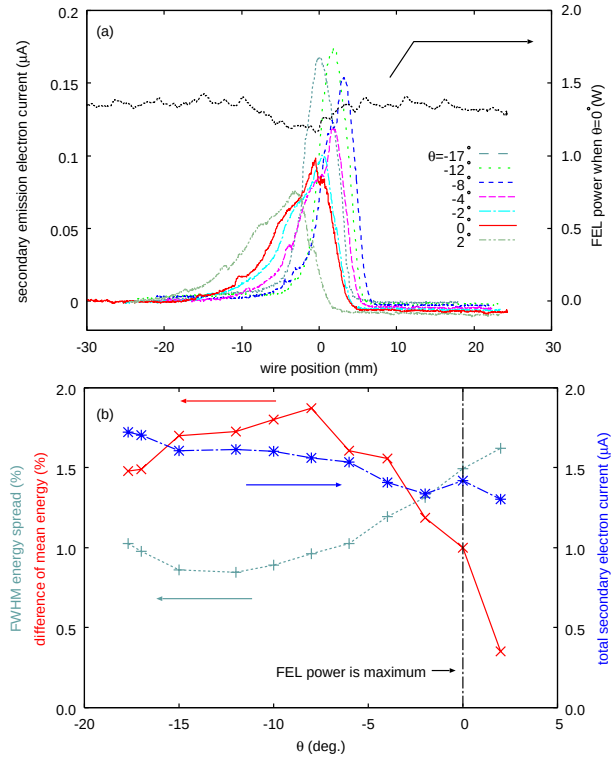

Figure 7: The top figure (a) shows horizontal beam profiles measured with a wire scanner placed just after the first bending magnet in the first arc, where horizontal dispersion is calculated as η = 0.50 m, with respect to the RF phase of the last SCA module M2 defined as θ. The black dotted line shows measured FEL power during a wire scan when $\theta = 0^\circ$, where the FEL power is maximum. The bottom figure (b) shows relative difference of the beam centroid energies (solid line), FWHM energy spreads (dotted line), and the total secondary emission electron current from the wire scanner as a function of θ. Those data are obtained from the top figure (a).

FEL oscillation. At the JAEA ERL, ballistic bunching, which is performed before the main SCA modules, had been considered to play a major role in the bunch compression [25]. Recently we measured powers of coherent synchrotron radiation (CSR) generated from three bending magnets in the first arc and found that the CSR power at the last magnet is much stronger than the remaining two. This indicates that another bunch compression occurs in the first arc. In order to confirm this magnetic bunch compression, we measured horizontal beam profiles with a wire scanner at a dispersive point as a function of the RF phase of the last SCA module (SCA M2). Hereafter we use θ as the RF phase of SCA M2. The horizontal dispersion at the wire scanner located just after the first bending magnet is estimated to be η = 0.50 m from the first-order matrix calculation. The measured beam profiles are shown in Fig. 7(a). Here we set $\theta = 0^\circ$ where the FEL power is maximum. The

black dotted line shows FEL power with respect to the wire position when $\theta = 0°$. The power decreases by 10% when the wire passes the beam centroid. The ratio of FEL power loss is consistent with the ratio of beam loss due to the presence of the wire scanner, which is calculated from the peak secondary current of 0.1 μA divided by the total secondary current of 1.4 μA.

Figure 7(b) shows difference of the mean energy, FWHM energy spread, and total secondary electron current with respect to θ. The energy spread is 1.5% when $\theta = 0°$, but it decreases down to 0.8% as θ decreases to $-12°$. The energy of beam centroid shifts toward higher energy side with decreasing phase and reaches maximum around $\theta = -10°$. The energy difference between $\theta = 0°$ and $\theta = -10°$ is 0.8% corresponding to 0.14 MeV for 17 MeV electron. Since the energy gain for each main SCA module is roughly 7.5 MeV, 11 degree off-crest acceleration yields the same amount of energy difference. From these results, we can conclude that $\theta = 0°$ is about 10 degree off-crest of the SCA M2 phase. The total secondary electron current gradually increases with decreasing θ, and the ratio of the current increases by 20% when $\theta = -17°$. The similar amount of beam loss is observed in another experiment. We have measured beam currents with a Faraday cup both in the straight section along the main SCAs and after the first arc, and observed that the beam loss through the first arc amounts to roughly 20% when the RF phase is adjusted for the FEL power to become maximum. This indicates that the lower energy side of the electron beam arising from the off-crest acceleration is lost at the beam duct of the first bending magnet in the first arc. We have a plan to replace the beam duct with one having larger bore and repeat the same measurement to study the energy spectra of the accelerated electron beam with respect to θ in more details.

We have also measured temporal beam profiles at the undulator center as a function of θ with a synchroscan streak camera (M1954-10, Hamamatsu) at macropulse length of 30 μs, as shown in Fig. 8(a). The centroid of beam profiles changes as a function of θ, since the beam arrival time shifts due to M_{56} from the SCA M2 to the undulator. The shift of arrival time and rms bunch length are shown in Fig. 8(b). The shortest FWHM bunch length of 12 ps is obtained when $\theta = 0°$, indicating that high peak current is indispensable for the high-efficiency FEL oscillation. The arrival time difference between $\theta = 0°$ and $\theta = -10°$ is 10 ps, and the corresponding momentum difference between the two acceleration phases is 0.8% from Fig. 7(b). This leads to M_{56} = 0.38 m, where the sign of M_{56} is determined from first-order matrix calculation of the first arc based on the magnet parameters used for actual operation. The calculation yields M_{56} = 0.6 for the first arc and M_{56} = 0.07 for the half chicane.

We will perform the same measurement somewhere downstream of the second arc to obtain M_{56} from the undulator center to the entrance to the main SCA modules. The value of M_{56} in the return arc should be the same as that to

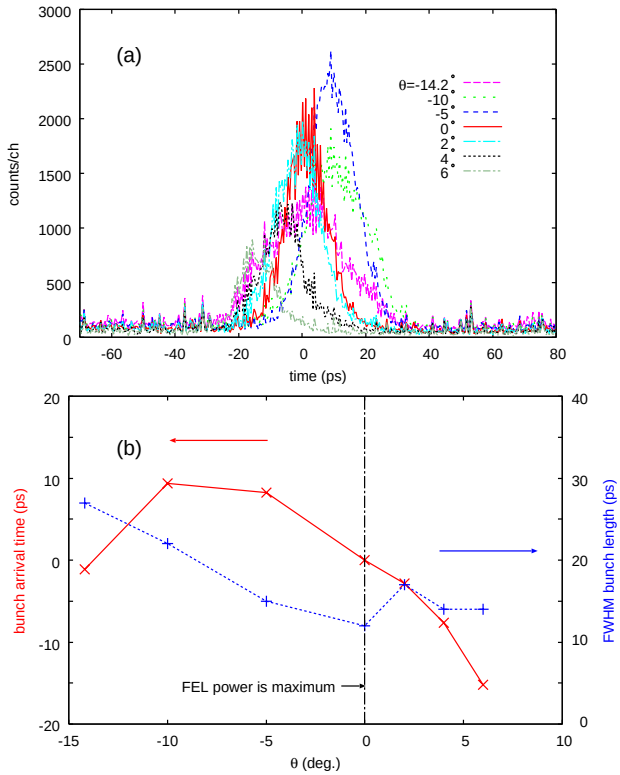

Figure 8: The top figure (a) shows temporal beam profiles measured with a synchroscan streak camera at the undulator center with respect to the RF phase of the SCA M2 (θ). The bottom figure (b) shows relative difference of the beam arrival time (solid line), and FWHM bunch length (dotted line). Those data are obtained from the top figure (a).

the undulator from the exit of SCA M2 except for its sign, if the energy compression in the return arc is properly executed. It is worth to mention that such a longitudinal phase space manipulation using magnetic bunch compression and decompression is performed in JLab FEL in an elegant way [5], where $M_{56} = -0.3$ m from the exit of SCA modules to the undulator for the bunch compression and M_{56} = 0.3 m from the undulator to the entrance of SCA modules for the energy compression.

APPLICATION

A laser-beam transport line has been built to deliver FEL pulses to an experiment room. We have upgraded an optical beam expander, which consists of two elliptic mirrors, at the end of FEL optical cavity to convert a diverging beam from a center-hole on a FEL cavity mirror into a parallel beam. The expanded beam is transported to the experimental room through a 24 m-long evacuated pipe. FEL transport efficiency 50% has been achieved [1].

For FEL applications, we investigate material processing using ultrashort FEL pulses. By using FEL pulse shorter than pico-second, it is possible to avoid thermally induced

stress and debris generation, which has been unavoidable in material processing with Q-switched YAG lasers or CO2 lasers [26]. Recently we found that non-thermal surface peeling of stainless steel by ultrashort laser pulses can be adopted to eliminate stress-corrosion-cracking (SCC), which is a critical problem in nuclear power plants [27]. A pilot experiment using Ti:sapphire laser showed that we can remove the residual stress and SCC susceptibility of cold-worked and hardened stainless steel by the laser peeling. Application of self-chirped FEL pulses is also studied. We reported that frequency chirp is induced in an FEL pulse, when the FEL oscillator has large gain and is operated at perfectly synchronized cavity length [28]. We demonstrated generation of an FEL pulse with frequency chirp of 14% and duration of 320 fs. A laser pulse with such large frequency chirp can be used for quantum control of chemical reaction: the resonant excitation of atomic or molecular systems, which have an anharmonic potential ladder [29].

REFERENCES

[1] H. Iijima et al.," Development of frequency-resolved optical gating for measurement of correlation between time and frequency of chirped FEL", in these proceedings.

[2] S. Benson et al.,"High power lasing in the IR Upgrade FEL at Jefferson Lab", Prof of the FEL-2004, 229 (2004).

[3] S. Benson,"Design challenges in high power free-electron laser oscillators", abstract of the FEL-2005, (2005).

[4] G.R. Neil et al.,"The JLab high power ERL light source", NIM A **557**, 9 (2006).

[5] D. Douglas,"The Jefferson Lab 1kW IR FEL", Prof of the LINAC-2000, 716 (2000).

[6] R. Hajima et al.,"First demonstration of energy-recovery operation in the JAERI superconducting linac for a high-power free-electron laser", NIM A **507**, 115 (2003).

[7] R. Hajima, E.J. Minehara,"Electron beam dynamics through a return-arc and a deceleration path of the JAERI energy-recovery linac", NIM A **507**, 141 (2003).

[8] R. Nagai et al.,"Beam current doubling of JAEA ERL-FEL", in these proceedings.

[9] N. Nishimori et al.,"High extraction efficiency observed at the JAERI free-electron laser", NIM A **475**, 266 (2001).

[10] R. Hajima et al.,"Design of energy-recovery transport for the JAERI FEL driven by a superconducting linac", NIM A **445**, 384 (2000); T. Shizuma et al.,"Simulated performance of the energy-recovery transport system for JAERI-FEL", *ibid* **475**, 569 (2001).

[11] N. Nishimori et al.,"20.8 MHz electron gun system for an energy recovery linac FEL at JAERI", Proc. of the APAC-2004, 625 (2004).

[12] V.P. Bolotin et al.,"Status of the Novosibirsk energy recovery linac", NIM A **557**, 23 (2006).

[13] M. Sawamura et al., "Status and development for the JAERI ERL-FEL for high-power and long-pulse operation", Prof of the EPAC-2004, 1723 (2004); Masaru Sawamura and Ryoji Nagai, "Status of RF system for the JAERI energy-recovery linac FEL", NIM A **557**, 287 (2006).

[14] R. Nagai et al.,"Improvement of RF low-level controller for JAERI ERL-FEL", Prof of the 1st annual meeting of Part. Acc. Soc. of Japan, 293 (2004) (in Japanese).

[15] R. Nagai et al., "Optical resonator optimization of JAERI ERL-FEL", NIM A **528**, 231 (2004).

[16] P. Chevtsov et al., "Non-invasive energy spread monitoring for the JLAB experimental program via synchrotron light interferometers", NIM A **557**, 324 (2006).

[17] A.P. Freyberger and G.A. Krafft, "Summary report on synchronization, diagnostics and instrumentation", NIM A **557**, 370 (2006).

[18] A.P. Freyberger, "Large dynamic range beam profile measurements", Proc of the DIPAC-2005, 12 (2005).

[19] T.I. Smith et al., "Status of the SCA-FEL", NIM A **296**, 33 (1990).

[20] W.A. Gillespie et al.,"Time-resolved electron spectrum measurement on the FELIX facility", NIM A **331**, 786 (1993).

[21] R.I. Cutler et al., "Performance of wire scanner beam profile monitors to determine the emittance and position of high power CW electron beams of the NBS-Los Alamos racetrack microtron", Proc of the PAC-1987, 625 (1987); M.A. Wilson et al., "Performance of the 5 MeV injector for the NBS-Los Alamos racetrack microtron", *ibid*, 322 (1987); D.B. Barlow et al.,"Prototype flying-wire beam-profile monitor", Proc of the PAC-1993, 2480 (1993).

[22] J. Camas et al.,"Observation of thermal effects on the LEP wire scanners", Proc of the PAC-1995, 2649 (1995).

[23] http://www.physics.nist.gov/PhysRefData/Star/Text/contents.html

[24] R. Hajima et al.,"Analyses of superradiance and spiking-mode lasing observed at JAERI-FEL", NIM A **475**, 270 (2001).

[25] R. Hajima et al.,"Development of an energy-recovery linac for a high-power FEL at JAERI", Proc. of the APAC-2004, 245 (2004).

[26] A. Nishimura et al., "Demonstration of material processing using JAERI-FEL", Proc of the FEL-2003, II-57 (2003).

[27] E.J. Minehara et al., "Preparation femtosecond laser prevention for the cold-worked stress corrosion crackings on reactor grade low carbon stainless steel", Prof of the FEL-2004, 665 (2004); E.J. Minehara et al., "JAERI 10kW high power ERL-FEL and its applications in nuclear energy industries", Prof of the FEL-2005, 305 (2005).

[28] Ryoichi Hajima and Ryoji Nagai, "Generation of a self-chirped few-cycle optical pulse in a FEL oscillator", PRL **91**, 024801 (2003).

[29] S. Chelkowski et al.,"Efficient molecular dissociation by a chirped ultrashort infrared laser pulse", PRL **65**, 2355 (1990).

ON THE DESIGN IMPLICATIONS OF INCORPORATING AN FEL IN AN ERL

G. R. Neil, S. V. Benson, D. Douglas, P. Evtushenko, and T. Powers
Thomas Jefferson National Accelerator Facility, Newport News VA 23606 USA.

Abstract

Encouraged by the successful operation of the JLab Demo in 1998, many high current ERLs are now being designed with not only short pulse synchrotron beamlines but also FELs. Such inclusion has major implications on magnet quality, rf feedback requirements, wiggler design, srf cavity Q_L, halo, etc.

Measurements on the JLab ERL FEL have identified new challenges. The JLab Upgrade was designed with a 160 MeV beam of 10 mA in 75 MHz, 300 fs bunches. FEL designers set transverse emittance and longitudinal bunching requirements, but to accommodate an FEL in our ERL also means setting stringent phase stability requirements of ($<6\times10^{-9}/f_m$ *rms*) based on a desired FEL detuning tolerance of 1.2 microns. Recovered beam RF loading on the subsequent accelerated beam complicates satisfying these requirements. Gain in the rf feedback limits the accuracy of energy stability when loaded Qs are ~10^7. Energy recovery to <10 MeV sets magnetic field tolerances at 10^{-4}. We present measurements on the JLab ERL showing how to set system requirements to tolerate such FEL lasing.

BACKGROUND

Given the rising interest in Energy Recovered Light Sources incorporating Free Electron Lasers [1], it is helpful to review what specifications of the light source may need revision in order to accommodate the strict demands of the FEL. The discussion below should not be viewed as inclusive but rather is a starting point for further analyses based on experience to date. We give examples of specific criteria based primarily on our experience with the JLab IR Upgrade machine, which has proven to be a great learning tool in the path toward the next generation ERLs. Key areas for discussion include:

1) impact of longitudinal phase space manipulation on rf phase and amplitude control and srf cavity specifications
2) magnetic field quality, higher order term management for transverse and longitudinal acceptance
3) wakefields and resistive wall effects

LONGITUDINAL PHASE SPACE

For an FEL ERL it is generally desirable to let the bunch length remain long during initial acceleration to minimize longitudinal emittance growth. By operating off crest, a correlated energy spread in imposed on the beam that can be used to compress the beam to high peak current at the wiggler. The FEL then imposes an energy spread during lasing with a full width on the order of 6 times the extraction efficiency. This large energy spread must be transported to the dump during energy recovery. In addition the centroid of the distribution loses energy according to the FEL efficiency. If an appropriate M_{56} and path delay in the transport is applied before deceleration the energy spread of the beam can be compressed as the beam decelerates so that the ultimate energy spread as a fraction of the energy is not much larger than the FEL-imposed spread. The offset deceleration angle must be chosen to be sufficient to handle the full energy spread of the beam or successful transport to the beam dump will not be possible (Figure 1). Given the large energy spread of the decelerating beam it is also necessary to match the higher order terms of the magnetics. The Upgrade FEL utilizes sextupoles to help match the rf curvature and minimize dE/E at the dump [2-4].

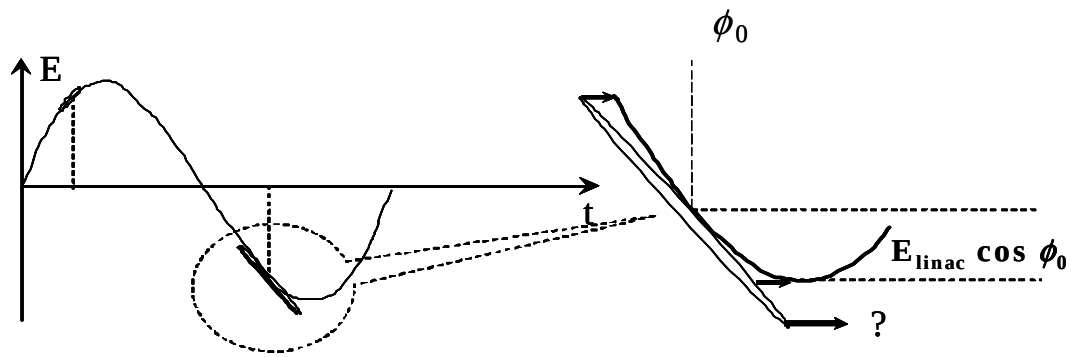

Figure 1. Electron distribution on the acceleration and deceleration rf phase. If the energy spread of the beam exceeds $(\Delta E/E)_{FEL}/2 < E_{linac} \cos \phi_0$ then there is not sufficient rf gradient to decelerate those electrons.

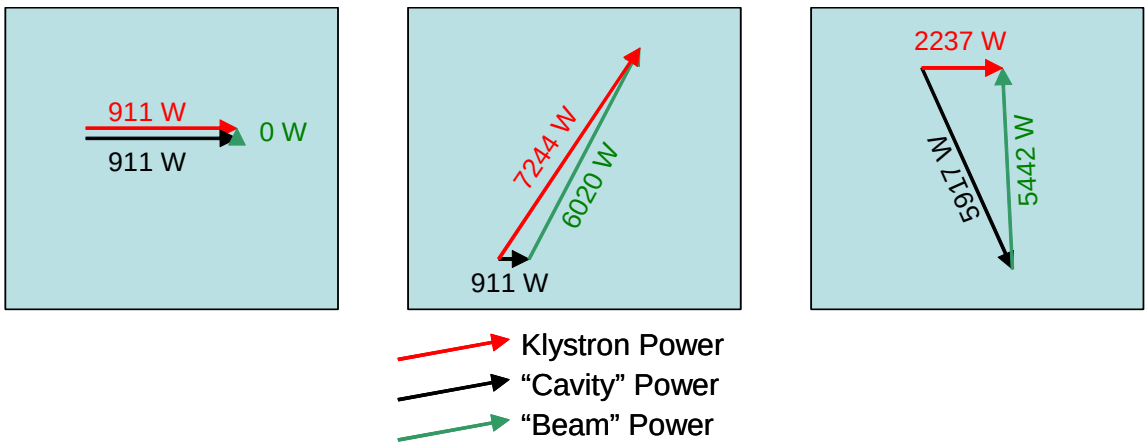

Figure 2. Loading of the rf with a) perfectly matched acceleration and deceleration, b) when the FEL turns on and instantaneously shifts in phase, c) after the srf cavity tunes its resonance to minimize power draw.

A practical rf control system must be able to manage transients associated with the FEL turning on and off. Figure 2 illustrates the beam load phasors in a typical rf cavity with the accelerated and decelerated beam initially perfectly canceling. For the example parameters, when the FEL turns on a phase shift of 7.2 degrees results and initially the rf power draw goes from 911 W at zero degrees to 7244 W at 50 degrees in the rise time of the laser: ~ 10 microseconds. Given time the srf cavity can retune to minimize the power draw (Figure 2c, 3). The resultant is then 2237 W at zero degrees. The energy of the accelerated beam must not change substantially during this transient or a relaxation instability between the FEL and accelerator can be initiated. It is important to note that although an ERL with perfectly opposed accelerating and decelerating beams can operate in principle with a very high loaded Q >> 10^7 such an arrangement makes this turn on and management of the FEL much more difficult. In practice, it may be more practical to trade the high CW power draw for ease of operation by having a lower Q_L [5].

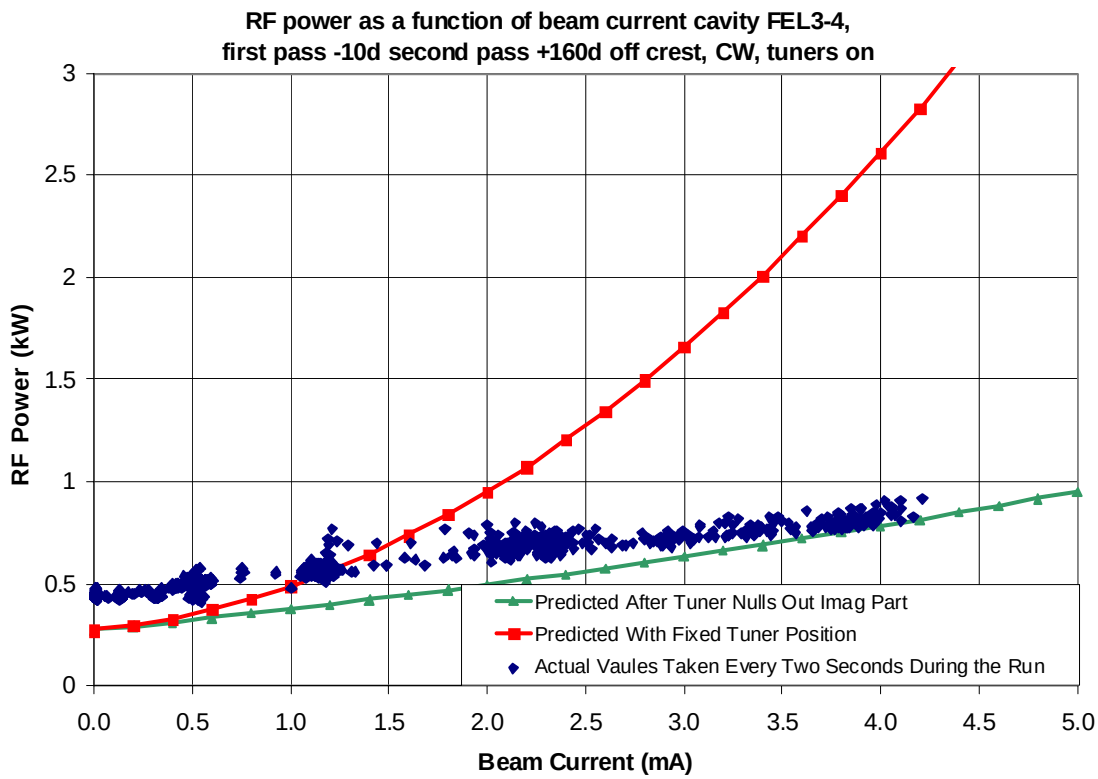

Figure 3. Measured and calculated RF power draw during lasing with cavity tuning for rf power minimum.

Having excess power available to stabilize fluctuations is crucial. The optical cavity must have its round trip travel time precisely matched to the arrival time of the electron bunches for stable lasing. To keep the peak-to-peak fluctuations smaller than 10% it is necessary to keep the cavity length stable to less than $0.05GN\lambda$. For example, in the JLab IR Upgrade for G of 0.5, a N of 32, and λ at 1.5 μm one must keep the cavity length constant to <1.2 μm peak to peak. The micropulse arrival time must be kept constant to the same precision:

$$\frac{\delta\omega}{\omega} < \frac{\delta L}{L} < \frac{1.2\times10^{-6}}{32} = 3.8\times10^{-8} \qquad (1)$$

From the frequency modulation constraint you get a timing jitter constraint of $\delta\tau < 6\text{x}10^{-9}/f_m$. Note that the FEL is fairly tolerant of slow timing jitter since the optical cavity can follow this.

FIELD QUALITY

Since the FEL and energy recovery is sensitive to the phase of the rf it goes without saying that magnetic field quality affects the path that any electron takes and therefore must have tight tolerances. A transverse variation in field ΔB leads to an erroneous angular spread across the beam of magnitude $\delta x' = \Delta Bl/B\rho \sim \Delta Bl/(33.3$ kG-m/GeV * $E_{linac})$. This evolves, via M_{52} a path length spread δl, which differential path length spread in turn translates to a final energy spread ΔE_{dump} which equals $2\pi \sin\phi_0 M_{52}(\Delta Bl/33.36$ kG-m)/λ_{RF} (GeV). From this one can conclude that the allowed error field integral ΔBl is *independent* of linac length/energy gain. In other words the tolerable relative field error falls as energy (required field) goes up. Higher energy ERLs will have increasing difficulty meeting this requirement. For the JLab Upgrade the tolerances are of order $\Delta E_{dump} \sim 3400$ MeV * ($\Delta B/B$) and ~ 0.16 keV/G-cm * (ΔBl); thus a 10^{-4} relative field error budget leads to a remnant momentum spread of 340 keV after energy recovery. This has led to the necessity of careful design, mapping, and hysteresis control of the magnets in the Upgrade. Major dipoles must be spectrometer grade with dB/B of 10^{-4} (see Figure 4 for an example of one of our IR Upgrade magnets).

A substantial amount of effort has gone into making the IR Upgrade FEL transport have the ability to linearize and control higher order transport terms so as to achieve the shortest possible bunch length at the wiggler and successfully transport beam energy spreads of up to 15% all the way to the beam dump with current losses less than 10^{-4}. A full discussion of this system is beyond the scope of this paper. We refer the reader to [3].

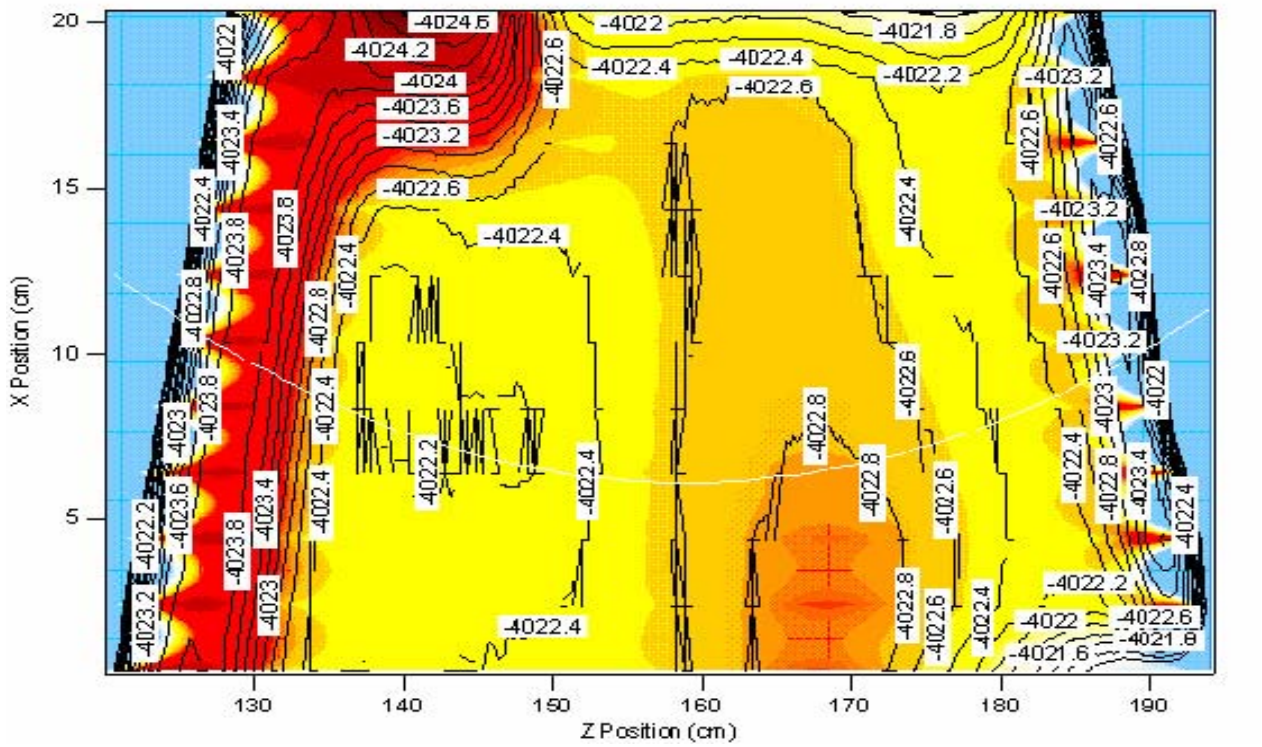

Figure 4. Measured field contours of a GX dipole at 0.4 G resolution. Precision measurements such as these must be made at all desired operating points (or ranges) and B• dl calculated for high order transport.

WAKEFIELDS

The wakefield produced by relativistic particles is an issue often dealt with in storage rings so techniques to address this are well known in the community. The issues with an ERL can be more severe than with such storage rings because of the short bunch lengths required at the FEL itself. This causes the high frequency collective emission cutoff to move to much higher frequencies, a benefit if one is looking for THz emission but a detriment in terms of resistive wall heating and excitation of unintended cavities along the beam pipe. Transitions between different size and shape chambers must be engineered to minimize wakefield problems or significant heating of the electron beam can result.

In addition, the narrow chamber required for wigglers exacerbates the problem since the longitudinal wake goes inversely with the square of the pipe diameter. Such effects can have dramatic consequences even at the modest currents (5 to 10 mA) of our first generation ERLs (Figure 5).

SUMMARY

We have illustrated a number of ways in which the demands of high longitudinal brightness at the input of the FEL, and large energy spread at the output of the FEL can drive tight specifications for the magnetic transport system and its apertures. In addition the need for output stability and the impact of laser transients sets additional strict requirements on the RF control system, and phase and timing stability of the beam. While existing engineered solutions meet the need of first generation machines, improvements will be needed to extend the performance to systems presently in the planning stage.

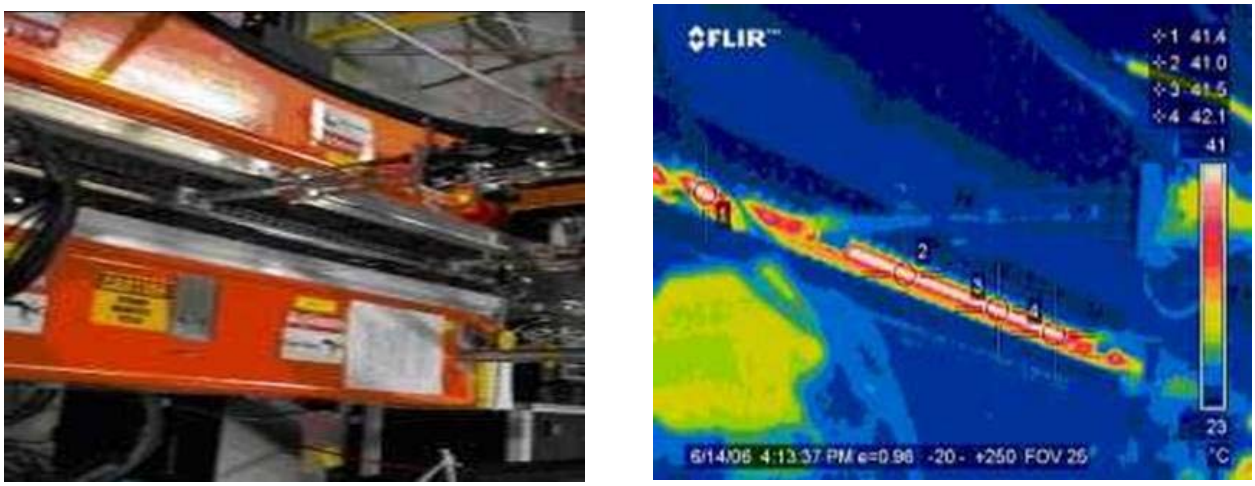

Figure 5. An image of the IR Upgrade wiggler chamber in the visible and infrared during 4.6 mA of beam. Heating is estimated at 35 W/m with the chamber reaching 42°C on top and 100°C at midplane.

ACKNOWLEDGEMENTS

We had the support of the entire FEL team in developing this work. We especially appreciate the help of Rui Li and Eduard Pozdeyev of CASA in analyzing the wakefield effects. This work was supported by U.S. DOE Contract No. DE-AC05-84-ER40150, the Office of Naval Research, the Air Force Research Laboratory, the Army Night Vision Laboratory, the Commonwealth of Virginia and the Laser Processing Consortium.

REFERENCES

[1] G.R. Neil, et al., *Nucl. Inst. And Meth. In Phys. Res.* **A557**, 9-15(2006).
[2] D. R. Douglas, et al., Proc. Linac 2000, Monterey, August 21-25, 2000.
[3] D. R. Douglas, JLab Technical Note JLABTN02002, (2002).
[4] S. Benson, *Nucl. Inst. And Meth. In Phys. Res.*, **A507,** 40-43 (2003).
[5] A.M. Vetter, *Nucl. Inst. And Meth. In Phys. Res* **A429,** 52-57(1999).

OPTICAL DESIGN OF THE ENERGY RECOVERY LINAC FEL AT PEKING UNIVERSITY*

Zhenchao Liu#, Kexin Liu+, Xiangyang Lu, Shengwen Quan, Guimei Wang, Baocheng Zhang, Jiankui Hao, Kui Zhao, Jiaer Chen

Institute of Heavy Ion Physics & MOE laboratory of Heavy Ion Physics, Peking University, Beijing, 100871, China.

Abstract

Peking University is currently designing an Energy Recovery Linac FEL (PKU-ERL-FEL). The system is consisted of a DC-SC photocathode injector, a superconducting linac which is composed of two nine cell TESLA-type cavities, an undulator and beam transport system. The objectives of the PKU-ERL-FEL are providing infrared FEL and building a test-bed for the study of beam dynamics and accelerator technology for energy recovery. In this paper the main parameters of the PKU-ERL-FEL are described and the optical design for the beam transport of PKU-ERL-FEL is presented. The simulation is carried out using the typical particle tracking codes such as *elegant*.

INTRODUCTION

Energy Recovery Linac (ERL) for FEL was approved in Jlab [1]. It is an economical operation mode for widely use in scientific research, industrial and other areas. As the benefit of reducing most of the energy loss, ERL would make it possible to construct large accelerators which need huge power and increase the beam current to a very high level that seems difficult nowadays. Recently many laboratories are developing ERL technology and some facilities are under constructing such as ERLP in Daresbury Laboratory [2][3][4]. Peking University also plan to build an Energy Recovery Linac FEL (PKU-ERL-FEL) based on the research work of RF superconducting technology. This facility will not only provide infrared FEL (IR-FEL) for users but also be used as a test-bed for the study of beam dynamics and superconducting linac techniques for energy recovery. In this paper we mainly discuss the optical issues of the PKU-ERL-FEL.

DISCRIPTION OF PKU-ERL-FEL

Similar with other facilities, PKU-ERL-FEL consists of a DC-SC photocathode injector, a superconducting linac which is composed of two nine cell TESLA-type cavities, an undulator with mirrors in each side and beam transport system. PKU-ERL-FEL is under design and the general parameters are determined. Figure 1 shows the layout and table 1 gives the main parameters of the PKU-ERL-FEL.

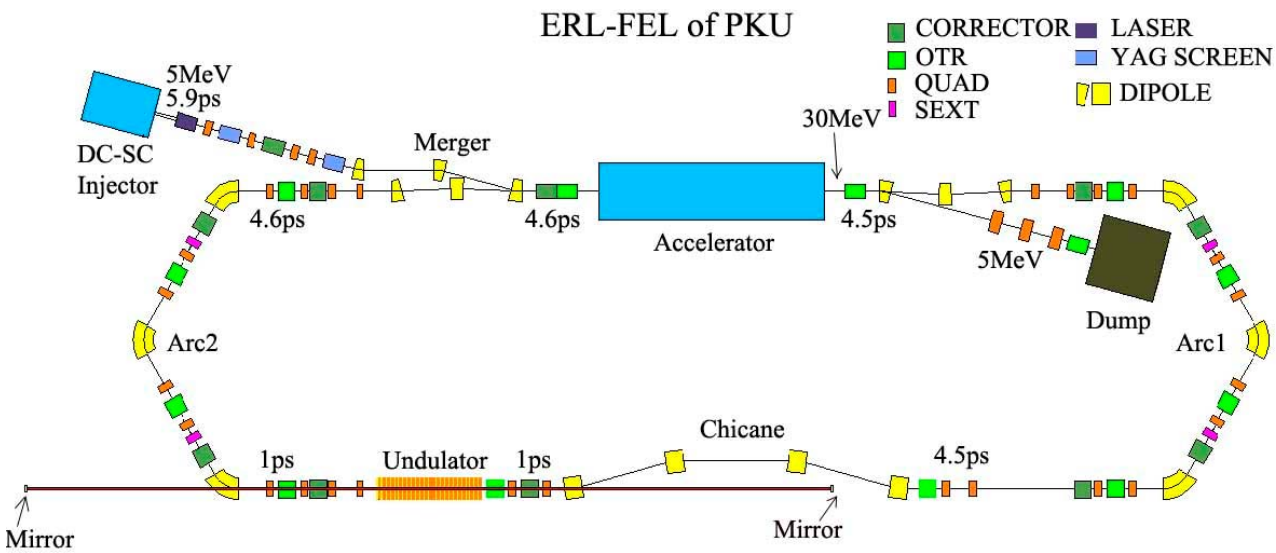

Figure 1: Layout of PKU-ERL-FEL.

*Work supported by National Basic Research Project
#lzhchao@pku.edu.cn
+kxliu@pku.edu.cn

Table 1: Main parameters of the PKU-ERL-FEL

Injection Energy	5MeV
Maximum Energy	30MeV
Bunch Frequency	26MHz
Bunch Charge	~60pC
Bunch length at Entrance of Undulator	~1ps
Macro Pulse Length	2ms
Rep. Frequency of Macro Pulse	10Hz
Energy Spread (rms)	0.24%
Transverse Emittance （rms, n.）	~3μm
Length of Undulator	1.5m
λ_u of Undulator	3cm
K of Undulator	0.5-1.4
Optical Cavity Length	11.52m
Wavelength of FEL	4.7-8.3μm

Injector

The injector is a three and half cell DC-SC photocathode injector working at 2K with a frequency of 1.3GHz. DC-SC photocathode injector has been studied at Peking University since 1999 and demonstrated with a one and half cell model [5]. The accelerating gradient of this three and half cell DC-SC photocathode injector will reach 15MV/m and the transverse emittance of the beam from the photocathode is less than 3.0μm.

Linac

The linac is composed of two nine cell TESLA-type cavities also working at 2K. Electron will be accelerated to 30 MeV from 5 MeV at a gradient of about 13MV/m. Then it goes through the whole loop and back to the linac to be decelerated to 5MeV at 180° phase shift which is exactly achieved by adjusting the length of the whole loop. The linac will be operated in pulse mode due to the limitation of the capability of the cryogenic system.

Undulator

The undulator is 1.5m long and with 50 periods. The wave length of the IR-FEL produced by the undulator is from 4.7μm to 8.3μm. As the bunch frequency is 26MHz, the length of the cavity is currently set at 11.52m. Before the undulator is a magnet compressor to compress the bunch length to about 1.0ps. The bunch length has to be lengthened for effective deceleration. There are two ways to lengthen the bunch after undulator, one is using a decompressing chicane and another is adjusting the R_{56} of return arc. We adopt the second way for saving cost and space. Therefore the undulator is put close to the second arc to make one mirror in the chicane and the other in the outside of the first bending dipole of the second arc.

Transport system

Considering the limited space, the transport loop should be at a smaller scale. The length between the outer side of the outward arc and return arc is near 17 meters and the width of the trajectories is about 4.2 meters. 3 bend merger is adopted for beam injecting to the linac. Following the linac is the extraction chicane which bends the decelerated beam to the dump. After the first arc which contains three 60° bending magnets the beam will be turned 180° to the opposite direction. Then the beam goes through the chicane with a bending angle of 15° and the undulator. The beam comes out from the second arc and goes back to linac through the merger chicane. The energy is recycled and the exhausted electron beam goes to the dump with an energy of about 5MeV.

DESIGN CONSIDERATION

It is well known that the lattice of an ERL-FEL system should be achromatic and the whole loop should be isochronous. Keeping the matrix elements

$$R_{16} = R_{26} = 0 \tag{1}$$

in each section is necessary to ensure the lattice to be achromatic. Keeping the matrix element

$$R_{56} = 0 \tag{2}$$

will make the whole loop isochronous. Because we will use the return arc to lengthen bunches, the R_{56} of the second arc should compensate the R_{56} coming from the compression chicane and other parts:

$$R_{56,arc2} = -(R_{56,chicane} + R_{56,other}) \tag{3}$$

The waist of the beta function should be removable and the beta function should match with the requirements of the undulator.

Energy spread is another important parameter to realize FEL and energy recovery successfully. The beam energy spread is determined by [6]

$$\delta < \frac{1}{4N} \tag{4}$$

N is the undulator period. The undulator in PKU-ERL-FEL has 50 periods so that the beam energy spread should be less than 0.5%.

Space Charge and Coherent Synchrotron Radiation (CSR) can cause the increase of beam emittance. Therefore they should be taken into account in our design.

In the optical design we also need to consider the second order matrix terms of T_{166}, T_{266} and T_{566}. Sextupoles should be used in the two arcs to reduce the value of second order matrix terms to a tolerable degree.

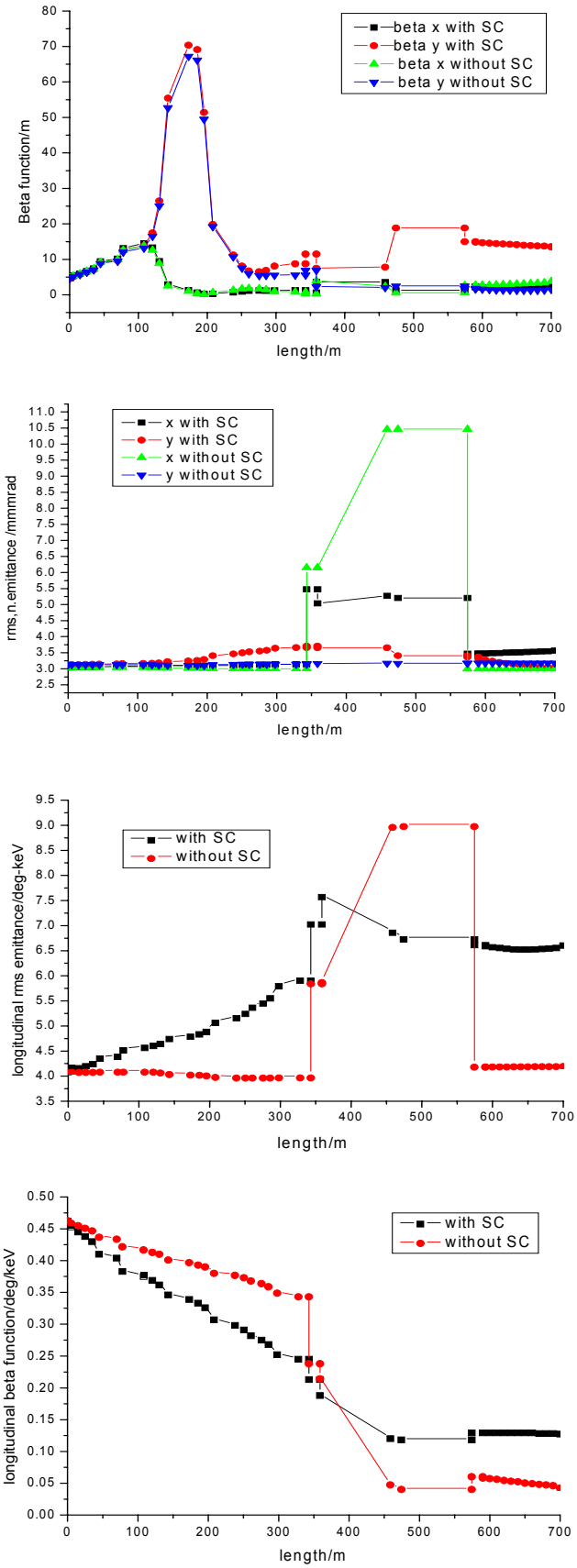

Figure 2: Beta functions and emittance from the injector to the linac

OPTICAL LAYOUT

Injector to linac

Considering the space charge, we have optimized the beam transmission with *parmela* in the injection line. Simulation has been carried out with and without space charge. The result shows that space charge takes little influence on beta function and emittance in x plane. In y plane, the emittance also doesn't change a lot but beta function changes obviously with and without space charge. Figure 2 shows the beta functions from the injector to the linac.

A waist of the transverse beta function has been made at the entrance of the linac but this requirement is not very strict. Simulation shows that the beta function does not change a lot in the exit of the accelerator when the waist is at different positions around the entrance of the linac.

Arc1 to arc2

In the first arc the beta function is symmetric but in the second arc is not. The beta function in x plane makes a waist in the middle of the undulator and keeps small within the undulator for higher radiation power gain. The energy spread is 0.24% (rms) at the entrance of the undulator which fulfills the requirement of lasing. The emittance and energy spread will increase greatly after undulator. We assume that the second arc has an acceptance of 30μm in emittance and 7% full width in energy spread according to the experiences of Jlab and JAERI [7]. The radius of beam envelope is up to 3.5cm in the outer quadrupole of the second arc due to this increase

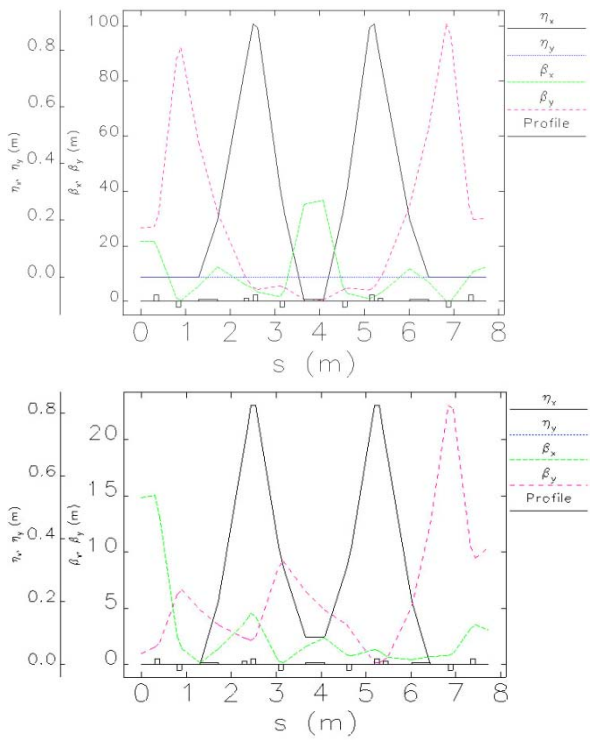

Figure 3: Twiss parameters in the two arcs (Top one is the first arc and bottom one is the second arc)

of emittance and energy spread. The diameter of the aperture of this quadrupole should be ~10cm for completely acceptance of the beam. Figure 3 shows the beta function and the dispersion in the two arcs.

CSR effect is taken into account from the first arc to the second arc in our simulation and it takes little influence on the emittance of the beam.

The second order matrix terms of T_{166} , T_{266} and T_{566} are decreased by using sextupoles in the two arcs. T_{166} and T_{266} are less than 0.02m and T_{566} is less than 1m after optimization.

Arc2 to linac and dump

The beta function of this section is well behaved in our design. The beta function of the beam from the second arc is adjusted by four quadrupoles and goes through the linac. After extraction it goes to the dump and the envelope is controlled well by three quadrupoles.

SUMMARY

The preliminary optical design of the PKU-ERL-FEL is carried out and the beta function of whole loop has been obtained. The result will be checked by further careful simulation with different particle tracking codes before the construction of the beam line of the PKU-ERL-FEL.

REFERENCES

[1] Lia Merminga, David R. Douglas, “HIGH-CURRENT ENERGY-RECOVERING ELECTRON LINACS”, Annu. Rev. Nucl. Part. Sci. 2003. 53:387–429.

[2] R. Hajima , M. Sawamura, “JAERI ERL-FEL: status and future plans”, The 14th Symposium on Accelerator Science and Technology, Tsukuba, Japan, November 2003.

[3] M.W. Poole, E.A. Seddon, “4GLS and the Prototype Energy Recovery Linac Project at Daresbury”, EPAC’04, Lucerne, July 2004.

[4] G. H. Hoffstaetter, I.V. Bazarov, “Status of a Plan for an ERL Extension to CESR”, Prodeedings PAC05, Knoxville/TN (2005), ERL-05-02.

[5] K. Zhao, et al, NIM, A475 (2001) 564.

[6] W. Colson, R. Freedman, “Oscillator evolution in free-electron lasers”, Phy. Rev. A, V.27 N.3, 1983.

[7] R. Hajima, T. Shizuma, “First Demonstration of Energy-Recovery Operation in the JAERI Superconducting Linac for a High-Power Free-Electron Laser”, FEL 2002, presentation.

PROSPECTS OF CASCADED HARMONIC GENERATION FELS*

G. Penn, Lawrence Berkeley National Laboratory, Berkeley, CA, USA

Abstract

Harmonic generation in Free Electron Lasers (FELs) encompasses many techniques for using an input seed laser to produce FEL radiation at a frequency that is multiples above that of the seed laser itself. This allows for the advantages of seeded FELs to be preserved, while extending the reach of these FELs to photon energies far above those produced by conventional laser sources. Many new projects are underway to make use of these methods, including the FERMI@Elettra [1] facility which envisions the use of two harmonic generation stages to reach photon energies above 100 eV. Different methods of harmonic generation are discussed, as well as the technical challenges to overcome in attempting to chain together multiple harmonic stages in an FEL.

INTRODUCTION

Harmonic generation in an FEL [2] is a promising technique for achieving high-intensity photon sources at short wavelengths. Among the benefits of this design is that the output is seeded by a laser signal, allowing for excellent frequency and timing control. The resulting output has the potential of being a transform-limited pulse, and the output power is not limited by the input power but instead by the saturation level of the FEL itself. In addition, the FEL output is at a harmonic of the laser signal, so that the required laser wavelength is longer than the desired output wavelength.

Multiple stages of harmonic generation can be combined into a cascade, where the output from each stage is used as the input seed for the next stage. A harmonic cascade allows conventional laser sources to be used to produce photons at extremely high energies. There are several facilities which plan to use a harmonic cascade as a source for experiments. Among these are FERMI@Elettra, which is to consist of two FELs, one with a single harmonic stage producing radiation in the 100 – 40 nm range, and one with two harmonic stages producing radiation in the 40 – 10 nm range. BESSY [3] is developing an FEL with up to four stages of harmonic generation, yielding wavelengths ranging from 50 nm down to as low as 1.2 nm. Both of these facilities plan to use conventional laser sources. An additional possibility is seeding with a High-Harmonic Generation (HHG) signal [4], which uses a short, intense laser pulse passing through a gas jet to generate many high harmonics of the initial laser. Such sources would drastically reduce the total harmonic conversion required in an FEL, but much work remains to be done to ascertain their suitability for use in this way.

This paper will begin with the FERMI@Elettra design to illustrate the harmonic generation process and to show some of the fundamental issues which need to be considered for a harmonic cascade. Sources of noise can degrade the FEL output, and phase noise is particularly important to consider for large harmonics. Simplified models are used to characterize the major constraints which must be considered for a harmonic cascade. Future prospects are

FERMI@ELETTRA SIMULATIONS

The electron beam parameters for FERMI@Elettra are: 1.2 GeV energy, 1.5 micron emittance, and depending on the beam compression the current can range from 400 A to 1 kA and the energy spread can range from 100 to 200 keV. The seed laser is tunable in the range 240 – 360 nm, has a peak power of 100 MW, and the pulse duration can be up to 1 ps. The first modulator has a period of 16 cm and is 3.04 m long. At the first harmonic, the undulators have a period of 6.5 cm and are in sections of 2.34 m length. The final radiator for the second harmonic has a period of 5 cm and is in sections of 2.4 m length. The initial modulator produces an energy oscillation in the electron beam with the same period as the wavelength of the seed laser, as the relative phase between the undulator field and the laser field when they both overlap the electrons determines the energy transfer. A dispersive chicane follows this modulator, converting the energy modulation into bunching at the wavelength of the seed laser. When this bunching is sufficiently strong, there are significant components at harmonics of the fundamental wavelength. Subsequently, the electron beam passes through undulators tuned to a harmonic of the seed laser, and radiates at that harmonic.

For the two-stage FEL, termed FEL-2, there are then two possibilities, as shown in Fig. 1. In the "fresh-bunch" approach, the radiation produced at the end of the first stage is made to overlap the electron beam in another modulating undulator after passing through a delay chicane. As a result, the radiation pulse produces an energy modulation in a region of the electron beam closer towards the head of the bunch, which was relatively unperturbed by the first stage of the FEL. The second stage produces a harmonic of the output from the first stage in the same way as the first stage generates a harmonic of the seed laser. In the "whole-bunch" approach, the first stage is continued until there is sufficient energy modulation at the harmonic to continue to the next stage. The electron beam is then passed through a dispersive chicane to enhance the bunching at the desired final harmonic. In the final radiator, the same section of

* This work was supported by the Director, Office of Science, High Energy Physics, U.S. Department of Energy under Contract No. DE-AC02-05CH11231.

electron beam radiates at this higher harmonic.

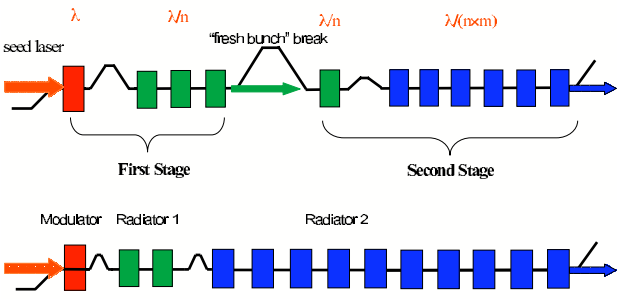

Figure 1: Two possible configurations for the FEL-2 line of the FERMI@Elettra facility: fresh-bunch (top) and whole-bunch (bottom).

An example from the FERMI@Elettra optimization study will motivate the topics discussed below. A realistic longitudinal beam distribution from accelerator studies is shown in Fig. 2. The central current is roughly 500 A. Note that there is a strong parabolic shape to the slice energy as a function of longitudinal position. More recent designs have advanced far towards removing this feature, but it serves as a useful reference. A whole-bunch configuration starting with a 240-nm seed laser with 1 ps duration FWHM produces 10 nm output with 0.1 mJ per pulse, and with peak power of 400 MW. The output power and phase (modulo 2π) resulting predicted by simulations using GENESIS [5] are shown in Fig. 3. The phase shows a strong quadratic dependence which mirrors the energy variation, and which leads to a broad, fluctuating spectrum as shown in Fig. 4. Applying an appropriate linear chirp to the seed laser is quite effective at cancelling the phase variation, resulting in the sharp spectrum shown on the same figure. While this demonstrates that a parabolic energy profile can be cancelled with a linear frequency chirp in the seed laser, proper tuning may be challenging and more complex phase space distributions will not be amenable to this type of a fix. Avoiding such features in the beam profile therefore becomes a high priority when high longitudinal coherence and spectral brightness are desired.

ENERGY AND PHASE ERRORS

A simplified view of harmonic generation in an FEL serves as a useful starting point for considering the challenges faced in designing a harmonic cascade FEL, as touched on above. In Fig. 5, a slice of the electron beam is modelled as a collection of mono-energetic beamlets, each one with a uniform distribution in longitudinal position (here expressed as phase). Note that phase increases towards the head of the bunch. After the modulator and dispersive chicane, the phase space distribution is folded over to produce significant bunching centered at the zero phase.

The spread in energies for the original beam results in a finite width for the microbunch, as a consequence of the

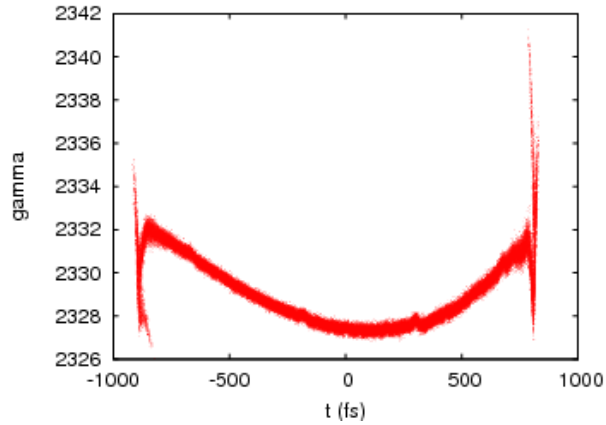

Figure 2: Preliminary phase space distribution from FERMI@Elettra study.

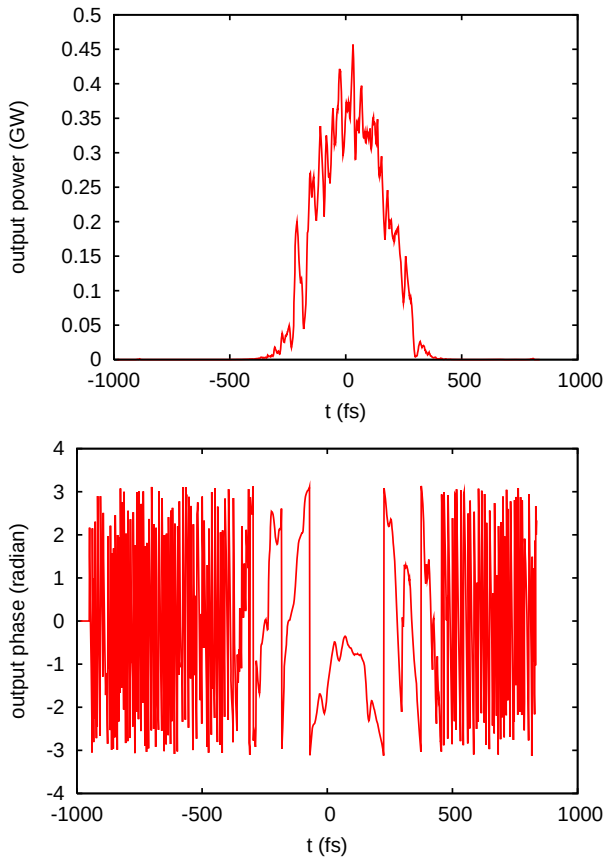

Figure 3: Output power and phase at 10 nm using whole-bunch approach.

conservation of phase space. There are more subtle issues which can be understood with this picture, however. Effective bunching, especially at higher harmonics, requires an energy modulation much larger than the initial energy spread. Roughly, this requires that the energy modulation, γ_M, satisfy

$$\gamma_M \geq (n-1)\sigma_\gamma, \quad (1)$$

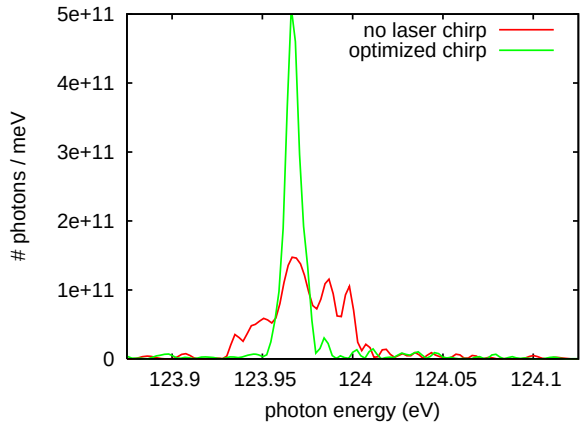

Figure 4: Output spectrum using laser seed with no chirp (red) and with optimized chirp (green).

where n is the harmonic number and σ_γ is the energy spread. The degree of bunching generated at the harmonic will be sensitive to the slice energy spread. Furthermore, because each energy value corresponds to a different phase for the microbunching, longitudinal variations in the average beam energy will lead to offsets in the timing of the microbunches. As the microbunches are separated by n wavelengths in terms of the harmonic output, these fractional timing offsets can have a large effect on the coherence of the output radiation.

To further understand the effect of longitudinal energy variation in the beam, we consider a similar effect where phase offsets are introduced within the seed laser itself. In Fig. 6, the bunching produced by a seed laser with a linear frequency chirp is compared to that produced by a seed laser with no chirp, but for an electron beam with a quadratic energy chirp. Both variations are greatly exaggerated compared to that which would be encountered in practice. The vertical bars indicate the phases of successive microbunches. It is apparent that a chirped seed laser can produce the same changes in timing structure as a chirp in the electron beam energy. This explains how a linear chirp in the seed laser can fix the output from an electron beam having a parabolic energy profile. Note that a linear energy chirp would simply produce a uniform offset in output wavelength. This is generated as the modulated electron beam passes through the dispersive chicane, where it is either compressed or stretched depending on the sign of the energy variation. Curvature in the energy profile leads to more complicated perturbations, as some sections of the beam are compressed and others are stretched. This can lead to sidebands in the spectrum or broadening, which would degrade the output radiation to be no longer transform-limited. This effect is made worse at high harmonics, as seen in Fig. 7. Here, an arbitrary small phase error is introduced to a pure Gaussian pulse. The effect is barely visible in the spectrum of the fundamental, but at the 24th harmonic the spectrum is drastically altered. At the fundamental, the signal is still transform limited, but

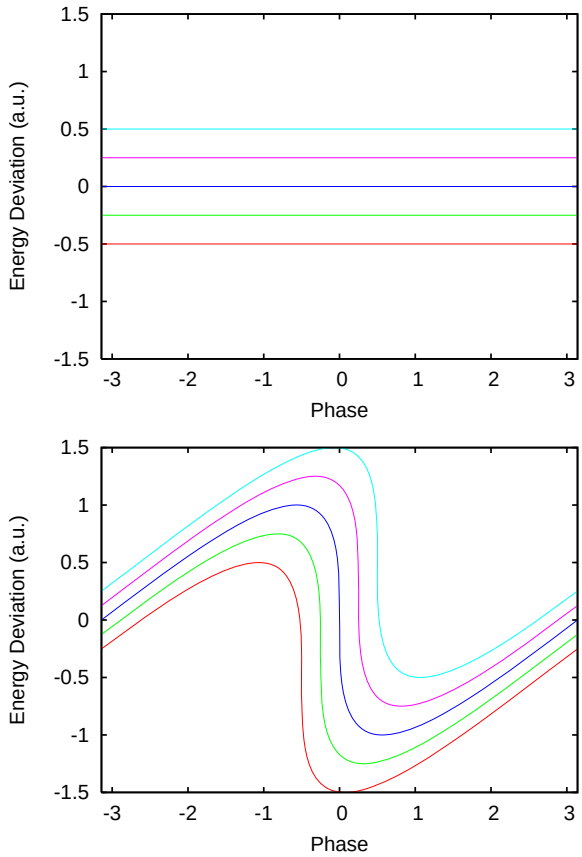

Figure 5: Illustration of bunching process as it affects electrons having different energies.

the pulse is still unsuitable for harmonic generation beyond a certain limit. This introduces added complexity to the design of the seed laser, as the constraints are more stringent than usual and are not a typical part of the vocabulatory of laser sources. In particular, even short pulses (i.e., a small number of wavelengths) will require a clock-like regularity of the field oscillation in order to function optimally as an FEL seed.

Macroparticle Noise

Because electrons at different energies are bunched at different phases, there are additional concerns for the proper simulation of harmonic generation. Typically, macroparticle noise in FEL simulations are controlled by starting with pseudorandom particle distributions, and using subsets of particles uniformly spaced in phase. Deviations from this uniform spacing are chosen to mimic the expected statistical fluctuations. However, an efficient bunching process will put most particles of a given energy at a single phase, so the final phase distribution will only depend on the initial energy distribution. In the example above, there will only be five bunches centered about the zero phase. Different choices of modelling the energy distribution will thus lead to different bunching pa-

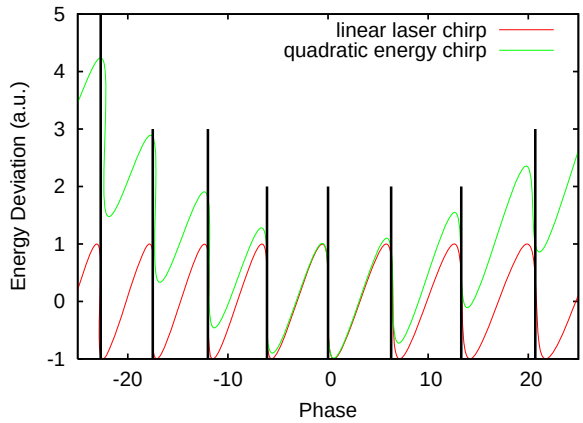

Figure 6: Comparison of bunching process for a flat beam seeded by a chirped laser, versus a beam with quadratic energy variation and no laser chirp. Vertical bars indicate the phases of successive microbunches.

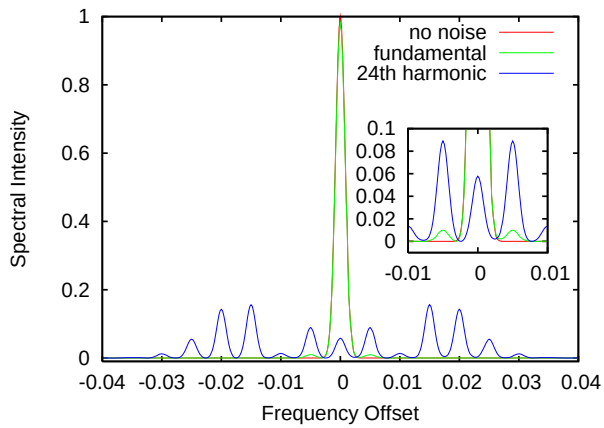

Figure 7: Spectra of Gaussian pulse with oscillating phase error, at original frequency and at 24th harmonic.

rameters. Furthermore, especially for large energy spread and harmonic number, the discrete nature of the bunching will lead to noise in the bunching parameter as the gaps between energy levels become resolved. The macroparticle noise for an optimally bunched beam will be given by $n\sigma_\gamma/N_\gamma\gamma_M$, where N_γ is the number of energies sampled by the distribution. Sampling more phases will not reduce this macroparticle noise, and may even make the problem worse if it is done at the expense of the number of discrete energies sampled. There is as of yet no known robust method to control this effect in simulations. It becomes increasingly difficult to get simulation results to converge as the initial energy spread in the electron beam is increased, especially when the nominal seeded bunching is already low.

POWER FLUCTUATIONS AND ENERGY OFFSETS

While phase distortions can reduce the longitudinal coherence of the FEL output, power fluctuations are also a major concern. There are many possible sources of power fluctuations, but typically the most important one is energy offsets in the beam. Note that while phase errors accumulate due to longitudinal variation of the slice beam energy, it is the difference between the slice energy and resonant energy which determines the output power. Shot-to-shot jitter in beam energy is thus a significant concern for output power flucuations. The sensitivity of the FEL to relative energy offsets is typically the larger of $1/N_U$ or the FEL parameter [6], $\rho_{\rm FEL} = \lambda_U/L_G$. Here, N_U is the number of undulator periods, λ_U is the undulator period, and L_G is the exponential gain length, all for the final undulator where the gain length is longest and the number of undulator periods is largest.

Reducing the sensitivity of the FEL involves a trade-off with trying to optimize the peak output power. One method is simply to reduce the number of undulator periods, at the cost of greatly reduced average power. A more efficient method is to introduce either variations in the magnetic field strength of the undulator, or phase offsets between undulator sections. Examples are shown in Figs. 8 and 10; the latter example is from a pseudorandom variation in the undulator field strength which drastically reduces the dependence on beam energy and reduces the peak power by a factor of 30. The evolution of the power and bunching for the example labelled “phase 3” are shown in Fig. 9. Note that the configuration is specific to the given length of undulator, at which point the various beam energies come close to each other in performance, but after passing through different dynamics.

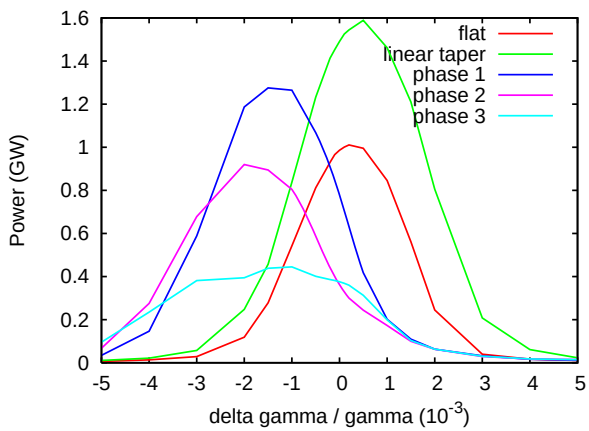

Figure 8: Sensitivity of FEL output power to beam energy offsets, for variations of the fine tuning.

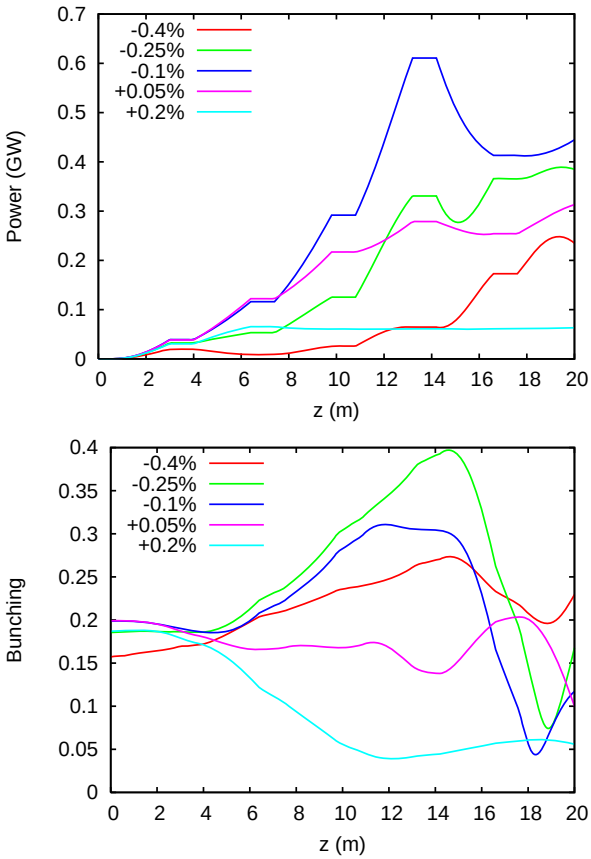

Figure 9: Power and bunching evolution in the FEL, for different electron beam energies, using the "phase 3" example in the previous figure.

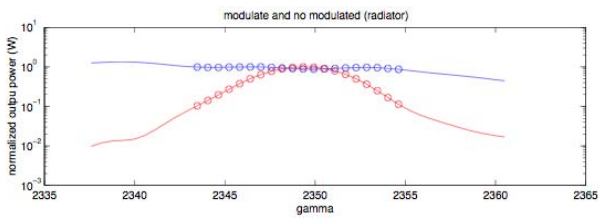

Figure 10: An example of extreme reduction in the sensitivity of FEL output to electron beam energy through pseudo-random tapering. Peak power in the tapered example (blue) is a factor of 30 below that in the nominal case (red), but is stable to much larger energy variations. Courtesy of G. De Ninno and E. Allaria.

CHALLENGES FOR HARMONIC CASCADES

The desire for even shorter wavelengths leads one to consider more ambitious harmonic cascade FEL designs, as in the BESSY multi-stage FEL. As the goal is moved to shorter wavelengths, the tendency is to consider more energetic electron beams. One motivation is the reduced effectiveness of the FEL when the normalized emittance is much larger than $\lambda_r/4\pi\gamma$, where λ_r is the radiation wavelength and γ is the relativistic factor of the beam. This is due to a combination of reduced electron density and increased spread in longitudinal velocities. Another is the challenge of satisfying the resonance condition,

$$\lambda_U = \frac{2\gamma^2}{1+a_U^2}\lambda_r, \tag{2}$$

where a_U is the normalized strength of the undulator field. The FEL parameter also tends to drop drastically as the beam energy is reduced, which further constrains tolerances on energy jitter and energy spread.

The high harmonic numbers involved also introduce complications. Attempting to take a single, large harmonic jump becomes very impractical, as the required energy modulation must be extremely large or the energy spread must be very low in order to satisfy Eq. 1. This leads to an additional problem, that for larger energy modulations the beam will debunch more rapidly. If the gain length is longer than the debunching length, the electrons will not be trapped in the ponderomotive well and the FEL will not reach saturation. A rough requirement to reach saturation is

$$\gamma_M \leq \gamma\lambda_U/16L_G. \tag{3}$$

Together with Eq. 1, this limits the range of acceptable energy modulations, and also imposes a maximum allowed energy spread.

Ultimately, many smaller harmonic stages become required. This adds to the complexity, and does not eliminate the sensitivity to phase noise and energy variations which depend on the total harmonic multiplication factor. The noise-to-signal power ratio within a given bandwidth can be expected to grow as the square of the total harmonic power through the harmonic generation process. The seeded FEL process must also compete with spontaneous FEL emission which may amplify the noise along the FEL, as well as spontaneous growth in energy spread.

As the energy modulation itself increases the slice energy spread with each harmonic multiplication stage, fresh-bunch delays between stages will ultimately be required. Each delay to an unseeded section of the electron beam introduces constraints on synchronization and reduces the maximum duration of the output pulse for a given electron distribution. While it may be possible to alternate between fresh-bunch and whole-bunch stages, these considerations lead to challenging electron source and acceleration requirements. Numerical simulations also require more resources and care when large harmonics are desired.

One attractive option is to take advantage of rapid advances in HHG sources, and seed the FEL at much shorter wavelengths than conventional lasers can achieve. There has been much recent activity studying the feasibility of HHG sources as an FEL seed [7, 8, 9]. While further characterization of these sources is clearly needed to make reliable predictions, some facts are already apparent. First, the typically low peak power in these signals is not an obstacle to their use. In particular, amplifying a signal is

much less difficult than conversion to a harmonic (hence the $(n-1)$ factor in Eq. 1). In addition, the HHG sources typically have durations of less than 100 fs, which favors experiments based on timing rather than spectral widths, and slippage between the radiation and the electrons will smooth out some phase noise components. Ultimately, HHG sources could be used to seed X-ray FELs which use only a single stage of harmonic generation.

While the challenges for developing cascaded harmonic FELs are daunting, they link together a large range of technologies; small improvements on many fronts may open up new horizons for seeded FELs in the future. It is clear that the lasers used as seeds for the FEL require more detailed characterization. In addition to improved or novel sources for seeding, advances in electron sources, acceleration, undulator design, and optics will enable more ambitious projects in the future. In the meantime, current facilities on the horizon will offer experience and testing grounds for new ideas, as well as provide opportunities for performing advanced scientific research.

ACKNOWLEDGMENTS

This paper discusses work performed in collaboration with many individuals, and much of this work came out of the collaboration to produce the FERMI@Elettra technical optimization study. The author would like to express his gratitude to Bill Fawley, Jonathan Wurtele and Sasha Zholents for their guidance in FEL studies, and John Corlett and Bill Barletta for their support and encouragement.

REFERENCES

[1] C. Bocchetta et al., Proceedings of the 2005 FEL Conference, (2005) 682.

[2] L.-H. Yu et al., Science **289** (2000), 932–934.

[3] The BESSY Soft X-ray Free Electron Laser, TDR BESSY March 2004, eds.: D.Krämer, E. Jaeschke, W. Eberhardt, ISBN 3-9809534-08, BESSY, BERLIN (2004).

[4] H.C. Kapteyn, M.M. Murnane, and I.P. Christov, Physics Today (March 2005) 39–44.

[5] S. Reiche, Nucl. Instr. Methods A **429** (1999), 243–248.

[6] R. Bonifacio, R. Corsini, and P. Pierini, Physical Review A **45** (1992), 4091–4096.

[7] G. Lambert et al., Proceedings of the 26th International Free Electron Laser Conference (FEL04), Trieste, Italy (2004), paper MOPOS21.

[8] B. Sheehy et al., Proceedings of the FLS 2006 Workshop, WG333.

[9] M. Gullans, J. Wurtele, G. Penn, Z. Zholents, submitted to Phys. Rev. ST:AB.

FEMTOSECOND SYNCHRONIZATION AND STABILIZATION TECHNIQUES*

J. Kim†, F. Ludwig‡, J. Chen, Z. Zhang§ and F. X. Kärtner, MIT, Cambridge, MA 02139, USA.

Abstract

High-precision synchronization and stabilization techniques are crucial for future advances in next generation light sources, seeded x-ray free electron lasers. In this paper, we present long-term stable femtosecond-precision optical-to-RF and optical-to-optical synchronization and stabilization techniques. For optical-to-RF synchronization, we demonstrate an optical-microwave phase detector that is capable of extracting an RF-signal from an optical pulse train in a long-term drift-free way. Extraction of an RF-signal with 3-fs in-loop timing jitter, integrated from 1 Hz to 10 MHz, from an optical pulse train is demonstrated. Optical-to-optical synchronization of two femtosecond lasers with sub-femtosecond precision over 12 hours is demonstrated. We also discuss how to use optically stabilized fiber links for timing distribution. Together with low-noise mode-locked lasers, a flexible femtosecond timing system can be constructed.

INTRODUCTION

Seeding of free electron lasers operating in the x-ray regime with radiation generated from ultrafast laser sources, either directly, via nonlinear crystals, or via high harmonics from noble gases, may result in a fully coherent x-ray laser. For seeding of such large-scale facilities spanning over several hundreds meters to a few kilometers, it is critical to synchronize low-level RF-systems, photo-injector lasers, seed radiation and potential probe lasers with low timing jitter, preferably in sub-10-femtosecond range, in a long-term stable arrangement [1].

Figure 1 shows the schematic of the envisioned timing distribution and synchronization system for the future next generation light sources, seeded x-ray free electron lasers (XFELs). The pulse repetition rate of an optical master oscillator implemented as a mode-locked laser is stabilized to an optical and/or microwave frequency standard. The pulse train is distributed to all critical subsystems, i.e., the pulsed klystron, the photo-injector laser, the low-level RF systems for linear accelerator, the seed laser as well as probe lasers, by use of timing stabilized fiber links. Finally, low-jitter, drift-free optical-to-RF and optical-to-optical synchronization between the distributed timing pulse trains and the remote RF- or optical subsystems will result in a tightly synchronized timing system over the large-scale accelerator facility.

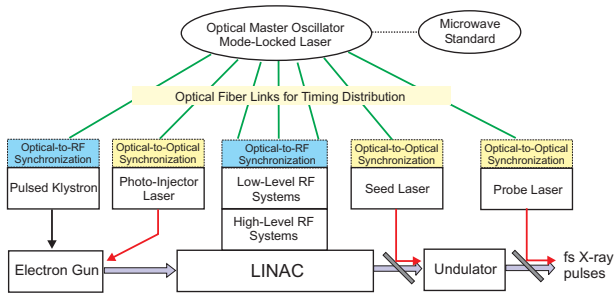

Figure 1: Schematic outline of timing distribution and synchronization for seeded X-ray free electron laser (XFEL) facilities.

Currently, the most promising candidates for ultra-low jitter optical master oscillators are passively mode-locked Er-doped fiber lasers [2], Yb-doped fiber lasers [3] and Er/Yb-glass lasers [4, 5]. Erbium and Ytterbium gain materials have long upper-state lifetime in the ms-range, and therefore, the high frequency fluctuations of the laser output in amplitude and timing are quantum noise limited [6]. Thus the timing jitter of mode-locked lasers is superior to that of conventional microwave oscillators in the high frequency range.

The crucial performance indicator for the optical master oscillator is the phase noise or timing jitter in the high frequency range. The bandwidth of optical/microwave reference locking is typically limited to tens of kHz range, and the high-frequency noise beyond locking bandwidth follows that of the free-running master oscillator. In addition, timing stabilization of fiber links based on the cross-correlation of the back-reflected pulse from fiber end with the fresh pulse also has a bandwidth limitation from the travel time of the reflected pulse. These limitations assure that a very low jitter mode-locked laser is a prerequisite for a high-precision timing system.

In Refs. [7] and [8], the timing jitter is characterized by measuring the phase noise of one harmonic (at 1.3 GHz) of the microwave signal obtained by direct photodetection of the pulse train. For standard Er-doped stretched pulse fiber lasers, the integrated timing jitter from 1 kHz to 22 MHz (Nyquist bandwidth) is measured on the order of 10 fs, which is already better than most commercial high-quality microwave signal generators (for example, Marconi 2041 signal generator). Note that the measurements are often limited in precision by the amplitude-to-phase (AM-to-PM) conversion from direct photodetection. A more detailed discussion on this conversion will be given in the next section. In theory, the high frequency timing jitter of pulse trains from mode-locked lasers can be below one femtosec-

* Supported by ONR, AFOSR, and EUROFEL.
† jungwon@mit.edu
‡ Permanent address: DESY, Hamburg, Germany
§ Permanent address: Peking University, Beijing, China

ond.

Once a timing signal in form of an optical pulse train is generated from a master oscillator, it should be distributed to the remote RF- or optical-subsystems that we aim to synchronize with minimal excess noise. Precise transfer of timing signals through fiber links for timing information dissemination has been demonstrated recently [7, 9, 10, 11] for short time spans, typically less than a minute. If the fiber length is L, we assume that no length fluctuations are faster than 2L/c, where c is the speed of light in the fiber. Relative fiber expansion by temperature change is typically on the order of 10^{-7}/K, which can be compensated by a fiber length control loop by referencing the back reflected pulse from the fiber end with the later pulse from the mode-locked laser. Recently, the demonstration of timing distribution over 500 meters in an accelerator environment was done with pure RF-techniques [7]. When the feedback loop is open, the jitter integrated from 0.1 Hz to 5 kHz is 66 fs; when the loop is closed, the in-loop jitter is suppressed down to 12 fs. More detailed information on this timing distribution experiment can be found in Ref. [7].

Although a short-term stabilization on the order of few tens of femtoseconds can be achieved with RF-techniques only, for long-term stabilization of fiber links with sub-10 fs accuracy over hours, balanced cross-correlation techniques [12] can be employed, as discussed later in this paper. Work is in progress to demonstrate long-term stable fiber links.

OPTICAL-TO-RF SYNCHRONIZATION

Once precise timing information encoded as an optical pulse train arrives at each remote location, the next task is to synchronize it with, for example, RF-subsystems. It is crucial to convert this optical signal into a low-jitter, drift-free RF-signal with a satisfactory power level in a long-term stable way. Recently, it has been shown that the extraction of an RF-signal from an optical pulse train using direct photodetection is limited in precision by excess phase noise [13]. The major contribution to this excess noise was identified to be the amplitude-to-phase (AM-to-PM) conversion in the photodetector. The intensity noise of the laser can be converted into a significant amount of phase noise and phase drift by this process. In Refs. [8] and [14], the AM-to-PM conversion factor was measured and it typically ranges 1 to 10 ps/mW depending on the bias and the bandwidth of the photodetector. The intensity noise of the delivered pulse train can be converted into a significant amount of excess timing jitter by this process. For a 12-GHz InGaAs photodetector at 6 V reverse bias that we tested, the AM-to-PM conversion factor was measured as 1.6 ps/mW [8]. For an Er-doped fiber laser with 0.03 $\%_{\mathrm{rms}}$ relative intensity noise (RIN), this may already result in 5-fs excess jitter when 10 mW of power is applied to the photodetector. In addition, direct photodetection has a limited extractable RF-power and signal-to-noise ratio (SNR) due to the damage threshold for the input optical power to the photodetector. Moreover, phase drifts in the diode due to temperature change as well as post-amplification to reach the required signal level can prevent a long-term stable regeneration of RF-signals.

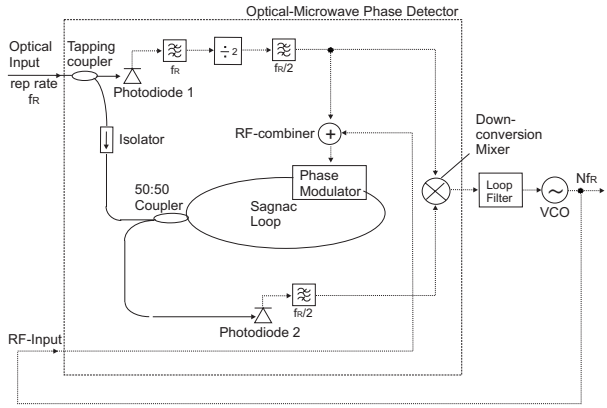

Figure 2: Schamatic of a balanced optical-microwave phase detector and its use for RF-signal regeneration from an optical pulse train. VCO, voltage-controlled oscillator.

Therefore, it is highly desirable to develop a phase-locked loop between an optical pulse train and a high-quality RF voltage-controlled oscillator (VCO) to prevent those undesired AM-to-PM conversion and drifts due to the photodetection process. In addition, one can leverage the fly-wheel effect of VCO. In doing so, the key issue is the development of drift-free, low-jitter phase detector which compares the relative phase between pulse trains and RF-signals in the optical domain before the photodetection is involved. Previously, we proposed and demonstrated a scheme to avoid the excess noise from direct photodetection by transfer of timing information in the optical domain [15]. However, due to acoustic vibrations and poor phase noise properties of the free-running VCO, the relative jitter was limited to 60-fs measured from 100 Hz to 10 MHz.

For the extraction of low-jitter, high-power, and drift-free RF-signals from optical pulse trains, a balanced optical-microwave phase detector is proposed and demonstrated. This phase detector is still based on the timing information transfer in the optical domain. The timing information transfer in the optical domain is implemented by use of a differentially-biased Sagnac fiber-loop and synchronous detection. We used the phase error signal from this balanced optical-microwave phase detector, which is robust against drifts and photodetector nonlinearities, to regenerate low-jitter RF-signals from optical pulse trains.

Figure 2 shows the schematic of the balanced optical-microwave phase detector. Part of the input pulse train is tapped off by Photodiode 1. This photodiode is used to generate a synchronous detection signal at half the repetition rate ($f_R/2$) of the optical pulse source. This signal is applied to both the phase modulator and the down-conversion mixer. The rest of the input pulse train is sent to

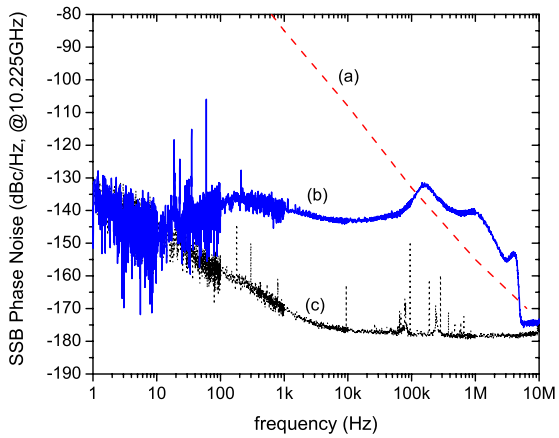

Figure 3: The single-sideband (SSB) phase noise spectra at 10.225 GHz. (a) Free-running VCO. (b) In-loop phase noise when it is locked. (c) Signal analyzer noise floor.

the Sagnac-loop with a phase modulator. The phase modulation in the Sagnac loop is converted into an amplitude modulated signal at $f_R/2$ at the output of the Sagnac-loop. The amplitude of this signal is, to the first order, proportional to the phase error between the optical pulse train and the RF-signal (which is, the output from the VCO). The detected signal at Photodiode 2 is band-pass filtered at $f_R/2$ and down-converted to the baseband by mixing with the reference signal. This error signal is filtered and controls the low-noise VCO to close the phase-locked loop.

For the demonstration experiment, a standard stretched-pulse Er-doped fiber laser [2] (repetition rate f_R = 44.26 MHz) is used as the optical pulse source. All optical components in the phase detector are implemented using commercial 1550-nm optical fiber and components. In the experimental implementation, we generated a signal with the frequency $10.5 f_R$ for the phase modulation in the Sagnac-loop in parallel with $f_R/2$ component to reduce the necessary fiber loop length. By closing the loop with a 10.225-GHz (231st harmonic of the fundamental repetition rate) VCO (PSI DRO-10.225), a long-term stable locking between the laser and the VCO is achieved.

Figure 3 shows the measured in-loop phase noise spectra at the output of down-conversion mixer. The voltage signal from the phase detector was amplified with a low-noise amplifier (G=10 non-inverting amplifier with AD797) and measured with a low-noise vector signal analyzer (Agilent 89410A), and converted into single-sideband (SSB) phase noise at 10.225 GHz. This measurement shows that the integrated in-loop jitter is 3.0 fs $\pm$ 0.2 fs integrated from 1 Hz to 10 MHz when it is locked. Currently, the system is limited by the thermal noise from electronic amplifiers and has not yet reached shot noise limited performance yet. We are currently pursuing to further suppress the timing jitter to below 1 fs by increasing optical and RF power levels as well as optimizing loop characteristics. In addition, the construction of a second loop is in progress to perform long-term out-of-loop measurements by mixing two VCO outputs in quadrature.

OPTICAL-TO-OPTICAL SYNCHRONIZATION

Tight synchronization is necessary not only between optical and RF-subsystems but also between different optical systems, for example, the photo-injector laser, the seed laser and the probe lasers as shown in Fig. 1. Conventional timing synchronization between two mode-locked lasers based on microwave mixers [16] suffers from high residual jitter and thermal drifts in the electronic amplifiers and mixers. To overcome this limitations, a balanced optical cross-correlator [12] can be used for the long-term optical-to-optical synchronization. This technique uses nonlinear optical processes for an extremely sensitive detection of timing differences between optical pulses.

Figure 4 shows the schematic of the balanced cross-correlator. The combined pulses from two mode-locked lasers with different spectra, denoted as wavelengths λ_1 and λ_2, are splitted by a broadband 50:50 beam splitter. The two beam paths have a different group delay (GD), for example, by inserting a glass plate in one of the arms. This group delay offsets the relative position between two pulses. Each combined pulse is focused into a nonlinear crystal to generate a sum-frequency component at $\frac{1}{\lambda_{SFG}} = \frac{1}{\lambda_1} + \frac{1}{\lambda_2}$. After bandpass filtering the sum-frequency generation (SFG) components, a balanced detector measures the intensity imbalance. For small timing differences (within the range of the group delay of the GD element), the output from the balanced detector is nearly proportional to the time difference between the two pulses. At the zero-crossing of the balanced detector output, the amplitude noise from each laser is balanced and does not affect the detected error signal. The signal from the balanced detector is used to lock the repetition rates of the two lasers by controlling the cavity length of one laser with cavity mirrors mounted on piezo-electric transducers (PZTs). This finally closes the loop. This method enables a drift-free and temperature-independent synchronization between two independent lasers.

The long-term timing synchronization performance using balanced optical cross-correlation is demonstrated using a 5-fs Ti:sapphire laser (centered at 830 nm) and a 30-fs Cr:forsterite laser (centered at 1250 nm). The pulses are combined and splitted by use of a broadband 50:50 beam splitter with matched group delay dispersion. LBO crystals with 1-mm thickness are used for SFG at 499 nm (1/830nm + 1/1250nm = 1/499nm). To generate a group delay offset of 45 fs between 830 nm and 1250 nm, a 3-mm thick fused silica plate is used.

Figure 5 shows the out-of-loop cross correrlation result for a timing jitter measurement between the Ti:sapphire and Cr:forsterite lasers. The black line shows the cross-

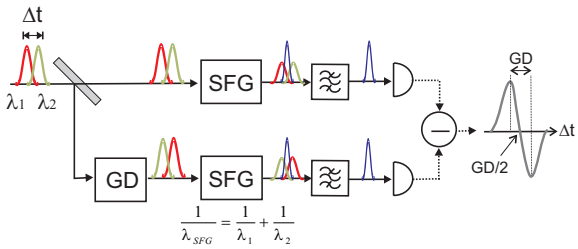

Figure 4: Schematic of a balanced cross-correlator. GD: group-delay element between two color pulses. SFG: sum-frequency generation.

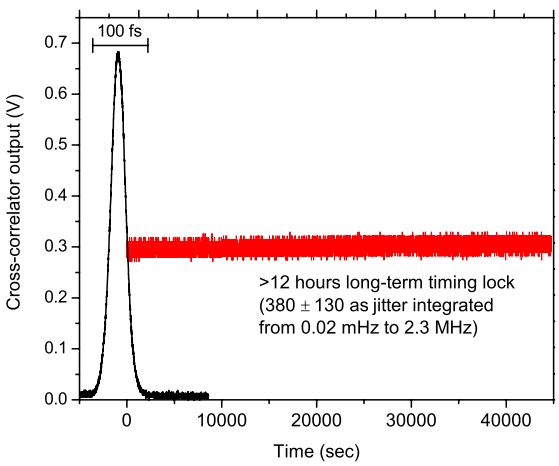

Figure 5: Long-term optical-to-optical synchronization result between Ti:sapphire and Cr:forsterite lasers. Drift-free sub-femtosecond synchronization over 12 hours were measured.

correlation trace when two lasers are not locked. The red line shows the cross-correlation trace when two lasers are locked adjacent to each other so that timing fluctuations are transferred into intensity fluctuations in the cross-correlation signal [16]. The pulse trains from the two lasers are locked with 380 attoseconds rms timing jitter over 12 hours without thermal drift in the bandwidth from 0.02 mHz to 2.3 MHz. Note that the duration of 12 hours does not constitute a limit to the locking scheme but was merely the duration of the experiment. In principle, as long as the lasers stay mode-locked, the timing lock can be maintained if the mechanical perturbations to the system are below a certain threshold value.

CONCLUSION

In summary, we reported on the progress toward a long-term stable and scalable timing distribution and synchronization system for future accelerator and seeded x-ray free electron laser facilities proposed in Ref. [1]. In particular, we demonstrated high-precision optical-to-RF and optical-to-optical synchronization techniques. We proposed and demonstrated the use of a balanced optical-microwave phase detector and balanced optical cross-correlator. By use of optical techniques, we could achieve a long-term femtosecond and sub-femtosecond accuracies which was not achievable with conventional pure RF-techniques.

REFERENCES

[1] J. Kim, F. Ö. Ilday, F. X. Kärtner, O. D. Mücke, M. H. Perrott, W. S. Graves, D. E. Moncton, T. Zwart, "Large-Scale Timing Distribution and RF-Synchronization for FEL Facilities," Proceedings of Free Electron Laser Conference 2004, p. 329, August 2004.

[2] G. Lenz, K. Tamura, H. A. Haus and E. P. Ippen, Opt. Lett. **20**, 1289 (1995).

[3] F. Ö. Ilday, J. R. Buckley, H. Lim, F. W. Wise and W. G. Clark, Opt. Lett. **28**, 1365 (2003).

[4] J. B. Schlager, B. E. Callicoatt, R. P. Mirin, N. A. Sanford, D. J. Jones and J. Ye, Opt. Lett. **28**, 2411 (2003).

[5] S. C. Zeller, L. Krainer, G. J. Spuhler, R. Paschotta, M. Golling, D. Ebling, K. J. Weingarten and U. Keller, Electron. Lett. **40**, 875 (2004).

[6] S. Namiki and H. A. Haus, IEEE J. Quantum Electron. **33**, 649 (1997).

[7] A. Winter, P. Schmüsser, H. Schlarb, F. Ö. Ilday, J. Kim, J. Chen, F. X. Kärtner, D. Cheever, T. Zwart, D. Wang, "High-Precision Optical Synchronization Systems for X-Ray Free Electron Lasers," Proceedings of Free Electron Laser 2005, p. 676, August 2005.

[8] F. X. Kärtner, F. Ö. Ilday, J. Kim, A. Winter, F. Grawert, H. Byun, J. Chen, "Progress in Large-Scale Femtosecond Timing Distribution and RF-Synchronization," Proceedings of 2005 Particle Accelerator Conference, p. 284, May 2005.

[9] J. Ye, J. Peng, R.J. Jones, K.W. Holman, J.L. Hall, D.J. Jones, S.A. Diddams, J. Kitching, S. Bize, J.C. Bergquist, L.W. Hollberg, L. Robertsson, and L. Ma, J. Opt. Soc. Am. B **20**, 1459 (2003).

[10] K. W. Holman, D. J. Jones, D. D. Hudson, J. Ye, Opt. Lett. **29**, 1554 (2004).

[11] D. D. Hudson, S. M. Foreman, S. T. Cundiff and J. Ye, Opt. Lett. **31**, 1951 (2006).

[12] T. R. Schibli, J. Kim, O. Kuzucu, J. Gopinath, S. N. Tandon, G. S. Petrich, L. A. Kolodziejski, J. G. Fujimoto, E. P. Ippen, and F. X. Kärtner, Opt. Lett. **28**, 947 (2003).

[13] E. N. Ivanov, S. A. Diddams and L. Hollberg, IEEE J. Sel. Top. Quantum Electron. **9**, 1059 (2003).

[14] A. Bartels, S. A. Diddams, C. W. Oates, G. Wilpers, J. C. Bergquist, W. H. Oskay and L. Hollberg, Opt. Lett. **30**, 667 (2005).

[15] J. Kim, F. X. Kärtner, and M. H. Perrott, Opt. Lett. **29**, 2076 (2004).

[16] R. K. Shelton, S. M. Foreman, L. Ma, J. L. Hall, H. C. Kapteyn, M. M. Murnane, M. Notcutt and J. Ye, Opt. Lett. **27**, 312 (2002).

CROSS-CORRELATION BETWEEN A VUV-FEL AND AN OPTICAL LASER

Theophilos Maltezopoulos, Ulrike Fruehling, Elke Plönjes, DESY, Hamburg;
Markus Drescher, Roland Kalms, Maria Krikunova, Marek Wieland, Uni HH, Hamburg;
Stefan Cunovic, Norbert Müller, Universität Bielefeld, Bielefeld

Abstract

At the Free Electron Laser in Hamburg (FLASH) a synchronized 800 nm optical laser is available for time-resolved VUV/vis pump-probe experiments. We crossed both femtosecond pulses in a Kr gas target and imaged the created photoelectrons with an energy-dispersive electron spectrometer. In the region where both pulses overlap in space and time, the photoelectrons are energetically shifted and form spectral sidebands. The imaging electron spectrometer projects the spectral- into an intensity modulation, thus, mapping time into space. This way, the technique delivers information about the relative timing between VUV- and visible pulse and is non invasive for both pulses. While observation of the cross-correlation signal currently requires data-averaging, with proper focussing single shot capability shall be reached, thereby enabling pulse-to-pulse jitter measurements.

PAPER NOT AVAILABLE

INVERSE FREE ELECTRON LASERS FOR ADVANCED LIGHT SOURCES

P. Musumeci, F. Germoni, M. Serluca, M. Mattioli
INFN-Roma1, P.le Aldo Moro 2, 00100, Rome, Italy.

Abstract

Laser accelerators hold the promise for high gradient acceleration and production of ultra short electron bunches. Among these, the inverse free-electron laser has recently demonstrated to be a mature and reliable scheme ready to step up from successful proof-of-principle experiments to cutting-edge applications. The very high gradient and the multi kAmp peak current of the output beam make it an attractive option in the hundreds of MeV to few GeV energy region. We examine the feasibility of using an IFEL driven by an high power Ti:Sa laser source to generate soft x-rays by FEL interaction in an undulator. A control of the slippage of the radiation over the ultrashort spikes of the IFEL-microbunched beam current is implemented to increase the gain and maintain the 200 as-long pulse structure in the radiation profile.

INTRODUCTION

While the wall plug efficiency of laser based accelerators still falls short of the requirements needed to cost-effectively build a high energy physics linear collider, high-gradient, short-wavelength advanced accelerator schemes are an attractive option to produce electron beams suitable to drive 4th generation x-ray lasers where one can choose peak brightness over average brightness. The small transverse emittances and high peak currents of current conventional radiofrequency based designs [1, 2] are within the reach of advanced state-of-the-art laser based accelerators. The requirements on the beam relative energy spread (less than few thousandths) could be tougher to satisfy but the progress in the experimental results in these last few years [3] brings closer to reality an advanced accelerator driven x-ray laser with an attractive reduction of the footprint and henceforth of the costs of such machines.

Among the various advanced accelerator schemes, the inverse free-electron laser (IFEL) is one of the most promising and well understood in terms of control of longitudinal phase space, trapping efficiency and final energy spread [4]. Using a high power laser and a properly designed undulator the IFEL has recently demonstrated accelerating gradients superior to conventional rf accelerators and very high energy gains [5]. Moreover, the IFEL is a far-field vacuum acceleration scheme which preserves the beam emittance through acceleration and it is in principle free of optics damage threshold limitations. Finally, the energy transfer mechanism, just the inverse of the well known FEL principle at the basis of the last generation light source facilities, is very efficient and one can design undulators able to transfer more than 75 % of optical power to beam power [6]. The final efficiency is in fact only limited by the wall-plug to optical conversion efficiency which for common high power laser systems is still quite low (below 1 %).

Even though many limitations arise when one considers the IFEL for multi-GeV energies mostly due to the synchrotron radiation losses from the wiggling electron trajectories, the tremendous progress and commercial availability of ultrahigh power laser sources makes the IFEL scheme a very feasible and convenient choice in the hundreds of MeV to few GeV energy, which is just the energy region for x-ray FEL drivers.

The detailed control over the electron beam longitudinal phase space obtainable with the interaction of a powerful laser and relativistic electrons passing through an undulator has already captured the interest of FEL physicists. In fact the IFEL mechanism in its not-accelerating prebunching version has been already proposed to be used at LCLS to enhance the SASE characteristics (ESASE). The short high current spikes obtained converting the IFEL-induced energy modulation into density modulation at the scale of the optical wavelength are foreseen to shorten the undulator distance needed to reach saturation and to produce sub femtosecond X-ray pulses [7].

In this paper we conjugate the advantages of using an IFEL as a prebuncher with its high gradient capabilities to design a soft X-ray source based on an IFEL accelerator. The design aims at producing coherent radiation in the so called water window region of the electromagnetic spectrum (λ = 3-4 nm) and it is tailored on the SPARC linac which is a state-of-the-art injector delivering a high brightness electron beam at 200 MeV energy in its final stage of construction at Frascati [8].

IFEL DESIGN

In Table 1 we report the input parameters considered for the IFEL design.

The electron beam input parameters like energy, energy spread and peak current are the nominal values of the SPARC linac [9]. In this design exercise we have considered to use a portion (20 TW out of 100 TW) of the high power laser foreseen to be installed in the same experimental area of the high brightness injector [10]. The ratio between the laser rayleigh range and the undulator length has been set to maximize the integrated gradient and so the final energy gain [11]. The choice for the IFEL coupling is

Table 1: IFEL input parameters

parameter	fixed value
Energy	210 MeV
Energy spread	0.5 %
Current	1 kA
Wavelength	800 nm
Peak Power	20 TW
Wiggler length	2 m
wiggler gap	7 mm
Rayleigh range	0.2 m
Waist position	1 m

a permanent magnet helical undulator. The particle transverse velocity is always different than zero and parallel to the electric field of a circularly polarized laser (easily obtainable from a linearly polarized pulse, using a high power quarterwave plate) so that the energy transfer mechanism between photons and electrons is always turned on. The undulator gap is set to 7 mm in order to be able to propagate without clipping along the undulator length both the laser and the electron beam. To ensure feasibility of the undulator construction, the Halbach relation

$$B_{max} = 1.79e^{-\lambda_w/g}[Tesla] \quad (1)$$

which yields the maximum attainable magnetic field amplitude for a given gap g and period λ_w has been used as an upper bound for the magnetic field. [12]. The optimized variations for period and field amplitude are reported in Fig. 1a. The resulting resonant energy

$$\gamma_r = \sqrt{\frac{\lambda_w(1+K^2)}{2\lambda}} \quad (2)$$

along the helical undulator is also shown (Fig. 1b). In (2) K is the normalized peak magnetic field amplitude and λ is the driving laser wavelength.

In order to guarantee an high quality final longitudinal phase space for the accelerated beam the ponderomotive resonant phase is varied along the undulator. In Fig. 2 we show the longitudinal phase space and its projection on the energy and time axis obtained tracking particles through the undulator and laser electromagnetic fields with the 3D IFEL code TREDI[13]. At the beginning the resonant phase is close to zero to improve capture efficiency while later in the undulator after the particles have been already captured and bunched its value grows to $\pi/3$ to maximize the accelerating gradient and reduce the final energy spread. The latter in particular is one of the most sensitive parameters for a 4th generation light source driver. The stable accelerating region of phasespace formed by the ponderomotive IFEL potential ensures that small variations in driving laser power and time/spatial jitter only affect the capture efficiency reducing slightly the final peak current and not the other parameters of the accelerator like final energy and

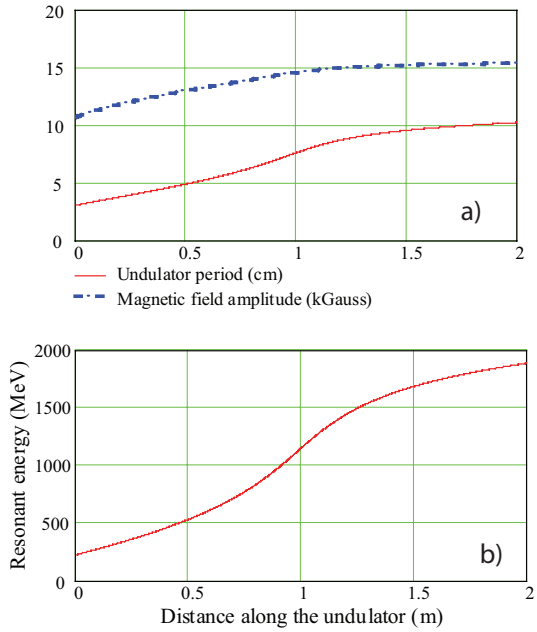

Figure 1: Variation of period and magnetic field amplitude along the undulator (a). The resonant energy is also shown (b).

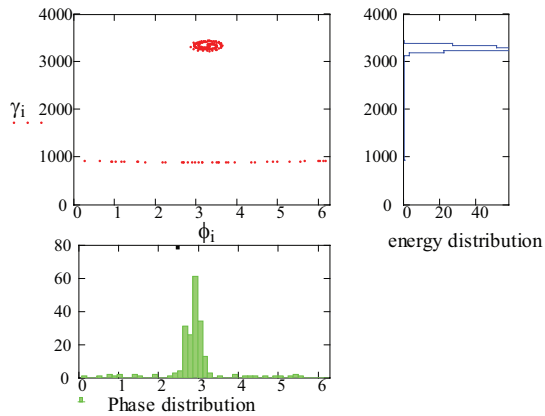

Figure 2: Simulated longitudinal phase space of the electron beam at the exit of the IFEL accelerator.

energy spread [13]. The output accelerator parameters are summarized in Table 2.

The average gradient obtained in this design is quite large, more than one order of magnitude larger than conventional rf-based designs. A length of just 2 m of undulator is sufficient to reach an energy of 1.5 GeV suitable to drive a x-ray laser at the water window wavelength (3 nm) which is the goal of our design exercise. The high peak current results from the bunching at the optical wavelength that takes place in the IFEL (see Fig. 3).

SLIPPAGE DOMINATED FEL

The undulator magnet envisioned to be used to generate the soft x-ray radiation is the same of the one being built

Table 2: IFEL output parameters

Energy	1.7 GeV
Energy spread	$< 0.5\,\%$
microbunch length	250 as
Peak current	6 kAmp
Avg. gradient	750 MeV/m

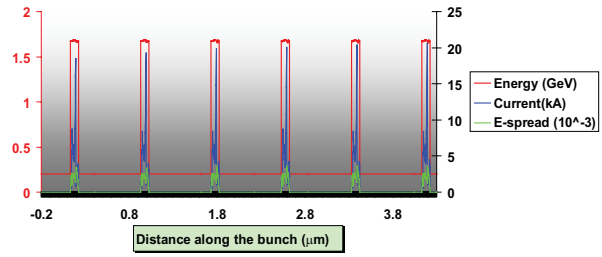

Figure 3: Electron beam current along the bunch. The current spikes are very short (250 as) and distant an optical period 2 fs between eachother.

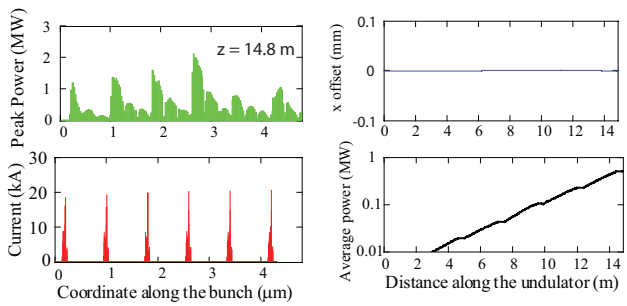

Figure 4: Output of the SASE simulation.

and installed for the SPARC project. The FEL parameters are reported in Table 3.

Start-to-end simulations of the entire system are performed using the output phase space from TREDI as the starting distribution in Genesis 1.3 [14]. Even though the physical mechanism of the interaction is the same along the system, it is required to use a different code to model the IFEL interaction since due to the strong tapering the period-averaged classical FEL approximation is not valid anymore, and the explicit 3d Lorentz-force equation solver is used for the particle dynamics in the simulation of the IFEL with TREDI. At the same time for the light generation section of the system, TREDI does not take into account the evolution of the electromagnetic field which has to be calculated using Genesis. The longitudinal phase space is periodic with period equal to the driving laser wavelength. The FEL simulation is performed over a window including a portion of the accelerated beam of a length such to include 6 to 8 periods of 800 nm. In Fig. 3 we show the beam parameters along the electron bunch coordinate inside the simulation window. The energy spread at the peak of the current is almost as large as the FEL ρ parameter and this degrades the interaction. Further work is needed in the optimization of the last section of the IFEL accelerator in order to minimize this effect.

The Genesis simulation result is shown in Fig. 4. The final peak power is limited to only few MW and in the longitudinal profile of the newborn radiation there is no trace of the attractive sub-fs structure of the incoming electron beam.

To explain these results, we must keep in mind that the the duration of the current spikes is only 1/10th of the optical wavelength, that is 250 attoseconds or ~ 90 nm. Considering the fact that in the undulator the radiation slips one radiation wavelength each undulator period, after only 30 periods of undulator the radiation has slipped over the peak

Table 3: FEL parameters

Radiation wavelength	3 nm
Undulator period	2.8 cm
Undulator K	1.65
Periods per section	77
Number of sections	6
ρ parameter	$4.5 \cdot 10^{-3}$

of its gain medium. An FEL driven by such beam would operate in a strongly slippage dominated regime. Clearly the problem is reduced if the IFEL accelerates the electron beam to higher energies enabling the production of shorter wavelength radiation. In this case in fact the length of each current spike would be the same, being fixed by the IFEL driver wavelength) and the shorter wavelength FEL radiation would experience a high gain for a larger number of undulator periods before slipping away of the high peak current region. Unfortunately the IFEL accelerator design gets more complicate for higher final energies since it requires a larger laser power and it also involves staging of two different IFEL modules. Moreover the planned extension of the SPARC photoinjector, SPARX [15], is foreseen to deliver coherent soft X-rays and user and diagnostics availability make attractive the few nm region of the electromagnetic spectrum.

One possible solution to the slippage problem is to take advantage of the microbunch train structure of the electron beam. In principle one could retard the charged particles inserting a magnetic path length between different undulator sections so that the radiation would slip faster over the electrons and take over the next high current spike at the beginning of the next undulator section. A cartoon illustration of this scheme is shown in Fig. 5. The advantage in this configuration is twofold: i) the FEL radiation only experience high gain and is amplified over the entire undulator length and ii) the magnetic chicane inserted to delay the electrons between undulator sections is a positive R_{56} element which helps the conversion of energy modulation into

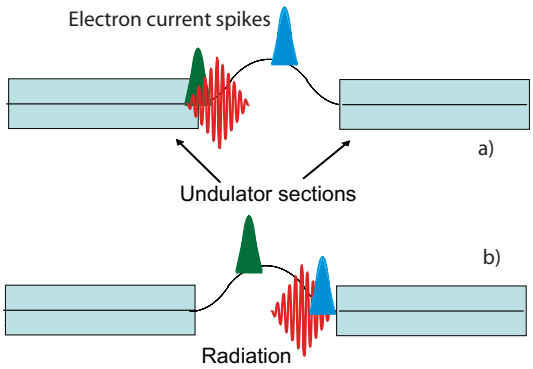

Figure 5: Schematics of chicane to compensate slippage inserted between undulator sections.

density modulation and so accelerates the microbunching process enhancing the FEL instability in a optical-klystron like configuration [16].

Without a coherent seed over all the electron bunch, on the other hand, the enhancement of the FEL interaction will not take place since the phase of the electromagnetic field and of the induced bunching starting in the different high gain high current regions is completely random being determined by the shot-noise in the electron beam. Suitable seeds at these short wavelengths are of course lacking at this time, but the strong progress in high harmonic generation in gas [17] could help in this regard. In Fig. 6 we show the results of the GENESIS simulation obtained introducing a coherent seed over the entire macrobunch length so that there is a definite phase relationship between the radiation and the bunching in the different current spikes and the FEL interaction can start constructively at the beginning of each undulator section. In the upper right corner the x-trajectory of the electron beam is represented. The bumps represent the magnetic chicanes located in between different undulator sections. The final peak power is > 1 GW and the radiation is composed by a train of sub-fs spikes locked with the 800 nm IFEL drive laser phase.

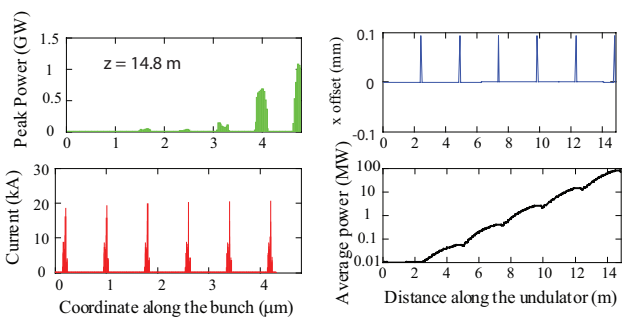

Figure 6: Output of the GENESIS1.3 simulation with a seed and with the magnetic chicanes between the undulator sections.

CONCLUSIONS

We propose the use of an inverse free electron laser to drive a 4th generation light source in the soft X-ray region of the electromagnetic spectrum. Taking advantage of the high gradient and of the precise control over the longitudinal electron beam phase space, the inverse free electron laser accelerator delivers a high current, high energy electron beam. The sub-fs structure on the current induces strong limitations due to the slippage on the FEL dynamics. If one wants to preserve the structure and increase the final power, some special precautions have to be taken. It is worthwhile to note that even if in this paper we considered the inverse free-electron laser as the advanced accelerator scheme to generate the electron beam, a similar output beam structure is likely to be found using other laser and/or plasma based accelerators. The considerations and the solutions discussed here are applicable to those cases also. Another benefit of the proposed laser driven source is the synchronization and phase-locking of the x-ray pulse with an external high power laser for pump-probe experiments.

REFERENCES

[1] J. Galayda et al. Linac Coherent Light Source Conceptual Design Report, SLAC-R-593, 2002.

[2] TESLA Technical Design Report TESLA-FEL-2002-9, DESY-2002-167, 2002.

[3] C. G. R. Geddes et al. *Nature*, 431:538, 2004.

[4] W. Kimura et al. *Phys. Rev. Lett.*, 92:054801, 2004.

[5] P. Musumeci et al. *Phys. Rev. Lett.*, 94:154801, 2005.

[6] P. Musumeci. *Proc. of 2006 Advanced Accelerator Concepts, Lake Geneva, WI*, 2006.

[7] A. A. Zholents and W. M. Fawley. *Phys. Rev. Lett.*, 92:224801, 2004.

[8] M. Bellaveglia. In *these proceedings*, 2006.

[9] D. Alesini et al. *Nuclear Instruments and Methods in Physics Research A*, 507:345, 2003.

[10] L. Serafini et al. In *Proc. of 2006 EPAC Conference*, 2006.

[11] W. Kimura et al. In *AIP Conf. Proc.*, volume 737, page 251, 2004.

[12] K. Halbach. *Journal de Physique*, C1:211, 1983.

[13] P. Musumeci et al. In *Proc. of 2001 Particle Accelerator Conference, Chicago, Illinois*, page 4008, 2001.

[14] S. Reiche. *Nuclear Instruments and Methods in Physics Research A*, 429:243–248, 1999.

[15] C. Vaccarezza et al. In *Proc. of 2006 EPAC Conference, Edinburh, Scotland*, 2006.

[16] Y. Ding et al. *PRSTAB*, 9:070702, 2006.

[17] J. Seres et al. *Nature*, 433:596, 2005.

TECHNICAL ASPECTS OF THE INTEGRATION OF THE OPTICAL REPLICA SYNTHESISER FOR THE DIAGNOSTICS OF ULTRA-SHORT BUNCHES INTO FLASH AT DESY*

P. van der Meulen, N. Javahiraly, M. Larsson, Department of Physics, AlbaNova, Stockholm University, Stockholm, Sweden
V. Ziemann, Department of Nulcear and Particle Physics, Uppsala University, Uppsala, Sweden
H. Schlarb, A. Winter, E. Saldin, E. Schneidmiller, M. Yurkov, DESY, Hamburg, Germany.

Abstract

In this paper we present an overview of current status of the Optical Replica Synthesiser at DESY. The method is based on producing an "optical copy" of the electron bunch with its subsequent analysis with optical techniques [1]. To this end, a near-IR laser beam is superimposed on the electron beam in the first undulated of an optical klystron. In the following dispersive section the laser-induced energy modulation is transformed into a density modulation. The modulated electron bunch then produces a strong optical pulse in the second undulator. Analysis of this near-IR pulse (the optical copy) then provides information about the profile, the slice emittance and the slice energy spread of the electron bunch. We discuss the implementation of such a measurement set-up at the FLASH facility at DESY and investigate the influence of various parameters on the performance of the device. Topics we address include the dispersive chicane, as well as the requirements for the seed laser pulses and the detection and analysis of the near-IR pulse.

INTRODUCTION

Monitoring and tuning the bunch properties are essential for the reliable operation of linac-based SASE free-electron lasers such as FLASH [2], XFEL [3], and LCLS [4]. This need has triggered the development of new diagnostic methods based on a transversely deflecting cavity [5] or electro-optical sampling [6]. The Optical Replica Synthesiser (ORS), a complementary scheme that was introduced in reference 1, is similar to an optical klystron FEL seeded by an infrared laser as is shown in figure 1. In the modulator the interaction of the laser with the transversely oscillating electrons causes an energy modulation. A dispersive section turns this energy modulation into a density modulation at the wavelength of the light. In a following radiator undulator the micro-bunched beam radiates coherently and the emitted light pulse has the same longitudinal profile as the electron beam. Hence the name optical replica synthesiser.

The optical replica pulse is analysed in a FROG (frequency resolved optical gating) device [7], which is based on recording the spectrally resolved signal of the auto-correlation. Subsequent application of a pulse retrieval algorithm reveals both amplitude and phase of the incident electric field and thus of the longitudinal profile of the electron bunch. A very compact second harmonic FROG device, Grenouille [8], which performs the analysis, is available commercially.

Following up on the signing of a letter of intent by DESY and the vice-chancellors of three Swedish universities in Uppsala and Stockholm the recently established SU-KTH-UU Free Electron Laser Centre has entered a collaboration with DESY to design and implement a prototype of the ORS in FLASH in order to establish the feasibility of the device for the X-FEL. In this note we present the status of the project as of August 2006.

SPACE AND TIME

The ORS will be installed in the beam line of FLASH between the collimating dog-leg and the VUV-undulator. The seed laser will be coupled in into the beam line just downstream of the dog-leg where a vacuum window is available. The modulator will be located about 10 m downstream of the vacuum window. The magnets will fit into 1.5m long unoccupied sections between quadrupoles and other equipment and the magnet gap of 40mm is sufficiently large to allow installation without modifying the existing beam pipe. The chicane consisting of four standard dipole magnets will also fit in between consecutive quadrupoles and can be mounted without breaking the vacuum. The housing of the extraction coupling mirror and some extra diagnostic for beam size measurements and alignment of laser and electron beam will require some vacuum intervention.

The distance between the modulator and the radiator will be on the order of 15m and it should indeed be short, because collective effects such a plasma oscillations [9] perturb the micro-bunching, caused by modulator, before it can generate the optical replica pulse in the radiator. The replica pulse in this case would not be a faithful replica of the electron bunch profile.

The laser system will be placed outside the linac tunnel with the shortest possible laser transfer line. For that an additional tunnel into the beam-tunnel will be drilled near the dog-leg. The installation of the ORS in the beam line is foreseen for a shutdown during spring 2007 which will be followed by commissioning and operating until the self-seeding option for FLASH will be installed in the beam line between the collimating dog-leg and the undulator.

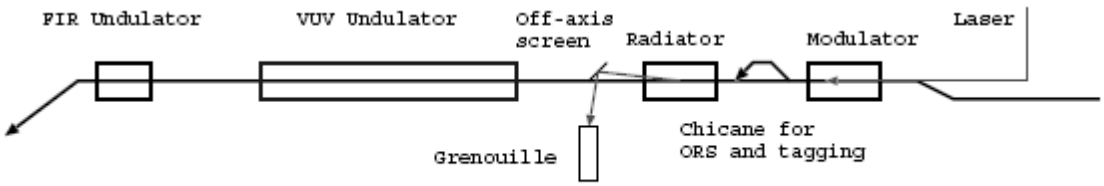

Figure 1: Schematic view of the Optical Replica Synthesiser.

SEED LASER

The seed laser will be based on an 1550 nm Erbium fiber oscillator that can be synchronised to the RF system of the linear accelerator. This oscillator has recently been constructed and the first, preliminary tests show that it is functioning properly. Stable mode locking is achieved and the pulse has the desired characteristics regarding pulse energy and spectral width. A schematic diagram of the Erbium fiber laser is shown in figure 2. As a next step the pulses will be compressed and frequency doubled. Subsequently the active synchronisation will be implemented and its effect on the laser operation will be tested.

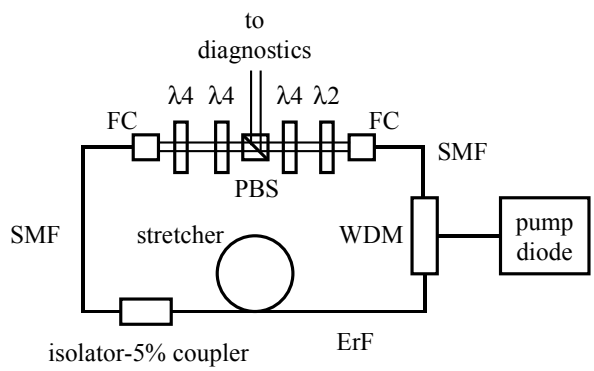

Figure 2: Schematic view of the Erbium fiber oscillator. FC: fiber coupler; SMF: single mode fiber; ErF: Erbium doped fiber, PBS: polarising beam splitter, WDM: wavelength division multiplexer, λ4: quarter lambda plate, λ2: half lambda plate.

As an amplifier we will use an existing Clark-MXR CPA2001 Ti:Sapphire laser from Stockholm University. The interfacing of the home-built oscillator and the amplifier will start soon. The choice for this amplifier is mainly motivated by budgetary reasons, as the CPA2001 is a highly compact laser system that is not easily adapted to this particular application. On the other hand, it has performed very reliably in our lab, with little maintenance and without major malfunctions for many years. The doubled output pulses of the Erbium fiber oscillator will be stretched before injection into the Ti:Sapphire amplifier cavity. We will attempt to use the stretcher currently installed inside the CPA2001. This means that we will have to separate the two layers of the CPA2001 in order to gain access to the lower level. No modifications of the amplifier cavity or the compressor are envisaged and only slight changes of control electronics are necessary, predominantly in the Pockels cell driver. The normal operating frequency of the CPA2001 is 1 kHz, but it can easily be reduced to 1-10 Hz to match the frequency of FLASH.

A seed laser intensity of about 4.5 GW/cm^2 is necessary to achieve required energy modulation of the electron bunch in a five period modulator undulator [1]. If we account for reflection losses during transport, the estimated maximum pulse energy of the modified CPA2001 laser system will be approximately 700 μJ inside the accelerator vacuum tube. The pulse length will be set to about 2 ps to attain a stable temporal overlap between the laser pulse and the electron bunch. This is achieved by deliberately misaligning the compressor of the CPA2001. The resulting longitudinal chirp on the laser pulse is not expected to influence the operation of the ORS significantly.

In order to estimate the beam diameter inside the modulator undulator we have performed a straightforward calculation using Gaussian optics. The results of this calculation, in which the beam is focussed by a Galilean telescope consisting of two achromatic lenses with focal lengths of 1.0 m and -0.8 m separated by 0.26 m, are shown in figure 3. The beam from the CPA2001 was assumed to be diffraction limited with an initial diameter of 6 mm (FWHM). From figure 3 we can see that a beam diameter of about 0.8 mm (FWHM) can be expected at the position of the modulator undulator located about 10 m downstream from the second telescope lens. This leads to a laser peak intensity of about 45 GW/cm^2 a factor of ten in excess compared to what should be required. A more realistic simulation that takes into account the transversal mode structure of the femtosecond pulses is under way using commercial beam propagation software. This simulation will also address the transport form the CPA2001 laser system to the focussing telescope.

In principle even higher laser intensities could be reached by focussing tighter, but here we are limited by the requirement that the intensity is essentially constant over the entire length (ca. 1.5 m) of the modulator and by the dimensions of the input vacuum window (16 mm diameter). Furthermore, the laser beam should easily accommodate the whole electron bunch, which has a diameter of 0.1-0.2 mm (FWHM), even while it is performing its oscillatory motion in the modulator, and by making the diameter of the seed laser beam too small we

may simply become too sensitive to the pointing stability of the laser system. In any case, the distance between the laser and the modulator is so large that probably active beam position stabilisers are required to maintain spatial overlap between the laser and the electron beam for extended periods of time. Existing beam position monitors and screens will be used to monitor the spatial overlap between the laser and the electron beams. Diagnostic stations to monitor the laser before the vacuum window as well as after the radiator undulator are foreseen, but not yet finalised.

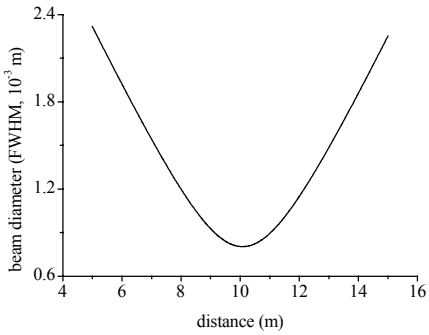

Figure 3: Seed laser beam diameter as a function of the distance to the focussing telescope showing a focus of 0.8 mm diameter (FWHM) inside the modulator.

One point of concern is the presence of a spatial chirp and / or a tilted wavefront on the CPA2001 seed laser pulse. At the moment it is not entirely clear how this will affect the detailed micro-bunching process or the subsequent analysis of the radiator pulse using the Grenouille FROG apparatus. We will perhaps be forced to take steps to correct the seed laser pulse for these imperfections.

UNDULATOR AND CHICANE

The undulators for the modulator and radiator with period l_0 and $K=93.4B_0l_0$ must fulfil the FEL resonance condition $\lambda=l_0(1+K^2/2)/2\gamma^2$ with an IR laser operating at λ = 780 nm and beam energies $E = \gamma mc^2$ between 500 and 1000 MeV. Together with the constraint to be shorter than 1.5 m we arrive at electromagnetic magnets that have 5 full periods plus two extra periods to zero the field-integrals with a period of 20 cm and a peak field B_0 below 0.5 T. In order to allow separating the high power seed laser from the weaker replica pulse by a polariser we will have one horizontal and one vertically polarised undulator. Both magnets are now ordered from Scanditronix in Sweden and will be delivered to DESY in spring 2007. The support structure for the undulators to move them in and out of the beam line will be designed by staff at DESY.

The standard steering dipoles with a peak excitation of $33x10^{-3}$ Tm are sufficient for chicane to provide an R_{56} of up to 0.3 mm. The transverse offset (ca. 10 mm) of the beam in the chicane can also be used to insert a mirror and extract a major portion of the seed laser pulse to avoid irradiating downstream equipment and disturbing the weak replica pulse.

LASER DIAGNOSTICS

Once the replica pulse is generated in the radiator undulator it has to be extracted from the beam pipe and transported to the diagnostic section with the Grenouille. Presently we are discussing several options to extract the light, either by pointing the radiator undulator at a downstream off-axis mirror. This option, however, would introduce significant wavefront distortion and is not favoured. In another option we add a second chicane downstream of the radiator with steering magnets to steer around an off axis screen. A third option would be to insert a mirror with a hole into the beam pipe such that the electron beam can pass the mirror, but the IR pulse is deflected out. These options will be scrutinised in the coming months.

The placement of the Grenouille either in the accelerator tunnel or in the new laser housing has not been decided yet. Placement of the Grenouille inside the tunnel has the advantage of a shorter beam path for the replica pulse as well as easier alignment and construction, but access to the tunnel during accelerator operation is impossible and parasitic operation without impeding other activities is, of course, much favoured.

CONCLUSIONS AND PROSPECTS

We have taken the first steps towards implementing the ORS in FLASH at DESY. Ordering the magnets which have a long lead time was the first major step and building the laser will be the next, together with solving all the other issues that we only mentioned in passing.

The infrastructure of lasers and undulators created for the ORS provides a fertile ground for further experiments with beams and lasers, especially regarding synchronisation. For example, using the FIR-undulator that will be installed downstream of the VUV-undulator as the radiator instead of the original radiator will allow to generate a coherent light pulse at the wavelength of the seeding laser close to the experimental hall where it can be cross-correlated with an external laser used for pump probe experiments. This will yield information about the relative timing of the external laser and the bunch arrival time, which also caused the VUV-pulse. In this way the relative timing between VUV-pulse and external laser can be determined.

Furthermore, passing the micro-bunched electron beam after the chicane through an optical transition radiation screen, will yield information about the bunching and this signal can be used for tuning.

REFERENCES

[1] E. Saldin, E. Schneidmiller, M. Yurkov, ``A simple method for the determination of the structure of ultrashort relativistic electron bunches,'' Nucl. Inst. and Methods A 539 (2005) 499.
[2] J. Rossbach, Nucl. Inst. Meth. A475 (2001) 13.
[3] P. Audebert, et.al., ``TESLA XFEL: The first stage of the X-ray laser laboratory - Technical Design Report,'' DESY 2002-167.
[4] The LCLS Design Study Group, ``LCLS Design Study Report'', SLAC-R-593, 2002.
[5] O. Grimm et al., ``Longitudinal bunch shape diagnostics with coherent radiation an a transverse deflecting cavity in TTF2", Proceedings of the 2004 FEL conference, 395.
[6] G. Berden, et al., ``Electro-Optic Technique with Improved Time Resolution for Real-Time, Nondestructive, Single-Shot Measurements of Femtosecond Electron Bunch Profiles,'' Phys. Rev. Lett. 93 (2004) 114802.
[7] R. Trebino, ``Frequency Resolved Optical Gating", Kluwer Academic, Boston, 2000.
[8] www.swanoptics.com
[9] G. Geloni, E. Saldin, E. Schneidmiller, M. Yurkov, ``Theory of space-charge waves on gradient-profile relativistic electron beam: An analysis in propagating eigenmodes,'' Nucl. Inst. and Methods A 554 (2005) 20.

INVESTIGATIONS OF THE LONGITUDINAL ELECTRON BUNCH STRUCTURE AT THE FLASH LINAC WITH A TRANSVERSE DEFLECTING RF-STRUCTURE

Michael Röhrs*, Christopher Gerth, Holger Schlarb
Deutsches Elektronen-Synchrotron DESY, D-22603 Hamburg, Germany.

Abstract

In the single-pass Free-Electron Laser FLASH, Self-Amplification of Spontaneous Emission (SASE) occurs in a small fraction of an electron bunch with a length in the order of micrometers. As a consequence, there is a need for bunch diagnostics with a time resolution in the femtosecond regime for understanding and improving the machine performance. At FLASH, a vertically deflecting structure (LOLA) is used to measure the longitudinal charge density profile and phase space distribution of single bunches with high time resolution. The horizontal slice emittance can be determined by additionally using quadrupole scan techiques. In this paper, we present results of measurements under conditions close to SASE operation at 13.7 nm. We reached a RMS resolution of 20 fs for the longitudinal profile measurements, and resolved the longitudinal phase space distribution and slice emittance with 50 fs and 60 fs, respectively. Strong indications for a substructure within the horizontal phase space distribution of the peak current region have been found.

INTRODUCTION

At the Free electron LASer in Hamburg (FLASH), electron bunches with peak currents of 1-3 kA are produced by longitudinal bunch compression in two magnetic chicanes. This results in a narrow high current region at the front of the bunch ("spike") with a width of less than 100 fs (FWHM) and a long trailing tail. The SASE process may be initiated within the spike, if transverse slice emittance and slice energy width are sufficiently small. However, these parameters are significantly degraded by coherent synchrotron radiation (CSR) effects in the dipoles of the magnetic chicanes, and by space charge forces along the linac. The SASE signal with a duration in the order of 10 fs suggests that only a fraction of the charge in the spike contributes to the lasing process. To resolve the longitudinal structure, bunch diagnostics with an appropriate time resolution is necessary.

The most powerful and multifunctional tools for this purpose are currently transverse deflecting rf-structures called LOLA [1, 2, 3]. LOLA structures operate in a hybrid mode (a superposition of a TM_{110} and a TE_{110} mode), which propagates with a phase velocity equal to the speed of light. A passing relativistic electron is subject to a deflecting force in vertical direction, which is independent of the transverse position of the electron within the structure and constant in time. The force sensitively depends on the phase of the fields at the arrival time due to a high frequency time variation at 2.856 GHz. Injection of a bunch at zero crossing of the deflecting force results in a shearing or "streaking" of the bunch without centroid deflection. As a consequence, the vertical positions of the bunch electrons downstream of the structure are linearly correlated with their longitudinal coordinates. Standard OTR screens then allow for measurements of the particle distribution in the longitudinal-horizontal plane. Alongside the measurement of the longitudinal charge density profile, this technique permits to determine the horizontal slice emittance by scanning quadrupoles upstream of LOLA [4]. Furthermore, the longitudinal phase space distribution can be obtained in a single shot measurement at locations with significant horizontal dispersion. An estimate for the time resolution is given by the vertical size of the bunches at the screen location without streak, i.e. with LOLA being switched off. Parameters of the LOLA structure are listed in Table 1 [3].

Table 1: Properties of LOLA [3]

Length	3.64 m
Frequency	2.856 GHz
Max. operating power	25 MW
Deflecting voltage at 20 MW	26 MV
Filling time	0.645 μs
Aperture	44.88 mm

EXPERIMENTAL SETUP

A schematic of the FLASH linac and the sections used for the measurements is shown in Fig. 1. Electron bunches are generated in an rf photocathode (gun) and accelerated in five superconducting modules ACC1 to ACC5. The bunches are longitudinally compressed in two magnetic chicanes BC2 and BC3 at energies of typically 127 MeV and 360 MeV, respectively. A dispersive section (dogleg) is used to collimate the beam before it enters the undulator section. For the presented measurements, the linac was operated with a bunch charge of 0.5 nC and a final energy of 677 MeV to produce a SASE signal at 13.7 nm wavelength. We obtained an average radiation energy of 5 μJ per electron bunch. The phase of module ACC1 was set to -7.6° from minimum energy width operation, which is 4.4 ° above the phase for maximum peak current (-12 °). The

* michael.roehrs@desy.de

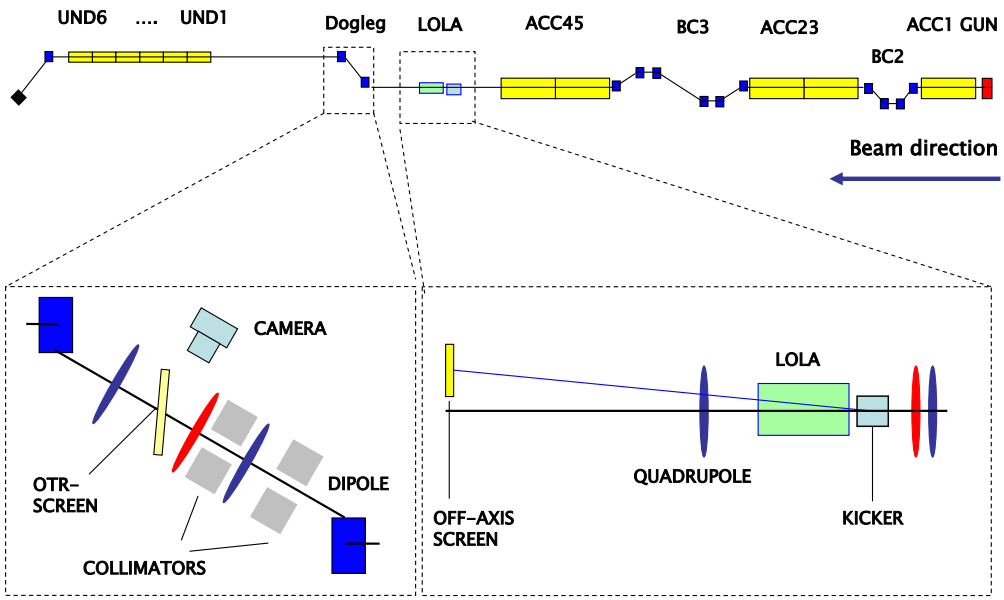

Figure 1: Schematic of the FLASH beamline and a zoom into the regions used for the measurements. Longitudinal profile and slice emittance have been measured on an off-axis screen (bottom right), the distribution in longitudinal phase space with a screen in the dogleg section (bottom left).

phases of modules ACC23 and ACC45 were set to -25° and 0°, respectively.

LOLA is located at the end of the linac. An off-axis screen with a hight of 17 mm has been used in combination with a horizontal kicker preceding LOLA to measure the longitudinal profiles. The time scale on the vertical axis of the screen has been calibrated by measuring the vertical bunch position while varying the phase of LOLA around zero crossing. The calibration constant or "streak strength" was 4.9 mm/ps in case of the density profile measurement. The input power of LOLA has been adjusted to observe entire bunches on the screen, including the long tails. In this way additional quantities may be infered, e.g. the charge portion within the spike, whereas the time resolution is slightly degraded. The horizontal slice emittance has been measured by varying quadrupoles upstream of LOLA. Several quadrupoles had to be scanned simultaneously in order to minimize the changes in time resolution (vertical beam size with LOLA switched off) while the phase advance in horizontal direction was varied.

An OTR screen in the horizontally dispersive dogleg section has been used for measuring the longitudinal phase space distribution. The dispersion generated by the upstream dipole has been determined to be 233 mm by measuring the horizontal beam position on the screen for different dipole currents.

Before the measurements, the optics downstream of BC3 had been modified in order to improve the resolution of the measurements. However, we expect only a negligible modification of the longitudinal bunch properties and the horizontal emittance. In case of longitudinal phase space measurements, also the optics upstream of BC3 had to be modified slightly, which may have altered CSR effects in the dipoles of BC3.

RESULTS

LONGITUDINAL PROFILE

Fig. 2 shows the measured longitudinal charge density profile of a single bunch. It consists of a sharp leading spike and a long tail. The width of the spike is ∼70 fs (FWHM). The time resolution is ∼50 fs FWHM and ∼20 fs RMS. The properties of the spike change slightly from bunch to bunch most likely due to phase and / or amplitude fluctuations of the first acccelerating module. An analysis for 100 successive bunches reveals a nearly gaussian-shaped distribution of the spike width with a mean of 74 fs and a sigma of 9 fs. The same applies to the charge in the spike defined by the coloured area in Fig. 2 and the corresponding current, which are 0.13 ± 0.01 nC (25 ± 1 % of the total bunch charge) and 1.7 ± 0.1 kA.

LONGITUDINAL PHASE SPACE

The particle distribution of a single bunch in longitudinal phase space, which is directly obtained from an OTR image of a streaked bunch in the dispersive dogleg section, is presented in Fig. 3 (top). It shows the expected overall

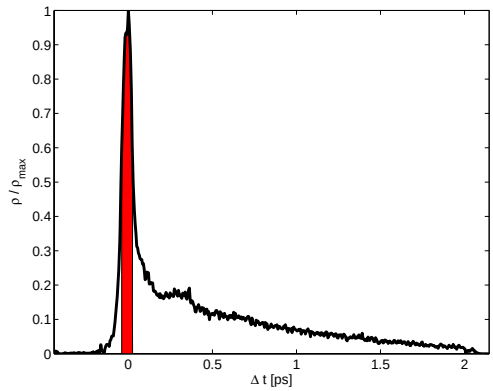

Figure 2: Normalized longitudinal charge density profile measured with LOLA. The width of the coloured region is equal to the width of the spike (FWHM). The specified charge fraction in the spike refers to this area.

correlation, which is characterized by a rapid energy variation at the head of the bunch leading to the observed sharp spike in the longitudinal profile, and an increasing energy along the tail due to off-crest acceleration. Within the high density region, there are deviations from the ideal shape in terms of spikes in time and energy direction. Tracking calculations with ASTRA [5] and CSR-Track [6] are in qualitative agreement with these results [7]. Some distinct distortion patterns are mostly related to longitudinal space charge (LSC) forces: On the way from BC3 to the screen, LSC causes an increase in energy width, which can clearly be seen in Fig. 3. The spike at the very front of the bunch in time direction is due to energy spread generated by LSC during the passage from BC2 to BC3, which is then sheared in longitudinal phase space in BC3.

The slice energy widths and the longitudinal density profile calculated from the measured phase space distribution are shown in the bottom plot in Fig. 3. The chosen slice widths is equal to the RMS resolution of 50 fs. The slice energy spread reaches a maximum value of $\sim$0.26 % or $\sim$1.8 MeV at the bunch head and decreases to $\sim$ 0.06 % ($\sim$406 keV) in the tail. Here, the values are limited by the residual transverse beam size without dispersion and provide an estimate for the energy resolution of the measurement.

The increase in energy width at the front is largely due to a non-gaussian energy distribution. Within this region, two local maxima of the energy profile can be observed (Fig. 4). This structure may arise from both, LSC and CSR, but we expect the LSC effects to be dominant. By dividing the phase space distribution between the two maxima as indicated by the dashed line in Fig. 4, the longitudinal density profile in the high current region can be considered seperately for the two regions, revealing a separation of the charge density maxima in time by $\sim$50 fs (see Fig. 4). It may be speculated that this is a true substructure of the spike in the longitudinal density profile, which could not be resolved here.

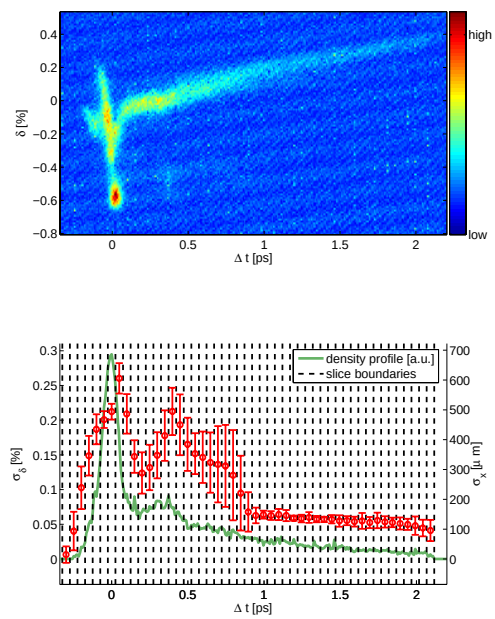

Figure 3: Longitudinal phase space distribution for a single bunch (top) and corresponding RMS slice energy width σ_δ (bottom). In the bottom image, the slice boundaries and the density profile are drawn in.

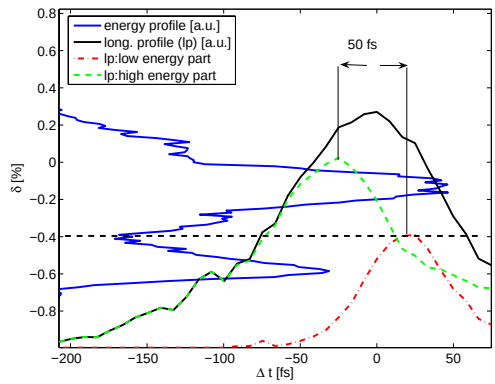

Figure 4: Projections of the longitudinal phase space distribution within the peak current region (Fig. 3) onto the time and energy axis. The longitudinal profile is splitted into two parts, as is indicated by the dashed horizontal line: The one for the low energy part and the one for the high energy part. The maximas of the profiles are seperated in time by $\sim$50 fs.

SLICE EMITTANCE

Figure (5) shows the measured horizontal 1σ slice emittance (normalized) along the bunch (bottom) with a resolution of 60 fs, and an OTR image of a bunch during the scan (top). Within the bunch tail the slice emittance ranges from 2 μrad to 3 μrad. There is a dramatic increase in slice emittance at the front of the bunch with a value of $\sim$16 μrad within the density spike, which is significantly larger than expected for SASE operation. Assuming an RMS energy

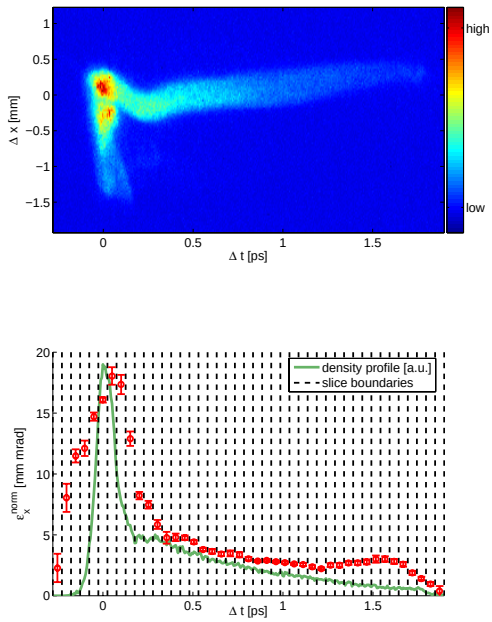

Figure 5: OTR image of a bunch during the quadrupole scan (top) and 1σ slice emittance along the bunch (bottom). In the bottom image, the slice boundaries and the density profile are drawn in.

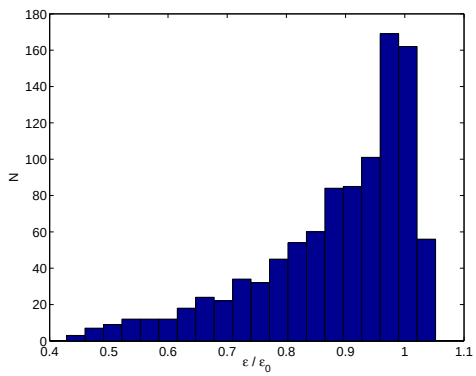

Figure 6: Result of a Monte Carlo simulation with 1000 seeds for the relative emittance error assuming 3 % peak to peak quadrupole gradient errors.

width of $\sim$0.2 % as measured in the spike, the emittance would have to be about $\sim$5 μrad to obtain the observed SASE power [8].

One contribution to this increase in slice emittance is due to a substructure in the horizontal profile of slices in the high current region. For certain quadrupole settings, two separate density maxima appear, as can be seen on the bunch image in Fig. 5. This suggests that there are two islands with high charge density in the horizontal phase space distribution, each for its own having a smaller emittance. Assuming that these density maxima correspond to the observed maxima in the energy profile of the head, the horizontal displacement of the two density maxima may be explained by dispersion in the order of 50 mm, which is a possible value at this location. The dispersion caused by the kicker amounts only to $\sim$10 mm and does therefore not explain this behaviour. In case CSR forces significantly contribute to the separation of the energy maxima, this would lead to a horizontal displacement as well. However, we have no proof yet that there is a connection between the observed structures in the energy profile and the horizontal profile.

Another contribution may come from a systematic error of the absolute emittance values. The accuracy is mainly determined by quadrupole gradient errors, since six quadrupoles have been used for the scan. Figure (6) shows the result of a Monte Carlo simulation for 3 % peak to peak errors of all quadrupole gradients (independently), which is a rather pessimistic assumption. The probability of having an error larger than 30 % is accordingly 15 %. The ratios of the given slice emittance values are not affected by gradient errors.

The shown results for the slice emittance suggest that a reasonable analysis of the emittance in the high current region can, at least for the time resolution given here, only be done by reconstructing the transverse phase space distribution. A main goal for the future is therefore to apply phase space tomography methods. Moreover, quantitative comparisons with simulations using ASTRA and CSR-Track will be done.

ACKNOWLEDGEMENTS

We would like to thank the FLASH team, in particular B. Faatz, M. Hüning and B. Beutner, for their support.

REFERENCES

[1] P. Emma *et al*, "A Transvers RF Deflecting Structure for Bunch Length and Phase Space Diagnostics", SLAC-PUB-8864, August 2000.

[2] M. Hüning *et al*,"Observation of femtosecond bunch length using a transverse deflecting structure", FEL Conference 2005, Stanford, August 2005.

[3] A. Bolzmann, "Investigations of the Longitudinal Charge Distribution of Electron Bunches at the VUV-FEL using the Tranverse Deflecting Cavity LOLA", Diploma thesis, Universität Würzburg,2005.

[4] M. Röhrs *at al*, "Measurement of Slice-Emittance using a Transvers Deflecting Structure", FEL Conference 2005, Stanford, August 2005.

[5] K. Flöttmann,"ASTRA - A Space ChargeTracking Algorithm" 2006, http://www.desy.de/ mpyflo/Astra dokumentation/

[6] M. Dohlus , "Two Methods for the calculation of CSR Fields", TESLA-FEL-2003-05.

[7] M. Dohlus, "Modelling of Space Charge and CSR Effects in Bunch Compression Systems", EPAC 2006, Edinburgh.

[8] B. Faatz, private communication.

A 3D MODEL OF THE 4GLS VUV-FEL CONCEPTUAL DESIGN INCLUDING IMPROVED MODELLING OF THE OPTICAL CAVITY

N. R. Thompson and D. J. Dunning, ASTeC, Daresbury Laboratory, Warrington WA4 4AD, UK*
B. W. J. M^{c}Neil, SUPA, University of Strathclyde, Glasgow G4 0NG, UK
J. G. Karssenberg, P. J. M. van der Slot and K.-J. Boller, Twente University, Enschede, Netherlands.

Abstract

The Conceptual Design Report (CDR) for the 4th Generation Light Source (4GLS) at Daresbury Laboratory in the UK was published in Spring 2006. The proposal includes a low-Q cavity (also called a regenerative amplifier) FEL to generate variably-polarised, temporally-coherent radiation in the photon energy range 3-10eV. A new simulation code has been developed that incorporates the 3D FEL code Genesis 1.3 and which simulates in 3D the optical components and radiation propagation within the non-amplifying sections of an optical cavity. This code is used to estimate the optimum low-Q cavity design and characterise the output from the 4GLS VUV-FEL.

INTRODUCTION

4GLS is a 4th Generation Light Source [1] proposed by CCLRC Daresbury Laboratory to meet the needs of the 'low photon energy' community. The Conceptual Design Report (CDR) was published in 2006 [2]. 4GLS will comprise synchrotron radiation sources, free-electron lasers and conventional lasers which will be combined synchronously to allow innovative pump-probe experiments.

A 600MeV high average current branch operating in energy recovery mode (80pC bunches at up to 1.3GHz) will feed spontaneous sources and a VUV-FEL. A 750-950MeV high peak current branch (1nC bunches at 1-10kHz) will feed a XUV-FEL[3]. There will also be an IR-FEL operating over 2.5–200μm.

This paper first summarises the VUV-FEL CDR design. The proposal is a low-Q cavity FEL, or Regenerative Amplifier FEL [4, 5], in which the high gain allows saturation to be reached in a few passes with mirrors of low reflectivity. It has been shown from 1D simulations [6] that the optimum outcoupling fraction is $\sim 75\%$ for mirrors of 60% reflectivity, using a hole for outcoupling. This fraction gives a near maximum output power but is a stable working point, such that the output power is relatively insensitive to small changes in outcoupling fraction or mirror reflectivity.

The next section presents 3D simulations of the CDR design, using Genesis 1.3 [7] and a new 3D optics simulation code developed at Twente University [8]. These simulations confirm the validity of the CDR design and the earlier 1D simulations which investigated the parameter space. The last section presents simulations to optimise the resonator.

* n.r.thompson@dl.ac.uk

Table 1: Baseline VUV-FEL parameters, as presented in the 4GLS CDR.

UNDULATOR	
Undulator Period λ_w	60 mm
Periods per module	37
Number of modules	5
ELECTRON BEAM	
Electron Beam Energy	600 MeV
Relative Energy Spread (rms)	0.1%
Bunch Charge	80 pC
Peak Current	300 A
Normalised emittance	2 mm-mrad
OPTICAL CAVITY	
Cavity length L_{cav}	34.6 m
Upstream ROC r_1	12.85 m
Downstream ROC r_2	22.75 m
Rayleigh length z_r	2.8 m
Fundamental mode waist w_0	0.34 mm
Waist position (measured from US mirror)	12.2 m
Outcoupling hole radius	2 mm
Cavity stability $g_1 \times g_2$	0.88

CDR PARAMETERS

The VUV-FEL will produce radiation of variable polarisation using APPLE-II undulator modules. The minimum gap is 10mm and the undulator period 60mm. The photon energy range 3–10eV is covered by gap tuning from 10–19mm in helical mode and 12–25mm in planar mode. For high enough gain for RAFEL operation, the undulator length, expressed in the universal scaling of [9], must give $\bar{z} \equiv 4\pi\rho N_u \geq 4$ over all wavelengths and polarisations. The required length is then 11m, achieved with five 2.2m modules of 37 periods. The intermodule gap is 0.6m to allow space for a quadrupole, BPM and phase matching unit. A FODO lattice is used with quadrupoles of length 0.12m and strength 9T/m. The electron beam parameters have been derived using the FEL design formulae of Ming Xie [10].

The resonator parameters are derived from simple assumptions, with the expectation they will be revised after 3D optics modelling. The fundamental cold cavity mode is focussed to maximise the overlap between radiation and electron beam over the first two undulator modules. This is done with a waist at the end of the first module, 12m from the upstream (US) mirror as shown in Fig.1. The *optimum* Rayleigh length z_R (for maximum overlap) is then approximately one third the total length of the two modules plus

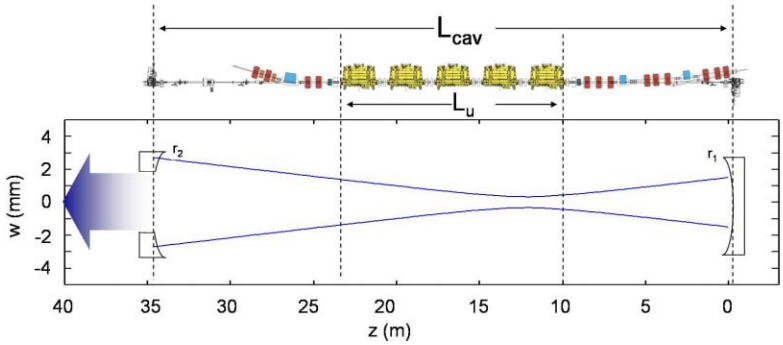

Figure 1: A schematic of the 4GLS VUV-FEL with the baseline CDR parameters. The fundamental cavity mode is shown on the same longitudinal scale as the engineering representation. The electron beam direction is right to left.

gap, i.e. around 1.7m. However, this z_R pushes the cavity geometry close to instability and gives an excessive spot size at the downstream mirror and some diffraction losses on the undulator aperture for the longer wavelengths. In addition the hole size on the downstream mirror is larger than the spot size of the spontaneous radiation emitted on the first pass and does not allow sufficient feedback. The Rayleigh length is therefore chosen so that the spot size of the fundamental cavity mode is the same as the estimated spot size of the spontaneous emission. This gives a Rayleigh length of 2.8m, somewhat larger than the value for maximum overlap.

The hole size is such that the outcoupling fraction of the fundamental cold cavity mode is 65%. This is slightly less than the optimum value (from 1D simulations) of 75% but the high gain FEL interaction is expected to guide the radiation reducing the spot size and increasing the outcoupling fraction towards its optimum value. The mirror material is protected aluminium with a reflectivity of 60% at 10eV. The CDR parameters are given in Table 1 and a schematic shown in Fig.1 where the fundamental cold cavity mode is shown on the same longitudinal scale as the machine layout.

3D SIMULATIONS

A new simulation code has been developed at Twente University that incorporates the 3D FEL code Genesis 1.3 and which simulates in 3D the optical components and radiation propagation within the non-amplifying sections of the optical cavity. Full details of the code are given elsewhere [8]. The code has been used to model the 4GLS VUV-FEL using Genesis 1.3 in steady-state mode. All the simulations presented here are for 10eV operation. Simulation results for 3eV will be presented in a later work.

Simulations of baseline design

The CDR parameters have been used for the initial simulations. The growth of output power and the measured outcoupling fraction, both as a function of pass number, are shown in Fig. 2. At saturation the output power is 350MW with a measured outcoupling fraction of 68%. The

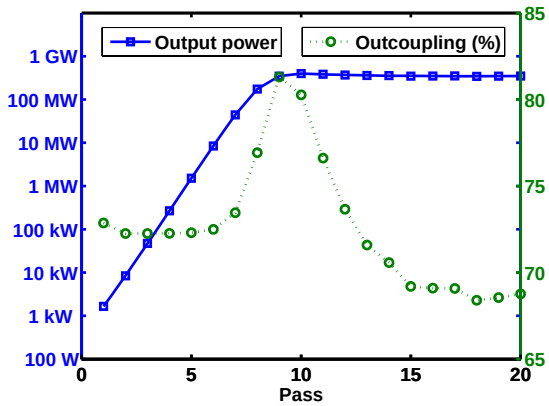

Figure 2: The growth of output power and the measured outcoupling fraction, both as a function of pass number, for the CDR parameters.

normalised power profiles at saturation, for different points within the optical cavity, are shown in Fig.3. A modal expansion algorithm is under development and will calculate the power distribution between the fundamental and higher order modes. It is clear however from Fig.3 that there is significant transverse HOM content in the radiation field. It is interesting to note that although the on-axis power of the radiation reflected from the downstream (DS) outcoupling mirror is zero, due to the large hole, by the time the radiation is reflected back off the upstream (US) mirror and back into the undulator the power is concentrated on-axis allowing good coupling with the electron beam for the next pass.

Cavity optimisation

Fig.4 shows the effect of varying the radius of the outcoupling hole and the mirror reflectivity on the output power after 20 passes (by which time the FEL has reached saturation for almost all parameter sets used here). The results show that the CDR working point (hole radius 2mm, reflectivity 60%) is satisfactory and stable—the output power is near optimum, yet small changes in hole size or reflectivity have a correspondingly small effect on the

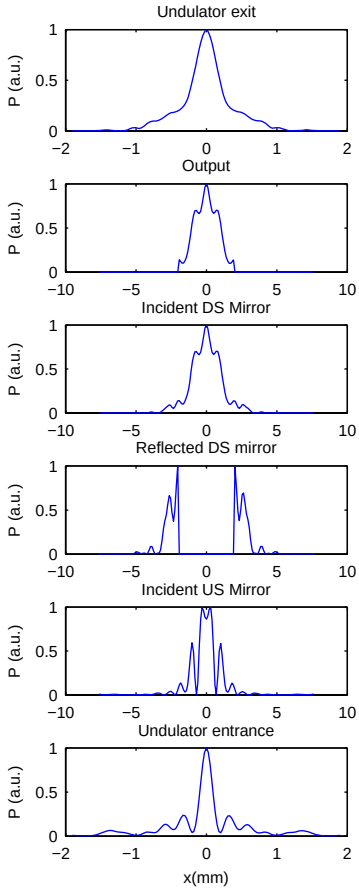

Figure 3: The normalised intensity cross sections at saturation, for different points within the optical cavity. The parameters are the CDR values (waist position 12 m, waist radius 0.34mm).

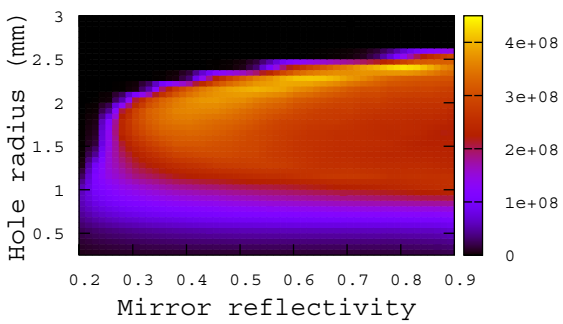

Figure 4: Output power (W) as a function of hole radius and mirror reflectivity. The CDR hole radius is 2mm and mirror reflectivity is 60%.

output power. In fact a reduction in reflectivity would cause a small increase in output power, as predicted by the earlier 1D simulations.

Different cavity configuration have been investigated by changing the ROC of the mirrors such that either waist size or waist position of the lowest order cold-cavity mode is kept constant and the other is varied. The dependence

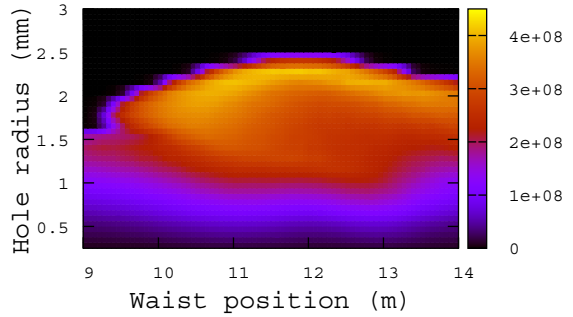

Figure 5: Output power (W) as a function of hole radius and waist position.

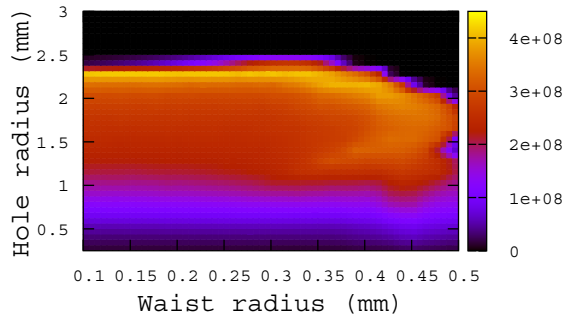

Figure 6: Output power (W) as a function of hole radius and waist size, for waist position 12.19m.

of the output power on hole radius and waist position is shown in Fig.5. It appears that moving the waist back 1m towards the undulator entrance (from 12m to 11m from the upstream mirror), i.e. to the centre of the first undulator module, gives a working point in a broader region of near maximum output power which would be beneficial.

The results of varying the waist radius from its CDR value of 0.34mm are shown in Fig.6 for a waist position of 12m where it is seen there is little dependence on waist radius even when the waist radius is 0.1mm which represents a cavity on the boundary of instability with $g_1 g_2 = 1.00$. Extensions of geometry into unstable resonator configurations will be investigated in the future. Similar results have been obtained for a waist position of 10.5m. These results demonstrate that considerations of cold cavity resonator modes are not very relevant to this design—the gain guiding of the high-gain FEL interaction strongly dominates.

This interpretation is supported by simulations investigating the effect of changes in waist position on the radiation profiles at different cavity positions. Shown in Fig. 7 are the far field intensity cross sections (calculated at 14m beyond the outcoupling hole, this being the position of the VUV-FEL optical diagnostic bench) and at the undulator entrance. The cross sections are displayed in arbitrary units. Again, the dependence on waist position is weak.

It is noted that the far field cross section in Fig.7 displays clear higher order transverse mode structure, with a

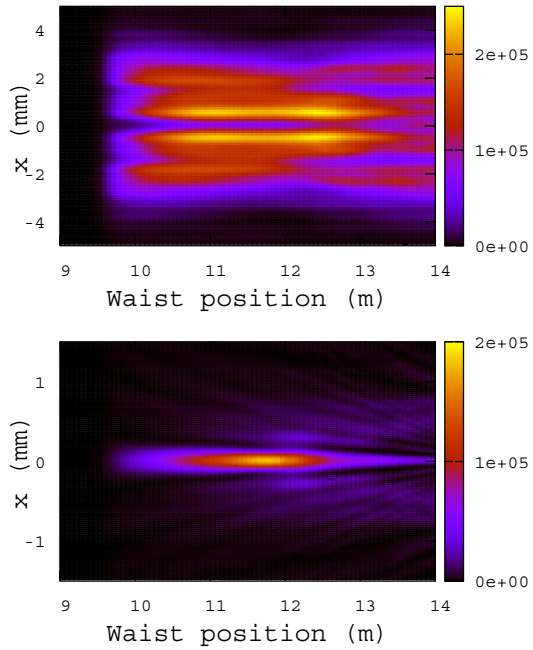

Figure 7: Intensity (a. u.) cross sections in the far field (top) and at the undulator entrance (bottom) as a function of the waist position of the cold-cavity fundamental mode of the resonator. The hole radius is 2mm.

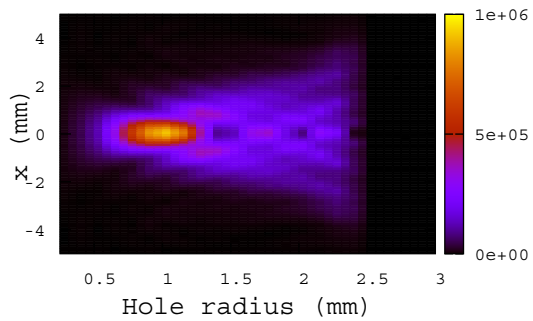

Figure 8: Intensity (a. u.) cross section in the far field as a function of hole radius, for waist position 12.19m.

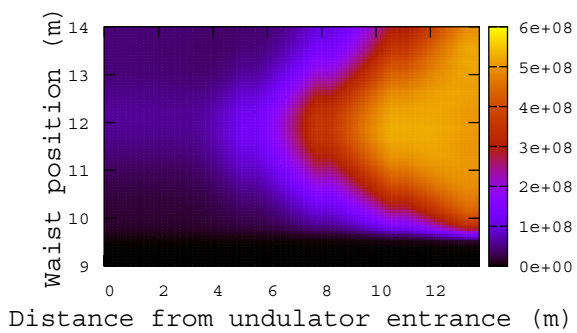

Figure 9: Power (W) growth along undulator as a function of waist position. The vertical bands are due to the gaps between the undulator sections.

minimum intensity on axis. A scan of the effect of hole radius on far-field cross section is shown in Fig.8 where it is seen that the far field cross section can be improved (i.e. brought closer to a fundamental gaussion mode) by reducing the hole radius. Further optimisation will now be done to maximise the output power while maintaining the optimum far-field cross section, including investigation of unstable resonators.

Finally, the total power within the undulator as a function of waist position is shown in Fig.9. The baseline waist position of 12m gives the strongest power growth.

CONCLUSION

Full 3D modelling of the VUV-FEL has been made possible with the new optics simulation package. The main conclusions are:

- The CDR parameters are close to the optimum values found with steady state simulations;
- The far field cross-section and total output power depend on hole radius but, for each hole radius, are otherwise relatively insensitive to the resonator configuration over a large range of ROC's around the CDR values;
- The high gain of the FEL ensures that optical guiding within the undulator and hole size are far more dominant in defining the radiation profile than the ROC of the mirrors.

These conclusions demonstrate that the VUV-FEL should be treated as a self-seeding amplifier FEL rather than as an oscillator FEL.

After 3eV simulations are complete it is expected that 3 mirror sets will be specified, one optimised for 10eV output, one for 3eV output and one for scanning over the full range.

REFERENCES

[1] M. W. Poole and E. A. Seddon, *4GLS and the ERLP Project at Daresbury Laboratory*, PAC05 Proceedings, (2005)

[2] *4GLS Conceptual Design Report*, CCLRC, `http://www.4gls.ac.uk/documents.htm#CDR`, (2006)

[3] B. W. J. McNeil *et al*, *The Conceptual Design of the 4GLS XUV-FEL*, (*ibid*), (2006)

[4] B. W. J. McNeil, IEEE Journal of Quantum Electronics, 26, 6, 1990, p1124

[5] D. C. Nguyen *et al*, *Regenerative Amplifier FEL*, Proceedings of the XX International Linac Conference, p731 (2000)

[6] N. R. Thompson *et al*, *A VUV-FEL for 4GLS*, Proc. 27th FEL Conf., Stanford (2005)

[7] `http://corona.physics.ucla.edu/~reiche/`

[8] J. G. Karssenberg *et al*, *FEL-Oscillator Simulations with Genesis 1.3*, (*ibid*), (2006)

[9] R. Bonifacio *et al*, Opt. Commun. 50, p373 (1984)

[10] Ming Xie, PAC Proceedings 1995, p183.

DEVELOPMENT OF FREQUENCY-RESOLVED OPTICAL GATING FOR MEASUREMENT OF CORRELATION BETWEEN TIME AND FREQUENCY OF CHIRPED FEL

H. Iijima, R. Hajima, E. J. Minehara, R. Nagai and N. Nishimori, Japan Atomic Energy Agency, 2-4 Shirakata-Shirane, Tokai, Naka, Ibaraki, Japan.

Abstract

A femtosecond infrared-chirped free-electron laser (FEL) is an effective tool of dissociating molecules without the intramolecular vibrational redistribution. The ultrashort FEL pulse with the broadband spectrum is achieved operating the long-pulse electron beam from an energy recovry linac at Japan Atomic Energy Agency. Until now, the broadband spectrum of ultrashort pulse was measured to be $\Delta\omega / \omega_0$ = 14% with the central wavelength of 23 μm and the pulse duration of 320 fs at FWHM by an autocorrelation of fringe-resolved second harmonic generation. However the information of pulse shape and variation of frequency depending on the time during the pulse were not obtained. Since it is essential to know both information in the pulse for the dissociation of the molecule, we will measure them by frequency-resolved optical gating (FROG).

INTRODUCTION

A femtosecond infrared-chirped free-electron laser (FEL) is an effective tool of dissociating polyatomic molecules without the intramolecular vibrational redistribution [1,2]. Coherent vibrational climbing proceeds from exciting a molecular vibration transitions by the ultrashort infrared pulse with the broadband spectrum which encompasses several vibrational transitions of the molecule. Indeed, these transition energies become smaller and smaller with climbing the ladder because of molecular anharmonicity. Therefore, the climbing efficiency can be increased dramatically when using a negatively chirped pulse so that its high-frequency components which resonant with the lower transitions of the ladder precede its low-frequency components which resonant with the upper transitions of the ladder. Coherent vibrational climbing can be viewed also as a rapid adiabatic passage leading to efficient excitation of the upper vibrational states with an efficiency that in theory can be close to 100% because of the coherent nature of the interaction.

At Japan Atomic Energy Agency (JAEA), an energy recovery linac (ERL) driven by superconducting accelerators has been constructed to produce a high-power far-infrared FEL(~20μm) [3,4]. Operating this device, it succeeds in generating ultrashort pulses with the broadband spectrum using a long macro pulse of electron beam by JAEA-ERL.

Until now, the broadband spectrum was measured to be $\Delta\omega / \omega_0$ = 14% at the central wavelength of 23 μm and the pulse width of 320 fs at FWHM by an autocorrelation of fringe-resolved second harmonic generation (FRSHG) [3]. However the intensity and the variation of frequency depending on the time during the FEL pulse were not obtained. Since it is essential to know both of the intensity and the variation of frequency in the pulse for the dissociation of the molecule, we will measure them by frequency-resolved optical gating (FROG) [5].

FREQUENCY-RESOLVED OPTICAL GATING

Principle of FROG

FROG is a technique to completely determine the intensity and phase versus time or frequency. The apparatus of FROG is only an autocorrelator followed by a spectrometer. In the autocorrelation and related techniques, the ultrashort pulse is measured purely in the time domain (autocorrelator), or in the frequency domain (spectrometer). In all these measurements, detectors can only measure the intensity of the signal. As a result, it is inevitable to lose the phase information, if the measurement is taken only in one domain. The measurement of FROG trace is taken in a hybrid domain: time-frequency domain. As time and frequency are two reciprocal domains connected by Fourier transform, the phase information in time domain is encoded into the intensity information in frequency domain, and vise versa. Therefore FROG trace contains the information of both intensity and phase of ultrashort FEL pulse by doing only intensity measurement in time-frequency domain.

As the time-dependent component of the pulse can be written in

$$E(t) = \mathrm{Re}\left\{\sqrt{I(t)}\exp(i\omega_0 t - i\varphi(t))\right\}, \qquad (1)$$

where $I(t)$ and $\varphi(t)$ are the time-dependent intensity and the variation of frequency, and ω_0 is a carrier frequency, FROG trace is described as

$$I_{FROG}(\omega,\tau) = \left|\int_{-\infty}^{\infty} E_{sig}(t,\tau)\exp(-i\omega t)dt\right|^2, \qquad (2)$$

where a quantity $E_{sig}(t,\tau)$ is a signal field defined by $E(t)g(t-\tau)$. The function $g(t-\tau)$ is a gate function with respect to the gate delay τ. Now, consider the Fourier transform of $E_{sig}(t,\tau)$ with respect to τ, Eq. (2) is transformed to

$$I_{FROG}(\omega,\tau)=\left|\int_{-\infty}^{\infty}\hat{E}_{sig}(t,\Omega)\exp(-i\omega t-i\Omega\tau)dtd\Omega\right|^2 . \quad (3)$$

Since Eq. (3) is the 2-dimensional Fourier transform with respect to t and Ω, the signal field $E_{sig}(t)$ implementing I_{FROG} is determined uniquely due to the fundamental theorem of algebra. As a result, the information of $I(t)$ and $\varphi(t)$ in Eq. (1) are obtained from the quantity $I_{FROG}(\omega,\tau)$.

Various non-linearities such as second-harmonic generation (SHG), third-harmonic generation, self-diffraction and polarized-gate are well known as the gate function [6]. In our measurement, SHG autocorrelation is used as the gate for FROG trace.

Simulation of SHG-FROG

In the SHG-FROG geometry, the pulse is split into two pulses which are then spatially overlapped in a piece of frequency-doubling crystal. In the frequency-doubling crystal, the two pulses induce a second harmonic due to the second-order optical non-linearity. Hence the signal field for SHG-FROG is given by $E_{sig}(t,\tau) = E(t)E(t-\tau)$. The main advantage of SHG-FROG is sensitivity: it involves only the second-order nonlinearity. Consequently, for a given amount of input pulse energy, SHG-FROG will yield more signal pulse energy.

In order to evaluate retrieval of the intensity $I(t)$ and phase $\varphi(t)$ of the ultrashort pulse from SHG-FROG trace, a numerical simulation for SHG-FROG was carried out using the JAEA-FEL parameters. As a temporal profile of input intensity, the previous simulation result was used [7]. The carrier frequency ω_0 was determined by an experimental measurement of λ_0 = 21μm. Three types of input variation of frequency were assumed for the simulation.

The simulation results are shown in Fig. 1, in which the top row shows false-color FROG trace for each phase; red means high intensity and violet means low intensity. The images of FROG trace in Fig. 1 are cropped, but the simulation was achieved in double range. The bottom row shows retrieval results of FEL pulse, where red closed (open) circle indicates the retrieval intensity (phase) respectively, and blue lines mean the input shape of FEL pulse. The each column indicates the difference of the

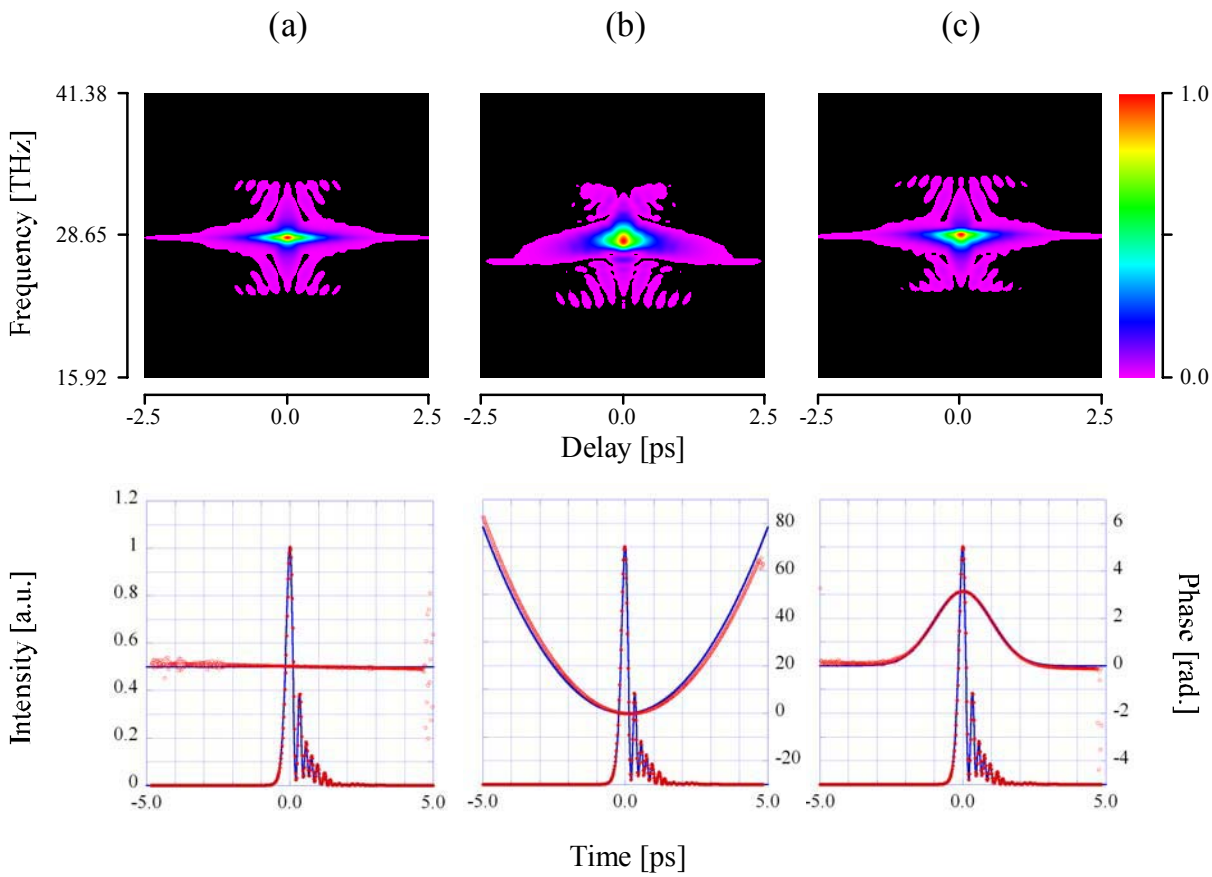

Figure 1: The top row shows false-color FROG trace for each phase; red means high intensity and purple means low intensity. The bottom row shows the retrieval result, where red closed (open) circle indicates the retrieval intensity (phase) and blue line indicates the initial parameter. The each column (a), (b), (c) indicates Fourier transformer-limited, negative chirp, self-phase modulated pulse respectively.

variation of frequency; (a) is a Fourier transformer-limited, (b) is a negative chirp, and (c) is a self-phase modulated pulse respectively. The retrieval intensity and phase were good agreement with the input intensity and phase.

MEASUERMENT SETUP

Focus and transport system

Since the FEL pulse is diverged by optical diffraction due to a ϕ2-mm pinhole on an output coupler mirror of FEL optical cavity, a pair of Au-coated elliptical mirrors is used to parallelize the FEL pulse with large beam size (approximately 5 cm in diameter). This optical focusing system is located near the output coupler. In an experimental room, the transported FEL is focused again by a pair of Au-coated parabolic mirrors. The whole set-up is mounted in vacuum boxes, which are evacuated up to 10^{-7} Torr, in order to avoid distortion of the FEL pulse due to absorption of the infrared radiation by ambient water vapour, and is connected to the 24-m FEL transport ducts. The optics design was determined to be close to 100% optical transport efficiency by a numerical simulation code GRAD [8].

Experimental setup of SHG-FROG

Figure 2 shows a schematic view of SHG FROG apparatus constructed now. As shown in Fig. 2, the incoming FEL pulse is split by a polyethylene terephthalate (PET) film, whose thickness is 23μm, into two beams. One of them is delayed by a movable retro reflector; the other has a fixed path length. The movable reflector can be achieved by a stepper-motor-driven linear stage on which the retro reflector is mounted. A parabolic mirror focuses both pulses onto the frequency doubling crystal consisting of 2mm thickness Tellurium (Te). The second harmonic generated in the crystal when both pulses have a temporal and spatial overlap propagates through a slit to the spectrometer. Finally a mercury-cadmium telluride (MCT) detector detects the intensity of signal.

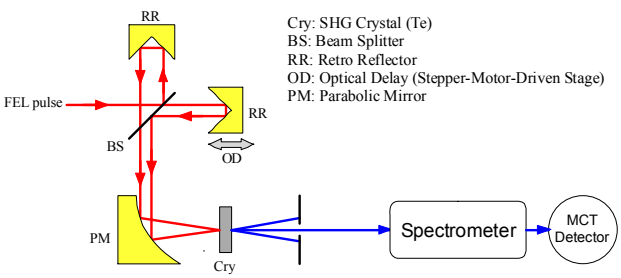

Figure 2: The schematic view of the SHG-FROG setup.

STATUS OF MEASUREMENTS

Spectrum of FEL pulse

Now, the whole optics is being adjusted precisely to provide the SHG signal from the Te crystal, therefore the focus, transport, and measurement system are in atmosphere. The atmospheric transport efficiency was measured to be 40 ~ 50 % due to the absorption by the ambient water vapour, and the average power of FEL pulses was measured to be 500 mW, typically.

Figure 3 shows a spectrum of the FEL pulse measured by a spectrometer. One can find the absorption by the ambient water vapour at 21.1, 21.8 and 22.6 μm.

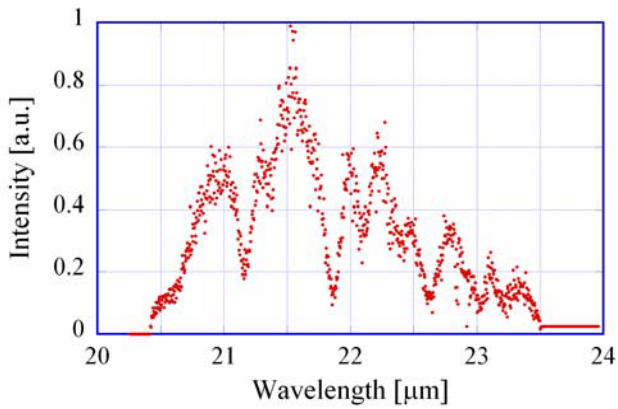

Figure 3: The spectrum of FEL pulse. The absorption of the infrared radiation by the water vapour can be seen at 21.1, 21.8 and 22.6 μm.

Polarization

High efficiency SHG is one of important points to perform SHG-FROG trace. The efficiency depends on an angle between a Te crystal orientation and a polarizing plane, and an input power of the FEL pulse dominantly. On the other hand, the surface of Te crystal is damaged if the pulse is strongly focused to generate the second harmonic. Therefore the angle between the Te crystal orientation and the polarizing plane of FEL pulse should be adjusted precisely.

Figure 4 shows a measurement result of polarizing angle of the FEL pulse at position of Te surface. The measurement was done using a polarizer. In this figure, zero degree corresponds to the horizontal direction. In our case, the FEL pulse has a vertical polarization at the output coupler. At the surface of Te crystal, the polarizing direction rotates to 133 degree due to the refractions via the mirrors in the transport system. The measurement value is good agreement with the designed value.

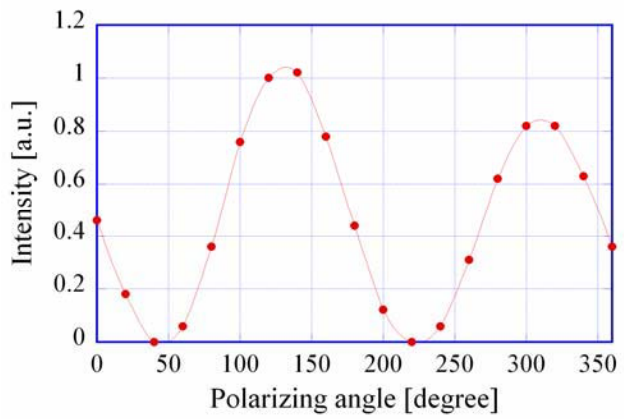

Figure 4: Polarizing angle on the surface of the doubling crystal.

SUMMARY

The femtosecond infrared-chirped FEL is the effective tool of dissociating molecules without the intramolecular vibrational redistribution. JAEA ERL-FEL has been constracted to provide a high-power far-infrared FEL. The ultrashort FEL pulse with the broadband spectrum is achieved operating the long-pulse electron beam from JAEA ERL-FEL. Since it is essential to know both of the intensity and the variation of frequency in the pulse for the high-efficiecny dissociation of the molecule, we consider to measure them by SHG FROG. The numerical simulation of SHG FROG using the FEL parameters can completely retrieves the intensity and phase of the pulse. In the following, we have start to develop the apparatus of SHG FROG. Now we are measuring basic parameters of the FEL pulse (beam size, power, wavelength, polarization and so on) in the experimental room.

ACKNOWLEDGEMENTS

This research is partially supported by MEXT KAKENHI 18740265.

REFERENCES

[1] S. Chelkowski, et al., Phys. Rev. Let., 65 (1990) 2355.
[2] Y. Fujimura, O plus E, No. 176, p. 102.
[3] R. Hajima and R. Nagai, Phys. Rev. Let., 91 (2003) 024801.
[4] N. Nishimori, et al., Nucl. Instrum. and Meth. A, 475 (2001) 266.
[5] R. Trebino, et al., Rev. Sci. Instrum., 68 (1997) 3277.
[6] B. A. Richman, et al., Opt. Lett., 22(1997)721.
[7] R. Hajima, et al., Nucl. Instrum. and Meth. A, 475 (2001) 270.
[8] GRAD; General Laser Analysis and Design program (Applied Optical Research, AOR).

BEAM CURRENT DOUBLING OF JAEA ERL-FEL

R. Nagai#, R. Hajima, H. Iijima, N. Kikuzawa,
E. Minehara, N. Nishimori, T. Nishitani, M. Sawamura,
Japan Atomic Energy Agency, Tokai, Ibaraki, Japan

Abstract

An energy-recovery linac (ERL) R&D program for a high-power free-electron laser (FEL) is in progress at Japan Atomic Energy Agency (JAEA; formerly JAERI and JNC). The first energy-recovery operation and FEL lasing was demonstrated in 2002 by remodeling the superconducting linac of the JAERI-FEL driver. In the first demonstration, the accelerated beam current was same as the original linac. One of the advantages of an ERL is that the accelerating beam current can be increased by only changing micro-pulse repetition rate without increasing the RF power of the main linac. The advantage of an ERL has been demonstrated by the current doubling.

INTRODUCTION

For the high-power free-electron laser (FEL), the FEL extraction efficiency or the drive beam power should be increased. Increasing of the drive beam power is more effective than increasing of the FEL extraction efficiency because the FEL extraction efficiency is limited in several percent. For the beam power increasing in a usual linac, there are some problems as follows: high-power RF source and coupler corresponding with the beam power are needed, high-power and high-energy beam should be dumped, radiation shield at the beam dump is very tough. A high-power beam can be accelerated by small RF power in an energy-recovery linac (ERL) because the beam power not extracted to the FEL light is recovered and used to the acceleration. The radiation shield and thermal design of the beam dump becomes easy because the dumped beam power and energy is reduced by the deceleration at the linac. Using an ERL as an FEL driver therefore solves the problems for the beam power increasing.

An ERL-FEL R&D program is in progress at Japan Atomic Energy Agency (JAEA; formerly JAERI and JNC). The first energy-recovery operation and FEL lasing was demonstrated [1] in 2002 by remodeling the superconducting linac of the JAERI-FEL [2]. In the first demonstration, the accelerated beam current was same as the original linac. One of the advantages of the ERL is that the accelerating beam current can be increased by only changing micro-pulse repetition rate without increasing the RF power of the main linac. To demonstrate the advantage, the e-gun, the injector RF source, the low-level RF (LLRF) controller, and the operation system have been improved. As a result of the improvement, the doubled beam acceleration and the FEL power improvement have been successfully achieved.

IMPROVEMENT OF THE JAEA ERL-FEL

The layout of JAEA ERL-FEL is shown in Fig. 1. The injector consists of a DC electron gun with thermionic cathode driven by a grid pulser, an 83.3 MHz sub-hermonic buncher, and two 499.8 MHz 1-cell superconducting modules. The merger is a two-step staircase type that consists of four bending magnets and three quadrupole magnets. The main linac consists of two 499.8 MHz 5-cell superconducting modules. The beam transport system to the undulator consists of a triple-bend achromatic (TBA) arc and a half-chicane achromatic system. The undulator is a hybrid type with period

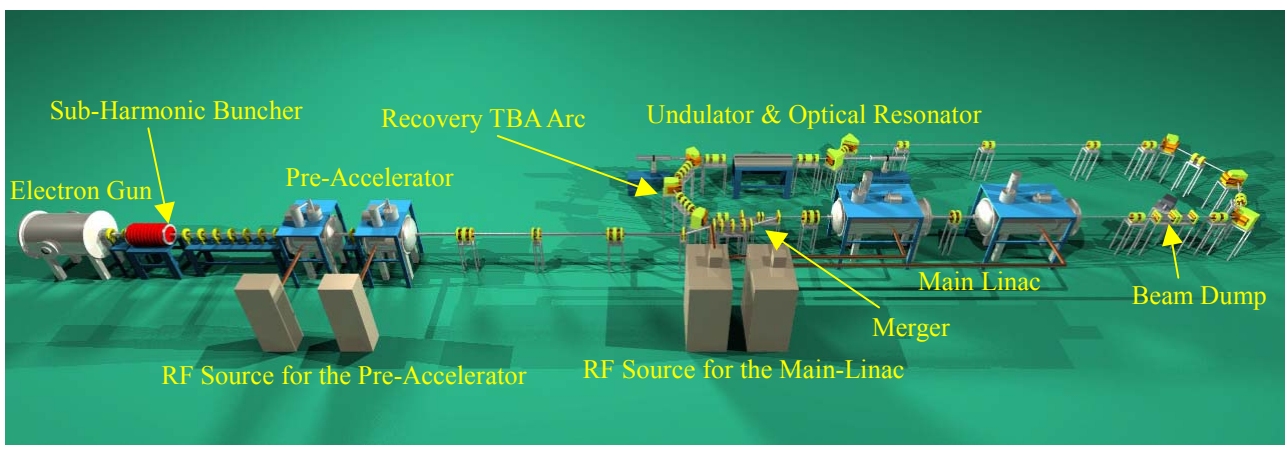

Figure 1: Layout of JAEA-ERL.

#Email: nagai.ryoji@jaea.go.jp

number of 52 and period length of 33 mm. The optical resonator is a near-concentric Fabry-Perot type that consists of two gold-coated mirrors with center-hole output coupler. The recovery beam transport system is a TBA arc.

In the original linac, the electron beam was accelerated in burst mode with 10 Hz macro-pulse and 10.4125 MHz micro-pulse repetitions. The macro-pulse average current was 5 mA that was mainly limited by the RF power sources and the grid pulser. To demonstrate that the higher beam current than the RF source capacity of the main linac can be accelerated, the ERL has been improved.

The electron gun is equipped with a thermionic cathode and operated at 230kV DC voltage. A train of electron bunch is generated by the grid pulser. To generate 20.825 MHz bunch train, doubled repetition of original one, a main-circuit of the grid pulser was replaced to new circuit [3]. The bunch length and timing jitter of the electron beam at the electron gun are 590 ps-FWHM and 12.8 ps-rms, respectively. The bunch length and timing jitter are compressed into about 1/100 through the beam transport system to the undulator.

In the original linac without energy-recovery, two 1-cell superconducting modules were driven by two 8 kW solid-state amplifiers for each, enough capacity for 5 mA operation. The solid-state amplifiers were replaced by two IOT of 50 kW [4], which is enough capacity for 40 mA operation.

Stable operation of an FEL depends much on the stability of an accelerator. In a superconducting accelerator, a LLRF controller is one of the key components for achieving good stability. The original LLRF controller was designed for phase flatness at ±1 deg. within a 1 ms macro-pulse. This LLRF controller contributed to the 10-year operation of JAERI-FEL. After the remodeling into the ERL, however, the original LLRF controller performance was insufficient for the ERL operation. The LLRF controller was replaced by new one. The new controller is based on analog phase and amplitude control of the cavity RF field coupled with a tuner controller, which is same as the original controller. In the new controller, the following functions were introduced for the better stability: the feedback gain, time constant and loop phase offset can be varied during operation to obtain good flatness of RF phase and amplitude within a macro-pulse, all the circuits are contained in a temperature regulated oven [5]. By the new controller, the phase and amplitude stabilities at the beam acceleration are 0.07 %-rms and 0.07 deg-rms, respectively. The original controller was placed at the control room, and the feedback loop involved 50 m cables to connect the controllers and the RF cavities. These long cables have large phase drift due to the temperature dependence of the electrical length. The new controller are installed just beside the cavities to make the cable length as short as possible. Furthermore the cables between the controllers and the cavities are contained in a temperature-regulated pipe to suppress the effect of the changing of the room temperature [6]. The phase stability in any season has been achieved less than 0.1 deg-rms by the temperature-regulated cable system.

The electron motion in the longitudinal and transversal phase space is very complex because the injector has long drift spaces before and after the pre-accelerator. The achromaticity of the merger and the bunch length of the electron beam are sensitive to the quadrupole magnets parameter. Therefore, the beam transport parameter adjustment of the injector and the merger is not easy. To support systematic parameter search, the accelerator operation system of the JAEA-ERL is equipped with a data-logging system and database services [7]. The initial parameter set of the injector was decided by the numerical optimization [8]. In the result, the electron bunch length of less than 10 ps has been achieved at the undulator.

The length of the optical resonator was changed along with remodeling to the ERL. The optical resonator geometry was optimized by a Fox-Li procedure utilized simulation code[9]. In the optimization, the center-hole thickness was not taking into account. The center-hole thickness causes additive loss. If the center-hole thickness is taking into account, the radius should be enlarged more than the ideal case. The center-hole radius of 1.0 mm was adopted in consideration of the loss by the center-hole thickness because the optimum radius was 0.8 mm in the ideal case. The misalignment tolerance of the resonator was estimated by the Fox-Li simulation code [10]. The offset and tilt tolerance for the FEL power fluctuation of 1% are 0.1 mm and 40 μrad, respectively. The vibration of the floor is less than 1 μm. The accuracy of the He-Ne alignment system of the optical resonator is less than 20 μrad. The offset and tilt tolerance of the optical resonator is therefore sufficiently large for the FEL power fluctuation of less than 1%.

ERL AND FEL DEMONSTRATIONS

In the adjustment of the beam transport, the higher current beam than the RF source capacity cannot be accelerated because the energy-recovery is not enough. The energy-recovery acceleration and beam transport have been adjusted in the condition of original micro-pulse repetition of 10.4125 MHz. Under the micro-pulse repetition in 10.4125 MHz, because the beam lost is allowed, the screen monitor can be used for the beam transport adjustment. After the adjustment, doubled beam in the repetition frequency of 20.825 MHz has been accelerated only changing of the micro-pulse repetition. The current increase only by changing the micro-pulse repetition is scalable. The successful current doubling shows that the current can be increased easily up to 40 mA corresponding with the repetition of the SHB frequency. Typical signal of the current monitor at the entrance of the main linac is shown in Fig. 2. These signals are the injection beam to the main linac and the re-circulated beam from the recovery beam transport system in the repetition of 20.4125 MHz. The amplitudes of the

injection and the re-circulated beam signal are the almost same.

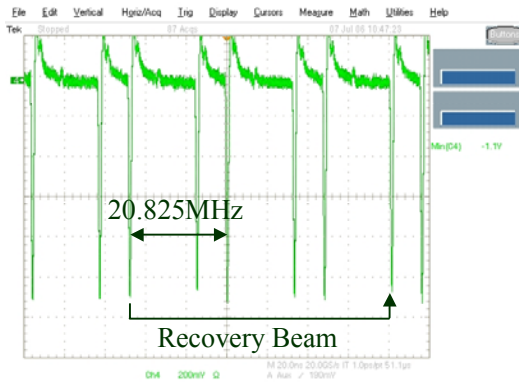

Figure 2: Typical signal of the current monitor at the entrance of the main linac.

Typical signal of output power of the main linac RF source is shown in Fig. 3. The RF source is operated in the pulse mode in the repetition of 10 pps and the pulse width of 2 ms. The electron beam has been accelerated with 1ms in the latter half. In the case of Fig. 3, the macro-pulse width of the electron beam is 230 μs. The RF output power with and without the electron beam are the almost same because the RF power is recovered by the decelerated electron beam. As shown in Fig. 3, the high-current electron beam can be accelerated if there is an RF power only of the amount of exciting the acceleration field. The spike at the edge of the electron beam macro-pulse is caused by the feedback of the RF low-level controller. In the pulse mode, the RF power to compensate the disturbance such as the edge of the electron beam macro-pulse is needed as shown in Fig. 3.

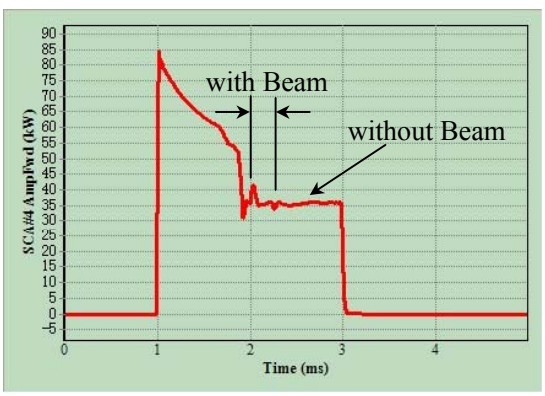

Figure 3: Typical signal of output power of the main linac RF source.

After the energy-recovery acceleration, the FEL lasing is successfully achieved by adjusting the length and the beam position of the optical resonator. The beam position is adjusted while monitoring the stored spontaneous emission with a liquid-nitrogen-cooled HgCdTe detector. The FEL extraction efficiency is obtained by measuring the energy loss of the electron beam. The energy loss and energy spectrum of the electron beam is measured by a wire-monitor set up on the way of the recovery TBA arc. The amount of the beam lost by the wire monitor is less than the RF power source capacity. The detune curve of the FEL extraction efficiency is shown in Fig. 4. The Maximum efficiency and power are 2.7 % and 0.7 kW, respectively. The output efficiency of the optical resonator is about 30 %. The output efficiency of the optical resonator is about 37 % in the numerical simulation. The difference of the measured value and calculated one is caused by the thickness of the output center-hole, and misalignment of the resonator.

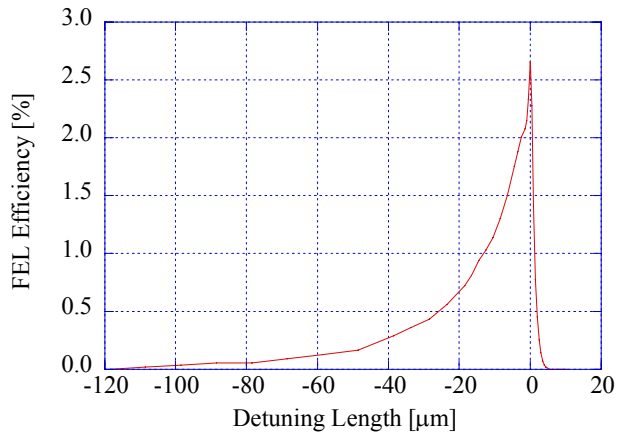

Figure 4: Detune curve of the FEL extraction efficiency.

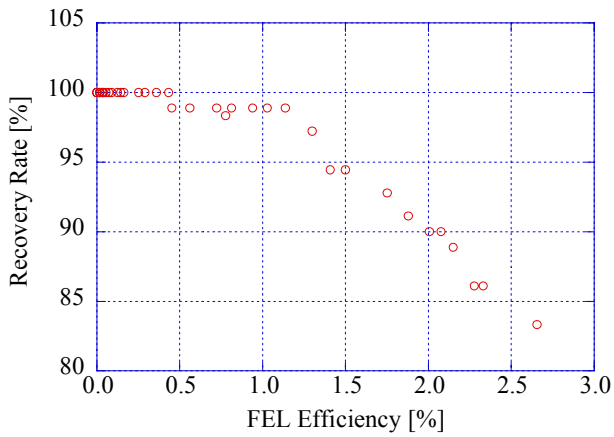

Figure 5: Recovery rate of the electron beam at the beam dump.

The recovery transport system with a large energy acceptance is necessary because after lasing the electron beam has large energy spread. The energy spread is about 5 times of the extraction efficiency. The recovery rate of electron beam at the beam dump is shown in Fig. 5. The electron beam is almost recovered up to the extraction efficiency about 1 %. Under the present condition, the beam loss at the FEL lasing is less than the RF source capacity. To increase the beam current, the recovery rate should be close to 100 %. Measured energy spread at the maximum output power is about 13.5 % (tail to tail). The energy acceptance of the recovery TBA arc is about 16 % in the calculation, and almost electron beam can be transported. There is actually little bremsstrahlung radiation in the arc part. The beam is therefore lost mainly in deceleration at the main linac. To recover the

almost electron beam, after lasing the energy spread of the electron beam should be compressed because it is too large into the energy after decelerating [11]. Therefore, R56 of the recovery TBA arc and deceleration phase should be optimized to achieve fully recovery. The optimization of the energy compression is in progress.

CONCLUSION

One of the advantages of an ERL is that the high beam current over the RF source capacity of the main linac can be accelerated. The advantage of an ERL has been successfully demonstrated by the current doubling with only changing of the micro-pulse repetition rate. The current increase only by changing the micro-pulse repetition is scalable. The successful current doubling shows that the current can be increased easily up to 40 mA corresponding with the repetition of the SHB frequency.

To achieve in the future the 10 kW class high-power FEL, the beam current will be increased by solving the problem of the recovery rate and increasing the repetition of micro-pulse up to the SHB frequency of 83.3 MHz. The RF sources of the pre-accelerators are ready for 40 mA beam. For the 83.3 MHz operation, the drive frequency of the grid pulser should be improved up to 83.3 MHz. Design of a grid pulser for the higher repetition rate is under investigation. A photo cathode electron gun driven by a laser as another option for the 83.3 MHz operation is under investigation also.

REFERENCES

[1] N. Nishimori, et al., Nucl. Instr. and Meth. **A475** (2001) 266-269.
[2] R. Hajima, et al., Nucl. Instr. and Meth. **A507** (2003) 115-119.
[3] N. Nishimori, et al., Proc. of the APAC2004 (2004) 625-627.
[4] M.Sawamura, et al., Nucl. Instr. and Meth. **A557** (2006) 287-289.
[5] R. Nagai, et al., Proc. of the Annual Meeting of Part. Acc. Soc. (2004) 293-295.
[6] R. Nagai, et al., Proc. of the 14th Symposium on Acc. Sci. and Tech. (2003) 362-363.
[7] N. Kikuzawa, Proc of the FEL2003 (2004) II-5.
[8] R. Nagai, et al., Proc. of the Annual Meeting of Part. Acc. Soc. (2004) 420-422.
[9] R. Nagai, et al., Nucl. Instr. and Meth. **A528** (2004) 231-234.
[10] R. Nagai, et al., Proc. of the FEL2004 (2004) 255-257.
[11] R. Hajima, E. Minehara, Nucl. Instr. and Meth. **A507** (2003) 141-145.

PERFORMANCE OF A CONVENTIONAL ANALOG Φ-A TYPE LOW-LEVEL RF CONTROLLER

R. Nagai[#], R. Hajima, H. Iijima, N. Kikuzawa,
E. Minehara, N. Nishimori, T. Nishitani, M. Sawamura,
Japan Atomic Energy Agency, Tokai, Ibaraki, Japan

Abstract

For a free-electron laser application and energy-recovery linac based light source, high-stability of accelerator RF amplitude and phase is required. A low-level RF controller of the JAEA-ERL has been improved to ensure high-stability accelerating RF field. The controller is a conventional analog Φ-A type controller. The controller performance is evaluated with a 499.8 MHz superconducting cavity and a 1300 MHz copper cavity. The phase and amplitude stabilities of the 499.8 MHz superconducting cavity within latter half of an RF pulse are 0.0055 deg-rms and 7.64×10^{-5}, respectively. For the 1300 MHz copper cavity, the performance of pulse and CW modes are evaluated. In the case of pulse mode, the phase and amplitude stabilities are 0.011 deg-rms and 7.64×10^{-5}, respectively. In the case of CW mode, the phase and amplitude stabilities are 0.011 deg-rms and 6.68×10^{-5}, respectively. Therefore, the performance of the analog Φ-A type low-level RF controller is sufficient for a free-electron laser stable operation and an energy-recovery linac based light source.

INTRODUCTION

Stable operation of a free-electron laser (FEL) and performance of an energy-recovery linac (ERL) based light source depend much on the stability of an accelerator. In a superconducting accelerator, a low-level RF (LLRF) controller is one of the key components for achieving good stability. An ERL R&D program for a high-power FEL is in progress at Japan Atomic Energy Agency (JAEA; formerly JAERI and JNC). A LLRF controller based on analog phase and amplitude feedback system was improved in the R&D program. An analog Φ–A system has the faster response than a digital feedback system because there is no delay caused by the computation. There is however the following disadvantages: the feedback parameters are not adjustable easily, the temperature coefficient of the circuit parts are larger than the digital feedback system. To solve the disadvantages, the following functions were introduced: the feedback gain, filter time constant and phase-lock loop (PLL) offset phase can be varied during operation, all the circuits are contained in a temperature regulated oven. As a result of the improvement, the accelerator phase stability of 0.06 deg-rms was achieved within latter half of an RF pulse [1].

The feedback filter of the LLRF controller is a low-pass filter of a single-pole RC circuit type. Only the resistance can be varied to change the time constant. The operation frequency of the PLL is 499.8 MHz, which is the same frequency of the superconducting cavity. To satisfy the requirements of the ERL based next generation light source, the following functions are added: the filter time constant can be varied by changing the resistance and capacitor, the frequency converter and band-pass filter can be added for the various frequency operation.

The improved controller performance is evaluated with a 499.8 MHz superconducting cavity and a 1300 MHz copper cavity. The stabilities are measured by the error signal of the controller. For the 499.8 MHz superconducting cavity, the RF mode is a pulse mode which is the same mode with the JAEA-ERL usual operation mode. For the 1300 MHz copper cavity, the phase and amplitude stabilities are measured in the pulse and CW modes. In the CW mode, the phase stability is estimated by also the phase noise measurement.

STABILITY MEASUREMENTS

Stability of the 499.8 MHz Superconducting Cavity

The RF field stability is measured for the 499.8 MHz superconducting cavity used as a pre-accelerator of the JAEA-ERL. The JAEA-ERL is operated by pulsed RF mode in the width of 2 ms and the repetition of 10 pps. The stability in the part of latter half used to accelerate the electron beam is measured in the setup as shown in Fig. 1. The setup is similar to the usual operation of the JAEA-ERL. The signal of 499.8 MHz from the master oscillator (Hewlett-Packerd 8665A) is input to the controller as a reference signal. The output of the controller is amplified with 400 W pre-amplifier (THAMWAY T145-56AAA) and 50 kW IOT (CPI CHK2500W5508) [2], and input to the superconducting cavity. The monitor signal of the superconducting cavity is returned to the controller for the feedback loop. The signals of the phase and amplitude of the cavity are output from the controller and measured by a signal monitor. The signal monitor consists of a digitizer (Yokogawa WE7000) and a computer. The signals of the phase and amplitude from the controller are digitized and acquired to the computer. The phase and amplitude stabilities are calculated with real-time from the digitized data. The feedback gain, filter time constant and PLL offset phase of the controller are adjusted in real-time monitoring of the stabilities.

Typical signal of the phase and amplitude within a pulse is shown in Fig. 2. The phase and amplitude stabilities within latter half of an RF pulse are 0.0055 deg-

[#]Email: nagai.ryoji@jaea.go.jp

rms and 7.64×10^{-5} rms, respectively. The accelerating gradient and loaded Q of the superconducting cavity are 5.2 MV/m and 1.3×10^{6}, respectively. In this case, main disturbance is an RF shaking due to the pulse operation.

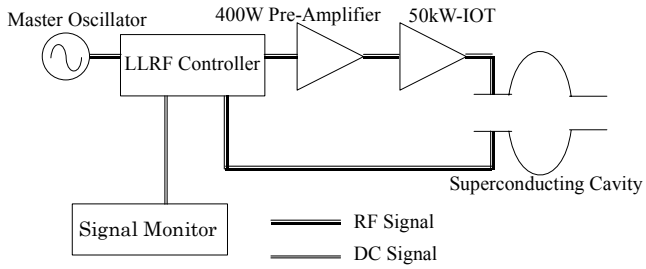

Figure 1: Stability measurement setup for the 499.8 MHz superconducting cavity.

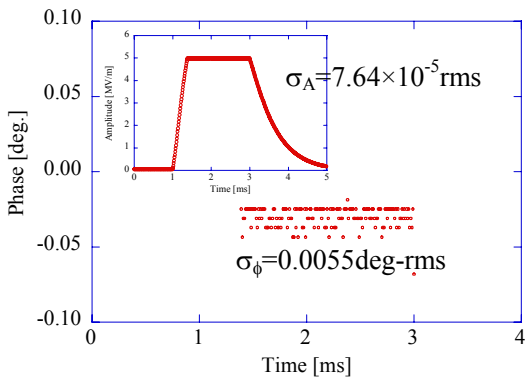

Figure 2: Typical result of the phase and amplitude (inset) within a pulse for the 499.8 MHz superconducting cavity.

Stability of the 1300 MHz Copper Cavity

To evaluate the performance of the LLRF controller at the 1300 MHz operation, the phase and amplitude stabilities are measured using a copper cavity in the pulse and CW modes. The loaded Q of the copper cavity is about 5800. The measurement setup is shown in Fig. 3. The signal of 1300 MHz from the master oscillator (Hewlett-Packerd 8341B) is input to the controller as a reference signal. The signal of 800.2 MHz from the local oscillator (Agilent 8662A) is input to the controller for a frequency conversion. The output of the controller is amplified with +28 dBm amplifier (Mini-Circuits ZHL-4240W), and input to the copper cavity. The monitor signal of the copper cavity is returned to the controller for the feedback loop. A part of the returned signal is input to a spectrum analyser (Tektronix RSA230) for the phase noise measurement in the CW mode. The master oscillator, local oscillator and spectrum analyzer are synchronized with the local signal of the master oscillator.

For the pulse mode measurement, the phase and amplitude stabilities are measured with the width of 3 ms and the repetition of 10 pps. The feedback parameters are adjusted according to the similar procedure of the superconducting cavity case. Typical signal of the phase and amplitude within a pulse is shown in Fig. 4. The phase and amplitude stabilities within latter half of an RF pulse are 0.011 deg-rms and 7.64×10^{-5} rms, respectively. For the CW mode measurement, the feedback parameters are re-adjusted. The phase and amplitude stabilities are 0.011 deg-rms and 6.68×10^{-5} rms, respectively.

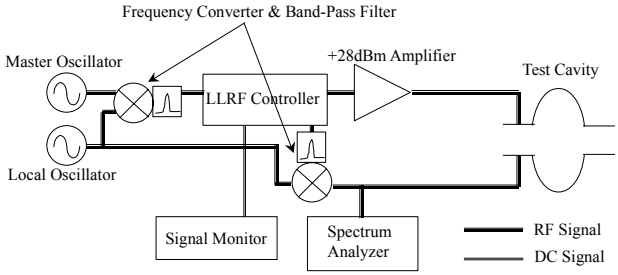

Figure 3: Stability measurement setup for the 1300 MHz copper cavity.

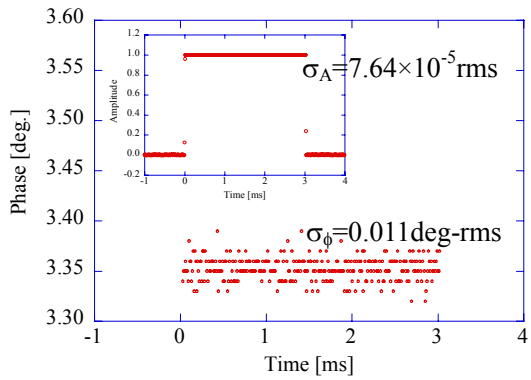

Figure 4: Typical result of the phase and amplitude (inset) within a pulse for the 1300 MHz copper cavity.

For the CW mode, the phase stability is estimated by also the phase noise measurement. The phase fluctuation (phase stability), σ_φ over a frequency range from f_1 to f_2 is given by

$$\sigma_\varphi = \left(\int_{f_1}^{f_2} 2L(f)\, df \right)^{1/2} \quad [rad], \qquad (1)$$

where $L(f)$ is a single sideband (SSB) phase noise [3]. In this measurement, the frequency range is 2 Hz to 10 kHz. The measurement accuracy of the spectrum analyzer used for this measurement is about -100 dBc/Hz. The phase noise of the master oscillator is not negligible small. The phase stability of the cavity is therefore estimated by

$$\sigma_\varphi = \left(\sigma_{\varphi m}^2 - \sigma_{\varphi 0}^2 \right)^{1/2}, \qquad (2)$$

where $\sigma_{\varphi m}$ is measured phase stability and $\sigma_{\varphi 0}$ is phase fluctuation of the oscillator and spectrum analyzer. The measured SSB phase noise against offset from the carrier frequency (offset frequency) is shown in Fig. 5. The inset is a phase noise of the oscillator and the spectrum analyzer. The phase stability is 0.013 deg-rms as a result of the measurement. Even if two phase noises in Fig. 5 are compared, the difference is hardly seen. The phase noise of the spectrum analyzer and the oscillator is not small enough to measure such a very high stability (less than 0.01deg-rms). The high-accuracy measurement of the phase noise by a low-noise measurement system is under arranging.

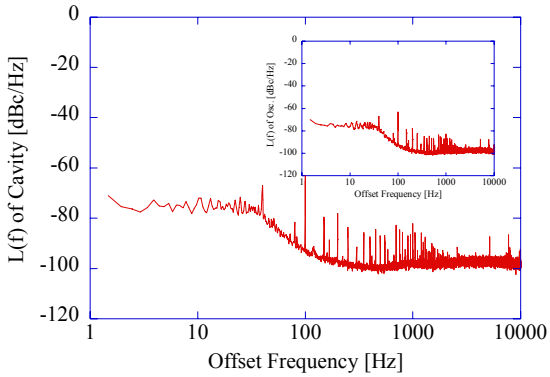

Figure 5: SSB phase noise of the copper cavity and the oscillator (inset).

The main disturbance of the ERL is a minute vibration of the acceleration cavity which is called microphonic [4,5]. To evaluate the microphonic disturbance, the phase noise is measured with the mechanical vibrated cavity. The phase and amplitude stabilities measured by the error signal of the controller are 0.014 deg-rms and 7.60×10^{-5}, respectively. The measured phase noise is shown in Fig. 6. The large phase noise (-37 dBc/Hz) due to the mechanical vibration is observed around 25 Hz without the feedback. When feedback is on, the phase noise is almost the same as the background level (-75 dBc/Hz). Therefore, the feedback gain of the phase around this frequency is 38 dB or more. The phase stability estimated from the phase noise is 0.034 deg-rms. The estimated value differs from the measured by the error signal due to the accuracy of the measurement system in this condition.

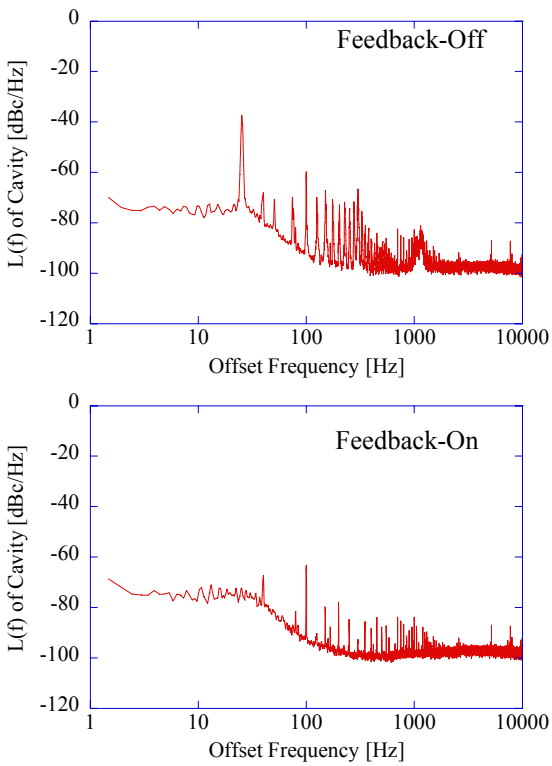

Figure 6: SSB phase noise with mechanical vibration.

CONCLUSION

The phase and amplitude stability requirements for an ERL based light source are 0.06 deg-rms and 3×10^{-4} rms, respectively [5]. The performance of the conventional analog Φ-A type LLRF controller is sufficient for the ERL-FEL stable operation and the ERL based light source as a result of the stability measurement.

The measurement of the SSB phase noise is useful for the performance evaluation of the controller with frequency resolved disturbance analysis.

REFERENCES

[1] R. Nagai, et al., Proc. of the Annual Meeting of Part. Acc. Soc. (2004) 293-295.
[2] M. Sawamura, R. Nagai, Nucl. Instr. and Meth. **A557** (2006) 287-289.
[3] E. Ezura, 'Characterization and Measurement of Frequency Stability' KEK Report 2000-6.
[4] C. Hovater, et al., Proc of the 20th Linac Conf. (2000) 518-520.
[5] M. Liepe, et al., Proc. of the PAC2003 (2003) 1329-1331.

JAEA PHOTOCATHODE DC-GUN FOR AN ERL INJECTOR

T. Nishitani, R. Hajima, H. Iijima, R. Nagai, M. Sawamura, N. Kikuzawa, N. Nishimori, E. Minehara, Japan Atomic Energy Agency, Tokai, Ibaraki, Japan
M. Tabuchi, Y. Noritake, H. Hayashitani, Y. Takeda, Nagoya Univ., Nagoya, Aichi, Japan.

Abstract

An ERL-based next-generation synchrotron light source and free electron laser require an electron beam of large current and small emittance. In order to realize an electron gun satisfying such requirements, we are developing an NEA-GaAs photocathode DC-gun. The gun is based on an existing DC-gun of Japan Atomic Energy Agency (JAEA) ERL-FEL and designed to provide a beam with energy of 250 keV and average current of 50 mA. Conditioning of a high voltage power supply has been completed up to design the target voltage of 250 kV. We have also decided to use superlattice semiconductor as a new type of photocathode with higher performance than an existing technology. We fabricated bulk-AlGaAs photocathode samples by molecular beam epitaxy in order to optimize the superlattice structure. We measured quantum efficiency and lifetime of the samples and achieved twice QE of a bulk-GaAs photocathode and longer NEA surface life than that of the bulk-GaAs photocathode.

INTRODUCTION

NEA-GaAs photocathodes have played very important roles as polarized electron sources in several fields of fundamental science [1]- [5], because polarized electrons is generated from an NEA-GaAs photocathode can be through the excitation of electrons by polarized photons tuned to the band-gap energy.

Now, an NEA-GaAs photocathode is also expected as a high-brightness electron source for ERL-based next-generation synchrotron X-ray light sources (ERL-LS). Ultimately high-brightness electron beam is required to realize the ERL-LS [6]. In order to realize such a high-brightness electron source, we need to control initial momentum spread of electrons as small as possible. An NEA photocathode can generate electron beam with such small initial momentum spread by excitation energy corresponding to the band-gap.

However, a conventional NEA-GaAs photocathode using a bulk type of GaAs semiconductor (bulk-GaAs) has serious problems, small quantum efficiency (QE) and short lifetime of the NEA surface.

In JAEA, we are developing a high-brightness electron gun for future ERL LS and FEL. In this study, we have decided to use a superlattice semiconductor for a high-brightness photocathode to fulfill the requirement of future ERL LSs. In the design of superlattice structure, we can optimize its electron affinity, band-gap energy and quantum confinement effect to improve the photocathode performance: higher QE, smaller momentum spread and longer lifetime.

DEVELOPMENTAL STATUS OF THE JAEA PHOTOCATHODE DC-GUN

An NEA photocathode has a fragile surface consisting of thin layer of cesium-atoms attached to gallium-atoms, which form electric dipole field to pull down the vacuum potential barrier. The NEA surface is easy to destroy by ion back-bombardment, which is ion generation by collision of extracted electrons and residual gas molecules followed by acceleration of the ions toward the cathode surface. Therefore, extreme high vacuum is essential to make an NEA surface of good quality and preserve it for long time.

A field emitting electrons also causes the ion back-bombardment. The field emission current can be suppressed using titanium and molybdenum as electrode materials [7] and isolating gun chamber from NEA activation chamber to prevent cesium contamination to the electrode.

The JAEA photocathode DC-gun consists of the gun chamber, the NEA surface preparation chamber and the load-lock system for transporting photocathode between these chambers. The preparation chamber is equipped with 200l/s NEG pump modules and a 500l/s ion pump. The gun chamber is equipped with 2000l/s NEG pump modules and two ion pumps, 500l/s and 200 l/s.

We have decided to use titanium alloy for the electrodes and these chambers. The titanium alloy shows out-gassing rate of 6×10^{-13} Pa m/s, which is much lower than that of standard vacuum materials by three orders of magnitude [8]. In our estimation of the ultimate pressure using the pumping speed and the out-gassing rate, the chambers is expected to be below 5×10^{-10}Pa

The ceramic insulator of the gun and the high voltage stack of the 250kV-50mA power supply are located side-by-side in a pressure vessel filled with SF6 gas of 2kgf/cm^2.

Figure 1 shows the gun chamber and the high voltage power supply.

Figure 1: JAEA photocathode DC-gun.

Conditioning of the high voltage power supply has been completed up to the design voltage of 250kV. Figure 2 shows leakage current of high-voltage terminal as a function of applied voltage. We confirmed the linear relationship between leakage current and supplying voltage without severe corona discharge.

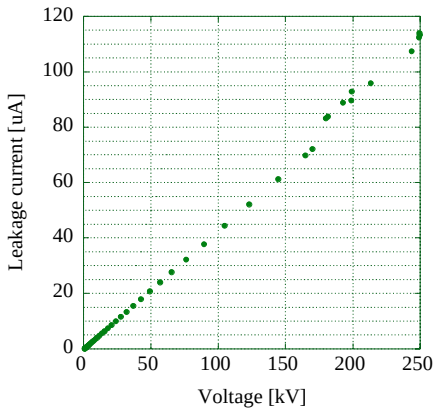

Figure 2: Leakage current of the high-voltage terminal as a function of applied.

STRATEGY OF A NEW TYPE OF PHOTOCATHODE

Superlattice photocathode

We have decided to use a superlattice photocathode as a new type of photocathode with higher performance than the existing technology [9]. A superlattice structure has periodically interchanging solid layers, well-layer and barrier-layer, thickness of which is less than 10nm. By selecting appropriate semiconductor for a each layer, a superlattice is possible to have larger band-gap energy and smaller electron affinity than that of a bulk-GaAs.

We consider the superlattice has intrinsic advantages in realization of higher QE, smaller initial momentum spread of photoelectrons and a longer lifetime of the NEA surface than those of a bulk-GaAs photocathode due to the following two reasons.

(1) Larger band-gap and smaller electron affinity than those of a GaAs is possible by optimization of a superlattice structure.

Experimental results of polarized electron sources have suggested that larger band-gap photocathode is more suitable for higher QE photocathode [10]. Moreover, we predict smaller electron affinity is more suitable for longer NEA life. Because a semiconductor with smaller electron affinity has lower vacuum level when the surface is NEA-activated.

(2) Electron density of state (DOS) for a superlattice is a step function of excitation photon energy because of quantum confinement effect.

In a semiconductor photocathode, QE is proportional to its DOS integrated from the band-gap energy to the excitation photon energy. A bulk GaAs, which has a monotonically increasing DOS function, requires rather higher energy photons to achieve high-QE operation at the expense of large momentum spread of electrons. A superlattice photocathode, on the other hand, enable one to achieve high-QE and small momentum spread simultaneously by choosing a photon energy just above the step energy of DOS [11].

NEA-ALGAAS PHOTOCATHODE

Advantages of bulk-AlGaAs in a high QE and a longer lifetime

In order to confirm the effect of band-gap energy and electron affinity on the photocathode performance, we have measured QE and lifetime of different materials: bulk GaAs and bulk AlGaAs, which has larger band-gap energy and smaller electron affinity than GaAs. It is known that the AlAs semiconductor has larger band-gap energy and smaller electron affinity than the GaAs semiconductor [12].

The measurement of the QE and the NEA surface lifetime as a function of band-gap energy and electron affinity is essential for optimization of the material fraction in the barrier layer of a superlattice structure. The bulk AlGaAs cathode is also expected to be a higher QE and a longer lifetime in comparison with a conventional GaAs photocathode.

Fabrication of crystal samples

We fabricated bulk-GaAs and bulk-AlGaAs samples with various Al fractions (=0.10, 0.17. 0.28). These samples have the same active-layer thickness for the photoelectron generation. Figure 3 shows samples fabricated by Molecular Beam Epitaxy at Nagoya University.

Exposure of a cathode surface to atmosphere results in adsorption of impurities such as oxide and carbide, which are harmful for NEA activation and hard to remove by heat cleaning. The samples have, therefore, covered by arsenide film in their preparation at the MBE chamber. The film is removed by heating in a vacuum chamber just before the NEA activation.

Figure 3: Photocathode samples: bulk-GaAs and bulk-AlGaAs.

Experimental setup

The measurements of QE and life time for GaAs and AlGaAs have been made at a test bench as shown in Figure 4.

The main chamber keeps extreme high vacuum of 3×10^{-9} Pa using the combination of a 500 l/s ion pump and a 1300 l/s NEG pump. The surface of samples is cleaned by radiation heating using a tungsten heater. The NEA surface is activated by alternatively adsorption of cesium and oxygen (yo-yo method).

Ti:Sapphire laser (720-870nm), He-Ne laser (633nm) and laser diode (690nm and 670nm) is used as a excitation laser.

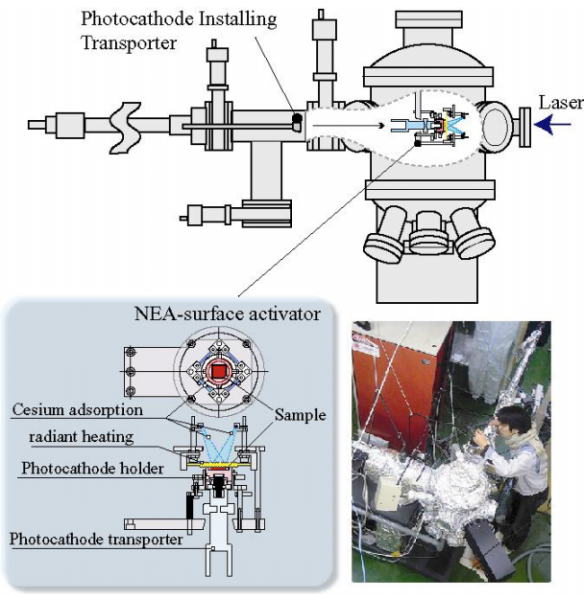

Figure 4: Experimental set up.

Quantum efficiency measurement

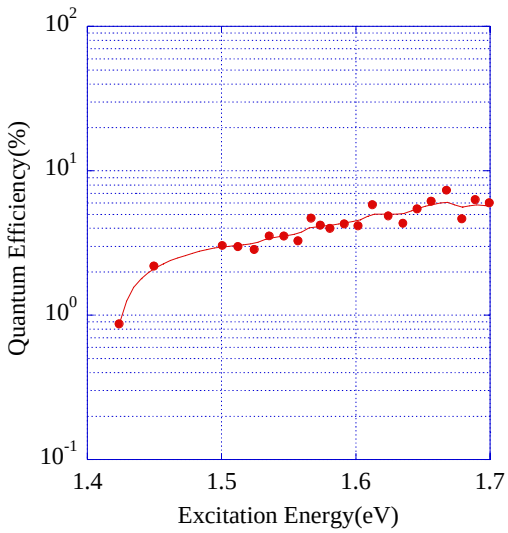

Figure 5: Quantum efficiency of the bulk-GaAs sample

Figure 5 shows measured QE spectrum of the bulk-GaAs sample. We can see a threshold around the band-gap energy (1.42eV) and QE of 2~3% from the band-gap energy to 0.1eV above the band-gap energy. These results are consistent with previous experiments [13].

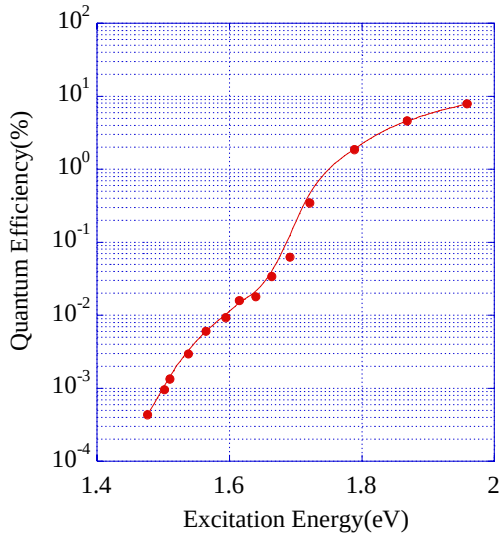

Figure 6: Quantum efficiency of the bulk-AlGaAs sample.

Figure 6 shows QE spectrum of the bulk AlGaAs sample. We can also see a threshold around the band-gap energy (1.79eV) calculated from the content of aluminum.. The QE from the band-gap energy to 0.1eV above the band-gap energy is 5~8%, which is two times higher than that of the bulk-GaAs sample.

NEA-surface life measurement

Figure 7 shows measurement results of NEA surface lifetime of samples, where laser photon energy was chosen at 0.1 eV above the band-gap for each sample. Photocurrent was below 100 nA and applied voltage was as low as 200 V to avoid NEA surface degeneration by ion back bombardment.

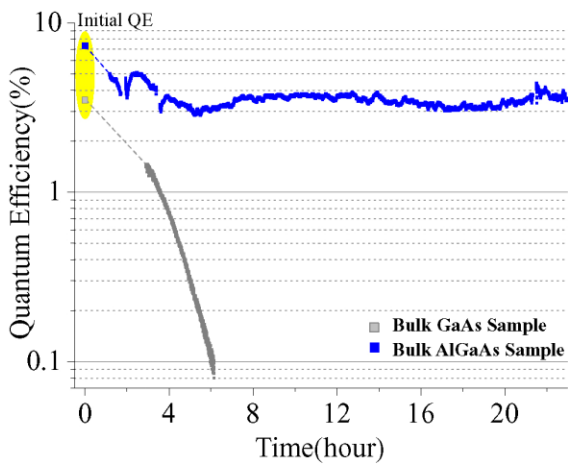

Figure 7: NEA-surface lifetime of bulk-GaAs (laser wavelength of 804nm) and bulk-AlGaAs (laser wavelength of 633nm).

In the case of the bulk-GaAs, QE, initially 3.5%, decreases below 1% 4hours after the NEA activation and the photocurrent ceases after 6 hours. In the case of the bulk-AlGaAs, QE shows initial drop from its initial value of 8% to 3% during 5 hours, but keeps 3% QE more than 26 hours.

From these results, we have found the bulk-AlGaAs has a longer lifetime of NEA surface than the bulk-GaAs. These results agree with our prediction that smaller electron affinity is suitable for longer NEA life.

SUMMARY

In JAEA, we are developing an electron gun for future ERL X-ray light sources and FELs. Fabrication of a DC gun and study on a photocathode for small emittance and high average current are in progress. We have proposed novel approaches, titanium alloy for the DC gun chambers and superlattice for the photocathode. The superlattice produces electrons with small initial momentum spread due to its quantum confinement effect, and realizes high QE, small emittance and long life time by optimizing well- and barrier-layers so that it has large band-gap and small electron affinity. Preliminary results from the measurements of QE and lifetime for the bulk GaAs and the AlGaAs photocathodes support our strategy. We will measure QE and NEA surface of samples with various fraction of aluminum to optimize the superlattice structure

ACKNOWLEDGEMENT

This work has been supported in part by Grant-in-Aid for Scientific Research for Ministry of Education, Culture, Sports, Science and Technology (Nos. 18740253).

REFERENCE

[1] D.T. Pierce et al., Appl. Phys. Lett. 26 (1975) 670.
[2] C.Y. Prescott et al., Phys. Lett. 77B (1978) 347.
[3] M. Meyerho¤ et al., Phys. Lett. B 327 (1994) 201.
[4] SLD Collaboration, Phys. Rev. Lett. 74 (1995) 2880.
[5] S. Mayer, J. Kessler, Phys. Rev. Lett. 74 (1995) 4803.
[6] Sol M. Gruner, et al., Review of Scientific Instruments, Vol. 73 Issue 3 pp. 1402-1406, 2002
[7] F. Furuta et al., NIM A 538 (2005) pp. 33–44
[8] H. Kurisu, et al., J. Vac. Sci Technol. A21 (2003) L10
[9] T. Rao, et al., Nuclear Instruments and Methods in Physics Research A557 pp.124–130, 2006
[10] T. Nakanishi, et al., AIP Conference Proceedings 421, (1998) pp. 300-310
[11] T. Nishitani et al. J. Appl. Phys. 97 (2005) 094907
[12] Sadao Adachi, J. Appl. Phys. 58 (3), (1985) pp. R1-R12
[13] T. Maruyama, et al., Appl. Phys. Lett. Vol82, 23, (2003) pp.4184-4186

HARMONIC LASING CHARACTERIZATION AT JEFFERSON LAB

S. V. Benson and M. D. Shinn, Jefferson Lab, Newport News VA 23606.

Abstract

Harmonic lasing is normally suppressed because of lasing at the fundamental wavelength. It can, however, be achieved using any of several methods that suppress fundamental lasing. In this paper we discuss two methods used at Jefferson Lab. The first is to use the characteristics of dielectric coatings to allow harmonic lasing at cavity lengths longer than the synchronous length for the fundamental. The second is to use a dielectric coating that has little reflectivity at the fundamental. This allows us to directly compare fundamental and harmonic lasing with the same optical resonator and electron beam. We present measurement carried out at Jefferson Lab using the IR Upgrade FEL operating at 0.53, 0.94, 1.04, 1.6, and 2.8 microns in which both schemes are used to produce lasing at both the 3rd and 5th harmonic of the fundamental.

INTRODUCTION

Harmonic lasing was predicted in 1980[1][2] and third harmonic lasing was demonstrated at Stanford and Los Alamos [3][4] in 1988. Since then many groups have demonstrated 3rd harmonic lasing and Jefferson Lab has demonstrated 2nd and 5th harmonic lasing as well [5][6]. In all cases the challenge has been two-fold: produce a sufficiently bright electron beam with high gain at harmonic wavelengths, and somehow suppress fundamental lasing. Photocathode injectors now routinely produce electron beams bright enough to lase well at harmonics. There are also several techniques that are available to suppress the fundamental. The first harmonic lasing demonstrations used a dispersive element to force the harmonic lasing to a longer cavity length or an aperture to preferentially diffract away the fundamental. Another way, more appropriate for a high power system, is to use dielectric mirrors to provide a high resonator Q at the harmonic and little or no Q at the fundamental. This is how lasing at the second and fifth harmonic were achieved at Jefferson Lab. In either case the gain was quite low so two high reflectors were used to produce lasing.

In this paper dielectric mirrors were used to produce harmonic lasing with relatively high gain at the third and fifth harmonic and a new mechanism was discovered that produces harmonic lasing using a resonator with high Q at the fundamental.

FEATURES OF DIELECTRIC MIRRORS RELATED TO HARMONIC LASING

Most high power resonator mirrors consist of a stack of layer pairs. The layers alternate between high and low refractive index materials, for example silicon dioxide/hafnium dioxide or thorium fluoride/zinc selenide. The thickness of each layer is one quarter of the center wavelength, or $\lambda/4n$ where n is the refractive index of the coating. The peak reflectivity is a function of the ratio of the refractive indices and the number of layer pairs. The spectral width of the reflectivity band is proportional to the square root of the ratio of the refractive indices. Note that the third harmonic center wavelength is not exactly one third of the fundamental wavelength because the refractive indices vary with wavelength, however in practice, if a quarter wave stack has good reflectivity for one wavelength, it will have similar reflectivity at the third harmonic of that wavelength.

As for the laser cavity, if a resonator has a high resonator Q at the fundamental wavelength, then it usually has high resonator Q for the third harmonic and possibly the fifth harmonic if the fundamental is a long wavelength. In our case the resonator Q is actually slightly higher for the third harmonic than for the fundamental. Since the gain at the fundamental wavelength is typically much higher than the third and fifth harmonic gain, the laser will almost always lase at the fundamental with a quarter wave stack. If the wiggler is set to a wavelength 5/3 as long as the center wavelength of the quarter wave stack coating, the third harmonic of the coating will be coincident with the fifth harmonic of the FEL. There is very little resonator Q at 5/3 of the center wavelength or at 5/9 of the resonator wavelength where the third harmonic is resonant. The laser then lases at the fifth harmonic of the FEL and the third harmonic of the coating. Note that it is also possible to lase at the fundamental of the FEL with the third harmonic of the coating.

CASE 1. LASING AT HARMONICS AT A FIXED WAVELENGTH

The first measurements were performed with the same resonator and center wavelength, while varying the wiggler strength. The resonant wavelength of the wiggler was set to 1.02 microns, 3.06 microns, and 5.1 microns. All three settings produced strong lasing. The detuning curves for the three settings are show in figure 1. It is very interesting to note that the fundamental, which has the highest gain of the three, has the shortest detuning curve. According to G. Dattoli's formulas [7], the detuning curve length should be proportional to $GhN_W\lambda$. where G is the small signal gain, h is the harmonic number, N_W is the number of wiggler periods and λ is the laser wavelength. The ratio of the detuning curve lengths using the measured gain should be 3.5:6.0:5.7 according to the formula. The third and fifth are a bit shorter than this would indicate but they are also closer to threshold, which shortens the detuning curve.

Table 1 shows a comparison of measured and predicted gain and power, where predicted values were obtained using Dattoli's formulas. The measured gain was inferred from the minimum turn-on time in the detuning

curve. Simulations indicate that the turn-on time to half power is 22.5 e-foldings and direct measurements of the gain support this observation. The power was measured using a high power laser power meter accurate to 5%. The gain and power are in good agreement for the fundamental and fifth harmonic but the experimental gain is lower and power is much larger than predicted for the third harmonic. This may have been due to differences in accelerator setup though no single accelerator parameter can explain the discrepancy.

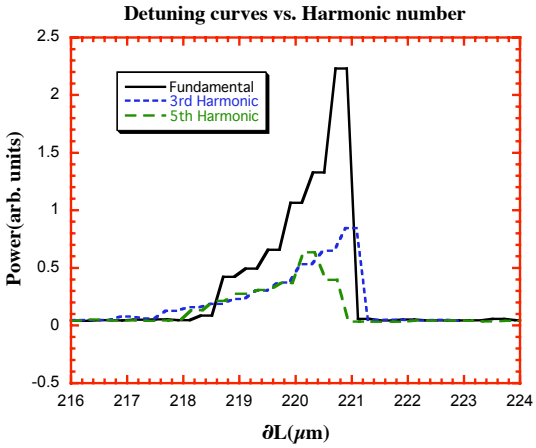

Figure 1. Power vs. cavity length for lasing at the fundamental, third, and fifth harmonic, with fundamental wavelength ~1.04 μm.

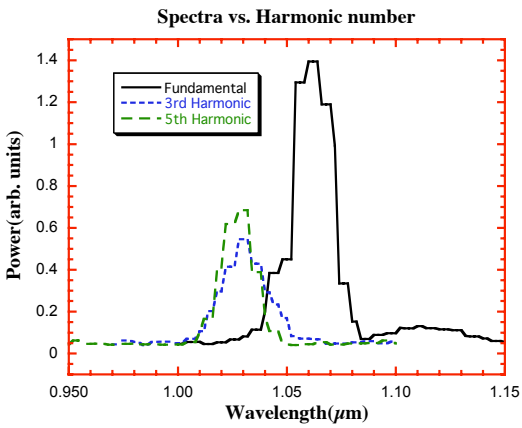

Figure 2. Spectra while lasing with 1.06 micron mirrors with the resonant wavelength equal to 1.02, 3.06, and 5.1 microns. The resonator losses were 3.5%/pass. Note the movement towards 1.02 microns as the harmonic number is increased.

Table 1. Measured and predicted gain and power when lasing at harmonics at ~1.04 microns.

h	Meas. Gain	Calc. Gain	Meas. Power(W)	Calc. Power (W)
1	48%	48%	700	885
3	20.4%	24%	275	180
5	11.6%	11%	63	65

Spectra for these three cases are shown in Figure 2. Note that the wavelengths are not the same. Simulations indicate that the lasing wavelength is typically a fraction $1/hN_W$ longer than the resonant wavelength. Since h is changing but the resonant wavelength is not, one expects the laser wavelength to get closer to the resonant wavelength. The fundamental is shifted further from the resonant wavelength because it is lasing harder than the harmonics, as is evident from the weak sideband at 1.11 μm.

CASE 2: LASING ON THE FIFTH HARMONIC OF THE LASER AND THE THIRD HARMONIC OF THE COATING

For both the 2.8 and 1.6 micron mirrors, it was possible to lase at the third harmonic of the laser coating and the fifth harmonic of the laser. For the 2.8 micron mirrors the wiggler was set to 4.65 microns and lased at 0.935 microns. For the 1.6 micron mirrors the wiggler was set to 2.74 microns and lased at 0.53 microns. In both cases the lasing was quite robust. Note that both mirror sets have higher reflectivity at the third harmonic than at the fundamental. The detuning curve at 0.53 μm was as long as 5 microns, which is comparable to the fundamental lasing curve. Dattoli's formula noted above, implies that the 5th harmonic gain is 3/5 of the fundamental gain. The gain inferred from the turn-on time and losses is about 1/3 the fundamental gain. Direct gain measurements will be necessary to resolve these discrepancies. The efficiency was not as good as the 1.06 micron lasing but we did obtain 35 W of CW light in the green.

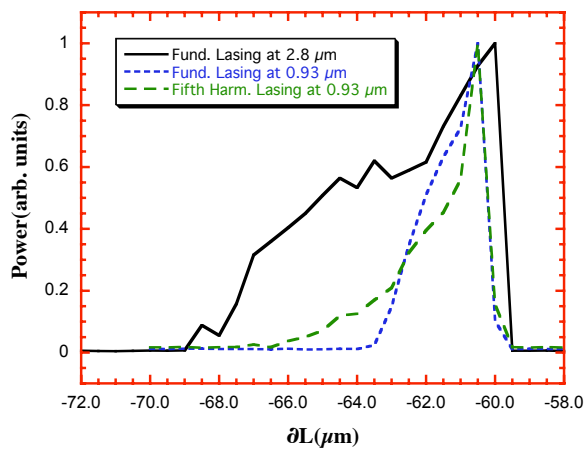

Figure 3. Detuning curves for three different configurations using the 2.8 micron mirrors.

In figure 3 we show the detuning curves while lasing at the fundamental using both the 2.8 μm and 0.935 μm reflectivity peaks. The detuning curves for the fundamental have a three to one ratio. Dattoli's formula then would indicate similar gain. In fact the gain at 2.8 microns is about 50% larger than at 0.935 microns. This apparent discrepancy has been seen before when varying the electron beam repetition rate [8]. Both curves have a convex shape (negative second derivative), which is common when the gain is well above threshold. The fifth harmonic curve at 0.935 μm should be five times as long as

the fundamental if the gain is similar. In fact it is only twice as long indicating a gain 40% of the fundamental. It also has a concave shape, which is typical for lasing close to threshold. The ratio between the fifth harmonic gain and fundamental gain is extremely sensitive to the energy spread. The ratio is 0.4:1 for an energy spread of 0.3%. This is a typical value for our machine, though the spread was not measured the day of these measurements.

CASE 3: A NEW WAY TO LASE AT THE THIRD HARMONIC

When the laser is very well tuned and the wavelength is very close to or slightly longer than the center wavelength of the mirror coatings, we see a very interesting phenomenon. The laser starts to lase sporadically at the third harmonic when the cavity length is very close to the synchronous cavity length where the round trip time in the resonator matches the arrival time of the electron bunches. This occurs for both the 1.6 micron and 2.8 micron mirrors. We sometimes use this as a measure of how well the laser is optimized. If the laser optimization is poor, harmonic lasing will not occur.

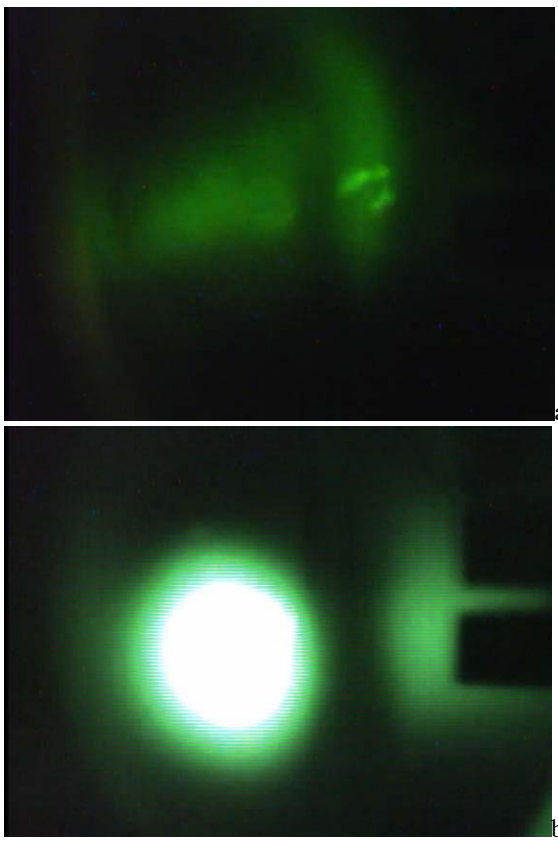

Figure 4. (a) coherent harmonics emitted during fundamental lasing on the output coupler of the laser. (b) Harmonic lasing at 0.53 microns obtained by lengthening the optical cavity by a fraction of a micron.

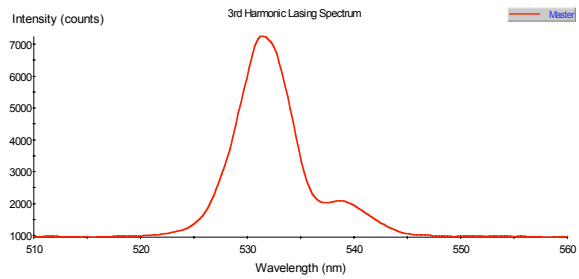

Figure 5. Lasing spectrum using an Ocean Optics visible spectrometer array. This is a single macropulse shot.

This behavior is shown in figure 4. In figure 4a we see the pattern of coherent spontaneous radiation that is always present when lasing at 1.6 microns. In figure 4b we have lengthened the optical cavity by a fraction of a micron and see very strong green emission with a TEM_{00} profile. The image here completely saturates the CCD camera. The spectrum of the third harmonic lasing is shown in Figure 5. This signal at 530 nm is not present when the cavity is tuned for strong fundamental lasing.

With the 2.8 μm mirrors the lasing can occur over a larger range of detuning and can be quite stable. In figure 6 we show a detuning curve obtained using a spectrometer at 0.935 microns. The detector did not show any signal when lasing at the fundamental but showed a strong signal when lasing at the 3rd harmonic.

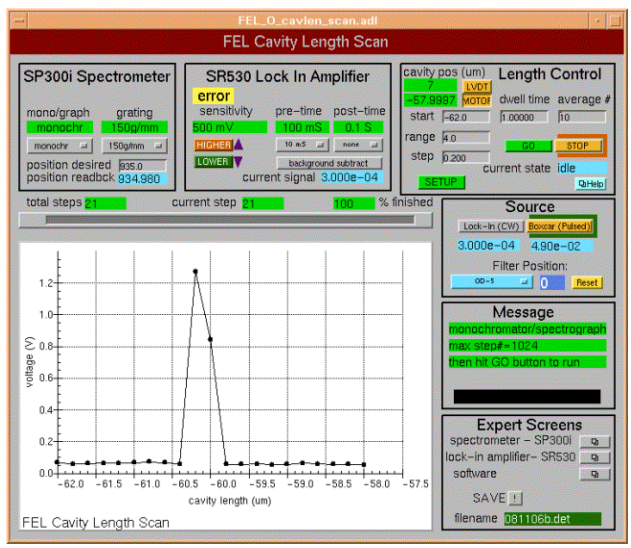

Figure 6. Detuning curve taken through a spectrometer set to 935 nm. The lasing occurs over about 0.5 microns in cavity length. The fundamental is not lasing over this range.

We do not understand exactly how this new lasing phenemonan works. It seems as though the round trip time in the resonator is less for the third harmonic than for the fundamental. This suggests that the fundamental light penetrates more deeply into the coating than the third harmonic light. The interference that produces the outgoing wave should be the same for the third harmonic as for the fundamental. The different penetration depth may

be related to the higher reflectivity of the coating at the third harmonic. Future experiments will study the wavelength dependence of the harmonic lasing and compare with reflectivity models of the coating.

CONCLUSIONS

The availability of a high brightness electron beam and a wiggler with large tuning range has opened up an interesting diagnostic device for free-electron lasers. Since the harmonic lasing is far more sensitive to beam parameters than the fundamental it allows one to more carefully optimize the laser. The presence of lasing at harmonics greatly restricts the laser modeling since the model must fit both the fundamental and harmonic lasing with the same optical resonator and electron beam.

In the future we plan to try to lase with an electron beam with half the energy spread of the one now used. This reduces the fundamental gain but greatly increases the harmonic gain. We should have a situation where the harmonic gain actually exceeds the fundamental gain. This should also allow lasing at the seventh and possibly the ninth harmonic.

ACKNOWLEDGEMENTS

George Neil was quite helpful in setting up the laser to take data. Shukui Zhang operated the Ocean Optics spectrometer to get the visible spectrum. This work was supported by U.S. DOE Contract No. DE-AC05-84-ER40150, the Office of Naval Research, the Air Force Research Laboratory, the Army Night Vision Laboratory, the Commonwealth of Virginia and the Laser Processing Consortium.

REFERENCES

[1] J. M. J. Madey, R. C. Taber, "Equations of Motion for a Free-electron Laser with a Transverse Gradient", In *Free-electron generators of coherent radiation*, **7,** Addison-Wesley (1979) 741.

[2] W. B. Colson, IEEE J. of Quant. Elec**. QE-17**, (1981) 1417.

[3] S. V. Benson, J. M. J. Madey, *Phys. Rev.* **A39**, (1989) 1579–1581.

[4] R. W. Warren, L. C. Haynes, D. W. Feldman, W. E. Stein, S. J. Gitomer, *Nucl. Inst. and Meth.* **A296** (1990) 84–88.

[5] George R. Neil, S. V. Benson, G. Biallas, J. Gubeli, K. Jordan, S. Myers, and M. D. Shinn, “Second Harmonic FEL Oscillation, Phys. Rev. Lett. **87**, (2001) 084801.

[6] S. Benson, M. Shinn, G. R. Neil, and T. Siggins, “First Demonstration of 5th Harmonic Lasing in a FEL”, presented at the 21st International FEL Conference, Hamburg Germany, August 1999.

[7] G. Dattoli, S. Cabrini, L. Gianessi, V. Loreto, and C. Mari, *Nucl. Inst. and Meth.* **A318** (1992) 495.

[8] S. Benson et al., *Nucl. Inst. and Meth.* **A429** (1999) 27–32.

A DESIGN STUDY OF A FIR/THZ FEL FOR HIGH MAGNETIC FIELD RESEARCH

M. Tecimer, L.C. Brunel, J. van Tol, NHMFL / FSU, Tallahassee, FL 32310, USA,
G. Neil, TJNAF, Newport News, VA 23606, USA.

Abstract

Presently a conceptual design for a NIR-FIR FEL system at the National High Magnetic Field Lab. - Florida State University (NHMFL-FSU) is being undertaken in collaboration with the FEL group at the Thomas Jefferson Laboratory. The system is expected to combine high magnetic field research with an intense, tuneable photon source spanning the spectral region ~ 2 - 1100 microns. Here, a design study involving the FIR/THz part of the NHMFL-FEL design proposal is presented. The suggested long-wavelength FEL encompasses in the first phase a thermionic injector with a ~2 mA average current and a ~10 MeV superconducting rf linac module operating at 1.3 GHz. The broadband outcoupling over the envisaged FIR/THz spectral range (100 - 1100 microns) can be accomplished by adopting a variable-outcoupler scheme in a waveguided cavity. Besides the performance predictions of the suggested long wave-length FEL, techniques for the generation of high peak power, nanoseconds long THz pulses (for magnetic resonance applications) are also briefly discussed.

Table 1:FIR FEL Specifications

PARAMETER	FIR FEL	UNITS
Wavelength	*100 to 1100*	μm
Micropulse Energy	*1 to 3*	μJ
Micropulse-width	*~ 5 to 60*	ps
Fract. bandwidth	*~ 0.3 - 5%*	
Resonator	*pp- waveguide, ~ 5.8*	m
Outcoupling	*Variable (others?)*	
Pulse rep. rate	*26 (13)*	MHz
Macropulse-width	*100μs to CW*	
Beam energy	*10 - 11*	MeV
Wiggler period	*70 (hybrid.)*	mm
Wiggler K	*0.6-3.5*	
Periods	*40*	

INTRODUCTION

In the framework of the NHMFL FEL initiative the design efforts for the construction of FIR/THz FEL radiation sources are twofold; the main effort is directed towards the generation of high peak power micropulses for time resolved measurements in the (tens of) picoseconds range. The planned rf-linac based system relies on relatively mature technologies developed at FELIX (FOM), Stanford, Jefferson Lab. and FZ-Rossendorf. The use of superconductive rf-linac cavities enables quasi-cw operation with the associated higher average THz radiation power levels (tens of Watts) and offers the possibility of an extension to an energy recovery linac (ERL) system (considered for the NIR-MIR FELs) as well. The second part of the FEL effort focuses on the development of techniques in producing relatively long ((sub-) nanoseconds), kW - level tuneable (sub-)millimetre wave pulses, in order to generate spin excitations at high magnetic fields and for possible pulsed magnetic resonance applications. While it has been shown that the FIR-FEL technology developed by the TeraHertz Center at UCSB with an electrostatic accelerator (EA) [1,2], this long wavelength range at the envisioned power levels have not yet been achieved with a rf linac system.

Here, we give an overview of the studied outcoupler design options and report on the simulated performance of a rf-linac driven waveguide FIR-FEL based on specified system settings. Finally, we discuss briefly on the current status of search for methods that would allow us to extend the inherently short pulse durations in the studied sc rf linac driven FIR FEL configuration into the ns range.

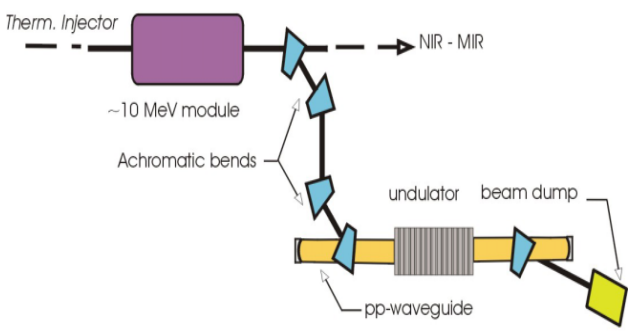

Figure 1: Layout of the FIR-FEL beamline option.

RF LINAC-FIR FEL DESIGN ISSUES

In the current design , the beam energy for the FIR FEL is provided by the first cryomodule (~10 MeV, operating at 1.3 GHz) which constitutes, along with the thermionic injector, the injector section of the NIR-MIR FELs. The thermionic injector system (a grid modulated DC gun followed by subharmonic and fundamental

mtecimer@magnet.fsu.edu

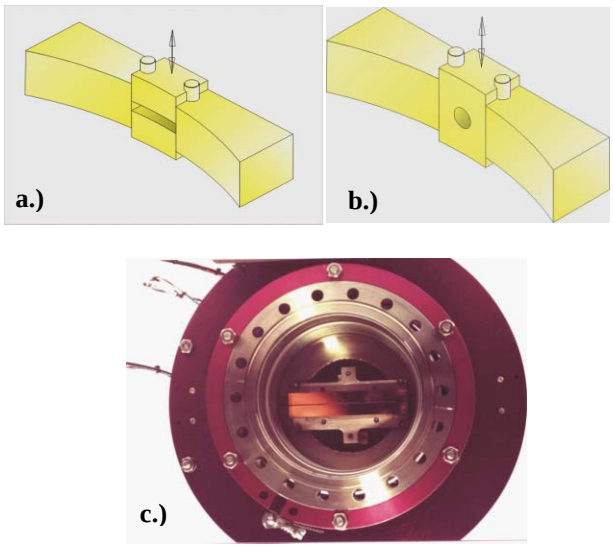

Figure 2 a-c: The lateral dimension of the outcoupler mirrors shown in a.) , b.) amounts to ~14 cm. The radius of curvature is ~3.5 m. The outcoupler mirror shown in c.) is constructed for an FIR FEL operating at ~230-650 μm.

bunchers) [3] is similar to the ones in use at FZ-Rossendorf and Stanford University. It is planned to provide ~2 mA average current at 26 MHz repetition rate. The NHMFL FIR-FEL is being designed to cover a large portion of the THz spectrum while employing a single wiggler, (possibly) a single cylindrical outcoupler mirror along with a waveguide structure that extends over the entire cavity (~5.8 meters). The latter option reduces the diffraction losses inherent in this long wavelength spectral region and avoids oversized cavity mirrors and mirror vacuum chambers. It requires the injection of the beam into the parallel-plate waveguide cavity (gap:10 mm) prior matching the beam into the undulator. After leaving the interaction section, the spent beam is directed into a beam dump. The design specifications along with the major system parameters are listed in Table 1.

The continuous tunability offered by the FEL over the envisaged large spectral range ideally would incorporate a broad-band feedback/outcoupling which can be accomplished by adopting a variable outcoupler scheme on one of the cylindrical metal-mirrors. The outcoupler option illustrated in Fig. 2a is a modified version of the variable height outcoupler (Fig. 2c) studied and realized in [4,5]. Adjusting the slot aperture in the vertical dimension between 0. – 3.0 mm continuously, the power output can be optimised over the entire 100 - 1100 microns. Hereby, the use of inserts with different lateral sizes (1.5mm, 3.0mm) allows one to keep the ratio of horizontal to vertical dimensions of the aperture < ~1.5 , at any slot aperture/wavelength configuration. In the second option, depicted in Fig. 2b, the middle insert (thus the centre of the hole aperture) is displaced in the vertical, sampling different areas of the hybrid waveguide mode on the mirror surface. The latter scheme covers the targeted wavelength range using max. three different hole apertures (or, alternatively, three cylindrical mirrors that could be moved up and down in the vertical, each having a different hole aperture). The optical beam transport accounts for the small (max. ~ 2 - 3 mm) off-axis displacement of the optical beam centre behind the outcoupler. Other variable outcoupler options such as FPI-meshes are being considered (as far as they remain operational at cw multi-kW level intracavity power), particularly for wavelengths above 500 microns.

The performance modelling of the FIR-FEL system is based on electron beam parameters (bunch charge, norm. transverse emittance, longitudinal emittance, energy spread) that are similar to those implemented at FZ-Rossendorf FEL, with the exception of an increase in the electron bunch repetition frequency up to 26 MHz, the latter being relevant in determining the resonator length and the average radiation power. Using the waveguide FEL code described in [5,6], that models the physics of a rf-linac driven, highly slippage dominated short pulse THz-FEL oscillator, the FEL performance for various

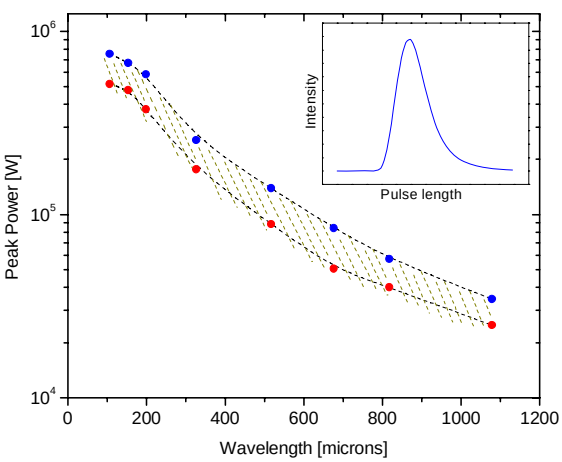

Figure 3: The upper peak power values (blue dots) are obtained at the peak of the detuning curve whereas the lower data points at cav. Detuning ~ -0.4·λ.

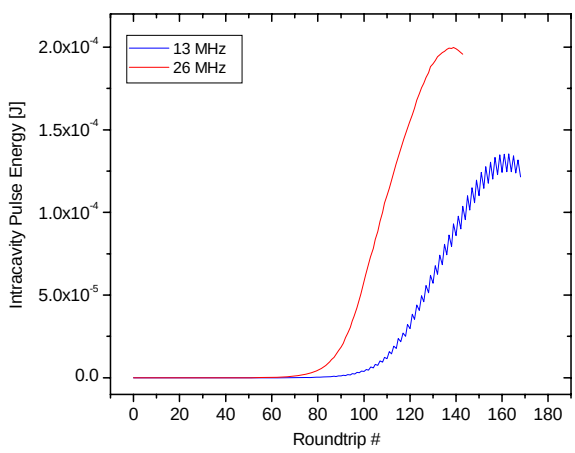

Figure 4: FEL operation at 13 MHz and 26 MHz pulse rep. rates with ~5.8 m cavity length , λ ~ 155 μm.

wavelength/wiggler settings (assuming a FEL operating at a fixed beam energy of 10.8 MeV) and outcoupling ratios (optimised by using the transmission characteristics of the scheme shown in Fig. 2a) are studied. An aspect that affects strongly the intracavity radiation build-up process and the evolution of the optical pulse structure is the use of ps-short electron bunches for the generation of (for rf-linac based systems unusually) long wavelength radiation in a waveguided propagation medium. Fig.3 shows the predicted (approximate) peak power levels achievable in the generated THz micropulses. The inset illustrates the simulated pulse shape whose leading edge exhibits a distinct exponential decay deviating from the Gaussian.

Another possible operational mode is driving the FIR FEL with 13 MHz rep. rate (limiting the average current to ~1mA), while keeping the waveguide resonator length 5.8 meters. In this case, the optical pulse interacts with the electron beam every other roundtrip, thus experiencing nearly twice as much cavity losses for each amplifying pass. The simulated evolution of the intracavity micropulse energy up to the saturation is shown in Fig. 4 at 155 microns (as an example) for both, 13 MHz and 26 MHz rep. rates. In the '13 MHz case' the outcoupling ratio is set to ~ 0.6 % (optimised to obtain the highest pulse energy coupled out), while the '26 MHz case' employs ~ 3.0 %. The calculated outcoupled pulse energies at different wavelengths indicate that 13 MHz rep. rate in combination with 5.8 m resonator length does not lead to a satisfying FEL operation. It results in a significant reduction in the pulse energies obtained. In addition, the micropulse energy fluctuations in subsequent roundtrips (by an amount defined by the cavity losses) may not be tolerable in many applications. In the following, simulated pulse energies are given for the '13 MHz and 26 MHz repetition rates' at two different wavelengths, 155 microns and 1080 microns respectively:

- '13 MHz 'case:

- outcoupled max. pulse energy ~0.7 μJ (@155 μm)
- outcoupled max. pulse energy ~0.3 μJ (@1080 μm)

- '26 MHz' case:

- outcoupled max. pulse energy ~3.1 μJ (@ ~155 μm)
- outcoupled max. pulse energy ~1.6 μJ (@ ~1080 μm)

GENERATION OF (SUB-) NS PULSES

For pulsed magnetic resonance excitations, the pulse length condition is given by $\gamma B_1 \tau \approx 0.5$ in which γ is 28 GHz/Tesla, B_1 is the amplitude of the oscillating magnetic field, and τ is the FIR pulse length. For the envisioned time resolution and the available power, the pulse length is of the order of 1 ns. At the present design stage, having optical pulse rep. rates of max. 26 MHz, the planned superconductive rf-linac FIR FEL configuration is not suitable for the implementation of interpulse phase-locking techniques described in [7] to generate narrow bandwidth, ns - long pulses. On the other hand, the flexibility offered by the variation of cavity desynchronization on modifying the pulse durations (thus the Fourier transform limited spectral bandwidth) falls short of providing the pulse lengthening effect that would be necessary to meet the requirements posed on the pulse durations and the associated spectral bandwidths. A possible (standard-) solution to lengthen the (rf-linac generated) picoseconds long optical pulses with sufficiently broad bandwidths is the use of grating stretchers [8], ending up with frequency chirped pulses of ns-duration. However, due to the introduced time frequency correlation within the pulse and the still existent broad bandwidth (not Fourier transform limited pulses), frequency chirped pulses remain restricted in their applications in the area of pulsed magnetic resonance experiments. Table 2 illustrates the parameters of a grating stretcher and the stretching factors achievable upon application of the device on the outcoupled FIR FEL pulses specified in Table 1. In Table 2, parameters *d*, *m*, *Z* denote the groove spacing of the blazed grating, the order at which the grating is used and the variable distance between the grating and the telescope mirror used in the setup, respectively.

Table 2: Grating Stretcher specifications

λ [μm]	*d* [μm]	*m*	*Z* [m]	*Initial* [ps]	*Final* [ns]
100	80	1	3.0	5.0	1.5
100	80	3	1.34	5.0	3.1
500	400	1	3.0	25.0	1.6
500	400	3	0.57	25.0	3.1
1000	800	1	3.0	65.0	1.2
1000	800	3	0.78	65.0	3.1

ACKNOWLEDGMENTS

We thank G. Ramian for helpful discussions. One of the authors (M.T.) acknowledges the input provided by P. Michel and J. Teichert regarding the sc rf-linac system at FZR-ELBE. This work has been supported by the NSF under grant no DMR-0520481.

REFERENCES

[1] G. Ramian, Nucl. Inst. and Meth. A 318, (1992) 225.

[2] Doty et al., Rev. Sci. Instrum., Vol.75, (2004) 2920.

[3] http://www.FZ-Rossendorf.de/ELBE

[4] M. Tecimer et al., Nucl. Instr. and Meth. A 528, (2004) 146.

[5] http://www2.hawaii.edu/~mtecimer

[6] M. Tecimer et al., Nucl. Instr. and Meth. A 528, (2004) 139.

[7] D. Oepts and W.B. Colson, IEEE QE-26, (1990) 723.

[8] E.B. Tracy and A.J. DeMaria, Phys. Lett., Vol. 29 A, 369.

EXPERIMENTAL STUDY OF A VOLUME FREE ELECTRON LASER WITH A "GRID" RESONATOR

V.G. Baryshevsky *, N.A.Belous, A.A.Gurinovich, A.S.Lobko, P.V.Molchanov, V.I.Stolyarsky,
Research Institute for Nuclear Problems, 11 Bobryiskaya str., 220050, Minsk, Belarus

Abstract

Operation of Volume Free Electron Laser with a "grid" photonic crystal, built from periodically strained metallic threads, was studied in the backward wave regime. Generation threshold was observed for different "grid" photonic crystals. Dependence of the generation threshold on the resonator length was investigated.

INTRODUCTION

Generators using radiation from an electron beam in a periodic slow-wave circuit (travelling wave tubes, backward wave oscillators, free electron lasers) are now widespread [1].

Diffraction radiation [2] in periodical structures is in the basis of operation of travelling wave tubes (TWT) [3, 4], backward wave oscillators (BWO) and such devices as Smith-Purcell lasers [5, 6, 7] and volume FELs using two- or three-dimensional distributed feedback [8, 9, 10, 11].

A challenge of precise electron beam guiding over the slowing structure (the electron beam should pass at the distance $\delta \leq \frac{\lambda\beta\gamma}{4\pi}$ over the diffraction grating, here δ is the so-called beam impact parameter, λ is the radiation wavelength, $\beta = v/c$, v is the electron beam velocity, γ is the electron Lorentz-factor) restricts application of Smith-Purcell lasers and the similar devices. Electrical endurance of resonator limits radiation power and current of acceptable electron beam. Conventional waveguide systems are essentially restricted by the requirement for transverse dimensions of resonator, which should not significantly exceed radiation wavelength.

The most of the above problems can be overcome in VFEL [8, 9, 10, 11, 12]. In VFEL the greater part of electron beam interacts with the electromagnetic wave due to volume distributed interaction. Transverse dimensions of VFEL resonator could significantly exceed radiation wavelength $D \gg \lambda$. In addition, electron beam and radiation power are distributed over the whole volume that is beneficial for electrical endurance of the system. One of the VFEL types uses a "grid" volume resonator ("grid" photonic crystal) that is formed by a periodically strained either dielectric or metallic threads.

The "grid" structure of dielectric threads was experimentally studied in [13], where it was shown that such "grid" photonic crystals have sufficiently high Q factors ($10^4 - 10^6$).

Theoretical analysis [14, 16] showed that periodic metal grid does not absorb electromagnetic radiation and the "grid" photonic crystal of metal threads is almost transparent for the electromagnetic waves in the wavelength range, where the skin-depth is less then the thread radius. The conclusions of [14] declared possibility of development of VFEL with the "grid" photonic crystal of metal threads.

First lasing of the volume FEL with a "grid" volume resonator, which was formed by the periodic set of metal threads inside a rectangular waveguide, was observed in the proof-of-principle experiment [15] and completely confirmed conclusions of [14].

In the present paper dependence of the generation intensity as a function of the grid photonic crystal length is studied for the backward wave oscillation regime.

THE CONCEPT

Waves propagation through photonic crystals is the subject for numerous studies both theoretical and experimental [17, 18, 19, 20].

Challenges, which appears when considering interaction of an electromagnetic wave with such a photonic crystal, are as follows: It is well known that a metal grid reflects electromagnetic waves perfectly. Therefore, the question arises as to whether a wave penetrate deep into resonator, especially since resonator contains a set of grids. Theoretical analysis [14, 16] showed that periodic metal grid does not absorb electromagnetic radiation and the "grid" photonic crystal, made of metal threads, is almost transparent for the electromagnetic waves in the frequency range from GHz to THz. In this range the skin depth δ is about 1 micron or less for the most of metals (for example, for 10 GHz $\delta_{Cu} = 0.66$ μm, $\delta_{Al} = 0.8$ μm, $\delta_W = 1.16$ μm and so on). Thus, in this frequency range the metallic threads can be considered as perfect conducting.

According to [14, 16] the refraction index for the "grid" photonic crystal, can be expressed as:

$$n^2_{\parallel(\perp)} = 1 + \frac{\eta_{\parallel(\perp)}}{k^2}, \qquad (1)$$

where

$$\eta_{\parallel(\perp)} = \frac{4\pi}{\Omega_2} \frac{A_0}{1 + i\pi A_0 - 2CA_0}, \qquad (2)$$

$n_\parallel$ and $n_\perp$ are the refraction indices for the waves with polarization parallel and perpendicular to the thread axis, respectively, $k = 2\pi/\lambda$ is the wave number, R is the thread radius, $\Omega_2 = d_y \cdot d_z$, where d_y and d_z are the photonic crystal periods along the axis y and z, respectively, $C = 0.5772$ is the Eiler constant. The values $A_{0(\parallel)}$ and $A_{0(\perp)}$ for perfectly conducting threads are defined as [15, 16]:

$$A_{0(\parallel)} = \frac{1}{\pi} \frac{J_0(kR) N_0(kR)}{J_0^2(kR) + N_0^2(kR)} + \frac{i}{\pi} \frac{J_0^2(kR)}{J_0^2(kR) + N_0^2(kR)},$$

* bar@inp.minsk.by

$$A_{0(\perp)}=\frac{1}{\pi}\frac{J_0'(kR)\,N_0'(kR)}{J_0'^2(kR)+N_0'^2(kR)}+\frac{i}{\pi}\frac{J_0'^2(kR)}{J_0'^2(kR)+N_0'^2(kR)}\,, \quad (3)$$

where J_0, N_0, J_0' and N_0' are the Bessel and Neumann functions and their derivatives, respectively.

To consider threads with finite conductivity one should use the following expressions:

$$A_{0(\parallel)}=\frac{i}{\pi}\frac{J_0(k_tR)J_0'(kR)-\sqrt{\varepsilon_t}J_0'(k_tR)J_0(kR)}{J_0(k_tR)H_0^{(1)\prime}(kR)-\sqrt{\varepsilon_t}J_0'(k_tR)H_0^{(1)}(kR)}, \quad (4)$$

$$A_{0(\perp)}=\frac{i}{\pi}\frac{J_0(k_tR)J_0'(kR)-\frac{1}{\sqrt{\varepsilon_t}}J_0'(k_tR)J_0(kR)}{J_0(k_tR)H_0^{(1)\prime}(kR)-\frac{1}{\sqrt{\varepsilon_t}}J_0'(k_tR)H_0^{(1)}(kR)}\,,$$

where ε_t is the dielectric permittivity of the thread material, $k_t=\sqrt{\varepsilon_t}k$, $H_0^{(1)}$ is the Hankel function of the zero order. The expressions (3) can be obtained from (4) considering $\varepsilon_t \to \infty$.

Difference in the refraction indices for different wave polarizations ($n_\parallel \neq n_\perp$) indicates that the system owns optical anisotropy (i.e. possesses birefringence and dichroism). To escape this anisotropy we can alternate the treads position in the grid: threads in each layer are orthogonal to those in the previous and following layers.

Smith - Purcell (diffraction) radiation in photonic crystal for an electron beam with the velocity $\vec{v}$ passing through the "grid"arises when the radiation condition is fulfilled:

$$\omega-\vec{k}n(k)\vec{v}=\vec{\tau}\vec{v}\,, \quad (5)$$

where $\vec{\tau}$ is the reciprocal lattice vector and $n(k)$ is the refraction index (see (1)). Suppose the electron beam velocity is directed along the axis OZ, then (5) can be presented in the form:

$$k-\tau_z\beta=k\,n(k)\,\beta\cos\theta, \quad (6)$$

where $\beta=\frac{v}{c}$, the angle between $\vec{k}$ and the electron beam velocity is denoted by θ and $\tau_z=\frac{2\pi m_h}{d_z}$, where $m_h=1,2,...$ is the number of harmonic. The roots of this equation give the spectrum of frequencies of diffraction (Smith-Purcell) radiation, which is induced by a particle moving in the above "grid" photonic crystal.

Diffraction radiation in a metal waveguide of the rectangular cross-section with the "grid" photonic crystal placed inside it is shown in [14, 16] to be described by the equation similar to (6):

$$(\frac{\omega-\tau_z v}{v})^2=(\frac{\omega}{c})^2-(\kappa_{mn}^2-\eta), \quad (7)$$

where η is determined by (2) and the eigenvalues κ_{mn} are determined by the waveguide transverse dimensions (width a and height b):

$$\kappa_{mn}^2=(\frac{\pi m}{a})^2+(\frac{\pi n}{b})^2\,. \quad (8)$$

The roots of equation (7) for $\frac{\eta}{\tau_z^2\beta^2}\ll 1$ can be obtained as:

$$\omega_1(m,n)=\frac{\tau_z v}{1-\beta^2}\left(1-\beta\sqrt{1-\frac{(\kappa_{mn}^2-\eta)}{\tau_z^2}\frac{1-\beta^2}{\beta^2}}\right), \quad (9)$$

$$\omega_2(m,n)=\frac{\tau_z v}{1-\beta^2}\left(1+\beta\sqrt{1-\frac{(\kappa_{mn}^2-\eta)}{\tau_z^2}\frac{1-\beta^2}{\beta^2}}\right).$$

It should be reminded here that $\tau_z=\frac{2\pi m_h}{d_z}$, where $m_h=1,2,...$ is the number of harmonic. From (9) it follows that higher harmonics provide for getting radiation with higher frequencies. For example, for the electron beam with the energy 200 keV, considering $\theta\sim 20^\circ$ and $d_z=1.6$ cm, the first harmonic ($m_h=1$) gives radiation frequencies ~ 10 GHz and ~ 40 GHz for the roots 1 and 2 of the equation (7), respectively, the 30-th harmonic ($m_h=30$) provides ~ 230 GHz and ~ 1 THz.

EXPERIMENTAL SETUP

The "grid" photonic crystal is built from tungsten threads with the diameter 0.1 mm strained inside the rectangular waveguide with the transversal dimensions $a=35$ mm, $b=35$ mm and length 300 mm (see Fig.1). The distance between the threads along the axis OZ is $d_z=12.5$ mm. A pencil-like electron beam with the diameter 32 mm, energy ~200 keV and current ~2kA passes through the above structure. The magnetic field guiding the electron beam is $\sim 1.55-1.6$ tesla. Period of grating is chosen to provide radiation frequency ~ 8.4 GHz. The "grid" structure

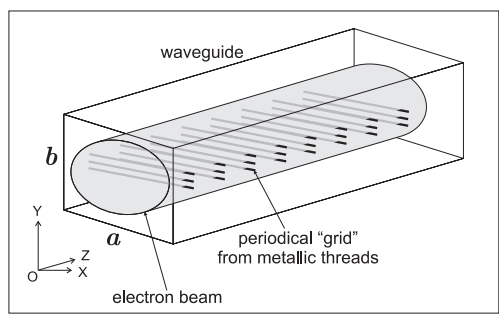

Figure 1: The "grid" diffraction grating placed inside the waveguide.

is made of separate frames each containing the layer of 1, 3 or 5 parallel threads with the distance between the next threads $d_y=6$ mm). Frames are joined to get the "grid" structure with the distance d_z between layers.

Frequency range was evaluated by means of tunable waveguide filters, which were tuned in the band 7.8 - 12.4 GHz with passbands 0.25 GHz, 0.5 GHz and 1 GHz. Attenuation of radiation in the suppressed band of this filter is ~ -25 dB.

EXPERIMENTAL RESULTS

The objective of the experiment is to study dependence of the generated radiation intensity on the "grid" photonic crystal length.

The maximal radiation power of VFEL generator in the this experiment was about 1.5 kiloWatt for one thread in the frame, 5 kiloWatts for three threads in the frame and 10 kiloWatt for five threads in the frame.

The sample oscillogram is shown in Fig.2, where signals marked 1 and 2 are the signals obtained from microwave detectors. Other two curves are the electron gun voltage and electron beam current. Time scale is 80 ns.

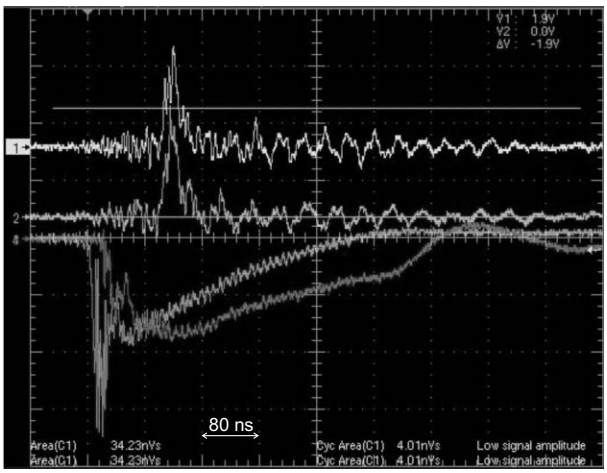

Figure 2: The sample oscillogram.

Two types of experiments are reported.

1. The radiation power was measured for photonic crystal with 4, 8, 10 and 24 frames each containing one thread equidistant from waveguide top and bottom walls (see Fig.3). The result of these measurements is presented in Fig.4, where the radiation power is normalized to the maximal detected power (1.5 kiloWatt).

2. The radiation power is measured for photonic crystal with 4, 6, 10, 12, 14 and 22 frames each containing five threads distant $d_y = 6$ mm each from other (see Fig.5).

The result of these measurements is presented in Fig.6, where the radiation power is also normalized to the maximal detected power (10 kiloWatt). The solid curve in this figure shows the numerically simulated radiation power, which also normalized.

CONCLUSION

Operation of Volume Free Electron Laser with a "grid" photonic crystal, built from periodically strained metallic threads, was studied in the backward wave regime. Generation threshold was observed for different "grid" photonic crystals. Dependence of the generation threshold on the resonator length was investigated. Use of volume resonators of the described type provides to weaken requirements for the electron beam shape and guiding precision,

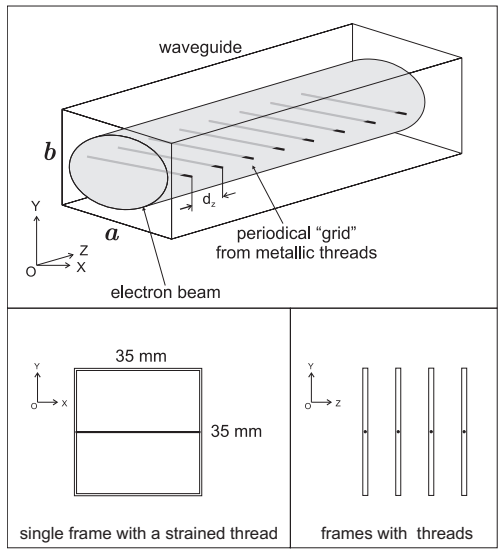

Figure 3: Photonic crystal with frames each containing one thread equidistant from waveguide top and bottom walls.

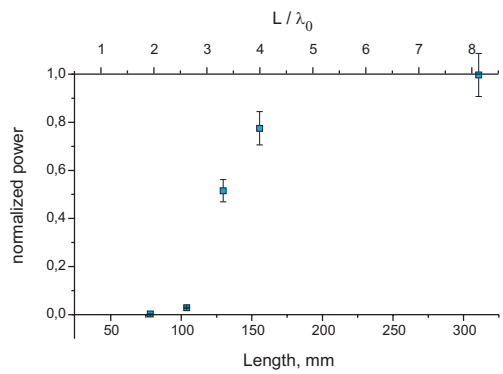

Figure 4: Dependence of the generation intensity on the length of the "grid" photonic crystal with one thread in the frame, the upper scale show the resonator length in the number of wavelength L/λ_0, where $\lambda_0 = 3.6$ cm.

because the electron beam passes directly through the photonic crystal.

REFERENCES

[1] V.L.Granatstein, R.K.Parker and C.M.Armstrong, Proceedings of the IEEE **87**, no.5 (1999).

[2] B.M.Bolotovskii and G.V.Voskresenskii, Usp. Fiz. Nauk. **88**, 209 (1966) (Sov. Phys. Usp. **9**, 73 (1966)).

[3] R.Kompfner, Wireless World **52**, 369 (1946).

[4] R.Pierce, Proc. IRE **35**, 111 (1947).

[5] S.J.Smith and E.M.Purcell, Phys. Rev. **92**, 1069 (1953).

[6] W.W.Salisbury, US Patent 2,634,372 (1953); J.Opt. Soc.Am. **60**, 1279 (1970).

[7] G.Doucas, J.H.Mulvey, M.Omori, J.Walsh and M.F.Kimmit, Phys.Rev.Lett. **69**, 1761 (1992); John E. Walsh US Patent 5,790,585 (1996).

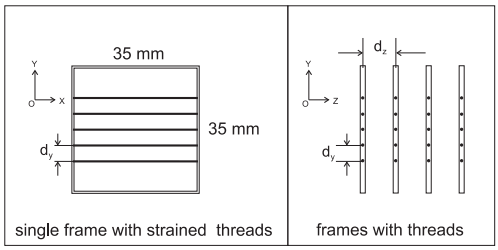

Figure 5: Photonic crystal with frames each containing five threads distant $d_y = 6$ mm each from other

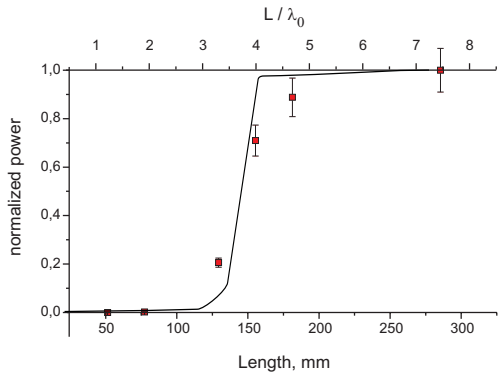

Figure 6: Dependence of the generation intensity on the length of the "grid" photonic crystal with 5 threads in the frame marked with squares and numerically simulated dependence of the wave amplitude on the "grid" photonic crystal length for the electron beam with the energy ∼200 keV and current density ~ 2 kA/cm^2

[8] V.G.Baryshevsky, NIM **445A**, 281 (2000); LANL e-print archive physics/9806039.

[9] V.G.Baryshevsky, K.G.Batrakov, A.A.Gurinovich et al., NIM **483A**, 21 (2002).

[10] V.G.Baryshevsky, K.G.Batrakov, A.A.Gurinovich et al., NIM **507A**, 137 (2003).

[11] V.G.Baryshevsky et al., Eurasian Patent no. 004665.

[12] V.G.Baryshevsky, I.D.Feranchuk, Phys.Lett. **102A**, 141 (1984).

[13] V.G.Baryshevsky,K.G.Batrakov,I.Ya.Dubovskaya,V.A.Karpovich, V.M.Rodionova, NIM **393A**, 71 (1997).

[14] V.G.Baryshevsky, A.A.Gurinovich LANL e-print archive: physics/0409107

[15] V.G. Baryshevsky, K.G. Batrakov, N.A. Belous, A.A. Gurinovich, A.S. Lobko, P.V. Molchanov, P.F. Sofronov, V.I. Stolyarsky, LANL e-print archive: physics/0409125.

[16] V.G.Baryshevsky, A.A.Gurinovich, to be published in NIM B, Topical Issue RC2005.

[17] A. L. Pokrovsky and A. L. Efros, Phys. Rev. **B 65**, 045110 (2002).

[18] A. L. Pokrovsky, Phys. Rev. **B 69**, 195108 (2004).

[19] E. I. Smirnova, C. Chen, M. A. Shapiro et al., J. Appl.Phys. **91**(3), 960 (2002).

[20] E. I. Smirnova and C. Chen, M. A., J. Appl.Phys. **93**(10), 5859 (2003).

[21] R.W. James, *The Optical Principles of Diffraction of X-Rays* (Ox Bow Press, 1982).

[22] Shih-Lin Chang, *Multiple diffraction of x-rays in crystals* (Springer-Verlag, 1984).

[23] V.V. Nikolsky , Electrodynamics and propagation of radiowave (Nauka, 1978)

ELECTRODYNAMICAL PROPERTIES OF A VOLUME FREE ELECTRON LASER WITH A "GRID" RESONATOR

V.G. Baryshevsky, A.A.Gurinovich *
Research Institute for Nuclear Problems, 11 Bobryiskaya str., 220050, Minsk, Belarus.

Abstract

The electrodynamic properties and lasing in Volume Free Electron Laser with a "grid" resonator ("grid" photonic crystal) with changing in space parameters are considered. The equations describing lasing of VFEL with such a resonator are obtained. It is shown that use of diffraction gratings (photonic crystal) with variable period increases radiation intensity and provide to create the dynamical wiggler with variable period. This makes possible to develop a double-cascaded FEL with variable parameters, which efficiency can be significantly higher then that of conventional system.

INTRODUCTION

Diffraction radiation [1] in periodical structures is in the basis of operation of travelling wave tubes (TWT) [2, 3], backward wave oscillators (BWO) and such devices as Smith-Purcell lasers [4, 5, 6] and volume Free Electron Lasers [7, 8, 9] (see also [10]).

Volume Free Electron Laser (VFEL) is a radiation generator using non-one-dimensional distributed feedback, which is created with the aid of Bragg diffraction gratings or photonic crystals.

One of the VFEL types uses a "grid" volume resonator ("grid" photonic crystal) that is formed by a periodically strained either dielectric [11] or metallic threads [12, 13, 14, 15].

In the present paper the electrodynamic properties and lasing in Volume Free Electron Laser with a "grid" resonator ("grid" photonic crystal) with changing in space parameters are considered. The equations describing lasing of VFEL with such a resonator are obtained. It is shown that use of diffraction gratings (photonic crystal) with variable period provide to create the dynamical wiggler with variable period. This makes possible to develop a double-cascaded FEL with variable parameters changing, which efficiency can be significantly higher that of conventional system.

THEORY OF LASING FOR VFEL WITH A "GRID" PHOTONIC CRYSTAL WITH VARIABLE PERIOD

To obtain equations, which describe VFEL lasing in the "grid" photonic crystal (see Fig.1), the Maxwell equations and motion equations for a particle in an electromagnetic field should be considered:

$$\mathrm{rot}\vec{H} = \frac{1}{c}\frac{\partial \vec{D}}{\partial t} + \frac{4\pi}{c}\vec{j},\ \mathrm{rot}\vec{E} = -\frac{1}{c}\frac{\partial \vec{H}}{\partial t},$$
$$\mathrm{div}\vec{D} = 4\pi\rho,\ \frac{\partial \rho}{\partial t} + \mathrm{div}\vec{j} = 0, \qquad (1)$$

here $\vec{E}$ and $\vec{H}$ are the electric and magnetic fields, $\vec{j}$ and ρ are the current and charge densities, the electromagnetic induction $D_i(\vec{r},t') = \int \varepsilon_{il}(\vec{r},t-t')E_l(\vec{r},t')dt'$ and, therefore, $D_i(\vec{r},\omega) = \varepsilon_{il}(\vec{r},\omega)E_l(\vec{r},\omega)$, the indices $i,l = 1,2,3$ correspond to the axes x,y,z, respectively. The current and charge densities are respectively defined as:

$$\vec{j}(\vec{r},t) = e\sum_\alpha \vec{v}_\alpha(t)\delta(\vec{r}-\vec{r}_\alpha(t)),\ \rho(\vec{r},t) = e\sum_\alpha \delta(\vec{r}-\vec{r}_\alpha(t)),$$

where e is the electron charge, $\vec{v}_\alpha$ is the velocity of the particle α (α numerates the beam particles),

$$\frac{d\vec{v}_\alpha}{dt} = \frac{e}{m\gamma_\alpha}\left\{\vec{E}(\vec{r}_\alpha,t) + \frac{1}{c}[\vec{v}_\alpha \times \vec{H}(\vec{r}_\alpha,t)] - \frac{\vec{v}_\alpha}{c^2}(\vec{v}_\alpha\vec{E}(\vec{r}_\alpha,t))\right\},$$

here $\gamma_\alpha = (1-\frac{v_\alpha^2}{c^2})^{-\frac{1}{2}}$ is the Lorentz-factor, $\vec{E}(\vec{r}_\alpha,t)$ and $\vec{H}(\vec{r}_\alpha,t)$ are the electric and magnetic field in the point of location $\vec{r}_\alpha = \vec{r}_\alpha(t)$ of the particle α.

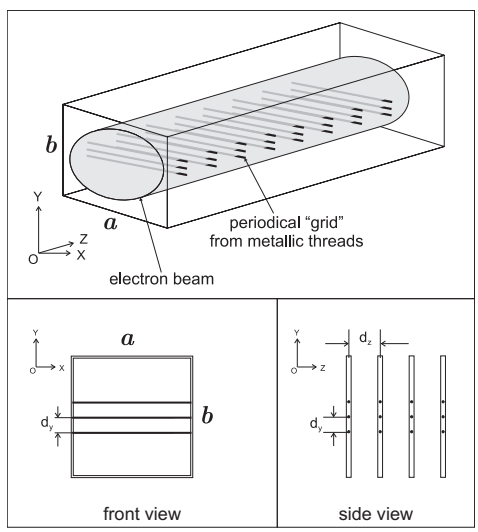

Figure 1: A "grid" photonic crystal.

The dielectric permittivity tensor can be expressed as $\hat{\varepsilon}(\vec{r}) = 1 + \hat{\chi}(\vec{r})$, where $\hat{\chi}(\vec{r})$ is the dielectric susceptibility.

* gur@inp.minsk.by

When $\hat{\chi} \ll 1$ the system (1) can be rewritten as:

$$\Delta\vec{E}(\vec{r},t) - \frac{1}{c^2}\frac{\partial^2}{\partial t^2}\int \hat{\varepsilon}(\vec{r},t-t')\vec{E}(\vec{r},t')dt' = \quad (2)$$
$$= 4\pi\left(\frac{1}{c^2}\frac{\partial\vec{j}(\vec{r},t)}{\partial t} + \vec{\nabla}\rho(\vec{r},t)\right).$$

When the grating is ideal $\hat{\chi}(\vec{r}) = \sum_\tau \hat{\chi}_\tau(\vec{r})e^{i\vec{\tau}\vec{r}}$, where $\vec{\tau}$ is the reciprocal lattice vector [16, 17].

Let the diffraction grating (photonic crystal) period is smoothly varied with distance, which is much greater then the diffraction grating (ptotonic crystal lattice) period. It is convenient in this case to present the susceptibility $\hat{\chi}(\vec{r})$ in the form, typical for theory of X-ray diffraction in crystals with lattice distortion [18]:

$$\hat{\chi}(\vec{r}) = \sum_\tau e^{i\Phi_\tau(\vec{r})}\hat{\chi}_\tau(\vec{r}), \quad (3)$$

where $\Phi_\tau(\vec{r}) = \int \vec{\tau}(\vec{r}')d\vec{l}'$, $\vec{\tau}(\vec{r}')$ is the reciprocal lattice vector in the vicinity of the point $\vec{r}'$. The expressions for $\hat{\chi}$ for the "grid" photonic crystal were obtained in [12, 14]:

$$\chi_{\parallel(\perp)} = \frac{4\pi}{\Omega_2 k^2}\,\frac{A_{0\parallel(\perp)}}{1 + i\pi A_{0\parallel(\perp)} - 2CA_{0\parallel(\perp)}}, \quad (4)$$

the symbols $\parallel$ and $\perp$ indicate the waves with polarization parallel and perpendicular to the thread axis, respectively, $k = 2\pi/\lambda$ is the wave number, R is the thread radius, $C = 0.5772$ is the Eiler constant, $\Omega_2 = d_y \cdot d_z$, where d_y and d_z are the photonic crystal periods along the axis y and z, respectively. The values $A_{0(\parallel)}$ and $A_{0(\perp)}$ for the threads with finite conductivity are defined as[14]:

$$A_{0(\parallel)} = \frac{i}{\pi}\frac{J_0(k_tR)J_0'(kR) - \sqrt{\varepsilon_t}J_0'(k_tR)J_0(kR)}{J_0(k_tR)H_0^{(1)\prime}(kR) - \sqrt{\varepsilon_t}J_0'(k_tR)H_0^{(1)}(kR)},$$
$$A_{0(\perp)} = \frac{i}{\pi}\frac{J_0(k_tR)J_0'(kR) - \frac{1}{\sqrt{\varepsilon_t}}J_0'(k_tR)J_0(kR)}{J_0(k_tR)H_0^{(1)\prime}(kR) - \frac{1}{\sqrt{\varepsilon_t}}J_0'(k_tR)H_0^{(1)}(kR)},$$

where ε_t is the dielectric permittivity of the thread material, $k_t = \sqrt{\varepsilon_t}k$, $H_0^{(1)}$ is the Hankel function of the zero order, J_0 and J_0' are the Bessel functions and their derivatives, respectively.

In contrast to the theory of X-rays diffraction, in the case under consideration $\hat{\chi}_\tau$ depends on $\vec{r}$. It is to the fact that $\hat{\chi}_\tau$ depends on the volume of the lattice unit cell Ω_2, which can be significantly varied for diffraction gratings (photonic crystals), as distinct from natural crystals.

It should be reminded that for an ideal crystal without lattice distortions, the wave, which propagates in crystal can be presented as a superposition of the plane waves:

$$\vec{E}(\vec{r},t) = \sum_{\vec{\tau}=0}^{\infty}\vec{A}_{\vec{\tau}}e^{i(\vec{k}_\tau\vec{r}-\omega t)}, \quad (5)$$

where $\vec{k}_\tau = \vec{k} + \vec{\tau}$.

In the case under consideration the solution of (2) can be written in the form (compare with [18]):

$$\vec{E}(\vec{r},t) = \mathrm{Re}\left\{\sum_{\vec{\tau}=0}^{\infty}\vec{A}_{\vec{\tau}}e^{i(\phi_\tau(\vec{r})-\omega t)}\right\}, \quad (6)$$

where $\phi_\tau(\vec{r}) = \int_0^{\vec{r}} k(\vec{r})d\vec{l} + \Phi_\tau(\vec{r})$ and $k(\vec{r})$ can be found as solution of the dispersion equation in the vicinity of the point with the coordinate vector $\vec{r}$, integration is done over the quasiclassical trajectory, which describes motion of the wavepacket in the photonic crystal with lattice distortion.

Let us consider now case when all the waves participating in the diffraction process lays in a plane (coupled wave diffraction, multiple-wave diffraction [17, 16]) i.e. all the reciprocal lattice vectors $\vec{\tau}$ lie in one plane. Suppose the wave polarization vector is orthogonal to the plane of diffraction.

Let us rewrite (6) in the form $\vec{E}(\vec{r},t) = \vec{e}\,E(\vec{r},t)$, where

$$E(\vec{r},t) = \mathrm{Re}\left\{\vec{A}_1e^{i(\phi_1(\vec{r})-\omega t)} + \vec{A}_2e^{i(\phi_2(\vec{r})-\omega t)} + ..\right\}, \quad (7)$$

$$\phi_1(\vec{r}) = \int_0^{\vec{r}}\vec{k}_1(\vec{r}')d\vec{l}, \quad (8)$$

$$\phi_2(\vec{r}) = \int_0^{\vec{r}}\vec{k}_1(\vec{r}')d\vec{l} + \int_0^{\vec{r}}\vec{\tau}(\vec{r}')d\vec{l}. \quad (9)$$

Then multiplying (2) by $\vec{e}$ one can get:

$$\Delta E(\vec{r},t) - \frac{1}{c^2}\frac{\partial^2}{\partial t^2}\int \hat{\varepsilon}(\vec{r},t-t')E(\vec{r},t')dt' = \quad (10)$$
$$= 4\pi\vec{e}\left(\frac{1}{c^2}\frac{\partial\vec{j}(\vec{r},t)}{\partial t} + \vec{\nabla}\rho(\vec{r},t)\right). \quad (11)$$

Substitution of (7) to (11) gives the following system:

$$\frac{1}{2}e^{i(\phi_1(\vec{r})-\omega t)}[2i\vec{k}_1(\vec{r})\vec{\nabla}A_1 + i\vec{\nabla}\vec{k}_1(\vec{r})A_1 - k_1^2(\vec{r})A_1 +$$
$$+\frac{\omega^2}{c^2}\varepsilon_0(\omega,\vec{r})A_1 + i\frac{1}{c^2}\frac{\partial\omega^2\varepsilon_0(\omega,\vec{r})}{\partial\omega}\frac{\partial A_1}{\partial t} + \frac{\omega}{c^2}^2\varepsilon_{-\tau}(\omega,\vec{r})A_2 +$$
$$+i\frac{1}{c^2}\frac{\partial\omega^2\varepsilon_{-\tau}(\omega,\vec{r})}{\partial\omega}\frac{\partial A_2}{\partial t}] + \text{ conjugated terms } =$$
$$= 4\pi\vec{e}\left(\frac{1}{c^2}\frac{\partial\vec{j}(\vec{r},t)}{\partial t} + \vec{\nabla}\rho(\vec{r},t)\right), \quad (12)$$
$$\frac{1}{2}e^{i(\phi_2(\vec{r})-\omega t)}[2i\vec{k}_2(\vec{r})\vec{\nabla}A_2 + i\vec{\nabla}\vec{k}_2(\vec{r})A_2 - k_2^2(\vec{r})A_2 +$$
$$+\frac{\omega^2}{c^2}\varepsilon_0(\omega,\vec{r})A_2 + i\frac{1}{c^2}\frac{\partial\omega^2\varepsilon_0(\omega,\vec{r})}{\partial\omega}\frac{\partial A_2}{\partial t} + \frac{\omega^2}{c^2}\varepsilon_\tau\,(\omega,\vec{r})A_1 +$$
$$+i\frac{1}{c^2}\frac{\partial\omega^2\varepsilon_\tau(\omega,\vec{r})}{\partial\omega}\frac{\partial A_1}{\partial t}] + \text{ conjugated terms } =$$
$$= 4\pi\vec{e}\left(\frac{1}{c^2}\frac{\partial\vec{j}(\vec{r},t)}{\partial t} + \vec{\nabla}\rho(\vec{r},t)\right),$$

where the vector $\vec{k}_2(\vec{r}) = \vec{k}_1(\vec{r}) + \vec{\tau}$, $\varepsilon_0(\omega,\vec{r}) = 1 + \chi_0(\vec{r})$, here notation $\chi_0(\vec{r}) = \chi_{\tau=0}(\vec{r})$ is used, $\varepsilon_\tau(\omega,\vec{r}) = \chi_\tau(\vec{r})$. Note here that for numerical analysis of (12), if $\chi_0 \ll 0$, it is convenient to take the vector $\vec{k}_1(\vec{r})$ in the form $\vec{k}_1(\vec{r}) = \vec{n}\sqrt{k^2 + \frac{\omega^2}{c^2}\chi_0(\vec{r})}$.

For better understanding let us suppose that the diffraction grating (photonic crystal lattice) period changes along one direction and define this direction as axis z.

Considering the right part of (2) let us take into account that microscopic currents and densities are the sums of terms, containing delta-functions, therefore, the right part can be rewritten as:

$$e^{-i(\vec{k}_\perp\vec{r}_\perp+\phi_{1z}(z)-\omega t)}4\pi\vec{e}\left(\frac{1}{c^2}\frac{\partial\vec{j}(\vec{r},t)}{\partial t}+\vec{\nabla}\rho(\vec{r},t)\right)=$$
$$=-\frac{4\pi i\omega e}{c^2}\vec{e}\sum_\alpha\vec{v}_\alpha(t)\delta(\vec{r}-\vec{r}_\alpha(t))e^{-i(\vec{k}_\perp\vec{r}_\perp+\phi_{1z}(z)-\omega t)}\times$$
$$\times\theta(t-t_\alpha)\,\theta(T_\alpha-t), \qquad (13)$$

here t_α is the time of entrance of particle α to the resonator, T_α is the time of particle leaving from the resonator, $\theta-$functions in (13) image the fact that for time moments preceding t_α and following T_α the particle α does not contribute in process.

Let us suppose now that a strong magnetic field is applied for beam guiding though the generation area. Thus, the problem appears one-dimensional (components v_x and v_y are suppressed). Averaging the right part of (13) over the particle positions inside the beam, points of particle entrance to the resonator $r_{\perp0\alpha}$ and time of particle entrance to the resonator t_α we can obtain:

$$e^{-i(\vec{k}_\perp\vec{r}_\perp+\phi_{1z}(z)-\omega t)}4\pi\vec{e}\left(\frac{1}{c^2}\frac{\partial\vec{j}(\vec{r},t)}{\partial t}+\vec{\nabla}\rho(\vec{r},t)\right)=$$
$$=-\frac{4\pi i\omega\rho\,\vartheta_1\,u(t)\,e}{c^2}\frac{1}{S}\int d^2\vec{r}_{\perp0}\frac{1}{T}\times \qquad (14)$$
$$\times\int_0^t e^{-i(\phi_1(\vec{r},\vec{r}_\perp,t,t_0)+\vec{k}_\perp\vec{r}_{\perp0}-\omega t)}dt_0=$$
$$=-\frac{4\pi i\omega\rho\,\vartheta_1\,u(t)\,e}{c^2}\langle\langle e^{-i(\phi_1(\vec{r},\vec{r}_\perp,t,t_0)+\vec{k}_\perp\vec{r}_{\perp0}-\omega t)}dt_0\rangle\rangle,$$

where ρ is the electron beam density , $u(t)$ is the mean electron beam velocity, which depends on time due to energy losses, $\vartheta_1=\sqrt{1-\frac{\omega^2}{\beta^2k_1^2c^2}}$, $\beta^2=1-\frac{1}{\gamma^2}$, $\langle\langle\ \rangle\rangle$ indicates averaging over transversal coordinate of point of particle entrance to the resonator $r_{\perp0\alpha}$ and time of particle entrance to the resonator t_α.

According to [19] averaging procedure in (14) can be simplified, when consider that random phases, appearing due to random transversal coordinate and time of entrance, presents in (14) as differences. Therefore, double integration over $d^2\vec{r}_{\perp0}\,dt_0$ can be replaced by single integration [19].

The system (12) in this case converts to:

$$2ik_{1z}(z)\frac{\partial A_1}{\partial z}+i\frac{\partial k_{1z}(z)}{\partial z}A_1-(k_\perp^2+k_{1z}^2(z))A_1+$$
$$+\frac{\omega^2}{c^2}\varepsilon_0(\omega,z)A_1+i\frac{1}{c^2}\frac{\partial\omega^2\varepsilon_0(\omega,z)}{\partial\omega}\frac{\partial A_1}{\partial t}+$$
$$+\frac{\omega^2}{c^2}\varepsilon_{-\tau}(\omega,z)A_2+i\frac{1}{c^2}\frac{\partial\omega^2\varepsilon_{-\tau}(\omega,z)}{\partial\omega}\frac{\partial A_2}{\partial t}=$$
$$=i\frac{2\omega}{c^2}J_1(k_{1z}(z)), \qquad (15)$$

$$2ik_{2z}(z)\frac{\partial A_2}{\partial z}+i\frac{\partial k_{2z}(z)}{\partial z}A_2-(k_\perp^2+k_{2z}^2(z))A_2+$$
$$+\frac{\omega^2}{c^2}\varepsilon_0(\omega,z)A_2+i\frac{1}{c^2}\frac{\partial\omega^2\varepsilon_0(\omega,z)}{\partial\omega}\frac{\partial A_2}{\partial t}+$$
$$+\frac{\omega^2}{c^2}\varepsilon_\tau(\omega,z)A_1+i\frac{1}{c^2}\frac{\partial\omega^2\varepsilon_\tau(\omega,z)}{\partial\omega}\frac{\partial A_1}{\partial t}=$$
$$=i\frac{2\omega}{c^2}J_2(k_{2z}(z)),$$

where the currents J_1, J_2 are determined by the expression

$$J_m=2\pi j\vartheta_m\int_0^{2\pi}\frac{2\pi-p}{8\pi^2}(e^{-i\phi_m(t,z,p)}+e^{-i\phi_m(t,z,-p)})dp,$$
$$\vartheta_m=\sqrt{1-\frac{\omega^2}{\beta^2k_m^2c^2}},\ m=1,2,\ \beta^2=1-\frac{1}{\gamma^2}\,, \qquad (16)$$

$j=en_0v$ is the current density, $A_1\equiv A_{\tau=0}$, $A_2\equiv A_\tau$, $\vec{k}_1=\vec{k}_{\tau=0}$, $\vec{k}_2=\vec{k}_1+\vec{\tau}$. The expressions for J_1 for k_1 independent on z was obtained in [19].

When more than two waves participate in diffraction process, the system (15) should be supplemented with equations for waves A_m, which are similar to those for A_1 and A_2.

Now we can find the equation for phase. From the expressions (8,9) it follows that

$$\frac{d^2\phi_m}{dz^2}+\frac{1}{v}\frac{dv}{dz}\frac{d\phi_m}{dz}=\frac{dk_m}{dz}+\frac{k_m}{v^2}\frac{d^2z}{dt^2}, \qquad (17)$$

Let us introduce new function $C(z)$ az follows:

$$\frac{d\phi_m}{dz}=C_m(z)e^{-\int_0^z\frac{1}{v}\frac{dv}{dz'}dz'}=\frac{v_0}{v(z)}C_m(z), \qquad (18)$$
$$\phi_m(z)=\phi_m(0)+\int_0^z\frac{v_0}{v(z')}C_m(z')dz'$$

Therefore,

$$\frac{dC_m(z)}{dz}=\frac{v(z)}{v_0}\left(\frac{dk_m}{dz}+\frac{k_m}{v^2}\frac{d^2z}{dt^2}\right). \qquad (19)$$

In the one-dimensional case the motion equation can be written as:

$$\frac{d^2z_\alpha}{dt^2}=\frac{e\vartheta}{m\gamma(z_\alpha,t,p)}\mathrm{Re}E(z_\alpha,t), \qquad (20)$$

therefore,

$$\frac{dC_m(z)}{dz}=\frac{v(z)}{v_0}\frac{dk_m}{dz}+ \qquad (21)$$
$$+\frac{k_m}{v_0v(z)}\frac{e\vartheta_m}{m\gamma^3(z,t(z),p)}Re\{A_m(z,t(z))e^{i\phi_m(z,t(z),p)}\},$$
$$\frac{d\phi_m(t,z,p)}{dz}|_{z=0}=k_{mz}-\frac{\omega}{v},\ \phi_m(t,z,p)|_{z=0}=p,$$
$$A_1|_{z=L}=E_1^0,\ A_2|_{z=L}=E_2^0,\ A_m|_{t=0}=0,\ m=1,2,$$
$$t>0,\ z\in[0,L],\ p\in[-2\pi,2\pi],$$

L is the length of the photonic crystal.

These equations should be supplied with the equations for $\gamma(z,p)$. It is well-known that

$$mc^2\frac{d\gamma}{dt} = e\vec{v}\vec{E}. \qquad (22)$$

Therefore,

$$\frac{d\gamma(z,t(z),p)}{dz} = \sum_l \frac{e\vartheta_l}{mc^2}\mathrm{Re}\{\sum_l A_l(z,t(z))e^{i\phi_l(z,t(z),p)}\}.$$

The above obtained equations (15,18,21,22) provide to describe generation process in FEL with varied parameters of diffraction grating (photonic crystal). Analysis of the system (21) can be simplified by replacement of the $\gamma(z,t(z),p)$ with its averaged by the initial phase value

$$\langle\gamma(z,t(z))\rangle = \frac{1}{2\pi}\int_0^{2\pi}\gamma(z,t(z),p)\,dp.$$

Note that the law of parameters change can be both smooth and stepped.

Analysis of such a system shows that its efficiency significantly exceeds efficiency of a system with constant parameters. Use of photonic crystals provide to develop different VFEL arrangements (see Fig.2). It should be noted

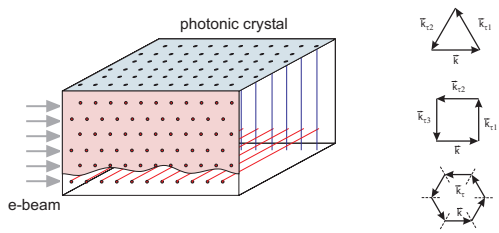

Figure 2: An example of photonic crystal with the thread arrangement providing multi-wave volume distributed feedback. Threads are arranged to couple several waves (three, four, six and so on), which appear due to diffraction in such a structure, in both the vertical and horizontal planes. The electronic beam takes the whole volume of photonic crystal.

that, for example, in the FEL (TWT,BWO) resonator with changing in space parameters of grating (photonic crystal) the electromagnetic wave with depending on z spatial period is formed (see eq. (6)). This means that the dynamical undulator with depending on z period appears along the whole resonator length i. e. tapering dynamical wiggler becomes settled. It is well known that tapering wiggler can significantly increase efficiency of the undulator FEL. The dynamical wiggler with varied period, which is proposed, can be used for development of double-cascaded FEL with parameters changing in space. The efficiency of such system can be significantly higher that of conventional system. Moreover, the period of dynamical wiggler can be done much shorter than that available for wigglers using static magnetic fields. It should be also noted that, due to dependence of the phase velocity of the electromagnetic wave on time, compression of the radiation pulse is possible in such a system.

CONCLUSION

The electrodynamic properties and lasing in Volume Free Electron Laser with a "grid" resonator ("grid" photonic crystal) with changing in space parameters are considered. The equations describing lasing of VFEL with such a resonator are obtained. It is shown that use of diffraction gratings (photonic crystal) with variable period increases radiation intensity and provide to create the dynamical wiggler with variable period. This makes possible to develop a double-cascaded FEL with variable parameters, which efficiency can be significantly higher then that of conventional system.

REFERENCES

[1] B.M.Bolotovskii and G.V.Voskresenskii, Usp. Fiz. Nauk. **88**, 209 (1966) (Sov. Phys. Usp. **9**, 73 (1966)).

[2] R.Kompfner, Wireless World **52**, 369 (1946).

[3] R.Pierce, Proc. IRE **35**, 111 (1947).

[4] S.J.Smith and E.M.Purcell, Phys. Rev. **92**, 1069 (1953).

[5] W.W.Salisbury, US Patent 2,634,372 (1953); J.Opt. Soc.Am. **60**, 1279 (1970).

[6] G.Doucas, J.H.Mulvey, M.Omori et al., Phys.Rev.Lett. **69**, 1761 (1992); John E. Walsh US Patent 5,790,585 (1996).

[7] V.G.Baryshevsky, NIM **445A**, 281 (2000); LANL e-print archive physics/9806039.

[8] V.G.Baryshevsky, K.G.Batrakov, A.A.Gurinovich et al., NIM **483A**, 21 (2002).

[9] V.G.Baryshevsky, K.G.Batrakov, A.A.Gurinovich et al., NIM **507A**, 137 (2003).

[10] V.L.Granatstein, R.K.Parker and C.M.Armstrong, Proceedings of the IEEE **87**, no.5 (1999).

[11] V.G.Baryshevsky, K.G.Batrakov, I.Ya.Dubovskaya, et al., NIM **393A**, 71 (1997).

[12] V.G.Baryshevsky, A.A.Gurinovich, LANL e-print archive: physics/0409107.

[13] V.G.Baryshevsky, K.G.Batrakov, N.A.Belous et al., LANL e-print archive: physics/0409125.

[14] V.G.Baryshevsky, A.A.Gurinovich, to be published in NIM B, Topical Issue RC2005.

[15] V.G. Baryshevsky, N.A. Belous, V.A. Evdokimov et al., LANL e-print arXiv: physics/0605122.

[16] R.W. James, *The Optical Principles of Diffraction of X-Rays* (Ox Bow Press, 1982).

[17] Shih-Lin Chang, *Multiple diffraction of x-rays in crystals* (Springer-Verlag, 1984).

[18] S.Takagi, Acta Crystall. **15**, 1311 (1962).

[19] K.G.Batrakov and S.N.Sytova, Computational Mathematics and Mathematical Physics **45**, No.4, 666 (2005).

LASER GAIN AND INTRA-CAVITY LOSSES OF THE ELBE MID-IR FEL

U. Lehnert, P. Michel, W. Seidel, J. Teichert, R.Wünsch
Forschungszentrum Rossendorf, PF 510119, 01328 Dresden, Germany.

Abstract

The U27-FEL of the ELBE radiation source allows to choose between five mirrors with different outcoupling holes. This allows to adapt the optical resonator to the required wavelength range to ensure the needed laser gain and to optimize the outcoupled laser power.

Another parameter which influences the achievable laser gain and output power is the detuning length of the optical cavity. While for CW operation often the minimum detuning point is choosen which maximizes the outcoupled power, for pulsed-mode operation about one wavelength of cavity detuning maximizes the laser gain and yields best stability of the laser.

To gain some insight into the behavior of the optical resonator we have measured the round-trip losses and the net laser gain and compared both to calulations. We have used a fast-readout MCT detector to measure the decay and rise-time of the outcoupled infrared beam caused by a 10 μs break in the electron beam micro-pulse train. We show gain and loss for 5, 10 and 20 μm wavelength with the typical detuning curves of an FEL.

INTRODUCTION

The U27 mid-IR FEL of the ELBE radiation source was designed to cover a wavelength range from 3 to 20 μm. The optical resonator is equipped with two spherical mirrors with a free propagating optical mode of fixed Rayleigh length. Therefore, the optical mode size at the mirrors shows a big variation over the whole wavelength range. To achieve a suitable outcoupling different sizes of the outcoupling hole are required. The mirror chamber containing the outcoupling mirror was designed with a mirror wheel which allows to choose between 5 different mirrors. At present outcoupling holes from 1.5 to 4 mm are available. Now, the fraction of outcoupling can be adjusted to ensure the needed laser gain and to optimize the outcoupled laser power.

GAIN AND LOSS MEASUREMENTS

For measurements of the laser gain and round-trip losses of the optical cavity we switch off the electron beam for a 10 μs period. An MCT detector with a fast readout electronics is used to measure the decay and rise of the optical power (see Fig. 1). The decay can easily be fitted by a single exponential giving the optical losses per round-trip.

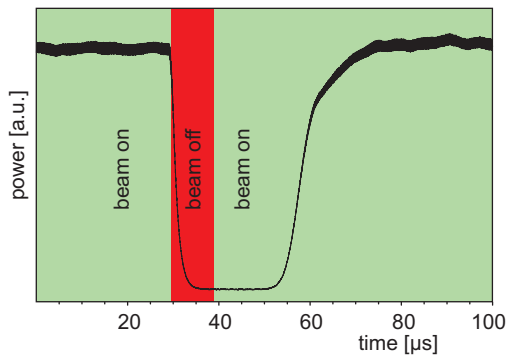

Figure 1: Decay and rise of the optical power caused by a 10 μs break of the electron beam.

ROUND-TRIP LOSSES

Round-trip losses inside the optical cavity were computed using the GLAD [1] code (see Fig. 2). The computation (totals shown with red triangles) includes the outcoupling of optical power (blue circles) as well as diffraction losses due to the aperture limits of the optical beam path in

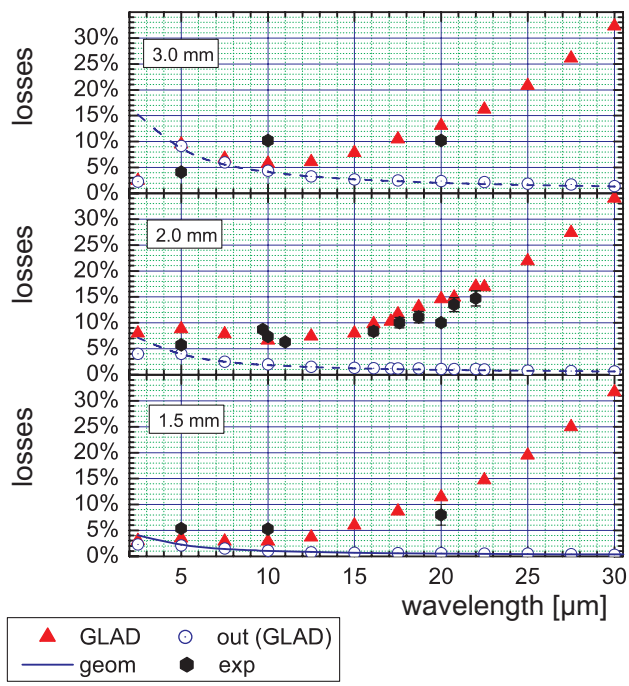

Figure 2: Comparison of measured and computed values of the round-trip losses inside the FEL resonator.

Table 1: Parameters of the optical resonator of the U27 FEL measured at 10 μm wavelength for different sizes of the outcoupling hole. The intra-cavity power is estimated using the computed fraction of outcoupling. To scale it to the saturation power a pulse length of 2 ps was assumed which was previously measured for a minimum-detuning setting of the optical resonator.

out-coupling hole size	1.5 mm	2.0 mm	3.0 mm
measured average power	16.8 W	24.8 W	13.9 W
measured round-trip losses	5.25 $\pm$ 0.25 %	7.25 $\pm$ 0.25 %	10.0 $\pm$ 0.6 %
computed round-trip losses	2.9 %	6.6 %	5.8 %
out-coupled fraction	1.1 %	2.0 %	4.4 %
average intra-cavity power	1600 W	1300 W	330 W
intra-cavity saturated power	62 MW	50 MW	13 MW

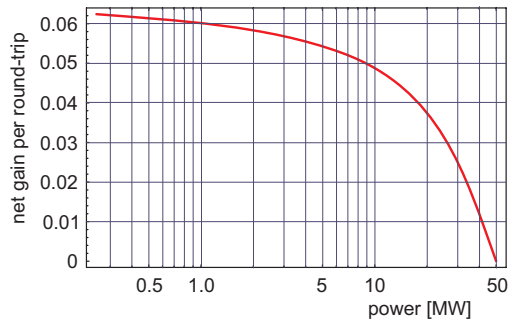

Figure 3: Analytical model of the gain drop at high laser powers approaching saturation.

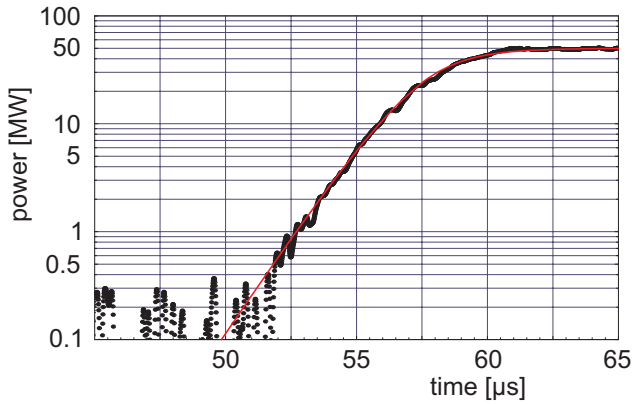

Figure 4: The rise of the optical power computed from the model in Fig. 3 very well fits the measured power data.

particular inside the undulator. The amount of outcoupling very well agrees with a simple geometrical model (blue line) except for very short wavelengths where the optical mode has a tendency to avoid the outcoupling hole. The latter effect was seen experimentally as well. At 5 μm wavelength the measured losses were significanly smaller when using the 3 mm outcoupling hole than with the 1.5 mm or 2 mm holes. In general, the measured round-trip losses show a quite reasonable agreement with the computation.

LASER GAIN AND POWER

The rise of the optical power is determined by the net laser gain. However, the rise curves shown in Fig. 1 need a more involved analysis as the gain itself depends on the optical power. We use a simple analytical model (see Fig. 3) to simulate the gain drop at high powers caused by overbunching and wave-breaking effects. This model very well fits the measured curves of the laser turn-on as shown in Fig. 4. In the example shown we have a 6% small-signal gain over 7% round-trip losses. The laser saturates at 50 MW optical power. At this point the gain has dropped to just match the losses.

THE OPTIMAL OUTCOUPLING

The measurements performed at 10 μm wavelength demonstrate that there exists an optimal outcoupling hole for a given cavity and beam setup. The data shown in Table 1 were measured with a 22 MeV electron beam with 50 pC bunch charge. The round-trip losses roughly correspond to the computed ones considering that the losses at the mirror surfaces are not included in the calculations. Going from 1.5 mm to 2 mm outcoupling hole size one sees the expected rise of the losses (approx. 2%) due to the outcoupling and the increased diffraction losses at the hole. At this power level the gain changes quite rapidly with the power. So the needed 2% higher gain translates only into a small drop of the intra-cavity power. The outcoupled power is increased. But when going further to 3 mm hole size the increased losses yield a much lower saturation power inside the cavity. Despite the higher outcoupling fraction the outcoupled power drops. The measured power levels again roughly confirm the gain model shown in Fig. 3.

REFERENCES

[1] GLAD, Applied Optics Research, Woodland, WA 98674, USA.

REMOTE CONTROLLED IR-DIAGNOSTIC STATION FOR THE FEL AT ROSSENDORF

W. Seidel, S. Friebel, R. Jainsch, M. Justus, K.-W. Leege, D. Proehl, D. Stehr, H. Weigelt, S. Winnerl, D. Wohlfarth
Forschungszentrum Rossendorf, Dresden, Germany

Abstract

The remote controlled diagnostic station delivers a small amount of the IR radiation by means of a system of relocatable mirrors, scraper mirrors and beam splitters to the spectrometer and to various power detectors working in different power ranges. Furthermore, a long wavelength MCT detector is integrated in the diagnostic station for gain and loss measurement in the whole wavelength range of the U27-FEL. The average FEL power for the users can be reduced by a remote controlled attenuator. We have built a non-collinear background-free autocorrelator as a part of the diagnostic station to characterize the optical micropulse duration. By using a CdTe single-crystal for second-harmonic generation a broad wavelength coverage is obtained. In order to decrease the average radiation power of the Rossendorf FEL, as required for certain experiments, the repetition rate can be reduced from 13 MHz to 1 kHz. For that aim a semiconductor plasma switch excited by a synchronized Nd:YAG amplifier is under commissioning and first results will be presented.

INTRODUCTION

The Radiation Source ELBE [1] at the Forschungszentrum Rossendorf in Dresden is centered around a superconducting Electron Linear accelerator of high Brilliance and low Emittance (ELBE), constructed to produce CW electron beams up to 1 mA beam current at 40 MeV. The electron beam is used to generate various kinds of secondary radiation, mainly to drive free-electron lasers in the infrared region (3-150 μm). Starting in the summer 2005, beam time is offered to external users in the frame of the EC funded "Integrating Activity on Synchrotron and Free Electron Laser Science" (FELBE project [2]). It is of great importance for routine user operation at ELBE that after changing the beam path or after beam interruptions stable operation in all wavelength ranges can be provided within a very short time (some minutes). Extensive diagnostics for the optical components of the FEL are very important to achieve fast availability.

DIAGNOSTIC STATION

Remote Controlled Power and Wavelength Measurement

We have developed an optical beam diagnostic system (see Fig. 1) to properly characterize and adapt the output of the two FELs (U27 and U100). The present system is

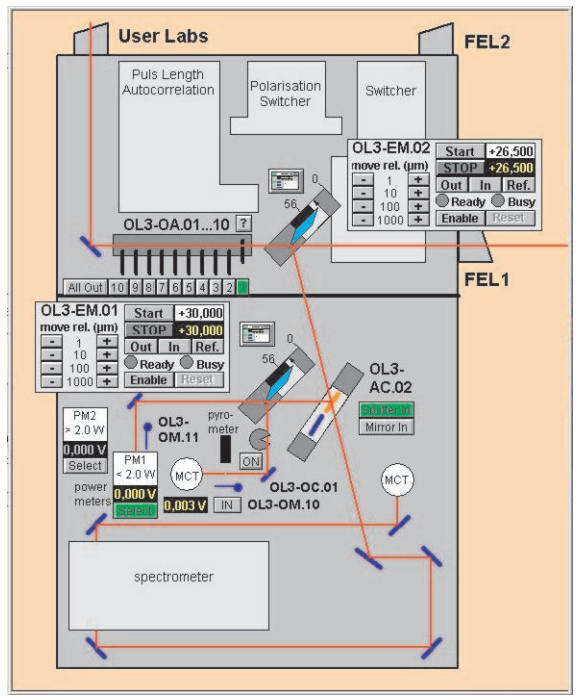

Figure 2: Interface of the remote controlled part of the IR-diagnostic station. One attenuator, two scraper mirrors on stepper controlled stages, one mirror and one beam splitter on a common pneumatic stage, spectrometer and different power meters are indicated. The red lines show different paths for the radiation when both scraper mirrors are not entirely within the beam.

compatible with a tuning range from 3 μm to 150μm, and can be extended beyond 150 μm, if necessary.

The FEL beam from each undulator will be transported separately from the resonator to the diagnostic area through beam pipes using reflective optics. Both lines will be merged on the diagnostic table, which may be purged with dry nitrogen to avoid absorption in air, if necessary. From here both the beams follow the same path. From the main beam, approximately 1-5 percent of the total power will be separated by a scraper mirror on a translation stage for wavelength measurement and power monitoring. The transmitted beam passes an attenuator and can be delivered to 6 optical laboratories. In this attenuator precisely fabricated metal grids diffract a calibrated (3,5, and 3 $\times$ 10 dB) percentage of power out of the beam. The rejected power is absorbed in the walls of the housing. The mode structure and other properties of the transmitted beam in-

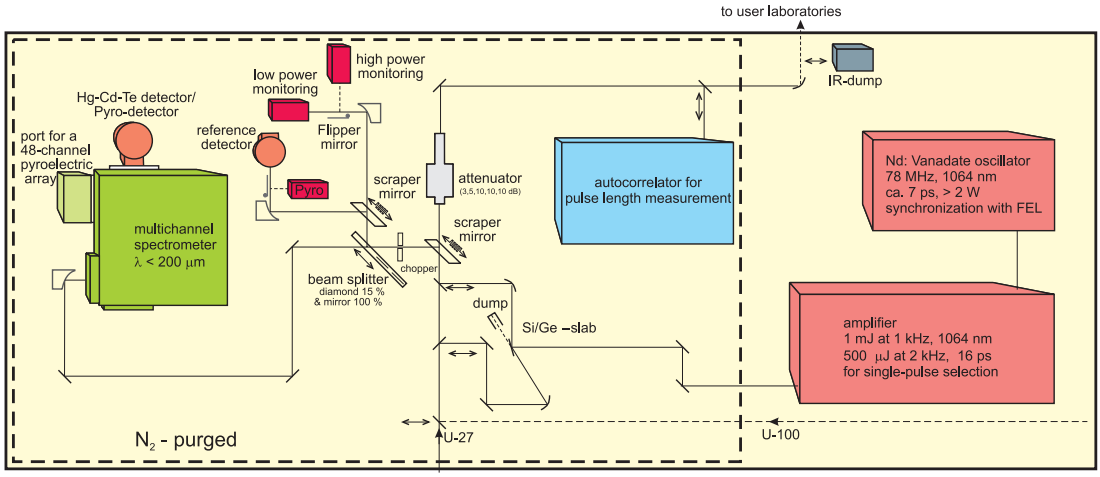

Figure 1: Arrangement of the different optical components and devices on the table.

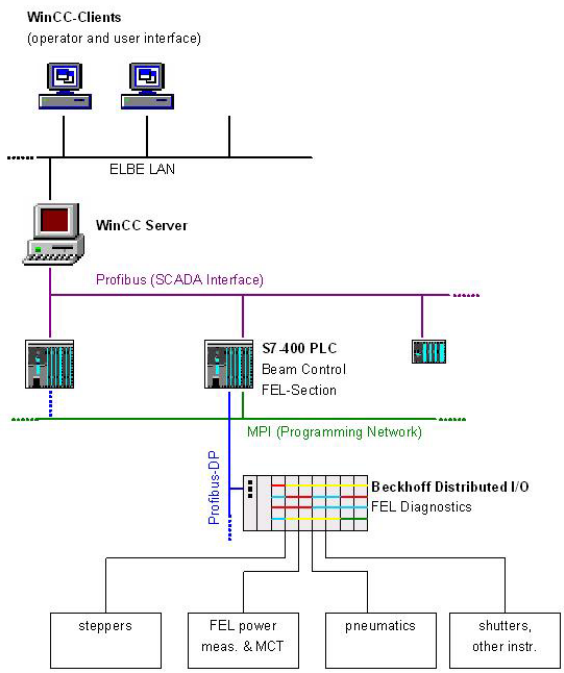

Figure 3: The existing Programmable Logic Control (PLC) and Human-Machine-Interface (HMI) environment of ELBE with the integrated FEL diagnostics instrumentation.

cluding the divergence and the M^2 parameters are fully preserved, the polarisation as well. The deflected part of the power goes through a synchronized chopper for measurement in CW-mode. Next to this the outcoupled beam is deflected by a mirror or a diamond beam splitter (350 μm thick, under 45 degrees, deflection 15 %) at a pneumatic translation stage. The beam transmitted through the diamond beam splitter (85 %) is transported to the spectrometer. The spectrum is measured with a Czerny-Turner type spectrometer which contains a turret with three different gratings to cover the whole wavelength range from 3 μm to about 200 μm. The monochromator will be equipped in near future with a 48-channel pyroelectric linear array detector. We use the second side exit slit equipped with a single Hg-Cd-Te or Ge-Ga detector for measurements with higher sensitivity. The part reflected from the pneumatic device is distributed with an other scraper mirror and two flipper mirrors to different power meters and reference detectors for monitoring the lasing process (see Fig. 2). The FEL diagnostic instrumentation has been integrated into the existing Programmable Logic Control (PLC) and Human-Machine-Interface (HMI) environment of ELBE (see Fig. 3). It ensures the access both for operators and users of the FEL. The basic technologies used are the WinCC server/client system, the SIMATIK PLC system and distributed I/O by Beckhoff Automation for control of pneumatic components (i.e. attenuators), analogue data logging (FEL power, MCT) and other instrumentation. The stepper control drivers for the scraper mirrors are integrated system components, whereby using (expensive) separate controllers could be avoided.

Characterization of the Optical Pulse

The optical pulse length can sensitively be tuned by varying the resonator length with respect to the nominal length resulting from the electron bunch repetition rate. At minimum detuning one yields the highest saturated power and the shortest optical pulse length. By detuning the resonator the spectral width can be decreased simultaneously increasing the pulse length. To characterize the ultrashort pulses generated by the FEL we built a non-collinear background-free autocorrelator system. We used a CdTe crystal as SHG medium [3], since it is transparent for a wide wavelength range in the FIR. We measured the autocorrelation function at maximum power in the detuning curve at a wavelength of 11.09 μm (see Fig. 4, upper part). We deduced a pulse duration of 0.89 ps (FWHM), assuming a Gaussian temporal pulse shape. The measured FWHM of the spectrum is approx. 176 nm. The cal-

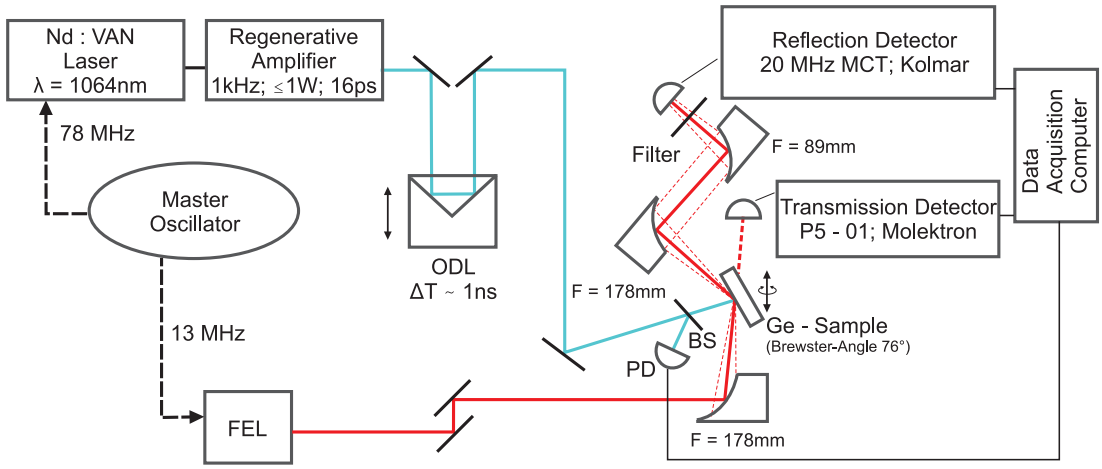

Figure 5: Setup for the plasma switch (see below).

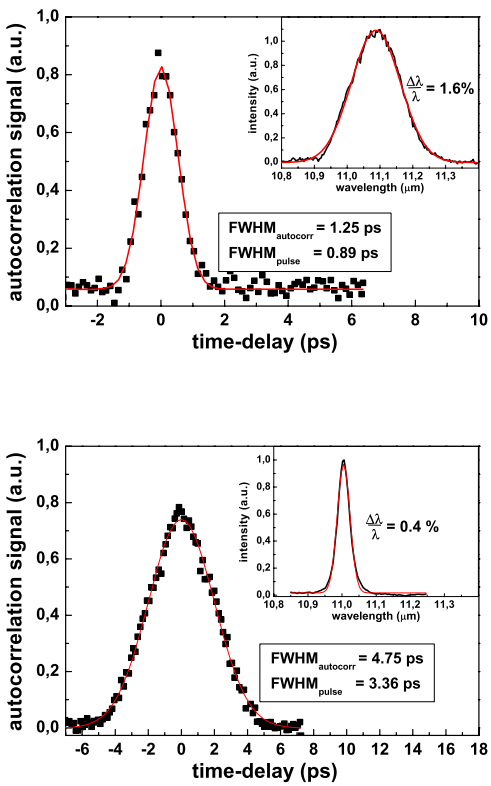

Figure 4: Pulse duration and the corresponding FWHM of the wavelength of 11 μm at maximum of the detuning curve (upper part) and from a detuned resonator (lower part).

culated time-bandwidth product is about 0.4 which indicates Fourier-transform limited operation. Long IR pulses with narrow bandwidth can be obtained from a detuned resonator (see Fig. 4, lower part).

Extraction of Single FEL Radiation Pulses Using a Laser-Activated Plasma Switch

In order to decrease the average radiation power of the Rossendorf free-electron laser FELBE, as required for certain experiments (high pulse energies but moderate or low average power), the FEL repetition rate can be reduced from 13 MHz to 1 kHz. To this end, plasma switching of FEL radiation pulses was demonstrated. The plasma switch bases on the principle of photo-induced reflectivity by an optically excited electron-hole plasma [4, 5]. Germanium serves as semiconductor material for the switch. The semiconductor was illuminated by a Nd:YAG laser amplifier system (1 kHz, λ = 1064 nm, $\tau \sim 16$ ps, $\leq$1 Watt), generating an electron-hole plasma on the front surface of the semiconductor. The generation of sufficient plasma density leads to a variation of the optical semiconductor properties for the infrared FEL-radiation (strongly focused and under Brewster's angle). For realizing the pulse selection the frequencies of both laser sources (FEL and Nd:YAG) were synchronised with RF electronics. For the exact timing of both laser pulses, when they hit the semiconductor, they were detected with a photon-drag detector or a fast pyroelectric detector (FEL) and a photo diode (Nd:YAG) and were adjusted on each other with cables, phase-shifter (trombone) and through moving a precision linear stage. Fig. 5 shows the experimental set-up. A gold mirror served as a reference for determining the reflectivity of the Germanium. The selected FEL pulses were detected by a fast MCT detector with a bandwidth of 20 MHz. Fig. 6 shows the switched pulse in two amplitude scales. The signal from the switch laser (photo diode) is shown in red. From the comparison of the black and blue curves we obtained an amount of dark pulses in the switched beam of about 0.5 % due to the angle of beam spread from the focussing. The time-resolved measurement of the reflectivity yields an exponential decay with a time constant of 590 ps. For the highest value of the Nd:YAG laser amplifier peak fluence of 25 mJ/cm^2, a reflectivity of Ge for FEL radi-

ation ($\lambda = 11\mu m$) of 100 % was achieved (see Fig. 7). We thus succeeded to extract single FEL radiation pulses out of the 13 MHz pulse train, indicating that this plasma switch is most suitable for the Rossendorf FEL. Further examinations will concentrate on achieving similar results for shorter wavelength. To integrate this plasma-switch into the existing diagnostic station we have to build an additional by-pass to the Germanium or Silicon slab which is under Brewster's angle (see Fig. 1). The selcted micro pulse will be refocused to the waist parameters outside of the by-pass line and transported to the user stations.

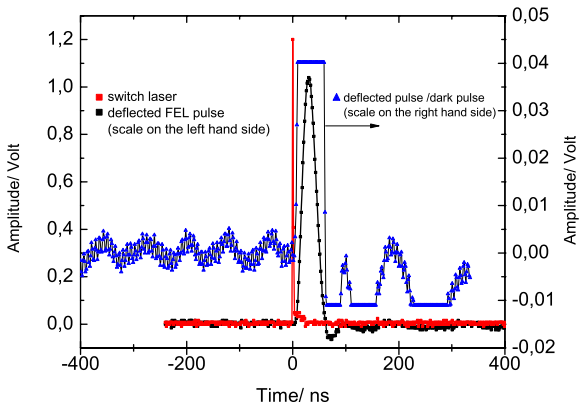

Figure 6: The switched FEL pulse at 11 μm in two different amplitude scales is measured by a fast MCT detector with a bandwidth of 20 MHz. The signal from the switch laser (photo diode) is shown in red. From the comparison of the black and blue curves we obtain an amount of dark pulse in the switched beam of about 0.5 %.

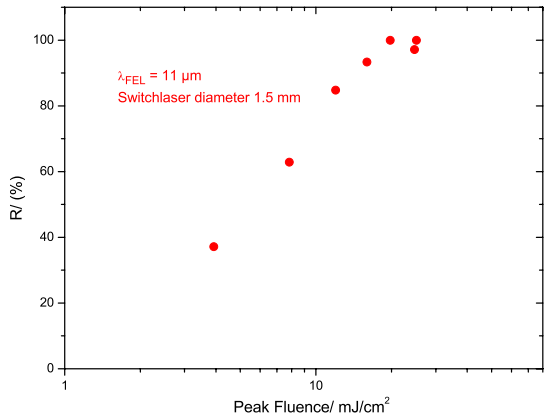

Figure 7: Dependence of reflectivity on the pump-laser peak fluence.

REFERENCES

[1] P. Michel et al., Proceedings of the 2004 FEL Conference, p. 8-13, Trieste, Italy

[2] www.fz-rossendorf.de/felbe

[3] J. Xu, G.M. Knippels, D. Oepts, and A.F.G. van der Meer, Opt. Comm. 197 (2001) 379-383

[4] P. Haar, Ph.D. thesis, Standford University (1996)

[5] E.H. Haselhoff et al., Nucl. Instr. and Meth. A358 (1995) ABS28

THE PARTIAL-WAVEGUIDE RESONATOR OF THE U100-FEL AT FZ ROSSENDORF

M. Freitag, R. Schlenk, W. Seidel, U. Willkommen, D. Wohlfarth, R. Wuensch, B. Wustmann,
FZ Rossendorf, Dresden, Germany.

THE U100-FEL

At the radiation source ELBE [1] an FEL with a permanent magnet undulator (U100) [2] has been constructed to extend the wavelength range to above 150 μm. Its lowest wavelength (20 μm) overlaps with the existing U27-FEL (Fig. 1). There is a first experimental evidence that wavelengths below 20 μm, maybe down to 15 μm, can also be reached.

The undulator is composed of 38 magnetic periods, each 100 mm long. The hybrid structure consists of SmCo magnets and soft-iron poles. It guarantees a sufficiently high magnetic field at a reasonable undulator gap, and a high radiation resistance. Increasing the gap from 24 to 85 mm the undulator parameter $K_{\rm rms}$ varies from 2.7 to 0.3.

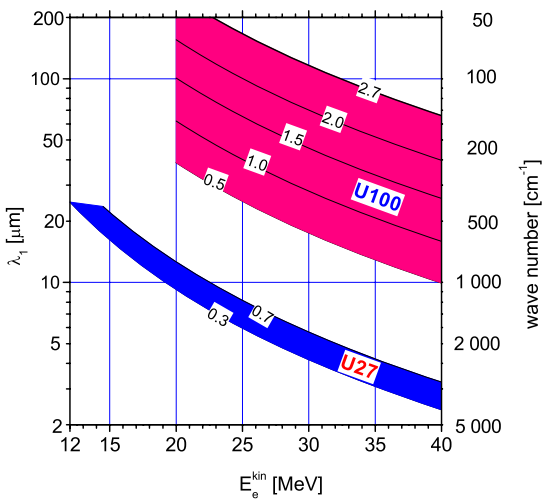

Figure 1: Wavelength λ_1 (fundamental harmonic) of the U27- and U-100 FELs as a function of the kinetic electron energy $E_{\rm e}^{\rm kin}$ calculated for the indicated undulator parameters $K_{\rm rms}$.

A waveguide was installed to fit the optical resonator mode into the undulator gap. It is 10 mm high and spans over 7.92 m from the undulator entrance to the resonator mirror M2 on the opposite side of the resonator (Fig. 2). The waveguide consists of two parallel plates, each 5 mm thick and divided into three pieces made out of non-magnetic stainless steel. In the horizontal direction the waveguide is wide enough to allow a free propagation of the optical beam. On the upstream side of the electron beam the optical beam propagates freely - both horizontally and vertically - through quadrupole and dipole magnets up to the toroidal mirror M1 with an outcoupling hole in the center.

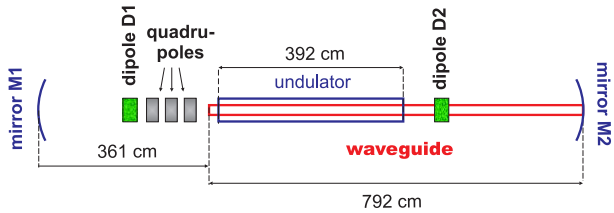

Figure 2: Scheme of the U100 resonator with partial waveguide. The electron beam enters the resonator at the dipole magnet D1 and leaves it at D2.

The partial waveguide causes a series of problems which are not present in the case of an open resonator. The mirrors must have different curvatures in horizontal and vertical direction. Although embedded in the waveguide, the downstream mirror M2 must be movable to adjust beam direction and resonator length. The narrow waveguide complicates the entering of screens and mirrors for beam diagnostics, and impedes the evacuation of the vacuum chamber.

RESONATOR MIRRORS

In the horizontal direction the infrared beam has a Gaussian shape. The curvature of the resonator mirrors corresponds to a Rayleigh length of 180 cm with a waist in the center of the undulator. Within the waveguide the vertical propagation is confined by the upper and lower plate of the waveguide. The downstream mirror M2 is cylindrical and focuses the beam only in horizontal direction. On the opposite side the vertical beam size increases rapidly behind the exit of the waveguide. The size of the beam at the surface of mirror M1 depends strongly on the wavelength. This is illustrated in Fig. 3. The size of the mirrors (black rectangle) covers more than 99% of the beam intensity even at 150 μm.

At the entrance into the waveguide, the optical mode must be converted from a freely propagating one into a waveguide mode and vice versa. This conversion causes optical losses which reduces the net gain of the laser. In general, the curvature of mirror M1 which minimizes the mode conversion losses depends on the wavelength. In our case, the waveguide is sufficiently far away from M1 and we can use a common radius of curvature for all wave-

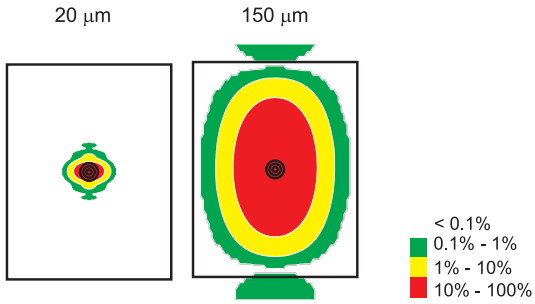

Figure 3: Transverse distribution of the light intensity at the surface of the outcoupling mirror M1 in comparison with the mirror size (black rectangle) calculated for the shortest (20 μm) and the longest wavelength (150 μm). The various colors represent the relative intensity in percent while the small circles in the center indicate the various outcoupling holes.

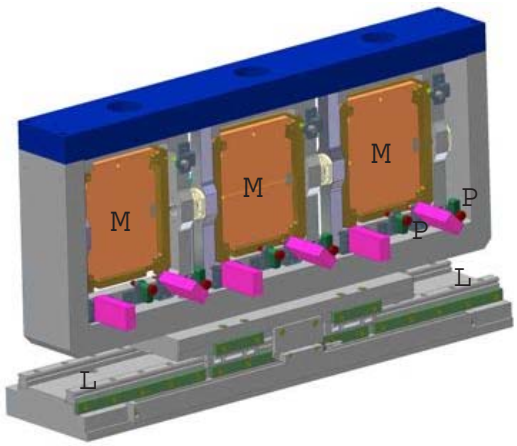

Figure 4: Support for the three mirrors M1. M: mirror, P: piezoelectric drives, L: linear translation stage,

lengths of the operating range of the U100-FEL. Above 35 μm the calculated coupling losses per round trip are below 5% [2]. Only at wavelengths below 25 μm they exceed 10% (simulations by means of the code GLAD [3]).

The beam is outcoupled through a circular hole in the center of mirror M1. Because of the large variation of the beam radius (factor 3) and of the expected laser gain (factor 5) in the operational range of the U100-FEL we need outcoupling holes of different size. We chose a set of 3 mirrors with the same curvature and holes with a diameter of 2, 4.5 and 7 mm. They are mounted on a support (Fig. 4). Using a linear translation stage the appropriate mirror can be shifted into the right position. The mirrors are gold-coated copper mirrors and cooled by water. They can be tilted horizontally and vertically by means of piezoelectric drives.

MIRROR ALIGNMENT AND CONTROL SYSTEM

Fig. 5 shows the scheme of the resonator alignment control system. It is similar to the system developed and used for the U27-FEL [4]. The correct location of the resonator axis is checked by means of two HeNe laser beams introduced into the resonator by auxiliary and pop-in mirrors.

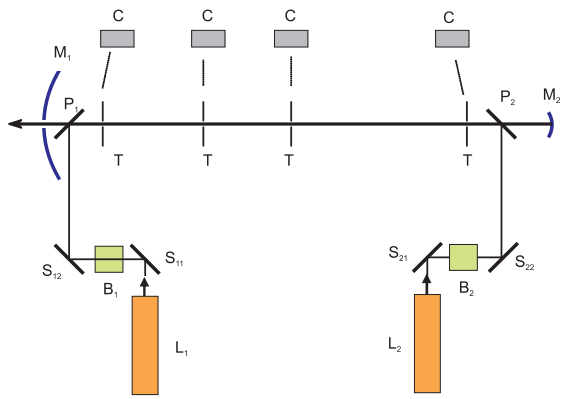

Figure 5: Schematic view of the resonator alignment system. $M_{1,2}$: resonator mirrors, $L_{1,2}$: HeNe alignment lasers, $B_{1,2}$: beam expander, $S_{11,12,21,22}$: steering mirrors, $P_{1,2}$: pop-in mirrors, T: adjustment apertures, C: monitoring cameras

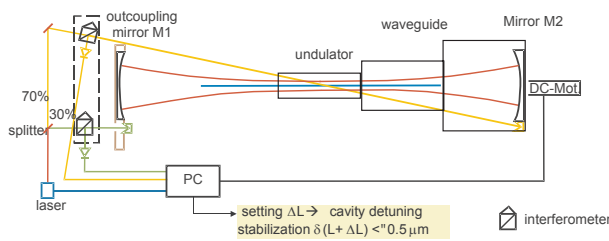

Figure 6: Schematic view of the resonator length control system.

A Hewlett-Packard interferometer system [5] is used for monitoring the resonator length (Fig. 6). It has also been taken from the U27-FEL.

The resonator has to be set and stabilized to a certain length and its axis has to be aligned to the electron beam. For that aim the mirrors are gimbal-mounted and can be tilted horizontally and vertically by means of piezoelectric (M1) and DC drives (M2). They allow the mirrors to be tilted up to 15 mrad in steps of 1 μrad. Moreover the cylindrical mirror M2 can be shifted along the resonator axis by 3.6 mm in steps of 100 nm (hysteresis 2 μm) by means of remote controlled DC drives (Fig. 7). Steps and hysteresis can additionally be reduced by a factor of about 30 by means of a beam in bending. Fig. 8 shows the opened mirror chamber M2.

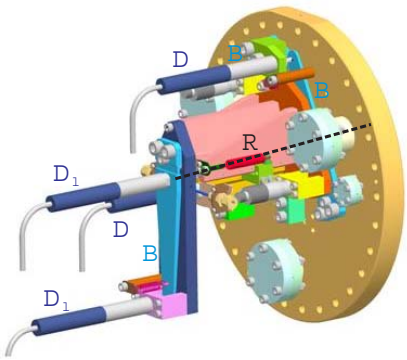

Figure 7: Back side of the flange of mirror chamber M2 with control elements. The mirror is mounted on the center of the front side. Schematic view with DC drives (D) for mirror tilting and shifting (D_l). The broken line (R) indicates the hidden driving rod, which transfers the motion onto the mirror on the front side. The beams in bending are labelled by B.

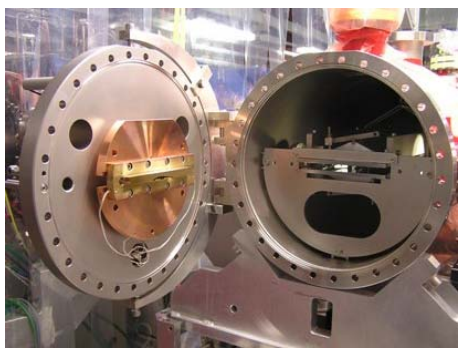

Figure 8: Open mirror chamber M2 with the rectangular cylindrical mirror (left side) and the end of the waveguide (right side).

BEAM DIAGNOSTICS

There is an extensive beam diagnostics system within the resonator region consisting of 20 view screens, markers and auxiliary mirrors. Most of them have to be inserted into the waveguide. They are not allowed to touch the polished surface of the waveguide, which is only 10 mm high. Fig. 9 shows the scheme of an auxiliary mirror with the corresponding insertion unit. The mirror is mounted at the end of a rod extending into the waveguide. The rod can be shifted into the waveguide by means of a pneumatic cylinder. It can precisely be moved along and perpendicular to the resonator axis, and allows an additional torsion of the rod which leads to a controlled and extremely sensitive tilting of the mirror at its head. The accuracy is 30 μm and 5μrad, respectively. Similar insertion units are used for OTR screens (7 mm high) made of beryllium with a 1 mm hole, foil screens consisting of a stretched aluminum foil, and markers (8 mm high) with a hole for the alignment and interferometer lasers. Among them are the pop-in mirrors and apertures used for the resonator alignment system (Fig. 5). CCD cameras in lead housings are used for observing the screens and markers through the viewports (Fig. 9).

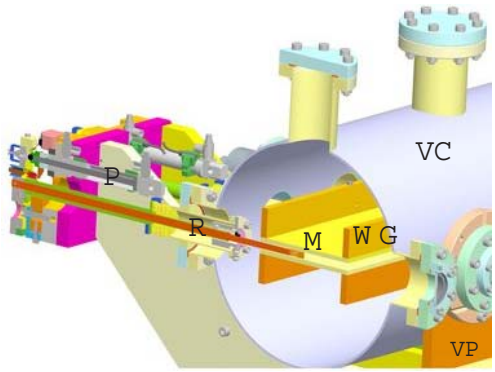

Figure 9: Diagnostic mirror for resonator axis tuning insertable into the waveguide. M: mirror, R: rod, P: pneumatic cylinder, VC: vacuum chamber, WG: waveguide, VP: view port.

Beam positioning monitors with an aperture of 75 mm have been developed for the online measurement of the electron beam position. One of them is located in front of the waveguide entrance.

VACUUM MANIFOLD

The presence of the waveguide does not allow to place the getter pumps directly below the beam line. A vacuum manifold with 6 getter pumps and 7 ports (Fig. 10) is installed below the waveguide instead. Their total throughput amounts to 520 l/s. An additional getter pump with 350 l/s throughput is fixed below each mirror chamber. The electron beam line can be separated by vacuum valves upstream and downstream the resonator. Another valve separates the mirror chamber M1 with the outcoupling window. Additionally, four powerful turbomolecular pumps

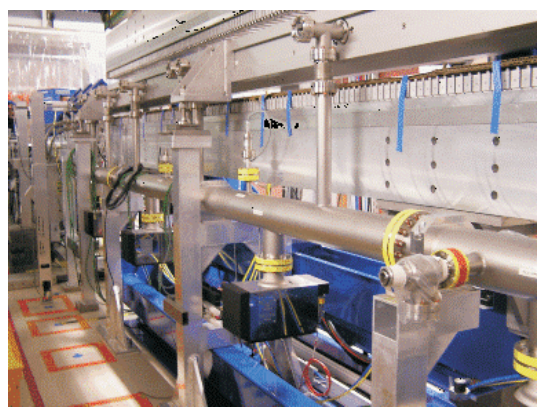

Figure 10: Collective vacuum line with getter pumps and connectors to the waveguide.

are linked to the manifold and to both mirror chamber as

well. They ensure to hold the vacuum in the whole system in the case of a local rise in pressure. Membrane pumps serve as fore-vacuum pumps. In stand-by mode the turbo- and membrane pumps can be switched off.

The system can be vented by means of needle valves with dry and particle-free nitrogen gas. A mass spectrometer allows to analyze the residual gas. The pressure in the vacuum line and in the mirror chambers is measured by means of Penning and Pirani vacuum gage heads.

SUMMARY

At the radiation source ELBE, another free-electron laser has started to produce light in the far infrared region. It is capable of producing IR radiation between 20 and 200 μm. Its resonator was equipped with a partial waveguide to allow a small undulator gap. Curvature and size of the resonator mirrors were adapted to minimimum optical losses. To optimize the outcoupled laser power three mirrors with circular holes of different size were installed on a linear translation stage. The resonator was equipped with a control and alignment laser system which allows to adjust and stabilize the resonator length and to align the resonator mirrors. Special beam diagnostic elements, which can be inserted into the waveguide, and a vacuum manifold were developed to fix the beam position and to ensure an extreme vacuum within the narrow waveguide.

REFERENCES

[1] http://www.FZ-Rossendorf.de/ELBE

[2] E. Grosse et al., FEL'05, Aug. 2005, SLAC, TUPP031, http://www.JACoW.org

[3] GLAD, Applied Optics Research, Woodland, WA 98674, USA.

[4] U. Lehnert et al., FEL'05, Aug. 2005, SLAC, MOPP032, http://www.JACoW.org

[5] U. Lehnert et al., FEL'05, Aug. 2005, SLAC, TUPP030, http://www.JACoW.org

NEW RESONATOR FOR THE ISRAELI FEL

A. Faingersh, Y. Socol, E. Dyunin, J. Dadoun, Kh. Garb, A.Gover#,
Dept. of Physical Electronics - Faculty of Engineering, Tel-Aviv University,
Tel-Aviv, Israel

M. Einat, B. Litvak, B. Kapilevich, Y. Pinhasi, A. Yahalom,
Dept. of Electrical and Electronic Engineering - The College of Judea and Samaria, Ariel, Israel

G. Denisov, M. Shmelev,
Institute of Applied Physics, Nizhniy Novgorod, Russia

Abstract

The Israeli FEL resonator (W-band 75-110 GHz) was re-designed in order to reduce the overall round-trip losses and to control the radiation out-coupling.

In its new configuration, the resonator consists of an overmoded corrugated rectangular waveguide and two radiation mode splitters, separating the high-energy e-beam from the mm-wave radiation. The electron input splitter is based on Talbot effect in an overmoded rectangular waveguide. The radiation out-coupling takes place in the output splitter. The splitter is based on a novel design. It combines Talbot effect between two parallel plates with free space propagation and with focusing by two curved cylindrical mirrors in a confocal imaging scheme.

The waveguide and the splitters were tested, showing improved performance in comparison with the former resonator. The measured unloaded Q-factor of the new resonator is increased by a factor of ~3, up to Q=25,000. Accordingly, the round-trip losses are ~23%. Rotating grids control the radiation out-coupling, allowing optimization of the radiation power and the extraction efficiency. The design layout and the testing results are presented.

NEW RESONATOR DESIGN

The Israeli FEL with Curved Parallel Plate (CPP) waveguide-based resonator was reported earlier [1-2]. Only a small part (~5%) of the generated RF energy was coupled out in these configuration. In order to minimize the total round-trip losses of the resonator, it was re-designed. The previously used CPP waveguide was substituted by a two-corrugated-walls rectangular waveguide. To separate the laser RF radiation from the electron beam and to out-couple the desired part of the RF energy, the beam output confocal splitter was also designed.

General Layout

The resonator consists of several waveguide sections of different profiles. It is integrated into

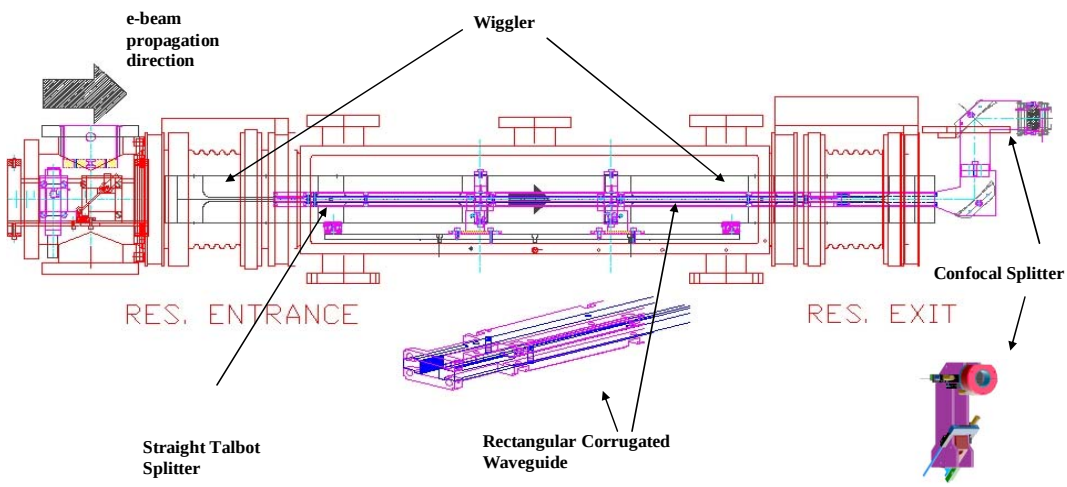

Fig. 1. The resonator lay-out and the scheme of installation of the resonator into the wiggler system.

Corresponding author. Email: gover@eng.tau.ac.il

the wiggler system, so that the interaction between the electron beam and the wiggler magnetic field of takes place inside the waveguide cavity - rectangular corrugated waveguide. The latter is assembled from 4 separate walls, 2 smooth and 2 mill-machined corrugated. This waveguide was designed in such a way that the electron beam at the design energy (1.4 MeV) can interact only with the fundamental mode TE_{01} according to the dispersion relation. The resonator layout installed into the wiggler system is schematically shown in Fig. 1.

In order to obtain positive feedback from the resonator mirrors, two wave splitters were placed at both terminations of the corrugated waveguide. These splitters are reflectors, based on overmoded rectangular waveguides shorted with a mirror at one end.

Confocal Splitter

The confocal splitter is a quasi-optical mm-wave component that based on a novel design. The splitter consists of an overmoded rectangular waveguide and two curved metallic mirrors. The splitter scheme provides the continuous waveguide propagation and Talbot effect in one dimension, and free-space propagation of the radiation in the other dimension (both orthogonal to the direction of propagation). The two parabolic (shaped in the plane of free space propagation) mirrors provide the dispersion-free focusing. The splitter prototype design and the manufactured model photo are shown at fig. 2. Computer simulation of the radiation propagation through the confocal splitter was also performed. The round-trip losses in the splitter were theoretically estimated as 12%, and later measured experimentally to be about 15 %.

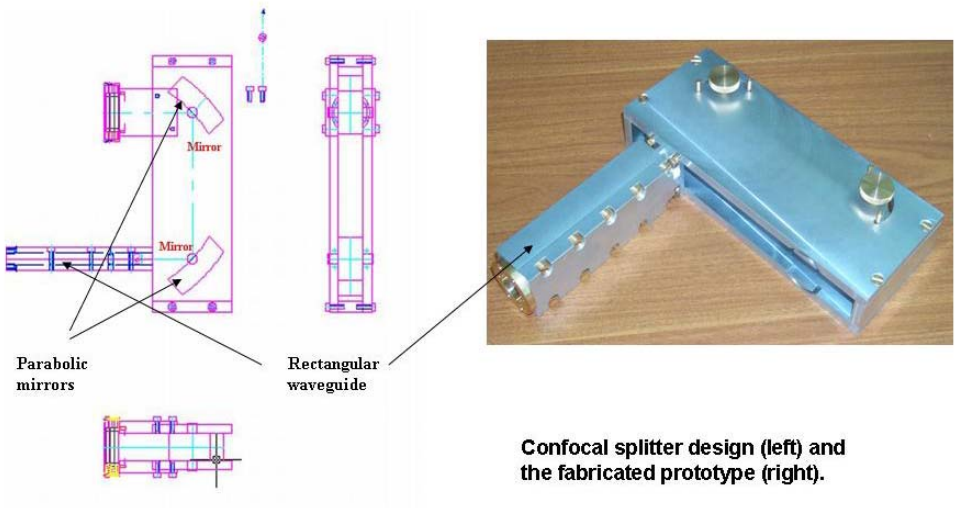

Fig. 2. Confocal splitter design (left) and the fabricated prototype (right).

The length of the input splitter equals to half of the Talbot-effect-optical-imaging length. At this distance, the overmoded (oversized) rectangular waveguide provides splitting of the original field distribution at the termination plane of the waveguide, where the reflecting mirror is placed. This effect allows to make a hole in the metallic mirror (as there is no field in the center), therefore to pass the electron beam through this hole.

The output confocal splitter is of the Talbot-effect-optical-imaging length and it provides the fundamental mode's field reconstruction at the plane of coupling grids that terminate the resonator.

MEASUREMENTS RESULT

After manufacturing of the resonator components, the whole resonator was assembled in the laboratory in order to enable experimental investigation outside the FEL tank. The round-trip reflectivity of the resonator was measured using excitation by special designed corrugated horn mode exciter through the 3-grid tuneable coupler system. In this experiment, the reflected signal from the excited resonator cavity was measured directly and the round trip reflectivity was calculated according to the theory presented in [2], [3].

Calculation of the round trip reflectivity

The algorithm of the round trip reflectivity is based on measurement of the reflection coefficient resonance curve and uses "optical" formulation. The reflection coefficient of the shorted Fabri-Perot resonator is

$$\Gamma = 1 - \frac{\left(R_1 - R_{rt}\right)\left(1 - R_1\right)/R_1}{\left(1 - \sqrt{R_{rt}}\right)^2 + 4\sqrt{R_{rt}}\sin^2\left(\delta 2\right)} \qquad (1)$$

were Γ is the power reflection coefficient, R_1 – reflection of the entering mirror (coupling condition), R_{rt} is the total round trip reflectivity and δ is a phase. On the other hand, choosing the Q factor definition as the ratio between the frequency f_0 (resonant wavelength λ_0) and bandwidth of the resonator mode $\delta f_{1/2}$ (or $\delta\lambda_{1/2}$):

$$Q = \frac{f_0}{\delta f_{1/2}} = \frac{\delta\lambda_{1/2}}{\lambda_0} \qquad (2)$$

As it shown in [2], one can derive:

$$Q = \frac{2\pi L}{\lambda}\frac{\sqrt[4]{R_{rt}}}{1 - \sqrt{R_{rt}}} \qquad (3)$$

were L is the resonator length and λ is wavelength. It should be noted that in Eq. 3 above, Q is the loaded Q-factor since both internal and external (coupling mirror) losses are included. Finally, the round trip reflectivity (or total losses, since R_{rt} = 1-Loss) can be found in terms of Q_{loaded} or directly in terms of FWHM ($\delta f_{1/2}$) of the measured resonator peaks:

$$R_{rt} = \left[-\frac{2\pi L}{\lambda_g Q_{loaded}} + \sqrt{\left(\frac{2\pi L}{\lambda_g Q_{loaded}}\right)^2 + 1} \right]^4 \qquad (4)$$

$$= \left[-\frac{2\pi L \delta f_{1/2}}{v_g} + \sqrt{\left(\frac{2\pi L \delta f_{1/2}}{v_g}\right)^2 + 1} \right]^4$$

were λ_g and v_g are the wavelength and velocity of wave propagation inside the resonator accordingly. The total round-trip reflectivity R_{rt} of the FEL resonator was calculated in the present work based on Eq. 4 and the direct measurement of the FWHM linewidth $\delta f_{1/2}$ of the resonant peaks. This linewidth was obtained from measurement of the power spectral reflection pattern.

CONCLUSIONS

The Israeli FEL resonator was re-designed in order to decrease the internal round-trip losses and thus to achieve threshold current reduction. The novel reflector and splitter based on the quasi-optical confocal scheme, were designed, manufactured and characterized. The round trip losses of the confocal splitter are about 15% (in good agreement with the theoretical limit estimation of 12%). The round trip losses of the overmoded corrugated waveguide and straight Talbot section were measured to be about 8 % for both waveguides. The total losses of the whole resonator system are therefore about 23%.

REFERENCES

[1] A. Faingersh, A. Gover, A. Eliran, and B.Kapilevich "Concluding report: measurements and calculation of round-trip reflectivity in the FEL waveguide resonator before and after modification and estimate of threshold current improvement", Internal report of the FEL group, 25-Aug-06, Tel-Aviv University.

[2] A. Gover, A. Faingersh, at al. "Radiation measurements in the new tandem accelerator FEL", Nuclear Instr. And Methods In Physics Research, A 528 (2004), pp. 23-27.

[3] B. Kapilevich, A. Faingersh, and A. Gover, **"**Accurate determination of Q-factor of a quasi-optical resonator", Microwave and Opt. Tech. Lett., vol.36, No.4, (2003).

PRESENT STATUS OF THE ISRAELI FEL: INCREASING FEL POWER BY ELECTRON BEAM ENERGY BOOSTING

E. Dyunin, M. Volshonok, A.Gover[#],
Dept. of Physical Electronics - Faculty of Engineering, Tel Aviv University, Tel-Aviv, Israel
M. Einat, Y. Lurie, Y. Pinhasi, Y. Socol, A. Yahalom,
Dept. of Electrical and Electronic Engineering – The College of Judea and Samaria, Ariel, Israel

Abstract

The status of a R&D work aimed on increasing the FEL power by boosting the electron beam energy after the radiation build-up is reported. A fine control of the electron beam energy during the radiation pulse is designed to compensate the small energy degradation during the pulse. Also, a controlled ramp (up or down) in the electron energy during the pulse will be applicable.

Theoretical estimations of the output power in the presence of an electron energy change during the pulse are presented. Two models, showing agreement between them are compared: Analytical model based on the pendulum equation, and, Rigorous 3D FEL interaction model solved numerically.

Another expected result of the design is to further extend the pulse duration with stable conditions and to obtain improved coherency.

The electrical and mechanical lay-outs of the high-voltage boosting (leading to electron beam energy boosting) are also presented.

INTRODUCTION

Electrostatic accelerator based FEL's (EA-FEL) are characterised by long pulse operation. Unlike RF-linac FEL's having a pulse width limited by the RF part, the EA-FEL's pulse width is incomparably longer and practically limited by the capability of the power supply to support the system with the required energy. In principle, an ideal power supply can support a CW operation of the FEL. Calculations of a long pulse operation of an FEL, show a saturation regime obtained at the end of the energy build up process, were the output power of the FEL is stable at its maximum. This maximum is related to the FEL characteristics and the operation conditions (such as electron-energy) which are kept constant.

In this paper the possibility of changing the electron energy during the pulse, after the radiation build-up, is considered. Calculations are made in two different methods to estimate the variations in the EA-FEL output power in saturation as a result of change in the electron energy during the pulse. Schematic of a high voltage boost system that supports a change in the electrons energy during the pulse is presented. This system allows a controlled ramp of the electron energy (up or down). This ramp can also be used to compensate the small degradation in the high voltage during the pulse to practically obtain constant electron energy for longer periods. That will lead to improvement of the coherency in the FEL radiation in view of the long pulse operation in constant conditions. In the following sections the two different models are presented and the results are given. Also the designed experimental setup to support the energy variations during the pulse is described.

THE FEL 3-D MODEL

The calculations were carried out in the framework of steady-state, three-dimensional, space-frequency approach, described in more details in [1]. In the approach, the total electromagnetic field oscillated at signal frequency f_s is presented in the frequency domain as an expansion in terms of transverse eigen-modes $\boldsymbol{\varepsilon}_q(x,y)$ of the cavity, in which the field is excited and propagates:

$$\tilde{\mathbf{E}}(\mathbf{r}) = \sum_q C_q(z)\,\boldsymbol{\varepsilon}_q(x,y)\,e^{-j\,k_{zq}\,z} \tag{1}$$

Here the time-domain field is

$$\mathbf{E}(\mathbf{r},t) = \mathrm{Re}\left\{\tilde{\mathbf{E}}(\mathbf{r})\,e^{+j\,2\pi\,f_s\,t}\right\} \tag{2}$$

and $C_q(z)$ is an amplitude coefficient of the mode *q*, which could be found from the excitation equation:

$$\frac{d}{dz}C_q(z) = -\frac{1}{2N_q}e^{+j\,k_{zq}\,z}\iint\tilde{\mathbf{J}}(\mathbf{r})\cdot\boldsymbol{\varepsilon}_q^{\,*}(x,y)\,dx\,dy \tag{3}$$

The power of the electromagnetic field emitted up to the point *z* can be found as follows:

$$P_{EM}(z) = \sum_q |C(z)|^2\,\frac{1}{2}\mathrm{Re}\{N_q\} \tag{4}$$

here N_q is the mode normalization power of the mode *q*.

* Work supported by the Israeli Ministry of Defence
# Corresponding author. E-mail: gover@eng.tau.ac.il

As usually accepted we consider the electron beam as consisting of a number of electron clusters or charged quasi-particles, distributed over the beam. Therefore the excitation current can be given in such a form:

$$\mathbf{J}(\mathbf{r},t) = -\sum_i q_i \mathbf{v}_i \, \delta(x-x_i)\delta(y-y_i)\,\delta[z-z_i(t)] \quad (5)$$

or in the frequency domain:

$$\tilde{\mathbf{J}}(\mathbf{r}) = -2\sum_i q_i \frac{\mathbf{v}_i}{v_{zi}} \delta(x-x_i)\delta(y-y_i)\, e^{-j\,2\pi\, f_s\, t_i(z)} \quad (6)$$

Substitution of the excitation current (6) into the excitation equation (3) enables one to re-write the last as follows:

$$\frac{d}{dz}C_q(z) = \frac{1}{N_q}\sum_i \frac{q_i}{v_{zi}} \mathbf{v}_i \cdot \boldsymbol{\varepsilon}_q^{\,*}(x_i,y_i)\, e^{+j\left[k_{zq}\, z - 2\pi\, f_s\, t_i(z)\right]} \quad (7)$$

In Eq. (5)-(7) q_i, $\mathbf{v}_i$ and $\mathbf{r}_i \equiv \{x_i, y_i, z_i\}$ are the charge, the velocity and the coordinates of the particle with a number *i*, and

$$t_i(z) = t_{0_i} + \int_0^z \frac{1}{v_{zi}(z')} dz' \quad (8)$$

is the moment when the particle number *i* comes to the point *z*.

With a known field, a next phase-space position of the particles can be found from the equations of motion:

$$\frac{d\mathbf{v}_i}{dz} = -\frac{1}{\gamma_i}\left\{\frac{e}{m}\frac{1}{v_{zi}}\left[\mathbf{E}(\mathbf{r}_i,t) + \mathbf{v}_i \times \mathbf{B}(\mathbf{r}_i,t) + \mathbf{v}_i \frac{d\gamma_i}{dz}\right]\right\} \quad (9)$$

$$\frac{d\gamma_i}{dz} = -\frac{e}{mc^2}\frac{1}{v_{zi}}\mathbf{v}_i \cdot \mathbf{E}(\mathbf{r}_i,t) \quad (10)$$

Figure 1 demonstrates schematically an FEL operated in oscillator regime. In that case some part of the radiation emitted by the beam is reflected by mirrors and returned to the interaction region, been forced to interact with a new portion of the driving current. Then the total electromagnetic field, emitted after *N* round-trips of the radiation in the resonator, may be found by:

$$\tilde{\mathbf{E}}_{tot}(\mathbf{r}) = \sum_q C_q^{tot}(z)\, \boldsymbol{\varepsilon}_q(x,y)\, e^{-j\,k_{zq}\,z} \quad (11)$$

Here the expansion coefficient of the total field is

$$C_q^{tot}(z) = \sum_{n=1}^{N} C_q^{(n)}(z) \quad (12)$$

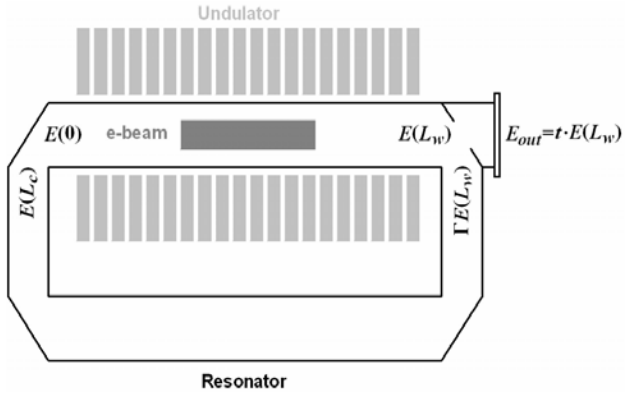

Figure 1: Principal scheme of FEL in an oscillator regime.

and the coefficients of the field emitted after *n* round trips of the radiation are defined by the recursion relation:

$$C_q^{(n+1)}(z=0) = \Gamma\, C_q^{(n)}(z=L_w)\, e^{-j\,k_{zq}\,L_c} \quad (13)$$

The above equations form a closed set of non-linear equations, which enables one to calculate the both radiated field and the beam trajectory. The model was realized in FEL3D numerical code and applied for the calculations considered in the next section.

THE "PARAMETRIC" PENDULUM EQUATION MODEL

The oscillation build-up and saturation process of the FEL oscillator were analyzed numerically in Ref. [3,4]. At saturation the radiation field inside the cavity is built up, and the small signal assumptions are not valid. The electron dynamics is described in the combined wiggler and radiation wave fields (the ponderomotive wave) in terms of the pendulum model [5]:

$$\frac{d^2\Psi}{dz^2} = -K_s^{\,2}\sin\Psi \quad (14)$$

$$\theta = \frac{d\Psi}{dz} \quad (15)$$

where $\Psi(z)$ is the phase of the electron relative to the ponderomotive wave: $\Psi(z) = \int_0^z \theta(\omega,z')dz' + \Psi_0$, and the detuning parameter is $\theta(\omega,z) = \frac{\omega}{v_z(z)} - k_{zq}(\omega) - k_w$. $k_{zq}(\omega)$ is the axial wavenumber of mode q, and $k_w = 2\pi/\lambda_w$ is the wiggler wavenumber. The Synchrotron oscillation wavenumber K_s is given by

$$P = A_p \overline{K}_s^4 \tag{16}$$

$$A_p = \frac{1}{2\pi^2} \cdot \frac{\left(\gamma_0 \gamma_z \beta_z^2\right)^4}{a_w^2} \cdot \frac{A_{em}\lambda^2}{L^4} \cdot \frac{\left(mc^2/e\right)^2}{Z_q} \tag{17}$$

where **E** and P are the circulating radiation field and power in the saturating oscillator cavity (we assume high round-trip resonator reflectivity, and therefore constant power -P along the resonator).

As well known, the pendulum equation (14) can be integrated once, resulting in a picture of open and closed trajectories in $\theta - \Psi$ phase-space (Fig. 2). This picture can also be viewed as a display of electron energy vs. phase trajectories, if one uses the differential linear relation between γ and θ near the synchronism energy γ_0 (Fig. 3).

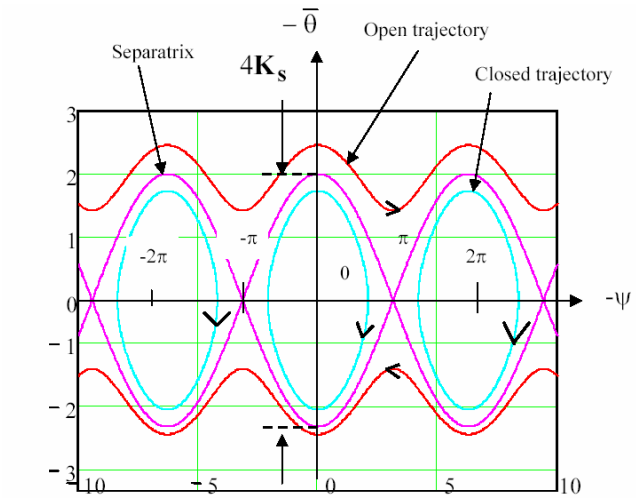

Figure 2: Phase-Space Trajectories of the Pendulum Equation.

OSCILLATION BUILD-UP EA-FEL

The oscillation build-up dynamics as a result of the two models are presented in Fig. 4. all the calculations are made for a single frequency. The result for a constant electron energy (1.42 MeV)) is shown in green. This calculation is done by the pendulum equation model. For the same frequency, a case with a step in the electron energy is calculated (red curve). The initial voltage is 1.4 MV and saturation is obtained. Than a voltage step is applied to 1.42 MV. As a result a new saturation level is obtained which is higher that the former level of a stable voltage. Thus, for the same final (i.e 1.42 MV) conditions two saturation levels are possible.

A verification of the red curve behaviour is obtained by the FEL 3D model (violet curve). Although different levels of saturation are obtained, the behavior is similar, where a jump in the saturation level is obtained. The differences between the models can be related to the differences in the assumptions in the models.

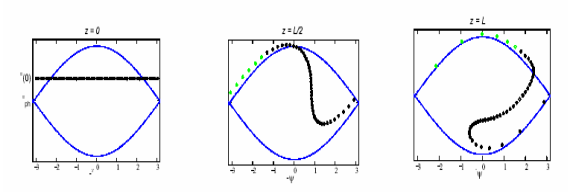

Fig. 3: Dynamics of electron beam trapping and synchrotron oscillation at steady state saturation stage of an FEL oscillator.

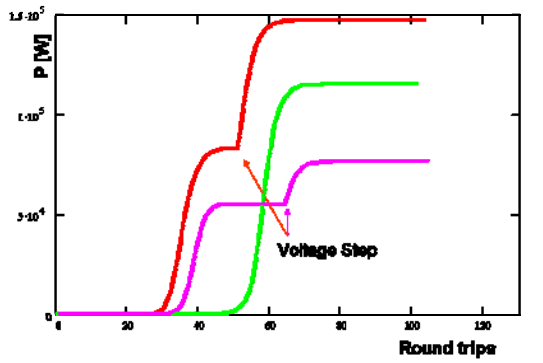

Fig. 4: The oscillations build-up in EA-FEL with constant electron energy and with a step in the energy during the pulse after saturation:
Constant Terminal Voltage 1.42 MV (PE) – Green,
Voltage Step from 1.4 to 1.42 MV (PE) – Red,
Voltage Step from 1.4 to 1.42 MV (FEL3D) – Violet.

ENERGY BOOST SYSTEM

Since the EA-FEL is capable of a long pulse operation, a coherent operation in high power is applicable [6]. Still. A practical experimental difficulty is the electrons the hit the terminal parts and reduce the voltage. These electrons can be related to non-ideal transport conditions and to returning electrons that could not reach the collector. This phenomena cause a drift in radiation frequency that is related to the drift in the voltage drop. Correcting this voltage drop was one of the motivations to the work presented here. But, if a correction system is designed, it can be used to more than a voltage correction but also to voltage control in a desired manner such as a ramp.

The voltage ramp control system is presented in Fig. 5. it is placed in the high voltage terminal and its output is added to the terminal voltage. A capacitor is charged to voltage of up to 30 kV. During the pulse it is partly discharge through a selected resistor to the terminal. Therefore the voltage of the terminal is raised. By selecting the resistor and voltage the rate of the voltage raise can be determined. Therefore a compensation to the electrons hitting the terminal can be achieved in order to stabilize the voltage conditions and as a result the frequency as well.

Also a ramp (positive or negative) in the voltage can be applied in order to enhance the saturation level as predicted by the theory.

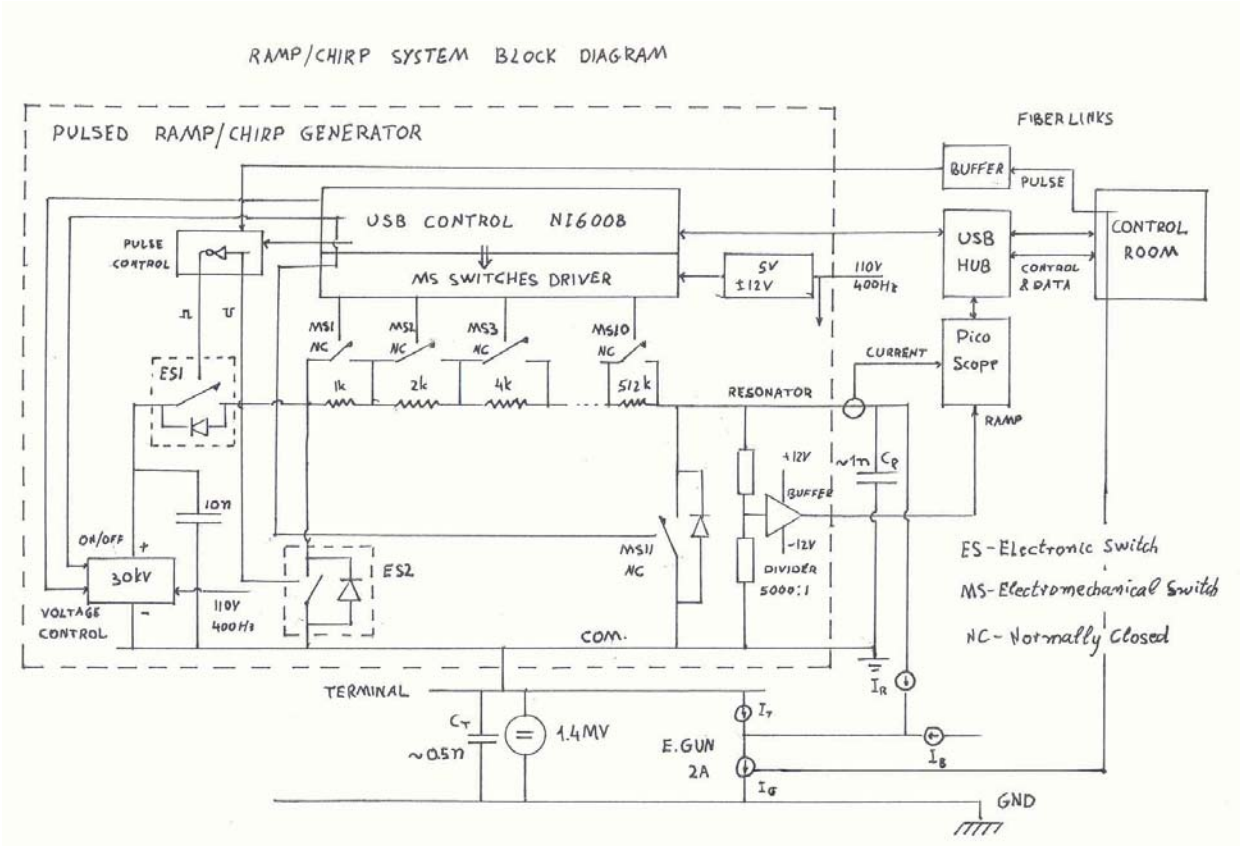

Fig. 5: The voltage ramp control circuit.

CONCLUSION

The possibility to achieve higher extraction efficiency and therefore higher operation power of the EA-FEL by electron energy step is theoretically possible.

Bi-stable saturation conditions are obtained for different initial conditions. An experimental setup is under construction in order to demonstrate the effect

REFERENCES

[1] Y. Pinhasi, A. Gover, and V. Shterngartz, Phys. Rev. E **54**, 6774 (1996)

[3] M.V. Krongaus, Y. Pinhasi, M. Tecimer, A. Gover, Nucl. Inst. and Meth .Phys. Res. A445, 28 (2000).

[4] M.V. Krongauz, Y. Pinhasi, A. Gover, "Dynamics and control of power build-up in a pre-bunched FEL", unpublished.

[5] A. Gover, E. Dyunin, Y. Lurie, Y. Pinhasi, M. V. Krongauz, "Superradiant and stimulated superradiant emission in prebunched electron-beam radiators - part II : Radiation enhancement schemes", Phys. Rev. ST – Acc. Beams Vol. 8, 030702 (2005).

[6] Y. Socol, A. Gover, A. Eliran, M. Volshonok, Y. Pinhasi, B. Kapilevich, A. Yahalom, Y. Lurie, M. Kanter, M. Einat, and B. Litvak, "Coherence limits and chirp control in long pulse free electron laser oscillator", Phys. Rev. ST – Acc. Beams Vol. 8, 080701, (2005).

DYNAMICS CONTROL OF THE ELETTRA STORAGE RING FREE-ELECTRON LASER WITH DIGITAL FEEDBACKS

E. Allaria#, G. De Ninno, Sincrotrone Trieste, 34012 Trieste, Italy
A. Antoniazzi, D. Fanelli, Dept. of Energetics, University of Florence, Florence Italy.

Abstract

The laser dynamics of a storage-ring free-electron laser has two main sources of instabilities. First of all, dynamical instabilities are developed as the free electron laser is moved away from the exact tuning between the period of the electron bunch(es) circulating into the ring and that of the photon pulse stored in the optical cavity. In addition, external (low-frequency) noise sources have a strong influence on the dynamical behavior of the system and can perturb its dynamics. Different feedback techniques have been proposed in order to control dynamical instabilities and stabilize the laser output. We present here a numerical and experimental investigation on the control of the Elettra storage ring free electron laser dynamics using different feedbacks techniques that can be experimentally implemented by means of a Field Programmable Gate Array.

INTRODUCTION

In a storage ring free electron laser (SRFEL) the electron bunch interacts with photons when passing through the optical klystron (Fig.1). The photons are stored in an optical cavity characterized by a traveling time ΔT and bounded by the two mirrors. The electron bunch, circulating in the storage ring, is characterized by the revolution period ΔT+ε which is determined by the storage ring radiofrequency.

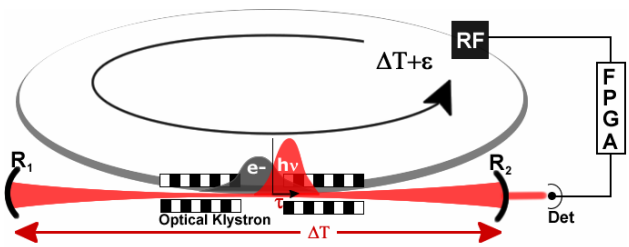

Figure 1: Layout of the storage-ring free-electron laser. The photon pulse (red) stored in the optical cavity interacts with the electron bunch (gray), circulating in the storage ring. The light intensity is acquired using an optical detector (Det). The resulting signal can be elaborated by an FPGA and used for slightly changing the electron revolution period (from ΔT to ΔT+ε) by varying the phase of the radio-frequency cavity (RF) of the ring.

Due to the impulsive character of the laser medium the laser intensity of a SRFEL is characterized by a sequence of micropulses whose duration is of the order of tens of picoseconds. Moreover its repetition rate is that of bunches in the ring (some MHz).

On a "slow" time scale (ms), the SRFEL behavior is strongly related to the temporal superposition of the photon and electron bunches inside the optical klystron. More precisely, the laser envelope displays a steady state regime for a perfect electron-photon tuning (ε=0 in Fig.1). Small light-electron detuning is sufficient to induce intensity oscillations on a slow time scale (Fig.2).

Due to these instabilities the quality of the laser temporal evolution is usually rather poor. Besides temporal detuning, the environmental noise (which is usually related to a residual 50Hz modulation coming from the power network) also perturbs the system and can strongly affect the SRFEL dynamics (Fig.2,5).

A simple model based on a recurrence map [1,2] can be used in order to describe the slow time-scale evolution of a SRFEL:

$$I_j(\tau) = R^2 I_{j-1}(\tau-\varepsilon)\cdot\left[1+g_{j-1}(\tau)\right]+i_s(\tau) \quad (1)$$

$$g_j(\tau) = g_0\frac{\sigma_0}{\sigma_j}e^{\left(-\frac{\sigma_j^2-\sigma_0^2}{2\sigma_0^2}\right)}e^{\left(-\frac{\tau^2}{2\sigma_{t,j}}\right)} \quad (2)$$

$$\sigma_{j+1}^2 = \sigma_j^2 + \frac{2\Delta T}{\tau_s}\left(\gamma_j + \sigma_0^2 - \sigma_j^2\right) \quad (3)$$

$$\varepsilon = \varepsilon + F(t) \quad (4)$$

$$F(t) = A\cdot\left[\frac{dI(t)}{dt}\right] \quad (5)$$

$$F(t) = A_1\cdot\left[I(t)-I(t-T_{d1})\right]+A_2\cdot\left[I(t)-I(t-T_{d2})\right] \quad (6)$$

Eq.1 describes the laser intensity at the j^{th} passage where τ is the temporal position with respect to the centroid of the electron bunch, R is the cavity mirror reflectivity, i_s stands for the spontaneous emission of the optical klystron, ε accounts for the detuning. The gain $g_j(\tau)$ is described by Eq.2 where g_0 and σ_0 respectively stand for the initial peak gain and energy spread respectively, $\sigma_{t,j}$ is the bunch length of the j^{th} interaction. The energy spread σ_j is described by Eq.3 where γ is the difference between equilibrium and initial energy spread, I_j the normalized laser intensity, ΔT the revolution period of electrons on the ring and τ_s the synchrotron damping time. For a more exhaustive description of the model we refer to Ref. [3].

Eqs.5,6 refers to the control signal $F(t)$ for the case of derivative and delayed feedbacks. Those signals are used to modulate the detuning (ε) according to Eq. (4) where $t = j\Delta T$.

#enrico.allaria@elettra.trieste.it

Table 1: Parameters used for the simulations of the Elettra SRFEL.

$\Omega = 16 \quad kHz$	$\sigma_{\tau,j} = \frac{\alpha}{\Omega}\sigma_j$	$R = R_1 \cdot R_2 = 0.96$
$\Delta T = 216 \quad ns$	$\alpha = 1.6 \cdot 10^{-3}$	$\gamma = \sigma_e^2 - \sigma_0^2 \quad \sigma_\varepsilon / \sigma_0 \approx 1.3$
$i_s = 4.3 \cdot 10^{-7}$	$\tau_s = 86 \quad ms$	$\varepsilon = \varepsilon_0 + \delta\varepsilon \cdot \sin(2\pi\nu t) \quad \nu = 50Hz$

The above model provides an ideal setting to investigate possible strategies for the stabilization of the SRFEL dynamics. The signal proportional to the laser output intensity extracted from the optical detector (Det in Fig.1) can be instrumental to the control of the system through dedicated feedback algorithms (Eqs. 4-6). More precisely, this signal can be used *ad hoc* to modify the electron revolution period (from ΔT to ΔT+ε) through the RF cavity of the ring (Fig.1).

Detuning and noise effects on SRFEL dynamics

By using the above model one can investigate the role of both the detuning and the external periodic noise modulation on the SRFEL dynamics.

Here we numerically simulate the Elettra SRFEL by using the model (Eq.1-3) assuming the values reported in Tab.1. We first assume an ideal case and neglect the external noise modulation at 50 Hz. In order to characterize the effect of a simple detuning ε_0 on the SRFEL dynamics, the bifurcations diagram of the laser output intensity (*I*) *vs* the detuning value (ε_0) has been reconstructed. Bifurcation diagrams are obtained by plotting the values of the laser intensity maxima and minima when dynamically varying the value of the photon-bunch detuning ε_0. In order to free our results from hysteresis effect we perform the scan both increasing and decreasing the values of ε_0.

Fig.2 (black curve) displays the results for the case of a non modulated detuning ε_0.

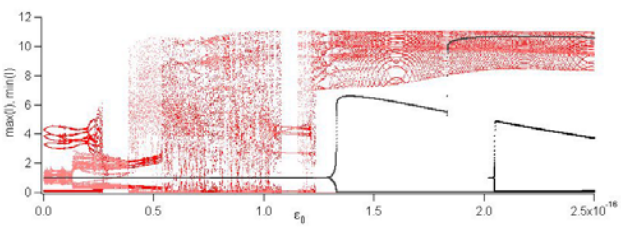

Figure 2: Bifurcation diagram of SRFEL intensity with respect of the detuning parameter ε_0. Black curve refers to the case without external perturbation of the detuning parameter ($\delta\varepsilon = 0$, see table 1). Red points refers to the case where also an external periodic perturbation is present ($\delta\varepsilon = 0.18$fs).

Results clearly show the presence of a steady state regime up to a detuning value of about 0.12fs where the transition to a pulsed regime occurs. Starting from $\varepsilon_0 =$ 0.12fs, the laser is characterized by high-intensity short pulses followed by long periods where the laser is off. If the detuning is further increased, the peak of the laser intensity decreases up to a second transition point ($\varepsilon_0 =$ 0.18fs). For larger detuning values the SRFEL achieves again a stable regime which falls outside the region considered in the subsequent analysis [4].

Results are instead different if one accounts for the presence of the external periodic noise signal. In Fig.2 (red curve) we report the bifurcation diagram of the SRFEL intensity *vs* the detuning value (ε_0) for a choice of the parameters which corresponds to the case of the Elettra SRFEL, i.e. $\delta\varepsilon_0 =$ 0.18fs [3]. The used value for the noise strength is sufficient to destroy the initial (i.e. small detuning) steady state region and the bifurcation diagram now shows a cascade of transitions between periodic and chaotic behaviors. However, depending on the detuning value, there exists regions where the laser is always turned on.

In the following we shall consider the Elettra SRFEL to be represented by the model of Eq.s1-3 with ε_0 and $\delta\varepsilon$ respectively equal to 0.5fs and 0.18fs [10].

CONTROL ALGORITHMS

The sensitivity of the system to the detuning ε can be exploited to implement a feedback system. A signal proportional to the laser can be used as an input in a feedback loop in order to control the system. To this aim an appropriate change to the electron revolution period is applied through the RF cavity of the ring (Fig.1, Eqs.1-6).

Recently, encouraging experimental results have been reported for a derivative feedback based on a low-pass filter [5]. In the near future we plan to implement a more sophisticated feedback system, exploiting the intrinsic flexibility of a FPGA to design innovative control algorithm. In the following we shall provide a first theoretical insight into this issue by comparing a digital derivative feedback (Fig.3,4) and a digital delayed feedback.

Derivative feedback

A derivative feedback enables to reduce the chaotic oscillations of the SRFEL dynamics.

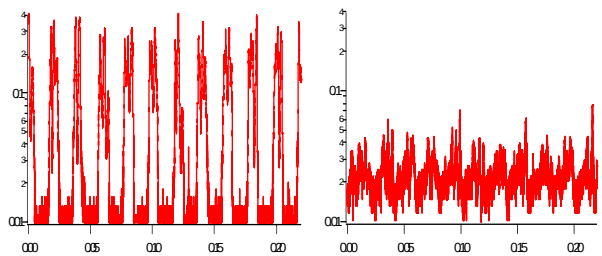

Figure 3: Time trace of the Elettra SRFEL showing the effect of the digital derivative feedback. a) Unstable behavior of the Elettra SRFEL. b) Controlled regime.

As appear evident from inspection of the experimental data reported in Fig.3, the digital derivative feedback control is able to prevent the laser to turn off. However, a small residual modulation at 50Hz is still present together with higher frequencies spurious contribution. In figure 4 we characterize the transition from the unstable pulsed

regime to the controlled one as a function of the strength of the control loop.

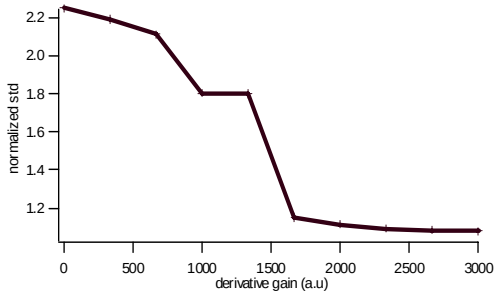

Figure 4: Transition from uncontrolled (Fig.3a) to controlled (Fig.3b) regimes: the normalized standard deviation of the SRFEL signal is reported as a function of the strength of the control signal.

One of the limitations of the derivative feedback is the fact that the sign of the controlling signal necessary for the stabilization of the SRFEL depends on the sign of the detuning [3]. For that reason in cases where the detuning (ε_0) is smaller or comparable to the perturbation of the external noise signal ($\delta\varepsilon$), a strong control signal cannot be employed. Otherwise, the control signal can induce detuning with the wrong sign and move the system away from the stability.

Delayed feedback

Delay control feedback can avoid the aforementioned problem because it involves a low correlation between the values of the laser intensities used for the calculation of the control signal.

Such a method consists in applying to the system a control signal *F(t)* described by Eq. (6): the loop gain A and the delay times $T_{d1,2}$ are the parameters to be set in order to stabilize the laser evolution.

Delayed feedbacks have been originally proposed for the stabilization of unstable periodic orbits of chaotic oscillators [6]. Recently two different incommensurable delays has been proposed to be used to obtain the stabilization of a steady state [7]. We further showed the possibility of using such a strategy in a SRFEL [8]. We are here interested in testing the robustness of the method to small fluctuations of SRFEL and/or algorithm parameters.

Figure 5 analyzes the performances of the method as a function of the two delay times. Results clearly show the existence of a region (blue) where the standard deviation of the signal has been strongly reduced (<0.5) thus pointing to the stabilization of the SRFEL signal. It is important to emphasize that those regions are located out from the diagonal which in turn enables one to conclude that at least two delays are necessary for the method to effectively work.

The possibility, and advantages, of using additional delay times should be addressed [9]. The robustness of the proposed method has been verified with respect of the variation of several input parameters.

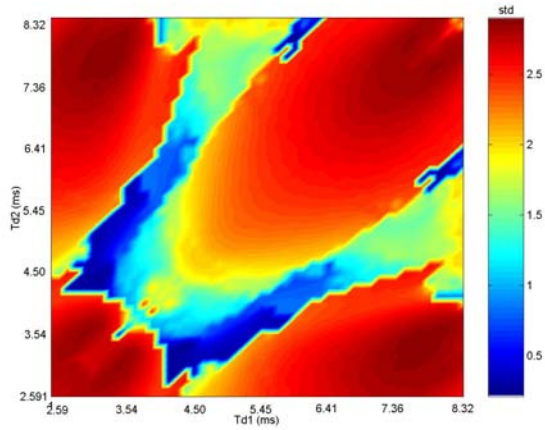

Figure 5: Color-scale plot of the standard deviation of the SRFEL output as a function of the delays used in the two delay lines of the control algorithm (A=1.9e-6). The plots clearly show the advantage of using two delays with respect to one (diagonal).

Numerical simulations indicate that the stable region (blue in Fig.4) is maintained when the input parameters (loop gain A, noise frequency and amplitude, electron-photons detuning …) are changed, as one would expect to occur in experimental conditions. This is a crucial observation in view of possible experimental realizations.

COMPARISON BETWEEN DERIVATIVE AND DELAYED FEEDBACK

In order to compare the performance of the delayed control algorithm and the derivative one we numerically tested both methods as a function of the strength of the external noise signal.

Figure 6 show the behavior of the SRFEL with ε_0=0.05fs as a function of the noise strength ($\delta\varepsilon$). The pulsed chaotic dynamics, which is usual for the Elettra SRFEL, is evident from the large range of fluctuation of the laser maxima for $\delta\varepsilon$ in the range 0.15-0.20fs.

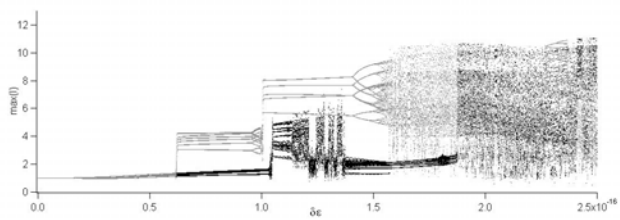

Figure 6: Bifurcation diagram of the SRFEL intensity as a function of the external noise modulation strength ($\delta\varepsilon$).

A proper setting of the derivative feedback [3] allows to stabilize the dynamics of the SRFEL in the region of $\delta\varepsilon \in$ (0.15-0.20fs) which is characteristic of the Elettra SRFEL. However, for larger values of $\delta\varepsilon$ the dynamics remains chaotic (Fig.7).

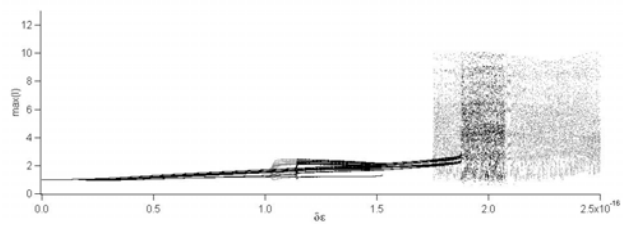

Figure 7: Bifurcation diagram of the SRFEL intensity with the use of the derivative feedback set for the stabilization (A=3.0e-2) of the unstable oscillations around the $\delta\varepsilon$ = 0.18fs case.

As clearly shown in figures 6,7,8 a dual delay algorithm results in a better stabilization of the SRFEL dynamics over a larger range of $\delta\varepsilon$.

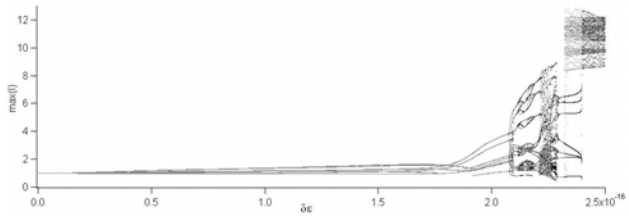

Figure 8: Bifurcation diagram of the SRFEL intensity with the use of the dual delay feedback set for the stabilization (A=1.9e-6, T_{d1}= 3.11ms, T_{d2}=4.24 ms) of the unstable oscillations around the $\delta\varepsilon$ = 0.18fs case.

Although the ultimate goal of obtaining a perfect steady state regime is beyond current possibilities, both methods are capable to stabilize the laser intensity for a large window of values of the noise strength $\delta\varepsilon$, a crucial quantity responsible for undesidered oscillations arising in the uncontrolled case (Fig. 6). A comparison between the proposed two methods in terms of extension of the allowed range of the noise strengthshow that the approach based on the multidelay performs better. This conclusion applies also as concerns the amplitude of the residual oscillations.

As previously anticipated, the reason for the above success is to be ascribed to the fact that the low correlation between delayed values in the case of chaotic signal allows us to implement a strong control term without facing the risk of producing opposite effects, reported instead for the case of the derivative feedback.

CONCLUSIONS

We presented a reliable model for the investigation of both detuned and noisy regimes in a SRFEL. The model has been applied to testing possible feedback algorithm to be developed with a FPGA. Preliminary experimental results have been reported concerning the stabilization of the Elettra SRFEL trough a digital derivative feedback. A proposed feedback method based on delayed signal has been presented and numerically investigated. The comparison of the delayed method with the derivative one shows the advantages of the former in terms of achieved stability and robustness to noise.

On the basis of these encouraging results, the experimental implementation of the delayed feedback control on the Elettra SRFEL is planned for the near future.

REFERENCES

[1] M. Billardon *et al.*, Phys. Rev. Lett. **69**, 2368 (1992).
[2] S. Bielawski *et al.*, Phys. Rev. **A**, **47**, 3276 (1993).
[3] G. De Ninno *et al.*, Phys. Rev. E **71**, 066504 (2005)
[4] M.E. Couprie *et al.*, Phys. Rev. E. **53**, 1871 (1996).
[5] S. Bielawski *et al.*, Phys. Rev. **E**, **69**, 045502 (2004).
[6] K. Pyragas, Physics Letters A, **170**, 421-428 (1992).
[7] A. Ahlborn and U. Parlitz, Phys. Rev. Lett. **93**, 264101 (2004).
[8] E. Allaria *et al.*, FEL05, JACoW/eConf C0508213, THPP005 (2005)
[9] Work in preparation.
[10] In the case of Elettra a detuning of 0.4fs correspond to a variation of 1Hz of the 500MHz RF frequency which is the limit of the accuracy of the instrument. Moreover to the time jitter of the master oscillator, that depending of the working conditions can be of the order of 1ps, can be associated a detuning of 0.02fs if we simplify the jitter to a 50Hz signal.

Q-SWITCH TECHNIQUES IMPLEMENTED AT THE ELETTRA STORAGE-RING FREE-ELECTRON LASER

F. Curbis*, M. B. Danailov, B. Diviacco, L. Romanzin, M. Trovò, G. De Ninno
Elettra, Basovizza, Trieste, Italy.

Abstract

In a Storage-Ring Free-Electron Laser (SRFEL) giant pulses can be produced by the interaction between the light stored in the optical cavity and an electron beam with low energy-spread (cold beam). This interplay produces the heating of the beam. After the generation of a single giant pulse the overlap between electrons and radiation is periodically prevented for a time necessary to dump the energy spread and recover the cold-beam condition. Two different methods are now implemented at Elettra for giant pulse generation. In the first, by modifying the radio-frequency of the ring, a change of the revolution time of electrons is induced. This avoids the temporal overlap between the electron beam and the optical field in the mirror cavity. The second method relies on a mechanical gating (chopper) which intercepts the light produced during previous interactions, inducing a periodic depletion of the optical cavity. The giant-pulses repetition rate is determined by the periodicity of the radio-frequency changes and the rotating velocity of the chopper, respectively. In this paper we compare the different techniques mentioned above for the case of the Elettra SRFEL.

INTRODUCTION

The customary layout of a Free-Electron Laser (FEL) in oscillator configuration takes advantage of an optical klystron. This magnetic structure is made up of two undulators and a dispersive section in between (see Figure 1). In the small gain case [1], which is indeed the oscillator case, the strong magnetic field of the dispersive section induces a delay between the radiation emitted in the first and in the second undulator. In comparison to the light the electrons spend longer time to pass through a magnetic chicane and, once in the the second undulator, their emission will have a different phase with respect to the light emitted formerly. This delay produces a constructive interference of radiation, changing the optical klystron spectrum in a more spiky structure and enhances the FEL process because its gain is proportional to the derivative of this interference structure. The other main component of an oscillator FEL is the optical cavity, composed by two mirrors on axis with the two undulators and the dispersive section, as depicted in Figure 1.

In the normal operational mode of a storage-ring FEL in oscillator configuration, the light emitted has a temporal structure depending on the ring filling and each pulse has a quite low power. When the electron beam interacts with the light stored in the optical cavity, emitting coherently, its energy spread grows up. This effect, called beam "heating", limits the maximum power achievable, because the gain is proportional to the electron density. Between the generation of two consecutive giant pulses it is necessary to wait few synchrotron damping times, this allows to restore the cold beam condition. In this period of time, in fact, if the light-electron interaction is prevented, the beam energy spread decreases to the initial value.

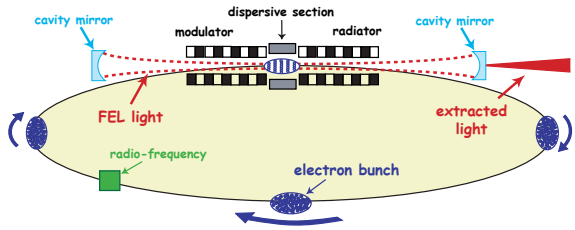

Figure 1: Layout of the Elettra storage-ring FEL in oscillator configuration.

Several methods have been studied and applied in oscillator FELs [2, 3, 4, 5] to create "giant pulses". There are basically three techniques that have been implemented:

- the gain modulation [6];
- the modulation of RF frequency [4, 5];
- the mechanical gating (chopper).

The first method is presently employed at Duke, where a dedicated magnet steers the electron beam orbit in the transverse direction. When the electron beam orbit is off-axis with respect to the optical cavity, the lasing is stopped and the electron beam can cool down. Once the electron beam orbit returns on-axis, a new giant pulse starts. The RF frequency modulation has been used in Super-ACO and is currently implemented at Elettra and UVSOR. This technique may excite synchrotron oscillations of the electron beam, or enhance them if already present. The induced oscillations can reduce the net gain at the laser start. While the first two techniques can be considered equivalent for generating giant pulses (as demonstrated for Duke in [7]), the mechanical gating is still under investigation.

The purpose of the Q-switch technique is twofold: to concentrate the average power of storage-ring FEL in a series of giant-pulses and to have a regular temporal dynamics of the light. This allows to use the light emitted for experiments, for example synchronizing an external trigger which drives the giant pulse repetition rate [8]. Besides, it

* francesca.curbis@elettra.trieste.it

is well known that the FEL light at the fundamental wavelength, which is reflected by the mirrors of the optical cavity, produces higher harmonics [9]. These harmonics survive just for a single pass in the optical cavity, because the mirrors do not reflect light with their wavelength. In normal operation mode the power of higher harmonics, which depends on the fundamental power, is too low to be detected. Giant pulse production is therefore a suitable way to enhance the fundamental power and accordingly the higher harmonic power. One example of harmonic generation in cavity is reported in Figure 2.

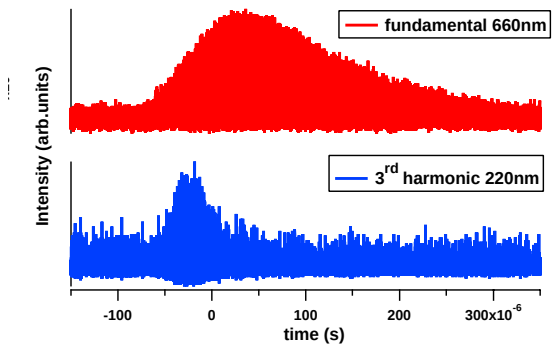

Figure 2: The fundamental (660 nm) and the third harmonic (220 nm) giant pulses. The harmonic signal is about a factor 25 above spontaneous emission.

The giant-pulse risetime provides also an estimation of the initial FEL gain. Between each pulse the electron beam is restored and when the giant pulse starts the only negative effect is due to the optical cavity losses. This allows to calculate the net gain of the FEL process, if the mirror reflectivity is known.

TWO DIFFERENT EXPERIMENTAL TECHNIQUES

In this section, we concentrate on the two techniques used at Elettra for the giant pulse generation, i.e., the RF frequency modulation and the Q-switch with the chopper.

RF frequency modulation

In a storage-ring FEL, in order to obtain the synchronization between the electron beam and the light stored in the optical cavity, the mirrors are placed at inter-bunch distance. Stepper or piezo-electric motors provide the fine tuning of the mirror position along the undulator axis. If the RF frequency of the storage ring changes the revolution time of electrons changes as well, causing the loss of synchronization with the optical filed in the cavity. Without temporal overlap the electrons do not interact with the radiation stored in the optical cavity and then the energy spread of the beam can decrease. The RF frequency modulation is based on a periodic detuning between the electron beam and the radiation stored into the optical cavity. When the system is detuned the lasing process is stopped. An external signal source induces the detuning and modifies the slope and the amplitude of the RF frequency jump. The detuned condition is maintained for few synchrotron damping times to allow the electron beam to cool down and the gain of the amplification process to recover its initial (i.e. laser-off) maximum value. Once this situation is reached, the system is led back to the perfect tuning condition which is maintained for a long enough time (order of dozens of milliseconds) to induce the onset of the laser giant pulse. Then the system is detuned again and the process repeated.

The main advantage of this technique is the fast transition time. The RF modulation is driven by a signal generator, therefore one can choose the slope of the signal to reach the maximum power. The unfavorable aspect is the beam perturbation caused by the RF modulation. The damping is regulated by the synchrotron frequency. Figure 3 shows a streak camera image of the synchrotron radiation and the FEL signal.

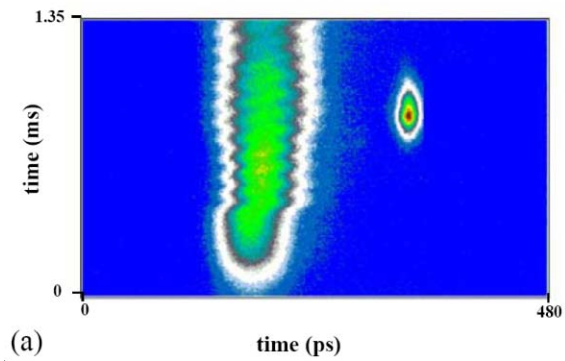

Figure 3: Streak-camera image of the electron beam (left trace) and of the FEL pulse (right trace) in Q-switch operation mode.

Along the vertical axis of the picture, the evolution in time of the distribution profile is reported and one can also see the excitation of synchrotron oscillation starting before the laser. The analysis in Figure 4 also shows the electron beam heating that begins before the giant pulse start.

Q-switch with chopper

In the Elettra storage-ring FEL a mechanical gating has been recently introduced in the optical cavity. This object, called chopper, is a molybdenum disc with a 115 mm radius with a little aperture positioned close to the border (see Figures 5). When the aperture is on-axis with the optical cavity the light stored can pass, otherwise the radiation is intercepted by the disc. The chopper is placed near the back mirror (see Figure 6) and rotates at constant speed, moved by a PHYTRON UHV stepper motor.

The rotating velocity determines the repetition rate of the Q-switch.

Generally speaking, when the electron beam interacts with the laser pulse (stored into the cavity) its longitudi-

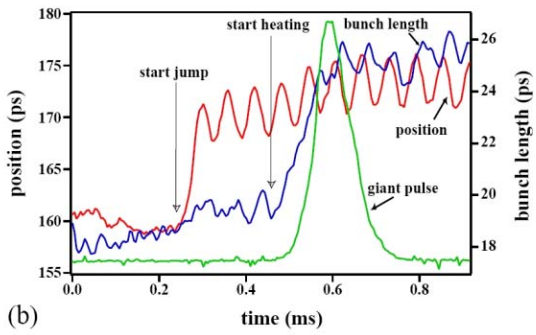

Figure 4: Analysis of the streak camera image in Figure 3. The longitudinal distributions are obtained by means of a horizontal cut of the picture.

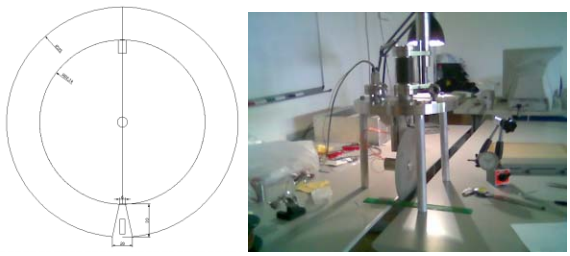

Figure 5: Left: schematic design of the metallic disc. Right: Preliminary studies in air.

nal dimensions grow up and the resulting energy spread reduces the FEL gain. The chopper allows the giant pulse creation because it prevents the electron-light interaction for a suitable time so that the energy spread reduces. This method does not generate beam perturbations and, as a consequence, higher power in the giant pulses is expected.

At the present the chopper technique can achieve only a limited repetition rate if compared to the RF modulation. Nevetheless we expect in the near future to operate the chopper at frequencies of 5 Hz or more. Furthermore, since the chopper Q-switch does not involve the RF frequency,

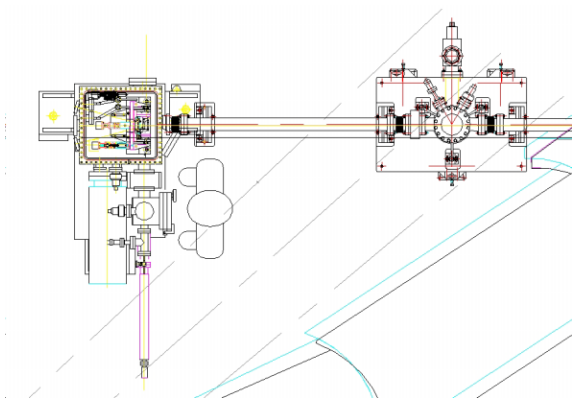

Figure 6: Schematic layout of the chopper chamber (at right), near the mirror chamber (at left).

Figure 7: Pictures of the chopper during the installation.

the latter can be used as a clock for cross-correlation measurement in order to characterize the harmonic signal.

A summary of the peculiarities of both methods is reported in Table 1.

Table 1: Chopper versus RF modulation

chopper advantages	**RF advantages**
no beam perturbation	fast transition time
chopper disadvantages	**RF disadvantages**
longer transition time	beam perturbation

Measurements and results

To compare the RF frequency modulation and the chopper Q-switch techniques, a campaign of measurement has been recently carried out using the Elettra SRFEL. Figure 8 and Figure 9 show preliminary risetime measurements for the RF modulation and the chopper case, respectively. The pictures report a train of giant pulses obtained at the same current and repetition rate. While the RF modulation method displays a quite constant level of the signal, the chopper exhibits an irregular behaviour. The reason is still under investigation.

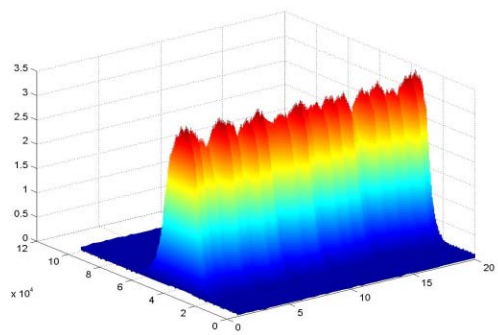

Figure 8: Sequence of 20 giant pulses, acquired by a fast photodiode, generated using the RF modulation. The electron beam current is about 10 mA and the repetition rate is 1.5 Hz

In Figure 10 we compare the two techniques for the 3 Hz case: the giant pulse risetime, calculated as a mean of 20 signals, is displayed as function of the total beam current.

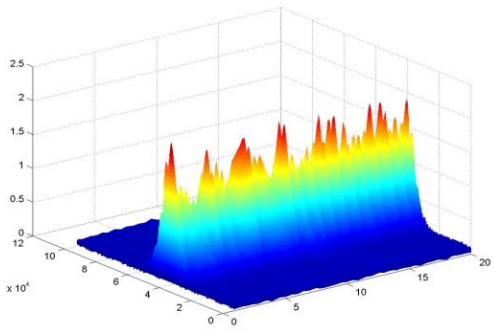

Figure 9: Sequence of 20 giant pulses, acquired by a fast photodiode, generated using the chopper Q-switch. The electron beam current is about 10 mA and the repetition rate is 1.5 Hz

For high currents the chopper and RF modulation seem comparable, while at medium-currents the chopper risetime is quite longer.

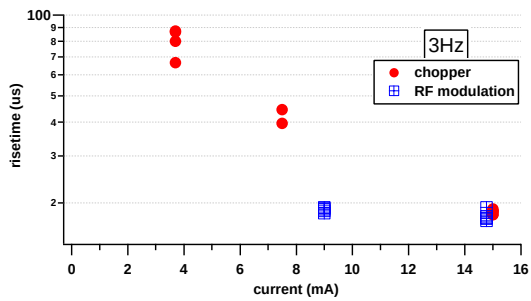

Figure 10: Comparison between chopper and RF modulation techniques, showing the risetime as a function of the total current at the same operational frequency (3Hz).

Figure 11 and Figure 12 report the risetime versus current for the RF modulation and for the chopper technique respectively. These data do not show any strong dependence of the risetime on the repetition rate.

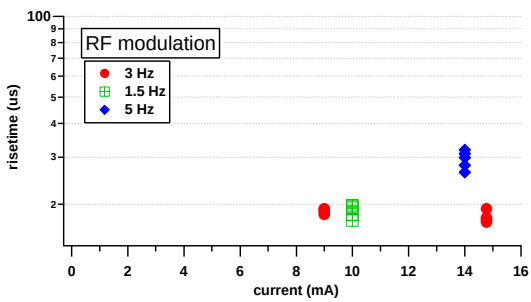

Figure 11: Efficiency of the Q-switch at different repetition rates using RF frequency modulation.

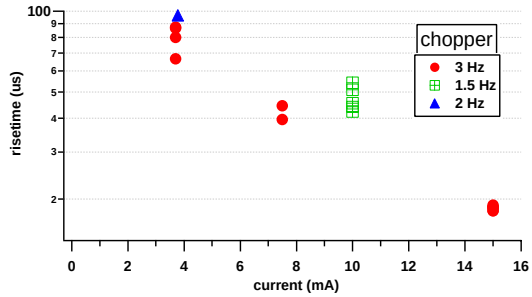

Figure 12: Efficiency of the Q-switch at different repetition rates using chopper.

CONCLUSIONS

The preliminary results presented here show the capability of the chopper method to generate giant pulses. This technique, although promising, needs more development in order to reach, and hopefully improve, the performance of the RF modulation method in terms of reproducibility and higher repetition rate.

REFERENCES

[1] J. M. J. Madey, J. Appl. Phys. **42**, 1906 (1971).

[2] G. N. Kulipanov, et al., *Nucl. Instr. and Meth. A* **296** (1990) 1.

[3] V. N. Litvinenko, et al., *Nucl. Instr. and Meth. A* **429** (1999) 151.

[4] T. Hara, et al., *Nucl. Instr. and Meth. A* **431** (1994) 21.

[5] G. De Ninno, et al., *Nucl. Instr. and Meth. A* **528** (2004) 278.

[6] I. V. Pinayev, et al., *Nucl. Instr. and Meth. A* **475** (2001) 222.

[7] G. De Ninno, et al., Elettra Internal Note.

[8] M. Amati, et al., these proceedings.

[9] V. N. Litvinenko, *Nucl. Instr. and Meth. A* **507** (2003) 265.

DEVELOPMENT OF A COMPACT CHERENKOV FREE-ELECTRON LASER IN TERAHERTZ SPECTRAL RANGE

M. R. Asakawa*[1], K. Nakao[2], N. Miyabe[1], M. Kusaba[2] and Y. Tsunawaki[2],
[1]Kansai University, Suita, Osaka, Japan,
[2]Osaka Sangyo University, Daito, Osaka, Japan.

Abstract

A Cherenkov free-electron laser (CFEL) generating terahertz radiation is now being developed under the joint research of Osaka Sangyo university and Kansai university. The main feature of the CFEL is its compactness. Microbeamlets from Spindt-type field emitter array are accelerated up to 50 keV and then injected into a silicon resonator with a path of 50 to 150 μ m spacing through which electrons propagate. Omitting the evacuation system and power supply, the size of CFEL section, including electron gun and resonator, is about $1 \times 1 \times 4$ cm^3. For the generation and the transport of the electron beam few μm in diameter, we investigated characteristics of the Spindt cathode, beam focusing by electrode and the magnetic field. A carbon nanotube field emitter was also tested for future application.

INTRODUCTION

Cherenkov free-electron lasers (CFELs) are one of the great candidates for compact tunable radiation sources. A pioneer work had demonstrated CFEL in 100 GHz frequency range using an electron beam with 35 to 75 keV acceleration energy [1]. In order to increase the operation frequency to terahertz frequency range, it is straightforward to scale down the optical resonator of CFEL. Fig. 1 shows a schematic view of a compact CFEL. Electron beamlets several μm in diameter are accelerated to 50 keV and then injected into a dielectric resonator. Electron beamlets passing through a channel bored in the dielectric resonator excite the Cherenkov radiation and interact with the evanescent part of that radiation.

The resonant frequency is determined principally by the radius of the channel: the resonant wavelength coms to severalfold of the channel radius. The dispersion curve of the evanescent wave in a circular dielectric waveguide is shown in fig. 2 with the dispersion of the light in vacuum and a beam-mode for 40 keV electron [2]. Because electrons moving along the channel transfer its kinetic energy to the radiation field via the interaction with the longitudinal component of the radiation field, the TM-mode which has that field component is important in such CFEL. Thus the dispersion relation for the TM_{01}-mode is shown in the figure. For the case of R_d=25 μm, the resonant frequency is 1.6THz. Note that the dispersion relations are scalable with the channel radius, thus the resonant frequency increases with decreasing the channel radius. CFELs are, therefore, capable to be operated in mid-infrared to sub-millimeter spectral range.

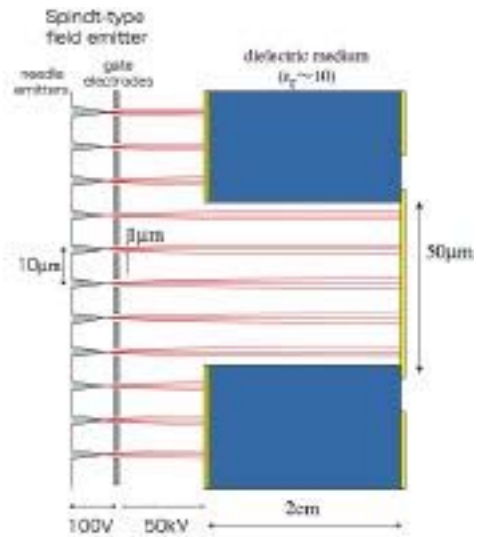

Figure 1: Schematic view of compact CFEL.

Our research aims a compact, more ambitiously, palmtop CFEL that can generate the radiation over the infrared spectral area. As the first step, we are developing the electron beam source which can produce μm beamlets. In following section, a CFEL test bench and experimental studies of the beam focusing will be described.

CFEL TEST BENCH

To produce the electron beam whose radius is order of micrometer, we used a Spindt cathode,[3] which contains 100,000 pairs of ultrasmall needles and gate electrodes in a 1 mm diameter array. Each pair of needle and electrode generate electron beamlet with diameter around 1 μm, and these tiny electron guns are arrayed with a spacing of 10 μm. Due to the needle-gate configuration and the high operation current density, Spindt cathode generates a diverging beam as shown in fig. 3. Therefore, the beam transport is the critical issue.

Figure 4 and fig.5 show the schematic view and the picture of a developing CFEL test bench, respectively. This system employs the magnetic field for the beam focusing. Main components, such as Spindt cathode, collector electrode and a optical resonator, are installed inside the bore

* asakawa@ipcku.kansai-u.ac.jp

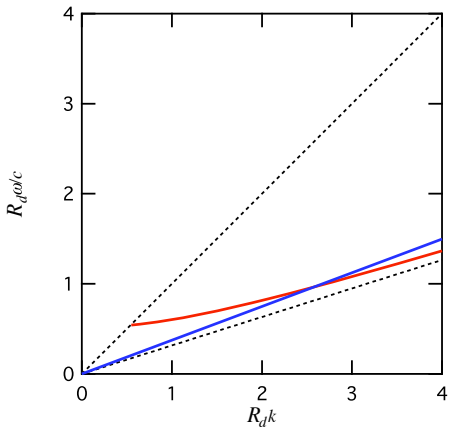

Figure 2: Dispersion relations of the evanescent wave for TM_{01} mode. The relative dielectric constant of the medium is 10.(red) Both axes are multiplied by the channel radius (R_d=25 μm) for the normalization. The blue solid line shows the dispersion of 40 keV beam mode. Upper and lower dashed lines denote the dispersion of the light in vacuum and the light in the dielectric medium, respectively.

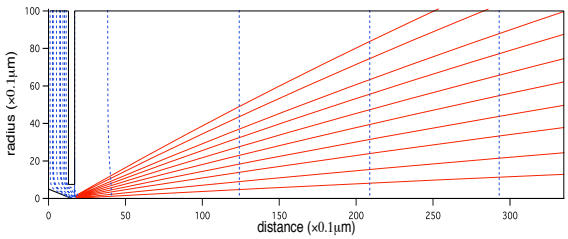

Figure 3: Calculated trajectories of electrons emitted by Spindt cathode. Red lines show the electron trajectories and Blue lines represent the equipotential lines. E-gun code was used for the calculation.

of a super conducting coil, which can produce magnetic flux density up to 5 T. The footprint of the whole system including the compressor unit for super conducting magnet is about 1 $\times$1 m^2.

Electron beamlets generated at the grounded Spindt cathode needles are accelerated toward the collector electrode, which is followed by the optical resonator. The resonator consists of a pair of silicon slabs gapped by thin spacers with thickness of 50, 100 or 150 μm. The resonant frequency increases from several hundreds GHz to few THz as decreasing the gap spacing. The end edges of slabs facing to the cathode are coated with Al and work as both the collector electrode and resonator mirror, while the other edges are left uncoated to extract Cherenkov radiation. One side of the gap between the slabs facing to cathode is opened for the beam injection, while the other side is blocked by the spacer for beam dumping and reflecting back of a part of radiation. The length of the laser interaction region is 2 cm.

Figure 6 shows the time trace of the gate voltage and the beam current. Pulsed voltage up to 100 V is applied to the gate electrode of Spindt cathode to generate a few

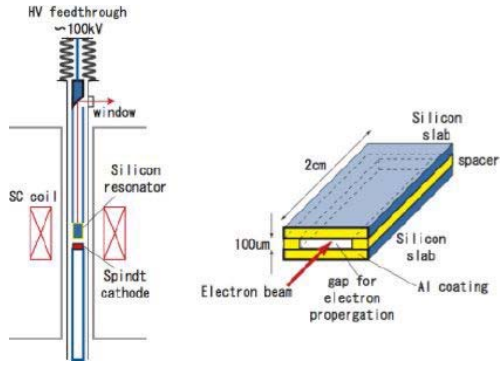

Figure 4: Schematic view of the CFEL test bench and the resonator. The left and right figures show the schematic view of the whole system and the detailed view of the resonator, respectively.

Figure 5: Picture of the CFEL test bench. The high voltage feedthrough, the 2-axis manipulator for resonator alignment and cryostat of the super conducting coil can be seen. The height and footprint of the device are 1.9 m (including a 0.7 m-height pedestal) and 0.7$\times$0.7 m^2, respectively.

milli-amperes beam current. The raise time of 50 μs was determined by the capacitance of the power feed cable and 100 kΩ resistance for current monitoring, and will be shorten by reducing the resistance in the laser experiments that higher beam current will be required. For the operation above the beam current shown in the figure, we suffered from the serious degassing and the following brake down. Such undesirable events were remarkable especially when the magnetic field was applied. This system is under aging process.

FOCUSING ELECTRODE

Because the magnetic focusing requires a large and expensive magnet, we also explored beam focusing using mid-electrode. A mid-electrode was located at a distance of 13 mm from the cathode. The spacing between the mid-

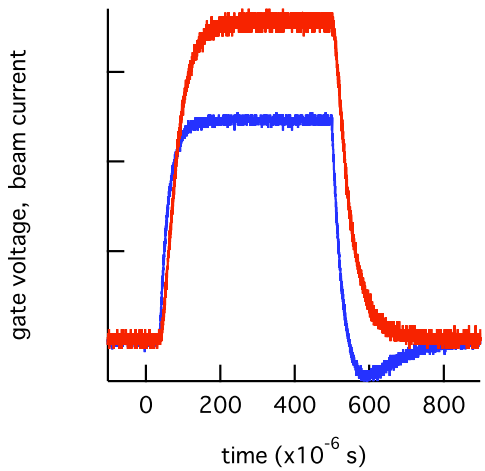

Figure 6: Time trace of the gate voltage (red) and the beam current (blue). Peak voltage is 50 V and peak current is 81 μA.

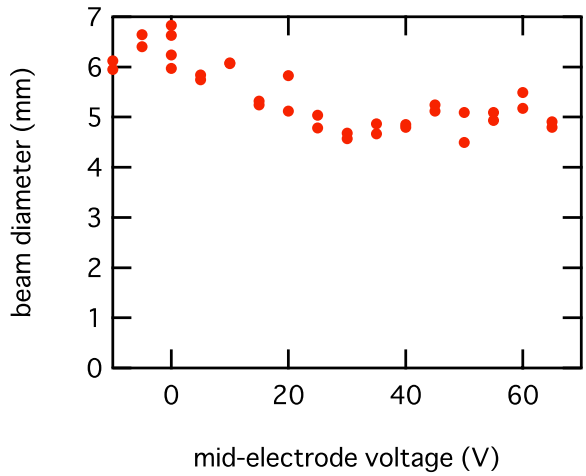

Figure 7: Beam diameter as a function of the mid-electrode voltage. During experiment, the collector voltage was held at 10 kV and pulsed 65 V voltage was applied to the gate electrode of Spindt cathode.

electrode and the collector electrode was set to 30 mm. Mid-electrode had a hole 5 mm in diameter through which the electrons pass through. The beam spot size at the collector electrode was evaluated from the fluorescence image on a phosphor screen placed at collector electrode. Figure 7 shows the beam diameters as a function of the mid-electrode voltage. The collector electrode voltage was held at 10 kV during the experiment. The gate voltage was set to 65 V and the pulse width was 10 ms to obtain luminance enough to observe. Note that these results show the diameter of the whole beam emitted from 100,000 tiny needles: the fine structure formed by each beamlet was smoothed out due to poor resolution of the measurement system. It is seen that the beam diameter decreases with mid-electrode voltage up to 30 V and then slightly increases with the voltage. It is inferred that the beam is over focused with the mid-electrode voltage above 30 V. This result indicates that the beam focusing by the focusing electrode is not enough to produce the electron beam with micrometer diameter. We are on the way to design optimal electrode configuration combined with the magnetic field configuration to find the reasonable focusing system.

CARBON NANOTUBE CATHODE

To develop the brighter electron beam source, we also tested a carbon nanotube cathode. As this test is a preliminary one: powdered carbon nanotubes were smeared over a 0.5 mm diameter plate of stainless steel and the gate electrode was not installed. Due to the lack of the gate electrode, the spacing between the cathode and the collector electrode was set to 0.2 mm to produce electric field enough for the field emission. Figure 8 shows the beam current vs. the collector electrode voltage. Electron emission stars at a voltage of 2.2kV and the current reaches to 2.4mA at 4.4 kV. Above 4.4 kV acceleration voltage, serious outgassing degraded the vacuum condition, thus we limited the supply voltage to this extent. It is worth to mention that the beam current was stable for long period of these experiment in spite of D.C. operation. Taking into account the fact that operation of Spindt cathode with D.C. 1 mA leads serious damage on Spindt cathode, we conclude that carbon nanotube cathodes are capable of generating denser electron beam. Installation of the gate electrode is the key issue for practical application.

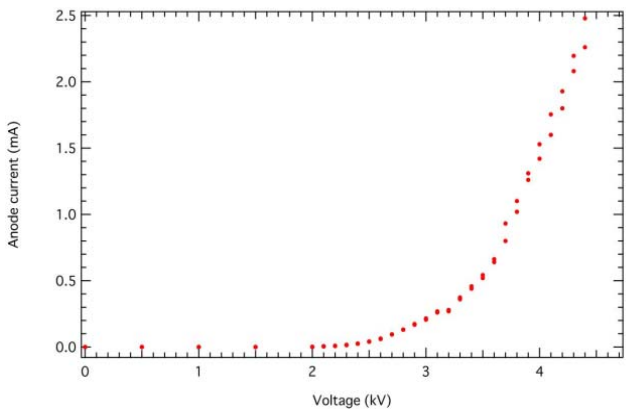

Figure 8: V-I curve for carbon nanotube cathode. D.C. voltage up to 4.4 kV was applied to the collector electrode.

SUMMARY AND RESEARCH PLAN

A compact THz CFEL driven by 50 keV electron beam is under development. Use of Spindt cathode and focusing of the electron beam are key technologies of this device. A CFEL test bench using super conducting coil for beam focusing was commissioned and is under conditioning. Beam focusing by mid-electrode was also studied. To

find the reasonable focusing system, we are investigating the beam focusing by the combination of the magnetic field and mid-electrode. First CFEL test will be started using high magnetic field up to 5 T after the aging conditioning of the test bench. The output frequency will be gradually increased from several hundreds GHz to few THz by reducing the gap spacing of the resonator. It is also planned to study Smith-Percell FEL and Cyclotron radiator on the test bench.

REFERENCES

[1] E. E. Fisch and J. E. Walsh: "Operation of the sapphire Cerenkov laser", Applied Physics Letter, Vol.60, No.11, pp.1298-1300 (1992).

[2] H.P. Freund and A. K. Ganguly: "Nonlinear analysis of the Cherenkov maser", Physics of Fluids B2, No.10, pp.2506-2515 (1990)

[3] K. Mima, S. Nakai, T. Taguchi, N. Ohigashi, Y. Tsunawaki, K. Imasaki , C. Yamanaka and M. Shiho: "A new FEL concept driven by a vacuum microfielf emitter", Nuclear Instruments and Methods in Physics Research SectionA, vol.331, pp.550-553 (1993).

HIGH POWER DEEP UV LASING ON THE UVSOR-II STORAGE RING FEL

M. Hosaka, M. Katoh, A. Mochihashi, M. Shimada, UVSOR Facility, Institute for Molecular Science, 38 Myodaiji-cho, Okazaki, Aichi 444-8585, Japan
Y. Takashima, Graduate School of Engineering, Nagoya University,Furo-cho, Chikusa, Nagoya, Aichi 464-8603, Japan
T. Hara, RIKEN/SPring8 1-1-1 Kouto, Mikazuki, Hyogo 679-5148, Japan

Abstract

Thanks to a recent upgrade of the UVSOR-II storage ring (lower beam emittance and higher peak current), an FEL gain has been enhanced much and we have succeeded in high power lasing in deep UV region. The highest extracted CW power so far is 0.25 W at wavelength of 215 nm and 1.1 W at 230 nm. Because of its variable wavelength even in deep UV region, high power and good coherence, the UVSOR-II FEL has come to be recognized as a useful tool by users inside and outside Institute for Molecular Science. Now UVSOR-II FEL has four users groups (solid state physics, surface physics, bio-moleculer science). Three different kinds of experiments have been successfully carried out in this year.

INTRODUCTION

On the UVSOR storage ring, a free electron laser has been developed as a new light source since early 1990s. In 1996, a helical optical klystron was installed and the performance of the FEL was improved much because of a smaller degradation of cavity mirrors and a higher FEL gain. Then the shortest wavelength (239 nm) of the storage ring FEL at that time was achieved [1].

Recently the storage ring was upgraded and the quality of the electron beam was much improved. With the increased FEL gain, a FEL lasing in shorter wavelength was expected, where more potential users exist. Here we report on an FEL experiment in the deep UV region at UVSOR-II aiming users application. The FEL should have enough power in addition to a good optical quality for application experiments. We also report recent upgrade of an rf accelerating cavity system, which plays an important role in the short wavelength lasing.

.

UPGRADE OF RF CAVITY SYSTEM

In 2003, the UVSOR storage ring was reconstructed toward a lower emittance ring; we call it “UVSOR-II” after the reconstruction [2]. The chief aim of this upgrade is to provide users with brighter synchrotron radiation. We still continue the upgrade of the ring. We replaced rf accelerating cavity system in 2005 [3]. The aim is to improve lifetime of the electron beam with higher accelerating voltage. At the UVSOR, 90.1 MHz rf cavity had been operated with a 20 kW transmitter but the rf accelerating voltage (55 kV at maximum) was limited by low shunt impedance (1 MΩ) of the former cavity.

Table 1: Basic parameters of previous/present rf cavity

	Previous	Present
Frequency	90.1 MHz	90.1 MHz
Cavity voltage	55 kV	150 kV
Shunt impedance	1 MΩ	2.45 MΩ
Unloaded Q	8370	20300
Coupling	1.75	1.34
Structure	Re-entrant ×1	Re-entrant×1
Inner diameter	1000 mm	964 mm
Bore radius	50 mm	55 mm
Material	SUS + Cu	Cu (OFHC)
Tuner	Plunge×1	Plunger ×2

Hence the new rf cavity was designed to have higher shunt impedance. Table 1 shows basic parameters of previous/present rf cavity. The new cavity was installed in the spring of 2005 and the high cavity voltage of 150 kV was achieved. With the new cavity system, observed Touschek beam lifetime was increased by a factor of 3. This upgrade is also favourable to the FEL because higher accelerating voltage leads to shorter electron bunch and higher peak current.

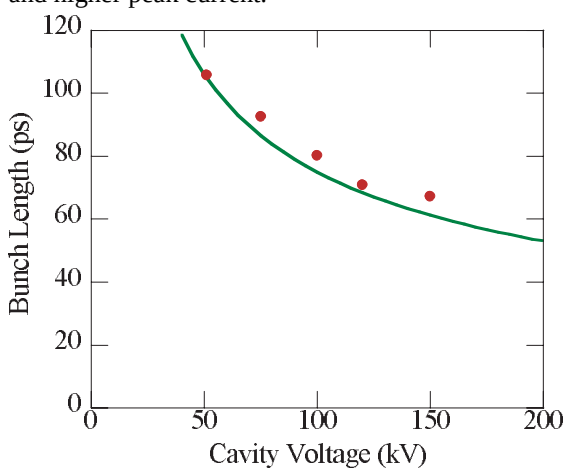

Figure 1: Natural bunch length in various rf voltage. The data points are measured values and the solid line is calculated bunch length.

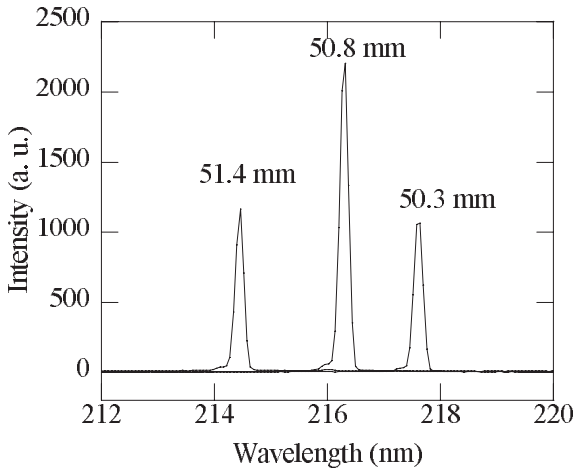

Figure 2: Typical FEL line spectra measured by changing gap width of the optical klystron. The resolution of the spectra is limited by that of the monochrometer used in the measurement.

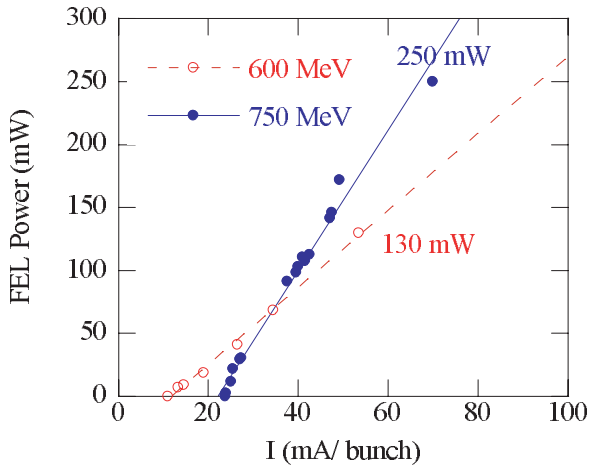

Figure 3: Measured extracted FEL power as a function of beam current at energy of 600 MeV and 750 MeV. The lines are guides to eyes.

Fig. 1 shows measured bunch length by using a streak camera after installing the new rf cavity. The bunch length at a cavity voltage of 150 kV is 67 psec; this value is 60 % of the previous one (110 psec). In this case FEL gain increased by a factor of 1.6 is expected. This leads the FEL lasing in the deep UV region where higher FEL gain is needed.

LASING AROUND 215 nm

We have planned an FEL lasing around 215 nm basically aiming to an user experiment. In the experiment, samples of bio-molecules are irradiated by a laser with the wavelength around 215 nm, where the absorption spectrum of the sample has a peak. The laser should have enough power in order to proceed the irradiation experiment quickly; otherwise the sample may be easily effected by bacteria.

In former UV lasing experiments at the UVSOR, multi-layers of HfO_2/SiO_2 had been employed for cavity mirrors. In a lasing experiment around 215 nm, the multi-layer can not be employed because the band gap energy of HfO_2 is about 5.6 eV (220 nm in a light wavelength) and a strong absorption is expected. Then we chose multi-layers of Al_2O_3/SiO_2; the band gap energy of Al_2O_3 is well above the laser photon energy requested. Since refraction index of Al_2O_3 is smaller than HfO_2, number of layers should be increased to attain reflectivity sufficiently high for lasing. On the other hand, transmission of a mirror becomes smaller and a less power is extracted through the mirror as increasing number of layers. Compromising reflectivity and transmission, we chose number of layer of 49 for downstream mirror and 37 for upstream mirror from which an FEL power is extracted. The expected round-trip reflectivity of the optical cavity is 99.3 % and the transmission of the upstream mirror is 0.5 %. Preparatory to the lasing experiment, we measured the round-trip reflectivity of the mirrors by ring-down method with a low electron beam current (~ 0.1 mA). The measured value was around 97.8 %, which was much smaller than the expected one. We suppose that the low reflectivity came from a degradation of the mirrors due to synchrotron radiation during reflectivity measurement. The mirrors degradation, however, seemed to stop after the first irradiation by synchrotron radiation. Even after exposure to SR of more than 1000 mA h during the lasing experiment, we did not observe the essential change of the reflectivity.

The lasing experiment was started with an electron energy of 600 MeV, with which UVSOR FEL experiment had been made so far. The storage ring was operated in two bunch mode with equal bunch spacing. As seen in Fig. 2. lasing from 214 nm to 218 nm was successfully obtained changing a gap width of the helical optical klystron. In Fig. 3, extracted laser power is plotted as a function of a stored beam current in the storage ring. The threshold beam current for lasing was 11 mA/bunch. The calculated FEL gain at a beam current of 11 mA/bunch is about 2.3 %. This value is very consistent with the measured cavity loss of 2.2 %.

As a next step of the lasing experiment, we raised the electron energy from 600 MeV to 750 MeV, with which the storage ring is operated for SR use. According to the Renieri limit [4], the extracted FEL power is proportional to the total synchrotron radiation power per turn from electron beam. Since the total radiation power is proportional to the 4th power of the electron energy, higher extracted laser power is expected at 750 MeV. Storing a rather high beam current in the storage ring, we have obtained successful lasing at this electron energy for the first time on UVSOR-FEL. The measured threshold current for lasing is about 2 times higher than that in the case of 600 MeV. But a higher laser power is extracted as is expected. The extracted FEL power at 750 MeV is about 1.6 times of that at 600 MeV at a beam current of 70 mA/bunch, that is well above the threshold current. This relation is consistent with that of synchrotron radiation power; the total synchrotron radiation power

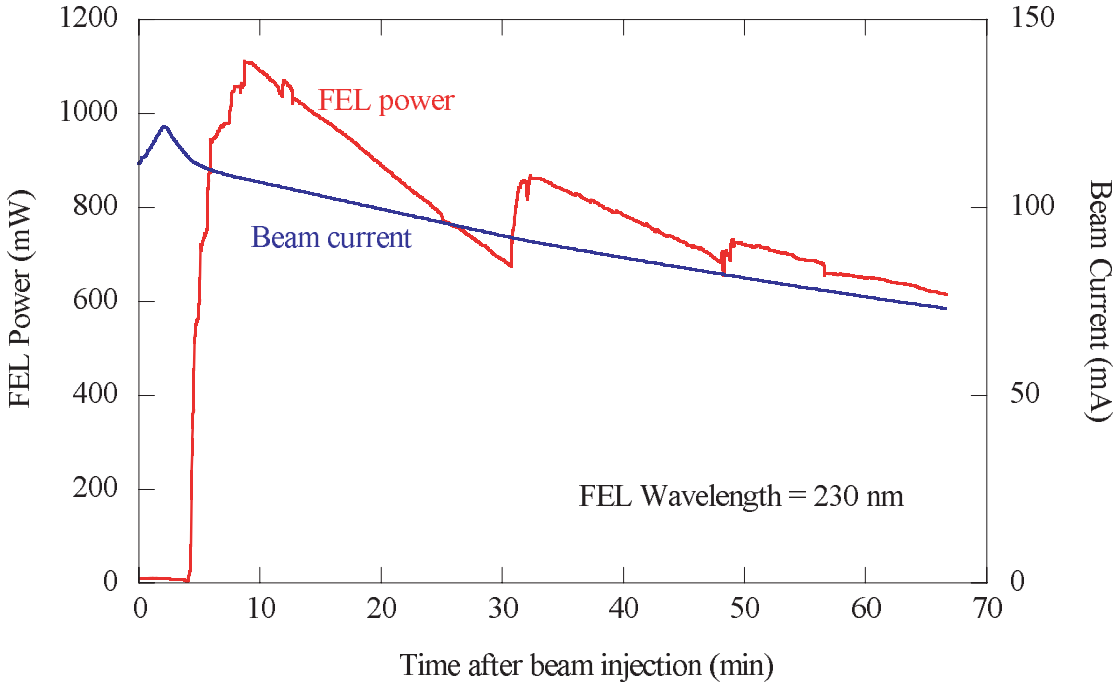

Figure 4: Extracted FEL power and beam current as a function of time. The FEL wavelength is around 230 nm. The maximum FEL power was 1.1 W.

from an electron at 750 MeV is about 2.4 times of that at 600 MeV. The higher electron energy has another advantage. The higher operating energy suppress Touschek effect, by which electron beam lifetime of UVSOR-II is limited. In the experiment at 750 MeV, we observed about three times longer lifetime, which resulted in longer lasing time for users experiment.

LASING AROUND 230 nm

Similar to the case of 215 nm-FEL, the lasing around 230 nm was planned oriented to users experiments. In the lasing experiment, multi-layers of Al_2O_3/SiO_2 were also employed for cavity mirrors. Measured round-trip reflectivity and transmission were 98.8 % and 0.8%, respectively. Therefore the optical characteristics of mirrors is advantageous for the FEL lasing as compared with mirror of 215 nm. The lasing experiment was carried out with an electron energy of 750 MeV. Fig 3 shows the extracted FEL power and the stored electron beam current as a function of time after the electron beam is stored. As is expected, higher extracted laser power was obtained and the observed maximum power reached 1.1 W at a beam current of 100 mA/bunch. During the experiment, drift of the laser power was observed especially at a high beam current as shown in the figure. The power could be recovered by adjusting the alignment with downstream mirror once again. Therefore the power drift can be explained by deformation of the cavity mirror due to heat-load from synchrotron radiation and from the FEL. The laser, however, became almost stable after about one hour exposure of synchrotron radiation.

The FEL around 230 nm was applied to two experiments on surface physics and photo-electron spectroscopy. The FEL extracted from the upstream mirror was transported to the experimental stations by using aluminium mirrors and was focused on samples by lenses. In the experiments, they started the measurement after the laser became stable. The FEL power around 0.5 ~ 0.2 W was actually applied. Although the experiments were made in limited machine time, the users succeeded in obtaining primary results.

CONCLUSION

We have succeeded in high power FEL lasing in deep UV around 215 nm and 230 nm. Users experiments of the FEL were carried out and primary results were obtained. The stability of the laser at the source position and also at the experimental station should be improved. Suppression of the thermal deformation of the cavity mirror and stability of the laser transport system are critical issues. We are going to lasing below 200 nm in near future. The shorter wavelength FEL is desired for the photo-electron spectroscopy experiment.

REFERENCES

[1] H. Hama et. al., Free Electron laser and its Applications in Asia, (1997) 17.
[2] M. Katoh et. al. Nucl. Instru. and Meth. A467 (2001) 68.
[3] A. Mochihasi et. al., UVSOR Activity Report 2004 (2005) 35. A. Mochihashi et. al., UVSOR Acitivity Report 2005 (2006) 37.
[4] A. Renieri, Nuovo Cimento, 53 (1979) 160.

SUPER COHERENT THZ LIGHT SOURCE BASED ON AN ISOCHRONOUS RING WITH VERY SHORT ELECTRON BUNCHES*

T. Tanaka#, T. Muto, F. Hinode, M. Kawai, K. Nanbu, K. Kasamsook, K. Akiyama, M. Yasuda and H. Hama, Laboratory of Nuclear Science, Tohoku University, 1-2-1 Mikamine, Taihaku-ku, Sendai, 982-0826, Japan
H. Tanaka, JASRI/Spring-8, 1-1-1 Koto, Sayo-cho Sayo-gun, Hyogo- pref. 679-5198, Japan

Abstract

A project to develop a coherent Teraherz (THz) light source has been progressed at Laboratory of Nuclear Science, Tohoku University. The coherent synchrotron light in the THz region is emitted from electron bunches with very short bunch less than 100 fs (rms) created by a thermionic RF gun and a sophisticated bunch compressor. The beam can circulate through the nearly complete isochronous ring for many turns, so that the average radiation power may be considerably enhanced. As an injector of this ring, we have developed an independently tunable cells (ITC) RF gun, which consists of two independent cavities to manipulate the longitudinal phase space. In order to generate short bunch with a significant bunch charge, a magnetic compressor is needed at downstream of ITC-RF gun. Two kinds of bunch compressor have been studied. This paper presents the isochronous THz ring design and describes ITC-RF gun, the magnetic bunch compressor and results of simulations. From simulation of the bunch compressor, we got a very short bunch length about 42 fs (rms).

INTRODUCTION

In these years, the coherent radiation in THz region has been observed in some 3rd generation light sources like BESSY-II [1]. However, it seems to be difficult on the storage ring to realize and/or maintain the short bunch with a significant beam current against bunch lengthening or other instabilities. On the other hand, when we focus on the condition of an isochronous beam transport, there is another possibility to generate the coherent radiation [2]. A very short electron bunch length around 100 fs is required to generate coherent THz radiation. To realize a coherent THz source based on the isochronous ring, total technologies of accelerators are required.

In this paper, a design study of an electron source and the bunch compressor for a novel coherent THz radiation source are described.

COHERENT THZ LIGHT SOURCE

Design of Isochronous Ring

The isochronous ring is the one of the candidates of the light source of coherent THz light [3]. Since this isochronous ring must keep a very short bunch length less than 100 fs (rms) from an injector in every place, it has been designed to have very small dispersion function. To keep bunch length for many turns at everywhere, the path difference for one turn should be much smaller than the bunch length. So that, the momentum spread of the injection beam must be order of 10^{-4} taking into account the momentum compaction factor which is designed as 0.0002. This ring has advantages; (1) multiple beam lines can be utilized, (2) a high average power of THz light can be generated since the electron beam can circulate ring for many turns. However, a betatron initial phase difference affects on the bunch lengthening larger than the effect of momentum compaction factor relatively. In order to reduce this bunch lengthening, an appropriate design of the phase advance in arcs is required [3]. We have designed the lattice of isochronous THz ring, then the effect of bunch lengthening in the bending arc has been calculated, and it is less than 40 fs which satisfies a condition to generate a coherent THz light. The major designed parameters of the isochronous ring are as follows. Tentative design parameters of this ring are shown in Table 1.

Table 1. Tentative design parameters of isochronous THz ring.

Circumference	C	45.691 m
Beam energy	E	200 MeV
Lattice type	-	Racetrack modified FODO
Bending radius	ρ	3 m (normal cell), 2 m (dispersion suppressor)
Momentum compaction factor	α	< 0.0002
Emittance of injection beam	ε_{rms}	5 π nmrad
Momentum spread of injection beam	$\Delta p/p$	2×10^{-4}

Coherent Synchrotron Radiation

The peak power of a coherent radiation from this ring has been calculated, and then it becomes about 100 kW with the bunch length of 100 fs (rms). This peak power of THz light is larger than other THz light sources (ex. FEL, other Lasers). This ring also has high performance in the average power of THz light. Radiation power of THz light sources is summarized in Table 2.

*Work supported by the Grants-in-Aid of Japan Society for the Promotion of Science, contract No. 17360035.
#takumi@lns.tohoku.ac.jp

Table 2. Radiation power from different THz light sources.

Source	Peak power (Micropulse length)	Average power
p-Ge Laser	1 W (10 ms)	100 mW
YAG + NOE	300 mW (4 ns)	60 nW
FEL	10 kW (1 ps)	10 mW
Isochronous THz ring	100 kW (250 fs)	350 mW

GENERATION OF VERY SHORT BUNCH

Design of a Thermionic RF Gun

As an injector of the isochronous ring, it is required to generate an electron beam with a very short bunch length less than 100 fs (rms) and with a very small normalized rms emittance less than 2 π mm mrad. To achieve high average power of coherent radiation, macropulse duration of the injector should be about 1.5 μs taking into account the circumference of the isochronous ring. In addition, the bunch charge should be as large as possible. To gather high bunch charge, the injector should have a large acceptance of momentum deviation. An acceptable momentum deviation is limited by acceptance of coherent THz ring. The coherent THz ring requires a momentum spread of the order of 10^{-4} for the injection beam. Because the beam is accelerated from 2 MeV to 200 MeV in the Linac, $\Delta p/p$ is limited to the order of 10^{-2} at the injector. To realize above parameters, a thermionic RF gun has been adopted for the injector. As a cathode material, a small single crystal of LaB_6 with a diameter 1.75 mm has been chosen. This cathode has a higher current density than conventional dispenser cathode. The normalized emittance can achieve a small value because of the small diameter. To reduce back-bombardment effect [4], this small diameter may be effective. In order to control a distribution of a longitudinal phase space at the exit of this RF gun, we employed independent two cells which don't couple with each other [5]. Parameters of ITC-RF gun are listed in Table 3.

Table 3. Design parameters of ITC-RF gun.

RF frequency	2,856 MHz (S-band)
Cathode material	LaB_6
Current density @ cathode	100 A/cm^2
Cathode diameter	1.75 mm
Number of cells	2
Feeding total power	～5 MW
E_{total} @ exit of gun	～2 MeV
Bunch length (rms)	～100 fs
Bunch charge	～several tens pC
$\varepsilon_{norm.\ rms}$	< 2 π mm mrad
$\Delta p/p$	< 2 %
Macropulse duration	1.5 μs

3D FDTD Simulation of ITC-RF Gun

In order to study the beam dynamics in ITC-RF gun and to design this geometry, we have used a 3D FDTD simulation code [6]. This code can include effects of the beam wakefield and of the space charge self-consistently. We have to design an appropriate distance between the cells and the strength of the accelerating field in each cell, because the longitudinal phase space strongly depends on these parameters. Since it is difficult for 3D FDTD code to calculate a precise geometry because of the mesh size, a 2D code: SUPERFISH [7] has been used to decide the precise geometry for manufacturing of ITC-RF gun. Because the RF coupling is a very small, accelerating fields are independent from each other. The prototype of ITC-RF gun is shown in Fig. 1.

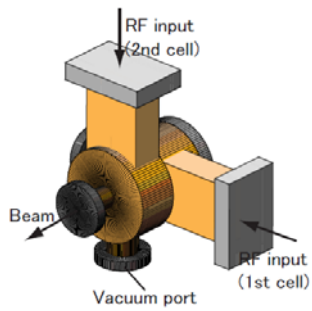

Figure 1. The prototype of ITC-RF gun. The RF input port is separated each other. This is now under manufacturing.

ITC-RF gun is designed to drive at π-mode basically. Peak accelerating fields of 1st cell E_1 [MV/m], 2nd cell E_2 [MV/m] and relative phase between cells Δθ are three degrees of freedom to control this gun. So as to compress the bunch length easier at the downstream of the gun, we have searched an optimum operating point of the gun to generate a beam with a linear dependence in the longitudinal phase space. At the optimization, the bunch charge from the gun should be as large as possible. The strength of E_1 was fixed around 25 MV/m in this gun, because the head of emitted electrons from a cathode must arrive at the middle point of between cells in time of a half RF cycle. With applying some suitable parameters (E_1, E_2) = (25, 50) MV/m and $\Delta p/p_{max}$ = 2 %, longitudinal and transverse phase spaces at exit of this gun are shown in Fig. 2 and Fig. 3 respectively.

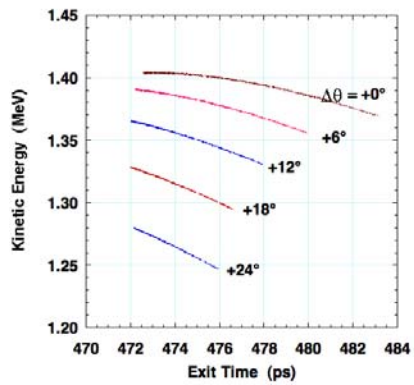

Figure 2. longitudinal phase space. Δθ is a variable in this simulation. (E_1, E_2) = (25, 50) MV/m.

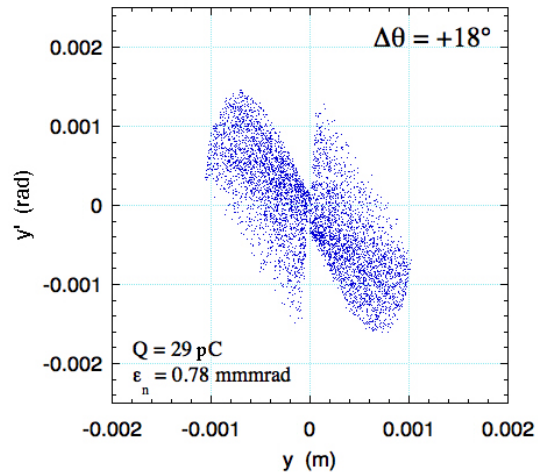

Figure 3. transverse phase space. (E_1, E_2) = (25, 50) MV/m, Δθ = +18 degree.

As shown in Fig. 2, a linearity of momentum distributions depends on the Δθ. From Fig. 3, the normalized rms emittance $\varepsilon_{norm.\ rms}$ = 0.78 π mm mrad satisfy the design value < 2 π mm mrad. Normalized rms emittances in other conditions also satisfy the design value. On the other hand, the bunch charge of this beam with momentum deviation $\Delta p/p$ = 2 % is about 30 pC which almost satisfy the design value. However the bunch lengths of these beams are far from the design value, so that the beams must be compressed at the downstream of the gun.

Magnetic Bunch Compressor

To compress the rms bunch length from several ps to less than 100 fs, a magnetic bunch compressor is needed. Magnetic bunch compression uses a difference of time of flight (TOF) for particles of different momenta p_0 and p_1 where these particles move from s_1 to s_2 along the beam axis. For these particles, the difference of TOF can be written as

$$\begin{aligned}\Delta t &= t_1 - t_0 \\ &= \frac{L_1}{c\beta_1} - \frac{L_0}{c\beta_0} \\ &= \frac{L_1}{c\beta_0\beta_1}\{-L_0(\Delta\beta) + \beta_0(\Delta L)\}\ , \qquad (1)\end{aligned}$$

where t is TOF from s_1 to s_2, L is a path length from s_1 to s_2, β is a relative velocity, index: 0, 1 represent particles with p_0 and p_1 respectively, $\Delta\beta = \beta_1 - \beta_0$ and $\Delta L = L_1 - L_0$. When we assume $p_0 < p_1$ and the longitudinal distribution in Fig. 2, a condition of the bunch compression leads $\Delta t > 0$. The first term of eq. (1) represents a difference of TOF caused by a difference of each particle velocity, and become negligible small when β goes to unity. The second term is caused by a difference of path lengths. In case of ITC-RF gun, the effect of the first term can not be negligible. When a total beam energy is 2 MeV, $s_2 - s_1$ = 1 m and p_1/p_0 = 1.02, the first term becomes about -5 ps. ΔL of the second term can be represented as

$$\begin{aligned}\Delta L &= \Delta L_{\Delta p/p} + \Delta L_{\beta} \\ &= \left\{\int \frac{\eta(s)}{\rho(s)} ds\right\}\frac{\Delta p}{p} + \int \frac{x_{\beta}(s)}{\rho(s)} ds\ . \qquad (2)\end{aligned}$$

The first term of eq. (2) means a path difference produced by an energy dispersion at bending section, and this term can be used for bunch compression. The second term of eq. (2) represents a path difference which comes from a different value of initial phase of a betatron motion, and this term can be suppressed by reducing the beta function and designing appropriate phase advances along lattice.

We have considered two kinds of magnetic compressor. The first is an α-magnet [8], and the second is a triple-bend achromat (TBA) lattice. An advantage of α-magnet is that this system has a larger energy acceptance, and has a possibility to gather larger bunch charge for a large $\Delta p/p$. An advantage of TBA lattice is that this system has a possibility to manipulate the higher order term of $\Delta p/p$ by adjusting optics. Each magnetic bunch compressor can apply different slopes of $(\Delta p/p)/\Delta t$ in longitudinal phase space. In case of TBA lattice, this system can vary the R_{56} by changing a dispersion function of the 2nd benging magnet without changing its reference orbit. When the α-magnet changes the field strength, reference orbit in it is changed correspondingly. Each system can be an achromat for the beam energy. At manufacturing the magnet of each system, it is easier for TBA lattice than α-magnet to design magnets. In order to select the method of a suitable bunch compression, studies have been continued. In the following, basic studies are shown.

In order to estimate a bunch compression, particle distributions in Fig. 2 and Fig. 3 have been used for both methods. The operating conditions of the gun are (E_1, E_2) = (25, 50) MV/m and Δθ = +18 degree. In case of α-magnet method, a beam tracking simulation has been done. In case of TBA lattice method, a design of optics and tracking simulations have been done by using SAD [9]. Since the bending angle of dipole magnets of TBA lattice are the same angle 60 degree, TBA lattice is 180 degree bending transport system totally. In addition, TBA lattice has four families of quadrupole which are used for two purposes mainly. The dispersion function in the 2nd bending magnet is controlled by quadrupole magnets between bending magnets to change the R_{56}. The other quadrupole magnets are used for matching of horizontal and vertical Twiss parameters at exit and reducing the beta function in bending magnets. One example of the TBA optics is shown in Fig. 4.

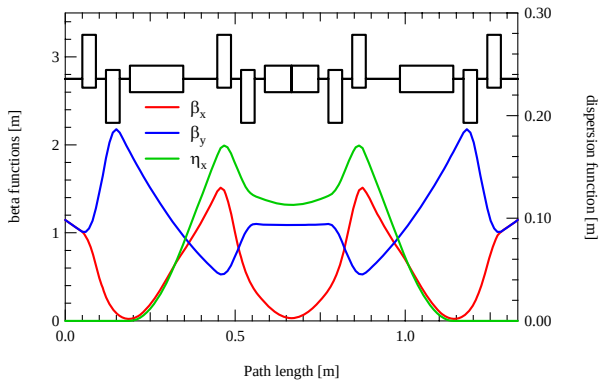

Figure 4. TBA optics. Left axis is for beta functions. Right axis is for dispersion function.

In case of an α-magnet, the first term of eq. (2) can be calculated by using following equation

$$\Delta L_{\Delta p/p} = \left\{ \int \frac{\eta(s)}{\rho(s)} ds \right\} \frac{\Delta p}{p}$$

$$= \frac{K_\alpha}{2} \sqrt{\frac{\beta\gamma}{g}} \frac{\Delta p}{p} \quad , \qquad (3)$$

where K_α = 191.655 Gauss$^{1/2}$cm$^{1/2}$ and g is the field gradient of α-magnet in Gauss/cm. The path length in α-magnet can be represented as $K_\alpha \sqrt{\beta\gamma / g}$. In order to estimate a difference of TOF in an α-magnet, the first term of eq. (1) and eq. (3) should be calculated, and then we can find the field gradient of an α-magnet for a suitable bunch compression. After optimizations of each bunch compressor, the longitudinal phase spaces and the particle time distributions are shown in Fig. 5.

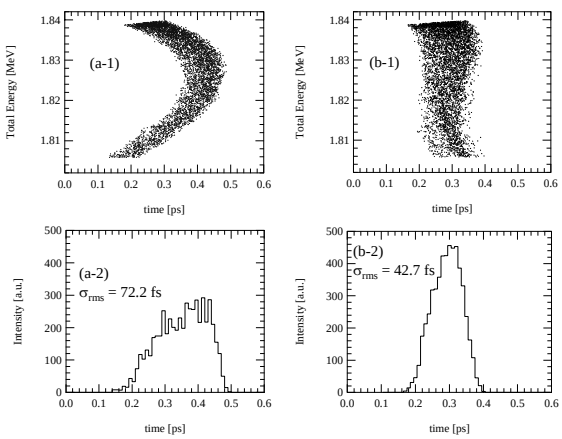

Figure 5. longitudinal phase space distributions and time distributions after bunch compression. (a-1), (a-2) α-magnet case, (b-1), (b-2) TBA lattice case.

As shown in Fig. 5, the compressed bunch lengths are 72.2 fs (rms) for the α-magnet system and 42.7 (rms) fs for the TBA lattice respectively. Both bunch compressors can achieve less than 100 (rms). TBA lattice can achieve shorter bunch length in this case, but more studies are needed for selecting a more suitable method.

SUMMARY

We have proposed the coherent THz light source by employing an isochronous THz ring and an injector which can generate a very short electron beam. From numerical calculations and simulations, the radiation power from the isochronous THz ring may achieve higher than other light sources of THz region. In order to generate the required short bunch beam for this ring, we have designed the injector which consists of ITC-RF gun and the magnetic bunch compressor. ITC-RF gun can generate a small normalized rms emittance value which satisfies the design parameter. For generating very short bunch, a magnetic compressor is needed at the downstream of ITC-RF gun. We have studied two kinds of bunch compressor: α-magnet transport and TBA lattice transport. Both of bunch compressors can achieve design bunch length less than 100 fs (rms). At a glance, TBA lattice seems to be better than α-magnet. However, we have continued to studied more detail about them including effect of the higher order momentum dependences and betatron initial phase difference.

REFERENCES

[1] M. Abo-Bakr, et al., Phys. Rev. Lett. 90 (2003) 94801.
[2] T. Nakazato, et al., Phys. Rev. Lett. 63 (1989) 1245.
[3] H. Hama, et al., Proc. of the 27th International FEL Conf., Stanford, California U.S.A., pp. 1.
[4] C.B. McKee and J.M.J. Madey, Nucl. Instr. and Meth. A 296 (1990) 716.
[5] T. Tanaka, et al., Proc. of the 27th International FEL Conf., Stanford, California U.S.A., pp. 142.
[6] H. Hama, et al., Nucl. Instr. and Meth. A 528 (2004) 371.
[7] http://laacg1.lanl.gov/laacg/services/download_sf.phtml
[8] H.A. Enge, Rev. Sci. Instr. 34 (1963) 385; M. Borland, Ph.D. Thesis, Stanford University, 1991.
[9] http://acc-physics.kek.jp/SAD/sad.html

RECENT EXPERIMENTS AND PROSPECT ON THE NIJI-IV VUV/IR FEL

H. Ogawa#, K. Yamada, N. Sei, M. Yasumoto, K. Yagi-Watanabe
Research Institute of Instrumentation, National Institute of Advanced Industrial Science and Technology (AIST), 1-1-1 Umezono, Tsukuba, Ibaraki 305-8568, Japan

Abstract

The NIJI-IV free electron laser (FEL) is being developed as a compact light source with very good optical quality and ultra-wideband tunability from the VUV to the IR. To obtain lasing at shorter wavelengths in the VUV region, continuous efforts to improve the cavity-mirror performance have been made, so that the original loss of mirrors was recently decreased around 195nm. A new optical cavity system, composed of two sets of a heavy granite base and a stable mirror manipulator, was installed to stabilize the lasing and also to extend the tuning range. As for the IR FEL, modification of the beam transport system to make space for installation of the optical cavity was completed.

INTORODUCTION

Storage ring FELs (SRFELs) are unique source and have advantages such as good spectral resolution, high repetition rate, and natural synchronisation with synchrotron radiation from insertion devices or bending magnets. These features of SRFELs are suitable for pump-probe experiments and observing a continuous change of a phenomenon without giving sample damage. Indeed, the use of SRFELs for the real-time surface observation has been investigated in combination with a photoemission electron microscopy (PEEM) at DUKE [1,2] and AIST [3,4]. Many efforts to shorten the wavelength in SRFELs have been made [5-7] for such applications. At AIST, an FEL research has been performed using the compact storage ring NIJI-IV and the FEL lasing down to 198nm was achieved [7]. The NIJI-IV is a racetrack-type storage ring whose circumference is 29.6m. The ring has two straight sections of 7.25 m and 4.1 m in length and a 6.3-m optical klystron ETLOK-II [8] is equipped in the longer straight section for the UV/VUV FEL experiments as shown in Fig.1. In 2004, a 3.6-m optical klystron ETLOK-III [9] was installed into the other straight section and the construction for lasing in the IR region is going on [10]. The optical klystron parameters are summarized in Table 1. Here we report recent progress in the NIJI-IV FEL.

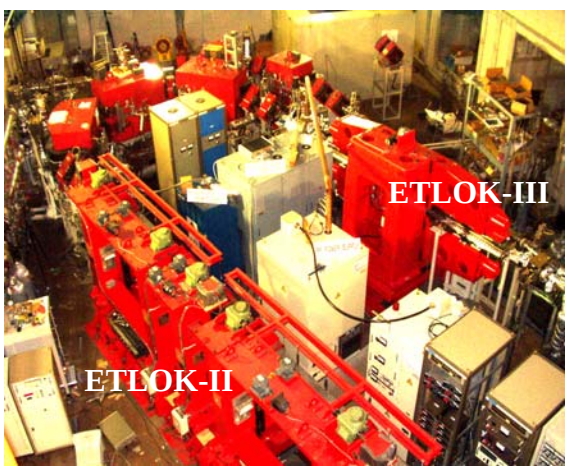

Figure 1: NIJI-IV FEL system.

Table 1: Parameters of optical klystron ETLOK-II and III

	ETLOK-II	ETLOK-III
Total length [m]	6.288	3.55
Magnetic period		
Undulator section [mm]	72	200
Dispersive section[mm]	216	720
Number of period N_u	42×2	7×2
Deflection factor K	<2.29	<10.04
Wavelength [μm]	0.198-0.595	(0.4-12)

DEVELOPMENT OF THE VUV/IR FEL

VUV FEL Mirror

To shorten the FEL wavelength, we have been upgrading the NIJI-IV FEL system. The replacement of NIJI-IV vacuum chambers as well as installation of thin sextupole magnets has been performed in order to increase FEL gain. As for the laser cavity, Al_2O_3/SiO_2 dielectric multilayer mirrors were adopted for the wavelength below 220 nm. In a previous study, we tried FEL oscillations below 195 nm with two kinds of Al_2O_3/SiO_2 mirrors but failed to obtain the oscillation. The original losses of the cavity composed of two mirrors around 195nm were small as 1.9%-2.6%, while the losses after irradiated by the undulator radiation from ETLOK-II were rapidly increased through degradation of dielectric multilayer mirrors as shown in Fig.2, so that the oscillation could not be realized [10]. To improve the mirror performance, the Al_2O_3/SiO_2 mirrors were manufactured again by tuning the dielectric coating condition. As a result, the original loss of the cavity was presently obtained to be down to 1.2%, which was sufficient to realize the lasing around 195nm. After measuring an evolution of degradation of the mirrors, we are planning to perform the FEL oscillation experiments below 195nm.

#ogawa.h@aist.go.jp

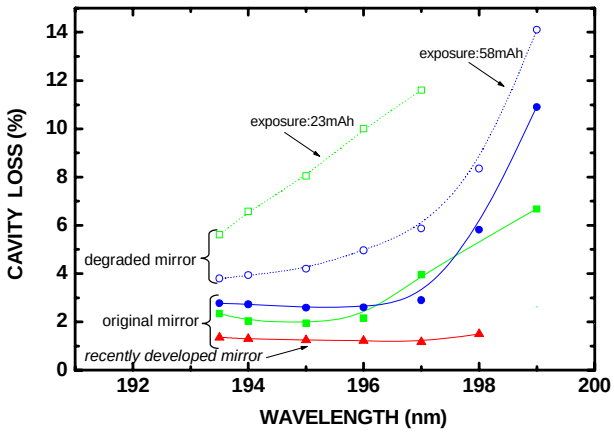

Figure 2: Wavelength dependence of the cavity loss of Al_2O_3/SiO_2 multilayer mirrors. The losses of mirrors manufactured in the previous work are shown by squares and circles, while the loss in the present work is represented by triangles.

Optical cavity system

It was observed that the intensity of the NIJI-IV FEL was modulated with a few to 10 ms period near the best cavity tuning condition and the lasing mode was not fixed at a stable CW mode [11]. Although its origin has never been identified, it is probably caused by a mechanical vibration of the mirror vacuum chamber, because the base of our mirror holders had a slender structure whose weight was only 20-30 kg. Therefore new optical cavity system has been made for the stabilization of the FEL oscillation, which is needed for FEL application research such as a photoemission electron microscopy. Figure 3 shows a photograph of the new system which was installed into an upstream side of ETLOK-II in this year. We chose heavy granite stone, whose weight was about 2 ton, as the base of the cavity, so that the vibration of the base in an optical axis was dumped below 0.1 mm, which was measured with a vibration sensor under frequency of 200 Hz. The mirror chamber is remotely manipulated by five-axis stage with gimbal optical mount and three linear stages (Newport SL20AN, M-MTM100PP.1, M-ILS50PP and M-MVN80 with precision motorized actuators LTA-HL). The cavity length and mirrors can be adjustable with resolutions of 0.1 mm and 0.8 mrad, respectively. In addition, a novel feature is that the chamber has two in-vacuum mirrors that are interchangeable with reproducible adjustment. This will enable us to extend FEL tuning range restricted by a narrow reflection bandwidth of dielectric multilayer mirrors. We will measure the stability of the FEL oscillation with the optical cavity system after commissioning of new beam transport system as described in the following subsection.

Figure 3: New optical cavity system.

Beam transport system

In order to extend lasing range toward a long-wavelength region, we have been developing the NIJI-IV FEL in the infrared (IR) region using ETLOK-III. The FEL gain in the visible and near-IR regions was evaluated to be over 2% from observed spectra of a spontaneous emission from the ETLOK-III [10]. The realization of FEL lasing can be expected in the visible and near-IR regions since high-reflection mirrors of 99.8% or more are available. We are preparing to make an optical cavity system for the IR FEL and its mirror diameter would be 50mm, which is larger than that for the UV/VUV FEL of 30mm, by considering diffraction loss.

However, there was no space to install the upstream cavity system for the IR FEL because a beam transport line was too close to the storage ring. Therefore we decided to modify the transport system to make a space for the cavity. The detail of design for new beam transport system was written in [10]. We have constructed the new transport system, as shown in Fig.4, which is 2.48m away from the former one and the beam commissioning has been started. The beam was transported from LINAC to

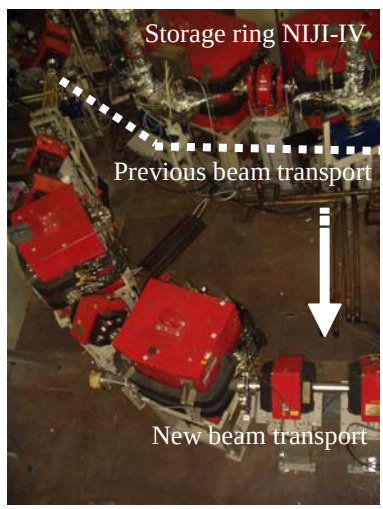

Figure 4: Photograph of a part of new beam transport system. The place where previous beam transport located is indicated by dashed line.

an entrance of the storage ring and focused into a septum chamber of NIJI-IV. The final tuning of beam parameter is now in progress.

DUV FEL APPLICATION

Recently, performance of the NIJI-IV FEL was improved at the deep UV (DUV) around 200 nm by both optimizing the transmittance of the output coupler and increasing stored electron-beam energy [3]. Thus we can make real-time observation of chemical reactions on a transition metal surface using a photoelectron emission microscopy (PEEM). The metal surface was irradiated by an FEL or spontaneous emission from ETLOK-II at a wavelength of 202 nm, and the catalytic CO-oxidation ($2CO + O_2 \rightarrow 2CO_2$) on a Pd(111) single crystal surface has been investigated by introducing CO and O_2 gases at a pressure of $\sim 10^{-5}$ Pa [4]. Figure 5 shows the setup for FEL-PEEM measurement. The PEEM system (STAIB Instrumente, type 350) is only applicable at pressures below $\sim 10^{-5}$ Pa, since a micro channel plate (MCP) image intensifier equipped in the system requires a vacuum of better than $\sim 10^{-5}$ Pa during operation. A differential pumping is necessary for observation of chemical reaction under higher pressure. Therefore we prepared a turbo molecular pump (Varian Turbo-V70LP) that is being added to a differential pumping port close to MCP. We are planning to observe chemical reactions on the transition metal surfaces at higher pressure of $\sim 10^{-3}$ Pa.

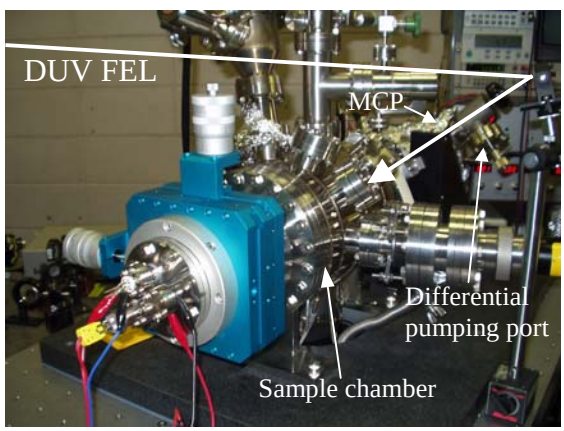

Figure 5: Photograph of the FEL-PEEM system.

SUMMARY

An FEL with wide wavelength range from the VUV to IR has been studied based on compact storage ring NIJI-IV. To shorten the lasing wavelength, Al_2O_3/SiO_2 multilayer mirrors optimized at 195nm were improved and the cavity loss of the original mirrors was successfully reduced by 30%, compared with that of previous ones. The preparation for the lasing in the IR region is also proceeding. The beam transport system in NIJI-IV has been modified to make space for the optical cavity of the IR FEL. Furthermore, in order to stabilize the FEL oscillations in the UV/VUV regions, new optical cavity system holding two in-vacuum interchangeable mirrors has been installed, which was composed of heavy granite base and five-axis manipulators. This will enable us to carry out reproducible FEL application experiments, such as real-time observation of surface chemical reactions.

ACKNOWLEDGEMENTS

This study was financially supported by the Budget for Nuclear Research of the Ministry of Education, Culture, Sports, Science and Technology, based on the screening and counseling by the Atomic Energy Commission of Japan.

REFERENCES

[1] W.-C. Yang et al., J. Appl. Phys. 94 (2003) 5720.
[2] W.-C. Yang et al., Phys. Rev. Lett. 90 (2003) 136102.
[3] K. Yamada et al., Proceedings of the 26th Free Electron Laser Conference, August 2004, Trieste, p.311.
[4] H. Ogawa et al., Proceedings of the 27th International Free Electron Laser Conference, August 2005, Stanford, p.467.
[5] F. Curbis et al., Proceedings of the 27th International Free Electron Laser Conference, August 2005, Stanford, p.473.
[6] V.N. Litvinenko et al., Nucl. Instr. and Meth. A470 (2001) 66.
[7] K. Yamada et al., Nucl. Instr. and Meth. A528 (2004) 268.
[8] T. Yamazaki et al., Nucl. Instr. and Meth. A331 (1993) 27.
[9] N. Sei et al., Jpn. J. Appl. Phys. 41 (2002) 1595.
[10] N. Sei et al., Proceedings of the 27th International Free Electron Laser Conference, August 2005, p.469.
[11] K. Yamada et al., Nucl. Instr. and Meth. A475 (2001) 205.

DISPERSION EFFECTS IN SHORT PULSE WAVEGUIDE FEL

N. S. Ginzburg, E. R. Kocharovskaya, A. S. Sergeev IAP RAS, Russia.

Abstract

The influence of waveguide dispersion on the FEL operation driven by short electron bunches is studied. Under the assumption of a high quality resonator, a parabolic equation for the evolution of the profile of electromagnetic pulse is derived. The condition of self-excitation are found by means of an analytical theory describing a structure of supermodes as the sum of resonator eigenmodes with locked phases. It is demonstrated that due to waveguide dispersion FEL is able to generate not only for positive but also for negative cavity detuning. The transient and nonlinear stages of the free-electron laser operation are analyzed by the computer simulation, and the optimal mismatches of group and cavity synchronism conditions are found.

INTRODUCTION

The mode-locking regime is typical for free-electron lasers (FEL) driven by a train of short electron bunches. In this regime, the electromagnetic radiation consists of micropulses with a duration nearly equal to that of the electron bunches. Both pulses (electron and electromagnetic) travel together through the resonator, but shift slightly away from each other due the difference between the wave group velocity and the electron velocity. Once they reach the right-hand mirror, the electron pulse escapes from the resonator, while the electromagnetic pulse reflects and comes back to the left-hand mirror at the time when the next current pulse arrives.

In short wavelength (optical, infrared) FEL experiments [1-4], the group velocity of electromagnetic pulses exceeds the velocity of electron bunches. To provide generation under such conditions, a specific mismatch between a period of electromagnetic pulse round trip over a resonator and a period of bunch injection was used. However, in some experimental investigations of long wavelength FELs [5-8], a waveguide may be used, so that the specific waveguide dispersion allows one to realize "zero-slippage" condition, for which the group velocity of electromagnetic pulse is equal to the longitudinal velocity of electrons. Under such conditions, mutual synchronization of radiation from different parts of electron bunches occurs due to dispersive spreading of the electromagnetic field, whereas localization of radiation near electron bunches is caused by its guiding properties [9,10].

In the present paper, a theoretical model of waveguide FEL is developed which takes into account the waveguide dispersion. Under the assumption of a high quality resonator, a parabolic equation for the evolution of the profile of electromagnetic pulse is derived. The linear, transient and nonlinear stages of the FEL operation are investigated, both analytically and numerically, and the optimal conditions are found.

THE MODEL AND BASIC EQUATIONS

Let us suggest that the radiation pulse propagating through a waveguide circulates between two mirrors (with reflection coefficients $R_{1,2}$), which are placed at some distance, L_0. Let FEL be fed by short electron pulses of duration τ_p, which is essentially less than both the round-trip of the radiation in the cavity $T_R = 2L_0 / v_{gr}$, and the repetition period of an electron bunch injection, T_i. During n-the pass through a resonator, the field can be represented as

$$A = \mathrm{Re}\left[E_s(r_\perp) \begin{Bmatrix} A_n^+(z,t)\exp(i(\omega_0 t - h_0 z)) + \\ A_n^-(z,t)\exp(i(\omega_0 t + h_0 z)) \end{Bmatrix} \right],$$

where E_S is a function, describing the profile of a given transverse waveguide eigenmode, ω_0 is the reference frequency, and $h_0 = h(\omega_0)$ the longitudinal wave number. Resonant electron-wave interaction takes place under the synchronism condition, $\omega_0 - h_0 v_\parallel \simeq \Omega_\perp$, where $\Omega_\perp = h_u v_\parallel$ is the bounce frequency, $h_u = 2\pi / \lambda_u$, λ_u the undulator period. We will consider the excitation of a resonator by a train of short electron bunches under the following conditions:

- the reflection coefficients are close to unity, $R_{1,2} \simeq 1$ and the changes of the wave amplitude during one pass are very small;
- dispersion spreading of the electromagnetic pulse during one pass over the resonator is small as well.

Under these approximations, we can replace the discrete variable n (pass number through the resonator) by a slow time τ with the period of one round trip, T_R taken as a time unit. Evolution of the pulse profile along the resonator can be described by the parabolic equation (for details see [9]):

$$\frac{\partial \alpha}{\partial \hat{\tau}} + \frac{\omega_0}{2Q}\alpha - \hat{\varepsilon}\frac{\partial \alpha}{\partial y} + i\frac{\hat{\nu} V_{gr}}{2}\frac{\partial^2 \alpha}{\partial y^2} = \frac{e\pi I_0 V_{gr}\kappa}{2m_e c^3 \gamma N_S h_0 l}\int_0^l f(y - z/V_{gr}) I_\omega dz, \quad (1)$$

where $I_\omega = \frac{1}{\pi}\int_0^{2\pi} e^{-i\Theta} d\Theta_0$ is the synchronous harmonic of the beam current, $V_{gr} = \partial\omega/\partial h$ the wave group velocity, $\hat{\nu} = |\partial^2 h / \partial \omega^2|$ the wave dispersion parameter,

$Q = \omega_0 l / V_{gr}(1 - R_1 R_2)$ the resonator Q-factor, I_0 the peak current of electron bunch, $\gamma = 1/\sqrt{1-\beta^2}$ the relativistic Lorentz factor, n_s the norm of the operating mode, κ the electron-wave coupling coefficient, $f(y)$ a function, describing the electron pulse profile, $\alpha = eA_n/(m_e c\gamma)$ the dimensionless wave amplitude. Taking into account the cavity detuning $\hat{\varepsilon} = (T_i - T_R)/T_R$, we use an independent time variable, $y = t - z/V_{gr} - \hat{\varepsilon}\hat{\tau}$.

Under assumptions described above, we can relay upon the periodical boundary conditions:

$$\alpha(\hat{\tau}, y) = \alpha(\hat{\tau}, y + T_R) \tag{2}$$

and expand the field and the beam current into Fourier series:

$$\alpha(\hat{\tau}, y) = \sum_{m=-\infty}^{\infty} a_m(\hat{\tau}) \exp(i2\pi m y / T_R),$$
$$I_\omega = \sum_{m=-\infty}^{\infty} J_m(\hat{\tau}) \exp(i2\pi m y / T_R). \tag{3}$$

An amplitude of each harmonic a_m, can be treated as an amplitude of cavity eigenmode with the longitudinal index m.

Assuming a small variation of electron energy $E = m_e c^2 \gamma$ and neglecting the Coulomb interaction, the electron motion equation can be presented in the form

$$\left(\frac{\partial}{\partial z} + \left(\frac{1}{V_\parallel} - \frac{1}{V_{gr}}\right)\frac{\partial}{\partial y}\right)^2 \Theta = \left(\frac{\omega_0}{c}\right)^2 \mu\kappa \,\mathrm{Re}\left(\alpha e^{i\Theta}\right) \tag{4}$$

with the boundary conditions:

$$\left(\frac{\partial}{\partial z} + \left(\frac{1}{V_\parallel} - \frac{1}{V_{gr}}\right)\frac{\partial}{\partial y}\right)\Theta\Big|_{z=0} = \Delta,\ \Theta\Big|_{z=0} = \Theta_0 \in [0, 2\pi],$$

where $\Delta = (\omega_0 - h_0 V_\parallel - \Omega_\perp)/V_\parallel$ is the initial mismatch of synchronism at the reference frequency, $\mu \simeq \gamma^{-2}$ the inertial bunching parameter. With the use of normalized variables,

$$\xi = \frac{\omega_0 y}{\chi} P,\ \tau = \frac{\omega_0 \hat{\tau}}{2Q},\ \zeta = z\frac{\omega_0}{c} P,$$
$$P = \left(\frac{4\pi e I_0 \mu \kappa^2 \beta_{gr} Q}{m_e c \gamma d b N_s h_0 l \omega_0^2}\right)^{1/3},$$

equations (1), (4) can be transformed to the following form:

$$\frac{\partial a}{\partial \tau} + a - \varepsilon\frac{\partial a}{\partial \xi} + i\nu\frac{\partial^2 a}{\partial \xi^2} = \int_0^L F(\xi - \zeta) I_\omega d\zeta, \quad (a)$$
$$\left(\frac{\partial}{\partial \zeta} + \frac{\partial}{\partial \xi}\right)^2 \Theta = \mathrm{Re}\left(a e^{i\Theta}\right), \quad (b) \tag{5}$$

with boundary conditions:

$$a(\tau, \xi) = a\left(\tau, \xi + T\right),$$
$$\Theta\Big|_{\zeta=0} = \Theta_0 \in [0, 2\pi],\ \left(\frac{\partial}{\partial \zeta} + \frac{\partial}{\partial \xi}\right)\Theta\Big|_{\zeta=0} = \delta,$$

where

$$a = \frac{\alpha\kappa\mu}{P^2},\quad T = \frac{T_R \omega_0 P}{\chi},$$
$$\nu = \left|\frac{\partial^2 h}{\partial \omega^2}\right| \frac{V_{gr}\omega_0 Q P^2}{\chi^2},\ \varepsilon = \frac{(T_i - T_R)}{T_R}\frac{2QP}{\chi},\ \delta = \Delta\frac{c}{\omega_0 P}.$$

$L = l\omega_0 P/c$ is the normalized interaction length, $F\left(\xi\right)$ the function describing electron-pulse profile, $\chi = \beta_\parallel^{-1} - \beta_{gr}^{-1}$ is the relative value of the detuning of "zero-slippage" condition. The normalized energy stored in electromagnetic pulse is give by relation

$$W = \frac{1}{T_c}\int_0^T |a|^2 d\xi.$$

THE LINEAR THEORY

Linearizing the equation of electron motion (see Eq. 5b), we obtain an equation for the electron current:

$$\left(\frac{\partial}{\partial \zeta} + \frac{\partial}{\partial \xi}\right)^2 I_\omega = -ia \tag{6}$$

Using the expressions (3) we find all harmonics of current

$$J_m = \left[\frac{i}{k_m^2} + \frac{\zeta e^{-ik_m\zeta}}{k_m} - \frac{ie^{-ik_m\zeta}}{k_m^2}\right] a_m, \tag{7}$$
$$k_m = 2\pi m/T + \delta.$$

As a result for the amplitude of each mode a_m from (5a) taken into account (7) we obtain

$$\left[\frac{d}{d\tau} + 1 - i\varepsilon\frac{2\pi m}{T} - i\nu\left(\frac{2\pi m}{T}\right)^2\right] a_m = \sum_{n=-\infty}^{\infty} C_n^m a_n, \tag{8}$$

where

$$C_n^m = \int_0^T\int_0^L \left[\frac{i\left(1 - e^{-ik_n\zeta}\right)}{k_n^2} + \frac{\zeta e^{-ik_n\zeta}}{k_n}\right]\frac{F(\xi - \zeta)e^{i\xi(k_n - k_m)}}{T} d\zeta d\xi.$$

Obviously the diagonal elements of the matrix C_n^m coincide with the expression for a complex electron permittivity found in [9, 10].

Representing the solution of Eq. 8 in the form $a_m = e^{i\Omega\tau}\hat{a}_m$ where Ω is a complex frequency, we get the algebraic equations for the supermodes of the resonator excited by a train of electron bunches:

$$i\Omega\hat{a}_m = \sum_{n=-\infty}^{\infty} D_n^m \hat{a}_n, \tag{9}$$

where $D_n^m = C_n^m - 1 + i\varepsilon(2\pi m/T) + i\nu(2\pi m/T)^2$.

Assumed for simplicity that the electron pulse has the

rectangular form with normalized duration $T_c = \tau_c \omega_0 P / \chi$, we obtain the following expression for the elements of the matrix D_n^m:

$$D_n^m = \frac{\left(e^{i(k_n-k_m)T_c/2} - e^{-i(k_n-k_m)T_c/2}\right)}{T} \frac{e^{-ik_m T_c/2}}{(k_n-k_m)^2} \times$$

$$\left[\frac{ie^{ik_m L}}{k_m^2} - \frac{ie^{ik_n L}}{k_n^2} - \frac{i}{k_m^2} + \frac{i}{k_n^2} + \frac{L}{k_m} - \frac{L}{k_n}\right] +$$

$$i\varepsilon\frac{2\pi m}{T} + i\nu\left(\frac{2\pi m}{T}\right)^2 - 1.$$

The starting condition of generation corresponds to the equality

$$\mathrm{Im}[\Omega] = 0. \qquad (10)$$

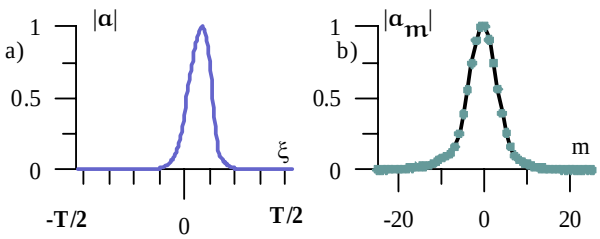

Figure 1: Normalized profile (a) and spectrum (b) of the supermode for the dimensionless parameters: $T_c = 4$, $\varepsilon = 1$, $L = 2.3$, $\nu = .3$. Resonator eigenmodes amplitudes are shown by blue dotes.

A spatial structure of supermodes calculated via eigen vectors of the matrix D_n^m is shown in Fig. 1a; it is a superposition of longitudinal resonator eigenmodes.

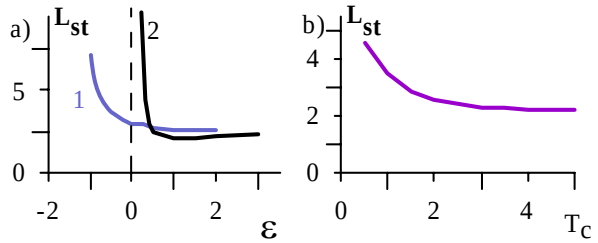

Figure 2: Dependence of the starting length, L_{st} a) on the cavity detuning ε: 1 for dispersive parameter $\nu = .3$, and 2 for the absence of dispersion and b) on the dimensionless electron bunch duration T_c.

Note that wave dispersion, playing a part of feedback, allows FEL to generate even in the case of negative values of the cavity detuning ($\varepsilon < 0$, see Fig. 2a, curve 1), for which the resonator can not be excited in the absence of dispersion (see Fig. 2a, curve 2). The increasing of the electron bunch duration leads to the decrease of the generation threshold (see Fig. 2b). For long electron bunch duration T_c this value as well as the cavity detuning does not practically influence the generation threshold.

COMPUTER SIMULATION OF THE NONLINEAR STAGE

The nonlinear stage of the electron-wave interaction was analyzed on the basis of computer simulation of Eqs. 5. The electron bunch profile has a rectangular form with normalized duration T_c. Three basic regimes of the FEL generation have been observed when the value of current exceeds the generation threshold: a) stationary regime (see Fig. 3), b) periodic self-modulation (see Fig. 4a), c) chaotic self-modulation (see Fig. 4b).

At a small excess over the generation threshold, a profile of the field and its spatial spectrum are closed to those found from the linear analysis (see Fig.1). The dynamics of electromagnetic pulse profile become more complicated with increasing the dimensionless resonator length, L (see Fig.3).

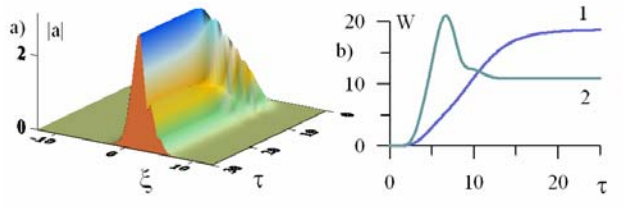

Figure 3: Regime of the stationary generation: $L = 4.4$, T=25.6, $\varepsilon = 0.5$, $T_c = 4$, $\nu = 0.3$,: a) time–space evolution of an envelope of the electromagnetic pulse; b) time dependence of the electromagnetic pulse energy W: for comparison the case of the absence of dispersion is shown by curve 2.

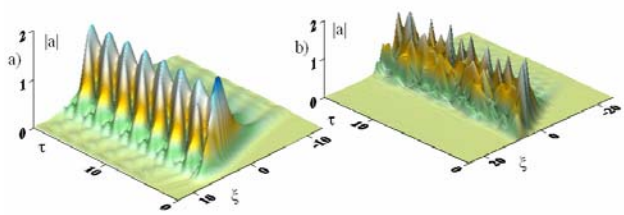

Figure 4:Time–space evolutions of an envelope of electromagnetic pulse in the regime of periodical (a) ($L = 4.4$, T=25.6, $\varepsilon = 4$, $T_c = 4$, $\nu = 1$) and chaotic self-modulation (b) ($L = 10$, T=51.2, $\varepsilon = 1$, $T_c = 6$, $\nu = 1$).

The self-modulation regime may be reached by two ways: via increasing the dimensionless length L and/or via enlarging the cavity detuning ε. Possible quasi-periodical behavior is demonstrated in Fig. 4a.

At large excess over the generation threshold, the chaotic regime of generation takes place (see Fig. 4b). At extremely large excess over the generation threshold, the pulse envelope evolves in a complicated stochastic manner, so that the generated radiation is distributed quasi-homogeneously over very wide spectral range of the resonator eigenmodes. According to estimates all these regimes are reasonable for the waveguide FEL to provide variety of applications (see Fig.5).

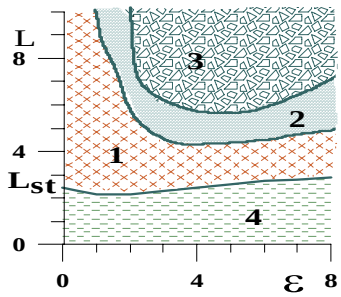

Figure 5: Zones of stationary (1), periodical (2) and chaotic (3) generation on the plane of dimensionless length L and cavity detuning ε for $\nu = 1$, $T_c = 4$, $T = 51.2$. Zone (4) is absence of generation.

The stationary regime, when one supermode is generated, has been investigated in detail for various parameters of dispersion, the detuning of "zero-slippage" conditions and cavity detuning. At the limit $\chi \to 0$ and $\varepsilon \to 0$ the equations (5) transform into the equations for the case of group synchronism [5, 6, 10]. Numerical simulation of the equations (5) at small values of the parameter ε, allows us to determine an optimal relation between all FEL parameters, χ, L, T_C and ν, which gives the maximum field amplitude, i.e., provides the most effective interaction between the electromagnetic pulse and the electron bunches.

Note also that a superradiant (nonstationary) type of operation regime [11] can be realized for small negative cavity detuning ε (see Fig. 6).

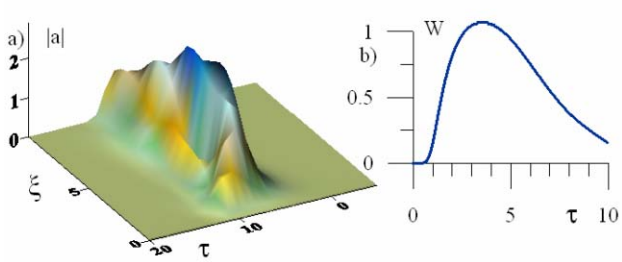

Figure 6: Superradiant operation regime: $L = 4.4$, T=51.2, $\varepsilon = -0.5$, $T_c = 16$, $\nu = 0.3$,: a) time–space evolution of an envelope of the electromagnetic pulse; b) time dependence of the field energy.

CONCLUSION

In conclusion, we develop both linear and nonlinear theory to describe regimes of operation of the waveguide FELs with finite detuning of "zero-slippage" condition and cavity detuning.

On the base carried out theoretical analyze it were estimated parameters of generated radiation for KAERI THz FEL ($\lambda = 100 \mu m$) [7, 8]. The experiments were done for an electron bunche of duration $\tau_p \simeq 30$ ps, an electron current ~ 0.5 A, particle energy ~ 6.5 MeV, the undulator period $\lambda_u = 25$ mm, the undulator length – 2 m, amplitude of undulator field ~ 6 kG, transverse sizes of the plane waveguide $d = 30$ mm, $b = 2$ mm, resonator losses ~ 10% Above physical parameters corresponds to dimensionless ones of length of interaction $L = 7$. From simulations the duration of electromagnetic micropulse is ~ 20 ps (relative spectrum width ~ 1.5%) and peak power 30kW. The value of spectrum width corresponds to experimental date, but experimental value of peak power is much less the theoretical limit that in particular can be explained by the parameter spread in the real electron bunches.

This research was supported by the grant RFBR-05-02-17553.

REFERENCES

[1] D.A.G. Deacon et al., Phys. Rev. Lett. 38 (1977) 892.

[2] D. Oepts et al., Phys. Rev. Lett. 68 (1992) 3543.

[3] D. C. Ngueyn et al., Nucl. Instr.&Meth. in Phys. Res. A 358 (1995) 27.

[4] V.P. Bolotin et al., "Status of the Novosibirsk High Power Free Electron Laser," IRMMW'2004, Karlsruhe, September 2004, p.55.

[5] F. Ciocci et al., Phys. Rev. Lett. 70 (1993) 928.

[6] A.J. Doria et al., IEEE J. Quantum Electron. 29 (1993) 1428.

[7] Y.U. Jeong et al., Nucl. Instr.&Meth. in Phys. Res., A 483 (2002) 195.

[8] Y.U. Jeong et al., "THZ imaging by a wide-band compact FEL", FEL'2004, Trieste, Italy 2004, p.667.

[9] N.S. Ginzburg and M.I. Petelin, Int. J. Electronics 59 (1985) 291.

[10] N.S. Ginzburg et al., Nucl. Instr.&Meth. in Phys. Res. A 407 (1998) 64.

[11] N. Piovella, Phys. Rev. E. 51 (1995) 5147.

THE EXPERIMENTAL RESEARCH OF THE SR-FEL CAVITY MIRRORS AT 355nm AND 248nm*

GAO Huailin#, WANG Donglei, WANG Yong, TAN Rongqing, WU Jin, Institute of Electronics, CAS, P.O. Box 2702-45, Beijing100080, CHINA

WANG Naiyan, China Institute of Atomic Energy, P.O. Box 275-7, Beijing 102413, CHINA.

Abstract

The cavity mirrors of the SR-FEL at 355nm and 248nm central wavelengths are developed experimentally with the fused silica substrate and "HfO2/SiO2+Al2O3/SiO2+M-SiO2" optical coatings. The electron-beam evaporation and ion-beams sputtering are used as the deposition technologies. After heating condition at 400°C×4hrs, the absolute reflectance and wavelength-tunable range is measured with VARIAN-Cary-5000 spectrophotometer. The experimental results show that R=99.45% and Δλ(R≥99.00%) =75nm at 355nm for the broadband mirror. For the mirror with the dual-central wavelength at 355nm/248nm, R= 99.69% and Δλ(R≥99.00%)=59nm at 355nm, and R=98.21%, Δλ(R≥99.00%)=9nm and Δλ (R≥98.00%) =51nm at 248nm.

INTRODUCTION

Storage-Ring Free-Electron Laser (SR-FEL) is a wavelength-tunable, high power, short pulse light source. With the optical resonator, SR-FEL will generate a laser radiation with the best spatial and temporal coherences, tunable wavelength and harmonic radiations, simultaneously [1-3]. It is also the best seed light for generating HGHG, X-ray laser and γ-ray laser with new FEL schemes [1-11]. All of these light sources have a potential application in the nuclear physics, atomic physics, molecular physics, bioscience and medicine. But the high power UV/DUV free electron laser and the synchrotron radiation will induce the mirror reflectance degradation or direct damage. These will limit the laser gain and the development of the SR-FEL toward to the shorter wavelength, shorter pulse and higher power in the UV/DUV region [1-3,8,12-13]. Thus, it's very important to develop the resonator mirror with the lowest absorption, highest absolute reflectance, needed wide wavelength-tunable range, highest damage threshold and the best resistance to reflectance degradation [1-13]. In this paper, report the progress on the experimental research of the SR-FEL resonator mirrors at 355nm and at 355nm/248nm.

PHYSICAL DESIGN TO MIRROR COATING

The physical design of the mirror coatings is based on the experimental results in the Inertial Confinement Fusion (ICF) driven by high energy laser and Storage-Ring Free Electron Laser (SR-FEL) researches from 1982 to 2006, so that it can integrate the all advantages of different physical designs, deposition technologies, film-growing parameters, post-deposition conditions, and so on. Here, a compound mirror coating is designed for the broadband mirror coating at 355nm central wavelength and the dual-band mirror coatings at 355nm and 248nm central wavelengths. It is "HfO2/SiO2+Al2O3/SiO2+M-SiO2", where Sub is the material of the mirror substrate, fused silica is chosen because of its stable physical characteristics. HfO2/SiO2 and Al2O3/SiO2 are two coating stacks, M=6 the layer number of the SiO2 top layers. Because the HfO2/SiO2 coatings has the largest bandwidth and Al2O3/SiO2 coatings has the highest damage threshold in the UV/DUV region, as found by LANL, LLNL, CIAE scientists in the research of ICF driven by high-energy laser [13-18]. And the top-layer SiO2 has an evident effect to increase the damage threshold of the mirror coating as found by above researchers [13-18], and to resist the reflectance degradation induced by the synchrotron radiation and the UV/DUV FEL as found by the ELETTRA scientists [8,12]. The theoretical design are listed in table.1, where H is HfO2, H` is Al2O3, L and L` are SiO2. Since the damage threshold of the Al2O3/SiO2 mirror coatings is higher than that of the HfO2/SiO2, the absorption coefficient of Al2O3 material is lower than that of HfO2 materials, and the laser intensity of the coherent standing-wave electric field in the topmost layers of mirror coating is higher than that in the inner. Thus, the Al2O3/SiO2 coating stack is set above the HfO2/SiO2, the top-layers SiO2 is put on the HfO2/SiO2 coating stack. The basic structures of the mirror coatings are "Sub.-LL-(0.5H-L-0.5H)[12-pair]/ 355nm-(0.5H`-L-0.5H`)[25-pair]-LL-4L`/320nm" for the broadband mirror at 355nm and "Sub.-LL-(HL)[11-pair] /355nm-H-(LH)[11-pair]/248nm-H`-(LH`)[20-pair]-LL-4L/212nm" for the dual-band mirror at 355nm/248nm.

DEPOSITION TECHNOLOGY AND PARAMETER

The past experiment research has shown that, for an optimized mirror coating design, the deposition technology and parameters have a strong and direct affection to the realization of the physical design. As found by LLNL scientists in ICF research, a mirror coatings will have a higher damage threshold when

* Work supported by NSFC, Grant No. 10475081.
# Corresponding author, Prof. GAO Huailin, email: gao.hl@mail.china

deposited by electron-beams evaporation (EBE) than by ion-beams sputtering (IBS) deposition [14]. But, as found by ELETTRA scientists in the SR-FEL research [8,12], when deposited by IBS technology, the oxide coating of the resonator mirror will have resistance to the reflectance degradation induced by FEL and synchrotron radiation. Thus, in our experimental research, the "HfO2/SiO2+Al2O3/SiO2+2-SiO2" part of the mirror coatings is deposited by EBE technology with LEYBOLD-APS-1104 machine; the rest 4-SiO2 film layers are deposited by IBS technology with VECCO-SPECTRA-IBS machine, so that these cavity mirror will have high damage threshold to laser radiation and resistance to synchrotron radiation, simultaneously. The deposition parameters are listed in table 2.

In Table 1, the leaked oxygen is used to re-oxide the dissociated oxygen molecular to increase the damage threshold of coatings further, as found by IECAS scientists in ICF and FEL researches [13]. Finally, the fresh sample is conditioned at 400°C×4hrs to decrease the absorption of the mirror coating and increase the absolute reflectance and damage threshold together. The step-size of temperature increase is 70°C/1hr. After 4-hour continuous treatment, the mirror sample will cool down naturally to room temperature. Then, they are measured.

Table 1: deposition technology and parameters for SR-FEL mirror coatings.

Deposition technology	Deposition parameter	
Electron-beams evaporation	V(HfO2)	0.5nm/s
	V(Al2O3)	0.5nm/s
	V(SiO2)	0.6nm/s
	T	185°C
	P(O2)	1.5×10[-4]mbar
Ion-beams sputtering	V(M-SiO2)	0.3nm/s
	T	120°C
	P(O2)	4.0×10[-4]mbar
Heating condition	400°C×4hrs	

EXPERIMENTAL RESULT AND DISCUSSION

The spectral performance of the SR-FEL mirror coatings is measured with the spectrophotometer VARIAN-Cary-5000. The parameters include the absolute reflectance at the central wavelength and the bandwidth corresponding to the absolute reflectance higher than 99.00%, i.e., the top width of the reflectance spectrum.

Broadband Mirror Coatings at 355nm

In Fig.1 was shown the spectra of the absolute reflectance for the broadband mirror coatings at 355nm before and after heating condition. The top width with the reflectance higher than 99.00% is listed in Table2. From Fig.1 and Tab.2, it shows, after heating condition, that the absolute reflectance at 355nm central wavelength is R(355nm)=99.45%, the wavelength-tunable range is from 406nm to 331nm, i.e., Δλ(R≥99.00%)=75nm. Relative to the R` and Δλ` of the fresh mirror sample without heating treatment, the average increases of the absolute reflectance and the wavelength-tunable range in the top region are ΔR= 0.39% and Δλ*=7nm, where ΔR and Δλ* are defined as

$$\Delta R = \frac{1}{N}\sum_{j=1}^{N}\left(R(\lambda_j) - R`(\lambda_j)\right)$$

$$\Delta\lambda^* = \Delta\lambda - \Delta\lambda`$$

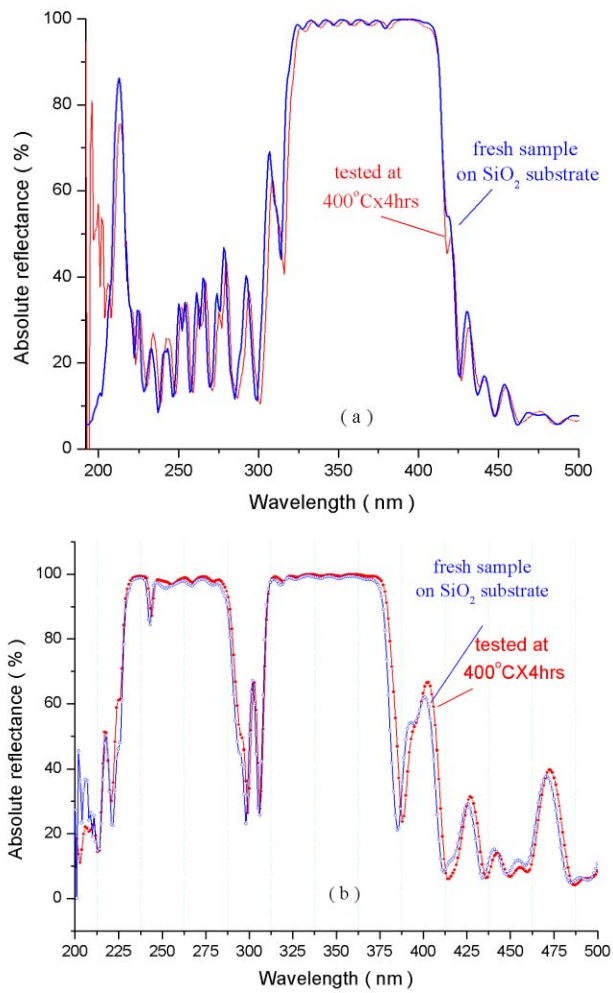

Figure 1: The spectral performances of the broadband (a) and dual-band (b) SR-FEL mirror with heating condition at 400°C×4hrs and without for the fresh samples. They are measured with varian-cary-5000 spectrophotometer.

Dual-band Mirror Coatings at 355nm/248nm

In the Figure 1 was also shown the spectra of the absolute reflectance for the dual-central wavelength mirror coatings at 355nm/248nm on fused silica substrate. The absolute reflectance higher than 99.00% is listed in Table 3. From these experimental data, it can be seen that, for the mirror coatings after heating condition, all the characteristics of the first band at 355nm is similar to that in Fig.1. It has a perfect shape. At the central wavelength 355nm, the absolute reflectance and wavelength-tunable range are R=99.69% and Δλ(R>99.00%)=373nm-314nm=59nm; Relative to the experimental data (R` and Δλ) in the Fig.1 for the fresh sample without heating treatment, the average increase of the absolute reflectance and wavelength-tunable range are ΔR= 0.73% and Δλ*=26nm, defined as above.

In the second band at 248nm for the sample with heating condition, the absolute reflectance is less than 99.00% at most of the wavelengths. The reflectance at 248nm central wavelength is only R(248nm)=98.21%. Only in the wavelength ranges of (275-272)nm and (240-234)nm, the absolute reflectance is higher than that 99.00% and Δλ(R≥99.00%)= (275-272)nm+(240-234) nm=9nm. At most of the wavelengths, the absolute reflectance is ranged from 98.00% to 99.20%, its corresponding wavelength-tunable range is Δλ(R≥98.00%) =33nm. Relative the optical spectrum of the fresh mirror coatings without heating treatment, its average increase of the absolute reflectance and wavelength bandwidth are ΔR(R≥98.00%)=1.04% and Δλ*(R≥98.00%)=9nm.

Table 2: The absolute reflectance and wavelength-tunable range of the SR-FEL broadband mirror at 355nm

λ/nm	406	405	401	400
R/%	99.02	99.10	99.55	99.67
R`/%	97.89	98.02	99.01	99.25
λ/nm	341	333	332	331
R/%	99.73	99.67	99.64	99.38
R`/%	98.65	99.02	98.53	97.73
Δλ/nm	Δλ (R>99.00%)=406nm–331nm=75nm, Δλ`(R`>99.00%)=401nm–333nm=68nm			

Table 3: The absolute reflectance and wavelength-tunable range of the SR-FEL mirror at 355nm/248nm.

λ/nm	373	364	363	355	330
R%	99.17	99.73	99.79	99.69	99.46
R`/%	97.54	98.83	99.01	99.14	99.04
λ/nm	323	322	316	314	283
R%	99.30	98.97	99.09	99.07	98.22
R`/%	98.87	98.77	97.81	98.39	96.45
Δλ/nm	Δλ(R>99.0%)=(373-314) nm=59nm,				
	Δλ`(R`>99.0%)=(363-330) nm=33nm				
λ/nm	275	272	271	270	248
R/%	99.19	99.12	98.8 79	98.49	98.21
R`/%	98.16	98.42	98.19	97.88	97.01
λ/nm	241	240	234	233	232
R%	98.83	99.17	99.12	98.82	98.09
R`/%	93.61	98.11	98.53	97.98	96.72
Δλ/nm	Δλ (R>98.0%) = (283-259)+(241-232)=33nm Δλ`(R`>98.0%) = (275-271)+(240-234)=10nm				

In additional, the highest reflectance is up to 99.19% at 275nm. The shortest wavelength with reflectance R≥99.00% is at 234nm. The shortest wavelength with reflectance R≥98.00% is at 232nm, its reflectance is 98.09%. The spectral breaking at 244nm may be induced by the bandwidth narrowing in the DUV region. Thus, it's necessary to improve the spectral continuity at 244nm further.

From the experimental results for tow types of the mirror coatings, we can get the following conclusion. (1) Heating condition to the fresh mirror coatings has an evident influence on increasing mirror's absolute reflectance and expanding spectral bandwidth. It implies that absorption coefficient of the mirror coatings have reduced after heating treatment. It's very important to develop the RS-FEL mirror toward the shorter wavelength and higher power output. (2) These resonator mirrors have get the designed absolute reflectance and spectral bandwidth. Thus, it can be used as the SR-FEL resonator mirror.

CONCLUSION

Today's experimental results show that it's possible to develop the SR-FEL cavity mirror with an absolute reflectance higher than 99.00% and wavelength-tunable range from 10nm to 75nm in the UV/DUV region. It is very effective to develop the SR-FEL mirror coatings with a compound optical design, a combined deposition technologies of electron beams evaporation and IBS, oxygen-leaked method, and heating treatment.

ACKNOWLEDGEMENTS

The research work is supported by the natural science foundation of China (NSFC) with the project No. 10475081. The authors gratefully thank NSFC for her support.

REFERENCES

[1] Patrick G. O'Shea and Henry P. Freund, "Free-Electron Laser: Status and Applications", Science, 292(2001) 1853-1858.

[2] S. V. Milton, E. Gluskin, N. D. Arnold, et al, "Exponential Gain and Staturation of a Self-

Amplified Spontaneous Emission Free-electron Laser", Science, 292(2001) 2037-2045.
[3] L. H. Yu, M. Babzien, I. Ben-Zvi, et al, "High-Gain Harmonic-Generation Free-Electron Laser", Science, 289(2000) 932-934.
[4] Jialin XIE, "Current FEL Development in China", Proc. 2nd Asian Particle Accelerator Conf., Beijing, China, 2001, 215-220.
[5] B. C. Zhang, K. Zhao, J. K. Hao, et al, "High Average Current Superconducting Accelerator At Peking University", Proc. 2nd Asian Particle Accelerator Conf., Beijing, China, 2001, 97-99.
[6] CHEN Nian, HE Duohui, LI Ge, at el, "General design of coherent harmonic generation storage-ring free-electron laser of NSRL", Nucl. Techn., 27(2004) 405-408, (in Chinese).
[7] D. NUTARELLI, D. Garzella, E. Renault, et al, "Super ACO FEL Oscillation at 300nm", Nucl. Instr. And Meth.. A 445(2000) 143-148.
[8] St. Gunster, A. Gatto, M. Trovo, et al, "VUV Optics Development for the ELETTRA Storage Ring FEL", Proc. 2004FEL Conf., 2004, 233-236.
[9] K. Yamada, N. Sei, H. Ohgaki, et al, "Characteristics of the NIJI-IV UV-VUV FEL System-Toward Lasing Down to 150nm Using a Compact Storage Ring", Nucl. Instr. And Meth.. A 475(2001) 205-210.
[10] Vladimir N. Litvinenko, Seong Hee Park, et al, "Operation of the OK-4/Duke Storage Ring FEL below 200nm", Nucl. Instr. And Meth.. A475 (2001) 195-204.
[11] M. Hosaka, S. Koda, M. Katoh, et al, "Recent Progress of the UVSOR", Proc. 2th Asian Particle Accelerator Conf., Beijing, CHINA 2001.
[12] A Gatto, J. Heber, N. Kaiser, et al, "High-performance UV/VUV optics for the storage ring FEL at ELETTRA", Nucl. Instr. And Meth.. A483 (2002) 357-362.
[13] GAO Huailin, WANG Naiyan and SHAN Yusheng, "Experimental Investigation on the Resonator mirror of the SR-FEL and ICF KrF Laser", High Energy Physics and Nuclear Physics, 29(2005)99-103, (in Chinese).
[14] Ralph Berggren and James D. Boyer, "Optics Technology for KrF laser", Inertial Confinement Fusion at Los Alamos, Progress Since 1985, Vol.I, Chapter VII, 1989, 1-8.
[15] F. Rainer, D. Milan and W. H. Lowdermilk, "Laser damage thresholds of thin film optical coatings at 248nm", NBS Special Publication, 638(1981) 339-343.
[16] GAO Huailin, SHAN Yusheng and WANG Naiyan, "Research on the UV Dielectric Coatings with High Damage Threshold", Chinese J. Laser, B6(1997) 229-237.
[17] Arthur H. Guenther, "Optical Damage: Boulder and Beyond", Lasers & Optronics, Oct.,1989, 57-62.
[18] Stephen R. FOLTYN and Brian NEWNAM, "Ultraviolet damage resistance of dielectric reflectors under multiple-shot irradiation", IEEE J. QE, 17(1981) 2092-20.

THE RESEARCH OF FIR-FEL IN CAEP

Xingfan Yang#, Ming Li, Xiao Jin, Weihua Li, Zhou Xu
Institute of Applied Electronics, CAEP, China.

Abstract

The research of FIR-FEL has been undertaken about 10 years in CAEP (China Academy of Engineering Physics) and first lasing at center wavelength 115 μm was observed in March 2005. The facility consists of RF-gun, alpha magnet, L-band SW accelerator, beam transport line, wiggler, optical cavity and measurement system. At present, a high brightness photo cathode RF-gun is commissioning, the cathode material is Cs2Te and the quadruple light is used. This injector will be used in the FIR-FEL project in the second half of this year. In this paper, the design consideration, the system layout and experiment results are introduced.

INTRODUCTION

The research work of FIR-FEL was started in 1997 in CAEP. In 1999 the 30MeV RF SW electron linac was built, the linac consists three accelerating sections, the resonant frequency is about 1.3GHz, a 1+1/2cell thermionic RF-gun was used as the injector. When doing the FIR-FEL, only the first accelerating section(ACC1) was used, the electron energy is about 6.5MeV~7MeV. The FIR-FEL facility consists of RF-gun, alpha magnet, ACC1, beam transport line, wiggler, optical cavity and measurement system (shown in Fig.1). Based on this facility the first lasing was observed in March 2005 and the center wavelength was 115 μm. As one important direction of FEL the high average power FEL was proposed. Two key technology of high average power FEL are the high brightness photo-cathode injector and the SRF ERL. The high brightness photo-cathode RF-gun injector was studied in our Lab in 1999 and the first photo-cathode injector with 2+1/2cell was operated in 2000.In order to study the SRF technology, cooperative with the Peking University, we built a superconducting cavity. This cavity includes a single cell (the frequency is 1.3GHz). This cavity was tested in our Lab in 2000, the energy gain is about 0.6MeV.

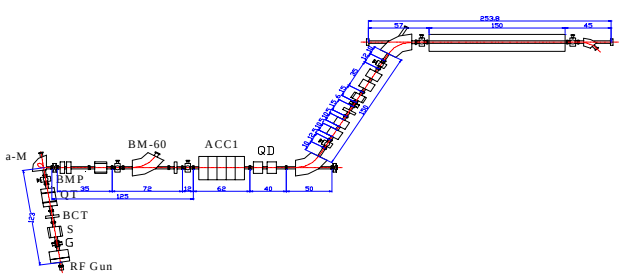

Fig.1: the schematic of the FIR-FEL facility.

#xingfan_y@caep.ac.cn

THERMIONIC CATHODE RF GUN INJECTOR

The study of FEL needs the high brightness electron beam with small energy spread. The beam quality is mainly determined by the injector. The development of high-brightness electron sources has been a challenging project for many years. RF gun is one kind of high brightness electron source which developed for the purpose of FEL research in 1984[1]. It has high electric field. The electron was accelerated to the light speed in a short distance, so the space charge effect has been reduced efficiently and easy to get the small emittance. There are two kinds of RF guns, one is the thermionic cathode RF-gun, the other is photo-cathode RF gun. The work of thermionic RF gun in our Lab is introduced in this section and the photo-cathode RF gun will be introduced in the next section. The advantages of thermionic cathode RF gun are the simple construction, operating reliability and low cost, it acts as an important role in the research of FEL especially at the beginning and it has been studied in detail. We built thermionic RF-gun as the injector for the 30MeV linac. The drawback of this kind of injector is the relative larger energy spread aroused by the wide capture phase and electron back bombardment. In order to decrease the electron back bombardment and obtain good quality electron beam, several guns with different structure have been built and experimented in our Lab. The SUPERFISH and PARMELA codes were used for the accelerating structure design. The ring cathode RF gun was tested also, but the experiment result was not good. Finally the 1+1/4cell gun was selected (shown in Fig.2), the electric field on the axis was measured using network analyser (shown in Fig.3). It was built in 2004(shown in Fig.4), the cathode material is LaB6, the diameter is 5mm and the electron energy of this injector is about 1.5MeV. Using this injector, the FIR-FEL stimulated emission was observed.

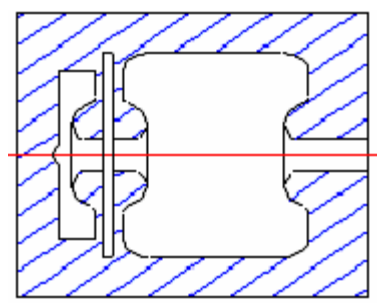

Fig.2: the schematic of the thermionic cathode injector.

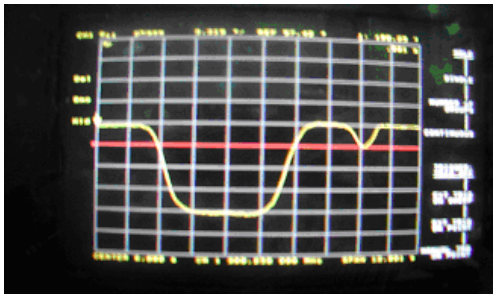

Fig.3: the electric field on the axis.

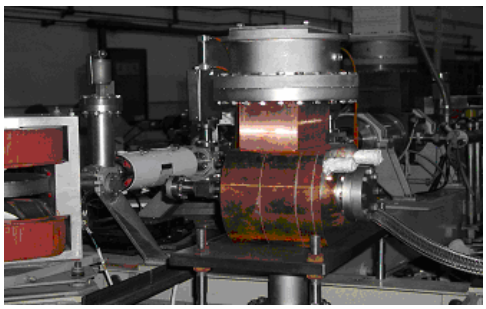

Fig.4: the thermionic cathode injector.

PHOTO-CATHODE RF GUN INJECTOR

The photo-cathode RF gun injector developed from 1985[2], comparing with the thermionic cathode RF-gun injector, the photo-cathode RF-gun is more adaptive to the research of FEL, it is easy to get the short pulse with high current and small energy spread. We started to study the photo-cathode RF-gun in 1999, and the first one was buil in 2000, the electron energy is about 3MeV. In order to develop the 3μm~8μm FEL, the second photo-cathode RF-gun with 4+1/2cell was studied in 2004(schematic was shown in Fig.5, the frequency is 1.3GHz), so the tota electron energy(including the injector and three accelerating sections) is about 37MeV. The electric field on the axis was measured using network analyser (shown in Fig.6). It was built in 2005(shown in Fig.7), the focusing solenoid and compensated solenoid were used This injector is commissioning at present.

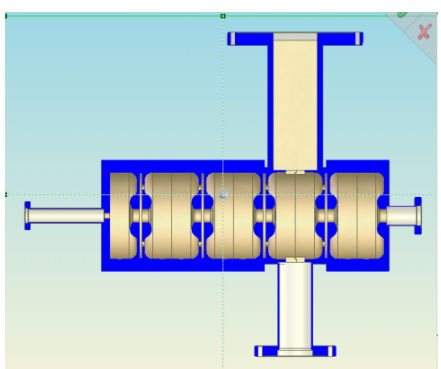

Fig.5: the schematic of the photo-cathode injector.

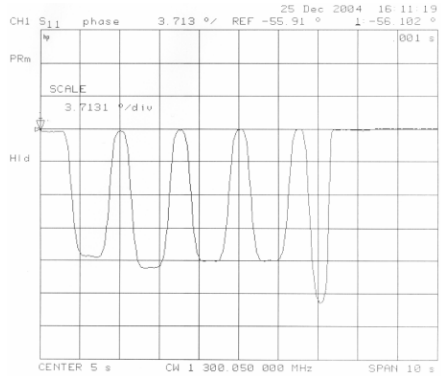

Fig.6: the electric field on the axis.

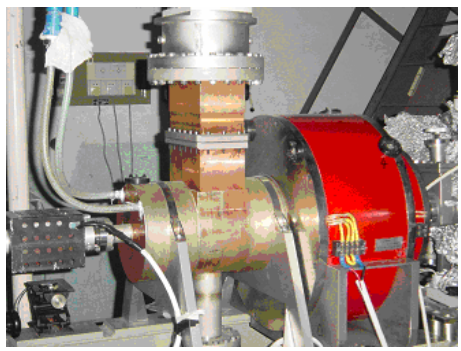

Fig.7: the 4+1/2cell photo-cathode injector.

The cathode material is Cs2Te and the quadruple light is used. The quantum efficiency is about 1%, the electron energy is 7MeV. The cathode-driving laser system(shown in Fig.8) of the RF photoinjector include the mode-locked oscillator(from Time-Bandwidth), diode-pumned amplifier and FHG (fourth harmonic generation). The average power of the oscillator is 10W , the timing jitter is 0.56ps, the width is 11.9ps at a repetition rate 54.167MHz . Micropulse energies is 3 μ J of 266nm light.

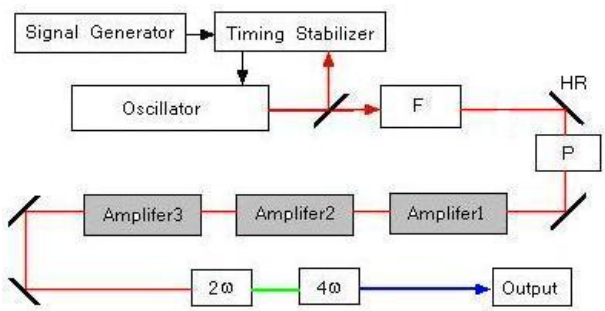

Fig.8: Optical Schematic of the cathode-driving laser system F, the Flady isolator.P, pockel .HR, high reflector.

THE WIGGLER

The Wiggler is one of the most important components for FEL and it is the region where the relative electron and the radiation field will interact. It's performance, such as the peak field, good field aperture etc. will determine

the FEL gain when we calculate the relative electron performance. A NdFeB-FeCoV hybrid wiggler has been designed and built for CFEL. More than 10mm good aperture and as high as 3235 Gs peak field were achieved with a 18 mm gap (shown in Fig.9). The trace simulation for a single electron showed that the center offset was less than 0.1 mm, the electron trajectory was simulated(shown in Fig.10), and the ratio of the small signal gain versus the ideal small signal gain was more than 98 percent. Recently, we've observed the resonance light in the 115 um FIR-FEL experimental study which used this wiggler.

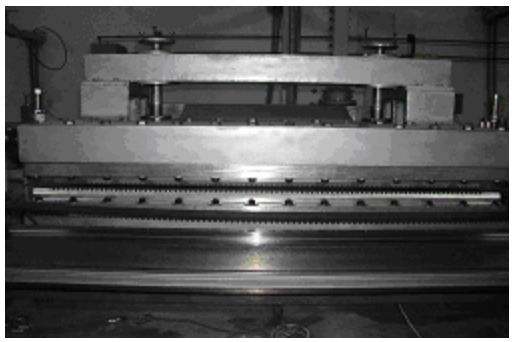

Fig.9: the wiggler.

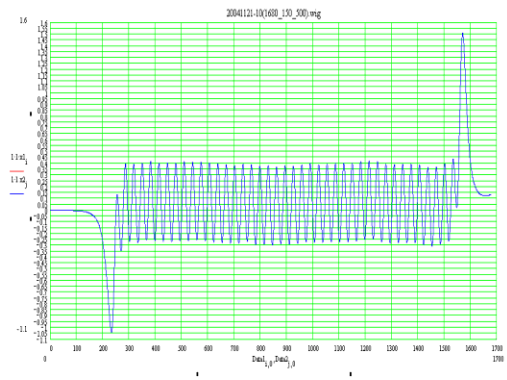

Fig.10: simulation trajectory of the electron in the wiggler.

THE STUDY OF SRF TECHNOLOGY

In order to get the high average FEL power, the high average electron beam power should be provided first, and the machine should be operated in the CW condition thus the SRF is required. SRF ERL technology is the practical way to obtain the high average power FEL and proved by JLAB[3]. Cooperate with the Peking University, we built a facility to study the SRF technology, (shown in Fig.11), at this facility the 2+1/2cell photo-cathode injector was used. The high average power FEL was proposed and we will begin to build the SRF ERL machine in the next years.

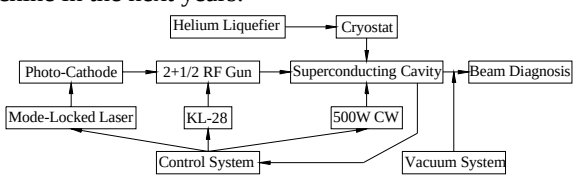

Fig.11: the schematic of the SRF test facility.

THE FIR FEL EXPERIMENT

The parameters of the FIR-FEL facility is shown in table 1.The macro-pulse current is measured by BCT and the beam currents are measured at the different position of the beam line, shown in Fig.12. The width of the micro-pulse is measured by the streak camera. The microwave power of the injector and ACC1 are provided by a klystron with 10MW. The stimulated signal is obtained in the March 2005, shown in Fig.13 and the spectrum of the stimulated signal is measured using grating analyser, shown in Fig.14, the center of the spectrum is 115μm, the width of spectrum is about 1%.

Table 1: parameters of the FIR-FEL facility

Energy 6.5MeV	Normalized emittance 20πmm·mrad
Macro-pulse current 130mA	Number of wiggler periods 44
Macro-pulse width 4μs	Period length 32mm
Micro-pulse current 4A	Wiggler gap 18mm
Micro-pulse width 25ps	Magnetic field 3250Gs
Energy spread 1%	Optical cavity length 2536mm

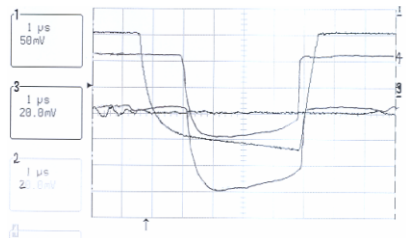

Fig.12: the beam current at the different position on the beam line, measured with BCT.

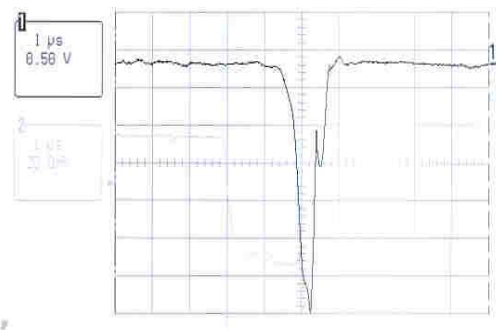

Fig.13: the FEL stimulated emission signal.

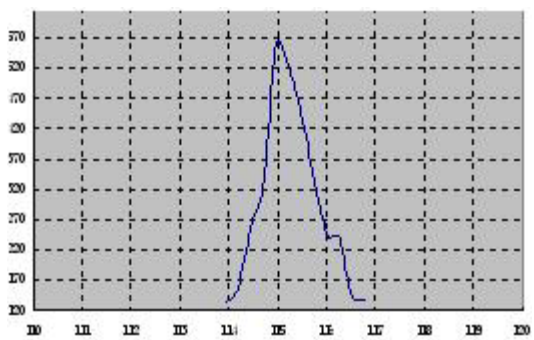

Fig.14: the spectrum of the stimulated signal.

CONCLUSION

We have made great efforts in the research of FIR-FEL, and obtained the stimulated emission in 2005. The thermionic-cathode and photo-cathode RF gun injectors have been built. The high power FEL project was proposed and a single cell superconducting facility was built and tested. The next step we will build the SRF energy recovery Linac.

REFERENCES

[1] A. Westenshop, J.M.J. Madey, “Microwave Electron Gun”, Laser and Particle Beam, 1984, 2(2), p223.

[2] C.H. Lee etc IEEE Trans Nucl Sci NS-225 1985, p3045.

[3] S. Benson, D. Douglas, M. Shinn, etc, “High Power Lasing in the IR Upgrade FEL at JEFFERSON LAB” Proceeding of FEL2004, p229-232.

DEVELOPMENT OF POWERFUL FEMS OF X, KA AND W BANDS FOR PHYSICAL AND INDUSTRIAL APPLICATIONS*

N. Ginzburg, N. Peskov, M. Petelin, Institute of Applied Physics RAS, N.Novgorod, Russia
A. Kaminsky, S. Sedykh, Joint Institute for Nuclear Research, Dubna, Russia
M. Einat, The College of Judea and Samaria, Ariel, Israel
A. Gover, Y. Socol, Tel-Aviv University, Israel
J. Lucas, The University of Liverpool, UK.

Abstract

The possibility to develop powerful FEMs capable for physical and industrial applications is being studied at Tel-Aviv University, IAP RAS, JINR and The University of Liverpool within the framework of the INTAS collaboration project. Present paper summarizes the progress in three successful FEM experiments: (1) Electrostatic-accelerator driven 70-130 GHz Tandem-FEM with kW-level pulse power (Tel-Aviv University); (2) Linac-driven 30-GHz FEM with pulse RF power of ~ 20 MW (JINR + IAP RAS); (3) Sub-relativistic e-beam industrial FEM tunable over X-band with output power up 1 kW (The University of Liverpool).

INTRODUCTION

Free electron masers (FEMs) are among the main sources of powerful microwave pulses from X to W-bands. Interest to such sources is caused by the large number of potential physical and industrial applications, requiring a wide variety of the radiation parameters. For example a new generation of the accelerators (SLAC, CERN etc.) requires sources of ~100 MW pulse power at 30-38 GHz with a narrow spectrum. Material processing stations require kW-level average power. Spectroscopic and imaging experiments as well as biological experiments, require lower power but fine control and tuning of the radiation spectrum.

Presently there are no ready industrial RF sources with parameters necessary for the applications mentioned above. Investigations carrying out in collaboration between aforementioned Institutes are aimed to partially fill up the gap with FEMs from X to W bands for different applications including testing components of high gradient accelerators and material processing. Present paper is devoted to the progress in the development of FEMs and their applications.

70-130 GHz TANDEM FEM

The Israeli FEM [1] resonator was re-designed in order to reduce the overall round-trip losses and achieve control on the radiation output-coupling. In its new configuration, the resonator consists of overmoded corrugated rectangular waveguide and two radiation mode splitters, separating the high-energy e-beam from the laser radiation. The electron input splitter is based on Talbot effect in an overmoded rectangular waveguide. The radiation out-coupling is done in the output splitter. It is based on novel design and it combines Talbot effect between two parallel plates with free space propagation, and focusing by two curved cylindrical mirrors in a confocal imaging scheme. The waveguide and the splitters were tested experimentally, showing improved performance in comparison with the former resonator. The measured unloaded Q-factor of the new version is increased by a factor of ~ 3, attaining up to Q = 25 000. Accordingly, the round-trip losses are ~ 23%. Rotating grids control the radiation out-coupling allowing wide variation for maximization of the radiation output power and extraction efficiency.

Additional R&D work was aimed on increasing FEM power by boosting the electron beam energy after the radiation build-up. A fine control of the electron beam energy during the radiation pulse is designed to compensate the small energy degradation during the pulse. Also, a controlled ramp (up or down) in the electron energy during the pulse will be applicable as well. We compared the theoretical estimations of the output power in the presence of electron energy change during the pulse, to the obtained experimental results. Two models, showing good agreement between them and with the existing data, were compared: low-gain analytical model based on the pendulum equation, and rigorous 3D FEM interaction model solved numerically. Another expected result of the design is to further extend the pulse duration with stable conditions and to obtain improved coherency.

30 GHz JINR-IAP FEM

The FEM-oscillator has been developed in Ka-band during last few years in a collaboration between JINR (Dubna) and IAP RAS (Nizhny Novgorod) [2]. These experiments aim to develop a pulsed power microwave source for testing behaviour of materials in high-Q structures under the influence of RF-pulses. Information about the life-time of different metals in strong RF-fields would be beneficial, in particular, when designing high-gradient accelerating structures for future linear colliders [3]. Such application requires a high power RF-source with a narrow frequency bandwidth. In addition, the

*This work is partially supported by INTAS (grant # 03-51-5319) and Russian RFBR (grants # 04-02-17118, # 05-02-16833, # 05-02-17036)

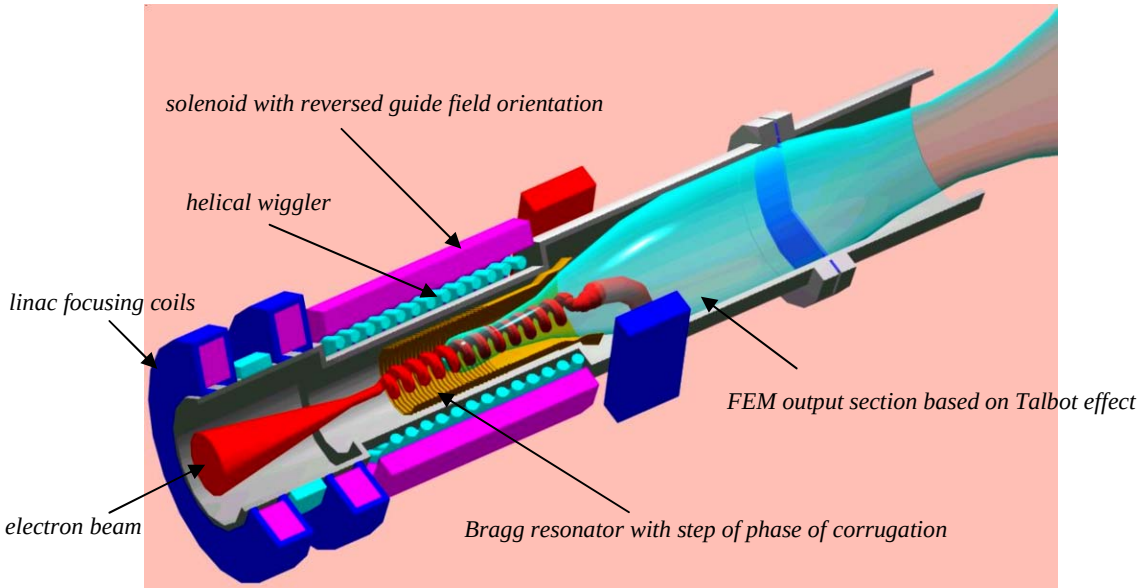

Figure 1: Schematic diagram of the JINR-IAP FEM.

radiation frequency should be exactly matched to the operating frequency of the accelerating structure, and therefore precise frequency tuning is essential for such a generator.

A schematic diagram of the JINR-IAP FEM experiments is shown in Fig.1. The induction linac LIU-3000 (JINR), which generates a 0.8 MeV / 200 A / 250 ns electron beam with a repetition rate of 1 Hz, drives the FEM-oscillator. Transverse velocity in the magnetically guided beam is pumped in a helical wiggler of 6 cm period. The main advantages of developed FEM is the use of a reversed guide field, which provides high-quality beam formation in the tapered wiggler section with a low sensitivity to the initial beam spread, alongside with Bragg resonator having a step of phase of corrugation, which possesses high electrodynamical mode selection. As a result, stabile single-mode operation with high electron efficiency was achieved in the FEM. At the present stage, the FEM generates 20 MW / 200 ns pulses at 30 GHz with the spectrum width of 6 - 10 MHz (Fig.2).

Precise tuning of the oscillation frequency of the FEM was performed by inserting short sections of smooth waveguide between the two Bragg structures. If the phase shift between the Bragg structures is varied from 0 to 2π the frequency of the fundamental eigenmode moves from the lower to the higher edge of the Bragg zone. It is important to note that only one high-Q eigenmode exists inside the Bragg zone at any value of phase shift, i.e. the high selective properties of the resonator are maintained over a sufficiently wide frequency band. For a phase shift equal to π the frequency of nearly 30 GHz was measured. In the experiments frequency tuning was achieved over a range of 6%, the spectrum width in all regimes of oscillations did not exceed 0.1% (Fig.3).

The test facility to study surface heating effects at 30 GHz, which was constructed based on the FEM source [4], is shown in Fig.4. The experimental set-up includes a two-mirror confocal transmission line and mode

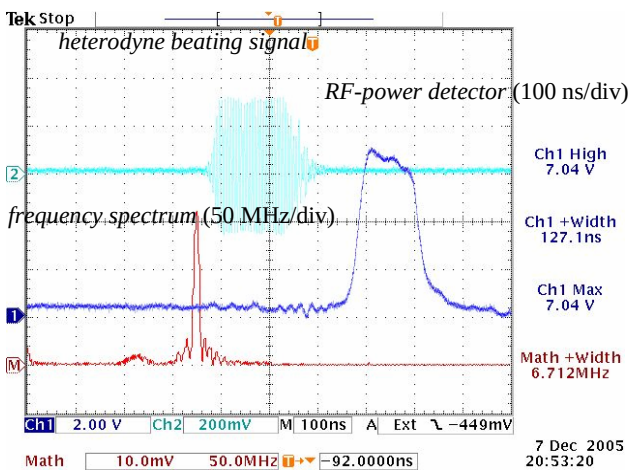

Figure 2: Typical oscilloscope traces of the RF-pulse generated by 30 GHz JINR-IAP FEM.

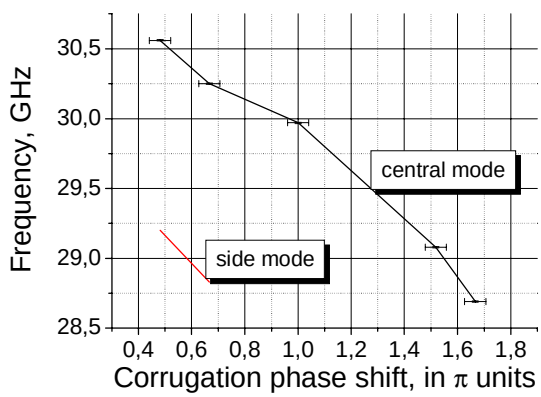

Figure 3: Measured dependence of the FEM oscillation frequency on the value of the phase shift of corrugation between the Bragg structures.

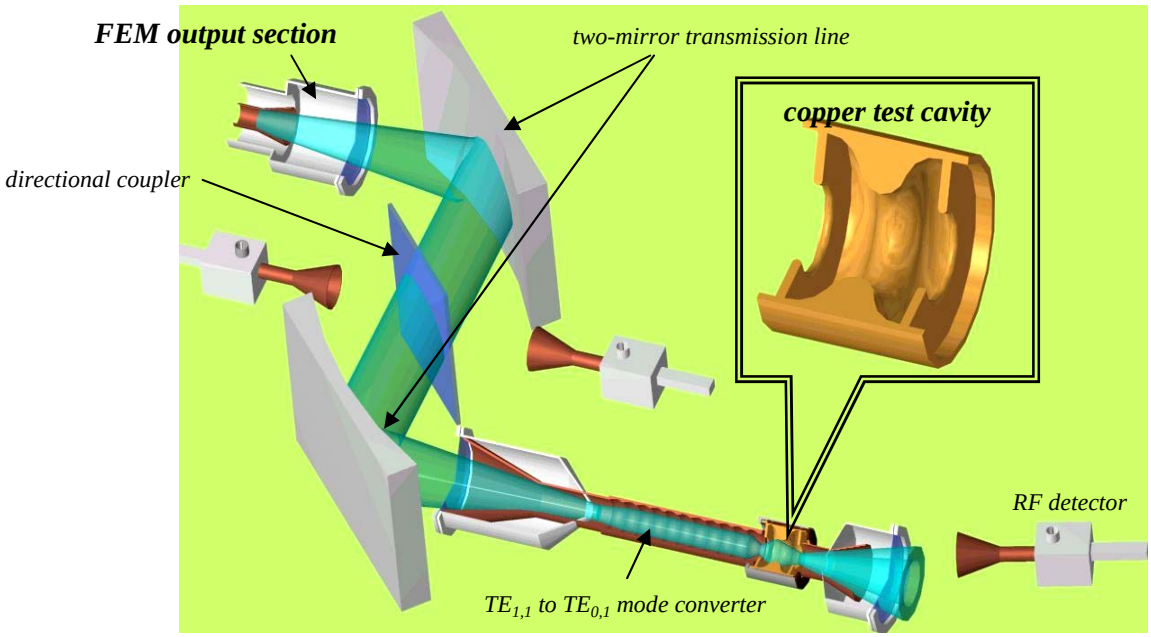

Figure 4: Schematic diagram of the test facility for studying surface heating effects based on JINR-IAP FEM.

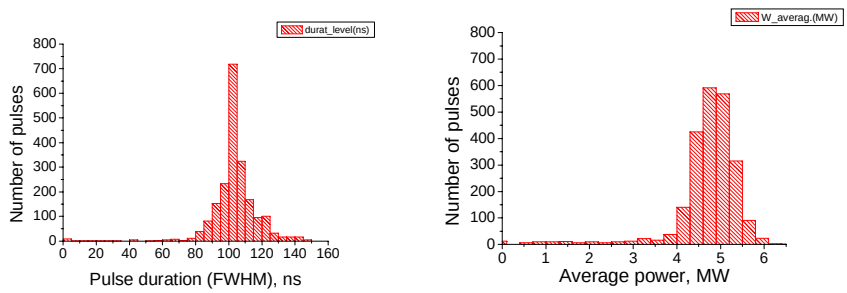

Figure 5: Statistic distributions of pulse duration and RF-power after the test cavity in the series of 10^4 pulses.

converters to transport the RF-power from the FEM to the test cavity. A special copper cavity operating with $TE_{0,1,1}$ mode and having Q-factor ~ 1500 was designed to model temperature regime in a high-Q accelerating structure of the CLIC project. The profile of the cavity surface was optimized to enhance the RF magnetic field in a certain zone and provide needed temperature rise during each RF-pulse. The resonant frequency of the cavities is also mechanically tuned to coincide with the frequency of the FEM source. A directional coupler is included to control both the incident and reflected powers. After a certain number of pulses the Q-factor of the cavity would be monitored using a network analyzer to detect early signs of surface damage. "Cold" tests of all components of the experimental set up were carried out and demonstrated good agreement with designed parameters.

Simulations carried out demonstrate principal ability of the FEM to be used for the aforementioned application. Results of the first experiments also proved possibility of the FEM to operate at the high-Q load. When frequency of the test-cavity was tuned to the FEM generation frequency it was observed that during the RF-pulse the reflected signal decreased and the test-cavity became transparent. As a result, accumulation of the RF-power in the load was achieved. At the present stage the effect of the copper surface degradation at 30 GHz was studied in the statistics of 10^5 pulses (Fig.5) at the temperature rise of 50 °C during each RF-pulse. The test cavity providing temperature rise at the certain zone up to 150 °C was designed and the experiments with the statistics of 10^6 pulses, which are important for design of CLIC collider components (CERN), are in progress currently.

REFERENCES

[1] A.Abramovich, M.Canter, A.Gover, e.a., Phys. Rev. Lett. 82 (1999) 5257.

[2] N.S.Ginzburg, A.K.Kaminsky, N.Yu.Peskov, e.a., Phys. Rev. Lett. 84 (2000) 3574.

[3] I.Wilson, CLIC Note 52, Oct. 1987.

[4] A.K.Kaminsky, A.V.Elzhov, I.N.Ivanov, e.a., Proc. of the 22nd Int. FEL Conf., Durham, USA, 2000, p.II-41.

A FEL AMPLIFIER BASED ON PLANAR BRAGG WAVEGUIDES*

Ginzburg N.S.#, Malkin A.M., Rozental R.M., IAP RAS, Nizhny Novgorod, Russia,
Dorfman K.E., Department of Physics, Texas A&M University, College Station, USA

Abstract

We study a new version of FEL amplifier on the base of wide sheet electron beams. We suggest using a transverse open Bragg structures which can provide radiation waveguiding with simultaneous effective mode selection (filtration). Theory of transverse current FEL amplifier based on planar Bragg waveguides is considered.

INTRODUCTION

A planar periodic Bragg structure can be used not only as resonant elements of FEL oscillators [1-3] but as selective waveguides in different new schemes of FEL amplifiers. Open Bragg waveguide where wave propagates in the direction transverse to the lattice vector (Fig.1) can provide high selectivity over the transverse coordinate when its size essentially exceeds wavelength. In a transverse current amplifier scheme it is beneficial to use a grating with a step of corrugation, which results in the existence of a single low dissipative mode located near defect. The sheet electron beam moves across the waveguide to be resonant to one of partial waves forming the operating mode. Another way is a traditional travelling wave amplifier scheme where electron beam moves along waveguide axis. To increase effective size of operating mode one ca use a structure with regular longitudinal corrugation that couples two partial waves propagating at some angle to the axis to the wave propagating directly along the axis. This wave, which in moving reference frame is transformed into a cut off mode, is excited by the electrons. Analysis shows rather high gain and efficiency of the novel schemes with simultaneous discrimination of parasitic modes.

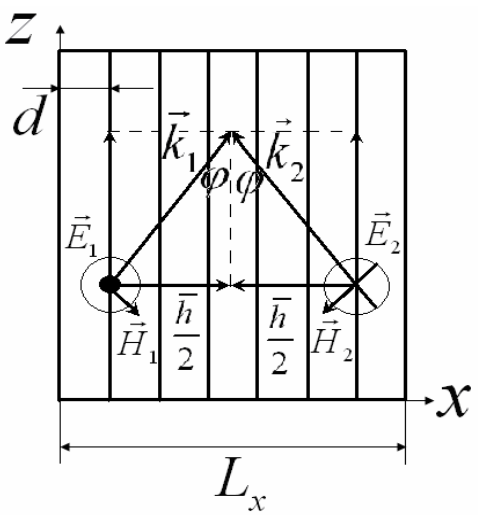

Figure 1: The diagram showing the coupling of waves on the Bragg lattice.

*Work supported by RFBR grants 06-02-17129-a and 05-02-17036-a and the Dynasty foundation.
#ginzburg@appl.sci-nnov.ru

This paper is organized as follows: in the Sect.1 we study wave propagation in the Bragg waveguide with a step of corrugation to find the mode spectrum of this structure. In the Sect.2 we investigate the model of the transverse current FEL amplifier. In Conclusion we briefly overview another scheme of Bragg amplifier based on coupling of some higher mode of the planar waveguide and two *TEM* modes.

EIGENMODES OF THE OPEN PLANAR BRAGG WAVEGUIDE WITH A STEP OF CORRUGATION

We consider a planar waveguide (Fig.4) with weakly corrugated walls

$$l = l_0 \cos(\bar{h}x) \qquad (1)$$

where $2\,l_0$ is the depth of corrugation. Assuming that lattice vector $\bar{h} = \frac{2\pi}{d}$, (d is the period of corrugation) is directed in x direction. The coupling exists for *TEM* waves with x- and z- wavenumbers satisfying Bragg resonance condition (see Fig.1)

$$h_{z1} = h_{z2} = h;\ h_{x1} = -h_{x2} = \bar{h}/2$$

We assume that the deflection of the waveguide surface $l(x)$ is much less than the wavelength λ and the corrugation period d: $l_0 << \lambda, d$. In this case perturbation of waveguide plates can be treated by using the equivalent surface magnetic current [4]. We seek the electric and magnetic fields as the linear combination of two TEM modes of a corresponding regular waveguide (Fig.5):

$$\vec{E} = \mathrm{Re}\left[\left(A_1(x,z)\vec{E}_1^{\,0}e^{i\frac{\bar{h}}{2}x} + A_2(x,z)\vec{E}_2^{\,0}e^{-i\frac{\bar{h}}{2}x}\right)\exp(i\omega t - ihz)\right],$$

$$\vec{H} = \mathrm{Re}\left[\left(A_1(x,z)\vec{H}_1^{\,0}e^{i\frac{\bar{h}}{2}x} + A_2(x,z)\vec{H}_2^{\,0}e^{-i\frac{\bar{h}}{2}x}\right)\exp(i\omega t - ihz)\right]$$

Slowly varying (in the wavelength scale) partial waves amplitudes, $A_{1,2}(x,z)$ satisfy the coupling equations:

$$\frac{h}{k}\frac{\partial A_{1,2}}{\partial z} \mp \frac{\bar{h}}{2k}\frac{\partial A_{1,2}}{\partial x} + i\alpha A_{2,1} = 0 \qquad (2)$$

where

$$\alpha = \frac{l_0}{4a_0}\frac{\bar{h}^2}{2k}$$

is the coupling parameter (a_0 is the distance between plates), $h = \sqrt{k^2 - (h/2)^2}, k = 2\pi/\lambda$. If we introduce an angle φ between the partial wave propagation directions ($\sin\varphi = \frac{\bar{h}}{2k}$), the coupling parameter can be represented as

$$\alpha = \frac{l}{4a_0}\bar{h}\sin\varphi \cdot$$

The maximum value of the coupling parameter takes place when the frequency tends to the cutoff frequency and the wave vectors of the two partial waves are counter directional $\left(\varphi = \frac{\pi}{2}\right)$. The coupling parameter and the angle φ tend to zero while the frequency shift from the cutoff increases. By seeking seek the solution of the eqs.(2) as $A_{1,2}\exp(igx + i\Gamma z)$, we have the dispersion equation for the unbounded grating

$$\left(\tfrac{\bar{h}}{2}g\right)^2 = (k\Gamma)^2 - (k\alpha)^2 \qquad (3)$$

where g and Γ are small amendment to the transverse and longitudinal wavenumbers $g << \bar{h}/2,\ \Gamma << h_0$.

The defect of corrugation in the middle of the waveguide can be entered as a $\pi/2$ phase step of the waveguide corrugation (1) which leads to the change of the sign of α in (2) at the point $x = L_x/2$:

$$\alpha = \alpha(x) = \begin{cases} +|\alpha|, & x < L_x/2 \\ -|\alpha|, & x > L_x/2 \end{cases}$$

Using the coupled waves equations (2) one can find the eigenmodes of an open in x direction planar Bragg waveguide with width L_x. In this case the boundary conditions for partial waves correspond to the absence of reflections and can be presented as follows:

$$A_1(0) = A_2(L_x) = 0 .$$

Taking (2) into account and using the fields continuity condition on the step of corrugation, the characteristic equation for the bounded grating can be presented in a form similar to the theory of Bragg resonators [2]:

$$\begin{aligned} 2\alpha^2 = &\left[\Gamma^2 - \Gamma\left(g\tfrac{\bar{h}}{2k}\right)\right]\exp(igL_x) + \\ &+\left[\Gamma^2 + \Gamma\left(g\tfrac{\bar{h}}{2k}\right)\right]\exp(-igL_x) \end{aligned} \qquad (4)$$

Equations (3),(4) can be solved approximately in the assumption of strong wave coupling ($\alpha L_x >> 1$). The spectrum of longitudinal wavenumbers consists of the single mode at the exact Bragg resonance ($\mathrm{Re}\,\Gamma = 0$) (which would be treated as "0"th mode):

$$\begin{cases} g_0 = \pm i\alpha\dfrac{2k}{\bar{h}} \\ \mathrm{Re}\,\Gamma_0 = 0 \\ \mathrm{Im}\,\Gamma_0 = -2\alpha\dfrac{k}{h}\exp\left(-\alpha\dfrac{2k}{\bar{h}}L_x\right) \end{cases} \qquad (5)$$

and a set of higher modes:

$$\begin{cases} g_N = 2\dfrac{\pi N}{L_x} - i2\dfrac{\pi N}{\alpha L_x^2}\dfrac{\bar{h}}{2k} \\ \mathrm{Re}\,\Gamma_N = \alpha\dfrac{k}{h}\dfrac{N}{|N|}\left(1 + 2\left(\dfrac{\pi N}{\alpha L_x}\dfrac{\bar{h}}{2k}\right)^2\right) \\ \mathrm{Im}\,\Gamma_N = -\alpha\dfrac{k}{h}4\dfrac{(\pi N)^2}{(\alpha L_x)^3}\left(\dfrac{\bar{h}}{2k}\right)^3 \end{cases} \qquad (6)$$

where $N = \pm1, \pm2, \pm3...$ are the mode numbers.

Fig. 2 demonstrates the dispersion diagrams for the different mode numbers and the diffraction losses curves via the frequency shift from the cutoff $\Omega = \frac{2k}{\bar{h}} - 1$.

It should be noted that expressions (5,6) diverge at $h \to 0$, while the frequency tends to the cutoff. These formally infinite diffraction losses appear when the applicability conditions of perturbation theory fail to fulfill. Nevertheless for practical use of Bragg waveguides it is interesting situation of rather large wave group velocities corresponding to large detuning of radiation frequency from the cutoff (Bragg frequency) where expressions (5),6) are non-divergent.

For $N>0$ the transverse structure of the N^{th} waveguide mode represents the distribution close to a standing wave with sine wave envelope having $|N|$ half-periods on the length L_x (Fig.3a), while the lowest mode distribution is localized near the defect and has the exponential transverse structure (Fig.3b).

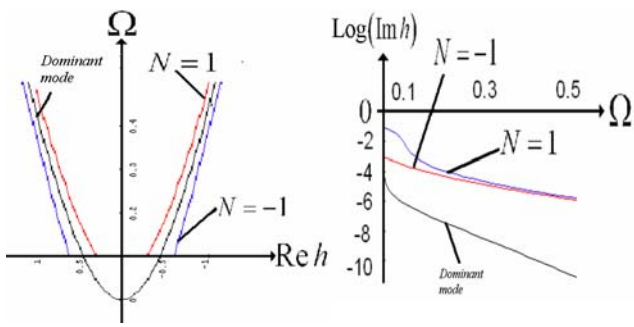

Figure 2: Dispersion diagrams for different mode numbers (left) and diffraction losses curves via the frequency shift (right).

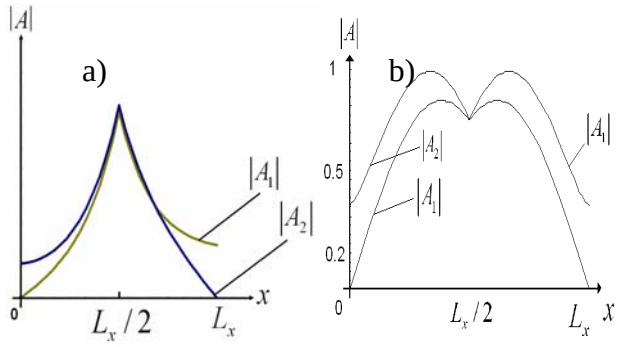

Figure 3: Transverse structure of modes with *N=0* (a) and *N=1* (b).

Diffraction losses of this mode ($\mathrm{Im}\,\Gamma$) are proportional to $\exp(-\left|2k\alpha L_x/\bar{h}\right|)$ and are very small at large L_x, while the high order modes have significantly greater decrements (they decrease as $1/L_x^3$) than the dominant mode decrement. Thus, such wide structures can be used for highly selective waveguiding.

TRANSVERSE CURRENT FEL AMPLIFIER

Transverse current amplifier schemes are well known in microwave electronics. In case of a rectilinear electron beams such type of interaction can be realized by means of oblique corrugation of slow wave structure [5]. In case of curves beams the synchronous interaction can be realized in smooth electrodynamical systems. One of the problems arising in such systems is distortion of the transverse field structure by the electron beam [6, 7]. This problem can be solved by means of using the open waveguides based on Bragg structures which provides high selectivity over the transverse mode index.

We consider a thin over the *y* coordinate sheet electron beam moving in the undulator field and in the uniform guiding magnet field $\vec{H}_0 = H_0\vec{\xi}_0$ (the directions of the coordinates and ξ are shown in the Fig.4). The beam is injected into the waveguide in the direction corresponding to the direction of propagation of the one of the coupled *TEM* waves in the waveguide described in the previous section and it is synchronous to this mode.

We consider the electron-wave interaction in the case of the undulator synchronism assuming the bounce frequency Ω is far from cyclotron synchronism with electrons:

$$\left|\omega - h v_{II} - \omega_H\right| T >> 2\pi, \quad \left|\Omega - \omega_H\right| T >> 2\pi,$$

where $\omega_{H0} = eH_0/m_0c\gamma_0$ is a cyclotron frequency, v_{II} is the longitudinal velocity of electrons, $\gamma_0 = \left(1 - v^2/c^2\right)^{-1/2}$ is relativistic factor, T is characteristic time of interaction. We also consider the ultra relativistic case $\gamma_0 >> 1$.

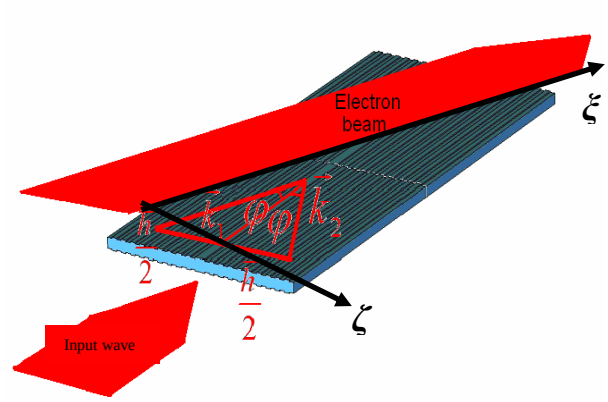

Figure 4: The scheme of a FEL amplifier with transverse current.

The process of monochromatic signal amplification in the transverse current FEL scheme can be described by the equations similar to the nonstationary equations of traditional FEL with 1D Bragg resonator [2] with time variable replaced by spatial one. These equations describe the formation of transverse structure of the fields together with their longitudinal structure

$$\begin{cases} \dfrac{h}{k}\dfrac{\partial a_1}{\partial \hat{z}} + \dfrac{\bar{h}}{2k}\dfrac{\partial a_1}{\partial \hat{x}} - i\delta a_1 + i\alpha a_2 = \dfrac{1}{\pi}\displaystyle\int_0^{2\pi} e^{-i\theta}d\theta_0 \\ \dfrac{h}{k}\dfrac{\partial a_2}{\partial \hat{z}} - \dfrac{\bar{h}}{2k}\dfrac{\partial a_2}{\partial \hat{x}} - i\delta a_2 + i\alpha a_1 = 0 \\ \left(\dfrac{h}{k}\dfrac{\partial}{\partial \hat{z}} + \dfrac{\bar{h}}{2k}\dfrac{\partial}{\partial \hat{x}}\right)^2 \theta = \mathrm{Re}\left(a_1 e^{i\theta}\right) \end{cases} \tag{7}$$

Here the normalizations, variables and parameters are defined as follows: $\hat{x}, \hat{z} = Ckx, Ckz$, $\hat{\alpha} = \alpha/(Ck)$, $a_{1,2} = eK\mu A_{1,2}/C^2$, θ is electron phase, C is Pierce parameter, μ is bunching parameter, K is electron-wave coupling parameter, δ is normalized synchronism detuning.

If the input signal is a *TEM* wave packet entering the system under the angle corresponding to the direction of propagation of the partial wave A_1, then the boundary conditions for (7) take the form

$$\begin{aligned} &\frac{d\theta}{dX}\Big|_{X=0} = 0,\ \theta\big|_{X=0} = \theta_0 \in [0, 2\pi), \\ &a_1\big|_{Z=0} = a_0,\ a_1\big|_{X=0} = 0,\ a_2\big|_{X=L_x} = 0 \end{aligned} \tag{8}$$

Results of direct numerical simulation of (7-8) are presented in Fig.5. In the Fig 5a the dependence of the amplification coefficient

$$\Gamma = \frac{\int_0^{L_x}\left(\left|A_1(X)\right|^2 + \left|A_2(X)\right|^2\right)dX}{\int_0^{L_x}\left|A_{0X}(X)\right|^2 dX}$$

on the longitudinal coordinate is depicted.

We can estimate the parameters of such system for an 8mm FEL basing that can be realized on the base of U2 high current accelerator at BINP RAS, Novosibirsk (width of the beam is ~150 cm, energy of electrons 1 MeV, $\gamma_0 = 3$, current density $j_0 = 1kA/cm$). We

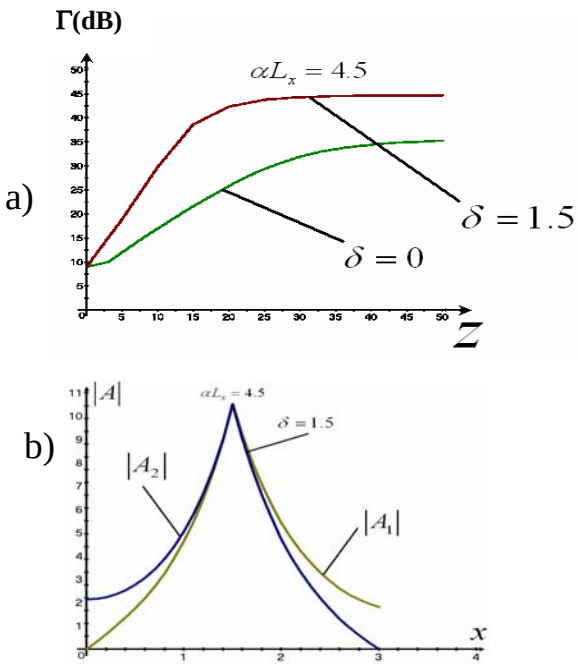

Figure 5: a) Dependence of the gain on the longitudinal coordinate, b) transverse structure of the fields.

assume the undulator period $d_u = 8cm$, undulator field amplitude $H_u = 2kOe$, guiding magnetic field $H_0 = 10kOe$, $a_0 = 1cm$ (the Pierce parameter is $C = 0.01$). At the following parameters of Bragg waveguide $l_0 = 0.4mm$, $d = 1mm$, $L_x = 50cm$, $L_z = 160cm$, $\varphi = 18^0$ one can get the gain up to 40 dB.

CONCLUSION

Another variant of using of an open Bragg structure for provision of higher selectivity in a FEL amplifier can be based on coupling between two TEM waves $A_\pm$ propagating at some angle to the axis and the wave *B* with a higher *y*-index propagating directly along the system axis. The latter wave is synchronous to the beam propagating directly along the axis, while the former waves provide the synchronization of radiation over the *x* coordinate. The coupling is provided by the regular corrugation with the following Bragg resonance conditions $\bar{h} = 2h_x$, where h_x is the transverse wavenumber of *TEM* modes. This interaction is described by the following equations.

$$\frac{\partial A_\pm}{\partial Z} \pm \frac{\partial A_\pm}{\partial X} = i\alpha B$$

$$\frac{\partial B}{\partial Z} + \frac{i}{2}\frac{\partial^2 B}{\partial Z^2} = -i\alpha(A_+ + A_-) + J$$

These equations are similar to those describing the excitation of the FEL oscillator based on coupling of the propagating and the trapped waves (see [10]) with excitation factor removed into the equations for the higher mode. Preliminary estimations show that in this case multiplication coefficient also should be rather high.

It should be noted in conclusion that the considered in section 1 system with defect of periodicity can be treated as a simple realization of photonic bandgap structures [8, 9]. Advantage of these Bragg waveguides is their compatibility with powerful sheet electron beam transportation system.

REFERENCES

[1] A. Yariv, Introduction to optical electronics (1976)

[2] V.L. Bratman , G.G. Denisov, N.S. Ginzburg, M.I. Petelin IEEE J. of Quant. Electr., v.9 E-19, N3, p.282 (1983)

[3] N.S. Ginzburg, A.S. Sergeev, N.Yu. Peskov, et al., IEEE Transactons on Plasma Science, Vol. 24, No. 3, pp. 770-780. (1996)

[4] N.F. Kovalev, I.M. Orlova, M.I. Petelin, Izv.Vuzov Radiofizika Vol.11 N.5 1968, p. 783.

[5] D.A.Dann, W.A.Harman, L.M.Field, G.S.Kino, Proc. IRE, 1956, p.879.

[6] Zhurahovsky A.V., Radiotehnika i electronika, 1969, p.8 (in Russian)

[7] Bykov Yu.V., Gaponov A.V., Petelin M.I., Izv. Vuzov Radiofizika, 1974, p.1219 (in Russian).

[8] R.J. Temkin, J.R. Sirigiri, K.E. Kreischer, et al., Phys. Rev. Lett., Vol. 86, p.5628 (2001)

[9] E. Yablonovitch, T.J.Gmitter, and K.M. Leung, Phys. Rev. Lett. Vol. 67, p.2295 (1991)

[10] N.S.Ginzburg, A.M.Malkin, N.Yu.Peskov, et al., Phys. Rev. ST Accel. Beams 8, 040705 (2005)

GENERATION OF NARROW BAND SHORT MM WAVE SUPERRADIANCE PULSES IN A NON-UNIFORM PLANAR WAVEGUIDE*

N. Ginzburg, R. Rozental#, A. Sergeev, I. Zotova, IAP RAS, N. Novgorod, Russia.

Abstract

A method for suppressing of spurious transverse modes excitation in the process of supperradiance from intense electron bunch is described. Such method based on the use of the waveguide with variable geometry (in the case of planar waveguide it is distance between plates). In such waveguide phase velocities of the different modes varied over longitudinal coordinate. For given waveguide profile variations are increased with increasing transverse mode indexes. As a result modes with large Brillouin angles (including near cut-off modes) which are responsible for low frequency radiation suppress more effectively than modes with small Brillouin angles. For the case of planar geometry this effect demonstrated both in the frame of the averaged equations and the full PIC-simulations.

INTRODUCTION

Recently significant progress was achieved in production of ultrashort pulses in millimeter wave band based on supperradiance from intense electron bunch [1-3]. One of the problems for advance generators based on such mechanisms in shorter (first of all sub-mm) wave bands is the spectrum broadening caused by the simultaneous excitation by an electron bunch several waveguide modes in oversized waveguide. For example at the fig.1 the dispersion diagram of the 1 MeV electron beam propagating through the planar waveguide with 1 cm gap is shown. Electron beam interacts simultaneously with three propagating modes (the interaction at the cut-off frequency with the TE_1 mode could be neglected): with TE_2 mode at the frequency of about 50 GHz, with TE_1 mode at the frequency of about 150 GHz and with the fundamental TEM mode at the frequency of about 200 GHz.

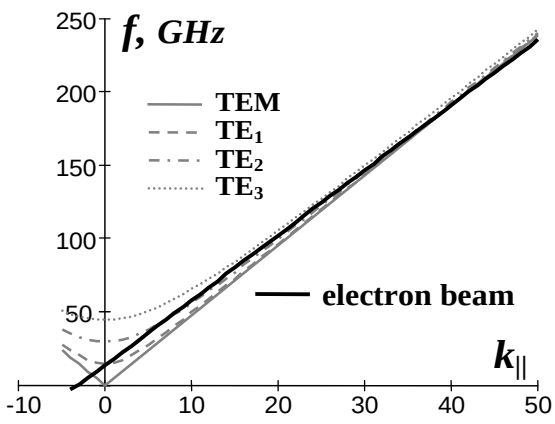

Figure 1: Dispersion diagram of the 1 MeV electron beam and planar waveguide with 1 cm gap.

*Work supported by Russian Fund for Fundamental Researches, grant 05-02-17553

#rrz@appl.sci-nnov.ru

To suppress spurious interaction we suggest using the non-uniform waveguide with tapered radius (cylindrical geometry) or distance between plates (planar geometry). In such a waveguide the phase velocities of the different modes varied over longitudinal coordinate. For given waveguide profile variations are increased with increasing transverse mode indexes. As a result modes with large Brillouin angles (including near cut-off modes) which are responsible for low frequency radiation suppress more effectively than modes with small Brillouin angles. In planar waveguide situation is even more preferable because phase velocity of fundamental TEM mode is totally independent on the distance between plates.

BASIC MODEL

Let us assume, that a sheet electron beam with initial velocity $\vec{v}_0 = v_0\vec{z}$ passes through a planar undulator with period *d* and homogeneous magnetic field with strength $\vec{H}_0$ in a planar waveguide with gap between plates *b* (Fig.2). We also assume that the system is infinite over the *y*-axis and the electron beam excites the TE_n-mode of a planar waveguide with *n* variations over the transverse coordinate *x*. Vector-potentials of the periodic undulator field (subscript *u*) and operating mode (subscript *s*) may be presented as

$$\vec{A}_u = \mathrm{Re}\{A_u ch(k_u x)\exp(ik_u z)\vec{y}\},$$
$$\vec{A}_s = \mathrm{Re}\{A_s(x,z)\exp(i\omega t - ik_\| z)\vec{x}\}$$

where $A_s(x,z)$ is the slowly-varying amplitude of the synchronous wave, $k_u = 2\pi/d$. The reference frequency ω was chosen to be the frequency at exact undulator synchronism $\omega - k_\| v_\| \approx \Omega$, where $k_\|^2 = k^2 - k_\perp^2$, $k = \omega/c$, $k_\perp = n\pi/b$, $\Omega = k_u v_\|$ is the bounce-frequency.

Using the independent variables

$$\zeta = \frac{kCZ}{\beta_\|^3\gamma_0^2},\ \tau = \frac{kC(t - z/v_\|)}{\beta_\|^3\gamma_0^2(1/v_\| - 1/v_{gr})}$$

superradiance process can be described by the following equations:

$$\frac{\partial a}{\partial\zeta} + \frac{\partial a}{\partial\tau} = f(\tau)\int_0^{2\pi} e^{-i\theta}d\theta_0$$
$$\frac{\partial u}{\partial\zeta} = \mathrm{Re}\{ae^{i\theta}\} \quad \frac{\partial\theta}{\partial\zeta} = u - \Delta \qquad (1)$$

with the boundary conditions

$$a|_{\tau=0} = a_0,\ a|_{\zeta=0} = 0,\ u|_{\zeta=0} = 0,$$
$$\theta|_{\zeta=0} = \theta_0 + r\cos(\theta_0),\ \theta_0 \in [0,2\pi)$$

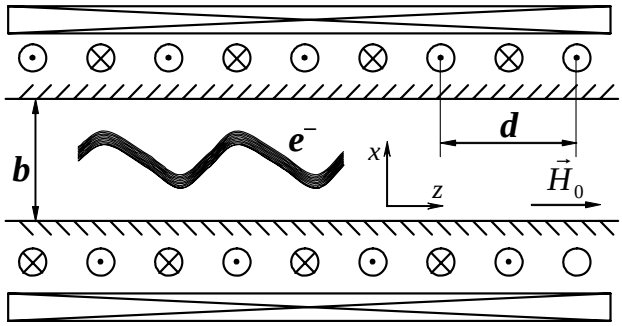

Figure 2: Scheme of the basic model.

The following dimensionless variables have been used:

$$a = \frac{eA_s}{2mc^2}\frac{eA_u}{2mc^2}\frac{\beta_\parallel^3 k_u c}{C^2}\left(\frac{1}{\Omega-\omega_H}-\frac{1}{\Omega+\omega_H}\right)$$

is the wave amplitude, $\theta = \omega t - (k_\parallel + k_u)z$ is the electron phase with the respect to the synchronous wave, $u = C^{-1}(1-\gamma/\gamma_0)$ is the relative electron energy,

$$C = \frac{eI}{mc^3}\frac{c\gamma_0}{4\pi N_s}\left[\frac{eA_u}{2mc^2}\beta_\parallel^3 k_u c\left(\frac{1}{\Omega-\omega_H}-\frac{1}{\Omega+\omega_H}\right)\right]^2$$

is the Pierce parameter, ω_H is the cyclotron frequency, I is the electron beam current, N_s is the norm of the operating wave,

$$\Delta = \frac{\beta_\parallel^3\gamma_0^2}{C}\left(\frac{k_\parallel + k_u}{k}-\frac{1}{\beta_\parallel}\right)$$

is the mismatch from the undulator synchronism, $f(\tau)=1$, $\tau\in[0,T]$, where T is the normalized duration of the electron bunch.

Let is consider the influence of the variation of the mismatch of the undulator synchronism over the longitudinal coordinate on the superradiance process. We choose the simplest linear dependence: $\Delta(\zeta)=\Delta_0\,\zeta/L-\Delta_0$. Fig.3 demonstrates the results of the simulation of Eqs. (1) for $L=T=30$ in the case of non-dispersive wave ($\Delta_0=0$, which corresponds to excitation TEM mode) and wave with dispersion ($\Delta_0=-1$, which corresponds to excitation TE_1 mode). In the first case we see formation of powerful superradaince spike. In the second case output radiation is practically suppressed.

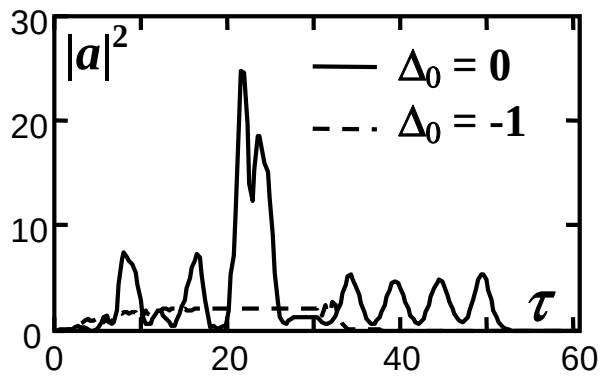

Figure 3: Simulation of averaged equations: output signal in case of uniform ($\Delta_0 = 0$) and non-uniform waveguide ($\Delta_0 = -1$).

PIC-SIMULATIONS

The 2-D version of the PIC-code KARAT was used for additional simulations. The 110 cm length planar waveguide was excited by the 1 MeV, 100 A/cm, 600 ps electron bunch which was transported through the periodic undulator with period 2 cm and 2 kOe strength and guiding magnetic field with strength of 22 kOe (Fig.4a). For regular waveguide simulation showed that the spectrum of the output signal includes three main frequencies (Fig.4c), which correspond to the simultaneous excitation of the TEM, TE_1 and TE_2 modes.

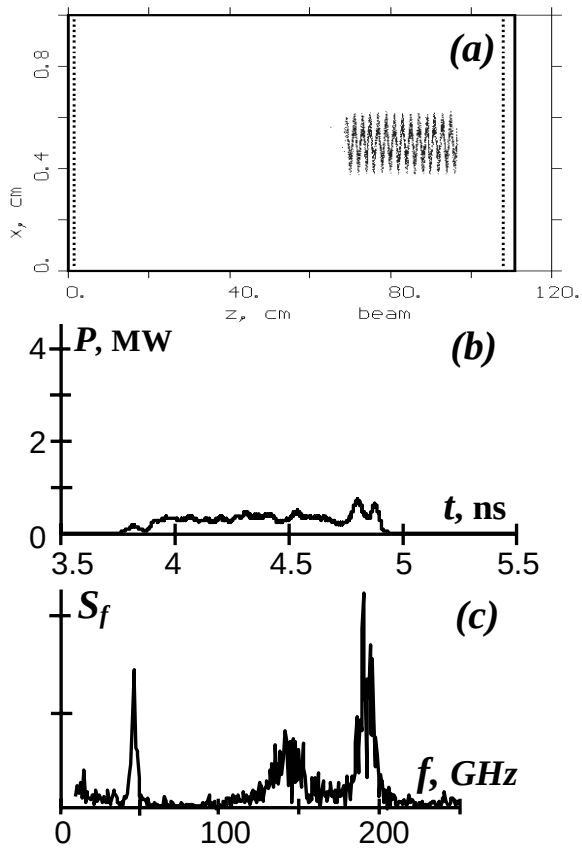

Figure 4: PIC-simulations of superradiance in the uniform oversized waveguide: *(a)* is the geometry of interaction space (solid lines denotes the ideal conductor, dash lines marked the boundary of the microwave absorption layers); *(b)* is the output signal and *(c)* is the spectrum of output radiation.

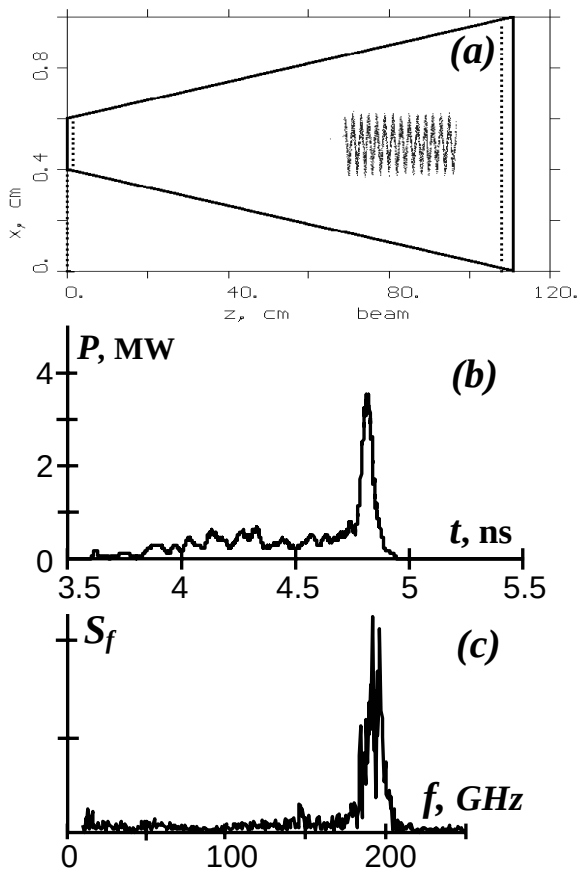

Figure 5: PIC-simulations of superradiance in the uniform oversized waveguide: *(a)* is the geometry of interaction space; *(b)* is the output signal and *(c)* is the spectrum of output radiation.

Fig.5 demonstrated the results of simulation of superradiance in the waveguide with linearly increased gap between plates from 0.2 to 1 cm (fig.5a). In this case all spurious modes were suppressed and the output radiation includes one powerful spike (fig.5b). As a result the spectrum of output radiation is concentrated near the operating frequency of 200 GHz corresponding to excitation fundamental TEM mode (fig.5c).

CONCLUSION

A method of suppressing excitation of spurious modes in the process of supperradiance from intense electron bunch in the planar oversized waveguide is considered. The simulations of the averaged equations and PIC-simulations were carried out and it was shown that in the planar waveguide with linearly increasing gap between plates the SR pulse associated with excitation of single transverse mode could be obtained.

REFERENCES

[1] Ginzburg N.S, et al., Nucl.Instr.Meth.Phys.Res., 1999, A429(1), 94.

[2] N.S.Ginzburg, et al., Opt.Comm., 2000, 175(1-3), 139.

[3] A.G.Reutova, et al. , JETP Lett., 2005, 82(5), 263.

GENERATION OF SUPERRADIANT PULSES BY BACKSCATTERING OF PUMPING WAVE ON THE INTENSE ELECTRON BUNCH*

V. Belousov, G. Denisov, N. Ginzburg, A. Sergeev, I. Zotova#, IAP RAS, N.Novgorod, Russia
A. Reutova, M. Ulmaskulov, A. Sharypov, V. Shpak, S. Shunailov, M. Yalandin, IEP RAS, Ekaterinburg, Russia.

Abstract

At the first time the generation of superradiance pulses in the process of stimulated backscattering of powerful pump wave by intense electron bunch (250 keV, 1 кA, 600 ps) has been observed experimentally. Using a relativistic 38 GHz BWO as a pump wave source, the short 200 ps superradiance pulses of scattered radiation with peak power ~1 MW were obtained. Due to the Doppler up-shift, in the spectrum of scattered radiation high frequency 150 GHz component was presented

INTRODUCTION

Recently a significant progress was achieved in the generation of subnanosecond pulses in the millimeter and centimeter wave bands utilizing the cyclotron and Cherenkov mechanisms of superradiance (SR) of electron bunches [1-3]. The maximal peak power in the case of Cherenkov SR exceeded gigawatt level [3]. This paper is devoted to the novel mechanism of superradiance in the case of the stimulated backscattering of powerful pump wave by intense electron bunch. In this situation, due to the Doppler up-shift effect the radiation frequency can significantly exceed the frequency of the pump wave:

$$\omega_s = \omega_i \frac{1+V_{||}/V_{ph.i}}{1-V_{||}/V_{ph.s}}, \qquad (1)$$

where $V_{||}$ is the translational electron velocity, $V_{ph.i,s}$ are the phase velocities of the pump wave (index *i*) and the scattered wave (index *s*). If the radiation of powerful laser undergoes backscattering at the electron beam with energy about 1-2 MeV the frequency of scattered radiation will belong to ultraviolet band. In the case when the pump wave is generated by relativistic microwave generator (for example BWO) it is possible to produce radiation at the short millimeter and submillimeter wave bands. In this paper we present a basic theoretical description of the superradiance regime of stimulated backscattering. The results of theoretical consideration are confirmed by the first experimental observation of above SR mechanism.

BASIC MODEL

Let us consider the backscattering of the powerful pump wave by the hollow electron bunch with injection radius R_b and duration Δt_b that moves through a cylindrical waveguide with radius *R* along homogeneous guiding magnetic field $\mathbf{H_0} = H_0\mathbf{z_0}$. Under assumption of the fixed pump wave amplitude, the generation of short single pulse of scattered radiation (SR pulse) can be described by the nonstationary equation for scattering signal amplitude A_s and the averaged equations for electrons' motion in the field of combination wave:

$$\frac{\partial a_s}{\partial\zeta}+\frac{\partial a_s}{\partial\tau}=if(\tau)a_i g\frac{I}{\pi}\int_0^{2\pi}e^{-i\theta}d\theta_0$$
$$\frac{\partial^2\theta}{\partial\zeta^2}=\mu\,Im\left\{a_s a_i\, g e^{-i\theta}\right\} \qquad (2)$$

Here $\zeta=\omega_c z/c$, $\tau=\omega_c c\left(t-z/V_{||}\right)\left(1/V_{gr}-1/V_{||}\right)^{-1}$, $a_{i,s}=eA_{i,s}/2m_0\gamma c^2$ are the dimensionless amplitudes of pump and scattered waves, $\theta=\omega_c t-k_c z$ is the electrons phase with respect to the combination wave, $\omega_c=\omega_s-\omega_i$, $k_c=h_s+h_i$, $h_{i,s}$ are the longitudinal pump and scattered wave numbers, $\mu=\gamma_0^{-2}\beta_{||}^{-3}$, $I=\left(eJ_0/mc^3\right)\cdot\left(2\gamma_0 h_s k_c R^2 N_s\right)^{-1}$, J_0 is the electron current, N_S is the norm of the scattered wave. Factor

$$g=J_{n_i-1}\left(k_{\perp i}R_b\right)J_{n_s-1}\left(k_{\perp s}R_b\right)\Omega/\left(\Omega-\omega_H\right) \qquad (3)$$

describes the increase of oscillation velocity of electrons near the cyclotron resonance, $\omega_H=eH_0/m_0c\gamma_0$ is the gyrofrequency, $\Omega=\omega_i+h_iV_{||}$ is the bounce frequency, $k_{\perp i,s}$ is the transverse wave number, $J_n(x)$ is the Bessel function, $n_{i,s}$ are the azimuth indices of the waveguide modes. Function $f(\tau)$ defines the profile of electron current with normalized duration $\tau_b=\Delta t_b\omega_c c\left(1/V_{gr}-1/V_{||}\right)^{-1}$.

Equations (2) describe the joint combinational action of the pump and the scattered waves on the electrons. Such an action leads to selfbunching that starts from small initial density perturbations. As a result the amplitude of scattered wave grows. In the absence of external feedback the synchronization of radiation from different parts of extended electron bunch is provided by slippage of the scattered wave with respect to electrons due to a difference between the electron velocity and the electromagnetic wave group velocity. As a result the scattered wave radiates in the form of a single short pulse, as is shown in Fig.1. The parameters of simulation are chosen in accordance with the performed experiment. The pump wave with 100 MW power and 38 GHz frequency has the transverse structure of the TE_{11} mode. This wave

*Work supported by Russian Fund for Fundamental Researches, grant 05-02-17553
#zotova@appl.sci-nnov.ru

undergoes the backscattering by the 250 keV, 1 kA, 200 ps electron bunch guided in 24 kG magnetic field. According to the simulation the duration of the scattered SR pulse is about 50 ps with peak power ~25 MW. According to waveguide dispersion the scattered wave frequency should be about 150 GHz.

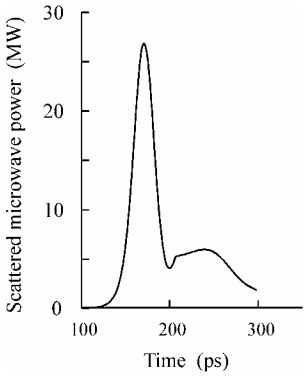

Figure 1: Superradiance pulse of scattered radiation.

KARAT PIC-CODE SIMULATIONS

The possibility of the observation SR in the process of backscattering has been tested also using the particle-in-cell (PIC) code KARAT. In simulation we used the simplified two-dimensional axial symmetric model of the scattering. The pump wave with frequency 38 GHz and power 100 MW represents the TE_{01} wave in contrast to the experimental situation. The guiding magnetic field was 28 kG.

As it is seen from Fig.2 scattered radiation has the form of the short pulse with the duration less than 100-200 ps and peak power about 3 MW. The radiation spectrum has a component with frequency about 150 GHz. Nevertheless the spectrum of radiation is rather wide. It may be explained by the dispersion of electron velocities as well as by excitation of several waveguide modes. Above factors also may result to the reduction of the peak power in comparison with the model described above.

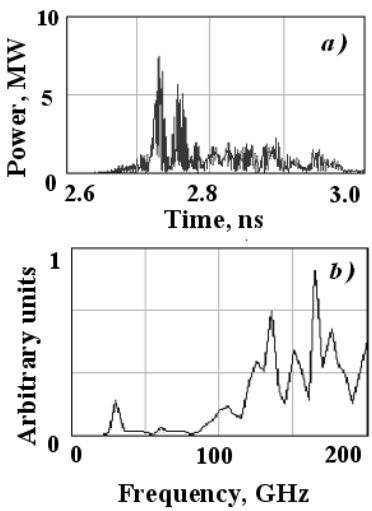

Figure 2: Results of KARAT PIC code simulations: (a) scattered SR pulse, (b) spectrum of SR pulse

EXPERIMENTAL SET-UP

Experiments on the observation of the stimulated backscattering in the superradiance regime were carried out at Institute of Electrophysics (Ekaterinburg, Russia) based on two synchronized nanosecond and subnanosecond high-current RADAN-303 accelerators [4-5]. The 4 ns electron beam from the first accelerator was used to drive the low frequency pump wave generator. The pump wave undergoes backscattering with frequency up-conversion on the subnanosecond electron bunch produced by the second accelerator. The general view of experimental set-up is shown in Fig.3.

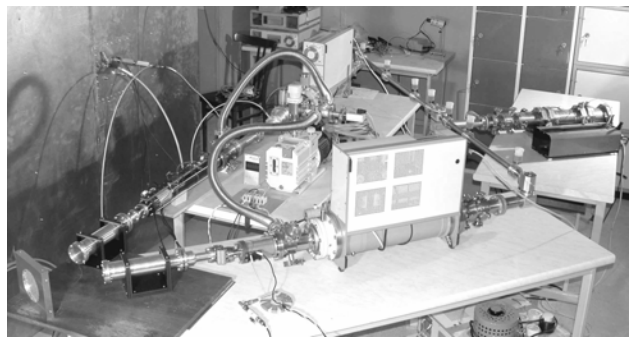

Figure 3: Experimental set-up

In experiments the pump wave was generated by relativistic BWO with operating frequency 38 GHz. For transmission of the pump wave to the scattering section a specially designed quasioptical mirror has been used. The mirror possessed the high reflectivity 95% at the pump wave frequency 38 GHz. The partial transparency of the mirror for the scattered radiation at frequencies above 60 GHz was provided by the mesh of holes with diameter of 3 mm having a step of 4 mm.

EXPERIMENTAL RESULTS

Oscilloscope trace of the 4 ns, 100 MW pump wave pulse with duration is shown in Fig.4a. In absence of subnanosecond electron bunch, the signal from BWO registered by detector installed after quasioptical mirror is shown in Fig.4b. This signal is caused by parasitic high-frequency radiation from the pump wave generator at the harmonics of operating frequency. Presence of such harmonics in a spectrum of the pump wave is confirmed by the direct simulation based on PIC-code KARAT.

In the scattering section with 30 cm length the low frequency pump wave underwent stimulated backscattering by the high current relativistic subnanosecond bunch (250 keV, 1 κA, 600 ps). It is important to note that in absence of the pump wave the background noise radiation of electron bunch was below the threshold sensitivity of a microwave detector. When the pump wave generator was switched on, the short powerful pulse could be observed, as is shown in Fig.4c. This pulse has rather short duration (about 200 ps) and can be interpreted as a superradiance pulse. SR pulses were observed in a large area of magnetic field detuning.

The maximal peak power was obtained for field strength 20-25 kG when the magnetic field strongly affects the amplitude of electron oscillations.

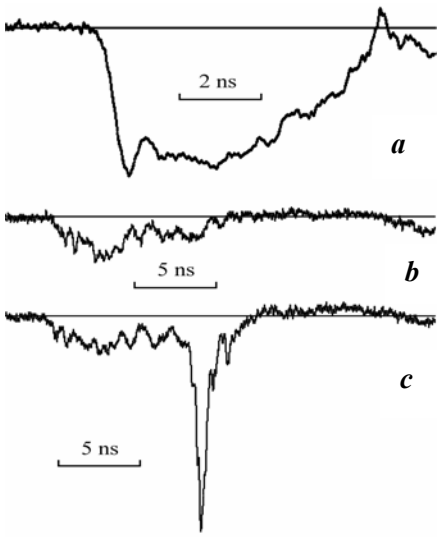

Figure 4: (a) Pulse of the pump wave. (b) High frequency component of BWO radiation in the absence of electron e-bunch registered by detector after quasioptical mirror. (c) Superradiance pulse caused by backscattering of pump wave by electron bunch.

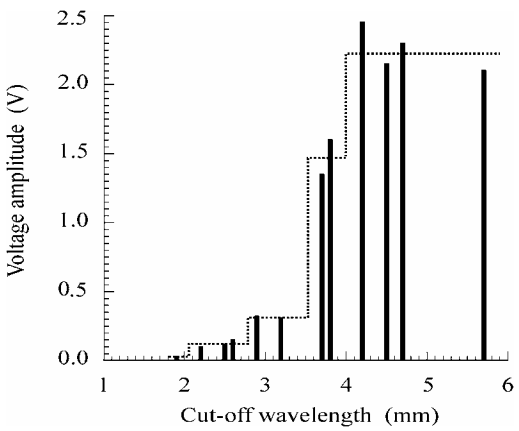

Figure 5: Spectrum measurements. Relative amplitudes of detector signal after filters with different cut-off frequencies.

To analyze the radiation spectrum a set of cut-off waveguides was used. Amplitudes of detector signals after filters with different cut-off frequencies are shown in Fig.5. Locations of vertical lines correspond to the cut-off wavelengths of different filters and the lengths of lines are proportional to the signals registered by the detector. Obviously the jumps of dashed line characterize the content of different spectrum components in the scattered radiation. The main components of radiation concentrate at the interval within wavelength $3.5 \div 4.2$ mm. But at the same time there are high frequency components with wavelength around 2 mm, which is rather close to the calculated one. However it should be noted that detector sensitivity decreases with frequency. So the real fall of intensity of high frequency components should be less than detector indications shown in Fig.4. A rather wide spectrum of scattered radiation can be explained by the spread of electron velocities in the real electron bunch as well as by excitation of several waveguide modes. Integral (over frequency spectrum) peak power of SR pulse amounts up to 1 MW. It was estimated basing on the power level indicated by microwave detector taking into account the aperture of the reception antenna, the distance from a radiator and the width of the radiation pattern.

CONCLUSION

As a result of the experiments the effect of generation of short electromagnetic pulses was observed in the process of stimulated backscattering of the powerful pump wave by the intense electron bunch. Scattered radiation had the form of ultrashort pulse with peak power of 1 MW and duration of 200 ps. Due to the Doppler frequency up-conversion the spectrum of scattered radiation included the frequencies up to 150 GHz that exceeded the pump wave frequency in several times. This process can be interpreted as a superradiance of electron bunch since the radiation of the short pulse occurs in the absence of external high frequency signal and in the absence of external cavity and correspondingly cannot be attributed to traditional amplification or oscillation regimes. Due to the development of selfbunching inside the extended electron bunch the peak power of scattered signal significantly exceeds the power of the spontaneous radiation of electrons in the pump wave and the duration of scattered pulse was essentially shorter than the duration of the background noise.

REFERENCES

[1] N. Ginzburg, I. Zotova, A. Sergeev, I. Konoplev, A. Phelps, A. Cross, S. Cook, V. Shpak, M. Yalandin, S. Shunailov and M. Ulmaskulov, Phys. Rev. Letters, 78(12) (1997) 2365.

[2] N. Ginzburg, Yu. Novozhilova, I. Zotova, A. Sergeev, N. Peskov, A. Phelps, A. Cross, V. Shpak, M. Yalandin, S. Shunailov and M. Ulmaskulov, Phys.Rev.E, 60(3) (1999) 3297.

[3] S. Korovin, G. Mesyats, V. Rostov, M. Ulmaskulov, K. Sharypov, V. Shpak, S. Shunailov and M. Yalandin, Technical Phys. Lett., 30 (2) (2004) 117.

[4] V. Shpak, S. Shunailov., M. Ulmasculov and M. Yalandin In Digest of the 12th IEEE Int. Pulsed Power Conf., USA,1999, 2, 1472

[5] G. Mesyats, S. Korovin, V. Rostov, V. Shpak and M. Yalandin. Proc. of the IEEE, 92 (7) (2004) 1166.

OPTIMIZATION OF THE INJECTION SYSTEM FOR MICROTRON-BASED TERAHERTZ FEL*

Grigory M. Kazakevich#, Viatcheslav M. Pavlov##, Gennady I. Kuznetsov, BINP, Novosibirsk, 630090, Russia,
Young Uk Jeong, Seong Hee Park, and Byung Cheol Lee, KAERI, Taejon, 305-600, South Korea.

Abstract

A compact widely-tunable microtron-based terahertz Free Electron Laser (FEL) has been developed and during last few years operates for users. The laboratory-size, stable facility at the macro-pulse power of tens of W is attractive for application in research laboratories and universities. Reliability in operation and stability of such microtron-based FEL is determined generally by the microtron injection system. Main parameters of the injection system were studied on the base of 2-D tracking considering the frequency drift of the accelerating cavity as a result of variation of the beam loading caused by cathode overheating due to back bombardment with non-resonance electrons. The obtained results show that the injection system based on a thermionic single crystal LaB_6 2.5 mm-in diameter emitter provides operation of the microtron-based FEL with standard deviation of the macro-pulse lasing power less than 10% during long-time work. Experimental check of the FEL during more than five years confirmed stable and reliable operation of the microtron-based FEL with the macro-pulse power of tens of W in the terahertz range.

INTRODUCTION

The injection system of the accelerator intended to drive the terahertz FEL has to provide a suitable bunch current with appropriate transverse parameters of the beam. The qualities are well matched in the system using the classical high-current microtron with an internal injection. In this case the acceleration starts in a high-gradient electric field that allows getting small beam emittance; the multi-turn motion of the electrons through the accelerating gap in the cavity provides good bunching of the beam. Worth to note that such system is simple and inexpensive in manufacturing but some drift of the beam loading during the macro-pulse is inherent to the system. The drift makes worse the intrapulse bunch repetition rate stability and the FEL operation as well because of the effective fluctuation of the FEL optical resonator length, detuning the resonator. The primordial source of the drift is a pulse overheating of the cathode emitting surface caused by back-streaming electrons.

*Work was supported in frames of the BINP-KAERI scientific collaboration and with Korea Research Foundation Grant (KRF-2004-042-C00053)
Corresponding author. Current affiliation:
FNAL, Batavia, IL 60510, U.S.A.
E-mail: gkazakevitch@yahoo.com (G.M. Kazakevich)
Current affiliation: University of Strathclyde, Glasgow, G4 0NG, UK.

To minimize the effect we optimized design and parameters of the microtron injecting system to operate with minimal acceptable cathode diameter. In this case the simplest and cheapest RF system employing the magnetron generator stabilized through the backward wave reflected from the accelerating cavity provides stable operation of the widely-tunable terahertz FEL based on the classical S-band microtron, [1]. For the optimization we calculated the accelerating cavity frequency drift caused by intrapulse variation of the beam loading as a function of the cathode diameter. The calculation was done for I-type injection, [2], basing on 2-D tracking in the microtron median plane. Comparison of the calculation with measured detuning curves of the FEL optical resonator showed that a single crystal LaB_6 emitter with diameter of 2.5 mm at a minimal acceptable detuning of the magnetron and the accelerating cavity can provide operation of the widely-tunable terahertz FEL with radiated macro-pulse power tens of W at a suitable stability and life time. Operation of the terahertz FEL during more than five years demonstrates that the optimized microtron injection system employing the thermionic cathode operating at the temperature of 1900^0 K at the strength of the electric field of > 10 MV/m provides reliable operation of the terahertz FEL. Results of simulations and measurements are presented and discussed in the article.

ANALYSIS OF THE EMISSION CURRENT IN THE MICROTRON WITH INTERNAL INJECTION

At operation of the high-current microtron with the internal injection the main part of electrons is emitted in non-resonance phases. The electrons could not reach the extracting channel, but they are participating in the process of acceleration and mainly hitting the cavity walls; a number of them hit the emitting surface making the back bombardment of the cathode. As was shown in [3], the back bombardment results in the pulse overheating of the emitting surface. This causes an additional emission including emission in resonance phases, thus the electron beam loading the cavity becomes increasing in time domain due to enhancement of number of synchronous electrons and non- synchronous as well.

To consider the effect of the back-streaming electrons hitting the cathode and increasing because of that the loading of the accelerating cavity we calculated the cathode overheats using 1-D analytic expression of the heat conduction along the emitter axis, [4]:

$$\Delta T^0(t_m) = \frac{P_{bs0}}{\pi \cdot r_C^2} \cdot \frac{1}{k_C} \cdot \sqrt{\frac{4\chi \cdot t_m}{\pi}}, \qquad (1)$$

where: k_C is thermal conductivity, χ is thermal diffusivity coefficient, r_C is the cathode radius, and t_m is the pulse duration of the emission current in the microtron. The average power of the electrons heating the emitter per the RF period, $P_{bs}(T)$, was calculated using expression:

$$P_{bs}(T) = \frac{1}{2\pi} \cdot \int_{\varphi_{bs}} \left[2\pi \cdot \int_0^{r_C} i_C(T,r,\varphi) \cdot \varepsilon(r,\varphi) \cdot r\, dr \right] d\varphi, \qquad (2)$$

where: $\varepsilon(r,\varphi)$ is the energy of back-streaming electron emitted in point with a coordinate r and with an initial phase φ, the average value of ε is approximately of 8.9 keV; $i_C(T,r,\varphi)$ is the emission current density of LaB_6 single crystal emitter depending on emitting radius r and initial phase φ; the term was calculated considering Schottky effect through the expression:

$$i_C(T,r,\varphi) = AT^2 \cdot \exp\left[\frac{-e\phi_C + 3.79 \cdot 10^{-4} \cdot \sqrt{E_{CS}(r,\varphi) \cdot 10^4}}{k \cdot T} \right], \qquad (3)$$

where $A = 73$ A / grad^2·cm^2 and $e\phi_C = 2.66$ eV are the Richardson constant and the work function for LaB_6, respectively, k is the Boltzmann constant and T is the emitter temperature in Kelvin deg; $E_{CS}(r,\varphi)$ is the electric field strength at the emitting surface with an initial phase φ. For cylindrical accelerating cavity employed in the microtron the E_{010} mode electric field strength was calculated for the emitting surface deepened relatively the cavity cover surface by d_C = 0.5 mm and emitter located in the center of the cathode hole, made in the cavity cover. The hole radius r_H is 2 mm; coordinate of the emitter center R_C is 30 mm. The $E_{CS}(r,\varphi)$ values were calculated using the expression:

$$E_{CS}(r,\varphi) = E_0 \cdot J_0(k_0 \cdot R_C) \cdot \cos(\varphi) \cdot \frac{J_0(k_r \cdot r)}{\mathrm{ch}(k_z \cdot d_C)}. \qquad (4)$$

Here: $E_0 \approx$ 35.53 MV/m is maximal field on the cavity axis corresponding to the microtron optimal regime, $k_0 = 2\pi/\lambda_0$, $k_r = \chi_{01}/r_H$, J_0 is the first kind Bessel function, $\chi_{01} = 2.405$ is the first square of Bessel function and $k_Z = \sqrt{k_r^2 - k_0^2}$.

Calculated maximal value of the current density at the emitter temperature of 1900^0 K is: $i_{C\max} = i_C(1900^0\ \mathrm{K}, 0, 0) \approx$ 49.5 A / cm^2. At this temperature the developed thermionic cathode with a single-crystal LaB_6 emitter, [3], has a life time approximately of 1000 h. The initial value of the emission cathode current was calculated using following expression, [3], for several values of the cathode diameter:

$$I_C(T) = \frac{1}{2\pi} \cdot \int_0^{2\pi} \left[2\pi \cdot \int_0^{r_C} i_C(T,r,\varphi) \cdot r\, dr \right] d\varphi. \qquad (5)$$

To calculate the loading current of the accelerating cavity we performed tracking of the electrons in the microtron using 2-D Lorentz equation in the median plane. The E_{010} mode electric and magnetic components of the cavity accelerating field and the permanent microtron magnetic field were considered. The electrons hitting the cavity walls (inside or outside the cavity) were non-participating in the tracking. The 2-D Lorentz equations were integrated up to last (12-th) orbit. The tracking in the microtron was done for several values of cathode diameter and the microtron parameter $Eps = E_0/cB$, where: B - is the value of the microtron permanent magnetic field (for our microtron the optimal value of $B =$ 0.1065 T).

Results of calculation of the cathode overheats vs. the cathode diameter for the microtron operating condition at the initial emitter temperature of 1900^0 K for several values of *Eps* parameter and the emission macro-pulse current having duration of 6 μs are presented in Fig 1. The values of k_C and of χ for LaB_6 at the high temperature were taken from [5].

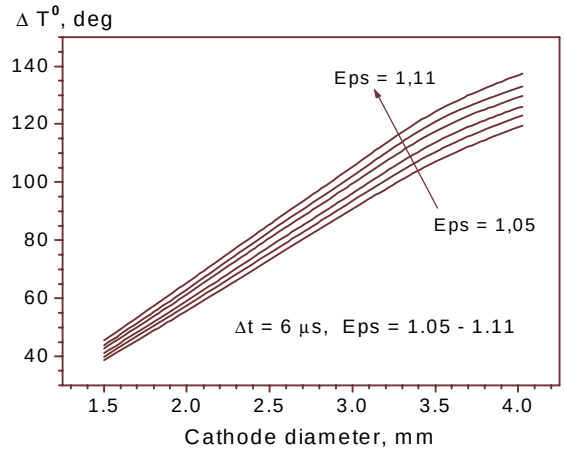

Fig. 1. Cathode overheats caused by back-streaming electrons during 6 μs macro-pulse vs. cathode diameter at the initial temperature of 1900^0 K. The arrow shows variation of the parameter Eps.

Note that we did not consider the heat losses caused by thermo-conductivity of the emitter holder and radiation of heat from the emitter. Because of that the $\Delta T°$ values and the overheating effects are overestimated.

Calculated values of the initial emission current at the initial temperature of 1900^0 K vs. the cathode diameter are plotted in Fig. 2.

Calculated values of the final emission current increased because of the overheating through the electron back-stream during the 6 μs- macro-pulse are plotted in this figure as well.

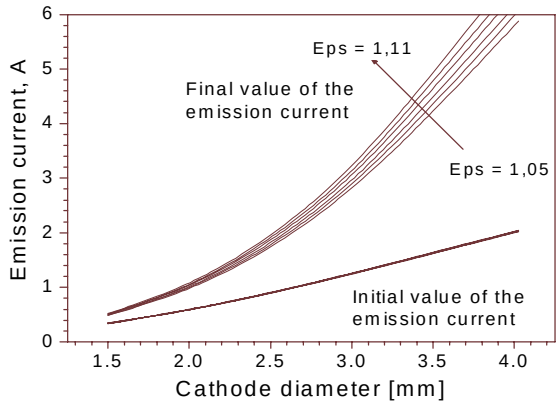

Fig. 2. Initial and final values of the emission current vs. cathode diameter at the initial emitter temperature of 1900^0 K and the macro-pulse duration of 6 μs. The arrow shows variation of the parameter *Eps*.

ESTIMATIONS OF THE FREQUENCY DRIFT IN A HIGH-CURRENT MICROTRON WITH INTERNAL INJECTION

Obtained data allow calculating the intrapulse variation of the accelerating cavity beam loading; that results in frequency drift of the cavity. Performing 2-D tracking of the electrons we calculated velocities of the electrons as well. That allowed us to determine the amplitude and phase of the fist harmonic cavity loading current. Note that the used method allows considering the cavity loading through all accelerated particles, synchronous and non-synchronous as well.

The highest possible frequency drift of the accelerating cavity caused by variation of the beam loading was calculated using following expression, [6]:

$$\Delta F \approx \frac{1}{2\pi} \cdot \frac{\eta_{e0} \cdot \omega_{0C}}{2Q_{0C}} \cdot \tan\varphi_W \cdot \left(1 - \frac{I_F}{I_0}\right), \qquad (6)$$

where: I_0 - initial emission current at the temperature of 1900^0 K, I_F - final value of the emission current increased because of additional heating of emitting surface through back-streaming electrons during 6 μs macro-pulse, Q_{0C} = 9800 is the accelerating cavity wall quality factor (measured value), ω_{0C} is the circular eigen frequency of the cavity, η_{e0} is the initial beam loading coefficient, and φ_W is the phase of the cavity loading current.

The value of η_e is determined as a ratio of the beam power P_e and the cavity wall loss power P_C:

$$\eta_e = \frac{P_e}{P_C} = \frac{[I \cdot V_C \cdot W \cdot \cos(\varphi_W)]}{\left[\frac{V_C^2}{R_{sh}}\right]} = \frac{R_{sh} \cdot I}{V_C} \cdot W \cdot \cos(\varphi_W). \qquad (7)$$

Here: R_{sh} = 1.08 MOhm is the effective shunt impedance of the accelerating cavity, I - is the averaged emission macro-pulse current, W and φ_W are dimensionless first harmonic current amplitude and the harmonic phase, respectively, depending on the cavity voltage amplitude, V_C. (V_C is equal to 0.586 MV for $Eps = 1.08$). The value of V_C is a constant (in steady-state); the values of W and φ_W are constants as well.

Note that using 2-D tracking without consideration of the vertical motion of the electrons causes overestimation of the contribution of the synchronous electrons in the beam loading; for the contribution of the non-synchronous electrons the 2-D tracking gives some underestimation.

From the tracking we determined the values of W and φ_W for various values of *Eps* parameter. For optimal value of *Eps* =1.08, W =2.607, φ_W =20.9º, and for I ≈1.07 A the calculated beam loading coefficient $\eta_e \approx$ 4.8. The value is higher by 10-20% than obtained from the measurements because of overestimation of the accelerated current as was noted above. Fig. 3 shows calculated maximal estimation for the frequency drift caused by overheating of the emitting surface with the electron back-stream vs. the cathode diameter.

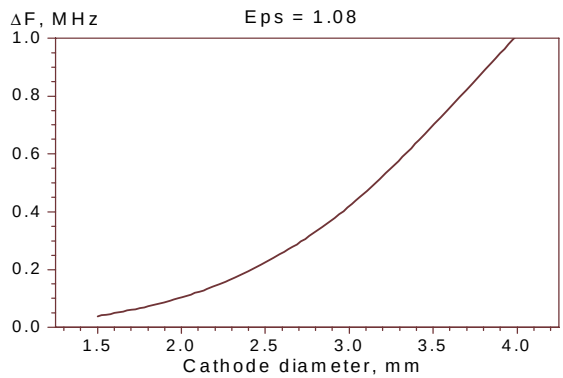

Fig. 3. The cavity frequency drift caused by overheating of the electron emitter with the electron back stream vs. cathode diameters at the initial emitter temperature of 1900^0 K and the value of *Eps* parameter of 1.08.

EFFECT OF THE FREQUENCY DRIFT ON THE TERAHERTZ FEL OPERATION

The described drift of the frequency of the accelerating cavity makes worse stability of the bunch repetition rate because of the stabilizing feedback through reflected wave coming to magnetron. Additional contribution in the bunch repetition rate instability causes increase of the magnetron current during the macro-pulse at a finite value of the frequency stabilization coefficient. The intrapulse increase of the magnetron current and the magnetron

power, respectively, is used to keep constant accelerating voltage and accelerated current at increase of the cavity loading, [1]. Both contributions result in the bunch repetition rate deviation during the macro-pulse; that effectively leads to intrapulse detuning of the FEL optical resonator.

Our terahertz FEL optical resonator, confocal free-space mode in horizontal plane and waveguide mode in vertical plane, was formed with two cylindrical mirrors mounted on the ends of a rectangular waveguide; one of the mirrors has a coupling hole to extract the FEL radiation.

The distance D between the mirrors was chosen using the expression:

$$D = 52 \cdot \frac{\lambda_b}{2} = 52 \cdot \frac{c}{2 \cdot F_b}, \qquad (8)$$

were: λ_b is the wavelength of the accelerating voltage, c is light velocity, F_b is the bunch repetition rate equal to the accelerating cavity frequency. For $F_b \approx 2.801$ GHz, $\lambda_b = \frac{c}{F_b} \approx 10.703$ cm. From expression (8) follows: $|\Delta D| = 26\lambda_b \cdot \frac{\Delta F_b}{F_b}$. I.e. for the optical resonator variation of the bunch repetition rate by 1 MHz approximately corresponds (in a signal level) to the detuning by 1 mm. Measured FEL optical resonator detuning curve at the lasing wavelengths of 113 μm is shown in Fig. 4.

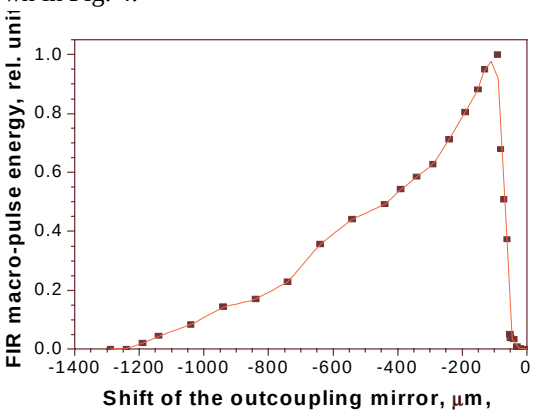

Fig. 4. Detuning curve of the FEL optical resonator measured at the wavelengths of 113 μm.

The measurements were done employing developed cathode assembly based on 2.5 mm-in diameter single crystal, face (100), LaB_6 emitter, operating at the initial temperature of ≈ 1900^0 K. The microtron operating parameters were chosen to provide the intrapulse bunch repetition rate deviations ≤ 0.25 MHz; that was measured using heterodyne method, [7]. At the measurements the microtron provided the beam current of 40 mA at the undulator entrance. The detuning of the FEL optical resonator was done by precise motion of the outcoupling mirror through a stepping motor.

The Fig. 4 curve shows that detuning by 0.2-0.25 mm, corresponding to variation in bunch repetition rate by 0.2-0.25 MHz, decreases the FEL macro-pulse energy by few tens of percents. The value can be used as an upper limit of the intrapulse bunch repetition rate deviations for the microtron intended driving the terahertz FEL. Considering curve plotted in Fig. 3, this points to a necessity in limitation of the emitter size though the emitter with larger diameter provides higher accelerated current at the same life time of the cathode.

Optimal diameter of 2.5 mm of the single crystal LaB_6 emitter for the microtron-terahertz FEL injector was chosen as a compromise considering requirements of reliable operation of the microtron and stable operation of the terahertz FEL. With the emitter at the microtron regime optimized for long-life operation of the cathode we obtained radiated macro-pulse lasing power of 40-50 W in the wavelength range of 100-200 μm. The measurements were done using calibrated pyro-electric detector measuring the lasing macro-pulse energy and the wide-band Schottky barrier detector measuring the lasing macro-pulse shape and the pulse width.

The thermionic cathodes with such emitters at optimized regime of the microtron have life time approximately of 1000 h, providing operation of the widely-tunable terahertz FEL with standard deviation of the lasing macro-pulse energy less than 10% during long-time work, [3].

SUMMARY

Effect of the back-streaming electrons bombarding the emitting surface of the thermionic cathode in a classical microtron with the internal injection on the lasing of the microtron-based FEL was analyzed. The results allow choosing the optimal size of the microtron thermionic cathode to provide stable and reliable operation of the microtron-based widely-tunable terahertz FEL with the macro-pulse lasing power few tens of W.

REFERENCES

[1]. G. M. Kazakevitch, Y. U. Jeong, V. M. Pavlov, B. C. Lee, NIM A 528 (2004) 115-119.
[2]. S. P. Kapitza and V. N. Melekhin, The Microtron London. Harwood, 1978.
[3]. G. M. Kazakevich, G. I. Kuznetsov, V. M. Pavlov, Y. U. Jeong, S. H. Park, and B. C. Lee "Injection system for microtron-based Terahertz FEL" Proceedings of the 27th International FEL Conference, JACoW / eConf C0508213.
[4] L. D. Landau and E. M. Lifshitz, in Course of Theoretical Physics ("Nauka" (In Russian), Moscow, (1986), Vol. **6**, Fluid Mechanics, p. 288-289.
[5] Takaho Tanaka, J. Phys. C **7**, L177-L180 (1974).
[6] E. L. Kosarev. Ph.D. Thesis, Inst. of Phys. Problems, Moscow, 1971, (in Russian).
[7] G. M. Kazakevitch, Y. U. Jeong, B. C. Lee, J. Lee, NIM A 483 (2002), 331-335.

FEL-OSCILLATOR SIMULATIONS WITH GENESIS 1.3

J.G. Karssenberg, P.J.M. van der Slot*, J.W.J. Verschuur, I.V. Volokhine † K.-J. Boller
Laser Physics and Non-Linear Optics Group, University of Twente
PO Box 217, 7500 AE Enschede, The Netherlands

Abstract

Modeling free-electron laser (FEL) oscillators requires calculation of both the light-beam interaction within the undulator and the propagation of the light outside the undulator. We present a paraxial Optical Propagation Code (OPC) based on the Spectral Method and Fresnel Diffraction Integral, which in combination with Genesis 1.3 can be used to perform either steady-state or time-dependent FEL oscillator simulations. A flexible scripting interface is used both to describe the optical resonator and to control the codes for propagation and amplification. OPC enables modeling of complex resonator designs that may include hard-edge elements (apertures) or hole-coupled mirrors with arbitrary shapes. Some capabilities of OPC are illustrated using the FELIX system as an example.

INTRODUCTION

Free-electron laser (FEL) oscillators are complex devices. They require simulation of both the amplification of the radiation field within the undulator and the propagation of the radiation field through the resonator, to correctly predict the spectral and spatial properties of the output of the laser. These properties are very important for the design of user experiments.

To date, several codes exist that can simulate an FEL amplifier or oscillator (see, e.g., [1]). However, the well-established Genesis 1.3 FEL code [2] is primarily used for FEL amplifier or SASE simulations. In this paper we present an optical propagation code (OPC) that works together with Genesis 1.3 to simulate FEL resonators. The full functionality of Genesis 1.3 is maintained and simulation of FEL oscillators can be done both in steady-state and time-dependent modes.

To propagate the radiation field between optical and gain elements, we have implemented three related paraxial methods: the Spectral Method [3], the Fresnel Diffraction Integral Method [4] and a modified Fresnel Diffraction Integral Method. The latter is based on the normal Fresnel Diffraction Integral, however, it includes the ABCD matrix of the optical system between input and output plane [5]. The radiation field produced by Genesis 1.3 at the undulator's exit is propagated using one of these methods to the first optical element. Then the action of that particular optical element is applied to the wave and one of the propagation methods is again used to propagate the wave to the next optical element. This procedure is repeated until the undulator's entrance is reached. Note that propagation through a cascaded set of optical elements can be done in a single step if this set can be represented by a single overall ABCD matrix and using the Modified Fresnel Diffraction Integral for the propagation.

We have chosen to separate the optical propagation model from the FEL simulation model for two main reasons. First, the optical propagation model can be used with different gain models and is, in principle, not limited to FELs. Second, the propagation model can then also be used to propagate the field outside the resonator and determine the field distribution, for example, in the far field or in a user area that can be located at a considerable distance from the laser in the case of FELs. The optical propagation code is available for download [10].

In the remainder of this paper, we first describe briefly the different propagation methods, then the OPC code and end with an example illustrating the capabilities of the combination of the OPC code with Genesis 1.3.

PARAXIAL OPTICAL PROPAGATION

By applying a Fourier transform over the transverse coordinates, the paraxial wave equation can be written as [5]:

$$(k_x^2 + k_y^2)\tilde{u} - 2ik\frac{\partial \tilde{u}}{\partial z} = 0, \tag{1}$$

where

$$\tilde{u}(k_x, k_y, z) = \int_{-\infty}^{\infty}\int_{-\infty}^{\infty} u(x, y, z)e^{-i(k_x x + k_y y)}\mathrm{d}x\mathrm{d}y \tag{2}$$

is the Fourier transform of the complex wave amplitude $u(x, y, z)$. Given a known optical field $u_0(x, y)$ at $z = 0$, the optical field after a propagation over a distance z can be obtained from eq. 1:

$$\tilde{u}(k_x, k_y, z) = \tilde{u}_0(k_x, k_y)e^{-i\frac{2z}{k}(k_x^2+k_y^2)}. \tag{3}$$

The propagation method described by eq. 3 is known as the Spectral Method and consists of applying the spatial Fourier transform eq. (2) to the input plane, propagate the field over a distance z (eq. 3) and applying the Inverse Fourier Transform to $\tilde{u}(k_x, k_y, z)$. This Inverse Fourier Transform is similar to eq. 2 with the roles of $\tilde{u}$, k_x and k_y interchanged with those of u, x and y, respectively, and a factor $1/4\pi^2$ added.

* p.j.m.vanderslot@tnw.utwente.nl
† Current address: Philips Research, High Tech Campus 34, 5656 AE Eindhoven, The Netherlands

It can be shown that paraxial wave propagation over a distance $z = L$ through a cascaded optical system can be realized in a single step using the elements of the overall ABCD matrix in Huygens' Integral for propagation [5]. If we use the following transform to remove the spherical portion of the wave at the input plane [5]:

$$v_0(\xi', \eta') \equiv \sqrt{a_1 a_3} u_0(\xi, \eta) e^{-i\frac{\pi(A_x - M_x)\xi^2}{B_x \lambda}} e^{-i\frac{\pi(A_y - M_y)\eta^2}{B_y \lambda}} \quad (4)$$

and at the output plane:

$$v(x', y') \equiv \sqrt{a_2 a_4} u(x, y, L) e^{+i\frac{\pi(D_x - M_x^{-1})x^2}{B_x \lambda}} e^{+i\frac{\pi(D_y - M_y^{-1})y^2}{B_y \lambda}}, \quad (5)$$

where $x' = a_1 x$, $\xi' = a_2 \xi$, $y' = a_3 x$, $\eta' = a_4 \eta$, and $A_{x(y)} \ldots D_{x(y)}$ are the ABCD matrix coefficients for the x- and y direction respectively, then Huygens' Integral can be written as a modified Fresnel Diffraction Integral:

$$v(x', y') = i\sqrt{N_{c,x} N_{c,y}} \times \int_{-1}^{1}\int_{-1}^{1} K(x', y', \xi', \eta') v_0(\xi', \eta') \mathrm{d}\xi' \mathrm{d}\eta', \quad (6)$$

where the kernel K is given by

$$K(x', y', \xi', \eta') = e^{-i\pi N_{c,x}(x' - \xi')^2} e^{-i\pi N_{c,y}(y' - \eta')^2}, \quad (7)$$

and the equivalent collimated Fresnel numbers $N_{c,x(y)}$ are given by

$$N_{c,x(y)} = \frac{M_{x(y)} a_{1(3)}^2}{B_{x(y)} \lambda}. \quad (8)$$

The arbitrary scaling factors $a_{1..4}$ in eqs. 4-5 define two magnification factors $M_{x(y)} = a_{2(4)}/a_{1(3)}$, if they correspond to either the size of a hard aperture or a size sufficiently large that the field is just negligible outside the area covered by that size. Note that for free-space propagation $A = D$ =1, C =0 and $B = L = z$, and using $M_x = M_y$ =1, reduces eqs. 6-8 to the normal Fresnel Diffraction Integral.

Both the Spectral and the Modified Fresnel propagation methods are implemented using Fast Fourier Transforms and therefor their computation time scales as $N^2 log_2(N^2)$ for a $N \times N$ grid. For an equal grid, the Spectral method is the faster of the two because it requires less operations [6]. However, care has to be taken with the Spectral Method that the field remains zero at the border of the grid to avoid artificial reflections. The Modified Fresnel Diffraction Integral has the advantage that propagation through an optical system, described be a single overall ABCD matrix, is obtained in a single step. Another advantage is that the scaling applied to this method allows a magnification factor for the grid so that the mesh size in the input plane does not have to be the same as the mesh size in the output plane.

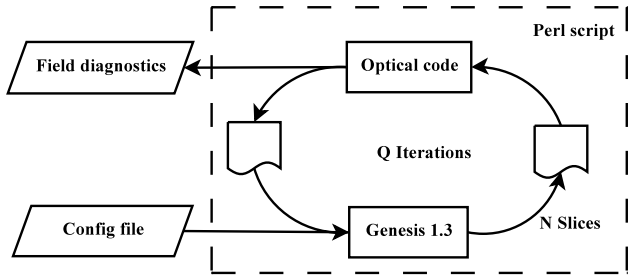

Figure 1: Flowchart of the simulation loop.

IMPLEMENTATION

Simulation of an FEL oscillator requires simulation of both the gain within the undulator and the propagation of the radiation through the remaining part of the resonator, that may contain multiple optical components. Genesis 1.3 [2] is used to propagate the optical wave through the undulator and calculate the amplification of the wave. The OPC receives the optical output from Genesis 1.3, and propagates it from optical element to optical element using one of the methods described above, until the undulator's entrance is reached and the next round trip can start. If a cascaded set of optical elements can be described by a single ABCD matrix, then propagation through the cascaded set can be done in a single step using the Modified Fresnel Diffraction Integral. Output can be produced at various positions, and by the optical elements, which is of advantage for beam diagnostics and for designing suitable optics for a further propagation of the output beam.

While the actual simulation algorithms are written in FORTRAN, the Perl scripting language is used to both control the program flow and define the resonator geometry. Fig. 1 shows schematically the program flow. The advantage of using a script to control the program instead of a config file is that it gives the user a lot of freedom to create complex models. Table 1 gives an example of a script for simulation of the FELIX system [7].

This example script contains all essential elements needed to simulate the FELIX system. The first three lines are headers needed to load a library. Then two objects are created, one that corresponds to the genesis program (l.5) and one that corresponds to the optical propagation code (l.6). The genesis object requires the standard configuration file for Genesis 1.3 as input. A Perl script function is provided that gives the user complete control over the parameters in the configuration file. This allows, for example, the use of a Gaussian seed for Genesis 1.3 in the first round trip and the resonator feedback as input for Genesis 1.3 in consecutive round trips.

To define the optical propagation through the resonator, the optics object (l.6) accepts a simple script that describes the propagation methods and optical components used (l.7-16). The available propagation methods are described above, and the optical components so far include diaphragms, square apertures, curved mirrors and thin

Table 1: Example script for simulating the FELIX FEL oscillator.

```
01:  #!/usr/bin/perl
02:  use lib './lib';
03:  use Physics::OPC;
04:
05:  $genesis = genesis('./felix.itdp.in');
06:  $optics  = optics( "
07:      fresnel z=1.062
08:      mirror  r=3 R=98%   # Downstream mirror
09:      fresnel z=5.89
10:      hole    r=0.0015 (    # Out-coupling
11:           dump var=output
12:           fresnel z=1       # Far field distance
13:           dump var=far  )
14:      mirror  r=4 R=98%   # Upstream mirror
15:      dump  var=reflected
16:      fresnel  z=2.358 "   );
17:
18:  for $i (1 .. 75) {
19:      run  $genesis;
20:      run  $optics;
21:      move $output   => "output.$i.dfl";
22:      move $far      => "far.$i.dfl";
23:      move $reflected => "reflected.$i.dfl";
24:      move $field    => "entrance.$i.dfl";
25:  }
```

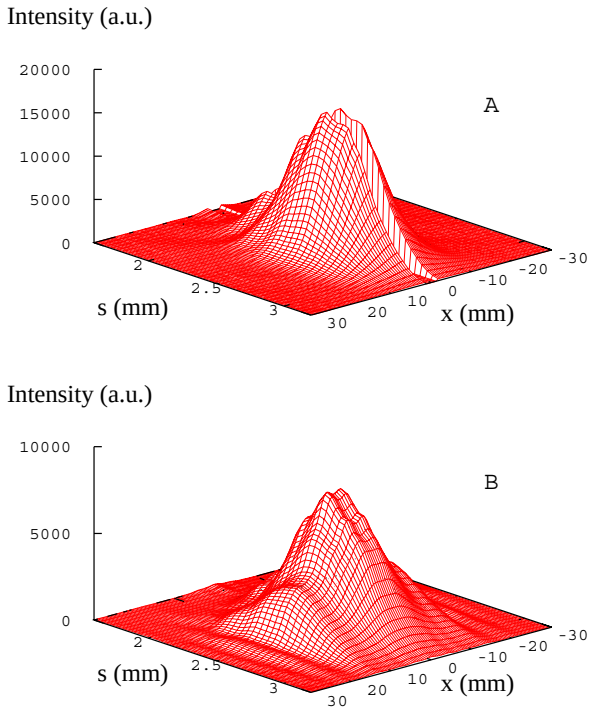

Figure 2: Radiation intensity just after reflection on the upstream mirror (A) and just before the undulator's entrance (B) as a function of the horizontal cross-section (at y=0) and the position within the optical micro pulse s after 75 round trips and for ΔL=-1.5λ.

lenses. Each optical component is defined by a set of parameters, for example the downstream mirror (l.8) for FELIX has a curvature ('r') of 3 m and a reflectivity ('R') of 98 %. Other possible parameters for a mirror are absorption ('A'), transmittance ('T'), offset ('xoff' and 'yoff'), and a small tilt ('xr' and 'yr'). The optical propagation starts with propagation over a distance z=1.062 m from the undulator's exit to the downstream mirror using the Fresnel Diffraction Integral (l.7). Then the downstream mirror is defined (l.8). After the downstream mirror the wave is propagated to the upstream mirror, again using the Fresnel Diffraction Integral (l.9). In FELIX, the output beam is extracted through a hole in the upstream mirror. In the model the "hole" component (l.10) is processed before the actual mirror component (l.14). The hole component creates two waves, one that is transmitted through the hole, and one that corresponds to the part outside the hole that remains within the resonator. In this case, the transmitted beam corresponds to the radiation extracted from the resonator. The output beam is propagated over a distance sufficiently large to be in the far field (l.11-13). At l.14 the script continues with the part outside the hole and this is reflected by the upstream mirror. The combination of the "hole" and "mirror" commands represent the upstream mirror with the hole. The resonator is closed by propagation from the upstream mirror to the undulator's entrance (l.16). The "dump" commands indicate positions where output is produced for further analysis.

The last part of the Perl script is the actual simulation loop where we run the two programs consecutively and save binary dumps (l.21-34) for each round trip at varies positions defined in the optical configuration. The binary files used by the propagation code have the same format as the field files produced by Genesis 1.3, so existing analysis tools can be re-used. Utilities to extract plain text data from these files are included with the OPC code. Using plotting tools such as Gnuplot, the user can create all kinds of views to analyze the optical pulse.

In steady-state mode Genesis 1.3 produces one field distribution, i.e., a single slice, as output, which is then processed by the propagation code. Genesis 1.3 can also run in time-dependent mode, which includes slippage effects. In this mode Genesis 1.3 produces a set of slices representing the radiation pulse as output. In time-dependent mode, the propagation code will process all slices produced by Genesis 1.3 consecutively. Each slice is propagated using the center wavelength of the optical pulse, which is valid only for a narrow bandwidth of the optical pulse. The slowly varying amplitude and phase approximation used by Genesis 1.3 limits the maximum bandwidth of the pulse. Furthermore, an analysis by Dattoli et.al. showed that the relative bandwidth is limit to about 10^{-3} to 10^{-2} for typical parameters of VUV, UV and IR FELs [8].

EXAMPLE

The script shown in Table 1 is used to illustrate some of the capabilities of the OPC code. The script describes the resonator for the FELIX system [7]. The script produces four binary dump files for each iteration (that is, for each round trip). The first gives the field distribution just outside the outcouple mirror (l.21), l.23 gives the field distribution just after reflection at the upstream mirror containing the hole for extraction of the radiation, and l.24 gives the distribution at the entrance of the undulator. The far-field distribution (l.22) will not be used here. It should be noted that the same script is used for both steady-state and time-dependent simulations, the only changes required are made in the genesis configuration file.

We performed a time-dependent simulation of the FELIX system. The horizontal cross-section (at y=0) of the radiation intensity just after reflection on the upstream mirror and just before the undulator's entrance are shown in Fig. 2 as a function the horizontal position x and the position s within the optical micro pulse after 75 round trips and for a cavity detuning ΔL=-1.5λ. This figure clearly shows the effect of the hole in the mirror (Fig. 2A) on the radiation profile and how this profile has changed when propagated to the undulator's entrance (Fig. 2B), that shows a near maximum on-axis intensity. Note that the broad radiation profile at the undulator's entrance may be clipped by the electron beam transport tube. Although not present in the current script, this can be included by adding a diaphragm component just after propagation to the undulator's entrance (l.16) in Table 1.

If we integrate the intensity over the cross-section of the optical pulse, we obtain the micro-pulse optical power as a function of the position s within the micro-pulse. This is shown in Fig. 3 as a function of the round-trip number. The oscillation in the micro-pulse optical power as a function of time (=round trip #) is known as the so called limit-cycle oscillations [9]. It is more clearly visible in the total micro-pulse energy that is shown in Fig. 4 for three different values of the cavity detuning ΔL.

CONCLUSION

We have developed an Optical Propagation Code that propagates an arbitrary radiation wave, in the paraxial approximation, through a complex optical system. In combination with a code to simulate the gain medium, such as Genesis 1.3 in case of FELs, this optical code can be used to model the output of a laser oscillator. The use of a flexible scripting interface allows a user to create both simple and complex resonator configurations. The OPC package is available for download at our website[10].

REFERENCES

[1] S. Biedron, Y. Chae, R. Dejus, B. Faatz, H. Freund, S. Milton, H.-D. Nuhn, and S. Reiche, Nucl. Instrum. Methods Phys. Res. A, Accel. Spectrom. Detect. Assoc. Equip. **A445**, 110 (2000).

[2] S. Reiche, *pbpl.physics.ucla.edu/ reiche*.

[3] E. Sziklas and A. Siegman, Appl. Opt. **14**, 1874 (1975).

[4] H.A. Hause, "Waves and fields in optoelectronics," 1984, Prentice-Hall, Englewood Cliffs.

[5] A.E. Siegman, "Lasers," 1986, University Science Books, Mill Valley.

[6] I.V. Volokhine, "Design and Numerical Analysis of TUE-FEL II", Ph.D. thesis, 2003 University of Twente.

[7] D. Oepts, A. van der Meer, and P. van Amersfoort, Infrared Phys. Technol. **36**, 297 (1995).

[8] G. Dattoli, H. Fang, L. Giannessi, M. Richetta, A. Torre, and R. Caloi, Nucl. Instrum. Methods Phys. Res. A, Accel. Spectrom. Detect. Assoc. Equip. **A285**, 108 (1989).

[9] D. Jaroszynski, R.J. Bakker, D. Oepts, A.F.G. van der Meer, and P.W. van Amersfoort, Nucl. Instrum. Methods Phys. Res. A, Accel. Spectrom. Detect. Assoc. Equip. **A331**, 52 (1993).

[10] OPC design team, *lf.tnw.utwente.nl/opc.html*.

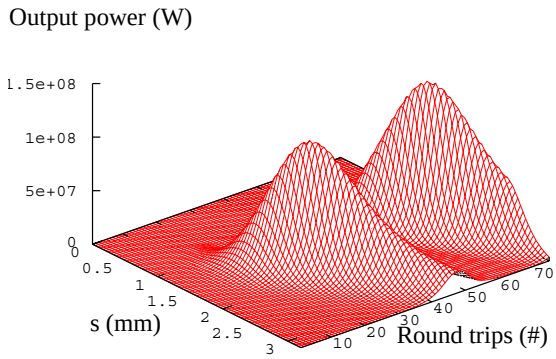

Figure 3: Micro pulse optical power as a function of both the position s within the pulse and the round trip number for a detuning ΔL=-1.5λ.

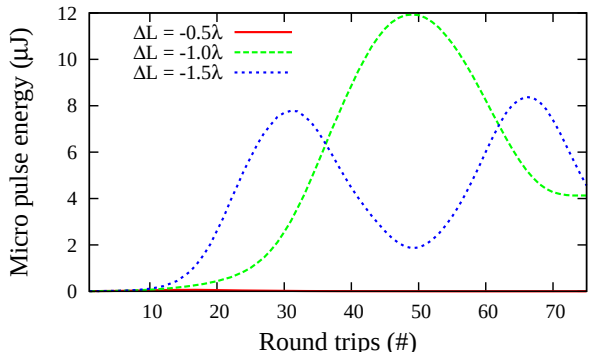

Figure 4: Total energy of the micro pulse as a function of round-trip number for a detuning ΔL of -0.5λ, -1λ and -1.5λ respectively.

COMMISSIONING OF S-BAND RF GUN AND LINAC FOR THE MARK-III FEL FACILITY AT DUKE UNIVERSITY

Y. Kim*, J. Gustavsson, P. Wang, G. Swift, M. Emamian, S. Hartman, P. Wallace, and G. Edwards
Free Electron Laser Laboratory, Duke University, Durham, NC 27708-0319, USA

Abstract

At the Free Electron Laser (FEL) Laboratory of Duke University, there is an S-band linac based Mark III FEL facility which can supply coherent FEL photon in the infrared wavelength range. To supply high quality electron beams and to have excellent pulse structure, we installed an S-band RF gun with a Lanthanum Hexaboride (LaB_6) single crystal cathode for the Mark III FEL facility in 2005. Its longest macropulse length is about 6 μs, and maximum repetition rates of a macropulse and a micropulse are 15 Hz and 2856 MHz, respectively. Therefore we can generate about 17142 bunches within a bunch train and about 257142 bunches within one second by the S-band gun. In this paper, we describe recent commissioning experiences of our newly installed S-band RF gun and linac for the Mark III FEL facility.

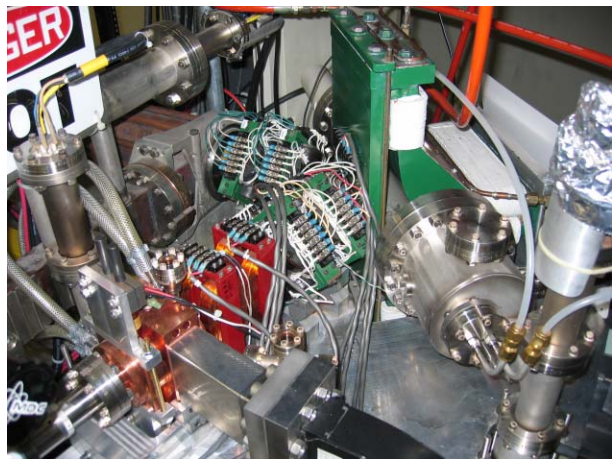

Figure 1: Photograph around the newly installed gun.

INTRODUCTION

The Mark III FEL is a wavelength-tunable light source facility which can generate coherent and ultra-bright FEL photon beams in the infrared wavelength range. Originally, the Mark III FEL facility was operated at Stanford University, then it was moved to Duke University in 1989 [1]. After relocating to Duke University, we had upgraded several machine components of the Mark III FEL facility [2], [3]. Recently, many FEL facilities started to use the laser driven RF photoinjector to generate high quality electron beams with a high peak current and a low transverse emittance. However, the laser driven RF photoinjector has a limitation to generate a good micropulse structure due to a low repetition rate of the gun driving laser. Since many users working for biophysical and biomedical science request high repetition rate of FEL photon beams, we have used an S-band thermionic RF gun with a LaB_6 cathode to supply excellent micropulse and macropulse structures [4]. After successful operation for several years, in 2003, we had met a strong back bombardment problem which caused malfunction of our gun [2], [5]. Therefore we re-installed a new S-band thermionic RF gun in 2005 to generate stable FEL photon beams continuously. In this paper, we describe our commissioning experiences of the new S-band RF gun and linac for the Mark III FEL facility.

LAYOUT OF GUN AND LINAC

The geometry and parameters of the newly installed gun are almost the same as those of our original gun. Its original shape and parameters can be found in reference [6] and [7]. In our new gun, we modified geometry of a deflection magnet and shifted its core position to backward by 3.175 mm for easy fabrication. Photograph around the new gun and layout of the Mark III FEL facility are shown in Figs. 1 and 2. And its main accelerator parameters are summarized in Table 1 where all emittances are estimated from ASTRA and ELEGANT simulations. As shown in Figs. 1 and 2, at the upstream of the gun cavity, there is the deflection magnet which bends electron beam orbit vertically to reduce the back bombardment on the LaB_6 cathode surface. At the downstream of the gun cavity, there are two vertical correctors to compensate vertically bended beam orbit which is intentionally generated by the deflection magnet. After those correctors, there is a quadrupole doublet (GQ1 and GQ2) and the first gun toroid (T1) to measure electron beam current in a macropulse or bunch train. Then electron beams are transferred to an α-magnet [8]. Since horizontal dispersion is not zero in the α-magnet, electron with a higher energy takes an outer or longer path, and electron with a lower energy takes an inner or shorter path in the α-magnet. In that manner, bunch length is compressed by the combined function of the nonzero momentum compaction factor R_{56} and nonzero energy spread in the α-magnet [6]. Since horizontal beam size becomes larger in the α-magnet due to nonzero dispersion as shown in Fig. 2, we chop tail or head part of electron beams by lower and higher energy filters to control beam energy spread, beam energy, and transverse emittance. Only electron beams which can go through two energy filters are transferred to linac [6]. Additionally, to supply macropulse with a frequency of 1 Hz,

* E-Mail : yjkim@FEL.DUKE.edu

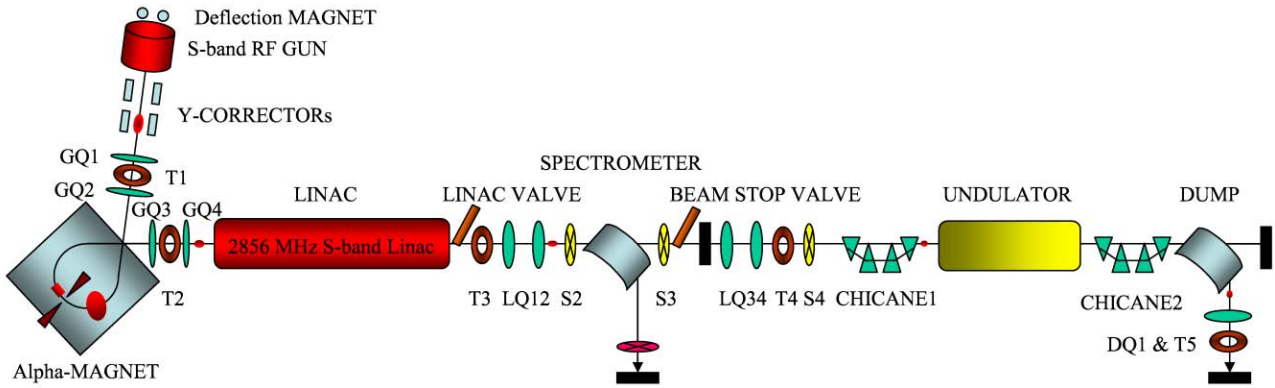

Figure 2: Layout of Mark III FEL Facility.

Table 1: Accelerator parameters of the Mark III FEL.

Parameter	Unit	Value
RF frequency of gun and linac	MHz	2856
number of gun cell	cell	1
cathode diameter	mm	1.75
cathode operation temperature	K	~ 1800
cathode energy spread	eV	~ 0.4
cathode work function	eV	2.69
cathode heater power	W	~ 11
operating vacuum in gun	Torr	$< 10^{-7}$
single bunch charge	nC	0.14
macropulse current at gun exit	mA	~ 400
macropulse current at α-magnet exit	mA	~ 180
klystron power	MW	30
gun forward RF power	MW	~ 1.8
max gradient on cathode	MV/m	~ 30
cavity cooling water temperature	deg	32.2
total beam energy at gun exit	MeV	~ 1.6
total beam energy at linac exit	MeV	$25 - 45$
beam energy spread at linac exit	%	0.3
peak current at linac exit	A	$15 - 45$
thermal emittance at cathode	μm	~ 0.35
projected emittance at linac exit	μm	~ 5
slice emittance at linac exit	μm	~ 1
macropulse length at linac exit	μs	$2 - 6$
max macropulse rate	Hz	15
micropulse length at linac exit	ps	$0.5 - 3$
micropulse rate	MHz	2856

there is a 11.5 kV kicker in the α-magnet. In this case, only one macropulse is transferred to linac in one second, and all other macropulses are dumped in the α-magnet by the kicker [6].

After the α-magnet, beams are focused by the second quadrupole doublet (GQ3 and GQ4). There are two toroids (T2 and T3) to measure beam current at the downstream of the α-magnet and linac. By accelerating electron beams with a 3 m long S-band accelerator, beam energy is increased up to about 45 MeV, and bunch length is more compressed to about 0.5 ps by the bunch compressor (CHICANE1). By optimizing two quadrupole doublets (LQ12 and LQ34) and steerers at the downstream of linac, we can get a beam waist in undulator which is helpful to increase interaction between electron beams and spontaneous emitted photon beams. After making the interaction to induce the microbunching in electron beams and lasing, electron beams are sent to the beam dump.

COMMISSIONING EXPERIENCES

To reduce space charge effects which increase transverse emittance and bunch length, we have to accelerate electron beams quickly in the gun cavity. By sending about 2 MW RF power to the gun cavity, electron beams can be accelerated to about 1.6 MeV in the gun. However, we could not send such a high power at the beginning stage of our commissioning due to too strong waveguide bangs, arcs, and poor vacuum at the gun region. Hence, first of all, we had to reduce gun reflected RF power by matching the resonance frequency of gun cavity with a driving RF frequency. By optimizing temperature of cavity cooling water, position of a gun cavity tuner, and position of the LaB_6 cathode, we could change volume of the gun cavity slightly, and we could get a best matched point which gives a minimum reflected RF power and the best beam emittance as shown in Fig. 3 [6]. Here the left means the head region of macropulse, and a large reflected RF power at the tail region was generated by a resonance frequency shift which was induced by the increased back bombardment and beam loading effect along the macropulse [5]. After reducing reflected power, by increasing gun forward power and macropulse length gently, we performed continuous gun cavity RF conditioning until we could get a stable vacuum status in gun region. Since gun reflected power is changed as forward RF power and macropulse length are increased, we had to re-optimize gun reflected RF power at a higher power and a longer macropulse. After performing continuous RF conditioning for three months, we

could obtain required basic beam parameters for the Mark III FEL operation, and vacuum at gun region was also stabilized as shown in Fig. 5. Here macropulse length is about 6 μs, the maximum beam current in the macropulse is about 400 mA at T1, and its maximum beam current at T2 is about 180 mA as shown in Figs. 3 and 4.

Although we optimized the deflection magnet to reduce the back bombardment on the cathode surface, we could not avoid the problem completely when macropulse length was longer than about 2 μs and beam current at T1 was higher than about 200 mA. Therefore, as shown in Figs. 3 and 4, beam current at T1 was continuously increased along the macropulse, and a large spike was generated at the tail region of the reflected power due to the resonance frequency shift. Generally, electron emission rate from a thermionic cathode becomes higher as the gradient on the cathode surface is increased. This increased current density J_s can be described by the well-known Schottky equation which is given by

$$J_s = A \cdot T^2 \exp\left[-(\Phi - e\sqrt{eE_c/(4\pi\epsilon_0)})/kT\right], \quad (1)$$

where $A = 120\,\mathrm{A/(cm^2 \cdot K^2)}$ is the Richardson constant, T is the cathode temperature, $\Phi = 2.69$ eV is the work function of the LaB_6 cathode, $k = 8.62 \times 10^{-5}$ eV/K is the Boltzmann constant, and E_c is the external electric field on the cathode surface [6], [9]. Therefore there are two ways to obtain a higher beam current at T1. One way is increasing RF forward power while keeping cathode temperature at a low value. The other way is increasing cathode temperature while keeping RF forward power at a low value. According to our experience, the latter way was useful to reduce the back bombardment along the macropulse. Hence during commissioning, we operated our gun with a high cathode temperature of about 1800 K.

After considering beam loading effect and the higher beam current at the tail region, we had to send more higher RF forward power along the macropulse to get a uniform energy distribution. If gun reflected power is close to unbalanced shape as shown Fig. 3(top left), head and tail parts in the macropulse are chopped by two energy filters in the α-magnet, and pulse length after the magnet became shorter. Therefore we optimized reflected and forward power signals to have a good linearity along the macropulse as shown in Fig. 3(bottom left) and (bottom right). From the information on position of the lower energy filter and magnetic field of the α-magnet, we could estimate total electron beam energy E at the gun exit which is given by

$$E\,[\mathrm{MeV}] \simeq 0.511\sqrt{1 + (0.205 \cdot I_\alpha[\mathrm{A}])^2}\,, \quad (2)$$

where I_α is the current of a power supply for the α-magnet, and the lower energy filter is located at 16 mm. By scanning I_α and monitoring T2 signal, we could estimate the lowest and the highest beam energies as well as energy spread in the macropulse, which are useful for us to keep reproducibility of gun RF amplitude and phase. Since peak current and beam loss along linac were sensitive to I_α, a

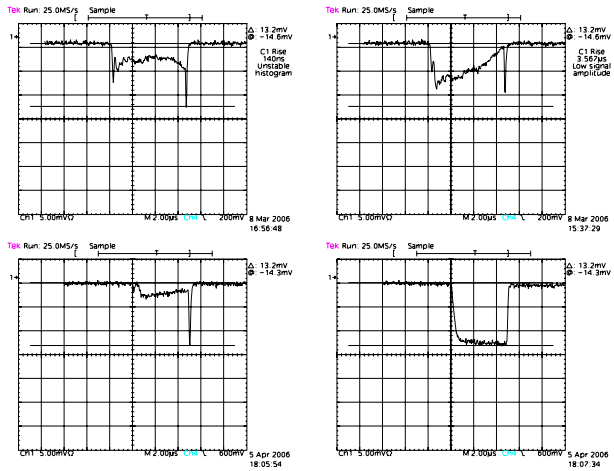

Figure 3: Signal of gun reflected RF power when reflected power are unbalanced at head and tail parts (top left), when head part has a high reflected power (top right), when reflected power is minimum and its slope along macropulse is optimized (bottom left), and signal of forward RF power when reflected power is optimized (bottom right).

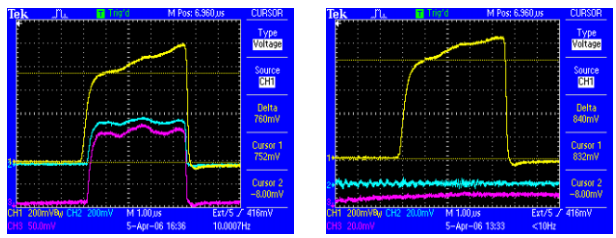

Figure 4: (left) signals of the first gun toroid (yellow), the second gun toroid (cyan), and linac toroid (magenta) when beam transmission from gun to linac and back bombardment along macropulse are optimized, (right) signal of the first gun toroid when there is no transmission in the α-magnet. Here calibration factors for T1, T2, and T3 are 0.4 A/V, 0.4 A/V, and 1.0 A/V, respectively.

fine tuning of I_α was also needed to get a lasing. After optimizing gun reflected power, quadrupoles, correctors, and the α-magnet properly, we could get about 45% transmission and a flat current distribution at the downstream of the α-magnet as shown in Fig. 4(left). If beam energy is too low or I_α is too high, we could not get any beam transmission at the α-magnet as shown in Fig. 4(right).

To optimize beam orbit and optics at gun and linac regions, we used signals from three radiation monitors which are distributed along linac. Although those signals were low during 1 Hz operation, they were significantly increased during 10 Hz operation as shown in Fig. 6. Due to the excellent pulse structures, those loss level were very high when beam orbit and optics at gun and linac region were slightly changed from a golden orbit and optics which give the minimum radiation loss and the best emittance for lasing. Therefore, we had to optimize all quadrupoles, steerers, and the α-magnet carefully to reduce those loss.

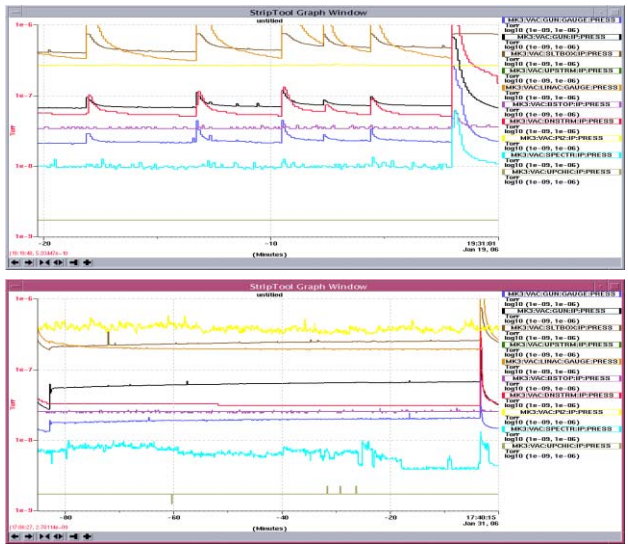

Figure 5: (top) spiky vacuum status on January 19, 2006 when gun generated 400 mA at T1 for the first time, (bottom) stabilized vacuum status on January 31, 2006 when gun generated 400 mA at T1 without any vacuum interlock for about 80 minutes.

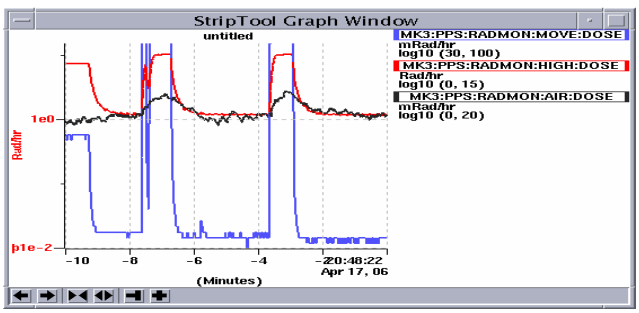

Figure 6: Signals of three radiation monitors along linac during 1 Hz and 10 Hz operations.

FUTURE UPGRADE PLANS

We are under developing and considering following upgrade plans to improve performance of the Mark III gun and linac. First of all, to keep electron beam current constant and to reduce the strong back bombardment problem, we need a real time cathode temperature monitoring system. By installing an infrared temperature detector and by giving a feedback to the power supply of a cathode heater, we can keep cathode temperature and beam current constant. And to remove the back bombardment problem completely, we are also under operating the other RF gun with the photoemission mode by shooting a Continuum Minilite-II Nd:YAG laser on the LaB_6 cathode surface [10]. Since the thermal emittance of the LaB_6 cathode is about 0.35 μm for a diameter of 1.75 mm, and quantum efficiency is about 0.05% at 266 nm, to improve transverse emittance, peak current, and energy spread more, we would like to use a high-class laser such an Nd:YLF laser whose the rms pulse length is about 4.4 ps, energy per a micropulse is about 1 μJ, and the maximum micropulse repetition rate is 9 MHz [11], [12]. This photoemission mode operation will be certainly helpful to increase the peak power of our Mark III FEL facility. Normally, electron beam quality and FEL performance are significantly changed even though RF amplitude and phase of gun and linac are slightly changed. Therefore we would like to develop a real time RF monitoring system to get a stable and reproducible FEL operation. And we want to develop an optical fiber based on-line beam loss monitor to stabilize beam orbit around undulator, which is certainly helpful to keep continuous and stable interaction between electron beams and spontaneous emitted photon beams in undulator. At the moment, we do not have a direct diagnostic tool to measure bunch length of about 0.5 ps long electron beam. To measure bunch length directly and to optimize FEL performance, we would like to install a small S-band deflection cavity in the near future. To control bunch length or peak current easily and to reduce geometrical wakefields and coherent synchrotron radiation, we are under developing a new bunch compressor with four electromagnetic dipoles. Now we are also under developing an emittance measurement system with a Flea digital camera of the Point Grey Research [13].

SUMMARY

By performing gun cavity RF conditioning for three months, we could get a stable vacuum status and required basic beam parameters. After optimizing reflected power, toroid signals, radiation loss along linac, and focusing around undulator, in January, 2006, we could send electron beams to the beam dump successfully. Since we could get a strong signal from a power meter in April, 2006, it is certain that our new gun and linac were optimized properly to generate FEL photon beams from our undulator. Authors thank to M. Pentico, O. Oakley, V. Rathbone, S. Huang, V. Popov, S. Mikhailov, and Y. Wu for their helpful comments and contributions for Mark III recommissioning project.

REFERENCES

[1] S. V. Benson *et al.*, Nucl. Instr. and Meth. A **296** (1990) 110.
[2] G.A. Barnett *et al.*, Nucl. Instr. and Meth. A **375** (1996) 97.
[3] I. Pinayev *et al.*, in *Proc. PAC2001*, 2001.
[4] G. S. Edwards *et al.*, Rev. Sci. Instrum. **74** (2003) 3207.
[5] Toshiteru Kii *et al.*, Nucl. Instr. and Meth. A **475** (2001) 588.
[6] G. A. Westenskow *et al.*, HEPL Tech. Note TN-86-1, 1986.
[7] C. B. McKee, Ph.D. dissertation, Duke University, 1994.
[8] Harald A. Enge, Rev. Sci. Instrum. **34** (1963) 385.
[9] Yu Song, IEEE J. Quantum Electronics **27** (1991) 898.
[10] J. G. Neumann *et al.*, Rev. Sci. Instrum. **76** (2005) 033303.
[11] J. M. Lafferty, J. Appl. Phys. **22** (1951) 299.
[12] S. Schreiber, in *Proc. FEL200*5, 2005.
[13] http://www.ptgrey.com/products/flea/.

BRIGHT ELECTRON BEAMS AND SMITH-PURCELL FREE-ELECTRON LASERS

Charles H. Boulware#, Heather L. Andrews, Jonathan D. Jarvis, Charles A. Brau
Department of Physics & Astronomy, Vanderbilt University, Nashville, TN 37235, U.S.A.

Abstract

We present further developments to the theory of Smith-Purcell free-electron lasers [1] (SPFELs) and characterization of a blunt needle cathode electron source in use to test the theory. The theory of SPFELs has been refined to include the effects of resistive losses on the evanescent surface wave supported by the grating and reflections of the wave from the ends of the grating. Losses are included directly in the grating dispersion relation and the reflections appear in the boundary conditions for the growing wave. Based on earlier work in sharp needle cathodes [2,3], an yttrium metal blunt needle cathode has been developed for the purpose of driving a SPFEL device. Space charge expansion of the beam in the transverse direction and aberration in the electron optics place limitations on the useful beam that can be generated. Both experimental and simple analytical characterizations of these limitations are presented and considered in light of the requirements of the SPFEL.

SPFEL THEORY

Smith-Purcell (SP) radiation is generated when an electron beam passes close to a grating. The virtual photons of the field of the electrons are scattered by the grating, and the wavelength λ_{SP} observed at an angle θ is

$$\lambda_{SP} = \frac{L}{|m|}\left(\frac{1}{\beta} - \cos\theta\right) \quad (1)$$

where L is the grating period, m is the diffraction order, βc is the electron velocity, and c is the speed of light. The angular spectral fluence of this radiation is described by several authors [4,5,6]. The intensity of the SP radiation falls off exponentially with the distance between the beam and the grating, with a characteristic length

$$h = \frac{\beta\gamma\lambda_{SP}}{4\pi} \quad (2)$$

where γ is the Lorentz factor for the electron beam [6].

When the electron beam current over the grating is sufficiently high, the interaction between the electrons and the fields above the grating becomes nonlinear, and the electrons become bunched. Periodic bunching of the electron beam intensifies the SP spectrum coherently [7]. Nonlinear emission with increasing beam current has been observed at Dartmouth College using a modified scanning electron microscope as a beam source [8,9].

The interaction between the electron beam and the fields above the grating is significant only for a grating surface wave whose phase velocity is equal to the electron velocity. The dispersion relation for a lamellar grating without external mirrors has been calculated by matching the boundary conditions for fields inside the grooves of the grating to a set of Floquet modes above the grating [10].

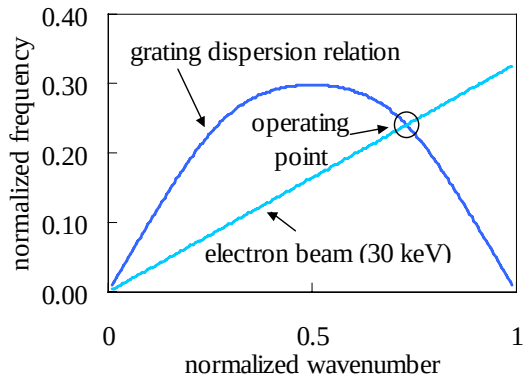

Figure 1. Grating dispersion relation showing synchronous solution

The electron beam is synchronous with a single evanescent mode of the grating, as shown in Fig. 1. The evanescent mode does not itself radiate except by scattering at the ends of the grating, and the wavelength of the mode is always longer than the lowest-order SP band. The SP radiation spectrum is coherently enhanced, however, at harmonics of the bunching frequency dictated by the wavelength of the synchronous evanescent wave.

The group velocity (the slope of the dispersion relation) at the synchronous point can be positive or negative, depending on the electron beam energy. The energy flow in the evanescent wave, therefore, can be copropagating or counterpropagating with respect to the electron beam. At high electron energy, the energy flow is copropagating, and the device operates on a convective instability as does a traveling wave tube amplifier. At low electron energy, the energy flow is counterpropagating and the device operates on an absolute instability in the manner of a backward wave oscillator. In the oscillator case, feedback is provided by the backward moving wave even in the absence of mirrors. At some intermediate energy, the synchronous point on the dispersion relation coincides with the Bragg point, where the group velocity v_g vanishes.

#charles.h.boulware@vanderbilt.edu

EFFECT OF LOSSES

The gain coefficient for the evanescent wave in either the amplifier or oscillator regime can be calculated by expanding the grating dispersion relation around the synchronous point. A dimensionless expression for this expansion (without losses) is

$$\left(\delta\omega - v_g\delta k\right)\left(\delta\omega - \beta c\delta k\right)^2 = \Delta \qquad (3)$$

where $\delta\omega$ is the frequency deviation from the synchronous point, v_g is the group velocity, δk is the wavenumber deviation, and

$$\Delta = \frac{\omega_p^2 G}{\gamma^3} \qquad (4)$$

where G is a constant that depends on the grating profile. The gain coefficient of the device varies as $\left|v_g\right|^{-1/3}$, which diverges near the Bragg point. However, the resistive losses in the grating have an attenuation coefficient that varies as $\left|v_g\right|^{-1}$, which diverges at the same point [1].

Resistive losses also introduce a real phase change. To see this, we consider a short section of grating as a resonant cavity by imagining perfect reflectors at each end. Small resistive losses in the grating surface then introduce a frequency shift given by

$$\delta\omega = -\frac{\langle Q\rangle}{2\langle U\rangle}(1+i) \qquad (5)$$

where $i=\sqrt{-1}$, Q is the power loss into the grating resistance, U the energy density in the surface wave, and the angled brackets represent averages over one period of the grating and one cycle of the wave [11]. The correct dispersion relation with losses is therefore

$$\left(\delta\omega - v_g\delta k + \frac{\omega_0}{2Q_c}(1+i)\right)\left(\delta\omega - \beta c\delta k\right)^2 = \Delta \qquad (6)$$

EFFECT OF REFLECTIONS

Equation 6 admits three solutions: a grating structure wave and so-called fast and slow space-charge waves. The three waves are locked together in frequency to form a single mode, but have slightly different wavenumbers and correspond to very different plasma dielectric susceptibilities. Interference allows the waves to satisfy boundary conditions at the ends of the grating. At the upstream end of the grating, the electron beam enters with uniform distributions of both density and velocity. In the absence of reflections, the electric field vanishes at the downstream end. These three boundary conditions are

$$\sum_{j=1}^{3}\frac{A_j}{\left(\delta\omega - \beta c\delta k_j\right)^2} = 0 \qquad (7)$$

$$\sum_{j=1}^{3}\frac{A_j}{\delta\omega - \beta c\delta k_j} = 0 \qquad (8)$$

$$\sum_{j=1}^{3} A_j e^{i\delta k_j Z} = 0 \qquad (9)$$

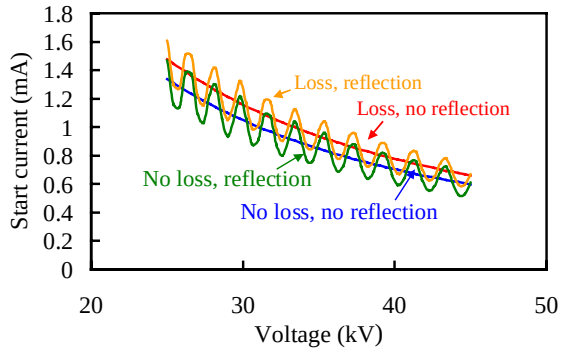

Figure 2. Effect of reflections on the start current as a function of beam voltage

where the index j represents the three different solutions of the dispersion relation expansion, A_j is the relative amplitude of the three waves, and Z is the length of the grating [1].

These boundary conditions can be refined to include reflections from the ends of the grating and losses in the reflected wave. When this is done, the last boundary condition becomes

$$\sum_{j=1}^{3}\left(e^{-i\delta_j Z} - Re^{i\delta_0 Z}\right) = 0 \qquad (10)$$

where

$$\delta_j = \frac{\delta\omega}{\beta c} - \delta k_j, \qquad (11)$$

$$\delta_0 = \frac{\beta+\beta_g}{\beta\beta_g c}\delta\omega + \frac{\beta+\beta_g}{\beta-\beta_g}\nu(1+i), \qquad (12)$$

R is the (complex) round-trip reflection coefficient, and $\nu = \langle U\rangle / 2v_g\langle Q\rangle$ is the empty grating loss coefficient. The boundary conditions are solved with the dispersion relation as a constraint. The effect of the reflection coefficient is to increase or decrease the computed growth rate according to whether the phase shift on reflection leads to constructive or deconstructive interference with the backward waves. The start condition for oscillation is that the growth rate, the imaginary part of the frequency, be positive. Details on the calculation of reflection at the grating ends and the inclusion of losses in the grating dispersion relation can be found elsewhere [12].

The condition for oscillation can be expressed as a start current. Figure 2 shows start current as a function of voltage for the parameters of the Dartmouth experiments [8]. The interference effects resulting from a nonzero reflection coefficient are clearly observed. The observed start current is on the order of 1 mA, in agreement with the experiments. However, the two-dimensional theory described here should underestimate the start current. We expect the diffraction width of the mode on the grating to be on the order of $\sqrt{Z_g / k} \approx 1\,\text{mm}$, where Z_g is the gain length of the evanescent wave, and k is the wavenumber at the operating point. This width is much greater than

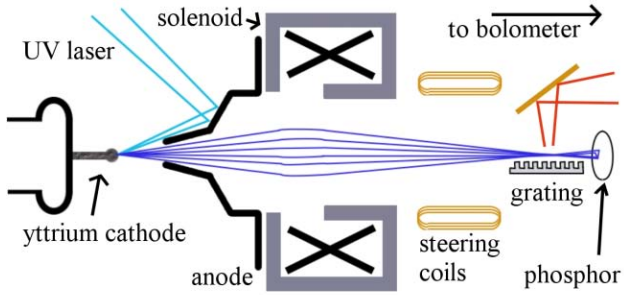

Figure 3. Schematic of electron source and focusing/steering magnets

the transverse size of the electron beam, thus reducing the effective interaction and raising the start current.

BLUNT NEEDLE CATHODES

The short vertical coupling length h between the electron beam and the grating makes necessary a high-brightness electron source for a SPFEL device. Sharp needle cathodes made of tungsten have been investigated as high-brightness electron sources [2,3]. The photoelectric quantum efficiency of photoemission from the tungsten metal is enhanced by several orders of magnitude at the high surface electric fields (up to 10^{10} V/m) that can be obtained at the 1 μm-radius tip of a chemically etched tungsten needle. At these fields, the Schottky effect reduces the barrier for electron emission by as much as 2.5 eV. The electron beams created from these sharp tips are highly divergent and difficult to focus.

A less divergent electron beam can be obtained from a blunt needle cathode with a tip radius on the order of 1 mm. The surface field is reduced to 10^7 V/m, but the loss in quantum efficiency can be mitigated by changing the needle material from tungsten to yttrium. Yttrium has a lower work function than tungsten (2.9 eV compared to 4.5 eV), so a reduction of the barrier by the Schottky effect is not necessary to enhance the quantum efficiency. At 10^7 V/m, for example, the Schottky effect is only 0.1 eV, but the effective work function of an yttrium cathode is similar to a tungsten cathode at 10^9 V/m.

The needle-cathode device at Vanderbilt University uses an yttrium cathode with a ≈ 700 μm radius spherical tip at the end of a 10 mm long square rod. Removal of adsorbate molecules from the yttrium surface is critically important to the quantum efficiency of the cathode. We use electron bombardment to raise the surface of the metal to its melting point (1800 K) for several seconds to produce a clean, smooth surface. The partially-covered cathode is held at a positive potential of 2-3 kV, and bombarding electrons are provided by a tungsten ion gauge filament positioned close to the cathode. The heating process is unstable when both the filament and the cathode tip are hot. Yttrium deposited on the tungsten filament lowers its work function, increasing the thermionic emission.

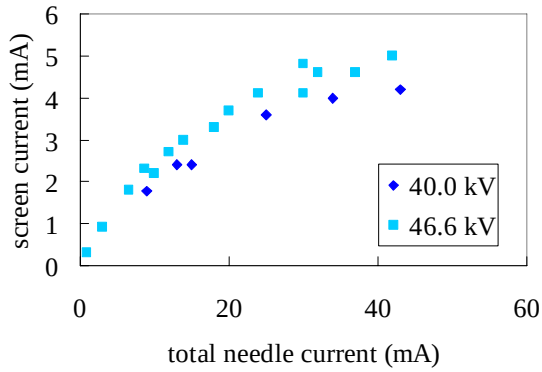

Figure 4. Current detected at the phosphor screen as a function of total needle current

After cleaning, the cathode is illuminated with a quintupled Nd:YAG laser (4-ns pulses at 20 Hz, <1 μJ per pulse, 5.9 eV per photon). Peak currents of 50 mA are produced reliably, corresponding to a QE of ~10^{-3}. The laser is focused on the cathode with a spot radius of 20 μm to give a current density at the source of $J_e \approx 10^7$ A/m^2. For an electron temperature $T_e \approx 1$ eV, the normalized brightness of the source is

$$B_N = \frac{m_e c^2 J_e}{2\pi k_B T_e} \approx 10^{12} \text{ A/m}^2\text{-steradian} \qquad (13)$$

where m_e is the electron mass and k_B is the Boltzmann constant [13].

A schematic of the experiment is shown in Fig. 3. A conical anode allows the ultraviolet laser light to enter the chamber from the side and be reflected by a mirror to the needle tip. The electron beam is focused by a 500-turn solenoid in an iron yoke designed to minimize the effective needle-lens distance, and therefore, the size of the beam in the lens. Steering coils direct the beam past an aluminum grating to a phosphor screen, which also serves as a Faraday cup. A fused quartz window above the grating allows millimeter-wave radiation to be collected by a He-cooled InSb bolometer. SP radiation above the bolometer noise level has yet to be detected.

The usable beam current from the needle cathode is limited by the fraction of the beam that can be collected and focused. Space-charge forces play a significant role in the divergence of the beam at the source, and the usable beam current increases sublinearly with total needle current at high laser intensities, as shown in Fig. 4. The importance of the space-charge effect is somewhat less at higher accelerating voltages. At 60 kV, with laser power at the needle damage threshold, 5 mA (about 10%) of the total beam current reaches the phosphor screen.

The spot size of the electron beam at the grating can be affected by aberration in the solenoid focusing magnet, beam emittance, and space charge at the beam focus [13]. The generalized perveance for a uniform round beam is

$$K = \frac{2I}{\beta^3 \gamma^3 I_0} \qquad (14)$$

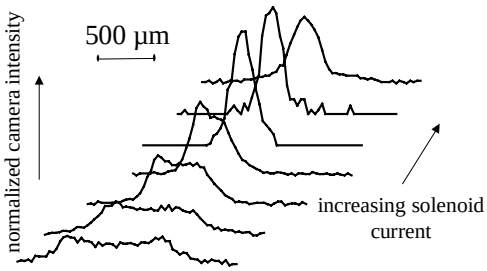

Figure 5. Transverse beam profiles show the effect of spherical aberration upstream of the electron focus

where I is the current in the beam, $I_0 = 4\pi\varepsilon_0 m_e c^3 / q_e$, ε_0 is the vacuum permittivity, and q_e is the electron charge. In terms of the generalized perveance, the space-charge dominated beam radius is

$$r = Ae^{\frac{-\alpha^2}{2K}} \tag{15}$$

where A is the beam aperture at the lens and α is the convergence angle. The space-charge limitation on the focal spot for the Vanderbilt device is less than 1 μm.

The calculated brightness of the yttrium blunt needle source corresponds to an emittance of $\varepsilon \approx 10^{-7}$ m for 5 mA current at the grating. The limitation posed by the emittance on the spot size at the focal point is

$$r = \frac{\varepsilon}{\alpha} \tag{16}$$

which corresponds to a 10 μm spot above the grating.

The limitation on the spot size resulting from spherical aberration in the focusing solenoid is independent of the beam current. Expanding the magnetic field near the axis and keeping terms up to third order in the transverse distance from the axis gives a radial dependence on the focal length of the solenoid (spherical aberration)

$$\frac{1}{f} = \frac{q_e^2}{4m_e^2\beta^2c^2}\left[\int_{-\infty}^{\infty} B_z^2 dz + \frac{5r^2}{8}\int_{-\infty}^{\infty}\left(\frac{dB_z}{dz}\right)^2 dz\right] \tag{17}$$

where B_z is the axial magnetic field and r is the transverse distance from the axis. The dependence of focal length on the transverse position of electrons entering the solenoid produces a spot size (at the circle of least confusion) of

$$r = \frac{5q_e^2}{128m_e^2\beta^2c^2} f_0 A^3 \int_{-\infty}^{\infty}\left(\frac{dB_z}{dz}\right)^2 dz \tag{18}$$

where f_0 is the paraxial focus of the lens. The aberration-limited spot size varies with the cube of the aperture size at the final lens. For the Vanderbilt experiment, this spot size is 125 μm at 60 kV and represents the dominant contribution to the radius of the beam at the circle of least confusion.

The size of the electron beam is measured by scanning the beam across a knife edge or by analyzing images of the phosphor screen. Images of the screen are captured with a CCD camera and provide differential current density across the beam. By changing the solenoid field strength, the beam is scanned through its focus. The effects of spherical aberration are observed clearly as an intense beam edge upstream of the electron focus. Several transverse current profiles at different lens strengths appear in Fig. 5. The measured radius at the beam waist is 200 μm, dominated by spherical aberration.

CONCLUSIONS

Detailed effects of losses and reflections have been incorporated into the theory of SPFELs. The modified dispersion relation for the grating evanescent wave gives both the attenuation and phase shift due to resistive losses. The effects of reflection at the grating ends are accounted for in the boundary conditions on the three waves that comprise the grating mode. The start current calculated in this way agrees with the Dartmouth experiments, though the two-dimensional treatment neglects diffraction of the evanescent mode in the transverse direction, which should increase the start current.

Experiments are underway using the yttrium cathode device at Vanderbilt to drive the oscillator-regime operation of a SPFEL. Spherical aberration limits the spot size of the electron beam in the Vanderbilt device, reducing the effective current interacting with the evanescent wave. Aperturing the beam to reduce spherical aberration also reduces the fraction of total needle current to the grating.

REFERENCES

[1] H. L. Andrews, C. H. Boulware, C. A. Brau, and J. D. Jarvis, Phys. Rev. ST-AB **8**, 050703 (2005).
[2] C. Hernandez Garcia and C .A. Brau, Nucl. Inst. Meth. Phys. **A483**, 273 (2002).
[3] C.H. Boulware and C.A. Brau, Free Electron Lasers 2002, K.-J. Kim, S.V. Milton, E. Gluskin (eds.), Elsevier Science B.V., II-47 (2003).
[4] P.M. van den Berg and T.H. Tan, J. Opt. Soc. Am. **64**, 325 (1974).
[5] L. Schaechter, *Beam-Wave Interaction in Periodic and Quasi-Periodic Structures* (Springer-Verlag, Berlin, 1996).
[6] Y. Shibata *et al*., Phys. Rev. E **57**, 1061 (1998).
[7] H. L. Andrews, C. H. Boulware, C. A. Brau, and J. D. Jarvis, Phys. Rev. ST-AB **8**, 110702 (2005).
[8] J. Urata *et al*., Phys. Rev. Lett. **80**, 516 (1998).
[9] A. Bakhtyari, J.E. Walsh, and J.H. Brownell, Phys. Rev. E **65**, 066503 (2002).
[10] H. L. Andrews and C. A. Brau, Phys. Rev. ST-AB **7**, 070701 (2004).
[11] J. D. Jackson, *Classical Electrodynamics*, 3rd edition (Wiley, New York, 1999), p. 374.
[12] H. L. Andrews, C. H. Boulware, C. A. Brau, J. T. Donohue, J. Gardelle, and J. D. Jarvis, submitted manuscript.
[13] J. D. Lawson, *The Physics of Charged Particle Beams*, *Clarendon Press*, Oxford, 1988.

EMITTANCE COMPENSATION OF SUPERCONDUCTING GUN AND LINAC SYSTEM FOR BEAMS WITH LARGE CHROMATIC VARIANCE

B. Buckley, Cornell University, Ithaca, NY 14853, USA
D. Kayran, V. N. Litvinenko,
Collider Accelerator Department, Brookhaven National Laboratory, Upton, NY 11973, USA*

Abstract

Among the methods of emittance compensation for a superconducting rf gun and linac system include utilizing a solenoid and drift space after the gun to achieve a specific beam envelope with zero beam divergence before entrance into the linac. Studies on this method have assumed minimal energy spread in the beam. However, in cases where chromatic effects cannot be ignored this one solenoid emittance compensation technique is inadequate. Proposed is a new method of emittance compensation utilizing two solenoids in order to minimize emittance in beams with large energy spread. We present a theoretical basis for the new technique along with a computer optimized configuration. The results are compared with previous methods of emittance compensation.

INTRODUCTION

First introduced by Carlsen [1] and expanded upon theoretically by Serafini and Rosenzweig [2] is a scheme for emittance compensation for an rf gun and linac system that uses a solenoid magnetic field to compensate for space charge defocusing. Chang et al. [3] extended the method for systems with a superconducting gun for which the solenoid must be placed outside the gun. Such studies and further experiments have achieved good emittance compensation results for beams with little energy spread [4].

Touched upon by Chang et al. are the effects on emittance caused by varying energy along the bunch. Energy dependence in solenoid focusing, space charge defocusing and linac ponderomotive focusing leads to emittance increases when large energy spread in the bunch is present. Previous studies have laid the foundation for cancelling out chromatic effects at the linac entrance [3]. However, there are other important chromatic effects that should be looked into.

In this paper we study the chromatic effects of the solenoid focusing and space charge defocusing. We introduce a method for compensating for emittance increases caused by these effects by adding a second solenoid. The mechanism of this emittance compensation scheme is studied with analysis of the beam through the system. The relationship between the placement and strengths of the two solenoids is studied theoretically and compared to a computer optimized setup. Finally, this two solenoid method is compared to the one solenoid method by running Parmela [5] simulations with both setups and comparing final normalized emittance values. We find that the two solenoid method is superior to the one solenoid method at minimizing emittance at the exit of the linac.

* Work performed under the auspices of the U.S. Department of Energy

EMITTANCE COMPENSATION

The essence of the emittance compensation method described in detail in Ref [2] involves focusing the diverging beam immediately after the gun with a solenoid and reaching a point of zero convergence after a drift space at which point the beam enters the linac. The solenoid field must be of a certain strength in order to have the beam enter the linac at the invariant envelope of the linac. This envelope is given by:

$$\hat{\sigma} = \left(\frac{2}{\gamma'}\right)\cdot\sqrt{\frac{I}{3I_A\gamma}} \tag{1}$$

where I_A= 17,054 A is the Alfven current, I is the current in the beam, and γ' is the average accelerating gradient of the linac. Entering at this envelope with zero divergence, the beam will exit the linac with zero divergence and with an envelope satisfying Eq. (1).

Chromatic Effects

Chromaticity comes into play in the energy dependence of the solenoid, space charge and linac focusing. As previously stated, we will not focus on the latter in this paper.

The envelope equation for a cylindrical space charge dominated beam through a focusing element, in this case a solenoid, is given by [2]:

$$\sigma'' = -\alpha_S\sigma + \frac{Q\beta c}{2I_A\sigma_z(\gamma\beta)^3\sigma} + \frac{\varepsilon_n^2}{(\gamma\beta)^2\sigma^3} \tag{2}$$

where ε_n is the normalized emittance and α_S is the solenoid focusing strength

$$\alpha_S = \left(\frac{eB}{2\gamma\beta mc}\right)^2 \tag{3}$$

where e is the charge of electron and B is the magnetic field of the solenoid. From the dependence on γ in each of these terms one can see that slices along the bunch with different energies will transform differently through the solenoid-drift space element.

ANALYSIS OF PHASE SPACE ANGLE

To illustrate these chromatic effects on the emittance we take a look at the transformation of the phase space angle

$$\theta = \frac{\sigma'}{\sigma} \tag{4}$$

through the solenoid and drift space elements.

Through Solenoid

In this analysis we will assume a small solenoid length in which no change in σ occurs, focusing only on the first term on the right hand side of Eq. (2). Taking the integral and dividing by σ we achieve

$$\Delta\theta = -\alpha_s L \tag{5}$$

with L the length of the solenoid.

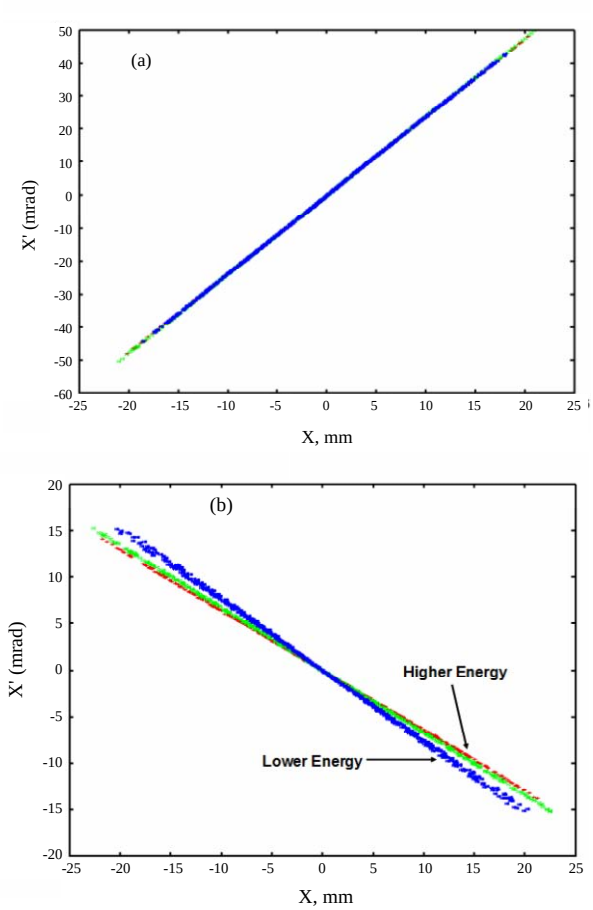

Figure 1: Phase space plots of three different slices of varying energy. Average energy of 2.5 MeV, energy spread of 3% and a total charge of 5nC, one of the possibilities for the RHIC e-cooling project at Brookhaven National Laboratory [6]. (a) Slices aligned before solenoid, immediately after gun. (b) Slices misaligned after solenoid focusing.

From Eq. (3) the dependence on energy is clear. Figures 1(a) and 1(b) illustrate the effect on the phase space distributions of three slices of varying energy. After the solenoid the phase space slices are no longer aligned leading to a rise in projected emittance.

Through Drift Space

For beam parameters typical for BNL's ERL injector (Q ~ 1 nC, γ ~ 5, $\sigma_z \sim \sigma$ ~ 1cm, and a normalized slice emittance of ε_n ~1 mm·mrad) the ratio between third and second terms on the right of Eq. 2 is very low: $I_A\sigma_z\gamma\varepsilon_n^2/Qc\sigma^2 \sim 5\cdot10^{-5}$. Hence, only the second term on the right side of the envelope equation is necessary:

$$\sigma'' = \frac{P}{\sigma}; \tag{6}$$

$$P = \frac{Q\beta c}{2I_A\sigma_z(\gamma\beta)^3} \tag{7}$$

with P being the perveance, a function of energy. Near the waist, the envelope can be approximated by a parabola [7]:

$$\sigma \cong \sigma_w + \frac{P(z-z_w)^2}{2\sigma_w} \tag{8}$$

with divergence of

$$\sigma' \cong \frac{P(z-z_w)}{\sigma_w} \quad . \tag{9}$$

Dividing the two we obtain a phase space angle of

$$\theta \cong \frac{2P(z-z_w)}{2\sigma_w{}^2 + P(z-z_w)^2} \quad . \tag{10}$$

The envelope at the waist is given by integrating the differential equation of Eq. 6 to obtain the equivalent first order differential equation and rearranging to achieve

$$\sigma_w = \sigma_i e^{-\frac{\sigma_i'^2}{2P}} \quad . \tag{11}$$

The position at the waist is found by taking the equivalent integral equation of Eq. 6 and using a polynomial approximate solution [3]:

$$z_w \cong \frac{\sigma_i}{\sqrt{P}}\left(.009165+.95449\frac{\sigma_i'}{\sqrt{P}}+.21824\frac{\sigma'^2{}_i}{P}\right) . \quad (12)$$

From these equations we are able to analyze how the spread in the phase space angle varies through the solenoid and drift space. In Fig. 2 we plot the difference in angle between the head and tail slices of the same bunch from Fig. 1, the head having a higher energy than the tail.

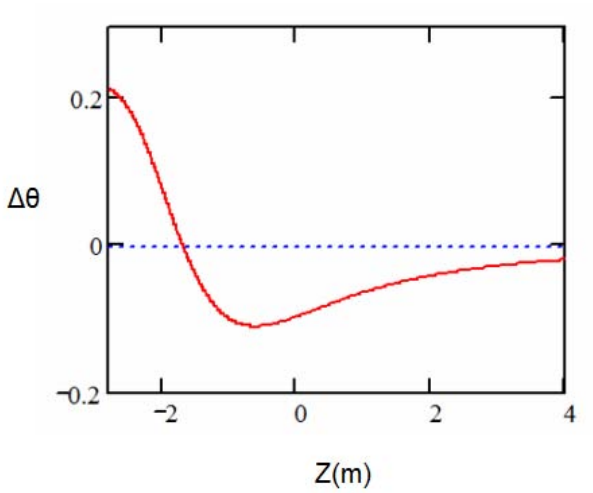

Figure 2: Difference between higher energy and lower energy slices in bunch immediately after solenoid. The beam waist occurs at z = 0 meters. The calculations and plots were done with Mathcad [8].

The plot begins after the solenoid at the maximum spread in angle and continues through drift space. We see that the slices align before z=0, the waist position, and are thus misaligned at the waist. This leads to a non-optimized emittance before entrance into the linac.

What one notices is that since the lower energy slices rotate past the higher energy slices it would be possible to use a second solenoid to realign the slices in phase space. The above equations allow one to calculate the spread in θ after an arbitrary distance and thus the relationship between the solenoid strengths of the first and second solenoids and the distance between them, which would result in realignment of the phase space slices.

OPTIMIZATION

A two solenoid, rf gun and linac system was optimized for lowest normalized emittance by optimizing position and field strengths of the two solenoids and position of the linac. Plots of normalized emittance and envelope can be found in Fig. 3 where they are compared to the same plots for a non-optimized one solenoid setup. The one solenoid configuration is set up following the invariant envelope method [2]. Since it is not optimized, looking at final emittances does not make for a definitive comparison. Instead, the plots serve to illustrate the overall advantage the two solenoid method has over the invariant envelope one solenoid method when dealing with large energy variation.

The optimized magnetic fields of the first and second solenoids and drift length between them are respectively 854 Gauss, 607 Gauss and 333.9 cm. To test the accuracy of the above equations describing the alignment of phase space slices we use them to calculate the magnetic field of the second solenoid, which would realign the phase space slices with all other optimized parameters unchanged. We obtain a theoretical magnetic field strength of roughly 520 Gauss for the second solenoid. This is significantly lower than the optimized value above. However, when comparing standard deviations in θ with 500 slices we find that the theoretical value has a lower spread in θ, .0846 inverse meters, than does the optimized value, .0897 inverse meters. This should not come as a surprise as the theoretical calculation minimized spread in θ after the second solenoid while the optimized value minimized normalized emittance after the linac, not necessarily minimizing spread in θ. What the comparison of spread in θ does is validate the accuracy of our theoretical approach, even if it should not be used as the exact value when attempting to minimize emittance.

DISCUSSION AND CONCLUSION

We have introduced a new method of emittance compensation that has advantages compared with previous methods using one solenoid in minimizing emittance of beams with significant energy spread. Our theoretical analysis of the transformations of phase space angle due to solenoid focusing and space charge defocusing has proven to be accurate and may serve as a basis for future analysis into this new emittance compensation scheme.

Further studies however must be undertaken in order to gain a better understanding of this new method. Firstly, alignment of sliced phase space angles is not the only parameter affecting total normalized emittance. Individual sliced emittances must also be minimized along with spread in slices and the two might not be simultaneously minimized. Studies into optimizing spread in θ after the linac have resulted in increases in normalized emittance.

Another aspect that should be looked into further are the chromatic effects of the linac focusing. As seen in Fig. 3, for the optimized two solenoid set up the beam does not enter the linac at the waist as is deemed necessary in previous one solenoid methods. Instead the beam enters at a significant convergence. Non-linearities

in the linac focusing due to this convergent entrance perhaps might be playing a large role in minimizing individual sliced emittances. Efforts at moving the linac further from the second solenoid have not resulted in lower values of normalized emittance.

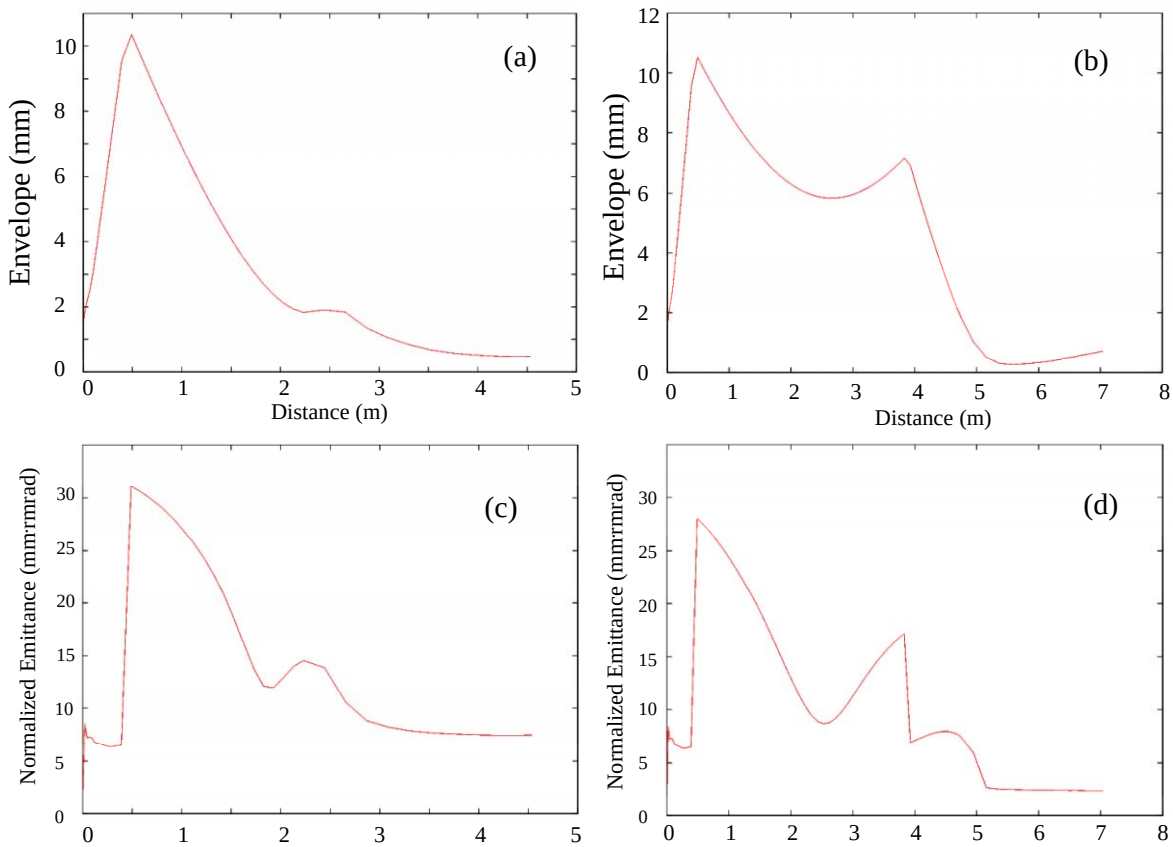

Figure 3: Comparison of one solenoid and two solenoid methods: Electron beam envelope with one solenoid (a) and two solenoids (b). (c) Normalized projected emittance with one solenoid (c) and two solenoids (d).

REFERENCES

[1] B. Carlsen, "New Photoelectric Injector Design for the Los Alamos National Laboratory XUV FEL Accelerator", NIM A285 (1989) 313-319.

[2] L. Serafini and J. B. Rosenzweig, "Envelope Analysis of Intense Relativistic Quasilaminar Beams in RF Photoinjectors: A Theory of Emittance Compensation", Phys. Rev. E 47, 2031 (1993).

[3] X. Chang, I. Ben Zvi, and J. Kewisch, "Emittance Compensation of Compact Superconducting Guns and Booster Linac System", PRST-AB 9, 044201 (2006).

[4] X. Qui, K Batchelor, I Ben-Zvi, and X-J Wang, "Demonstration of Emittance Compensation through the Measurement of the Slice Emittance of a 10-ps Electron Bunch", Phys. Rev. Lett. 76, 3723-3726 (1996).

[5] L. M. Young, Los Alamos National Laboratory Report No. LA-UR-96-1835 (revised 2001).

[6] V. Parkhomchuk and I. Ben-Zvi, Brookhaven National Laboratory Report No. C-A/AP/47, 2001.

[7] M. Reisner, Theory and Design of Charged Particle Beams (John Wiley and Sons, New York, 1994), p. 201

[8] Mathcad 2000, Reference Manual, MathSoft Inc., 101 Main Street Cambridge, Ma 02142, USA

FREE ELECTRON LASER STUDY OF FREE CARBON CLUSTERS

C. Spezzani*, E. Allaria, M. Coreno, F. Curbis, B. Diviacco, G. De Ninno, L. Romanzin, S. Tileva, M. Trovò, Sincrotrone Trieste, Strada Statale 14 - km 163.5, 34012 Basovizza, Trieste ITALY

M. Amati, G. Bongiorno, C. Lenardi, T. Mazza, P. Milani, T.A. Mostefaoui, P. Piseri, L. Ravagnan, Dipartimento di Fisica and CIMAINA, Università degli Studi di Milano, I-20133 Milano, ITALY.

Abstract

UV absorption from carbon nanoparticles is a very interesting astrophysical topic. The prominent hump centred at 217.5 nm is the most dominant feature in the interstellar extinction curve and also the most controversial and a long-standing problem in astrophysics. At the University of Milano an experimental set-up based on a Pulsed Microplasma Cluster Source has been developed for the investigation of free clusters at the Elettra Gas Phase beamline. The cluster source produces very intense cluster beams with tunable size distribution. The design of the apparatus is extended with a chamber for gas phase reaction (water vapour, CO, H_2...) providing a unique opportunity to study the gas phase properties of carbonaceous particles in different environments.

We plan to investigate Resonant Raman scattering of free carbon particles tuning the high brilliance UV/VIS storage ring FEL of ELETTRA across the region of 217.5 nm where the UV absorption hump in astrophysical data is observed and where a number of electronic transitions exist for variable size linear carbon chains.

INTRODUCTION

Since its discovery by Stecher (1965), the ultraviolet extinction curve feature observed at 217.5 nm has been attributed to π-electron plasmon absorption or π-π * band transitions in small graphite particles or amorphous carbon grains. Despite the early assignment to carbonaceous material, the exact physical nature of the carrier is still unknown and strongly debated. One peculiar behaviour of the 217.5 hump is the constancy of its spectral position regardless of the choice of the astronomical object under observation [1]. On the other hand, the peak position of the bump predicted for graphite particles is quite sensitive to grain size, shape and adsorbate coatings, which is inconsistent with the observations.

Many different models have been proposed to explain the experimental observation and many different attempts have been made to reproduce in laboratory an adequate prototype for cosmic dust [2,3,4]. Experiments conducted on hydrogenated carbon nanoparticles isolated in noble gas matrix pointed out the relevance not only of particle shape and size but also of their chemical environment [1]. Other observations indicate that the presence of an ice mantel surrounding the carbon particles strongly influence their UV optical response [3]. Other authors have succeeded in synthesizing carbon aggregates that show optical constants fitting quite well the extinction curve [4, 5], but, the adopted methods don't match very well with the environment conditions where carbon grains in the intergalactic medium are expected to form.

Actual models of dust astrophysics lack of experimental data about carbon dust in gas phase, their optical proprieties, mass distribution, reactivity and of course their absorption of the UV light in the 217 nm region. In order to attempt a meaningful reproduction, at the laboratory scale, of this astrophysical system it is important to study carbon clusters in isolated condition, as a function of their dimension and chemical environment. Recently the potential of optical spectroscopy in free jet expansion for experiments on astrophysically relevant species has been demonstrated [6].

Resonant Raman Scattering (RRS) is a powerful technique for the characterization of such a system. It combines the sensitivity to vibrational properties of carbon structures relevant for astrophysics like carbyne [7, 8] with a selective transfer of energy when the exciting photons are tuned at the energy corresponding to a given resonance, increasing in this way the scattering cross-section.

We present here an experimental setup for a RRS study of free carbon clusters which make use of the storage ring Free Electron Laser (SRFEL) radiation.

EXPERIMENTAL SETUP

This section quickly reviews the experimental setup that we are developing at ELETTRA in the framework of the collaboration between the CIMAINA of Milan University and the SRFEL group of ELETTRA, Trieste.

CESyRA

CESyRA (Cluster Experiments with Synchrotron RAdiation) [9] is a research project of the CIMAINA focused on free cluster spectroscopy with the high intensity UV and soft X-ray light from the ELETTRA synchrotron radiation facility.

* e-mail: carlo.spezzani@elettra.trieste.it

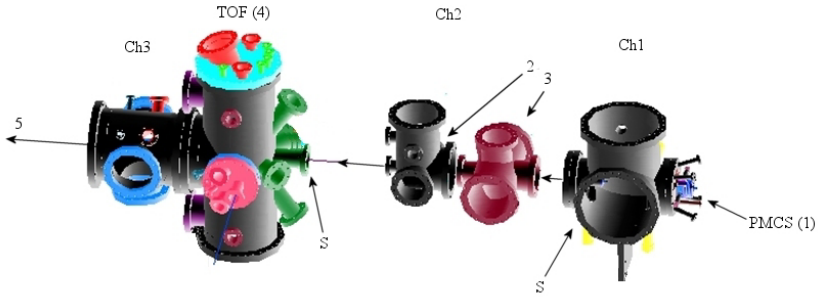

Fig. 1: Main elements of CESyRA apparatus: (Ch1) expansion chamber, (Ch2) deposition and gas exposure chamber, (Ch3) TOF, (1) PMCS, (2) manipulator, (3) gas line, (4) TOF, (5) to dumping chamber and quartz microbalance.

The experiments are implemented in a UHV compatible supersonic cluster beams apparatus. The main constituents of the system are sketched in figure 1. Briefly, it consists of three differentially pumped, high-vacuum chambers (Ch1, Ch2 and Ch3) separated by two skimmers (S). Heart of CESyRA apparatus is the Pulsed Microplasma Cluster Source (PMCS) [10,11], developed at the Molecular Beam and Nanocrystalline Materials Laboratory in Milano, which is able to deliver highly collimated and intense seeded beams of clusters from refractory materials (typical deposition rate for carbon: 100 μm/h at 500 mm source-substrate distance, ~ 0.8 cm^2 covered area). The PMCS is based on target ablation obtained by He plasma sputtering: a pulse of He flux is directed against a target by means of a valve driven by an electromagnet (opening time of about 300 μs). The gas is then ionized by a pulsed discharge fired between the target rod (cathode) and the anode. The sputtered particles are carried through an aerodynamic lens system by the He flow and the mixture eventually undergoes a supersonic expansion into a high vacuum chamber. In order to prevent the formation of holes on the cathode rod and to reduce the need for source maintenance, since the ablation is extremely localized, the target rod is maintained in rotation during source operation (see figure 2). The clusters are emitted in pulses that propagate at a speed of about 1000 m/s and that last typically 15 ms. Lighter aggregates are mostly located at the head of the pulse while the heavier ones at the tail.

The PMCS is located outside vacuum and communicates through the nozzle with the expansion chamber (Ch1). The beam passes through a skimmer that, due to particle focusing on the beam axis [12], efficiently separates the clusters from the carrier gas. In the second chamber a gas cell is installed to allow gas exposure of the free particles in the beam (3). A diaphragm separates the second from the third chamber (2) to produce differential vacuum and finally the beam is directed into an interaction chamber where a short linear time of flight (TOF) mass spectrometer is mounted perpendicularly to the plane formed by the intersection of the light and cluster beams (4). A sample manipulator is mounted, in order to intercept the beam and thus to allow cluster deposition onto a substrate. Finally, the beam is dumped onto a quartz microbalance (5) that monitors the cluster flux.

The SRFEL of ELETTRA

The CESyRA setup has primarily been thought for application with synchrotron radiation on refractory materials in gas phase, demonstrating for the first time the possibility of performing XAS measurements on free Ti nanoparticles [13]. However, for this particular application on carbon clusters, the requirements on the light source that has to be used make the SRFEL of Elettra [14] the best candidate for our objective. To probe the cluster beam in gas phase, we need a very high flux of photon with a wavelength that can be precisely tuned around 217.5 nm (5.7 eV). In this respect, the Elettra SRFEL can produce a very bright monochromatic beam that can be directed into the interaction volume by means of few optical elements, minimizing the photon flux losses due to radiation transport.

The maximum average lasing power that can be achieved using a SRFEL is limited by the heating of the electron beam induced by the laser onset [15, 16]. The increase of the electron-beam energy spread is indeed responsible for the diminution of the optical gain while, at

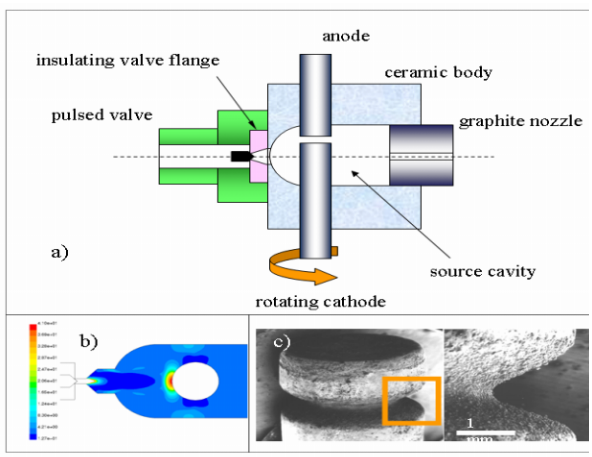

Fig. 2: a) schematic diagram of the PMCS source; b) pressure contour plot of He jet inside the PMCS cavity (see ref [11]); c) scanning electron microscope micrographs of the cathode region eroded by the plasma. The cathode is continuously rotated in order to prevent the formation of holes. A very smooth and precise trace formed by plasma erosion is clearly distinguishable.

saturation, the latter reaches the level of the optical cavity losses. However, for applications requiring a high peak power, the FEL power can be ‘‘concentrated’’ into a series of giant pulses, applying the so-called Q-switching regime. In this case, the peak power is considerably enhanced (one to few orders of magnitude) while the average power is only slightly reduced [17]. To operate the SRFEL in Q-switching, we apply a modulation on the radiofrequency (RF) that drives the electron bunches in the storage ring (figure 3a) [18]. The giant pulses that we obtain are typically 100 μs long (figure 3c). The development of a giant pulse introduce a quite big energy spread that implies a recovery time for the dumping of the electron beam of the order of 10~100 ms. For this reason Q-switching is normally operated at a repetition rate of few Hz (figure 3a and 3b). In RRS experiment setup, the RF modulation is triggered after a variable delay by the opening of the He valve in the clusters source. Adjusting the delay we are able to probe, with the highest power available, different parts of the cluster pulse and therefore sample cluster populations with different average size.

In order to probe the clusters with the Raman scattering in the spectral region of interest, we use mirrors for the FEL optical cavity especially designed for that wavelength. The interferential coating has been prepared at the Laser Zentrum Hannover.

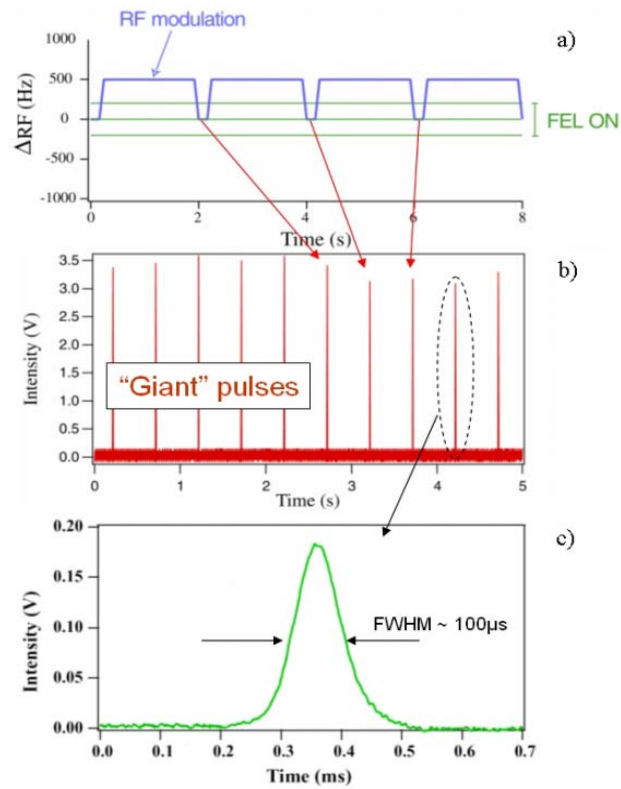

Fig. 3. Q-switching of the SRFEL: a) the RF modulation can be triggered by the opening of the He valve of the clusters source, b) development of a sequence of giant pulses, c) detail of a giant pulse: typical duration is 100 μs.

PRELIMINARY TESTS AND FUTURE DEVELOPMENT

The CESyRA system is in the experimental hall of ELETTRA since May 2006 for the long term project approved on the Gas Phase beamline [9,13,19]. When the chamber is not in use for this project it is available for the preparation of the RRS experiment.

In Raman spectroscopy, one of the most frequently encountered problems is related to the presence of the elastic background. Since the Raman cross section is typically 4-5 orders of magnitude smaller then the elastic one (Thomson scattering), the Raman signal risks to be submerged by the tails of the elastic peak. Moreover, in our setup, the interaction volume is in vacuum, separated from the spectrometer and the SRFEL by quartz view-ports. This introduces an additional source of scattered light that further decreases the "peak to background" ratio. The first step in the preparation of the Raman experiment has been the measurement of a total scattering yield, i.e. the collected light signal regardless of its spectral distribution, in order to evaluate the relevance of the background and to assess the interaction between the clusters and the radiation. For this purpose, we used a photomultiplier tube (PMT) to detect the photons that are collected by a small quartz lens focusing in the interaction volume about 5 mm far from the PMCS nozzle, where the cluster density is close to the maximum. When the setup will be optimized, the PMT will be replaced with a spectrometer.

Since now, few hours have been dedicated to optimize the experimental setup. FEL light at 217.5 nm has been generated with a very good stability. We expect to extract a power of few tenth of mW in free-run mode that should correspond to a flux of 10^{17}~10^{18} ph/s in the Q-switching regime. The FEL light has been used to perform the alignment of the chamber as well as some preliminary tests aimed at optimizing the Raman setup. The light was focused on the cluster beam by means of a lens located outside the chamber and one mirror in vacuum at 45º that deflect the light in the vertical direction. A second mirror at 45º was used to extract the light from the chamber. The focus of the collecting lens was placed at the intersection of the laser and clusters beams, so that the collection was done in the direction perpendicular to both of them. A multichannel time to digital conversion board has been used to record the detected events keeping track of their delay with respect to the opening of the valve. The full range temporal window of detection is 20 ms, with a time resolution of 82 ps. The acquisition software allows integration over an undefined number of consecutive pulses. To obtain a good background subtraction despite the possible drifts in laser and cluster source operation, the measurements have been done alternating acquisition of pulses with and without clusters; this was obtained by firing the vaporization discharge in the PMCS every second gas pulse only. Typical integration time was 5 min at a repetition rate of 5 Hz that corresponds to acquisition

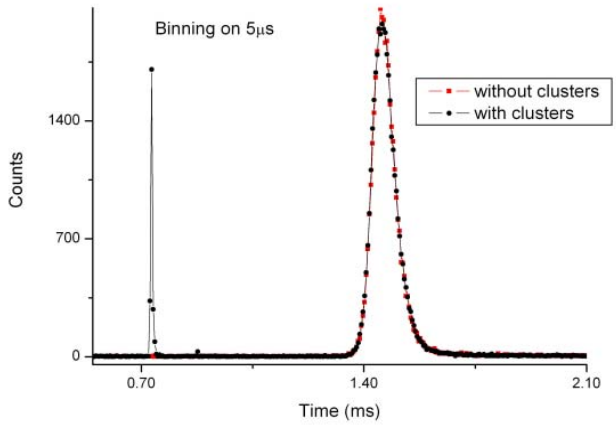

Fig. 4: Acquisition with PMT of the scattered intensity. Black line (circles) SRFEL pulse plus clusters pulse. Red line (square) SRFEL pulse with only the carrier gas (notice the absence of the HV discharge noise).

of about 750 laser pulses with clusters in the beam and 750 without clusters.

Figure 4 shows an example of detected events for an acquisition obtained setting a nominal delay of 1.2 ms between the He valve and the RF modulation. The peak at 1.45 ms corresponds to the photon counts collected under the giant pulses of the SRFEL. The black line with circles is associated to the pulses with clusters and the red one (squares) without clusters. The sharp spike at 0.73 ms is due to electrical noise introduced by the HV discharge in the PMCS and thus occurs only in the pulses where the generation of clusters is on; excluding this instrumental effect, no significant differences were measurable between the two curves at any delay. An expanded view of the peak at 1.45 ms (figure 5) shows that photon counts are detected with a time structure that closely follows the microtemporal structure of the FEL radiation. The fact that the detection rate is of the order of one photon count per micropulse indicates that the intensity of light scattered inside the chamber by the optical elements is hindering the signal of interest as the detector is probably saturated by background counts.

Those preliminary results show the importance of screening the detector from the intensity scattered by the optical elements. At present, we are developing a new optical scheme to minimize this source of background that certainly would prevent the detection of the weak Raman signal. We are also implementing a Nd:YAG table top laser that, even if not tunable at the proper wavelength, will be helpful for off-line preparation of the experiment with the SRFEL.

Considering the small number of shifts that for the moment have been dedicated to the experiment, we can be optimistic for the future developments. The CESyRA apparatus and the SRFEL reveal to be stable enough for the acquisition of data with good statistic.

We acknowledge the storage ring control group of Elettra for collaboration and Stefan Günster of LZH (Hanover) for the realization of FEL optics.

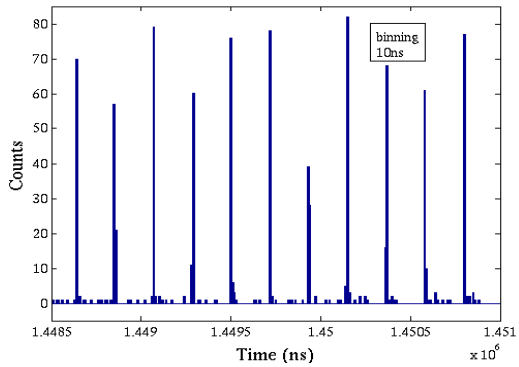

Figure 5: Expanded view of the microtemporal structure of photon count peak under FEL giant pulse in the Q-switch mode.

REFERENCES

[1] M. Schnaiter, et al., Astr. J. 498:486-496, 1998.

[2] W. Kraetschmer, Astrophysics and Space Science 128:93-99, 1986.

[3] D.C.B. Whittet, et al. Astr. J. 602:291-297, 2004.

[4] W.W. Duley and S. Lazarev, Astr. J., 612:L33-L35, 2004.

[5] Manish Chhowalla, et al., Phys. Rev. Lett. 90:155505, 2003.

[6] T. Motylewsky, et at., Astrophys. J. 531:312-320, 2000.

[7] L. Ravagnan, et al., Phys. Rev. Lett. 89:285506, 2002.

[8] L. Ravagnan, *"Synthesis and Characterization of Carbynoid Structures in Cluster Assembled Carbon Films"*, PhD thesis (2005).

[9] C. Lenardi, et al., Elettra Highlights 2003-2004, 92.

[10] E. Barborini, et al., J. Phys. D 32:L105-L109, 1999.

[11] H. Vahedi Tafreshi, et al. J. Nanosci. Nanotechnol. 6:1140-1149, 2006.

[12] P. Piseri, H. Vahedi Tafreshi, P. Milani Curr. Op. Solid St. Mater. Sci. 8:195-202, 2004.

[13] P Piseri, et al., New J. Phys. 8:136, 2006.

[14] R.P. Walker, et al., Nuclear Instruments and Methods in Physics Research A, 429: 179–184, 1999.

[15] N.A. Vinokurov, et al., preprint INP77.59 Novosibirsk, (unpublished) 1977.

[16] A. Renieri, Il Nuovo Cimento 35:161, 1979.

[17] I.V. Pinayev, et al., Nucl. Instr. and Meth. A 475:222, 2001. proceedings.

[18] G. De Ninno, et al., Nuclear Instruments and Methods in Physics Research A, 528:278–282, 2004.

[19] K.C. Prince, et al., J. Sync. Rad. 5:565, 1998.

FREE ELECTRON LASER PULSE CONTROL BY ACOUSTO- OPTIC MODULATORS

Taizou Kanai*, Sachiko Yoshihashi-Suzuki, Kunio Awazu, Institute of Free Electron Laser, Graduate School of Engineering, Osaka University, Japan

Abstract

The free electron laser (FEL) at Osaka University can be continuously varied over a range from 5.0 to 20.0 μm when using the 30 MeV electron beam. The FEL has a double pulse structure. The structure consists of a train of macropulses with a pulse width of 15 μs, and each macropulse contains a train of 330 micropulses with a pulse width of 5 ps. The FEL's tunability and short pulse make possible new medical applications, such as investigating protein dynamics and ablating soft tissues. Precise control of the micropulse train is essential for FEL medical applications because macropulses of long pulse duration lead to undesirable thermal effects. An FEL pulse control system, using an acousto-optic modulator (AOM), was developed to investigate the non-thermal effects of FEL on living tissues. This system provides efficiency (~ 65%) and a fast switching speed (> 200 ns), and we predict that FEL will serve as a novel tool in many new applications.

INTRODUCTION

The free electron laser (FEL) at Osaka University is a pulsed, tunable infrared source. It is designed to work in the region from 5 to 20 μm at an average power of up to 50 mW. The FEL applications research is broadly interdisciplinary, including measurements of investigation of protein dynamics, the ablation of soft tissues and narrow band-gap materials [1-4].

An electron beam of 30 MeV energy is the laser gain medium for the FEL. It is accelerated with a linear, pulsed RF accelerator. This leads to the pulsed beam current and complex temporal intensity profile of the emitted IR light as shown in Fig.1. The accelerated electron pulses have up to 20 μs duration and each of them generates one optical "macropulse" have duration of 15 μs. The mode locked pulse or "micropulse" have duration of approximately 5 ps with 44.8 ns spacing between pulses. For many FEL application 15 μs duration of the macropulse leads to undesirable thermal effects or obscures signals from fast optical process. The FEL user community has identified the need for selecting the number of micropulse. The switching device to achieve this should have the following properties;

(1) Operating wavelength of 5 to 12 μm;
(2) Variable pulse duration between 500 nanoseconds and the full macropulse length, with fast rise and fall times;
(3) High efficiency;
(4) Easy pulse duration adjustment; and
(5) Portability between different experimental stations.

An acousto-optic modulator (AOM) has therefore been chosen as the best solution for the Osaka University FEL system. Section 2 describes the principles of AOMs and pulse control systems. Section 3 details the performance evaluations of the pulse control system, and Section 4 reports the results of these evaluations.

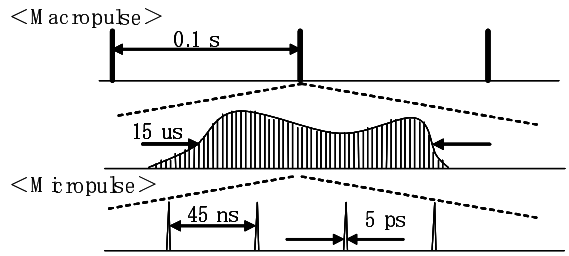

Figure 1: Pulse structure of FEL.

MATERIALS AND METHODS

The principle of an Acousto Optic Modulator

An AOM is a device that allows control of the power, frequency, or spatial direction of a laser beam using an electrical drive signal. It is based on the acousto-optic effect, i.e., refractive index modification by the oscillating mechanical pressure of a sound wave. The geometry of the input and output laser beams relative to the acoustic column is shown in Figure 2. An AOM's key element is a transparent crystal (or a piece of glass) through which the light propagates. A piezoelectric transducer attached to the crystal is used to excite a high-frequency sound wave. Light can then be diffracted at the periodic refractive index grating generated by the sound wave. The scattered beam has a slightly modified optical frequency (increased or decreased by the frequency of the sound wave) and a slightly different direction. The frequency and direction of the scattered beam can be controlled via the frequency of the sound wave, while the acoustic power allows control of the optical power. For sufficiently high acoustic power and to align the input laser beam for a true Bragg input angle, more than 70% of the optical power can be diffracted as the first order beam. When a supersonic wave intercepts the incident beam, the AOM generates a first order beam. Therefore, the rise time of first order beam depends on the diameter of the incident beam and the speed of the supersonic wave. The rise time of the first order beam is given by equation (1). The following

* kanai@fel.eng.osaka-u.ac.jp

equation describes the time required before the primary light output rises from 10% to 90% [5].

$$TR = S/ (v*1.56), \quad (1)$$

where:

TR = Rise time of first order beam,
S = Diameter of incident beam,
V = Speed of supersonic wave,
1.56 = correction factor.

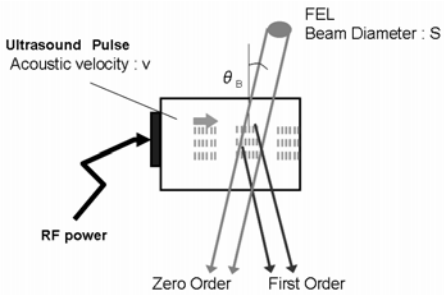

Figure 2: Principles of an AOM.

Pulse control system design

The diameter of the original FEL is about 50 mm Φ. To control the high efficiency/high speed pulse, it is necessary to incident para-parallel/diameter of very small beam into AOM. A schematic diagram of an FEL pulse control system is shown in Figure 4. The FEL beam (50 mm Φ) diameter was reduced in size to 1.5 mm Φ by two mirrors with either long (radius of curvature = 385 mm) or short (radius of curvature =50.0 mm) focal lengths. Table 1 shows the specifications of a standard AOM (AGM-402A1, IntraAction Corp).

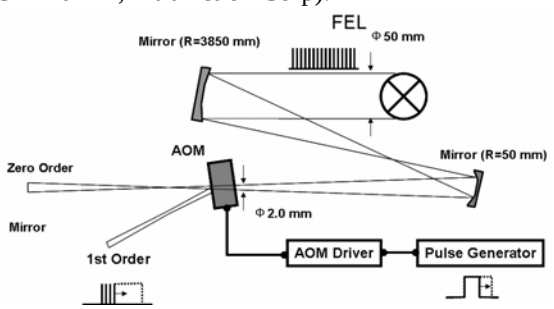

Figure 3: Experimental setup for pulse control.

Table 1: Specifications of Ge-AOM

Optical Wavelength	@10.6 µm
Acousto-optic Material	Single Crystal Germanium
Acoustic Velocity	5.5 mm/µsec
RF Center Frequency *	40 MHz
Optical Insertion Loss	<7 %
Optical Power Capability	25 Watts
Laser Polarization	Parallel to Base
Rise Time (diameter)	116 nsec (1 mm)
Bragg Angle	38.5 mrad
Beam Separation	77 mrad
Diffraction Efficiency	<70 %

*Other frequency available

PERFORMANCE EVALUATIONS

The laser damage threshold for Ge was determined empirically for the FEL. Surface damage occurred at 20 mW of average power, less than 1.5 mm Φ beam diameter, and 6.3 µm wavelength. The absorption by Ge does not change significantly between 6 and 12 µm. Our experimental setup is shown in Figure 5. The FEL enters the AOM at a diameter of 1.5 mm Φ and the pulse duration is controlled by adding a supersonic wave pulse to the AOM. First order beam is detected by infrared detector (MCT; VIGO Systems, R005). MCT signal is recorded by an oscilloscope (LeCroy, WaveMaster 8000).

RESULTS 1

Wavelength-dependence of pulse control system

The wavelength dependence of the pulse control system is shown in Figure 4, Input/picked FEL average power vs. wavelength in the range from 5.4 to 12 µm.

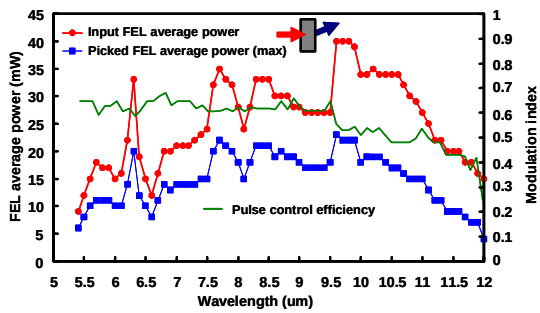

Figure 4:Wavelength-dependance of pulse control system.

Measurement of first order FEL

The MCT signal of the FEL first order beam is shown in Figure5. This pulse control system can control the FEL pulse width in the range of 10 micropulses (>200 ns) to the full macropulse (15 µs). A 630 ns first order FEL is produced by a control signal of 500 ns, a 360 ns first order FEL is produced by a control signal of 200 ns. Based on these results, the rise/fall time of this pulse control system is about 100 ns. This result aligns closely with the theoretical value derived from equation (1).

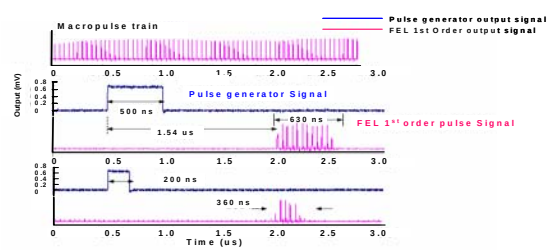

Figure 5: The pulse structure of the picked FEL.

EXPEREMENT

In case of FEL irradiation to gelatin, interaction arrives at depth of 2mm, at the maximum. However, Photo penetration depth = 3 μm. Interaction extends to much deeper from the region where light can arrive at. It is thought that this reaction depends on a shock wave.

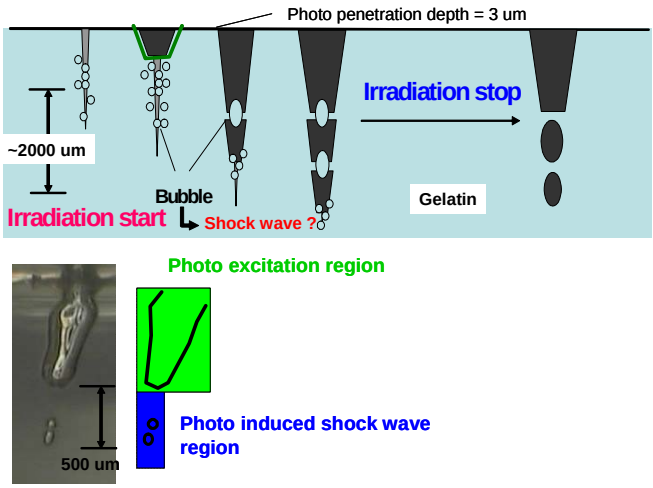

Figure 6: The process of gratin cut.

Experiment setup

Experiment setup for proof experiment of pulse control effect is shown in Fig 7. In this experiment, change of a shock wave is estimated by an image analysis and wave pattern analysis.

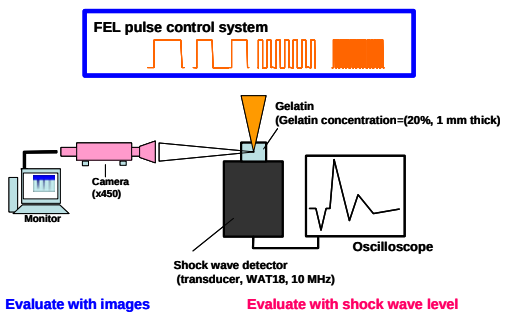

Figure 7: Experiment setup for proof experiment of pulse control effect.

RESULTS 2

A difference of a level of shock wave by a difference of pulse structure is shown in Figure8. Figure 9 illustrates the maximum shock wave level (peak to peak)/ maximum shock wave arrival depth (image analysis) vs. FEL pulse width. From these results, the same tendency was seen in an analysis result by an image and an analysis result by a wave pattern. A shock wave grows up to 1-2 μs and reaches saturation afterwards.

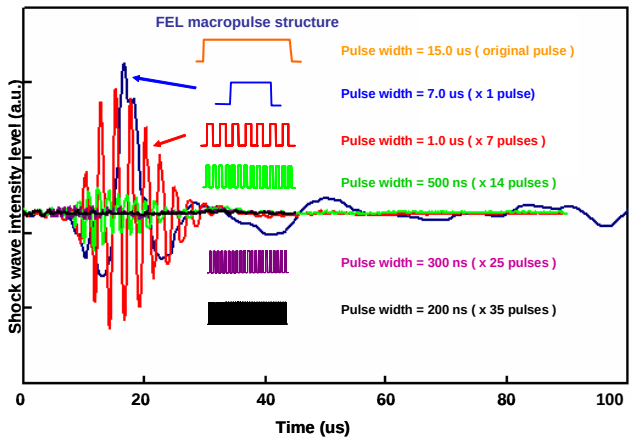

Figure 8: A difference of a level of shock wave by a difference of pulse structure.

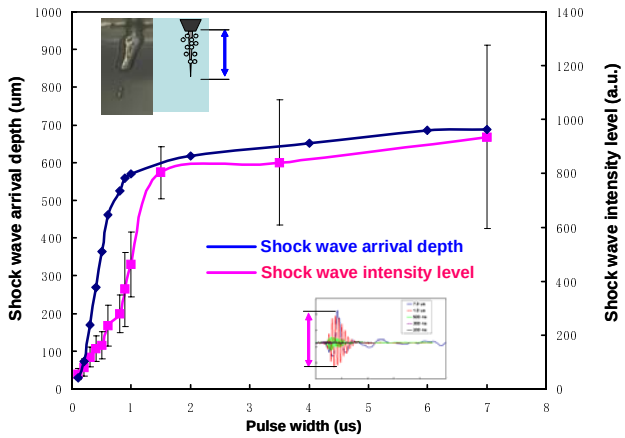

Figure 9: A difference of shock wave by a difference of pulse structure.

CONCLUSIONS

FEL pulse control system using an AOM was developed in order to investigate of non-thermal effect between the FEL and living tissue. With a time scale of 200 ns ~ 15 μs, this system provides the efficiency of ~65 % and a fast switching speed.

From results of pulse control effect proof experiment, the same tendency was seen in an analysis result by an image and an analysis result by a wave pattern. A shock wave grows up to 1-2 μs and reaches saturation afterwards. This system made it possible to control a shock wave by controlling a thing of pulse structure.

Picking out a single micropulse is impossible using this device with a time scale from 200 ns to 15 μs; it is, however, a very successful pulse control technique.

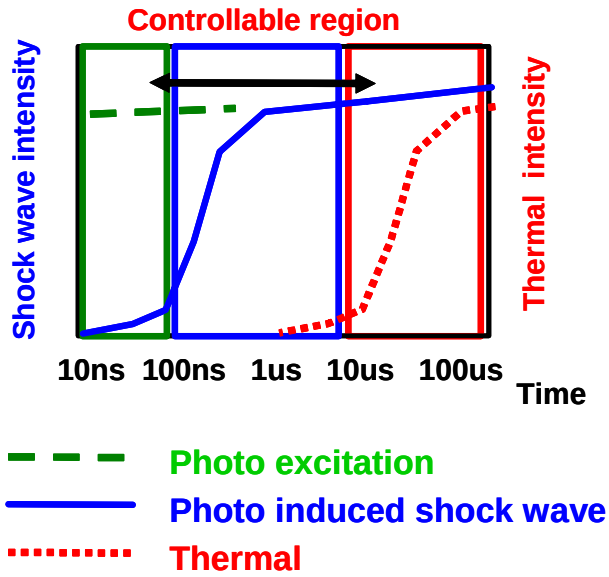

Figure 10: Controllable region by pulse control system.

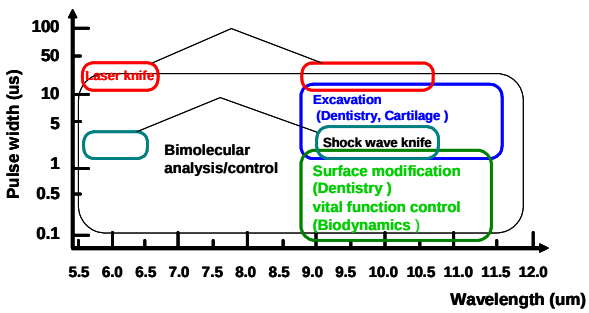

Figure 11: New regions that FEL can apply.

DISCUSSIONS

Using this system, the pulse width becomes the third parameter of the FEL system, in addition to the two conventional irradiation parameters of wavelength and power density. This system allows more precise FEL-biomolecular interactions, and was thereby able to produce a new irradiation effect of FEL that was not previously available (Figure 11). Improvement of the pulse control system (higher speed, higher power density) affords more selective excitation of biomolecules on a pico- and nanosecond time scale. In addition, by using FEL as the excitation light, we can introduce the picosecond time resolution vibration minute light method to the field of chemistry and biology.

REFERENCES

[1] GS. Edwards, D. Evertson, W. Gabella, TL. King, J. Kozub, M. Memdenhall, J. Shen, RH. Traeger: IEEE J. Sel. Top. Quantum Elec. Vol.2 (1998), p.810
[2] K. Awazu, A. Nagai, K. Aizawa, The Reveiew of Laser Engineering. Vol.26, No.5 (1998), p.369
[3] K. Awazu, The Reveiew of Laser Engineering.Vol.28, No.5 (2000), p.291
[4] Klaus Becker, J. Bruce Johnson, Gleen Edwards, Rev. Sci. Instrum. Vol.26, No.5 (1998), p.1496
[5] Mike Hillier: Acousto Optic Tuneable Filters Basic Theory And Design Considerations, Isomet corporation (1998)

ABSOLUTE AND CONVECTIVE INSTABILITY OF SMITH-PURCELL FREE ELECTRON LASER

D. Li#, K. Imasaki, ILT, 2-6 yamada-oka, suita, Osaka 565-0871, Japan
Z. Yang, UEST, Chengdu, 610054, P.R.China
Gun-Sik Park, SNU, Seoul 151-747, Korea
S. Miyamoto, S. Amano, T. Mochizuki, LASTI, 3-1-2 Koto, Kamigori, Hyogo 678-1205, Japan.

Abstract

The effect of dissipative loss in the grating surface on the Smith-Purcell free-electron laser is investigated with the help of a two-dimensional particle-in-cell simulation. The simulation model supposes an open aluminium grating driven by a continuous electron beam. With the present parameters, it has been shown that such a device can oscillate on both the convective and absolute instability when ignoring the surface-loss. The growth rate is found to be dependent of the beam energy, and it decreases when the surface-loss is involved. The results are compared with the recent theory.

INTRODUCTION

As a promising alternative in the development of a compact, tuneable and powerful THz source, the Smith-Purcell free-electron laser (SP-FEL) has attracted many attentions in recent years [1-5]. The SP-FEL can be realized on the configuration of an open grating [6-10], which is different from the conventional configuration, "orotron" or "ledatron" [11,12].

When an electron passes close to the surface of the grating, it not only emits Smith-Purcell radiation, but also excites the evanescent wave [13,14]. The evanescent wave, with the frequency below the lowest frequency of the Smith-Purcell radiation, travels along the grating and undergoes partial diffraction and partial reflection at both ends of the grating. The diffraction potion is radiative in the free space and can be utilized. The dispersion relation of the evanescent wave, as shown in Fig. 1, is similar to the backward-wave oscillators (BWOs) and traveling-wave tubes (TWTs), since the grating could be regarded as a kind of slow-wave structure. The frequency of the evanescent wave is determined from the intersection point of the dispersion curve and the beam line, as shown in Fig. 1, meaning that the beam velocity is synchronous with the phase velocity of the wave. The group velocity can be positive, negative or zero. When the interaction happens in the positive group velocity, the wave and the beam moves in the same direction. Such an interaction induces convective instability, and the device operates in the manner of TWTs [15]. When the group velocity is negative, the wave and the beam moves in the opposite direction. In this case, the interaction leads to absolute instability, and the device can operate without external feedback, like BWOs [15].

The case of absolute instability has been much addressed [6-9]. Andrews and co-workers predicated that there is possibility for device to start oscillation based on the convective instability, since the wave reflects at both ends of the grating, playing the role of external feedback [15]. In this paper, we address on the oscillation induced by absolute and convective instability, respectively, with the help of a two-dimensional particle-in-cell code, MAGIC [16], a code for simulating processes involving interactions between space charge and electromagnetic fields. The simulation is performed with and without involving the surface-loss of the grating, respectively, to demonstrate the effect of the loss on the operation of the device.

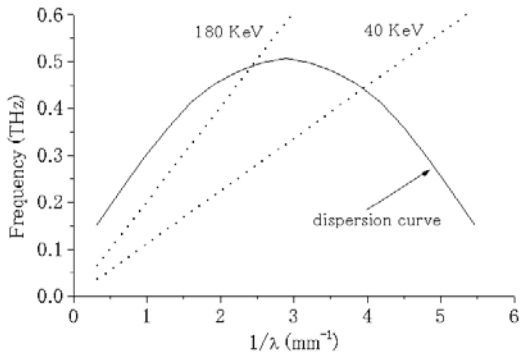

Figure 1: Dispersion relation for our grating.

SIMULATION DESCRIPTION

The simulation geometry is shown in Fig. 2. A grating with rectangular form is set in the centre of the bottom of the simulation box. The surface of the grating is assumed to consist of conductor whose grooves are

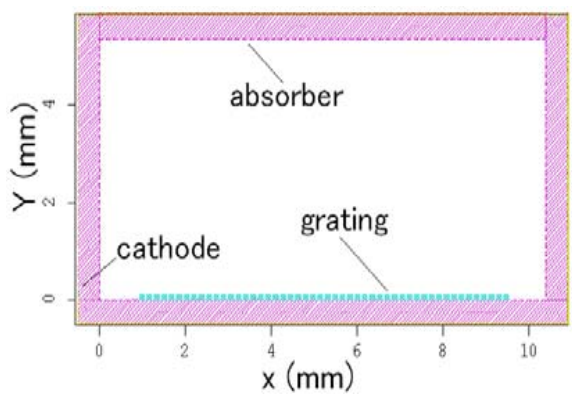

Figure 2: Simulation geometry.

#dazhi_li@hotmail.com

parallel and uniform in the *z* direction. We use a sheet electron beam with thickness of 24 μ m, and place its edge 34 μ m above the top of the grating. It is a perfect laminar beam produced by the MAGIC algorithm and is generated from a cathode located at the left boundary of the simulation box. The electron-wave interaction and radiation propagation happen in the vacuum area, which is enclosed by a special region (called *free-space* in MAGIC language), where the incident electromagnetic waves and electrons can be absorbed. The whole simulation area is divided into a mesh with rectangle cells of small size (δ x=17.3 μ m, δ y=17.3 μ m) in the region of beam propagation and grating, and large size (δ x=17.3 μ m, δ y=51.9 μ m) in the rest of the region. The Cartesian coordinate system is adopted with the origin at the centre of the grating. Since it is a two-dimensional simulation, it assumes that all fields and currents are independent of the z coordinate. And it should be noted that the current value mentioned in this paper represents the current per meter in the z direction.

The main parameters of the grating and electron beam are summarized in table 1. The electron beam

Table 1 Main parameters for simulation

Grating period	L=173 μ m
Groove width	w=62 μ m
Groove depth	d=100 μ m
Period number	N=50
Electron beam energy	E=40 ~140 KeV
Beam current	I=648A/m
Beam thickness	σ =24 μ m
Beam-grating distance	δ =34 μ m
External magnetic field	B_x=2T

energy will be varied in the following simulation. The external magnetic field is used in order to ensure stable beam propagation above the grating. It should be noted that some parameters of the grating and electrons, such as period length, groove depth and width, and electron's energy, used in our simulation are the same as those in Dartmouth experiment [1]. Consequently the radiation occurs in the THz regime. However, the grating length in our simulation is shorter than the one used in Dartmouth

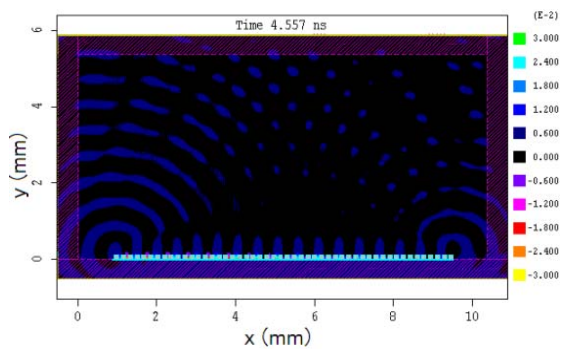

Figure 3: Contour plot of Bz for the case of 50 KeV electron beam.

experiment because of the limited capacity of our computers. In addition, the form of the beam is different, since we use a sheet beam and the experiment used a round beam.

As to the diagnostics, MAGIC allows us to observe a variety of physical quantities such as electromagnetic fields as functions of time and space, power outflow, and electron phase-space trajectories [16]. We can set the relevant detectors anywhere in the simulation area.

SIMULATION RESULTS

Ignoring Surface-loss

We first perform the simulation at the ignorance of the surface loss, i.e., the grating is supposed to be perfect conductor. The choice of beam energy spans the regions of absolute and convective instability. According to the theory of Andrews and Brau, the beam line intersects the point of zero group velocity, called Bragg condition, with the energy of 125 keV[15]. Fig.3 and 4 show the contour plot of B_z and energy modulation for the beam energy of 50 keV, at the time of 4.703 ns. In this case, the device operates on the absolute instability, and the energy modulation tells that the oscillation happens. If the beam energy is 140 keV, the device operates on the convective instability. From Fig. 5 we understand that the ends of the grating reflect the wave, and therefore provide feedback.

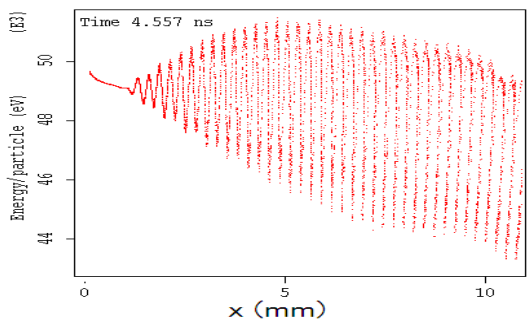

Figure 4: Energy modulation for the case of 50 keV eelectron beam.

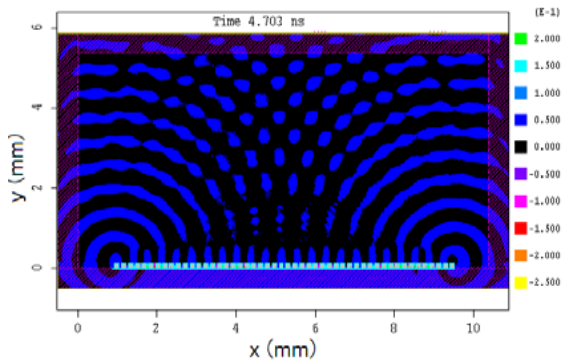

Figure 5: Contour plot of B_z for the case of 140 KeV electron beam.

The reflected waves form the interference pattern. Fig. 6 illustrates the modulation of the energy, meaning that the

device oscillates. The electric field component of the evanescent wave is observed near the grating surface, as examples, simulation results for some chosen energies are given in Fig.7. It is seen that the evolution of the

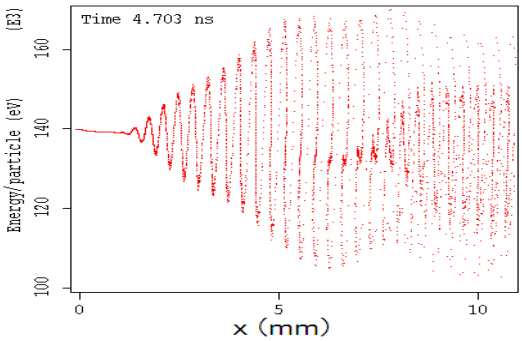

Figure 6: Energy modulation for the case of 140 keV electron beam.

amplitude of the electric field component in the x direction shows the exponential growth for all chosen energy, which means the device can oscillate by both absolute and convective instability, even at the Bragg condition. We noticed that when the beam energy is 125 KeV or more, the curves illustrate several sharp decreases as the amplitude growing.

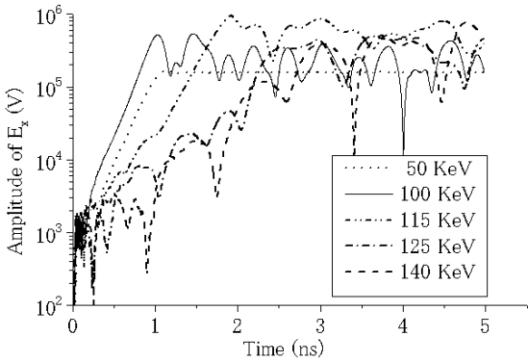

Figure 7: Evolution of amplitude of E^x with respect to time.

Involving Surface-loss

To be more practical, the grating should not be perfect conductor and it has loss in the surface. In this paper, we consider aluminium grating, which has the conductivity of 3.72×10^7 mhos/m. With involving the surface-loss, the evolution of the electric field amplitude corresponding to Fig.7 is as shown in Fig.8. It is understood that only the curves for 50KeV, 100KeV and 115KeV (operating on absolute instability) demonstrate the exponential growth, while for the case of 140KeV electron beam (operating on convective instability) the oscillation refuses starting. Further analysis of the simulation data shows that with the present parameters the device can only oscillate on the absolute instability. Comparing with Fig.7, the curve of 50KeV comes to saturation ahead of the curve of 100KeV in Fig. 8, which means the effect of surface loss strongly depends on the beam energy.

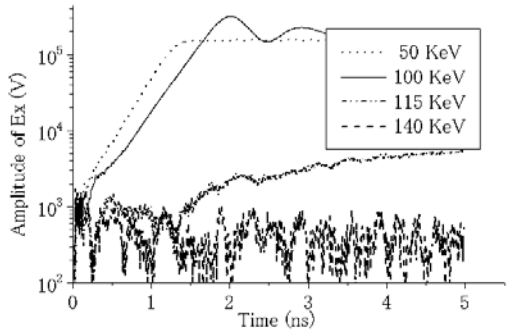

Figure 8: Evolution of amplitude of Ex with respect to time.

Growth rate

The growth rate of the evanescent wave can be derived from the simulation data. From the plot of amplitude of $E_x(t)$ vs t we can extract the slope of the linear envelop, which is the imaginary part of the frequency, Im(ω) [9]. Plenty of simulations are carried out with the variation of electron beam energy, and the growth rate for the particular energy is acquired by the way described above. The dependency of growth rate on beam energy is illustrated in Fig.9, for the cases of with and without surface loss, respectively. It has been shown that, the growth rate decreases when the surface-loss is involved. With the present parameters, the maximum growth rate appears at the energy of ~65 KeV for the case of with surface loss, then it goes down quickly to zero before the Bragg condition. That is the reason that the device can only operate on the absolute instability. If we expect the device oscillate at the convective instability, much higher current of electron beam is required to get the net gain. Also plotted in Fig.9 are the theoretical results from the recent theory [17], which show about two times larger than the simulation results.

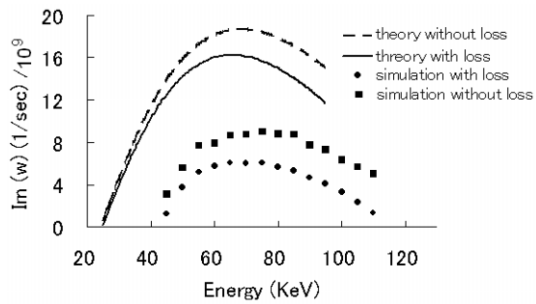

Figure 9: Growth rate with respect to beam energy.

CONCLUSION

The operation of a SP-FEL on absolute and convective instability is discussed in this paper. We demonstrate that the ends of the grating can provide the external feedback, which is possible to make the device oscillate at the

convective instability. The surface-loss will decrease the growth rate, especially in the region of convective instability. The growth rate drops down to zero before the Bragg condition with the present parameters. Higher beam current is predicted to provide the net gain if we expect the device to oscillate on the convective instability when the practical metal, such as aluminium, is used to make the grating.

ACKNOWLEDGMENTS

The authors gratefully acknowledge helpful discussions with Charles Brau and Heather Andrews.

REFERENCES

[1] J. Urata, M. Goldstein, M. F. Kimmitt, A. Naumov, C. Platt, and J. E. Walsh, Phys. Rev. Lett. **80**, 516 (1998).
[2] A. Bakhtyari, J. E. Walsh and J. H. Brownell, Phys. Rev. E **65**, 066503 (2002).
[3] L. Schachter and A. Ron, Phys. Rev. A **40**, 876 (1989).
[4] S.E.Korbly, A.S. Kesar, J.R.Sirigiri and R.J.Temkin, Phys. Rev. Lett. **94**, 054803, (2005).
[5] K. –J. Kim and S. –B. Song, Nucl. Instrum. Methods Phys. Res., sect. A **475**, 158 (2001).
[6] H. L. Andrews and C. A. Brau, Phys. Rev. ST Accel. Beams **7**, 070701 (2004).
[7] H.L.Andrews, C.H.Boulware, C.A.Brau and J.D.Jarvis, Phys. Rev. ST Accel. Beams **8**, 110720 (2005).
[8] V. Kumar and K.-J. Kim, Phys. Rev. E 73, 026501 (2006).
[9] J.T.Donohue and J.Gardelle, Phys. Rev. ST-AB, **8**, 060702 (2005).
[10] J.T.Donohue and J.Gardelle, Phys. Rev. ST-AB, **9**, 060701 (2006).
[11] R. P. Leavitt, D. E. Wortman, and C. A. Morrison, Appl. Phys. Lett. 35, 363(1979)
[12] K. Mizuno, S. Ono and Y. Shibata, IEEE Trans. Electron devices, ED-20, 749 (1973)
[13] D.Li, Z. Yang,K.Imasaki and Gun-sik Park, Phys. Rev. ST-AB **9**, 040701 (2006)
[14] D.Li, K.Imasaki , Z. Yang and Gun-sik Park, Appl. Phys. Lett. 88, 201501 (2006)
[15] H.L.Andrews, C.H.Boulware, , and J.D.Jarvis, Phys. Rev. ST Accel. Beams **8**, 050703 (2005).
[16] L. Ludeking, The MAGIC user's manual.
[17] C.A.Brau (private communication).

SUPERRADIANT SMITH-PURCELL RADIATION IN THE TERAHERTZ-WAVE REGION FROM BUNCHED ELECTRON BEAMS*

Zongjun Shi#, Ziqiang Yang, Zheng Liang, Institute of High Energy Electronic, University of Electronic Science and Technology of China, Sichuan, Chengdu, 610054, P. R. China
D.Li, K.Imasaki, Institute for Laser Technology, 2-6 Yamada-oka, Suita, Osaka 565-0871, Japan

Abstract

This paper presents an analysis of a possible method of producing the bunches and obtaining the coherent THz radiation. With the help of a two-dimensional particle-in-cell (PIC) simulation, the simulation proposes a model with two sections consisting of a square-toothed grating with a flat conducting roof above it and an open grating. In the first section, an initially continuous beam interacting with TM modes is bunched by using an external signal. In the second section, the coherent THz radiation is produced by the well bunched beam interacting with the open grating. The strongest radiation is at 120^0 and at frequency 266.5GHz.

INTRODUCTION

In recent years, there is a substantial interest in development of coherent radiation sources, especially to the coherent THz radiation. An important source of radiation in the THz region is Smith-Purcell(SP) radiation[1].

It is well known that the SP radiation may occur at angles θ measured from the direction of the electron beam and order *n* such that $\lambda = L(1/\beta - \cos\theta)/|n|$, where *L* is the grating period, βc the electron velocity, and c the speed of light. The coherent SP radiation has been observed in the THz region from experiments. One example is the Dartmouth experiments [2] with an initially continuous beam. The other is the MIT experiments [3] using the beam already bunched when it reaches the grating. The bunched beam from a linac operating at 17.14Ghz delivers pulses of duration 1ps. Quite recently, the PIC code simulations related to the coherent and superradiant SP radiation are performed by Li et al [4], Donohue and Gardelle, respectively [5,6]. In their simulations, the Dartmouth experiment and MIT experiment have been presented. These simulations are able to clearly observe coherent SP radiation at harmonics of imposed bunching frequency. Those results support the viewpoint of Andrews and Brau [7]. In the theoretical side, Kumar and Kim have performed a detailed 2D analysis in which the SP free-electron laser is treated as a BWO [8]. And a thorough discussion of the radiation emitted by prebunched beams has been given recently by Gover [9].

We know it is necessary for generating coherent SP radiation that the bunches are short comparing with the radiation wavelength. However, for the short electron bunches high quality electron accelerator which is expensive is needed. The bunches are unstable both in time and along the grating for the bunching of the initially continuous beam by an evanescent wave that is operating in backward wave region.

In this paper, with the help of a two-dimensional PIC simulation we discuss and analyze a new method of making the bunches and obtaining the coherent THz radiation. The simulation proposes a model with two sections consisting of a square-toothed grating with a flat conducting roof above it and an open grating. In the first section, an initially continuous beam interacting with TM modes is bunched by using an outer incoming signal. The electron-wave interaction is operating in the travelling-wave region, which resembles a Cerenkov amplifier. Due to the Mechanism for TWT, the bunches are relative stable compared with what is operating in backward wave region. In the second section, the coherent THz radiation is produced by the well bunched beam interacting with the open grating.

DETAILS OF THE NUMBER ANALYSIS

Geometry and parameters of the simulation

The simulations are carried out using the PIC code CHIPIC[10]. It is a finite-difference, time-domain code for simulating plasma physics process. Our simulations use a 2D PIC code in this paper. The geometry is given in Fig. 1. The basic structure consists of a grating bounded above by a roof and an open grating .The surface of the grating and the roof are assumed to consist of a perfect conductor whose rectangular groove are parallel and uniform in the z direction. A sheet electron beam propagates along the x-direction. It is a perfect beam produced from a small cathode located at the left boundary of the simulation. The drive signal is also

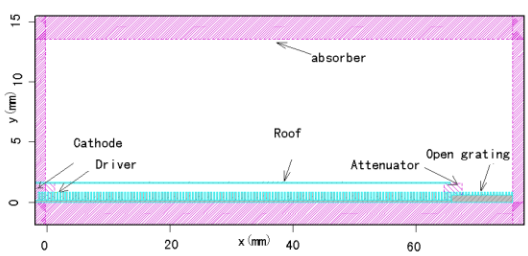

Figure 1. Simulation geometry.

*Work supported by National Nature Science Foundation of P.R.China (60571020),#shizongjun@163.com

Table 1. Parameters of the simulations

Parameters	First section	Second section
Beam energy	120 kV	
Current	200 A	
Beam thick	0.4 mm	0.4mm
Beam -grating distance	0.1 mm	0.1mm
Grating period	0.5mm	0.5mm
Grating groove depth	0.625mm	0.2mm
Grating groove width	0.25mm	0.3mm
Number of period	135	20
External magnetic field	2T	
Drive signal	2kW	
Mesh size	$(50um)^2$	$(50um)^2$

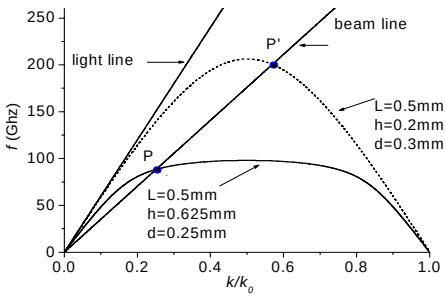

Figure 2.Dispersion relation for the grating

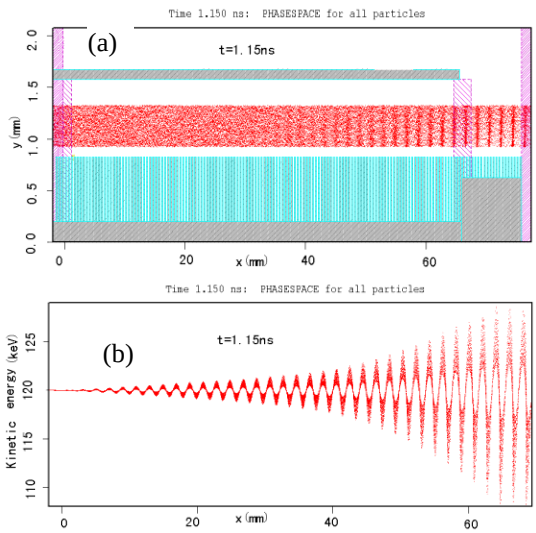

Figure 3. Phase-space distribution (a) density of electrons in the x-y plane at 1.15ns.Bunching is evident.(b) kinetic energy-*x* density at the same time

imposed on the left, which provides a 2kW power to the device. The beam-wave interaction and radiation propagation happen in the vacuum box. The boundary is enclosed with absorbers. At the end of the first section, there is an attenuator, which prevents most of the electromagnetic wave reaching the second section from perturbing the bunching and interpreting the coherent radiation. The grating parameters we choose have a period L=500*um*, a width of slots d=0.25*mm*, and a depth h=0.625 *mm*. The distance from the tops of the teeth to the roof is 0.75 *mm*. We assume a beam voltage of 120kV, a current of 200A, a beam thickness of 0.4mm, and beam-grating distance 0.1*mm*, external magnetic field B_x=2T. The main parameters of the grating and electron beam are summarized in Table 1.

Description of our idea

In fig. 2, the solid line shows the lowest order TM mode dispersion relation for the grating with a roof, and the dash line for open grating. Due to the choice of parameters, the lowest-order TM mode will be resonant with the beam in the neighborhood of 90-100GHz. At the operating point P, the group velocity is positive, which means electron-wave interacts at the traveling-wave region, as in the traveling-wave tube (TWT). The working process of the device is explained as follows. By using an initial injected signal with frequency 88.5GHz, the electron beam interacts with TM mode electromagnetic wave through the first section, and gets density bunching. The bunching wavelength will be the same as the spatial wavelength of the operating point P .In the second section in order to clearly observe coherent SP radiation at harmonics of the bunching frequency, we varied the parameters of the grating. In fig.2, the point P' is the operating point. Then the operating point frequency of the evanescent wave is different from the bunching frequency.

Through the second passage, which also acts a drift tube, the well bunched beam interacts with the grating, and the coherent radiation is produced.

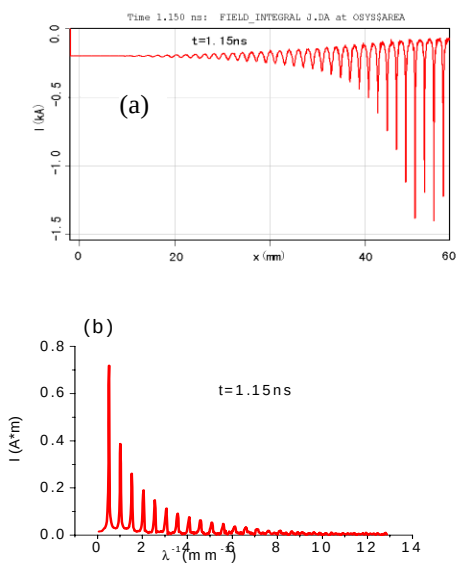

Figure 4. Space dependence of current (a) current I(x), (b) corresponding FFT.

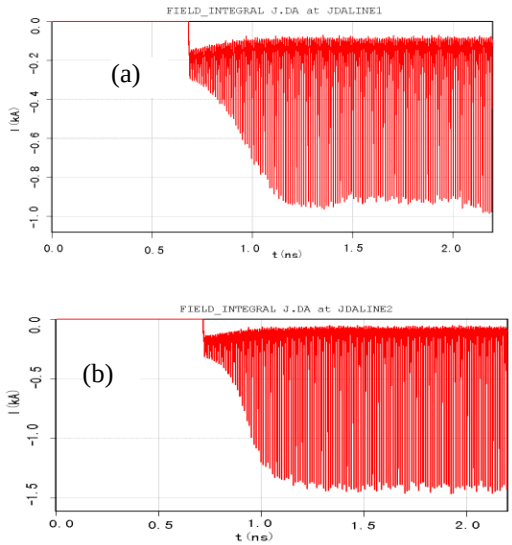

Figure 5. (Color) Current as a function of time: (a) at end of the first section .(b) at the center of the open grating .

SIMULATIONS RESULTS

Electron bunching

In this simulation, the main goal of the first section is not gaining the maximum output power of the beam-wave interaction, but obtaining the well stable bunches. Hence, by using of an outer injected wave, choosing a reasonable period numbers, an initial continuous beam travels through the first section and gets velocity modulation and density bunching, then passes through the open grating and the stable bunches are generated. The bunching can be clearly observed as a function of both space and time. In fig.3, we observe the beam bunching: phase-space plots at time 1.15ns and energy modulation of the electron .We note that the mean energy loss is about 5keV of the beam energy. The spatial modulation of the current displayed in fig.4 increases with *x*, and the period of the modulation is 1.94*mm*. The beam is well bunched at the downstream of the first of passage. We note that the bunching is relative stable along the open grating. In fig.4 (b) shows the bunching is nonlinear when it becomes strong. In fig.5 the beam current is a function of time, for locations at the end of the first of the passage and the center of the open grating. One clearly sees the bunching current is stable in time after time about 1ns. This is an advantage compared to the bunching of the initially continuous beam by an evanescent wave that is operating in backward wave region. In fig.5(b), the bunching current shows the beam is well bunched at the center of the open grating compared with that at the downstream of the grating with roof displayed in fig.5(a). It shows that the open grating also resembles a drift tube.

Coherent terahertz radiation

Here we analyze the radiation from the periodic bunching interacting with the open grating. The results of the simulation are given in fig.6, and three radiations are clearly observation. It has be shown that the dominant radiation is with the frequency of third harmonic of bunching wave, 88.5GHz peaked at the angle of about 120 deg which corresponds to the SP radiation angle. While the other two radiation are with the frequency of the fourth and fifth harmonics ,respectively, and also corresponds to the SP radiation angle. From the contour plot of fig.7 we can observe that the dominant third harmonic radiates at the angle of about 120^0, in agreement with that shown in fig.6.Of course, due to the interacting of the beam-wave which reduces the value of the particle velocity, the discrepancy appears somehow for the simulation data for the radiation angle compared to the theoretical value.

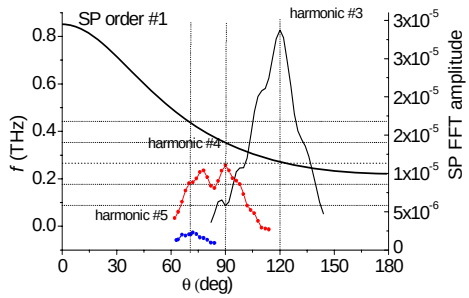

Figure 6. Radiation frequency and the peak of FFT amplitude of B_z as a function of angle, detected at the distance 10.58*mm* from the grating center.

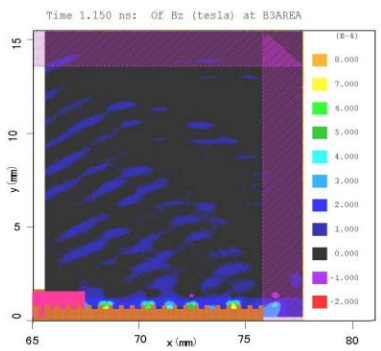

Figure 7. (Color) Contour plot of B_z for coherent radiation

CONCLUSIONS

We have presented results of the coherent THz radiation through the simulations of electron bunching of continuous beam interacting with an open grating. The results show that the bunching is stable in time and along the grating. The strongest radiation is at 120^0 and at frequency 266.5GHz at the simulation parameters. The coherent radiations are emitted at frequencies that are integer multiples of the bunching frequency, and at the corresponding SP angle.

REFERENCES

[1] S.J.Smith,E.M.Purcell. “Visible light from localized surface charges moving across a grating”.*Phys. Rev*. 1953， **92**（15）:1069

[2] J. Urata，M.Goldstein ,M.F. Kimmitt *et al*.. “Super radiation Smith-Purcell emission” .Phys. Rev. Lett., 1998,**80**(3): 516~519

[3] S.E.Korbly,A.S.Kesar,J.R.Sirigiri et al.. “Observation of frequency-Locked coherent terahertz Smith-Purcell radiation”. Phys.Rev.Lett.2005,94(5):054803-1~4.

[4] D. Li, Z. Yang, K. Imasaki, and Gun-sik Park. “Particle-in-cell simulation of coherent and superradiant SP radiation” .Phys. Rev. ST Accel. Beams **9** 040701 (2006). [5] J.T. Donohue and J. Gardelle. “Simulation of Smith-Purcell radiation using a particle-in-cell code”.Phys.Rev. ST Accel. Beams **8**,060702 (2005).

[6] J.T. Donohue and J. Gardelle.“Simulation of Smith-Purcell terahertz radiation using a particle-in-cell code”.Phys.Rev. ST Accel. Beams **9**,060701 (2006).

[7] H.L. Andrews, *et al*.. “superradiant emission of Smith -Purcell radiation”. Phys. Rev. ST Accel. Beams **8**,110702 (2005).

[8] Vinit Kumar and Kwang-Je Kim. “Analysis of Smith-Purcell free-electron lasers”Phys. Rev. E 73.020501(2006)

[9]A.Gover and Dyunin. “Superradiant and stimulated superradiant emission in prebunched electron-beam radiators”. Phys. Rev. ST Accel. Beams *I* 2005,**8**(3):030701-1~15

[10]Di Jun ,Zhu Da-jun ,and Liu Sheng-gang ,*et al*.. “Electronmagnetic field Algorith of the chipic code”.

STUDY ON SUPERRADIANT SMITH-PURCELL RADIATION

D. Li#, K. Imasaki, ILT, 2-6 yamada-oka, suita, Osaka 565-0871, Japan
Z. Yang, UESTC, Chengdu, 610054, P.R.China
Gun-Sik Park, SNU, Seoul 151-747, Korea
S. Miyamoto, S. Amano, T. Mochizuki, LASTI, 3-1-2 Koto, Kamigori, Hyogo 678-1205, Japan.

Abstract

An analysis of superradiant Smith-Purcell radiation is carried out with the help of performing a three-dimensional simulation in GHz regime using a particle-in-cell code. The simulation model supposes a rectangular grating with limited length and width, to be driven by a single electron bunch, a train of periodic bunches and a continuous beam, respectively. Besides the Smith-Purcell radiation, the evanescent wave is clearly observed, which holds the frequency lower than the allowed minimum Smith-Purcell frequency. It is also shown that the superradiant radiations excited by periodic bunches are emitted at higher harmonics of the bunching frequency and at the corresponding Smith-Purcell angles. The distributions of the radiation intensity are presented and compared with a recently proposed theory. The "start current" for a continuous beam to make the device start oscillation is addressed as well.

INTRODUCTION

The superradiant Smith-Purcell (SP) radiation has attracted many attentions since Urata and co-workers observed this phenomenon in their experiments [1,2]. It is a promising alternative in the development of a compact, tuneable and high power THz sources. To better understand the physics of the superradiant SP radiation is necessary for improving the performance of such kinds of devices.

It is known that the SP radiation is emitted as an electron passes close to the surface of a periodic metallic grating [3]. The wavelength λ of the radiation observed at the angle θ measured from the direction of electron beam is given by

$$\frac{\lambda}{d} = \frac{1}{|n|}\left(\frac{1}{\beta} - \cos\theta\right), \qquad (1)$$

where d is the grating period, βc the electron velocity, c the speed of light, and n the order of the reflection from the grating. The incoherent SP radiation has been analysed in many ways, such as diffraction theory, integral equation method and induced surface current model [4-8]. The experimentally observed superradiant effect is regarded as the result of the appearance of periodic electron bunches. Several theories have been proposed to reveal the physics of the superradiant phenomenon [9-13], and a three-dimensional simulation is supposed to be necessary.

#dazhi_li@hotmail.com

In this paper, we perform a three-dimensional particle-in-cell simulation for the coherent and superradiant SP radiation using MAGIC [14], a code for simulating processes involving interactions between space charge and electromagnetic fields.

SIMULATION MODEL

The simulation model involving a rectangular grating and a cylindrical electron beam is shown in Fig. 1, where d is the periodic length, s the groove width, h the groove depth and w the width of the grating. The main parameters are summarized in table 1, and we note that the grating period, groove width and depth and initial electron's energy are same as those in Ref. [15]. The length of the grating is set differently for particular simulation case, which will be mentioned lately. The grating, assumed to be a perfect conductor, is set in the

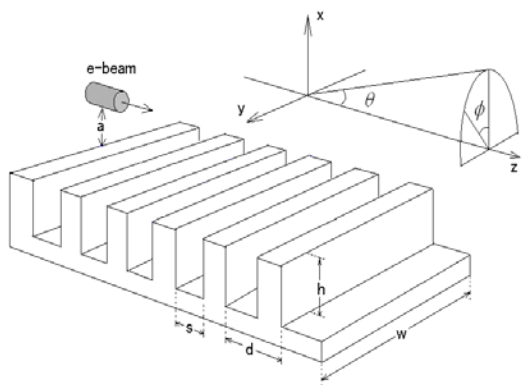

Figure 1: Three-dimensional simulation model of grating and electron beam.

centre of the bottom of a vacuum box, which is bounded by an absorption region. A perfect laminar beam produced from a cathode moves in the z-axis. The simulation area is divided into mesh with rectangular cell of very small size in the region of beam propagation and large in the rest.

Table I: Main Parameters for Simulation

Electron beam energy (injection)	E=100 keV
Beam radius	r=2.5 mm
Beam-grating distance	a=2 mm
Grating period	d=2 cm
Grating groove depth	h=1 cm
Grating groove width	s=1 cm
Grating width	w=10 cm

SIMULATION RESULTS

Single Bunch

We first perform the simulation of a single electron bunch. The grating is arranged to be 10 periods. The bunch length is chosen as 0.1 ps with the current of 1A. It is short compared to the radiation wavelength, so the radiation is coherent. In our simulation we focus on the first order SP radiation since the high orders are not evident. Fig. 2(a) illustrates the temporal behaviour of B_y, detected at the point of θ =120°, ϕ =0°. We notice that the SP radiation pulse consists of 10 periods and is separated in time from the evanescent wave. The corresponding FFT is given in Fig. 2(b), where one can find two clear peaks. The one peaked at 6.5 GHz is the SP radiation, while the other at 4.5 GHz is the evanescent wave. Not like the SP radiation, the evanescent wave frequency is angle independent. The dependency of the SP frequency and the amplitude of B_y on the angle θ is as shown in Fig. 3, observed at the same distance 36.35 cm to the centre of the grating. For comparison, we also plot the analytical result calculated from the theory of Andrews and co-workers [16]. It is seen that the simulation data for the SP radiation frequency agrees well to the theoretical curve as θ over 90°, somehow the discrepancy appears for the rest. Our best guess is that the detector is not far enough for far-field detection. We also see that the maximum amplitude of B_y appears at 125°. There are slight differences between the analytical and simulation results, which might be due to the fact that we use a broad electron beam that nearly reaches the grating, whereas they use a narrow electron beam model. In Fig.4, we give the distribution of field amplitude with respect to the azimuthal angle ϕ. The observation angle cannot vary in a large range due to the limit of the simulation geometry. The distribution shows maximum at the centre point ϕ =0 for cases of θ =130° and θ =80°, but minimum for θ =50°.

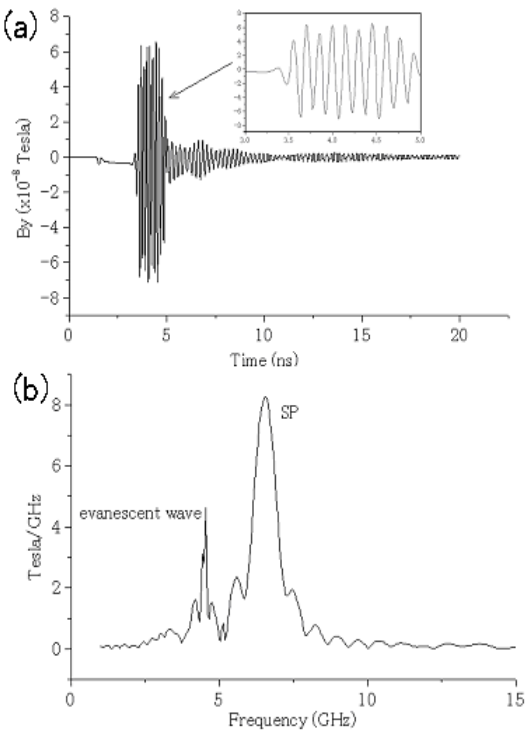

Figure 2: Time signal of B_y (a), and its corresponding FFT (b).

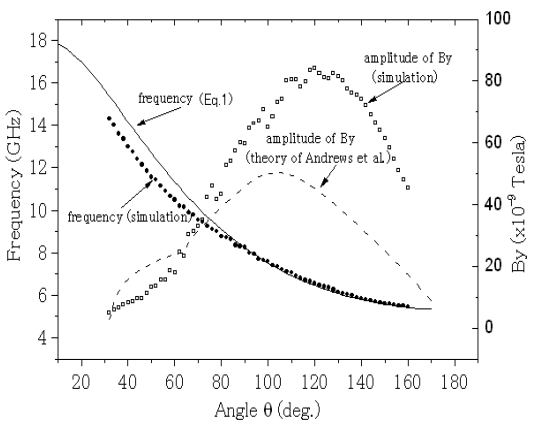

Figure 3: Distribution of SP frequency and its By amplitude.

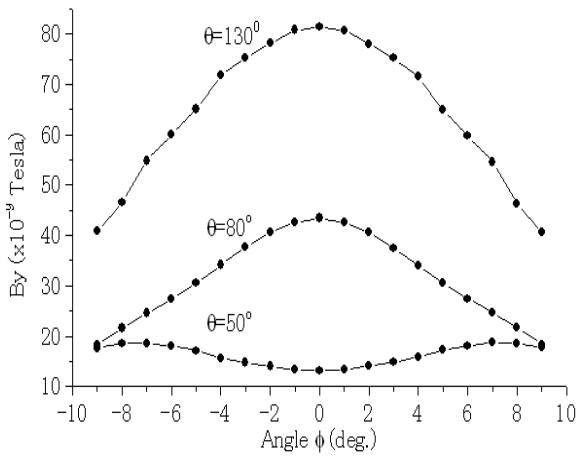

Figure 4: The dependency of By amplitude on azimuthal angle.

Periodic Bunches

In all radiation sources using an intense electron beam, the mechanism leading to superradiance is beam bunching. The spectral intensity of the radiation is enhanced at the bunching frequency and its harmonics. Recently Korbly and co-workers have carried out a SP experiment at MIT with using a pre-bunched electron beam [17]. When certain conditions are satisfied, a continuous beam can be bunched by the interaction with the evanescent wave, which has been discussed by Donohue and Gardelle [15]. In order to demonstrate the properties of superradiant radiation more clearly, we avoid the problem of bunching from an initially continuous beam. Instead, we generate a train of bunches to drive the grating.

The repetition frequency of bunches is chosen as 3 GHz, and the parameters for grating length and each single bunch are same to those mentioned earlier. Within the time of code running, 30 bunches are generated and enter the simulation area. From the FFT of the temporal behaviour observed by B_y detectors we know that the radiation focused on three frequencies, the second, third and forth harmonic of bunching frequency, as shown in

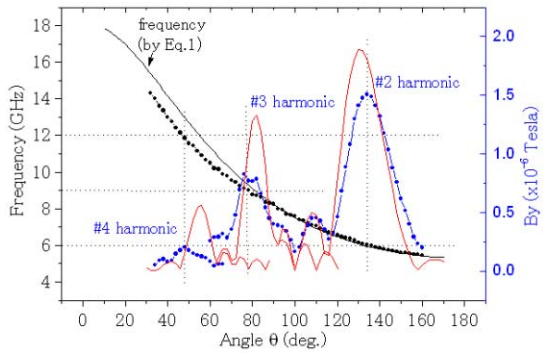

Figure 5: Distribution of superradiant SP radiation frequency and its B_y amplitude. The dotted blue line is the simulation results, and the red line the analytical result multiplied by 10.

Fig. 5. The dominant radiation is the second harmonic peaked at the angle 134°, which corresponds to Eq. 1. Also plotted In Fig. 5, is the analytical result according to Ref. [16], and we find the differences are smaller than one order of magnitude. Another evidence to show the fact that the radiations emit only at certain angles can be found in the contour plot of B_y, as shown in Fig. 6, where the second harmonic radiation is observed to radiate at the angle of about 134°, corresponding to what is shown in Fig. 5. These results strongly support the viewpoint of Andrews and co-workers.

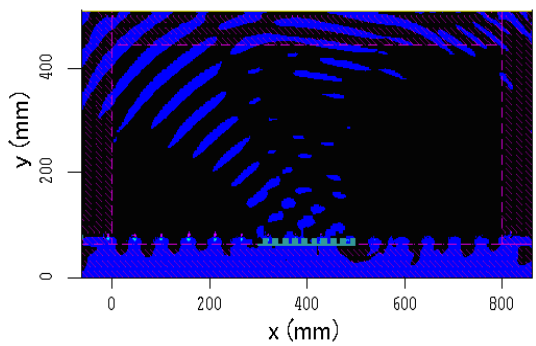

Figure 6: Contour plots of B_y.

Continuous beam

From the theoretical analysis in Ref. [15], we know that the beam line intersects the dispersion curve at a point representing a backward wave, which means the device operates in the mode of backward-wave oscillator (BWOs). Such a device is possible to start to oscillate without external feedback. When the beam current of an originally continuous beam is high enough to get the net gain, the beam will be bunched by the enhanced evanescent wave and the oscillation starts. The bunched beam consequently excites the superradiant SP radiation as discussed early. The value of the current starting the oscillation is called "start current", which needs careful analysis. In this section, we concentrate on determining the "start current" by three-dimensional simulation.

Considering the limit of the capacity of our computers, a grating consisting of 46 periods was employed in this simulation. The electron beam from the cathode is continuously generated, and an external magnetic field of 2T is introduced to prevent the beam from diverging. We vary the beam current and observe the amplitude of E_x of the evanescent wave. The appearance of exponential growth of E_x means that the oscillation happens.

The simulation results are given in Fig. 7. It is shown that, the electric field shows no growth when the current is lower than 0.4 A, while it shows evident growth as the current is above 0.5 A. And the radiation can reach saturation if the current is higher that 0.6 A. From Fig. 7, we can roughly estimate that the "start current" is ~0.5 A. The precise value can be reached if more simulations are performed.

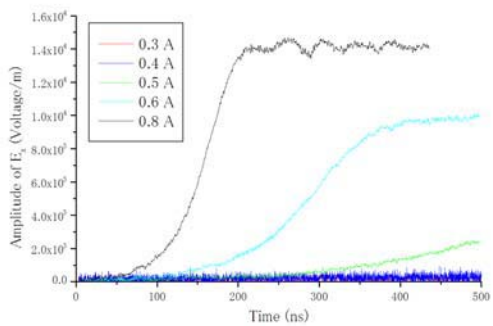

Figure 7: Evolution of amplitude of E_x.

CONCLUSION

In conclusion, we have studied the coherent and superradiant SP radiation through the three-dimensional simulation of an open grating system driven by different modes of electron beam. The single bunch simulation helps us to distinguish the true SP radiation from the evanescent wave. They are different in both frequency characteristics and generation mechanism. The amplitude of the SP radiation is angle dependent. The strongest radiation appears at 125° at the present parameters. The supperandiant effect is demonstrated with the simulation of a pre-bunched beam. We provide powerful evidence showing that the superradiant radiations are emitted at frequencies that are integer multiples of the bunching frequency, and at the corresponding SP direction. The simulation of an originally continuous beam determines the "start current" for the present parameters.

ACKNOLOWEDGEMENTS

The authors gratefully acknowledge helpful discussions with Charles Brau, John Donohue, and Heather Andrews.

REFERENCES

[1] J. Urata, M. Goldstein, M. F. Kimmitt, A. Naumov, C. Platt, and J. E. Walsh, Phys. Rev. Lett. **80**, 516 (1998).

[2] A. Bakhtyari, J. E. Walsh and J. H. Brownell, Phys. Rev. E **65**, 066503 (2002).

[3] S. J. Smith and E. M. Purcell, Phys. Rev. **92**, 1069 (1953).

[4] P. M. van den Berg, J. Opt. Soc. Am. **63**, 689 (1973).

[5] P. M. van den Berg and T. H. Tan, J. Opt. Soc. Am. **64**, 325 (1974).

[6] Y. Takaura and O. Haeberle, Phys. Rev. E 61,4441 (2000).

[7] J. Walsh, K. Woods and S.Yeager, Nucl. Instrum. Methods Phys. Res. A **341**, 277 (1994).

[8] Y. Shibata, S. Hasebe, K. Ishi, S. Ono, M. Ikezawa, T. Nakazato, M. Oyamada, S. Urasawa, T. Takahashi, T. Matsuyama, K. Kobayashi, and Y. Fujita, Phys. Rev. E **57**, 1061 (1998).

[9] L. Schachter and A. Ron, Phys. Rev. A **40**, 876 (1989).

[10] K. –J. Kim and S. –B. Song, Nucl. Instrum. Methods Phys. Res., sect. A **475**, 158 (2001).

[11] H. L. Andrews and C. A. Brau, Phys. Rev. ST Accel. Beams **7**, 070701 (2004).

[12] H.L.Andrews, C.H.Boulware, C.A.Brau and J.D.Jarvis, Phys. Rev. ST Accel. Beams **8**, 050703 (2005).

[13] V. Kumar and K.-J. Kim, Phys. Rev. E 73, 026501 (2006).

[14] D. Smithe and T.M. Abu-Elfadi, Comput. Phys. Commun. 106, **95** (1997).

[15] J.T.Donohue and J.Gardelle, Phys. Rev. ST-AB, **8**, 060702 (2005).

[16] H.L.Andrews, C.H.Boulware, C.A.Brau and J.D.Jarvis, Phys. Rev. ST Accel. Beams **8**, 110720 (2005).

[17] S.E.Korbly, A.S. Kesar, J.R.Sirigiri and R.J.Temkin, Phys. Rev. Lett. **94**, 054803, (2005).

FUTURE FEL STUDIES AT THE VISA EXPERIMENT IN THE SASE AND SEEDED MODES*

G. Andonian, M. Dunning, A. Murokh, C. Pellegrini, S. Reiche, J. Rosenzweig,
UCLA, Los Angeles, CA 90095, USA
M. Babzien, I. Ben-Zvi, V. Yakimenko, BNL, Upton, NY 11973, USA.

Abstract

The VISA (Visible to Infrared SASE Amplifier) experiment at BNL (Brookhaven National Laboratory) has previously demonstrated saturation at 840 nm in 2001. Further SASE studies, in 2003, have demonstrated an anomalously large bandwidth spread of the FEL spectrum due to off-angle emissions. This paper disseminates the current and future program of the VISA experiments at BNL. This includes a study of a seeded FEL, using a 1 micron YAG laser as a seed, and the accompanying diagnostics to characterize the radiation. Diagnostics include the double differential spectrometer, a mode converter to investigate the orbital angular momentum of light in the FEL, and an optical pepper-pot for coherence measurements. Start-to-end simulations, which are reliabily used for experimental modeling, are presented.

INTRODUCTION

The advent of the X-ray free electron laser (FEL) is on the horizon [1, 2]. The creation and diagnosis of ultra-short pulses is of great importance to the FEL community. The generation of femtosecond long, Ångstrom wavelength radiation will open doors to a myriad of scientific endeavors at ultra-short time scales [3].

The VISA program was developed to investigate properties of a high gain self amplified spontaneoous emission (SASE) free electron laser. A proposal to obtain ultra-short pulses [4], by manipulating frequency chirped FEL output, is the inspiration for the VISA II experiment. The frequency chirped radiation produced from an undulator is monochromatized and is used to seed a second undulator. The ultimate goal of the VISA II project is to operate the high gain SASE FEL with a large electron beam chirp.

The current mode of operations expands on this goal by utilizing the optimized capabilities of the facilities employed. Under these conditions, the VISA FEL operates in the seeded mode, using a 1 micron YAG laser as the seed. The experimental mission of the seeded FEL is to investigate high gain radiation properties with studies focusing on the far-field angular distribution and coherence of the radiation.

*This work supported by Dept. of Energy Contract no. DE-FG-98ER45693, and Office of Naval Research no. N000140210911

THE VISA EXPERIMENTAL PROGRAM

VISA I

The VISA project is hosted by the Accelerator Test Facility (ATF) of Brookhaven National Laboratory (BNL). The experimental layout is described in detail in Ref. [5] (Fig. 1 shows a schematic). The VISA I project succesfully demonstrated saturation of a SASE FEL within a 4 meter undulator at 840 nm. The high peak current, a result of nonlinear electron bunch compressoin along the dispersive line of the transport, was ultimately responsible for the observed high gain lasing. A start-to-end simulation suite of codes, PARMELA [6], ELEGANT [7], and GENESIS 1.3 [8], modeled the beam dynamics in the gun, transport and undulator, respectively. SASE FEL properties, such as pulse energy, profile, and angular distribution were computed with GENESIS. The complete characterization of the SASE FEL properties included gain lengths, spectra, energies, angular distributions and observation of nonlinear harmonics, and was successfully benchmarked against the simulation suite [9].

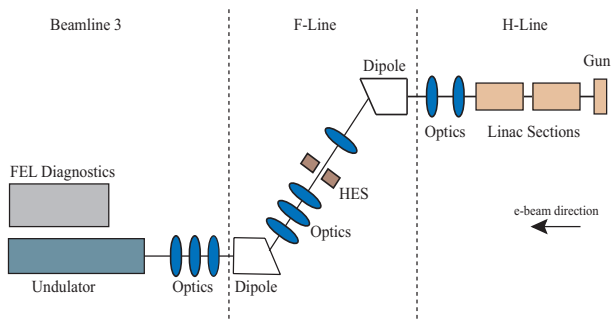

Figure 1: Layout of the ATF beam transport (not to scale). The VISA undulator is located along Beamline 3 after the 20 degree dogleg.

VISA IB

Subsequent measurements at VISA, informally referred to as VISA IB, also took place at the ATF in 2003. An anomolously large bandwidth, up to 15% full width, was observed at high gain (Fig. 2), accompanied by atypical far-field angular radiation patterns.

The electron beam (330 pC, 1.7% energy spread) was subjected to the same nonlinear bunch compression mechanism as in VISA I, except with a much higher degree of compression and thus a higher peak current. The SASE

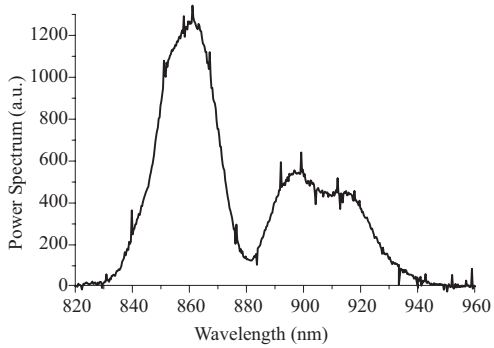

Figure 2: Sample shot of observed SASE FEL spectrum displays an anomalously large bandwidth.

FEL output (2 μJ average energy), was extremely stable and insensitive to RF and laser timing jitter. The spectrum is notable for a characteristic double peak structure, accompanied by a mean bandwidth value of 12% full width (greater than 100 nm), as seen in Fig. 2.

GENESIS simulations reproduced the features of the radiation (large bandwidth and double spiked structure). After transport, the electron beam displayed a highly nonlinear longitudinal phase space. The secondary spike was due to amplification of an off-axis mode. The mode was excited by the non-ideal centroid and envelope motion of the beam through the undulator's quadrupole focusing lattice. The lasing core of the beam was mismatched to the undulator focusing lattice yielding significant excursions in beam size in both transverse planes. Additional transverse motion causes a red-shift in the radiated wavelength and amplification of the off-axis modes [10].

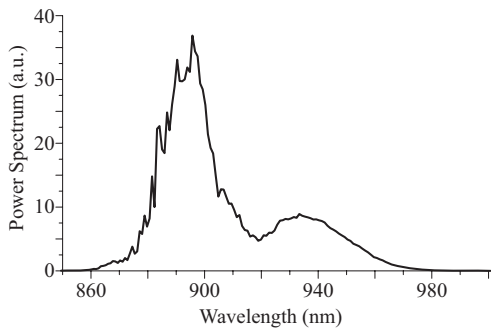

Figure 3: SASE FEL power spectrum obtained from GENESIS. The large bandwidth and the double hump feature observed in measurements were reproduced with simulations.

Double Differential Spectrometer The double differential spectrometer is diagnostic developed to unfold the relationships between frequency and angle of the FEL radiation. A slice of the FEL ouput is passed through graduated slits, then focused onto a set gratings (1200 in^{-1}). The resulting image displays the photon beam with frequency along one axis, and transverse angle along the other axis, and is a direct study of the intensity of the beam presented in the familiar form, $\frac{d^2I}{d\omega d\theta_y}$.

Raw data from a preliminary prototype of this diagnostic is presented in Fig. 4. The overall parabolic structure of the beam, from red shifting, in (θ, ω) space is evident, with even richer multi-mode patterns also present. Upgraded GENESIS post-processing tools were used to further understand this data and indeed displayed the parabolic structures along with the presence of higher order modes.

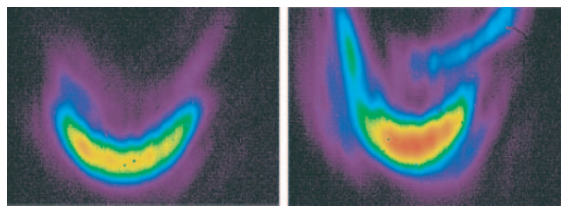

Figure 4: The parabolic structure (left) is evident in the images from the double differential spectrometer, where the angle is represented along the horizontal axis and the frequency along the vertical. Richer structures have also been observed (right).

Far-field Angular Distribution This far-field angular distribution measurement was made by propagating the output radiation, without optical focusing, to a screen located 3 m (10 Z_R) downstream. Observed patterns were hollow in nature, like previous VISA results, except more pronounced in angle (with spiral shaped patterns accompanying the hollow modes). The helicity of this patterns will be studied via a mode converter.

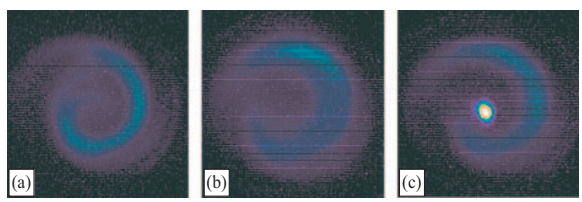

Figure 5: Far-field angular distribution profiles display an atypical spirality and helicity (a,b); superimposed with a reference alignment laser (c).

Chirped Beam FEL

The goal of the VISA II experiment is to inject a linearly chirped electron beam into the undulator to produce frequency chirped SASE FEL radiation. The bunch compression mechanism facilitates high-gain lasing, however, it restricts the management of beam properties through transport. Preservation of the electron beam chirp applied at the linac will be accomplished by the manipulation of nonlinear longitudinal compression by the addition of sextupole magnets placed at high horizontal dispersion points. The sextupoles will mitigate second order effects, particularly by diminishing the T_{566} element, of the transport matrix, to a negligible value [11]. Three sextupoles have been installed and commissioned at the ATF.

Frequency Resolved Optical Gating A frequency resolved optical gating (FROG) [12] system will be used to measure the frequency chirped, short pulse radiation. This method was successfully used elsewhere, to measure both the amplitude and phase of the radiation [13].

The frequency resolution of the FROG spectrogram is a concern at the VISA experiment. The diagnostic system is constrained by the doubling crystal and can not adequately resolve the radiation expected from the VISA II FEL. The thick lens must be replaced by a thin lens to increase the resolution; a dedicated spectrometer must be added to compensate for the loss of functionality of the thin lens. The CCD camera (several megapixel) must be able to cover a large range of wavelengths to resolve the observed bandwidth.

GENESIS outputs for the chirped beam case show a clear effect for idealized beam shapes and have been analyzed for varying degrees of chirp. Indeed, the inversion algorithm is robust enough to handle other exotic shapes and patterns which have been simulated and reconstructed via the commercial FROG software (Femtosoft) for the VISA II experiment. Fig. 6 shows an example of a spectrogram obtained from GENESIS for the running conditions of the VISA II FEL. This structure shows the complex nature of the FEL pulse, which is expected to contain several spikes. This longitudinal pulse profile was retrieved when the spectrogram was analyzed with the FROG reconstruction algorithm.

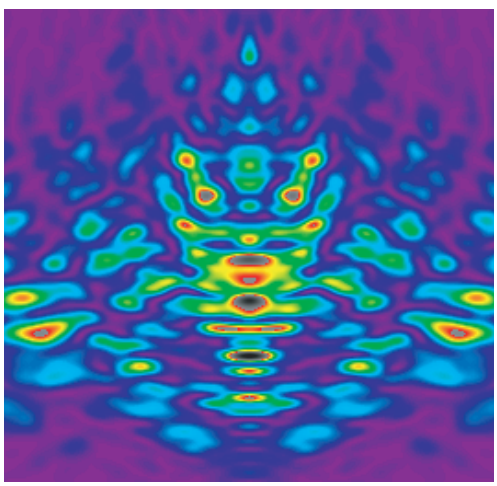

Figure 6: Spectrogram (with frequency along the vertical axis and time delay along the horizontal) of the expected radiation from the VISA II experiment. Further processing of this spectrogram has yielded the longitudinal profile of the pulse used in simulations.

Mode Converter The investigation of hollow mode and spiral shaped far-field angular radiation patterns at VISA is conducted with the introduction of a diagnostic mode converter. The mode converter is designed to transform light with planar polarization to circular polarization, and vice versa [14]. The $\pi/2$ mode converter is constructed of two cylindrical lenses, separated by a distance of $d = \sqrt{2}f$, and the resultant light will have distinct observable properties. This data will yield insight into the underpinnings of the unusual angular distribution patterns observed throughout the tenure of the VISA program. The cylindrical lenses for the mode converter have been setup and will be placed in the diagnostic station downstream of the undulator.

Polarizer The VISA project will also examine the study of coherent transition undulator radiation [15], the radiation emitted by the electron bunch as it passes through the entrance and exit of the undulator, due to the change in longitudinal velocity. Theoretically, the radiation is radially polarized, describing yet another possible explanation for the helicity of the observed far-field patterns from the planar undulator at VISA. The quantization of this effect requires minimal alteration of already existing diagnostics with the addition of grid polarizers to determine the polarization of the radiation. The effects of coherent transition radiation, from the electron beam striking a metal mirror, will have to be addressed (by the placement of a kicker magnet) before useful data is recovered from this measurement.

SEEDED FEL MEASUREMENTS

The results of the far-field angular distribution patterns at the VISA experiment have motivated further studies of the FEL in the seeded regime. The seeding pulse (a 1 micron YAG laser) will establish transverse and longitudinal coherence of the FEL (low bandwidth, high brightness). Such a radiation source will provide a short Rayleigh length FEL beam.

Further motivation for seeded FEL studies arises from controlling and managing the high power FEL in the far-field. Increasing the emission angles will decrease the intensity in the far-field (hollow modes) which will be technically useful in delivering high power radiation with minimal damage to sensitive optical elements.

The proposed experiment involves the VISA undulator with the ATF YAG laser as a seed. The YAG laser (1064 nm) serves as the drive laser for the photoelectron beam at the ATF and some its energy is transported to the experimental hall for deposition into the VISA undulator. A longitudinal delay line is currently being used to ensure adequate timing overlap with the electron beam and seed laser. The electron beam energy for the seeded FEL operations is lowered to 61 MeV to account for the higher wavelength operations

The experiments that will be carried out revolve around the detuning parameter of the FEL. Start-to-end simulations have been conducted for ideal and virtual particle sets. The results of the far-field angular distribution patters are presented in Fig. 7. It is apparent that detuning the electron beam indeed changes the angles and produces hollow

modes in the far-field. The power gain curves derived from GENESIS simulations (Fig. 8) have also been studied.

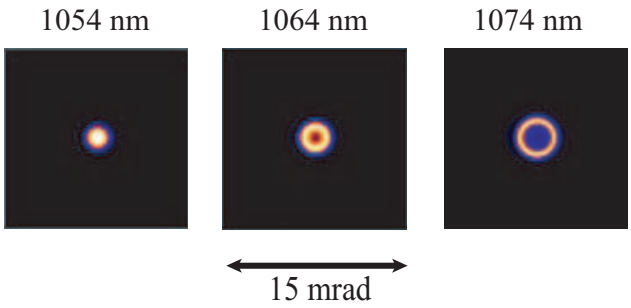

Figure 7: GENESIS simulation of the far-field angular distribution patterns of the seeded FEL for different values of detuning (1064 nm is the nominal wavelength).

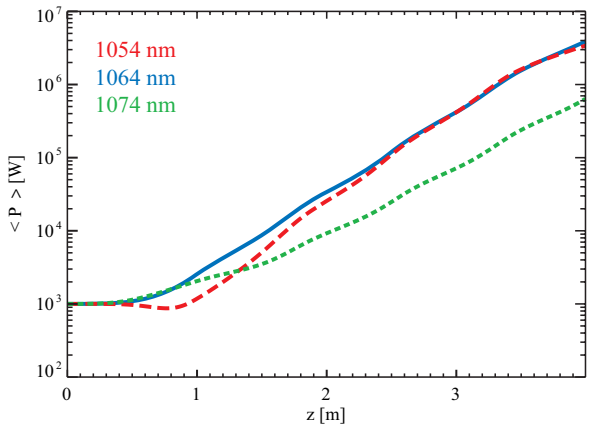

Figure 8: Power gain curves (GENESIS simulations) for varying detuning parameters.

Transverse Coherence

Transverse, or spatial coherence is an important figure of merit of any FEL. The transverse coherence for the seeded FEL will be verified with an arrangement of slits, by performing variations on the classical Young double-slit experiment. The FEL radiation diffracts at the slits, and the transverse coherence is calculated by measuring the ratio of the sum and difference of the maximum and minimum observed intensities [16]. Since the transverse coherence is a function of longitudinal position, it is measured at different positions downstream of the undulator exit. Several variations of slits have been fabricated for the transverse coherence study, including double-slits of various widths and spacings, crossed-slits, circular apertures of differing diameter, and a pepper-pot pattern of circular apertures. The use of these slits will be expanded after the seeded FEL experiment to also encompass SASE coherence measurements. The pepper-pot pattern is of particular interest because the emitted radiation from the uncorrected chirped-beam FEL experiments yielded intensity distributions with radial (helical) characteristics that provoke further investigation.

REFERENCES

[1] M. Cornacchia *et al.*, Linac Coherent Light Source Design Study Report no. SLAC-521 (1998)

[2] TESLA-FEL, Deutsches Elektronen Synchrotron 2001-05 (2001)

[3] R. Neutze *et al.*, Nature **406**, 752 (2000)

[4] C. Schroeder *et al.*, J. Opt. Soc. Am. B **19**, 1782 (2002)

[5] A. Murokh *et al.*, Phys. Rev. E **67**, 066501 (2003)

[6] L.M. Young, J.H. Billen, Los Alamos National Laboratory Report No. LA-UR-96-1835 (rev. 2000)

[7] M. Borland, Advanced Photon Source LS-287 (2000)

[8] S. Reiche, Nucl. Instrum. Methods A **429**, 243 (1999)

[9] A. Tremaine *et al.*, Phys. Rev. Lett. **88**, 204801 (2002)

[10] G. Andonian *et al.*, Phys. Rev. Lett. **95**, 054801 (2005)

[11] J. England *et al.*, Phys. Rev. ST Accel. Beams **8**, 012801 (2005)

[12] R. Trebino, *Frequency Resolved Optical Gating*, Kluwer Academic Publishers (2000)

[13] Y. Li *et al.*, Phys. Rev. Lett. **89**, 234801 (2002)

[14] M.W. Beijersbergen *et al.*, Optics Comm. **96**, 123-132 (1993)

[15] S. Reiche *et al.*, Procedings of the 2004 FEL Conference, 193-196, Trieste, Italy.

[16] R. Ischebeck, et al., Nuc. Inst. and Meth. in Phys. Res. A **507**, 175, 2003.

MAGNETIC CHICANE RADIATION STUDIES AT THE BNL ATF*

M. Dunning, G. Andonian, A.M. Cook, E. Hemsing, A. Murokh, S. Reiche, J. Rosenzweig,
D. Schiller, Particle Beam Physics Laboratory, Department of Physics and Astronomy, UCLA,
Los Angeles, CA 90095, USA
M. Babzien, K. Kusche, V. Yakimenko, Accelerator Test Facility, Brookhaven National Laboratory
Upton, NY 11973, USA.

Abstract

Radiation emitted by relativistic electrons traversing the magnetic eld gradients of a chicane bunch compressor has been studied in an attempt to characterize coherent edge radiation (CER). The studies performed at the Accelerator Test Facility (ATF) at Brookhaven National Laboratory (BNL) include frequency spectrum, angular distribution, and polarization measurements. A reconstruction of the longitudinal charge pro le from the measured spectrum shows that the bunch has been compressed to approximately 30 μm FWHM, with a peak current exceeding 1.5 kA. Measurements of radiation from the short pulses are compared to predictions from `QUINDI`, a new simulation code developed at UCLA to model the radiation.

INTRODUCTION

The chicane compressor studies are a collaboration with the Particle Beam Physics Laboratory (PBPL) at UCLA and the ATF, the user facility which hosts the experiment. The chicane was designed to compress the electron beam to yield the high peak current necessary to drive a self-ampli ed spontaneous emission free electron laser (SASE FEL) to saturation [1] and to expand the ATF core capabilities. Recent experiments have focused on the creation of very short electron beam pulses ($\sim$30 μm), and measurements of CER and coherent synchrotron radiation (CSR) emitted by such short bunches. The correlation between these radiative effects and microbunching instabilities are under investigation, as are other parasitic effects of the radiation. These are signi cant issues for larger projects, such as the Linac Coherent Light Source (LCLS), which will employ similar devices and diagnostics for the production of short duration pulses. CER has also been shown to be a bright source of infrared radiation, which makes it well-suited for certain types of microscopy and spectroscopy [2].

* Work supported by DOE grant DE-FG02-98ER45693 and NSF grant PHY-0355048.

EXPERIMENT DESCRIPTION

Chicane Compressor

The chicane compressor is currently installed along the high-energy line (H-line) of the ATF. The operating beam energy is 60-61 MeV for the present chicane radiation studies. The compressor consists of four dipole magnets oriented in a chicane layout, as in Fig. 1.

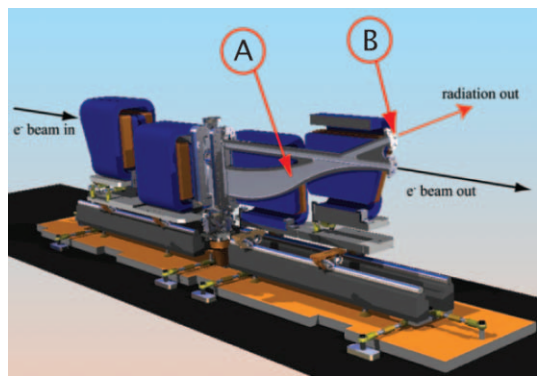

Figure 1: A rendering of the four dipole chicane compressor. The cutaway view shows the approximate radiation source between the third and fourth dipoles (A) and the radiation extraction port (B).

The chicane features a dedicated radiation extraction port that enables viewing of the region (Fig. 1A) which extends through the downstream edge of the third magnet to the upstream edge of the fourth magnet. The rectangular exit port (Fig. 1B) has transverse dimensions of 26 mm $\times$ 11 mm, with the longer dimension in the bend plane [3].

Table 1: Chicane design parameters

Parameter	Value	Units
B-Field	2015	Gauss
Bend Angle	20	deg
Geometric Length	41	cm
Magnet Gap	2.1	cm

Terahertz Radiation Transport

Radiation exits the chicane compressor through a fused silica vacuum window located on the extraction port (Fig. 1B). The radiation is guided with three adjustable mirrors (gold-coated) and a translatable Picarin lens, through metallic pipes (56 mm diameter) to an external diagnostic station. The entire length of the radiation transport line is approximately 7 m. The Picarin lens is positioned one focal length (1.25 m) from the approximate radiation source (between the third and fourth dipoles) to achieve a point-to-parallel transport con guration.

Diagnostic Station

The diagnostic station located at the end of the radiation transport is designed to be modular for versatility. It consists of focusing/turning mirrors, two individual l-ter wheels containing room temperature and cryogenically cooled lters, a wire grid polarizer, an iris on a two-dimensional translation stage, a silicon bolometer, and a Michelson-type interferometer.

Silicon Bolometer

In order to characterize the chicane radiation, a cryogenically cooled silicon bolometer (IR Labs model HDL-5) is employed. The bolometer is cooled with liquid helium and has a built in lter wheel, loaded with cut-on lters (long-pass) with wavelengths of 13, 27, 45, 103, and 285 μm. The detector element incorporates a Winston Cone collector, protected by a wedged polyethylene window (that provides an additional cut-on wavelength of 13 μm) [4].

Interferometer

The radiation spectrum is measured at the output of a Michelson-type interferometer as a function of bolometer voltage. The interferometer is optimized for the 15 μm to 1 mm wavelength range, and has a translatable mirror along one orthogonal leg with 1 μm spatial resolution [5].

CHICANE RADIATION OVERVIEW

Radiation exiting the chicane contains features of both synchrotron and edge radiation due to the measurement position and the magnet geometry. For electrons emitting under the same radiation process, the far- eld intensity distribution is expressed as

$$\mathscr{I}(\omega) = \mathscr{I}_0(\omega)[N_e + N_e(N_e - 1)F(\omega)], \qquad (1)$$

where $\mathscr{I}_0(\omega)$ is the single electron intensity distribution and $F(\omega)$ is the bunch form factor. For wavelengths longer than the bunch length ($\sim$ 30 μm), each type of radiation is coherently enhanced by a factor of N_e, the number of electrons in a bunch. Typically, $N_e \sim 10^9$ for the present ATF running parameters.

The edge radiation emitted from electrons entering and exiting the edges of bend magnets is expected to have greater intensity at longer wavelengths than synchrotron radiation [6]. The characteristics of CER also depend on the topology of the eld gradient. In the *zero-edge length model* [7], the eld of the bending magnet is approximated by a step function. The resultant radiation is radially polarized, with a cylindrically symmetric spatial distribution characterized by a null on the straight section axis and maxima at $\theta \sim 1/\gamma$, analogous to transition radiation. Analytic nite edge length models result in complicated expressions, requiring numerical calculations [8].

Simulations

Start-to-end simulations for the experiment were conducted with `PARMELA` [9] for the electron beam dynamics in the accelerating modules. The code `QUINDI` was used for the beam transport and radiation studies.

`QUINDI` is a parallel-computing code speci cally developed to model the emitted radiation from electron bunches within the ATF chicane. The program avoids the sequential approach of a magnetic lattice, relying instead on an object-driven description of magnetic elements. The observed radiation eld is calculated on a user-de ned plane based on the acceleration eld of the Liénard-Wiechert potentials.

MEASUREMENTS AND ANALYSIS

Frequency Spectrum

Spectral measurements of the emitted chicane radiation were conducted at the ATF. Interferograms were obtained from scans with the Michelson-type interferometer to provide information about the spectral content. This data was used to reconstruct the longitudinal charge distribution of the beam.

Interferometer signal amplitudes from the output of the silicon bolometer were recorded for N shots per mirror position. An averaged, normalized interferogram with the corresponding measured electron beam charge is shown in Fig. 2(a). Each point on the interferogram records the mean value and the error bars depict the standard deviation.

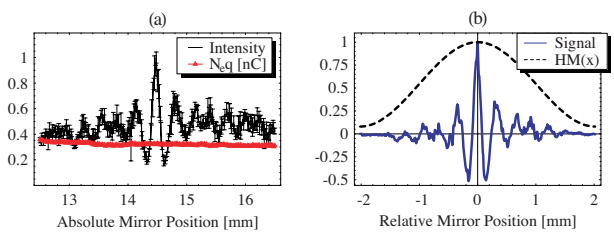

Figure 2: (a) Normalized, averaged signal amplitudes from interferometer scans of chicane radiation. (b) Apodized signal via a Hamming function.

For an accurate spectral reconstruction with a Discrete Inverse Fourier Transform (DIFT), the non-zero offset of the interferogram is removed and the signal is multiplied by an apodization function. Fig. 2(b)

shows the results of apodization by a Hamming function $\mathrm{HM}(x) = 0.54 + 0.46\cos(\frac{\pi x}{a})$, where $2a = 4$ mm is the length of the interferometer scan centered on the maximum peak. This standard procedure removes arti cial low-frequency components and corrects for the spurious tails that arise from the nite sum in the DIFT [10],

$$\tilde{I}_k = \frac{1}{n}\mathrm{Re}\sum_{j=1}^{n} I_j e^{2\pi i(k-1)(j-1)/n}, \qquad (2)$$

where n is the number of equally spaced interferometer mirror positions recorded over a nite distance $[ct_{min}, ct_{max}]$. This yields $n/2$ non-repeating intensity values, I_k, up to the maximum frequency, where I_j is the j^{th} intensity point in the modi ed interferogram.

Fig. 3(a) displays the resulting spectrum of the apodized signal. The peak at $f_{peak} \approx 0.5$ THz coincides with the dominant frequency given by results from QUINDI simulations.

Kramers-Kronig Reconstruction

The forward far- eld radiation intensity spectrum produced by the bunch is given by Eq. 1, where the longitudinal form factor $F(\omega)$ is

$$F(\omega) = \left| \int \hat{\rho}(z) e^{i\omega z/c} dz \right|^2, \qquad (3)$$

with $\hat{\rho}(z) = \rho(z)/N_e q$, the normalized longitudinal charge density. Following a minimal-phase reconstruction technique, a discretized Kramers-Kronig relation is used to extract $\hat{\rho}(z)$ [11].

The minimal phase is

$$\psi(\omega_i) = \frac{2\omega_i}{\pi}\sum_{j\neq i}^{N_{max}} \frac{\ln[\xi(\omega_j)/\xi(\omega_i)]}{\omega_j^2 - \omega_i^2}\Delta\omega, \qquad (4)$$

where $\xi^2(\omega_i) = F(\omega_i)$, and $\Delta\omega$ is the resolution from the spectrum. The normalized pro le $\hat{\rho}(z)$ then has the form

$$\hat{\rho}(z) = \frac{1}{\pi c}\sum_{i=0}^{N_{max}} \xi(\omega_i)\cos\left[\psi(\omega_i) - \frac{\omega_i z}{c}\right]\Delta\omega. \qquad (5)$$

The bunch distribution is calculated from the form factor, determined by tting well-behaved asymptotes to the measured normalized spectrum. Results of this reconstruction are shown in Fig. 3(b). The values for current are scaled to the average measured charge of $N_e q \approx 330$ pC. Due to experimental limitations (discussed below) and numerical tting of the form factor, this reconstruction technique is useful as an approximation of the true bunch distribution. Nevertheless, the reconstructed pro le shows general agreement with predictions from PARMELA simulations in the overall structure of the asymmetric bunch and the compressed head of ~ 30 μm FWHM.

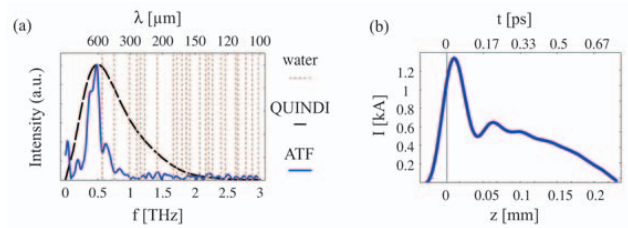

Figure 3: (a) Spectra from apodized interferogram and from simulation. Prominent water absorption frequencies are shown as vertical dotted lines. (b) Minimal phase Kramers-Kronig bunch reconstruction for the measured spectrum.

Limitations on Spectral Analysis

The simulated and measured spectra show that the radiation is dominated by frequencies below 1.5 THz, however, several experimental factors contribute to spectral l-tering which affect the measured frequency distribution and the longitudinal bunch reconstruction. The primary experimental artifact near the dominant frequency band is the selective ltering from water absorption (due to high levels of humidity encountered through the radiation transport on the dates of data acquisition). This effect is exempli ed by strong absorption troughs located near $f = 0.57$ and 0.75 THz. Signi cant absorption frequencies are plotted in Fig. 3(a) for a 7 m travel path [12]. The spectrum is also affected by the radiation transport line, which acts as a high pass lter due to its inherent nite apertures and acceptance angles. Further, the fused silica vacuum port window maintains a transmission coef cient that slowly decreases for frequencies greater than 0.3 THz, but rapidly approaches zero for frequencies greater than 6 THz.

Polarization

The transverse radiation pro le and polarization were measured in an effort to observe the distinctions between CER and CSR. Fig. 4 shows the measured intensity (normalized to maximum) as a function of polarizer rotation angle. The wire grid polarizer was mounted at the end of the transport and rotated in 15° increments, and the focused signal intensity was measured with the bolometer. The linearly polarized component of radiation (sinusoidal) is consistent with that expected from synchrotron radiation. The non-linearly polarized component, which introduces a vertical offset, is a clear signature of edge radiation. Analytic studies show that pure synchrotron radiation would give a ratio of approximately 7:1 between the maximum and minimum signal [13], while the observed ratio is approximately 4:1. QUINDI results are consistent with the measured data (Fig. 4).

Transverse Spatial Distribution

The transverse far- eld spatial intensity distribution of the emitted radiation was measured by scanning a small iris

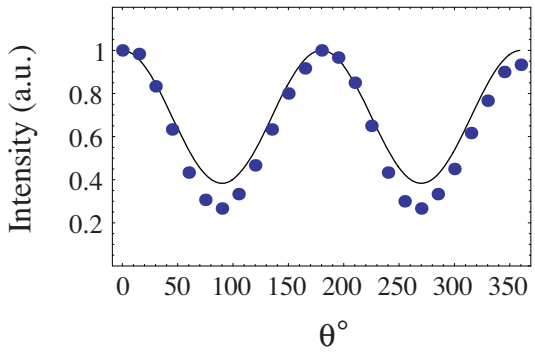

Figure 4: Normalized polarization intensity of the chicane radiation. Solid line is from QUINDI, dots are measured at the bolometer. The zero angle is arbitrary.

(3 mm diameter) in a 19 mm × 23 mm rectangular array of discrete points (Δd =3.8 mm). The iris was scanned across the transport tube exit and the signal was focused into the bolometer. Iris scans were performed for varying radiation polarizations with the aforementioned wire-grid polarizer (Fig. 5).

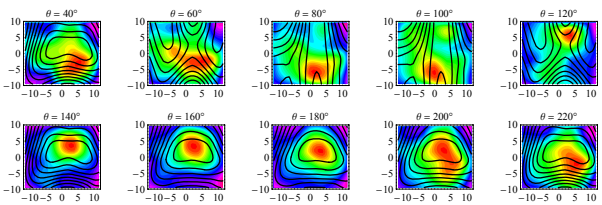

Figure 5: Interpolated far- eld radiation intensity distributions for 20 degree polarizer angle increments, with results from QUINDI simulations (contours) overlayed for comparison. The x and y scales have units of mm.

CONCLUSION

The chicane radiation studies at the ATF display telling signatures of edge radiation. The transverse spatial distributions show patterns consistent with simulations, namely strong peaks shifting into multiple peaks for varying degrees of polarization with identi able nulls in the distribution on-axis. The non linearly polarized component of radiation observed as an offset to the sinusoidal signal in the overall polarization curve is a clear indication of the actuality of prominent edge radiation.

Future plans to improve the measurements include radiation transport modi cations such as replacement of the fused silica chicane radiation port window with a diamond or z-cut crystalline quartz window; this will greatly improve the spectral range of the measurements. In addition, enclosing and ushing the transport line with dry nitrogen will mitigate the effects of water absorption lines in the measured spectrum. Also, a Czerny-Turner type monochromator is currently being built in order to more ef ciently resolve the chicane radiation spectrum.

REFERENCES

[1] G. Andonian, *et al.*, *Proceedings of the 2003 Particle Accelerator Conference*, 944, 2003.

[2] T. E. May, R. A. Bosch, and R. L. Julian, *Proceedings of the 1999 Particle Accelerator Conference*, 2394, 1999.

[3] R. Agustsson, *UCLA M.S. Thesis* (2003).

[4] http://www.irlabs.com/.

[5] http://www.radiabeam.com/.

[6] O. V. Chubar and N. V. Smolyakov, *J. Optics (Paris)* **24**, 117 (1993).

[7] R. A. Bosch, *Il Nuovo Cimento* **20D**, 483 (1998).

[8] O. V. Chubar and N. V. Smolyakov, *Proceedings of the 1993 Particle Accelerator Conference*, 1626, 1993.

[9] E. Colby, *UCLA PhD Thesis*, FERMILAB-THESIS-1997-03 (FNAL, 1997).

[10] J. F. Rabolt and R. Bellar, *Applied Spectroscopy* **35**, 132, 1981.

[11] R. Lai and A.J. Sievers, *Phys. Rev. E* **50**, 5 (1994).

[12] P.U. Jepsen, *private communication*.

[13] J.D. Jackson, *Classical Electrodynamics*, John Wiley and Sons, New York, 1999.

BEAM PICKUP DESIGNS SUITED FOR AN OPTICAL SAMPLING TECHNIQUE

K. Hacker, F. Loehl, H. Schlarb DESY, Hamburg, Germany

Abstract

The beam arrival-time monitor and large horizontal aperture chicane BPM at FLASH are important tools to stabilize the arrival-time of the beam at the end of the linac. The pickups for these monitors will be paired with a front-end that samples the zero-crossing of the transient through the use of electro-optical modulators (EOMs) and sub-picosecond-long laser pulses delivered by the master-laser oscillator (MLO). The design of pickups for this front-end requires the consideration of the transient shape as well as the amplitude. Simulations and oscilloscope traces for pickups that use or will use the EOM based phase measurement and the expected limitations of each pickup are presented. In particular, a method to reduce the beam position sensitivity of the beam arrival-time pickup, the potential resolution of a button pickup arrival-time measurement, and the design for a 5 μm resolution BPM with a 10 cm horizontal aperture are described.

INTRODUCTION

A beam arrival-time stability of 30 fs (~10 μm at v=c) is desired for pump-probe experiments and is mandatory for laser-based electron beam manipulation at FLASH and the XFEL [1]. With the accelerating LLRF goal energy stability of 10^{-4} at FLASH, the transverse position jitter in the dispersive section of the first chicane becomes 34.5 μm and results in a longitudinal position jitter of 18 μm. A monitor for a feedback system should be able to measure the beam energy by a factor of three better than the desired energy stability of $5*10^{-5}$ and this means that the resolution for a beam position measurement in the chicane must be better than 6 μm and a longitudinal time-of-flight path-length measurement should resolve 3 μm.

A longitudinal time-of-flight energy measurement can be made with two beam arrival-time monitors: one before and one after the chicane, but a chicane BPM energy measurement has an advantage given by the ratio of the R_{16} to the R_{56} terms. In the case of the first bunch compressor for the XFEL, this advantage in the required sensitivity of the monitor is a factor of six.

The arrival-time monitor and the chicane BPM can distinguish the energy jitter that results from injector timing jitter from the energy jitter caused by the acceleration RF phase and amplitude jitter. A bunch length monitor and the chicane BPM can distinguish the RF amplitude jitter from the RF phase jitter. BPMs before the chicane can be used to remove incoming orbit jitter from the chicane BPM's energy measurement.

The pickup transients for these energy measurements will be paired with the sub-picosecond pulses from the master laser oscillator (MLO) from the timing and synchronization system to sample the zero crossing of the beam transient through an electro-optical modulator (EOM). The beam arrival-time monitor installed in the tunnel, a perpendicularly mounted stripline to be installed in the dispersive section of the chicane in October 2006, and button-style pickups are analyzed with Microwave Studio simulations and compared to measured oscilloscope traces with regard to their suitability for the EOM phase measurement technique. The front-ends for beam transient pickups typically filter the transient down to 2 GHz or less and utilize the ringing or amplitude of the signal to get the desired beam information, but this EOM front-end works at 10 GHz or more and samples the zero-crossing, so attention must be paid to the transient shape.

EOM PHASE MEASUREMENT

Test Bench

To date, 30 fs resolution has been achieved with the EOM phase measurement and a limited but not combined output of the ring shaped arrival-time monitor pickup [2]. It utilizes a short optical pulse (< 1 ps) from a master laser oscillator that is locked to the 1.3 GHz reference of the machine. The light pulse travels via fiber optics through an electro-optical modulator (EOM) which encodes the amplitude information of an RF pulse into the laser pulse energy. Essentially, the laser pulse samples the beam transient. The modulated laser pulse is then detected with a 50 MHz bandwidth photo diode and read out by a 100 MHz, 12bit ADC that is clocked with the laser pulse at twice the repetition rate of the laser.

Since changes in the RF pulse arrival-time produce a change in laser intensity, the measurement is limited by the steepness of the RF signal slope and the precision of the laser amplitude detection. Slope changes can distort the measurement, so a feedback is used to maintain the measurement at the zero-crossing. The slope at the zero crossing for the 30 femtosecond resolution measurement was 250 mV/ps and the single-shot noise with which the laser pulse intensity was detected was 0.3%. Shot-noise of spontaneous emission from the laser is a suspected noise source, but as of yet there is no conclusion.

Future Applications

It is anticipated that for each pickup output, the transient signal will be split for a low-resolution (large range) phase measurement and a high-resolution (small range) phase measurement. A delay-line will use the low-resolution measurement to put the high-resolution measurement in range. The phase measurement is given by the position of this delay-line plus the fine

measurement given by the laser amplitude. This delay line must have sub-micrometer resolution over 10 cm and be adjusted between macro-pulses (10 Hz) in order to keep the system measuring the beam transient at the zero crossing, thereby reducing the systematic errors of slope variation.

The EOM setup will be standardized and duplicated several times for use with two or more beam arrival-time pickups and two large horizontal aperture chicane BPMs.

PICKUP DESIGN

Beam transient pickups for the EOM phase measurement must produce a steep slope for sampling of the zero-crossing with a picosecond-long laser pulse to give maximum resolution. They must also have a minimum of ringing so that the transient of a bunch that comes earlier is not detected. The bunch spacing will be 200 ns for the XFEL. A steep slope requires the high bandwidth and voltage that are produced by short bunches and pickups with a large area exposed to the beam. Bunches that are longer than ~25 ps (RMS) will have reduced resolution because the slope of the transient becomes less steep (e.g. 50% for 25 ps) for longer bunches. Minimal ringing can be achieved through tapering from the pickup to the feedthrough.

Position Monitor

The design utilizes a cylindrical pickup within a cylindrically shaped vacuum chamber channel that lies over and perpendicular to the path of the electron beam (see Fig. 1) [3]. It was originally proposed by [4]. When the electron beam travels beneath this pickup, short electrical pulses travel to opposite ends. The arrival-times of the pulses are then measured with the EOM technique and used to determine the position of the electron beam.

In Fig. 1, the perpendicularly mounted stripline is depicted in 3-D as well as in cross-section.

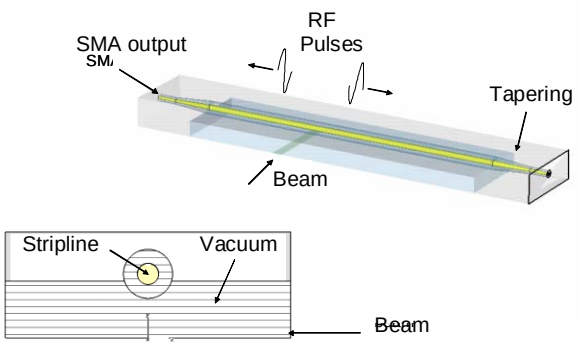

Figure 1: Perpendicularly-mounted stripline BPM pickup.

In the 3-D depiction, only the upper-half of the BPM is shown, since the lower-half is identical. The beam is represented by a thick line underneath the stripline. The central piece of the stripline is tapered on both ends from a 3 mm diameter to an SMA sized connector pin. The vacuum feedthroughs to SMA connectors are at the ends of the stripline.

Standard stripline designs do not have tapering from the pickup to the feedthrough, but instead have a larger radius pickup connected at a sharp angle to a smaller SMA connector sized feedthrough. The tapered design was chosen because in simulation it transmits 20% more signal amplitude and has 80% less ringing amplitude compared to the non-tapered design.

In a Microwave Studio simulation, a 50 GHz bandwidth (FWHM) Gaussian pulse was applied to the monopole mode of a waveguide port in order to simulate the electron beam. The output signals of the SMA connector ports were scaled according to a 1 nC electron bunch charge (Fig. 2).

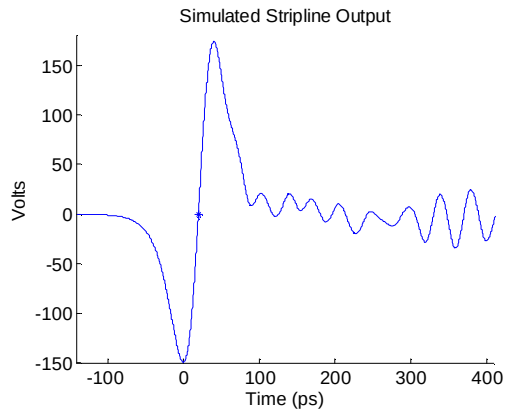

Figure 4: Simulated stripline output with a marker at the sampling location. The slope at the marker is 10 V/ps.

A similar simulation for an existing pickup also predicted such a high voltage, and when the pickup output was measured in the tunnel, the results matched the simulation within a few volts. The transient without a long cable is most interesting because the EOM front-end will be installed in the tunnel within a temperature stabilized enclosure, thus minimizing cable lengths and temperature dependent signal drifts.

The BPM's horizontal response is linear over the entire horizontal aperture and is insensitive to small changes in the beam shape. Vertical position changes and charge changes influence the amplitude of the signal but not the phase. The average of two outputs' phase measurements can also be used to measure the beam arrival-time, as long as the energy spread is constant. Alternatively, if the electron beam arrival-time is known, the energy spread can be measured through changes in the sum of the BPM outputs' phase measurements with a projected sensitivity of 1.5 fs/μm (Fig. 3), but this is only possible when the beam width is larger than the length.

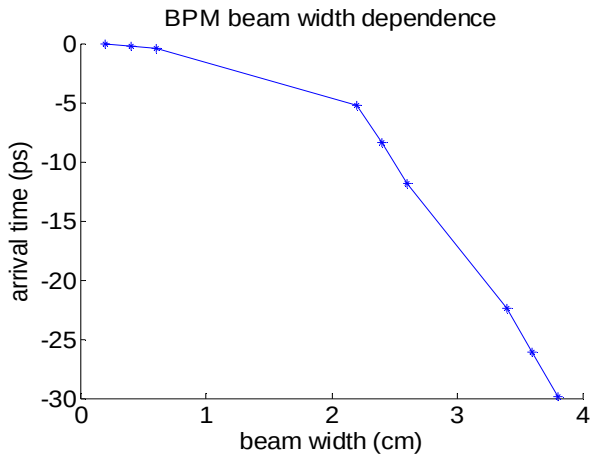

Figure 3: Energy spread measurement with BPM.

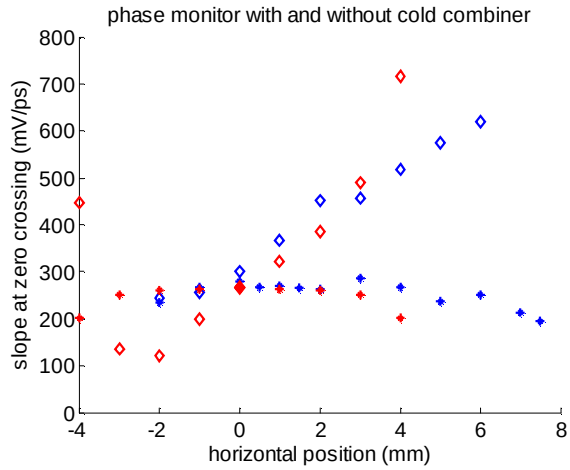

Figure 3: Slope at zero-crossing of arrival-time pickup with (star) and without (diamond) combiner. Simulation (red) and oscilloscope (blue) results are shown.

An important thing to note about pickup transients is that a measurement of the zero-crossing gives the RMS value of the beam position, in the case of the transverse stripline, or, in the case of the beam arrival-time monitor, it gives the RMS value of the arrival-time. This is different from measurements with devices that can measure the peak intensity of an electron distribution, such as synchrotron light monitors and electro-optical sampling. For non-linear, inhomogeneous compression schemes the RMS value and the peak value can differ, but for linear, homogeneous compression, they should be one and the same. About 30 fs difference between the peak and RMS values has been measured for the current compression scheme. The 3rd harmonic cavity will be installed in summer 2007 to linearize the compression.

Arrival-time Monitor

The arrival-time monitor pickup is a ring electrode in a thick flange with two SMA feedthrough sized pins attached to the ring in the horizontal plane. The frequency response of the ring shows a notch at 5 GHz which corresponds to a quarter-length of the ring circumference, implying that the beam does not couple strongly to the second harmonic of the ring. A position dependence of the output signals is therefore seen through a beat between the fundamental and third harmonic of the ring. This problem reflects the original intended use of the pickup in a lower-resolution RF down-mixing phase measurement that was not affected by the transient shape. For the EOM phase measurement the two outputs were combined to remove this effect (Fig. 3). The, so called, cold-combiner that was designed for a toroid-based charge measurement crossed the output pins of the SMA connectors in a circular void and terminated one of the arms of the cross with 50 Ohms [4].

The output from the monitor was measured with an 8 GHz bandwidth oscilloscope and simulated with a Gaussian 'beam' in Microwave Studio. Simulation and oscilloscope results agree well when cable, bandwidth, and combiner attenuation are taken into account (Figs. 3 and 4).

Button Pickups

Button pickups are installed in a few locations in the FLASH linac. Their output amplitude is proportional to the button size and distance from the beam and it can be comparable to that observed from the ring shaped pickup. Buttons can be more desirable than the ring electrode due to the lack of a notch in the frequency response that causes zero crossing changes with beam position changes. No detectable change of the transient zero crossing occurs for beam position changes. Buttons also produce a steeper, very linear slope with a lower peak-to-peak voltage.

Measurements of the beam transient with button pickups at FLASH were conducted with an 8 GHz bandwidth oscilloscope inside the tunnel and steep slopes of 1-2 V/ps were observed. The large changes in the slope due to beam position changes make the challenge of measuring on the zero crossing more critical. If the slope changes prove to be unworkable, a combiner could again be used.

The main problem with the pickups that were measured was that the signal was still ringing 200 ns after the transient with an amplitude that was 0.7% of the peak voltage. This would be a problem for the 200 ns XFEL bunch spacing because 10 fs resolution requires almost 10 times less ringing amplitude (Fig. 5).

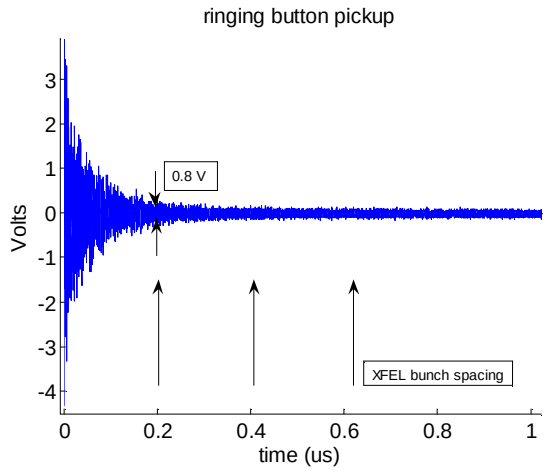

Figure 5: Ringing of button pickup with 120 Volt peak to peak transient. The ringing must be smaller than 10 mV by the time a new bunch comes for a 10 fs resolution phase measurement.

A few button pickup designs were simulated to look for ways to reduce or characterize the sources of the ringing. It was noted that for a large amplitude output, the pickup pin needed to be long or have a large button attached to it. For a long pin or a large cylindrical button, the transient amplitude was good, but the ratio between the transient amplitude and the ringing was bad. For a short pin without a button, there was practically no ringing, but the transient amplitude was insufficient (Fig. 6). More work needs to be done to understand and optimize the design.

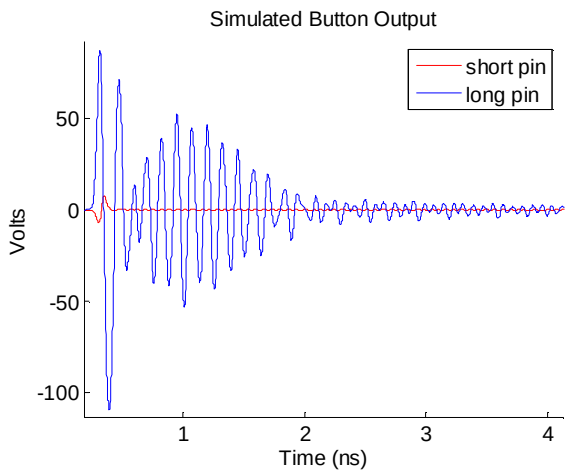

Figure 5: Button pickup with a long or short pickup pin. The long pin is more like a pickup in a cavity BPM.

EOM DAMAGE

The EOMs in the front-end are damaged by high voltages and care must be taken to preserve the steep slope of the transient while protecting the electronics from high voltage. Following a voltage surge through the arrival-time pickup caused by electron beam spray or incidence, the EOM's Lithium Niobate crystal was rendered opaque to the laser light. No limiter was in place and the damage occurred over less than a minute.

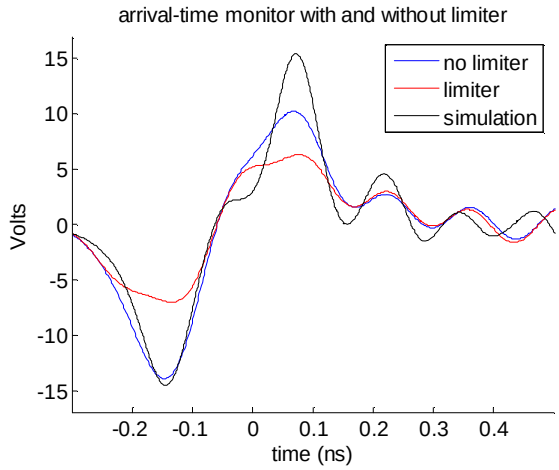

Figure 7: Limited and combined ring output from oscilloscope measurement and simulation including attenuation and dispersion from the cable, splitter, and combiner.

The Agilent N9355C 26.5 GHz bandwidth limiter that was in place throughout most tests of the EOM setup (Fig. 7) appeared to protect the EOM crystal from standard beam operation. With the limiter in place, even extreme off axis kicks from the transverse deflecting cavity upstream did not appear to damage the EOM. A conclusive study of the long-term effects of high voltage with the limiter has not, however, been done. The temperature dependent drifts of the limiter have also not been studied and are of interest even though the component will be used in a temperature controlled enclosure in the tunnel. It has also not bee used, long-term, in the tunnel, where 120 Volts peak to peak have been measured from the combined ring pickup.

SUMMARY

- EOM technique makes high resolution phase measurements possible.
- Optimal pickups for the EOM technique must maximize the slope and minimize ringing and transient distortions.
- EOMs must be protected from high voltage.

REFERENCES

[1] X-FEL Technical Design Report Sect. 4.8 2006.
[2] F. Loehl et. al., "Beam Arrival-time Monitor", EPAC'06, Edinburgh, June 2006.
[3] K. Hacker et. al., "BPM with Large Horizontal Aperture", EPAC'06, Edinburgh, June 2006.
[4] Manfred Wendt, personal communication.

DESIGN OF AN XUV FEL DRIVEN BY THE LASER-PLASMA ACCELERATOR AT THE LBNL LOASIS FACILITY*

C. B. Schroeder, W. M. Fawley, E. Esarey, W. P. Leemans
Lawrence Berkeley National Laboratory, Berkeley, CA 94720, USA

Abstract

We present a design for a compact FEL source of ultra-fast, high-peak flux, soft x-ray pulses employing a high-current, GeV-energy electron beam from the existing laser-plasma accelerator at the LBNL LOASIS laser facility. The proposed ultra-fast source would be intrinsically temporally synchronized to the drive laser pulse, enabling pump-probe studies in ultra-fast science with pulse lengths of tens of fs. Owing both to the high current ($\sim$10 kA) and reasonable charge/pulse ($\sim$0.1–0.5 nC) of the laser-plasma-accelerated electron beams, saturated output fluxes are potentially $10^{13} - 10^{14}$ photons/pulse. We examine devices based both on SASE and high-harmonic generated input seeds to give improved coherence and reduced undulator length, presenting both analytic scalings and numerical simulation results for expected FEL performance. A successful source would result in a new class of compact laser-driven FELs in which a conventional RF accelerator is replaced by a GeV-class laser-plasma accelerator whose active acceleration region is only a few cm in length.

INTRODUCTION

Recent advances in laser-plasma-based accelerators have demonstrated generation of low energy spread, $\sim$100 MeV electron beams [1]. These experiments used an ultra-intense $\sim 10^{19}$ W/cm^2 laser pulse focused on a gas jet, with typical length of a few millimeters, to generate plasma waves with accelerating fields on the order of 100 GV/m. By using a gas-filled discharge capillary for creating a plasma channel, the laser-plasma interaction length can be extended to a few centimeters, resulting in high-quality GeV electron beams [2]. In addition, the electron bunches emerging from a laser-plasma accelerator have naturally short durations (tens of fs) [3], and are intrinsically synchronized to the short-pulse laser driver, making such a source ideal for ultra-fast pump-probe applications. These laser-plasma accelerator experimental results [1, 2] open the possibility of a new class of compact, high-peak flux, x-ray free-electron laser (FEL) in which the conventional radio-frequency (RF) accelerator (10–100 m length) is replaced by a GeV-class laser-plasma accelerator (several cm length), in principle greatly reducing the size and cost of such light sources [4].

In this paper we discuss the design of an XUV FEL driven by the existing laser-plasma accelerator at the LOASIS laser facility at LBNL.

* Work supported by the U.S. Department of Energy under Contract No. DE-AC02-05CH11231.

LASER-PLASMA ACCELERATOR

The LOASIS Laboratory at LBNL presently produces ultra-short ($<$50 fs), relativistic electron bunches with high charge ($\gtrsim$100 pC/bunch) via a laser-plasma interaction. The bunches are generated by a laser wakefield accelerator (LWFA): radiation pressure from a short pulse, intense laser excites high-field plasma waves (wakefields) that accelerate electrons [5]. The LWFA at LBNL uses a 10 Hz, Ti:Sapphire laser system to focus ultra-short ($\sim$30 fs) laser pulses of relativistic intensity ($>10^{18}$ W/cm^2) into a plasma channel. GeV-energy electron beams have been demonstrated [2] using the LBNL 100 TW-class laser system and a gas-filled capillary discharge waveguide [6] for plasma channel production, which allows for low plasma densities ($\sim 10^{18}$ cm^{-3}) and long ($\sim$cm) laser-plasma interaction lengths. These LWFA-produced electron beams are high current ($\sim$10 kA) and ultra-short ($<$50 fs), properties which are attractive as an input beam for an FEL generating ultra-short x-rays.

In recent experiments using the plasma-channel-guided LWFA at LBNL, a 18-TW, 72-fs laser (25 μm focused spot size) is guided in capillary waveguide (which generates a plasma channel via a discharge in the hydrogen filled capillary), producing 0.5 GeV with 5% RMS *projected* relative energy spread, 2.0 mrad RMS divergence, and 50 pC of charge [2]. Experimental results using 2 J of laser energy have produced 1-nC electron beams at 0.5 GeV. At present, *slice* energy spread σ_γ measurements of the electron beam have not been performed, but simulation results [7] predict that the slice energy spread is an order of magnitude smaller than the projected value.

FEL DESIGN

We consider interaction of the LWFA-generated 0.5-GeV electron beam in a conventional magnetostatic undulator. For this study we will consider the LWFA electron beam and undulator parameters listed in Table 1; the latter correspond to the existing "THUNDER" device (see Ref. [8] for a detailed description), which provisionally will be transferred to LBNL from Boeing in late 2006. THUNDER contains 220 periods divided into ten 50-cm sections, each separated by a 4-cm diagnostic and steering space. The maximum RMS undulator strength parameter is $a_u = K/\sqrt{2} \simeq 1.31$ ($\approx$1.0 T peak magnetic field) which may be tapered section by section. Wiggle-plane

focusing is provided by a canted pole configuration with the expected matched beta-function $k_\beta^{-1} \approx 3.6\,\mathrm{m}$ for the peak field and 0.5-GeV beam. Conventional magnetic optics will transport the electron beam from the laser-plasma accelerator to the undulator. Note that there could be non-trivial beam transport issues concerning the required degree of achromaticity and preservation of pulse duration (*i.e.*, peak current). At 0.5 GeV, the beam is sufficiently "stiff" that pulse lengthening via drift will be small; for example, a 5% energy chirp results in less than 1 fs of pulse lengthening over a transport distance of a few meters.

Table 1: Electron Beam, Undulator and HHG Source Parameters

LWFA electron beam:	
Beam energy, γmc^2	0.5 GeV
Peak current, I	5 kA
Charge, Q	0.1 nC
Bunch duration (FWHM), τ_b	20 fs
Energy spread (RMS, slice), σ_γ/γ	0.25%
Normalized transverse emittance	1 mm mrad
Undulator:	
Undulator type	planar
Undulator period, λ_u	2.18 cm
Peak magnetic field	1.02 T
Undulator parameter (peak), K	1.85
Magnetic gap	4.8 mm
Beta-function, k_β^{-1}	3.6 m
HHG seed:	
HHG radiation wavelength	31 nm
Coherent HHG radiation power	15 MW
HHG pulse duration	20 fs

FEL PERFORMANCE

We consider two modes of FEL operation: self-amplified spontaneous emission (SASE) and seeding by a high-harmonic generation (HHG) source. Results from FLASH at DESY [9] and SSCS at Spring-8 [10], operating in the XUV wavelength regime, have confirmed the applicability of the basic SASE physics at XUV wavelengths. Existing laboratory HHG sources have demonstrated production of ultra-short (tens of fs) coherent soft x-ray (*e.g.*, 31 nm, 26th harmonic of a 0.8 μm drive laser) pulses with 0.3 μJ of energy (see, *e.g.*, Ref. [11]). HHG seeding has significant advantages over the simpler SASE mode of operation as it will provide improved temporal coherence and a much reduced power saturation length.

The resonant wavelength for the beam and undulator parameters of Table 1 is $\lambda = \lambda_u(1 + K^2/2)/(2\gamma^2) \simeq 31\,\mathrm{nm}$ (40-eV photons), while the matched electron beam size in the undulator is $60\,\mu$m. The FEL parameter is $\rho \approx 5 \times 10^{-3}$ and the ideal 1D (*i.e.*, no emittance, energy spread, or diffraction effects) exponential power gain length is $L_{1D} = \lambda_u/(4\pi\sqrt{3}\rho) \simeq 0.19\,\mathrm{m}$. Including these non-ideal effects via the Xie gain length formula [12] can increase the gain length (L_g) 1.5–3 fold compared to the ideal 1D gain length, depending upon the assumed value of σ_γ. For the parameters of Table 1, the 3D gain length is $L_g \approx 0.3\,\mathrm{m}$. Figure 1 displays contours of gain length as a function of peak current I and relative energy spread σ_γ/γ. If one presumes empirically that the product $I\sigma_\gamma$ remains constant, one sees that it is best to operate at relatively large currents. However, consideration of slippage effects over the full THUNDER undulator ($\tau_s = \lambda N_u/c \approx 24\,\mathrm{fs}$) suggests that reducing the electron beam pulse duration τ_b below τ_s will have diminishing returns. Hence, we believe peak currents of $I \sim 2.5$–$10\,\mathrm{kA}$ for a bunch charge of $Q \approx 100\,\mathrm{pC}$ is the likely region of interest. Space charge effects will not degrade the FEL performance in this high-current regime provided $(\lambda_u/\lambda_p)^2/\gamma^3 \ll (2\rho)^2$ (*i.e.*, the characteristic wavelength of the space charge oscillation in the lab frame is much greater than the FEL gain length), where λ_p is the plasma wavelength of the electron beam. This condition is satisfied for the parameters of Table 1.

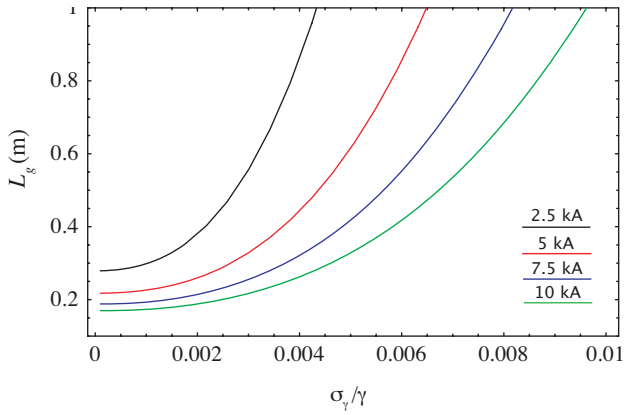

Figure 1: Exponential gain length as a function of incoherent energy spread for various electron beam currents as determined from the Xie [12] empirical fitting function.

We performed a series of time-independent GINGER [13] simulations to examine in detail the predicted FEL output from such a device, examining both the SASE and HHG-seeded cases. We adopted electron beam and undulator parameters as given in Table 1 with the exception that we also considered 7.5-kA peak current (150 pC charge) SASE and HHG-seeded cases and a 10-kA peak current (200 pC charge) SASE case, in addition to the nominal 5-kA HHG-seeded FEL. The simulations used a parabolic temporal profile for the electron beam; the details (*i.e.*, the sub-20 fs structure) of the actual experimental electron beam profile have not been measured. All the SASE results presented here are from one single simulation run for each of the two currents. Note that an ensemble average over many different runs, each with a different initial shot noise presentation would give smoother profiles for $P(t)$ and $P(\omega)$.

Figure 2 shows the maximum power for the HHG-seeded case (FEL in amplifier mode with 15 MW initial HHG

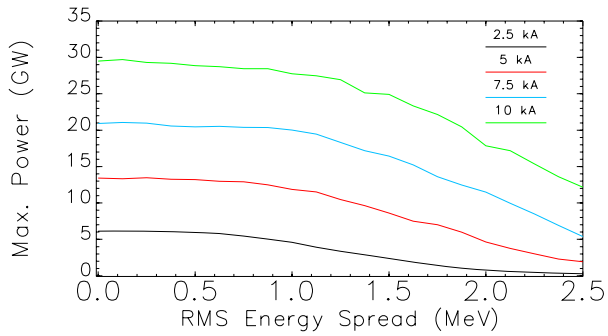

Figure 2: Predicted (GINGER calculations) maximum power in amplifier mode (with 15 MW initial HHG seed) over the THUNDER undulator (5 m) as a function of initial incoherent energy spread for various beam currents.

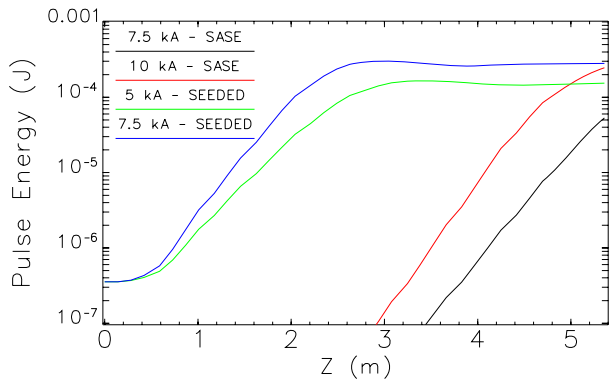

Figure 3: Predicted (GINGER calculations) radiation pulse energies as a function of undulator length z for both SASE and HHG-seeded cases.

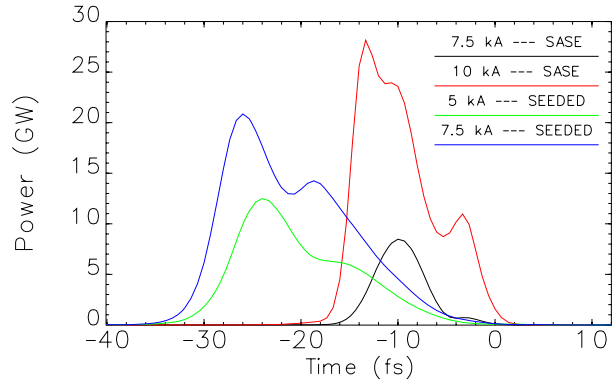

Figure 4: Predicted (GINGER calculations) output power temporal profiles for the cases associated with Fig. 3. The electron beam center is at $t = 0$.

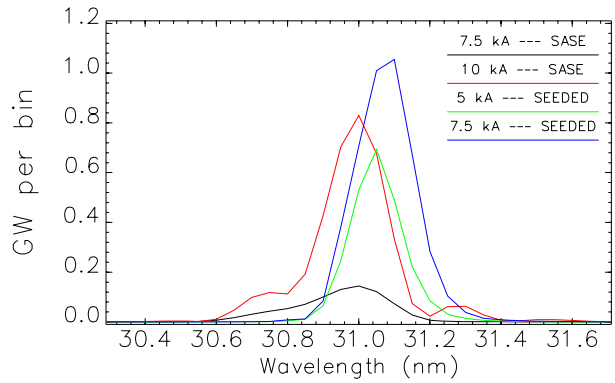

Figure 5: Predicted (GINGER calculations) output spectra at the 31-nm wavelength fundamental for the various SASE and seeded cases. Each bin is 64.6 meV wide while 1 GW is equivalent to 1.0×10^{13} photons.

seed) versus initial incoherent RMS energy spread for several beam currents. As the figure shows, for the nominal beam current (5 kA), greater than 10 GW of power can be achieved provided the RMS energy spread is $\lesssim$1.25 MeV ($\sigma_\gamma/\gamma \lesssim 0.25\%$).

Figure 3 displays time-integrated radiation pulse energies as a function of undulator length z; for reference, 1 μJ of energy corresponds to 1.5×10^{11} photons at 40 eV. The SASE results show a strong current dependence that is attributable to the sensitivity of L_g to current in this short-pulse regime with normalized σ_γ comparable to ρ. One sees in Fig. 3 that the 7.5-kA SASE case is about a gain length away from saturation, while the 10-kA SASE case reaches saturation. Given that we presumed idealized Gaussian transverse distributions with no offsets, tilts, *etc.*, additional current and charge might be required to reach full saturation with the assumed energy spread of 1.25 MeV. Earlier saturation in z might also be achieved by employing additional focusing (by adding focusing optics between the THUNDER undulator sections) thereby reducing the beta-function. Saturation is achieved in <3-m distance for the HHG-seeded cases.

Figure 4 shows output power temporal radiation profiles; one sees that the radiation pulse remains temporally close to the electron beam (whose center is at $t = 0$) when compared with slippage ($\tau_s \approx 24$ fs). Since the electron beam duration τ_b is only a few times the steady-state coherence length $c\tau_c \equiv \lambda/(4\pi\rho_{3D})$, the output profile is dominated by a single longitudinal mode, which results in spectral purity (at the price of reduced gain). This is apparent also in Fig 5 which shows quite clean power spectra for all cases except the 10-kA SASE run where there appear to be weak "sidebands" to either side of the central line; we expect ensemble average over many shots would likely show a simple Gaussian shape whose width would be slightly wider than this specific run.

For the HHG-seeded cases shown in Figs. 3, 4, and 5 we presumed an input seed with a 20-fs FWHM Gaussian temporal profile and peak power of 15 MW. The results indicate significantly improved performance of the HHG-seeded FEL, compared to the SASE cases (*e.g.*, compare the 7.5-kA cases). As seen in Fig. 3, saturation occurs before 3 m in the undulator, and peak powers exceeding 10 GW appear possible with FWHM durations ~15 fs (Fig. 4). Despite the early saturation, both HHG-seeded cases (5 kA and 7.5 kA) show essentially single mode spectral output with inverse normalized bandwidths (RMS) for the on-axis far field of $\omega/\Delta\omega \approx 500$ and autocorrelation times $\sim$ 12 fs. Predicted third harmonic power (due to

Table 2: FEL Performance

Radiation wavelength, λ	31 nm
Resonant photon energy	40 eV
FEL parameter, ρ	5×10^{-3}
3D Gain length	0.3 m
Slippage length	7.2 μm
Spontaneous radiation power	4 kW
Steady-state saturation power	12 GW
Photon/pulse (at saturation)	3×10^{13}
Peak brightness[a] (at saturation)	2×10^{16}
Saturation length (HHG-seeded, 5 kA)	2.4 m
Saturation length (SASE, 10 kA)	5 m

[a] photons/pulse/mm^2/mrad^2/0.1%BW

the nonlinear harmonic microbunching associated with the strong fundamental bunching) is about 0.4% and 0.8% of the fundamental for the 5-kA and 7.5-kA cases, respectively. The normalized spectral bandwidths for the third harmonic are narrower than the fundamental by slightly more than a factor of two; one expects less than the theoretical maximum of three due to the variation in temporal microbunching fraction [*i.e.*, the third-harmonic bunching parameter $b_3(t)$ has a narrower pulse shape than the fundamental $b_1(t)$]. Despite the much lower photon/pulse value of the third harmonic radiation, it may, nonetheless, be of interest for certain experiments.

DISCUSSION AND CONCLUSIONS

Recent advances in laser-plasma-based accelerator experiments [1, 2], and, in particular, the demonstration of high quality GeV electron beams [2], have enabled the possibility of a new class of compact laser-driven FELs in which the conventional RF accelerator is replaced by a cm-scale laser-plasma accelerator, greatly reducing the size and cost of the FEL. The natural short bunch length of the laser-plasma accelerator (tens of fs), and the intrinsic temporal synchronization between the short-pulse laser generating the electron beam and the FEL radiation, make the laser-driven FEL an ideal source for ultra-fast pump-probe applications. As discussed above, seeding of the FEL by an HHG source (generated from the same LWFA drive laser, and, therefore, temporally synchronized with the electron beam) has significant advantages over the simpler SASE mode of operation. The coherent amplification of the HHG source in the FEL leads to reduced undulator length and improved longitudinal coherence.

In this paper we have discussed the design of a XUV FEL employing the 0.5 GeV laser-plasma-generated electron beam produced at the LOASIS laser facility at LBNL. Table 2 shows the expected FEL performance employing a 31-nm HHG seed assuming the input parameters given in Table 1. Presuming a reasonably small incoherent energy spread of 1.25 MeV, a 15 MW HHG input seed provides sufficient initial power for the FEL to reach saturation in a few meters using the THUNDER undulator. For SASE, higher currents (*e.g.*, 10 kA) are needed to reach saturation in the 5 m undulator distance. The proposed HHG-seeded FEL, using the existing 0.5 GeV-LWFA at LBNL and the THUNDER undulator would capable of producing ultra-short ($\sim$15 fs) XUV (40 eV) pulses with $>10^{13}$ photons/pulse. The predicted third harmonic emission would be ~ 2.5 orders of magnitude less. A key beam parameter is the actual incoherent (*i.e.*, slice) energy spread. Values much above 1.25 MeV (0.25%) would require peak currents $\geq$ 10 kA for saturation to occur within the THUNDER undulator.

REFERENCES

[1] S. P. D. Mangles *et al.*, Nature 431 (2004) 535; C. G. R. Geddes *et al.*, *ibid.* 431 (2004) 538; J. Faure *et al.*, *ibid.* 431 (2004) 541.

[2] W. P. Leemans *et al.*, Nature Phys. 2 (2006) 696.

[3] J. van Tilborg *et al.*, Phys. Rev. Lett. 96 (2006) 014801.

[4] D. A. Jaroszynski *et al.*, Phil. Trans. R. Soc. A 364 (2006) 689.

[5] E. Esarey *et al.*, IEEE Trans. Plasma Sci. 24 (1996) 252.

[6] D. J. Spence and S. M. Hooker, Phys. Rev. E 63 (2001) 015401.

[7] C. G. R. Geddes *et al.*, Phys. Plasmas 12 (2005) 056709.

[8] K. E. Robinson, D. C. Quimby and J. M. Slater, IEEE J. Quantum Electron. QE-23, (1987) 1497.

[9] V. Ayvazyan *et al.*, Eur. Phys. J. D 37 (2006) 297.

[10] T. Shintake, "First Lasing at SCSS", Paper MOAAU04, these proceedings.

[11] E. Takahashi *et al.*, Phys. Rev. E 66 (2002) 021802(R).

[12] M. Xie, Nucl. Instrum. Methods Phys. Res. A445 (2000) 59.

[13] W. M. Fawley, LBNL Technical Report No. LBNL-49625 (2002); see also paper MOPPH073, these proceedings.

COMPARATIVE STUDY OF DIGITAL AND ANALOG SYNCHRONIZATION TECHNIQUES FOR LASERS IN ACCELERATORS

Axel Winter, Universität Hamburg, Hamburg, Germany,
Wojtek Jalmuzna, Warsaw University, Warsaw, Poland.

Abstract

Pulsed laser systems play an important role in present and future light sources. These lasers need to be synchronized very precisely to the accelerator RF. One approach is using an analog controller, which offers low-noise performance and has been demonstrated to achieve sub-50 fs stability. A digital controller based on a high-performance FPGA offers more flexibility, for instance the possibility to implement notch filters to evade the limitations by resonances of the piezo crystal used to adjust the laser cavity length. This paper presents results obtained with both approaches.

INTRODUCTION

A mode-locked laser serves as an ultra-stable laser master oscillator (LMO) for the proposed optical synchronization system for the European XFEL, which will be tested at the FEL facility FLASH [1]. Fiber lasers are well suited to realize such an optical master oscillator, because of the ease of coupling to the fiber distribution system, their excellent long-term stability, and the well-developed and mature components that are available at the optical communications wavelength of 1550 nm. A detailed description of the laser master oscillator can be found elsewhere [3]. Erbium-doped fiber lasers exhibit an extremely low phase noise at high offset frequencies making these lasers competitive with the best low-noise microwave oscillators around. Environmental effects like microphonics and vibrations cause excessive low-frequency phase noise, which can be significantly reduced by phase-locking the fiber laser to a ultra-low noise reference oscillator. Due to the extremely high upper state life time of erbium (1 ms), noise for frequencies above 1 kHz, due to for instance the pump laser, is suppressed.

SETUP OF THE LMO SYSTEM

A schematic of the setup of the LMO system is shown in Figure 1. Two fiber lasers run at a repetition rate of 54 MHz, which is the 24th subharmonic of the accelerator RF frequency of 1.3 GHz. Part of the laser pulse train is detected using a high-bandwidth photodiode. In frequency domain, the ultrashort pulses consist of harmonics of the repetition rate with equal energy and a spacing of the repetition frequency. Using a bandpass filter of appropriate

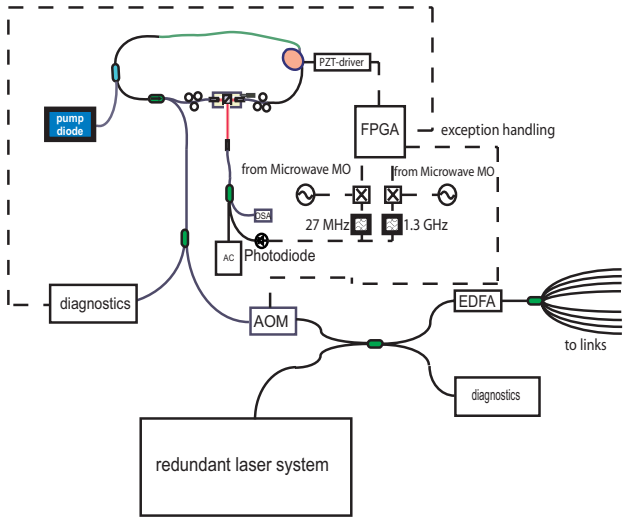

Figure 1: Schematic of the proposed FLASH LMO system.

bandwidth, the 23rd harmonic is selected and amplified to a level of around 5 dbm. The reference signal comes from a low phase noise RF oscillator at 1.3 GHz. Both signals are fed to a analog double-balanced diode ring mixer. The resulting error signal is now amplified by the loop filter, which is either a digital or analog proportional-integral controller. The proportional and integral part are in parallel, so the advantages of an integrator at low frequencies can be obtained without compromising the phase margin at higher frequencies. After being amplified to higher voltage levels to fit the range of piezo crystals, the signal is fed to a piezo-based fiber stretcher, onto which a substantial part of the optical fiber making up the laser cavity is wound. This adjusts the repetition rate of the LMO.

To achieve the required uptime of the LMO system, it is built redundant. Both lasers run continuously and should one of the lasers fail, the backup unit will take over. To enable an ultra-low residual jitter performance, the highest possible comparison frequency is selected which is 1.3 GHz in our case. This however leaves 24 possible positions where the PLL can catch. If the phase-lock of a failed unit is reestablished, it cannot be guaranteed that the laser pulse position is identical to the one of the backup laser which is now seeding the synchronization system. The solution to this problem is the introduction of a second PLL into the system. It runs at a comparison frequency which

is equal to the repetition rate of the LMO. This leaves only one zero-crossings where the PLL can catch per revolution of the laser pulse inside the cavity. The lower frequency PLL catches first and thus selects the phase of the laser pulse. Once the lock is established, the second PLL running at 1.3 GHz will take over.

There are two fundamental approaches which can be considered for the controller of this system. One choice is to use a conventional analog controller. It has been shown, that excellent synchronization performance can be achieved using such a system [4]. The limits of an analog controller lie in the flexibility it can offer. It is very difficult to realize more complex transfer functions than that of a simple PI controller. One aspect of where this is helpful is the implementation of a notch-filter to counteract the effects of the resonance of the piezo crystal in the fiber stretcher to obtain a higher gain in the PLL. Furthermore the switching of two PLL's is significantly easier using a digital controller which will be described in the next section.

DIGITAL CONTROLLER

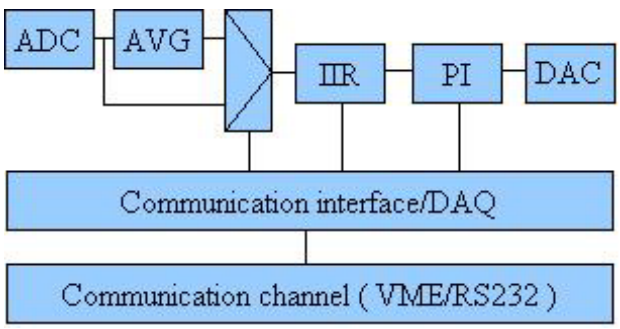

Figure 2: Schematic of the digital controller architecture.

The digital PI controller was implemented using an in-house developed controller board for the low-level RF control, called SIMCON 3.1[5]. The application utilizes the Virtex 2 Pro FPGA, located on the controller. The internal structure of the controller is shown on Figure 2. The digital controller offers the same functionality as its analog pendant, namely a parallel PI-controller with an optional second order infinite impulse response low-pass filter. The error signal from the double balanced mixer is sampled with a sampling frequency of 50 MHz. Then the data is decimated to provide one valid sample every 1 μs. Optionally averaging of 50 samples of the error signal can be used to reduce the ADC noise. The controller transfer function is applied to the resulting digital signal which is then converted with a DAC and fed to the piezo driver. For diagnostic purposes, a flexible data acquisition system was used. It saves 16 signals over 64 ms (64000 samples of each signal) to the external SRAM memory of the SIMCON controller. Two forms of communication were were implemented: a VME interface and an RS232 serial link.

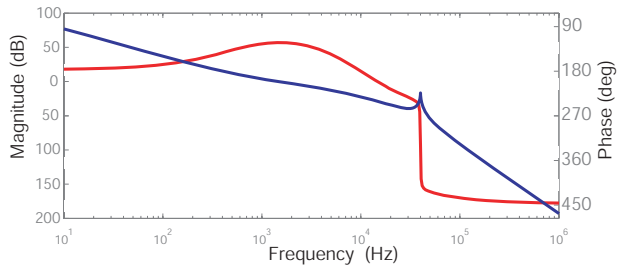

Figure 3: Bode Plot of the open loop transfer function (magnitude - blue, phase - red).

All the controller's parameters can be set with MATLAB software using a channel independent interface [6].

CONTROLLER TYPE AND SIMULATION

The feedback acts on the cavity length through the piezo which stretches the optical fiber. Care has to be taken not to disrupt the laser dynamics through introduced birefringence which occurs if the fiber is bent. The fiber stretcher is constructed such that bending is avoided and only the length of the fiber is varied by the piezo. Hence laser dynamics will to first order not be influenced and the laser will in terms of phase act as an integrator with the transfer function $G_l = \frac{k_l}{s}$, where k_l is the gain of the piezo inside the laser cavity (in our case is 0.35 $\frac{Hz}{V}$). Mechanical resonances of the piezo have to be considered (~ 40 kHz), which can be modeled by a harmonic oscillator. This yields a transfer function of $G_{piezo} = \frac{(2\cdot\pi\cdot f_{res})^2}{s^2+4\pi\gamma f_{res}\cdot s+(2\pi f_{res})^2}$ which ultimately limits the achievable gain of the PLL. A linear response is assumed for the phase detector around the locking point, which is valid for analog mixers around the zerocrossing, i.e. $\Delta\phi = 0, \pi, 2\pi \ldots$. The controller consists of a PI-controller ($G_{PI} = K_P + \frac{K_I}{s}$) and an optional low pass filter with a corner frequency of $f_{lp} = 10$ kHz.
The simulated open loop transfer function is shown in figure 3. The unity gain bandwidth is at 1 kHz which is in good agreement with the experimental results. It can be seen from Figure 5, that the phase noise spectra of the locked laser and reference oscillator start deviating just above 3 kHz which is the point of unity gain.

RESULTS

The first step to compare the performance of the two systems was to lock one LMO to a 1.3 GHz reference and evaluate the residual jitter. Figure 4 shows the power spectral density of the error signal when the system is locked for both analog and digital controller. The integration of these signal yields the respective residual jitter for either the analog or the digital controller. It amounts to 74 fs for the analog controller and 107 fs for the digital controller, both in a bandwidth from 1 Hz to 112 kHz. The difference in performance of the two controllers is almost entirely due

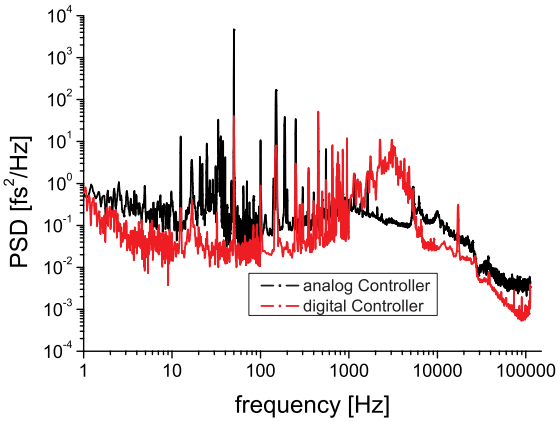

Figure 4: Power spectral density of the closed-loop error signal for both analog (black) and digital (red) controllers.

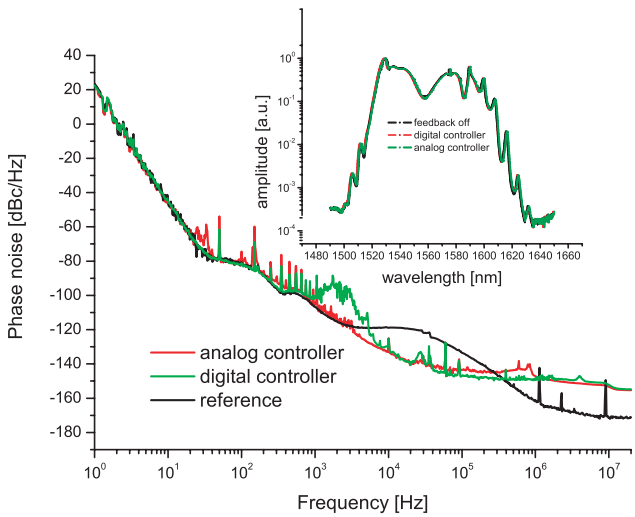

Figure 5: Phase noise for the locked fiber laser with both analog (red) and digital (green) controllers and the reference (black). Insert: Optical spectrum of the fiber laser without feedback (black), with digital controller (red) and analog controller (green).

to the PLL peaking of the digital controller. This is due to a slightly higher proportional gain which limits the phase margin of the system and leads to the power spectral density increase around 2 kHz. Reducing the proportional gain will yield a comparable result to the analog controller. It should be noted, that a significant part of the jitter in the digital controller is due to the 50 Hz line. The magnitude of this perturbation does not change with proportional and integral gain settings of the controller, making a crosstalk from the power supply to the DAC a likely candidate for the cause. It can possibly be improved in the next redesign of the digital controller board. An advantage of the digital controller is the possibility to average the ADC data. The sampling rate of the ADC is a lot higher than needed for the regulation (60 MHz), so an average was employed reducing the sampling rate to 1 MHz. This reduces the uncorrelated noise of the ADC by a factor of almost 8.

It is important, that the activated PLL does not increase the phase noise at higher offset frequencies. The measured phase noise with and without feedbacks is depicted in figure 5. There is no significant increase in the high frequency phase noise when locking with either system.

A further important issue is the possible change of the optical properties of the laser pulses due to the phase locking. The insert to Figure 5 shows the optical spectrum of the fiber laser without any feedback and with either controller. No significant change was observed for either feedback option.

CONCLUSION AND OUTLOOK

An optical master oscillator system requires a precise phase-lock of the fiber lasers to an external RF clock. This can be achieved by either using a digital or an analog controller. The measured performance for either system was comparable. No significant differences in the high frequency phase noise or the optical spectrum could be observed. This indicates that the more flexible approach using an FPGA as a digital loop filter is feasible without compromising the locking performance.

REFERENCES

[1] J. W. Kim et. al., “Large scale timing distribution and RF-synchronization for FEL facilities,” FEL Conference 2004, Trieste, Italy, 2004.

[2] J. Kim, F. X. Kärtner, and M. H. Perrott, “Femtosecond synchronization of radio frequency signals with optical pulse trains,” Opt. Lett. **29**, 2076-2078 (2004).

[3] A. Winter et. al., “Towards high-performance optical master oscillators for energy recovery linacs,” Nucl. Inst. Meth. A **557**, 299-304 (2006).

[4] A. Winter et. al., “Femtosecond Synchronisation of Ultrashort Pulse Lasers to a Microwave RF Clock,” Proceedings of the PAC 2005, Knoxville, TN.

[5] W. Giergusiewicz et. al., “Low latency control board for LLRF system SIMCON 3.1,” Proc. of SPIE Vol. 5948, (2005).

[6] J. Szewinski et. al., “Software for Development and Communication with FPGA Based Hardware”, TESLA Report 2005-16.

FIRST TOLERANCE STUDIES FOR THE 4GLS FEL SOURCES

D.J. Dunning, N.R. Thompson, J.A. Clarke and D.J. Scott, ASTeC, CCLRC Daresbury Laboratory
B.W.J. McNeil, SUPA, Department of Physics, University of Strathclyde, Glasgow, UK.

Abstract

The Conceptual Design Report for the 4th Generation Light Source (4GLS) at Daresbury Laboratory in the UK was published in Spring 2006 [1]. 4GLS features three distinct FEL designs, each operating in a different wavelength range: an externally seeded amplifier operating in the photon energy range 8-100eV (XUV-FEL); a regenerative amplifier FEL operating over 3-10eV (VUV-FEL); an FEL oscillator operating from 2.5-200μm (IR-FEL). Preliminary results of tolerance studies for the FEL designs are presented. In particular, the effects of the relative timing offset between the seed pulse of the XUV-FEL and the electron bunch, as well as the effects of electron bunch timing jitter in the VUV-FEL, are presented.

INTRODUCTION

4GLS is a 4th Generation Light Source proposed by CCLRC Daresbury Laboratory in the United Kingdom to meet the needs of the 'low photon energy' community. The 4GLS facility will combine energy recovery linac (ERL) and FEL technologies. This paper summarises the results of first tolerance studies for the XUV-FEL and the VUV-FEL. For the XUV-FEL, Genesis 1.3 [2] has been used to simulate the effects of a temporal offset between the electron bunch and the seed. For the VUV-FEL simulations, a one-dimensional, time-dependent FEL oscillator code which includes the effects of electron bunch arrival time jitter has been used.

The XUV-FEL design [3] consists of an undulator system directly seeded by a tuneable HHG laser source. It is capable of generating short, tuneable, high-brightness pulses of 8-100 eV photons with peak output powers of ~2-8 GW and typical FWHM pulse length < 50 fs. The FEL undulator consists of a lattice of undulator modules separated by beam focusing elements and diagnostics. The first eight undulator modules of the FEL will be planar, while the final five will be of APPLE-II design in order to produce variably elliptical polarised radiation.

The VUV-FEL [4] is a regenerative-amplifier-type FEL (RAFEL) [5] designed to deliver intense sub-ps pulses of tuneable coherent radiation in the photon energy range 3–10eV. A hole-outcoupled low-Q cavity using robust low reflectivity optics provides sufficient feedback to allow high gain type FEL saturation after only a few cavity round-trips. In its standard operating mode the VUV-FEL will generate temporally coherent photon beams with peak power ~500 MW and FWHM pulse lengths of ~170 fs. Cavity length adjustment may allow superradiant operation with enhanced peak powers of ~3 GW and FWHM pulse lengths of ~25 fs. These figures are the maximum values across the full wavelength range.

To enable variable polarisation, APPLE-II type undulator sections are employed throughout with a strong FODO focussing lattice and beam diagnostics distributed between sections.

XUV-FEL SIMULATIONS

100 eV Pulse Amplifier Lasing

A simulation of the XUV-FEL operating at 100 eV is performed, using the CDR parameters for the case of seed/electron bunch synchronism. The full set of planar and variable undulator modules are used with the APPLE-II undulators set to helical mode so that circularly polarised radiation is generated. Figure 1 shows the seed pulse of peak power P = 30kW and duration 30 fs FWHM. Also plotted is the electron beam current of peak current I_{pk} = 1.5kA and duration 626 fs (188μm) FWHM.

At the end of the FEL a peak saturated power of $P_{pk} \approx$ 2.4 GW is shown in Figure 2. A 'clean' central seeded region upon a noisier pedestal is seen. The pedestal is the pre-saturation SASE - as the shot noise power is only a few tens of watts, the seed power of 30 kW saturates first.

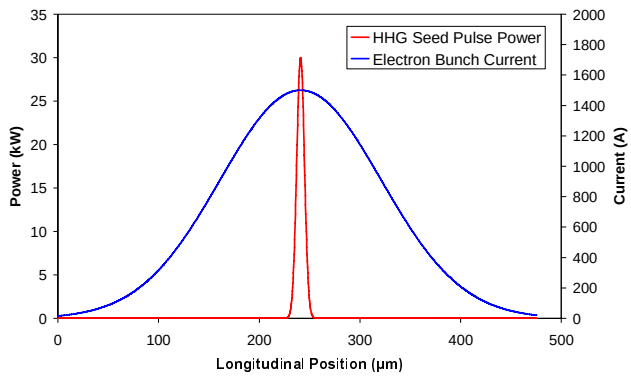

Figure 1. Input HHG seed power and electron bunch current as a function of longitudinal position.

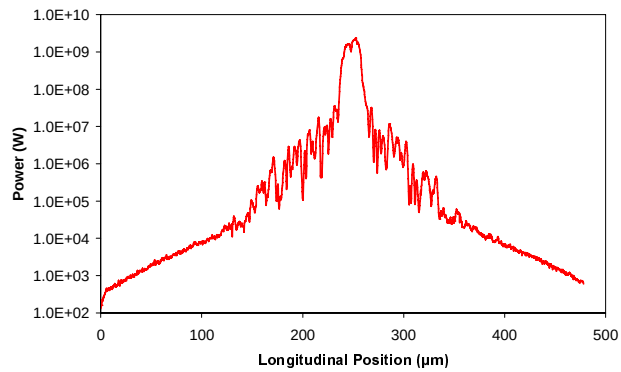

Figure 2. Radiation power at the exit of the XUV-FEL showing peak power $P_{pk} \approx$ 2.4 GW.

100eV Pulse Amplifier Lasing with Offset Seed

The above results are for synchronism between the peak HHG power and the peak of the electron bunch current. However, there may be an inherent noise associated with the arrival time of each bunch which results in a relative timing offset of magnitude Δt. Simulations have been carried out in which Δt is varied, as in Figure 3 (top). Also shown (bottom) is the radiation power at the end of the FEL, with the synchronous seed case for comparison. For seed offset of Δt = 100 fs, the peak power is reduced from 2.4 GW to 1.7 GW.

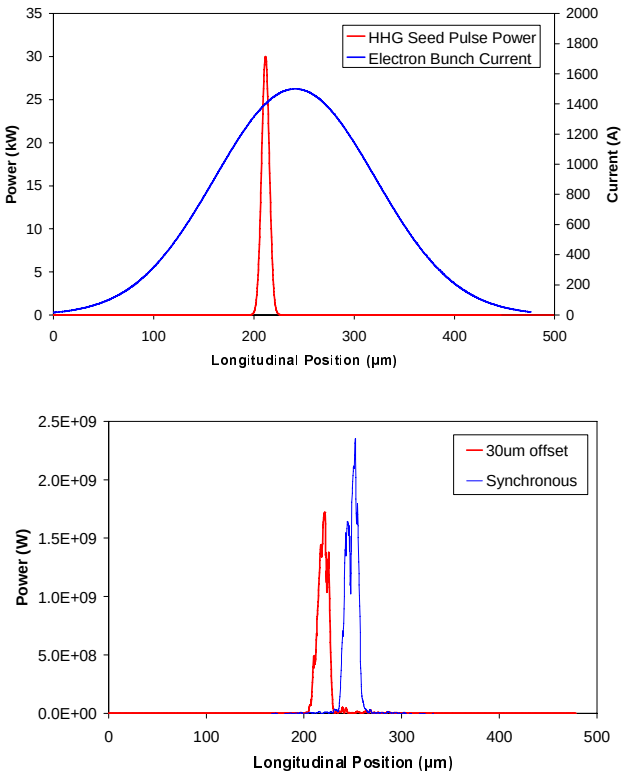

Figure 3. (Top) Seed offset by 100 fs (30 μm) behind the electron pulse and (bottom) radiation power at the end of the FEL for the offset case (red) and synchronous case (blue).

The offset, Δt, was varied between ± 250 fs and results of peak power against offset plotted in Figure 4. These results suggest that electron bunch offset should be limited to approximately ± 45 fs for peak output power to lie within 90% of the synchronous peak power P_{pk}.

From Figure 4, it is noted that the peak output power at the end of the FEL is higher for a negative Δt (seed pulse arriving behind the electron bunch) than for a positive offset of the same magnitude.

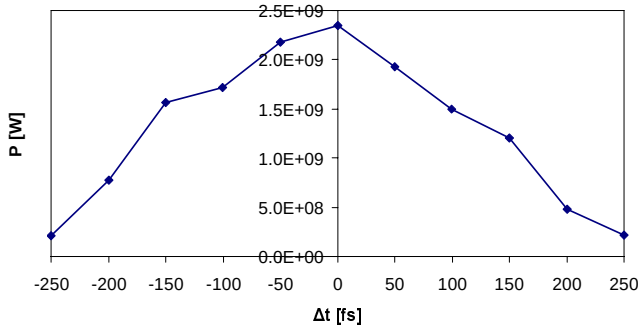

Figure 4. The effect of an offset Δt from electron/seed pulse synchronism upon the peak output power at the end of the FEL, for 100 eV operation.

Comparison with FEL design formulae

The Xie design formulae [6] have been used to estimate the effects of timing offset on the saturation power. This has been done by correlating the timing offset Δt with the beam current via the relation:

$$I(\Delta t) = I_{pk} \exp\left(-\frac{(\Delta t)^2}{2\sigma_e^2}\right).$$

This was carried out for the planar modules only. In Figure 5 these results are compared with the results of Genesis simulations which are seen to yield a slightly more stringent restriction on Δt.

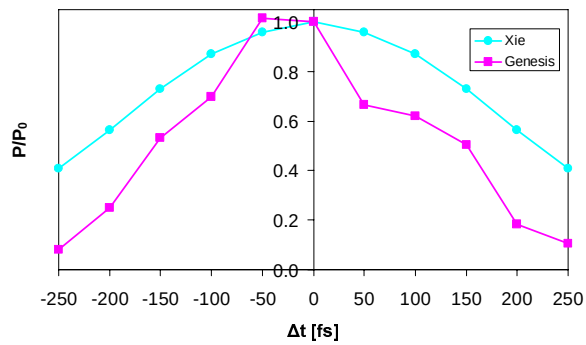

Figure 5. Simulations of the effect of an offset Δt from electron/seed pulse synchronism upon the peak power at the end of the FEL. The results are scaled with respect to their synchronous values at Δt = 0.

VUV-FEL SIMULATIONS

A one-dimensional, time-dependent FEL oscillator code (FELO [7]) has been used. The code includes the ability to model a temporal jitter in the electron bunch arrival into the FEL cavity (this effect is simulated by adding a jitter to the cavity length).

The simulated output power and pulse width variation with cavity length detuning is shown in Figure 6 for 10eV operation in planar mode. For cavity length detuning of 18μm, the pulse width is at a maximum. Typical pulse shape evolution with cavity pass number is shown in Figure 7. These simulations replicate start-up from shot-

noise, with the output pulse typically developing to saturation over 10-15 passes.

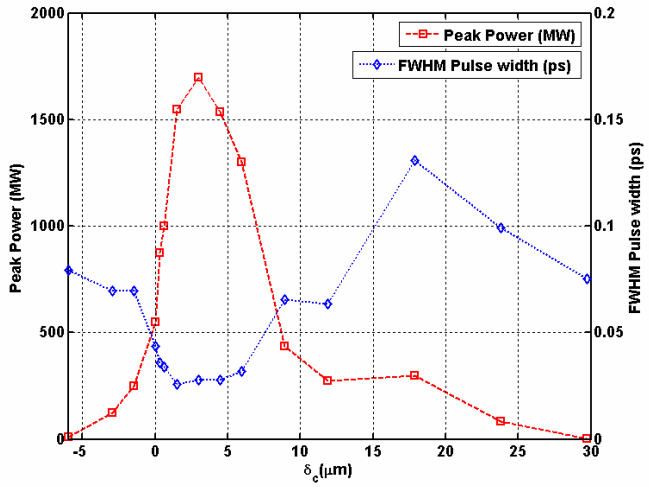

Figure 6. Plots of peak power and pulse width against cavity length detuning (δ_c) for simulations of the VUV-FEL operating at 10eV in planar mode.

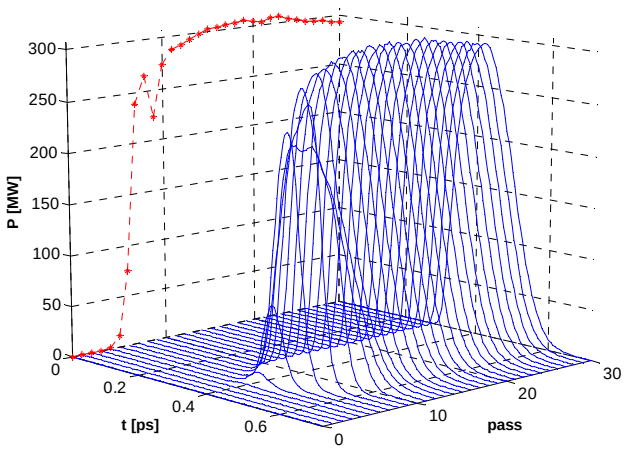

Figure 7. FELO simulation of the VUV-FEL at 10eV and cavity length detuning of 18μm with zero electron bunch arrival time jitter. The red points show the peak intensity of the pulse at each pass.

Simulations with Electron Bunch Time Jitter

In Figure 8 the variation of pulse shapes for different cavity pass numbers are plotted for three different electron bunch arrival time jitter values. Increasing jitter shows increasing variation of the pulse shape with pass number. The pulse shape remains approximately Gaussian for the cases where jitter $\leq \pm$ 80 fs. For the greater jitter value of ± 120 fs, the output pulse is seen to have a less stable shape.

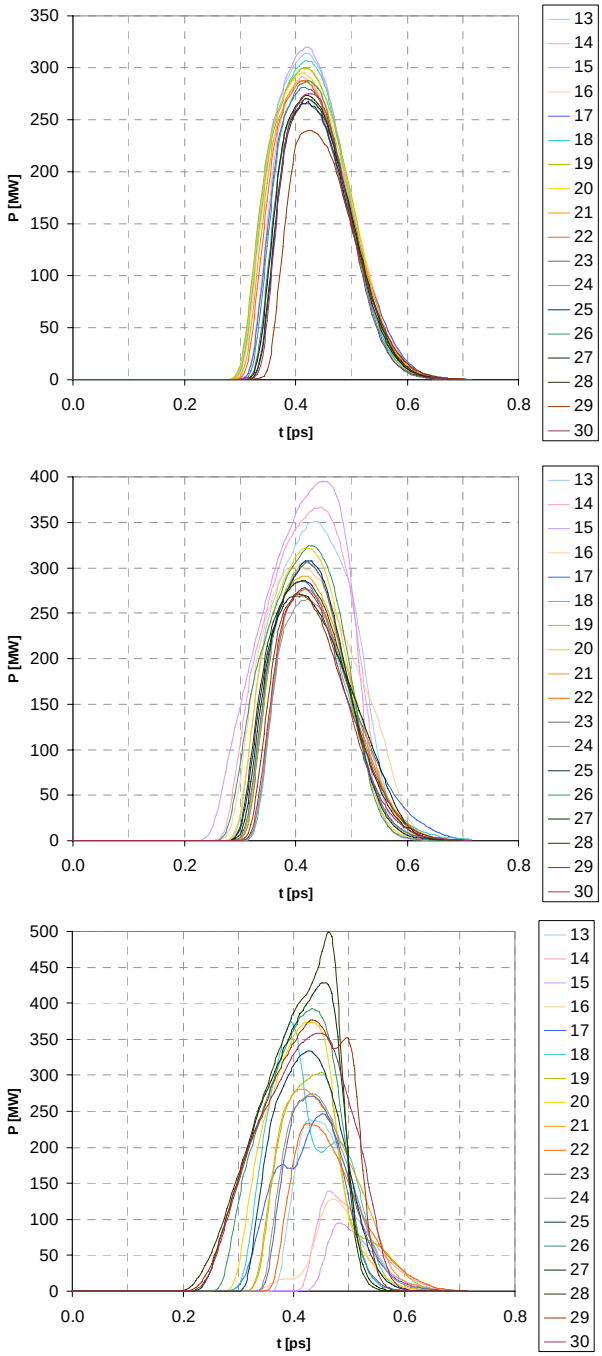

Figure 8. Variation of pulse shape with cavity pass number for electron bunch arrival time jitters of ± 40 fs (top), ± 80fs (middle) and ± 120 fs (bottom). Only passes 13 to 30 are shown. Increasing the temporal jitter shows increasing variation of the pulse shape.

Analysis of output power

Due to shot noise, repeat runs from the same input data yield slight variations in output. For jitter = 0, five runs were carried out and an average peak power was plotted as shown in Figure 9.

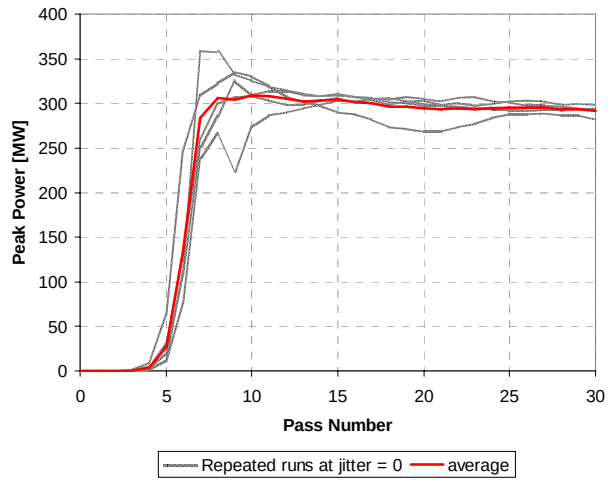

Figure 9. Peak power of pulse with pass for repeated runs at jitter = 0. The variation between different runs is due to the effect of shot noise only.

Repeated runs were carried out for different jitter values and the RMS variations from this average (at saturation) were calculated and are presented in Table 1.

Table 1. Variation of saturation power for different values of electron bunch arrival time jitter.

Jitter (fs)	Saturation Power (MW)
± 0.0	300 ± 2.5%
± 20	300 ± 4.1%
± 40	300 ± 6.0%
± 80	300 ± 8.0%
± 120	300 ± 18.8%

For the case of maximum jitter where the pulse shape remains approximately Gaussian (jitter = ± 80 fs), the output power at saturation is ~300MW ± 8%. The evolution of pulse shape with pass is shown for jitter of ± 80 fs in Figure 10.

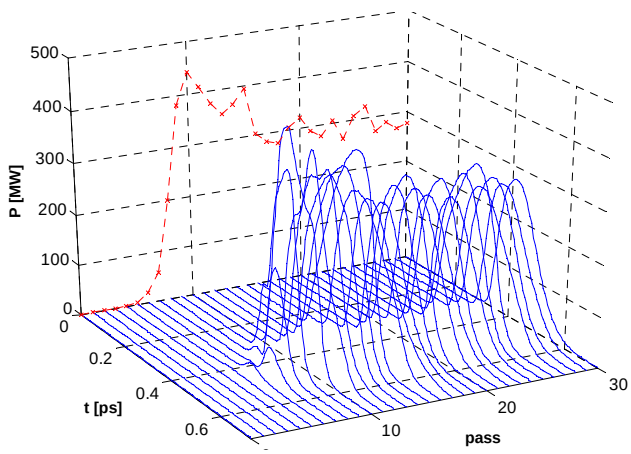

Figure 10. FELO simulation of the VUV-FEL at 10eV for cavity length detuning of 18μm with jitter of ±80 fs. The red points show the peak intensity of the pulse at each pass.

Short-pulse operation of the VUV-FEL

For a cavity length detuning of 1.5μm, operation is in superradiant mode, peak output power is near maximum and the pulse width is at a minimum (see Figure 6). Simulations using the FELO code show that at this cavity length detuning, it is possible for the side-spikes to develop into the peak with maximum power [8]. The evolution of the pulse where electron bunch arrival time jitter = ± 40 fs is shown in Figure 11.

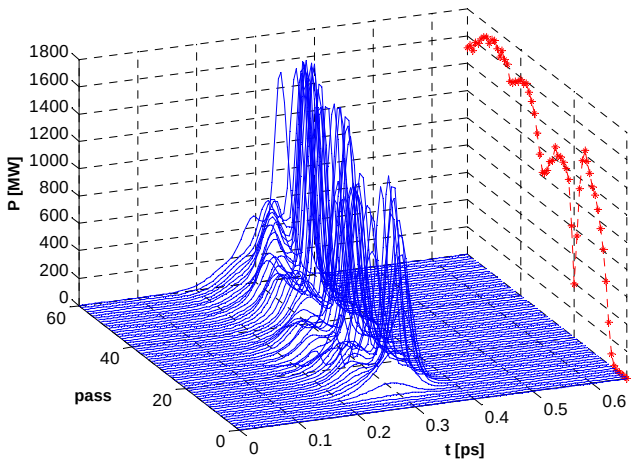

Figure 11. Pulse shape evolution for short-pulse operation with electron bunch arrival time jitter of ± 40 fs.

CONCLUSION

First tolerance studies for the 4GLS XUV-FEL and VUV-FEL have been carried out. For the XUV-FEL, increased offset between seed and electron pulse has been shown to decrease saturation power. For the VUV-FEL electron bunch arrival time jitter has been shown to result in increased instability in the shape of the output optical pulse. It has been concluded that for the XUV-FEL, temporal electron bunch offset should be limited to approximately ± 45 fs for output power to be within 90% of optimum. For the VUV-FEL, jitter should be limited to approximately ± 80 fs for approximate Gaussian output with peak power within ± 8 % of optimum.

REFERENCES

[1] 4GLS Conceptual Design Report, Council for the Central Laboratory of the Research Councils, UK (2006), available from: http://www.4gls.ac.uk/documents.htm#CDR
[2] S. Reiche, Nucl. Inst. Meth. Phys. Res. A, 429, 243, (1999)
[3] B.W.J. McNeil et al, 'The Conceptual Design of the 4GLS XUV-FEL', these proc.
[4] N.R. Thompson et al, 'A 3D Model of the 4GLS VUV-FEL Conceptual Design Including Improved Modelling of the Optical Feedback Cavity', these proc.
[5] B. W. J. McNeil, IEEE J. of Quantum Electron., 26, 1124 (1990)
[6] Ming Xie, Proc of 1995 Part. Accel. Conf., (1996) p183.
[7] B.W.J. McNeil et al, 'FELO, a one dimensional time-dependent FEL oscillator code', these proc.
[8] D.J. Dunning, 'Results of simulations varying the electron bunch arrival time jitter for the 4GLS VUV-FEL', Internal Report fgls-upcdr-rpt-0013, 2006.

PHASE NOISE COMPARISON OF SHORT PULSE LASER SYSTEMS

S. Zhang, S. Benson, J. Hansknecht, D. Hardy, G. Neil, and M. Shinn
TJNAF, Newport News, VA23606, USA.

Abstract

This paper describes phase noise measurements of several different laser systems that have completely different gain media and configurations including a multi-kW free-electron laser. We will focus on state-of-the-art short pulse lasers, especially drive lasers for photocathode injectors. Phase noise comparison of the FEL drive laser, electron beam and FEL laser output also will be presented.

INTRODUCTION

The stability of the drive laser plays a very important role in the performance of photogun-based accelerators and free-electron lasers (FELs). With the increasing demand for shorter wavelengths (including XFEL) and shorter pulse duration (sub-50 fs), phase noise and timing jitter issues are drawing more and more attention. Over the past decade, short pulse lasers technology has seen dramatic advancement due to the rapid development of solid-state materials and high power semiconductor laser diodes. Some state-of-the-art femtosecond lasers have shown superior performance in terms of both amplitude and phase stability. These lasers provide a unique opportunity to overcome challenges in the development of the next generation accelerator light sources.

The photogun drive laser is used to extract the electron beam that provides the gain medium for numerous FELs worldwide. Drive laser instabilities will limit high power FEL operation. Of all the instabilities associated with short pulse high repetition rate lasers, timing jitter appears to be the most important and most difficult to control. In this paper, we present phase noise and timing jitter measurements of several different lasers that can be used to drive photoguns. We believe a comparison of these lasers provides valuable information about the pros and cons of each system in their specific applications.

METHOD AND SETUP

Phase noise is a drive laser quantity that is often discussed. Phase noise is a direct representation of the timing jitter of a mode-locked laser system. Timing jitter can be quantified by measuring the phase noise. There are two basic methods widely used to measure the phase noise (and timing jitter) of optical pulse trains; a) the Phase Detector Technique (PDT) and, b) the Power Spectral Density Technique (PSDT) [1]. The PSDT provides better precision and was used for all of the measurements described below. The measurement requires a fast photodiode and a spectrum analyzer. In this case the timing jitter of the mode-locked or gain-switched optical pulse train is determined by measuring the phase noise spectral density.

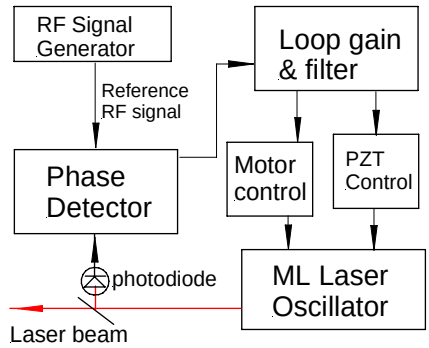

Fig.1. Schematic of a generic phase locking system.

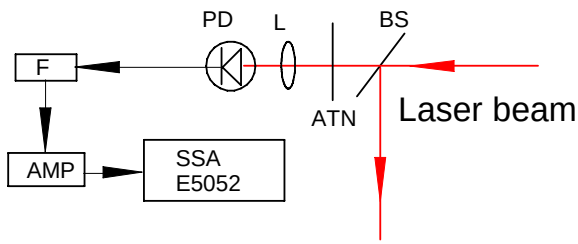

Fig.2. Schematic of the timing jitter measurement setup. BS, beam splitter. ATN, attenuator. L, lens. PD, photo-diode. F, RF filter. AMP, RF amplifier.

Fig.1 shows the basic principle of a generic phase-locking system used by many lasers. The laser phase error is detected and corrected by the RF feedback loop. The measurement setup is shown in Fig.2. The detectors used in the experiment were fast photo-diodes with bandwidth between 2 to 20 GHz. A Signal Source Analyzer (SSA, Agilent E5052A) was used for the phase noise and timing jitter data acquisition. This instrument presents faster speed and better precision compared with some other spectrum analyzers. The phase noise is usually measured at 1.497 GHz, the 20th harmonic of the 74.85 MHz laser pulse frequency in order to minimize the laser amplitude noise. The 1.497GHz signal was filtered out using an RF filter and amplified by a low noise RF amplifier before being fed into the SSA. For higher repetition rates, it was sometimes difficult to perform the measurement at the 20th harmonic. The noise added to the measurement from the RF amplifiers and filters was determined to be negligible.

DIFFERENT LASER SYSTEMS

Flash-lamp-pumped Active Mode-locked Laser

The first laser system tested was a frequency doubled CW mode-locked Nd:YLF laser pumped by flash lamps

(Coherent Antares laser made in early 90's). It has served as the drive laser for the photocathode injector at the JLab FEL facility for more than ten years. We studied the stability of this laser in the past [2]. Here we will focus on the phase noise characteristics. The laser has a folded cavity design and intracavity acousto-optic modulator (AOM) for mode-locking. The AOM can be driven with RF supplied by the laser power supply (internal RF) or with RF from the accelerator (external RF). The laser phase is monitored and controlled by the RF control module. A fast photodiode detects the optical pulses signal from the infrared light leaking through the high reflector. Unlike most other laser systems that use active laser cavity length adjustment to minimize the phase noise, the RF to the acoustic mode-locker on this laser is tuned to compensate the phase change. To detect the phase error and complete the phase loop, the 20th harmonic of the laser frequency (74.85 MHz) is filtered out, amplified and sent to an RF control module.

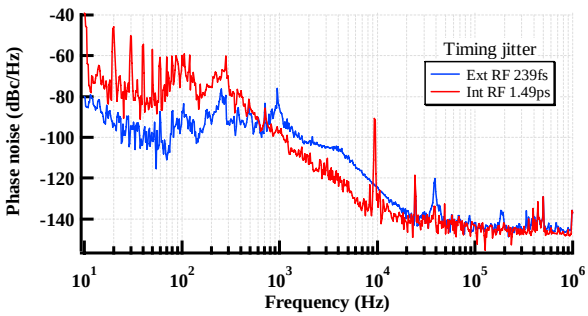

(a)

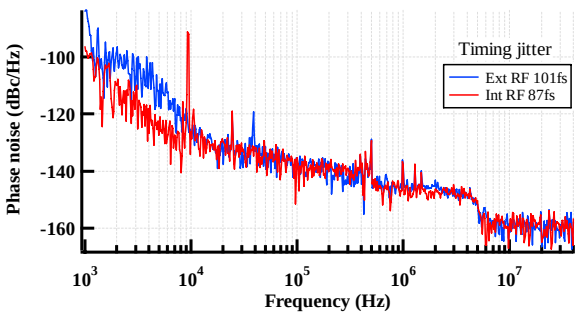

(b)

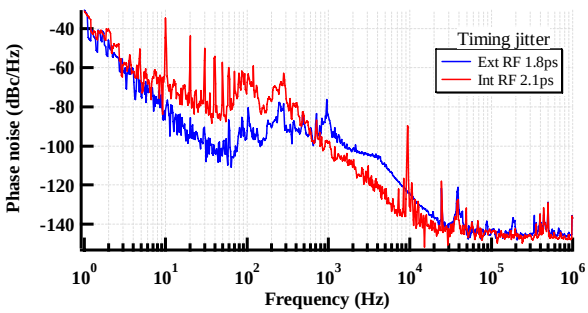

(c)

Fig.3. Phase noise spectral density plots of flash-lamped pumped Antares Nd:YLF laser at different offset frequency. (a)10 Hz~1 MHz. (b)1 kHz~40 MHz, and (c)1 Hz~1 MHz. As explained in the text, Ext and Int refer to external RF and internal RF, respectively.

From the results shown in Fig.3, the excellent performance is primarily due to the fact that the laser cavity was designed to have a particularly stable length: all components are mounted to an Invar rod to reduce temperature dependence. In addition, the phase control loop associated with the RF reference signal is very important, as can be seen by comparing the two RF sources, internal and external. The laser performs significantly better when using RF supplied by the accelerator, with timing jitter five times less compared to that obtained with RF supplied by the power supply. Most of the phase noise comes from the lower frequency band below a few hundred Hz. There are always more noises below 10Hz and the feedback loop does little to reduce them (Fig.3(c)). Usually a flash-lamp pumped laser tends to have noticeably higher phase noise than those pumped by diodes. But this measurement clearly indicates that the phase noise of a flash-lamp pumped system can be controlled to a very low level.

SESAM Mode-locked Laser

The SESAM mode-locked Nd:YVO_4 laser serves as the master oscillator, providing seed pulses for a multi-stage amplifier that provides over 50 W average power at 1.064 um and 25 W at 532 nm. This Maser-Oscillator-Power-Amplifier (MOPA) system will be used to drive a 100mA photoinjector. A detailed system description can be found in another paper [3]. The passively mode-locked Nd:YVO_4 laser is diode-pumped and produces over 500 mW at 1064 nm with 74.85 MHz pulse repetition rate and 25 ps pulses (Time-Bandwidth Product, GE100). It uses a semiconductor saturable-absorber mirror (SESAM) to initiate mode-locking. The laser cavity length is actively stabilized and the phase of the optical pulse train can be locked to an external RF reference signal.

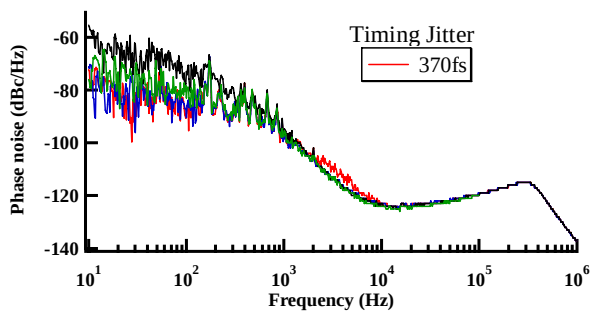

Fig.4. GE100 laser phase noise spectral density plots obtained over few minute time period. Mostly, the timing jitter is less than 400 fs but occasionally larger values are obtained.

When the laser cavity is optimized, it runs very well with timing jitter around 300 fs. Random fluctuations can be seen from time to time, which may be caused by environmental disturbances. Phase noise spectral density plots for this laser are shown in Figure 4. These plots were obtained over a few minutes and mostly timing jitter

is less than 400 fs but occasionally values surge over 500fs. We also intentionally unlocked the cavity length feedback loop. This has a profound affect, with timing jitter increasing to 4 ps (Fig.5). The overall timing jitter also depends highly on the laser cavity alignment and optimization. Timing jitter values can exceed 1ps in the case of poorly aligned cavity.

Phase noise measurements were also made downstream of the power amplifier section of this laser system. The Master oscillator (MO) seed light from the passively mode-locked Nd:YVO_4 laser passes through four Nd:YVO_4 amplifiers, with total output power at 1.064 um greater than 50 W. As expected, the diode-pumped amplifiers do not add much noise to the system (Fig.6). The added noises are most likely from the environment.

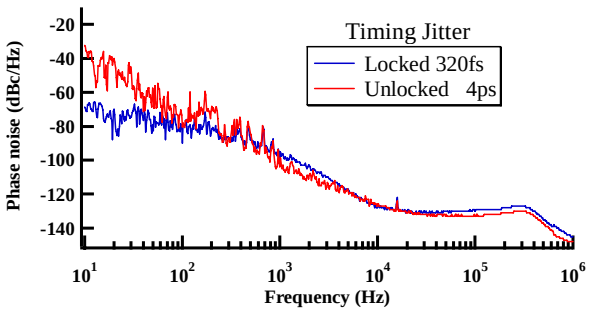

Fig.5. GE100 laser phase noise spectral density plots with laser cavity length feedback loop open and closed.

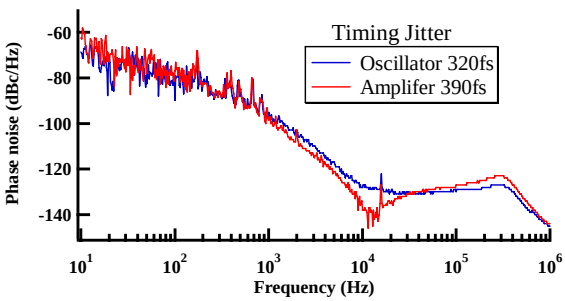

Fig.6. MOPA laser: GE100 laser and multistage power amplifier. Phase noise spectral density plots comparing MO and MOPA signals.

KLM Ti:sapphire Laser

Widely used fs-pulse Ti:sapphire lasers rely on self-mode-locking (KLM), a passive technique that relies on Kerr lensing within the Ti-sapphire crystal and a gain aperture effect that provides more gain for shorter pulses. These lasers are broadly tunable and can generate extremely short pulses because of the exceptionally broad gain bandwidth of the lasing medium.

Phase noise measurements were carried out using a Spectra Physics Kerr mode-locked Ti:sapphire laser (Tsunami, 100fs, 1W at 800nm) pumped by a frequency-doubled and diode pumped Nd:YVO_4 laser (Millennia, CW 10 W at 532 nm). The laser has a phase-locking unit that detects and corrects the laser phase by adjusting the cavity length with a pico-motor and PZT attached to the high reflector (HR) end mirror. A photodiode picks up the laser signal from a beam splitter and the phase is compared to the reference RF to create a phase error signal. The pulse repetition rate is 74.85 MHz, the same as for measurements with other laser systems. Phase noise spectral density plots are shown in Fig.7 for measurements at two different times. As with the SESAM mode-locked laser, phase noise was closely related to cavity alignment and optimization. The timing jitter was observed to jump up and down, but mostly values stay within a range between 200 and 400 fs (Fig. 8). When the feedback loop was turned OFF, timing jitter values surge upward by a factor of ten.

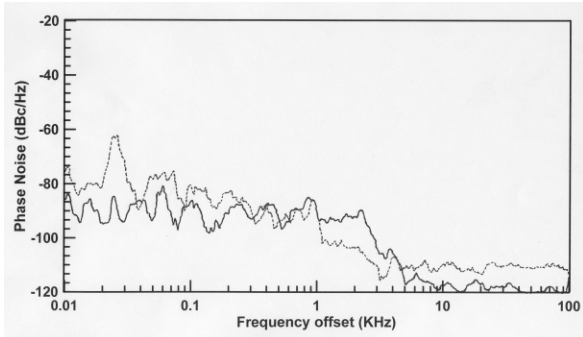

Fig.7. Tsunami laser phase noise spectral density plots at two different times.

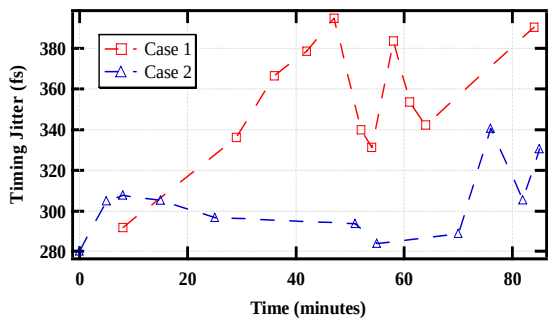

Fig.8. Tsunami laser. Timing jitter versus time. The square and the triangle stand for the data taken at two separate times.

The Tsunami laser uses an intracavity AOM to initiate and stabilize mode-locking. We investigated the influence of the AOM on timing jitter by making phase noise measurements with the AOM on and off. Measurements indicate that the AOM does not introduce additional instability. This confirms that AOM only helps to start the KLM process and set the fundamental frequency for the feedback loop to lock the cavity length. Once the cavity is optimized and loop is closed, AOM is not needed.

Gain-switched Diode Laser

Gain-switched diode lasers have a number of advantages over mode-locked lasers such as simplicity,

good stability and low cost. They also provide a wide range of pulse repetition rates independent of laser cavity length. While there is no doubt about amplitude stability, we did an investigation of phase noise performance. The laser system consists of a sub-milli-watt gain-switched InGaAs laser at 1.56 um and a fiber amplifier to boost the power to a level suitable for the measurement. Gain-switching at frequencies below 100 MHz produces longer optical pulses with tails, so a step-recovery diode (SRD) was used to improve the temporal profiles of the laser pulses. There is no cavity length adjustment for this system.

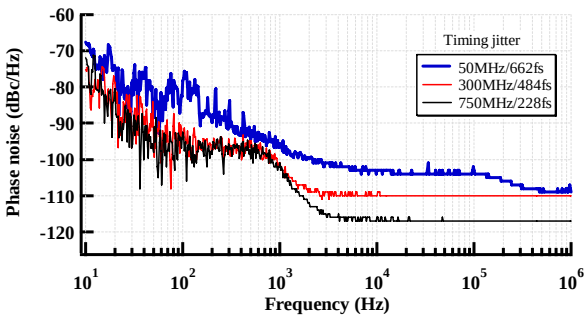

Fig.9. Phase noise spectral density plot and timing jitters of gain-switched diode laser and fiber amplifier at three different repetition rates.

Phase noise spectral density plots for the gain-switched diode laser at three pulse repetition rates are shown in Figure 9. The timing jitter increases inversely with the pulse frequency. At the lowest frequency 50 MHz, the timing jitter is larger than lasers mentioned previously. Note for the 50 MHz case, the phase noise at frequencies > 1 kHz is noticeably higher. The RF generator used here is the same as the previous lasers. The possible contribution to the noise is poor impedance matching at the SRD and driving circuits. The signal from the SRD shows different waveforms as the RF frequency and power changes. It requires a good balance between these parameters including the near threshold DC bias. Further work is needed to improve the performance before they can be adapted into the FELs.

High Power FEL

So far we have only talked about lasers with cavity lengths of 1.5 m or shorter. We also studied the phase noise properties of the high power JLab FEL, with output power over 1kW (pulse-width about 200 fs and wavelength 1.6 um). The FEL laser cavity is composed of two mirrors separated by 32 m. The mirrors sit inside vacuum chambers: the laser cavity length can be tuned over 1 cm with resolution sub-micron but there is no active cavity length control.

Phase noise measurements were made under different FEL operating conditions. Results are presented in Fig.10, together with the noise spectrum of the Antares drive laser. The FEL timing jitter is on the same level as other lasers, even operating without cavity length stabilization. The phase noise rises dramatically at all off-set frequencies, especially at the higher bands. If we look at the electron bunches in the wiggler region, they actually appear to be very quiet (timing jitter less than 60 fs). The phase noise actually gets suppressed compared to the drive laser. The two curves in Fig.10 for FEL were taken at two different times to show the random fluctuation during the same machine operation. In view of the exceptionally long FEL laser cavity length, the FEL output is remarkably stable. However, this measurement suggests that the FEL phase noise could be reduced using feedback mentioned in earlier sections.

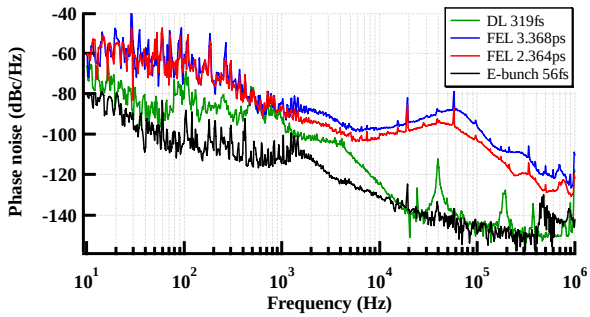

Fig.10. FEL phase noise spectra. The carrier frequency is 1.49 GHz. Laser frequency is 9.37 MHz. Lasing wavelength is 1.6 um. DL, drive laser. E-bunch, electron bunches.

SUMMARY

We have presented the phase noise characteristics of several lasers that can be used to drive GaAs photoguns. The performance of each laser depends on the phase locking mechanism. Active cavity length adjustment remarkably reduces the phase noise. The overall phase noise appears unrelated to the optical pulse length. The flash-lamp-pumped system does not necessarily have to be noisier. Diode-pumped amplifiers present very minor noise addition to the seed pulse. The gain-switched laser is good for repetition rates over 100 MHz but needs improvement to be used at sub-hundred MHz band.

ACKNOWLEDGMENT

The authors would like to thank M. Poelker for reviewing and extensive editing. This work is supported by the Office of Naval Research, the Joint Technology Office, the Commonwealth of Virginia, the Air Force Research Laboratory, and by DOE Contract DE-AC05-84ER40150.

REFERENCES

[1] D. von der Linde, Appl. Phys. B **39**,201 (1986).
[2] S. V. Benson, M. Shinn, 16th IEEE Particle Accelerator Conference (PAC 95) and International Conference on High-energy Accelerators (IUPAP), Dallas, Texas, May 1995. PAC, vol. 2(1052-1054).
[3] S. Zhang, S. Benson, et al., in Proceedings of the 27th International FEL Conference, SLAC, CA, August, 2005, pp. 351-354.

A MECHANICAL SHUTTER TO SELECT SINGLE BUNCH TRAINS AT THE FLASH FACILITY AT DESY

Martin Bräuer, now at SIEMENS Medical Solutions, 91052 Erlangen, Germany
Ulrich Hahn, and Sven Toleikis, Deutsches Elektronen-Synchrotron DESY, 22603 Hamburg, Germany.

Abstract

A fast mechanical shutter to select single photon bunch trains of the free electron laser FLASH is described. FLASH is installed at the Deutsches Elektronen-Synchrotron DESY in Hamburg and is based on superconducting linear accelerator technology. The accelerator provides bunch-trains with a repetition rate between 5 and 10 Hz. This time interval of down to 100 ms makes it possible to use a mechanical shutter system to select single bunch-trains for sample excitation.

A programmable logic controller (PLC) is used to steer a servo system based on an electronically commutated (EC) low-voltage motor. To select a bunch-train, the motor is started at the time when one train passes the station. During the following 100 ms, the cylinder is turned by 180°, leading to a movement of the shutter by 48 mm to the fully open position, thus allowing the passage of the following bunch-train. During the next 100 ms the rotation is continued to the 360° position, thus blocking the next bunch-train by pushing the shutter back to the fully closed position.

INTRODUCTION

Since 2005 the first FEL user facility for soft X-ray coherent light experiments FLASH is in operation at DESY [1]. The facility consists of a superconducting accelerator in combination with a 30 m long undulator producing highly intense (~GW) and extremely short (~10 fs) photon pulses. The superconducting linear accelerator creates and accelerates bunch-trains with up to 7200 bunches within 800 µs (at 10 Hz).

The experimental hall of the user facility is located approximately 30 m behind the last dipole magnet which separates the electron and the photon beam. The photon beam transport system delivers the FEL radiation under ultra high vacuum conditions to the five different end stations, which can be used alternatively.

The photon pulses energies are generated with an average energy of 10 µJ. Solid state samples irradiated in normal incidence are easily destroyed when the photons are focused to a spot size of ~20 µm. To study such damage processes it is important for FEL users to control the irradiation process. The 5 to 10 Hz repetition rate of the bunch trains allows the use of a mechanical shutter to select single bunch trains for sample irradiation.

The fast mechanical shutter is installed in the shared part of the first three beamlines. Figure 1 shows the shutter installed in the beamline system.

The fast shutter consists of a glassy carbon [2] shutter blade with a thickness of 4 mm. The blade motion is generated by a special linear drive developed for fast wire scanners for FEL electron beam diagnostics [3, 4]. The shutter covers the beam aperture of 20 mm.

In this paper, we report on the technical layout of the fast shutter, and first experimental results of a time-resolved damage and ablation measurement are presented.

TECHNICAL LAYOUT

Mechanical Set Up

Figure 2 shows the mechanical design of the fast shutter. The central part is the glassy carbon blade connected to the linear drive unit. Glassy carbon is chosen because of its low density of 1.6 g/cm^3 combined with high mechanical stability, good reflectivity in the spectral

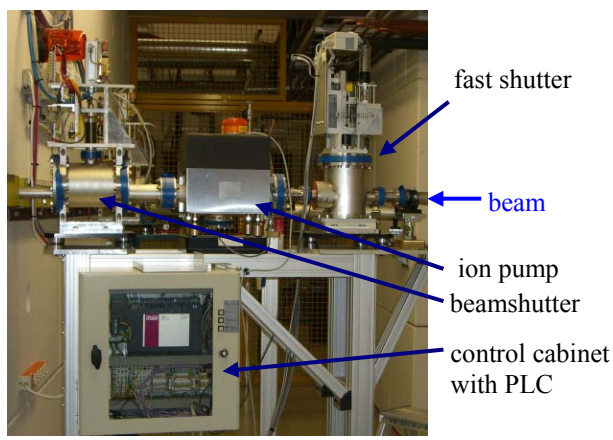

Figure 1: The fast shutter installed in the FLASH beam-line system

range of the FEL and the thermal robustness of carbon. The fast shutter has to be operated under ultra high vacuum conditions. As linear vacuum feed through a welded bellow is used. An incremental length gauge for position detection is connected to the linear drive. The essential features of the fast shutter are the stroke of 48 mm combined with a maximum shutter speed of 1 m/s in the linear velocity range of 24 mm. The speed is needed to shorten the opening and closing times into the ms range. The movement of the shutter blade is based on a slot winding cylinder (see Fig. 2 + 3) transforming the rotation of the servo motor into a linear motion [3, 4].

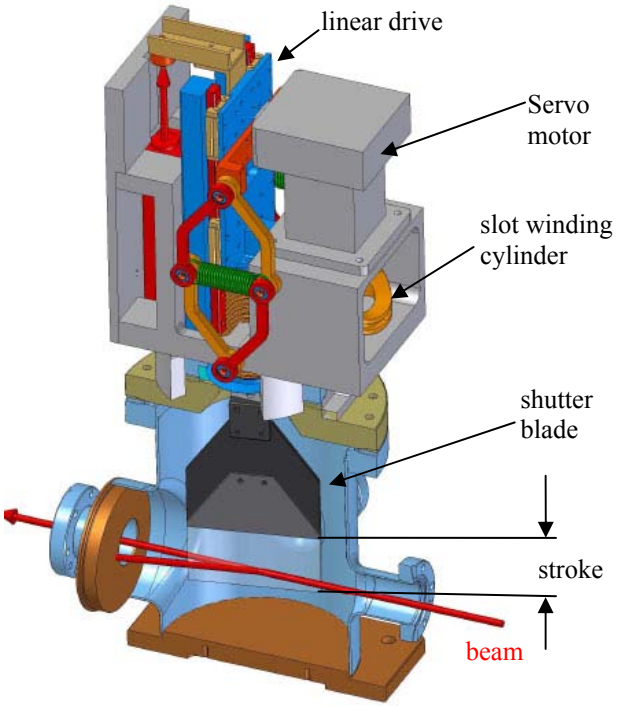

Figure 2: The mechanical layout of the fast shutter.

The cam of the slot winding cylinder uses the transfer function of a Bestehorn-sinuide (see Fig. 3):

$$S = s_0 \left[\omega t - (1/2\pi)\sin(2\pi\omega t)\right]$$
$$0 \le \omega t \le 1$$

where S is the stroke of the run up and down phase, s_0 the maximal stroke of 24 mm and ωt the normalized transmission angle. The region ωt = 0 until ωt = 1/2 represents the run up phase while ωt = 1/2 until ωt = 1 describes the run down phase. The speed and acceleration is given by

$$S' = s_0\,\omega\left[1 - \cos(2\pi\omega t)\right]$$

$$S'' = s_0\,\omega^2\,2\pi\sin(2\pi\omega t)$$
$$0 \le \omega t \le 1$$

At a stroke of 0mm the shutter is totally closed. The start up range between 0 and 12 mm accelerates the shutter to the opening speed of 0,36m/sec. Between 12 and 36 mm the shutter blade releases the photon beam aperture of 20mm. In the range from 36 to 48 mm the shutter blade changes the moving direction. When the blade transfers this range the photon bunch train can pass the shutter. Figure 3 shows the stroke, speed and acceleration of the blade during one turn, assuming that the shaft is rotating with constant speed.

The motor is connected to the slot-winding cylinder with a gearing-ratio of 15:1. For 10Hz operation, rotation speeds of the shaft of 450rpm and accelerations of 6750rpm/s are needed.

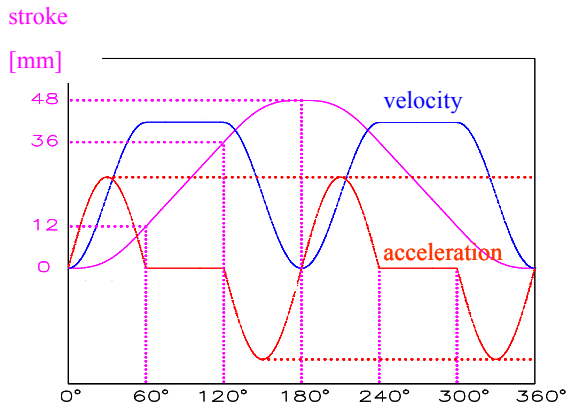

Figure 3: The transfer functions of the slot winding cylinder (Bestehorn sinuide).

Electronic Set Up

The electrical setup of the fast shutter is shown in Fig. 4. The central part is a PLC-controller with IO-Modules [5]. The controller acts on a servo system via a field-bus (CAN open [6]). The servo system consists of the servo controller/amplifier, the motor and two integrated feedback systems [7]. These components alone allow the

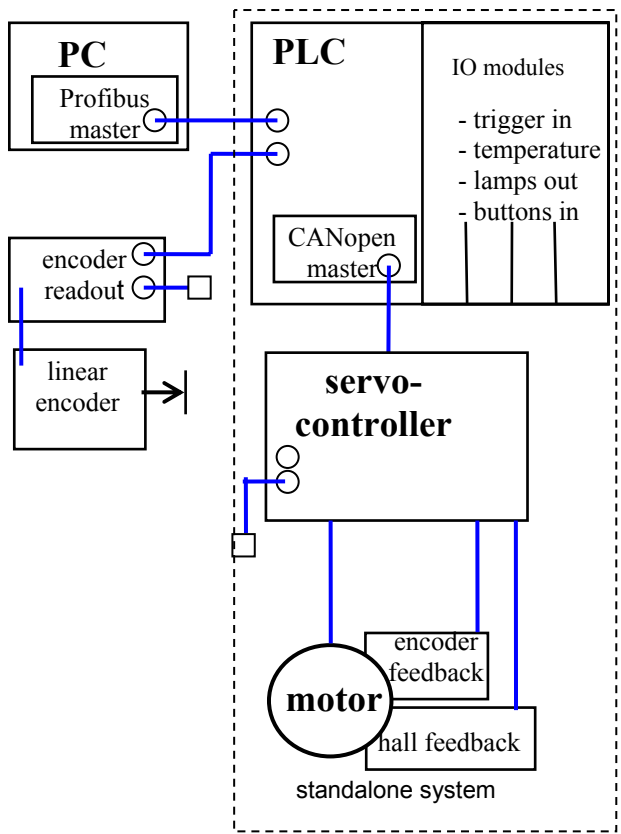

Figure 4: Layout of the electronic set-up.

operation of the fast shutter. In addition a PC, housing a Profibus-master card, was connected to the PLC. With the PC the parameterization and programming can be performed. Furthermore a Profibus-interface to read out the linear gauge is connected to the Profibus line. The linear gauge can only be accessed by the PC and be used for an independent feedback of the shutter position for diagnostics. All major components are described in the following.

All electronics parts are standard components from the general automation market. They are contained in a standard compartment, as shown in Fig. 1. Most space is occupied by the power supplies and the terminals to route the various electrical signals.

The PLC controller is programmed and parameterised from an external PC, but operating in a standalone mode afterwards. The cycle time for the SPS program was chosen to run at 3ms, which means that the whole program is running within 3ms under any condition while sampling inputs and setting outputs. The controller acts as a client on the Profibus and reactions to Profibus commands can be programmed. This allows the control from a master PLC in our case running on the PC. The connection to the beamline interlock system can be routed via this bus.

For the CANopen subsystem, the controller acts as a master. The CANopen subsystem is running with the cycle time of the PLC, allowing a fast reaction on events. Inputs and outputs are provided by appropriate IO-modules. Most important inputs are the user commands, generated by output cards of the FLASH experimental control system, by button states and the bunch signal. The bunch signal, derived from the FLASH-timing, announces the arrival of a photon bunch. This signal is stretched to 10 ms to be detected by the PLC.

The servo system uses an electronic commutated motor. While the controller/amplifier is connected to 48V DC, the motor is provided with two sinusoidal voltages to its static coils. The rotating permanent magnet follows the generated current. In contrast to a stepper-motor, the rotor position is measured by hall-elements to determine the absolute position of the magnet. To reach the ultimate precision for the velocity and position-control loops, an additional incremental encoder is attached to the motor shaft.

The controller firmware enables the user to work with the three nested servo-loops (current, velocity and position) in an easy way. Parameters are determined by an automatic tool and are stored together with further application specific data on the internal flash memory. Due to the CANopen standard, devices of various vendors can be mixed and exchanged, securing investments over the coming years.

In contrast to stepper-motors, the servo system can use a much larger speed-torque parameter space due to the active regulation.

Operational Principle

The shutter can be opened and closed by electrical signals, i.e. generated by buttons. The user commands are routed by the FLASH-control system via output-cards to 5V inputs of the PLC. Status information is transferred from the PLC via 5V terminals and input-cards to the user.

The states of the shutter are: ‘open’, ‘close’, ‘single shot’, ‘synchronized shot’ and ‘home’.

The home-mode is needed to orient the controller after power up. The shutter is driven to the open position until a precision switch mounted close to the open position is triggered.

All other movements are always executed synchronously to the bunch-trains.

After an open or close signal, the next following bunch-train-clock is waited for. When the PLC detects a rising edge on the bunch-signal, the motor is commanded to perform a 180ºrotation of the cylinder. This is thus changing the state of the shutter from closed to open or vice-versa.

After the detection of a single-shot signal, the procedure is executed in the same way but initiating a 360º turn of the cylinder. The timing of the later procedure is depicted in Fig. 5.

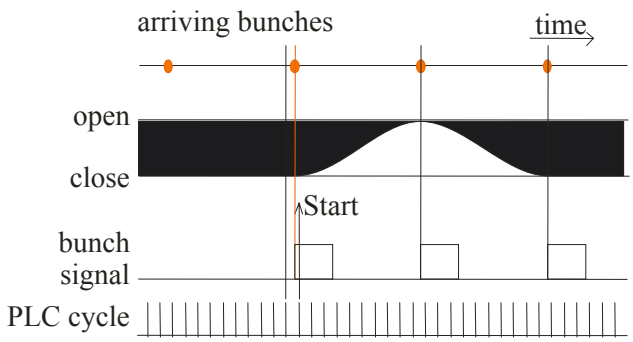

Figure 5: Timing scheme of the synchronous movements.

The synchronised move allows to trigger a single shot on an external 5V or TTL signal, generated by users instrumentation.

Since the bunch-train-frequency of FLASH can be adjusted by the operation-crew, a part of the PLC-software evaluates the frequency of detected bunch signals and automatically adjusts the appropriate velocity and acceleration values.

FIRST EXPERIMENTS

One of the first experiments that used the fast mechanical shutter at FLASH was a time-resolved damage and ablation measurement [8]. The aim of this experiment was to study the interaction of ultra short FEL pulses in the VUV wavelength range with solid state surfaces at moderate irradiation intensities ($I=10^{11}$-10^{14}

W/cm²). The irradiation with ultra short VUV pulses permits a high degree of electronic excitation but essentially without any non-linearity. In addition, the increased absorption depth for some materials helps to minimize the influence of transport effects, e.g., carrier diffusion and heat conduction. Therefore, ultra short VUV pulses allow the preparation of rather well defined excitation conditions in relatively large sample volumes as compared to femto second optical pulses. To directly study the dynamics of ultra fast VUV-induced phase transitions and ablation, time-resolved measurements of the optical reflectivity have been performed in a VUV pump - optical probe configuration. The VUV pulse (λ=32 nm) is used for sample excitation and a delayed visible probe pulse (λ=532 nm) serves as illumination in an optical microscope. This allows to follow the reflectivity evolution of the VUV irradiated surfaces with both temporal and spatial resolution.

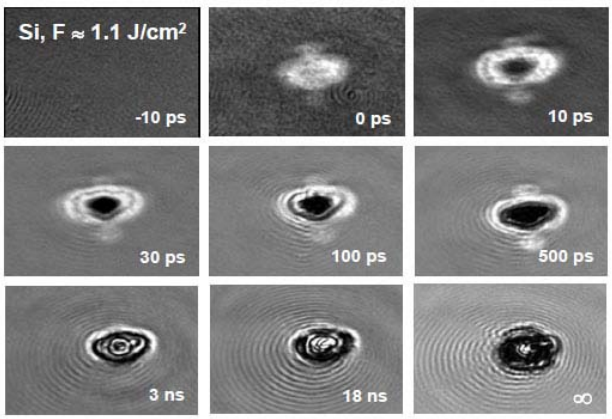

Figure 6: Surface of Si-wafer after irradiation with a <50 fs FLASH pulse (λ=32 nm) with a fluence of 1 J/cm². Frame size is 120 x 80 µm².

During the measurement FLASH was running in a single bunch operating mode having only one bunch in the bunch train. The mechanical shutter allowed the irradiation of the samples with exactly one ultra short VUV pulse of known intensity which was measured with a gas monitor detector system [9]. After irradiation the sample is moved to a new non-irradiated position and the reflectivity of the optical pulse is then measured at a different time delay. Figure 6 shows a sequence of time-resolved snapshots obtained on a bulk silicon sample for an excitation fluence of ~ 1 J/cm².

At early time (10 ps) a pronounced increase of the reflectivity is observed which can be attributed to a solid-liquid phase transition of the material. Although the temporal resolution was limited by the probe pulse duration to about 10 ps, this transition is most likely of electronic nature and occurs on sub-ps time-scales. Already after 10 ps the decrease of the reflectivity in the centre of the spot, where the fluence is highest, marks the onset of ablation. However, even after 18 ns ablation has not come to an end and the irradiated surface has not reached its final state.

The main goal of this measurement at FLASH was to establish the experimental technique and to obtain a first overview of the dynamics of the induced processes. Further measurements with enhanced temporal (<100 fs) and spatial resolution will follow which would provide a more detailed picture of these processes. Compared with femto second optical excitation distinct differences in the material response have been observed that are attributed to the larger absorption depths of the VUV radiation and the absence of non-linearity.

CONCLUSIONS

On the basis of existing wire scanner technology a fast shutter has been implemented in the FLASH beamline system. This allows users to choose single bunch trains with a repetition frequency of up to 10 Hz. First experimental results show the benefit of the fast shutter.

REFERENCES

[1] V. Ayvazyan, et al., "First operation of a Free-Electron Laser generating GW power radiation at 32 nm wavelength", Eur. Phys. J. D 37, (2006), 297-303

[2] Glassy carbon, SIGRADUR®, HTW Hochtemperatur Werkstoffe GmbH, Germany

[3] H. J. Grabosch, U. Hahn, M. Sachwitz, and H. Thom, „Wire Scanner System for Undulator Section of VUV-FEL at DESY", MEDSI-2004, Proceedings – 04 – 31

[4] P. Castro, U. Hahn, O. Hensler, S. Karstensen, M. Sachwitz and H. Thom, "Wire scanner system for FLASH at DESY", to be published

[5] BX3100 controller, Beckhoff Industrie Elektronik, 33415 Verl, Germany.

[6] CANopen, Controller Area Network, Can in Automation group, 91058 Erlangen, Germany.

[7] Servo system with EPOS 70/10 controller/amplifier and an EC-max 40 Motor with HEDL5540 Encoder by Maxon Motor AG, CH-6072, Switzerland.

[8] K. Sokolowski-Tinten, et al., to be published

[9] A.A. Sorokin, et. al., "Gas-Monitor Detector for Intense and Pulsed VUV/EUV Free-Electron Laser Radiation", Proceedings SRI2003, San Francisco, AIP Conf. Proc.705 (2004), 557-560

COMMISSIONING OF A NEW EMITTANCE MEASUREMENT SYSTEM AT PITZ*

L. Staykov†, J. Bähr, H.J. Grabosch, S. Khodyachykh, S. Korepanov, M. Krasilnikov,
A. Oppelt, B. Petrosyan, F. Stephan, DESY, 15738 Zeuthen, Germany
J. Rönsch, Hamburg University, 22761 Hamburg, Germany
G. Asova, I. Tsakov, INRNE-BAS, 1407 Sofia, Bulgaria.

Abstract

The goal of the Photo Injector Test facility in Zeuthen (PITZ) is to test and optimize high brightness electron sources suitable for FEL's like FLASH and the European XFEL. Such sources are characterized by very low emittance at high bunch charge. The new Emittance Measurement SYstem (EMSY) described in this paper uses YAG and OTR screens to measure the transverse beam size and thin Tungsten slits to measure the divergence of the beam. It has been optimized to measure emittance for a beam of 1 nC in the energy range 5 - 30 MeV. The new EMSY was developed in a cooperation between DESY Zeuthen and the Institute for Nuclear Research and Nuclear Energy (INRNE) in Sofia. It was installed in the PITZ tunnel in the beginning of June and commissioning and first measurements are ongoing.

INTRODUCTION

The Photo Injector Test Facility at DESY in Zeuthen (PITZ) was built to test and to optimize electron sources which are capable for SASE FEL operation. The main PITZ components are a photocathode laser, an L-band RF gun and space charge compensating solenoids. A major upgrade on the existing PITZ facility is ongoing since last year [1]. This upgrade includes the installation of an additional accelerating RF booster cavity and various diagnostics elements. The laser system was also upgraded in the last year, by improving the transverse imaging to the photo cathode (see [2]) and the overall stability. One of the goals of the facility is to study and optimize the conditions for the conservation of emittance compensated electron beam with short pulse length and low transverse emittance [3, 4]. Extended optimization of the photoinjector with ASTRA [5] showed that transverse emittance smaller than 1 mm.mrad at 1 nC charge can be reached (fig. 1). The Emittance Measurement SYstem used at PITZ was upgraded for better performance in the extended momentum range [6]. Three of such devices were produced by the HITECH HEP Group in INRNE Sofia and are already installed in the PITZ tunnel. In this paper details about the new EMSY as well as first experience from the commissioning are given.

* This work has partly been supported by the European Community, Contract Number RII3-CT-2004-506008, and by the 'Impuls- und Vernetzungsfonds' of the Helmholtz Association, contract number VH-FZ-005.

† Presenting author, e-mail: lazaraza@ifh.de

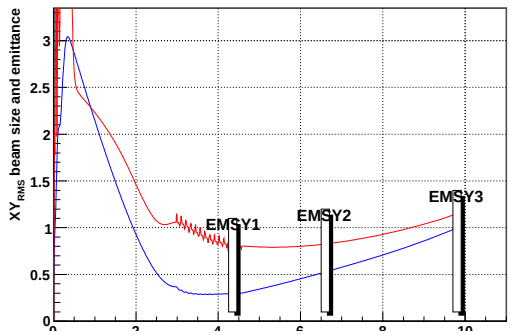

Figure 1: ASTRA simulation of the rms beam size in mm (blue) and normalized emittance in mm·mrad (red). The charge is 1 nC; accelerating gradient at the gun is 60 MV/m, phase of maximum energy gain; the focusing solenoid is at 385 A; the gradient of the booster cavity is 28.9 MV/m, phase of maximum energy gain.

PITZ SETUP

A detailed layout of the current PITZ setup is shown on Fig. 2. The electrons are produced in the RF gun (on the right hand side) and transported through the low energy diagnostic section, further acceleration up to the maximum of 30 MeV is given in the booster cavity after which the high energy diagnostic section is installed.

The low and high energy diagnostic sections consist of different view screens, BPM's, charge measurement devices and longitudinal phase space diagnostics. The charge per bunch can be monitored non-destructively at four positions along the beamline using Integrated Current Transformers (ICT's). The beam momentum and momentum spread are measured at two dispersive dipole arms, one in the low energy section and one after the booster cavity. The low energy dispersive dipole is also equipped with a streak camera readout providing full knowledge about the longitudinal phase space distribution (see [7]). Three EMSY's are located after the booster cavity in positions 4.3, 6.6 and 9.8 m from the cathode.
For the transverse phase space characterization we rely on YAG and OTR screens and the so called slit scan technique [8]. For this technique the uncorrelated local divergence is estimated by cutting the electron beam into thin slices and measuring their size on a screen after a drift. The so called sheared normalized RMS emittance is then calculated us-

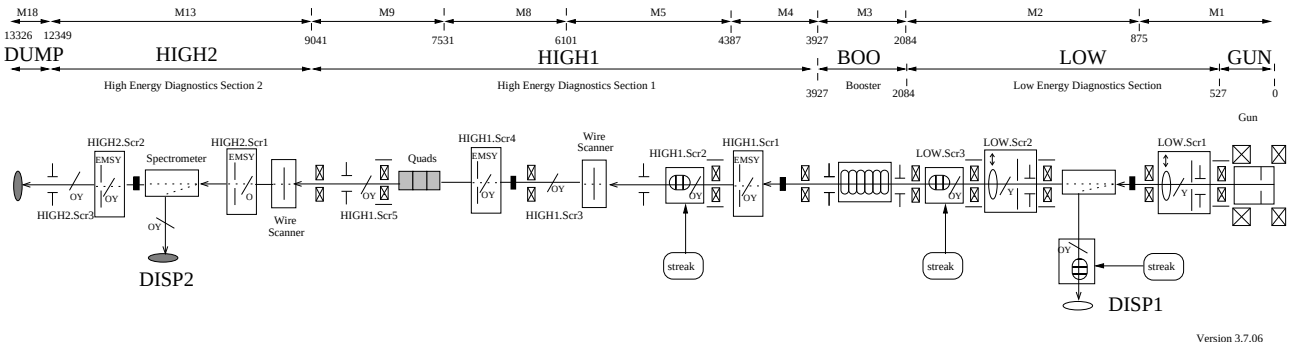

Figure 2: Layout of PITZ.

ing the following definition (1) taken from [8]:

$$\varepsilon_n = \beta\gamma \cdot \sqrt{\langle x^2 \rangle \cdot \langle x'^2 \rangle}. \quad (1)$$

Here $\langle x^2 \rangle$ and $\langle x'^2 \rangle$ are the second moments of the distribution of the electrons in the so called trace phase space where $x' = \sqrt{\langle p_x^2/p_z^2 \rangle}$ represents the divergence of the beam. The RMS beam size is measured on an OTR or YAG screen at the position of the slits along the beam axis. The uncorrelated divergence is obtained by analyzing the profiles of the beamlets produced from the slits which drift some distance L_d downstream where the spatial distribution of the beamlets corresponds to the local uncorrelated divergence, x' can be derived from the size of the beamlet using the formula in Eq. 2.

$$x' = \frac{\sqrt{\langle x_b^2 \rangle}}{L_d}. \quad (2)$$

Here x_b is the RMS size of the beamlet on the screen after distance L_d. The $\beta\gamma$ is measured using a dispersive arm after EMSY.

THE NEW EMITTANCE MEASUREMENT SYSTEM

EMSY consists of two orthogonal actuators (Fig. 3) which can be inserted separately to penetrate the beam in order to take images or to cut beamlets in the beam transverse planes. The actuators are driven into the beam line with stepper motors and positioned with precision better than 10 μm, their angular orientation with respect to the electron beam can be adjusted during the measurement again using stepper motors. Each actuator is equipped with an YAG or OTR screen for measurement of the transverse RMS beam size $\sqrt{\langle x^2 \rangle}$ and a single slit mask for estimation of the local divergence, multi slit masks are in production and will be mounted on the actuators in the next shutdown period. The design of the system enables us to measure the beam transverse parameters expected in PITZ with uncertainty less than 10 % (see [6]).

During the design the following considerations were taken into account:

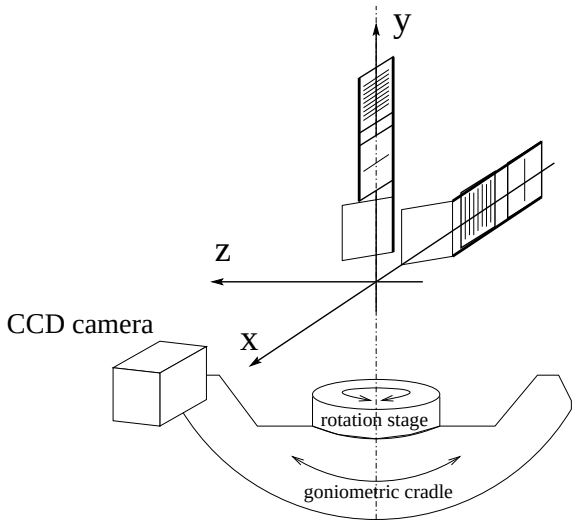

Figure 3: Layout of EMSY.

- The slit opening must be small enough to produce emittance and not space charge dominated beamlets, but still large enough to provide good transmission.
- The contribution of the initial beamlet size to the measured one at the screen of observation must be as small as possible.
- The distance betwen the slit mask and the screen must be big enough to resolve small beam divergence. But still short enough to prevent the space charge forces to degrade the beamlet and the overlapping of different beamlets from the multi slit mask.
- The mask thickness must be large enough to scatter the residual electrons from the beam in order to produce an uniform background for the beamlets measurements and still it must be thin enough provide sufficient acceptance angle.

The design of the slits was made using the above considerations, and GEANT4 [9] simulations for transport of the electrons through the masks and to assess the performance of the YAG screens to be used. Slits are made from 1 mm thick Tungsten with 10 μm slit opening, the slits of the multi slit mask are separated with 0.3 mm. The screens are made from 0.3 silica waffers coated with YAG powder

or with Al (for the OTR screens). The YAG screens are placed at 90 degrees with respect to the electron beam and an Al coated silicon mirror is used to direct the light to the CCD chip, the OTR screens are with 45 degrees orientation. Both the screens are observed with 8 bit CCD camera. It was found from the beam dynamics simulations, that in some cases 8 bit camera cannot provide the desired sensitivity, therefore 12 bit cameras are ordered and are soon to be installed. On fig. 4 a scan of the position of the slit trough the beam is shown, a good signal from the camera is obtained (blue line), with red the RMS beamlet size is plotted.

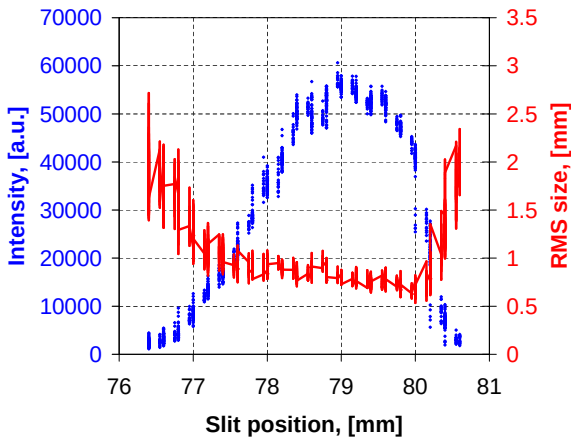

Figure 4: Scan with the 10 μm slit.

Further optimization of the readout can be made by adjusting the angular orientation of the slit, as can be seen in fig. 5. The slit at position 79 mm in fig. 4 was selected for the angular optimization, improvement of the intensity of the signal from the camera is seen (blue dots) as well as stable reading for the beamlet size (red line) in the angular range -10 to +8 mrad, for larger angular deviations lower signal transmission takes place as well as additional effects such as scattering of the electrons from the inner surface of the slit, etc.

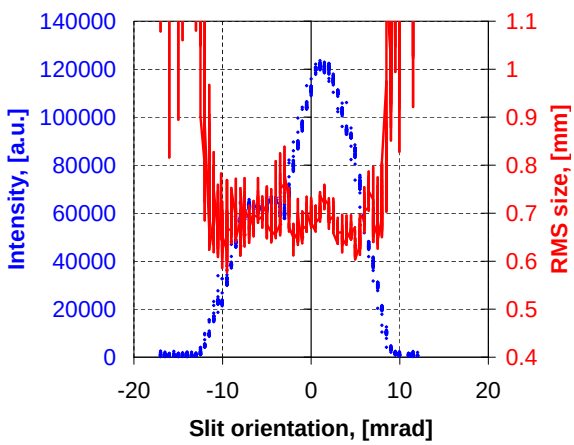

Figure 5: Scan of the angular orientation of 10 μm slit.

CONCLUSIONS

The 10 μm slits can provide sufficient signal for beamlet measurements with proper angular orientation. The emittance measurement system in PITZ is installed and commissioned. All the component from the system are tested and ready for use.

ACKNOWLEDGMENT

We would like to thank to Evstati Apostolov, Hristo Yotov and Luchezar Yotov from INRNE for the precise construction and Alexander Donat, Hartmut L¨udecke and Jochen Bienge from DESY Zeuthen for their outstanding support on the mounting and aligning the devices in the PITZ tunnel.

REFERENCES

[1] A. Oppelt, “Status of the PITZ facility upgrade”, LINAC 2006.

[2] J. B¨ahr et al., “Upgrades of the Laser Beam-line at PITZ”, FEL’05.

[3] M. Krasilnikov et al., “Recent developments at PITZ”, PAC’05, May 2005, Tennesy USA.

[4] L. Serafi ni, J. Rosenzweig, “Envelope analisys of intense relativistic quasilaminar beams in rf photoinjectors: A theory of emittance compensation”, Phys. Rev. E, Vol. 55, 1997.

[5] K. Floetmann,ASTRA,http://www.desy.de/˜mpyflo

[6] L. Staykov et al., “Design Optimization of an Emittance Measurement System at PITZ”, DIPAC’05.

[7] J. R¨onsch et al., “Investigations of the Longitudinal Phase Space at PITZ”, EPAC’06.

[8] V. Miltchev, “Investigations on the transverse phase space at a photo injector for minimized emittance”, PhD thesis.

[9] GEANT collaboration, CERN/LHCC 98-44, GEANT4: “An Object Oriented Toolkit for Simulation in HEP”; see also website: http//wwwinfo.cern.ch/asd/geant4/geant4.html

SIMULATION OF MIRROR DISTORTION IN FREE-ELECTRON LASER OSCILLATORS*

H.P. Freund#, Science Applications International Corp., McLean, VA 22102, U.S.A.
M. Shinn and S.V. Benson, Thomas Jefferson National Accelerator Facility, Newport News, VA 23606, U.S.A.

Abstract

Thermal distortions in high-average power FEL cavity mirrors can alter mode quality and degrade performance. We address these issues by developing simulation tools, and then benchmarking the simulation against observations on the 10 kW-Upgrade experiment at the Thomas Jefferson National Accelerator Facility in Newport News, VA. The modelling and simulation will rely on the MEDUSA code, which is a three-dimensional FEL simulation code that is capable of treating both amplifiers and oscillators in both the steady-state and time-dependent regimes. MEDUSA employs a Gaussian modal expansion, and treats oscillators by decomposing the modal representation at the exit of the wiggler into the vacuum Gaussian modes of the resonator and then analytically determining the propagation of these vacuum resonator modes through the resonator back to the entrance of the wiggler in synchronism with the next electron bunch. Knowledge of the power loading on the mirrors allows us to model the mode distortions using Zernike polynomials, and this technique will be incorporated into MEDUSA.

INTRODUCTION

Thermal distortions in cavity mirrors in high-average power FELs can alter mode quality and negatively impact performance; hence, it is important to predict the character and magnitude of the distortions and to be able to model their effect on FEL performance. To this end, we address these key issues by developing modelling and simulation tools that can accomplish these goals, and then benchmarking the simulation against observations on the 10 kW-upgrade experiment [1] at the Thomas Jefferson national accelerator facility in Newport News, VA (henceforth referred to as Jefferson Laboratory). The facility is undergoing continual upgrades; in particular, a new permanent magnet wiggler has been installed that will be used in comparing the experimental and simulation results (see Table 1). The modelling and simulation will rely on the MEDUSA code [2,3], which is a three-dimensional FEL simulation code that is capable of treating both amplifiers and oscillators in both the steady-state and time-dependent regimes. MEDUSA employs a Gaussian modal expansion, and treats oscillators by decomposing the modal representation at the exit of the wiggler into the vacuum Gaussian modes of the resonator and then analytically determining the propagation of these vacuum resonator modes through the resonator back to the entrance of the wiggler in synchronism with the next electron bunch. Knowledge of the power loading on the mirrors allows us to model the mode distortions using Zernike polynomials [4], and this technique will be incorporated into MEDUSA.

In this paper, we report on the progress to date in this activity. The first step is to compare MEDUSA predictions with the observed performance of the experiment at low duty factor where mirror distortions are unimportant. We then go on to determine the effects of the so-called first order properties, which include changes in the Rayleigh range and shifts in the position of the mode waist. Higher order distortions such as coma, astigmatism, and spherical aberration, collectively known as third-order aberrations, will be incorporated in the future. The organization of the paper is as follows. In the second Section we discuss the formulation used in MEDUSA. A description of the experiment is given in the third Section, and of the numerical results in fourth Section. A summary and discussion is given in the fifth Section.

THE NUMERICAL FORMULATION

The MEDUSA code [2,3] employs a three-dimensional formulation that includes the slippage of the radiation relative to the electron beam. MEDUSA can model both helical and planar wiggler geometry and treats the electromagnetic field as a superposition of either Gauss-Hermite or Gauss-Laguerre modes in the slowly-varying amplitude approximation, where

$$\delta\mathbf{A}(\boldsymbol{x},t)=\hat{\boldsymbol{e}}_x\sum_{l,n} e_{l,n}(x,y)\left[\delta A^{(1)}_{l,n}\cos\varphi(x,t) + \delta A^{(2)}_{l,n}\sin\varphi(x,t)\right], \quad (1)$$

where "l" and "n" are transverse mode numbers, "h" is the harmonic number, $e_{l,n,h} = \exp(-r^2/w_h^2)H_l(\sqrt{2}x/w_h)H_n(\sqrt{2}y/w_h)$, H_l is the Hermite polynomial of order l, and w_h is the spot size, $\varphi_h = h(k_0z - \omega_0t) + \alpha_h r^2/w_h^2$ ($k_0 = \omega_0/c$). We assume that $\delta A^{(1,2)}_{l,n,h}$, w_h, and α_h, vary slowly in z and t. The dynamical equations are

$$\left(\frac{d}{dz}+\frac{w_h'}{w_h}\right)\begin{pmatrix}\delta a^{(1)}_{l,n,h}\\ \delta a^{(2)}_{l,n,h}\end{pmatrix} + K_{l,n,h}\begin{pmatrix}\delta a^{(2)}_{l,n,h}\\ -\delta a^{(1)}_{l,n,h}\end{pmatrix} = \begin{pmatrix}s^{(1)}_{l,n,h}\\ s^{(2)}_{l,n,h}\end{pmatrix}, \quad (2)$$

where $\delta a^{(1,2)}_{l,n,h} = e\delta A^{(1,2)}_{l,n,h}/m_ec^2$, $d/dz = \partial/\partial z + c^{-1}\partial/\partial t$, the "prime" superscript denotes the total z-derivative,

$$K_{l,n,h} = (l+n+1)\left(\alpha_h\frac{w_h'}{w_h} - \frac{\alpha_h'}{2} - \frac{1+\alpha_h^2}{hk_0w_h^2}\right), \quad (3)$$

*Work supported by the Joint Technology Office.
#henry.p.freund@saic.com

$$\begin{pmatrix} s^{(1)}_{l,n,h} \\ s^{(2)}_{l,n,h} \end{pmatrix} = \frac{2\omega_b^2}{h\omega_0 c}\frac{F_{l,n}}{w_h^2}\left\langle \frac{v_x}{|v_z|} e_{l,n,h} \begin{pmatrix} \cos\varphi_h \\ -\sin\varphi_h \end{pmatrix} \right\rangle , \quad (4)$$

where $\omega_b(z,t)^2 = 4\pi e^2 n_b(z,t)/m_e$ for a beam density n_b, and $F_{l,n} = [2^{l+n} l!n!]^{-1}$, and <(…)> describes an average over the complete 6-D phase space. The spot size and radius of curvature for each harmonic component are given by

$$w_h' = \frac{2\alpha_h}{hk_0 w_h} - w_h Y_h \ , \quad (5)$$

$$\frac{\alpha_h'}{2} = \frac{1+\alpha_h^2}{hk_0 w_h^2} - \left(X_h + \alpha_h Y_h\right) \ . \quad (6)$$

These equations constitute the source-dependent expansion [5], which is a self-consistent adaptive eigenmode representation that tracks the optical guiding of the mode based upon the interaction with the electron beam. The field equations are integrated simultaneously with the complete three-dimensional Lorentz force equations for an ensemble of electrons. No wiggler-average orbit approximation is used so that the spatial step size must be small enough to resolve the wiggler motion.

Table 1: Nominal experimental parameters

ELECTRON BEAM	
Energy	115 MeV
Peak Current	310-370 A
Normalized Emittance	9 mm-mrad/7 mm-mrad
Energy Spread	0.35%
Bunch Length	380-420 fsec
Bunch Charge	79 pC
Initial Beam Size	257 microns/212 microns
Twiss-α Parameter	1.25
WIGGLER	
Amplitude	3.746 kG
Period	5.5 cm
Length	30 periods/1.65 m
OPTICAL MODE	
Wavelength	1.57 microns
Rayleigh Range	1.5 (±0.30) m
Mode Waist Position	1.03 (±0.05) m

THE JEFFERSON LAB EXPERIMENT

The Jefferson Lab IR-Upgrade FEL operates an energy recovery accelerator with a high power FEL wiggler and resonator. The electron beam consists of a core distribution and a halo distribution. The charge, emittance, and peak current are of that core beam. The wiggler is very well characterized and is essentially ideal. The optical resonator is nearly concentric, and consists of a high reflector at the upstream end and a transmissive element at the downstream end that out-couples approximately 10% of the power. The Rayleigh range can be varied in the experiment by changing the radius of curvature of the high reflector. However, the cavity is slightly astigmatic and can lead to a difference between the Rayleigh range in the two axes. The uncertainty in the Rayleigh range is about 20%. The measured gain and efficiency are 70±5% and 1.6±0.1% respectively.

The nominal parameters for the experiment that are used in simulation are given in Table 1. Observe that the normalized emittances and beam dimensions shown in the table refer to the wiggle-plane and the plane transverse to the wiggler-plane respectively. In addition, the Twiss-α parameter shown corresponds to a beam that is focused to a waist near the center of the wiggler. The estimate of the Rayleigh range and the location of the mode waist contain some uncertainty, and the values given are the best estimate at the present time. In particular, we note that the mode waist is located about 15 cm downstream from the wiggler center.

NUMERICAL RESULTS

As we mentioned previously, our first goal is to determine whether MEDUSA is in substantial agreement with the experiment when distortion is absent or minimal. This is the case when the experiment operates at low average powers (*i.e.*, low duty factors), where a single pass gain of the order of 65-75% is measured for a peak current of 310 A and a bunch length of 380 fsec.

The parameters shown in Table 1 are the nominal experimental parameters, and we note that the optical waist is located about 15 cm downstream from the wiggler center. The experiment was optimized by focusing the electron beam to a waist near the center of the wiggler, which provides an optimal match to the resonator mode. This was also found in simulation, and is obtained for a Twiss-α parameter of 1.25 in simulation. The single pass gain found using MEDUSA operating in steady-state mode for these parameters is of the order of 400%. However, the slippage time through the wiggler for this experiment is of the order of 160 fsec, which is a substantial fraction of the bunch length. Hence, slippage is important and can be expected to substantially reduce the single pass gain with respect to steady-state predictions.

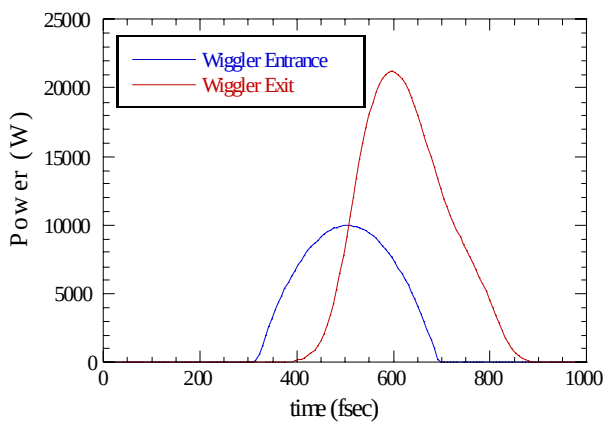

Figure 1: Plot of the power versus time through the pulse at the wiggler entrance and exit.

The slippage of the electromagnetic pulse through the wiggler is illustrated in Fig. 1 where we plot the pulse shapes at the entrance and exit from the wiggler. It is evident from the figure that while the pulse is assumed symmetric at the entrance to the wiggler, it has slipped by at least half the total pulse length over the course of the wiggler. Amplification of the peak power over the pulse has shrunk from the value of 400% found in steady-state simulation to just over 100% when slippage is included. However, in the time-dependent simulation, gain must be calculated based on the overall energy of the pulse, not the peak power. To this end, we plot the amplification of the total pulse energy through the wiggler in Fig. 2. The incident energy is 2.53 nJ and the energy at the output is 4.68 nJ yielding a single pass gain of about 84%. Given the uncertainties in the measured parameters, this represents reasonable agreement with the experiment. For example, there is a 20% uncertainty in the measurement of the Rayleigh range that would result in a reduction of the predicted gain to 73%.

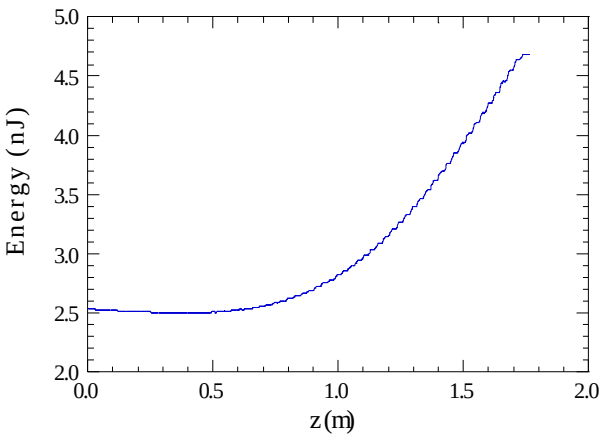

Figure 2: Plot of the amplification of the total pulse energy through the wiggler.

The lowest order mirror distortions involve variations in both the location of the optical waist and the Rayleigh range. In order to study the effects of these distortions, we (1) varied the position of the optical waist while holding the Rayleigh range fixed at 1.5 m, and (2) varied the Rayleigh range for an optical waist that is located at the wiggler center optical and 30 cm downstream from the wiggler center. These results are shown in Figs. 3 and 4 respectively. Figure 3 indicates that, for these parameters, the FEL gain is maximized when the optical waist is located about 20 cm upstream from the wiggler center, in contrast to the actual location that is 15 cm downstream from the wiggler center. Observe that we show the gain variation with Rayleigh range in Fig. 4 for an optical waist that is wiggler-centered and shifted downstream from the wiggler center by 30 cm. However, the optical waist is located 15 cm downstream from the wiggler center, and the actual location was used in the simulations shown in Figs. 1-3. We chose to use the larger displacement in Fig. 4 to better illustrate the performance sensitivity to these parameters, and the actual variation with Rayleigh range in the experiment is between these two lines. It is clear from Fig. 4 that the single pass gain would be larger if the Rayleigh range were smaller, and the optimal Rayleigh range found in simulation varies from about 0.5 m for a wiggler-centered resonator mode to 0.6 m when the mode waist is located 30 cm downstream from the wiggler center. The advantages that accrue from using a short Rayleigh range resonator were first pointed out by W. Colson and his collaborators [6]. The results shown in Figs. 3 and 4 indicate that were mirror distortions to either decrease the Rayleigh range or shift the mode waist upstream, then the single pass gain and FEL performance may actually be enhanced. Whether such an effect can actually be allowed for in the design of a high power FEL oscillator is currently under consideration.

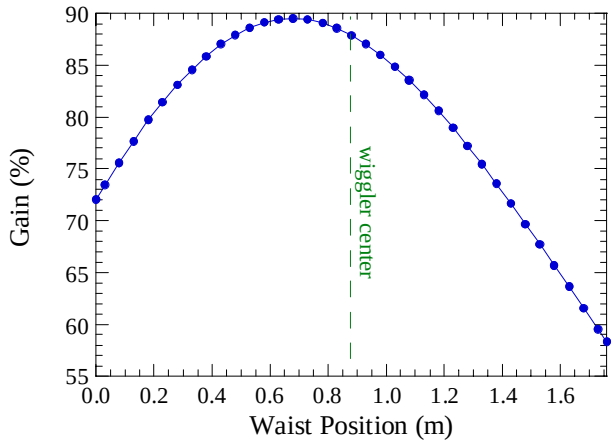

Figure 3: Variation of the single pass gain with the position of the optical waist.

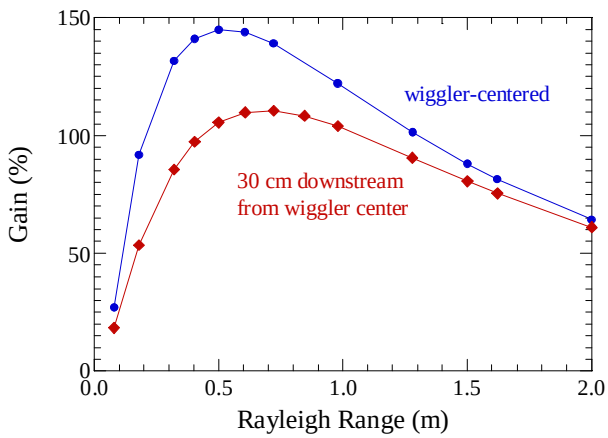

Figure 4: Variation of the single pass gain with the Rayleigh range.

SUMMARY AND DISCUSSION

In this paper we report on the initial work involved in a study of the effect of mirror distortions on the performance of a high power FEL oscillator using the MEDUSA simulation code. To this end, we first undertook to validate MEDUSA for low power (and duty factor) operation where mirror distortion was small. In this case MEDUSA predicted a single pass gain of 84%, which is in reasonable agreement with the measured range of 65-75% given the experimental uncertainties in the Rayleigh range, location of the optical waist, astigmatism in the resonator, and uncertainties related to the electron beam distribution. Experimentally, one derives the mode waist and position from the radii of curvatures (ROC) of the cavity mirrors. Repeated measurements set this uncertainty at ±5 cm. In turn, this creates a 20% uncertainty in the value of the Rayleigh range, but a relatively small (±5 cm) change in the waist position. There are also uncertainties associated with the electron beam parameters, especially those associated with the longitudinal distribution. Simulations indicate that the predicted gain is very sensitive to uncertainties of this magnitude. For example, a 20% uncertainty in the Rayleigh range and a ±5 cm uncertainty in the optical waist position can lead to a variation in the predicted gain of between 71% - 96%. As a consequence, the simulation is in substantial agreement with the experiment. Given the agreement between the simulation and experiment, we then undertook to investigate the variation in performance versus the Rayleigh range and the location of the optical waist. We found that the small signal gain would be substantially larger for much smaller Rayleigh ranges and for an optical waist located upstream from the wiggler center.

Future work will involve the inclusion of higher order mirror perturbations mentioned earlier, as well as validation of the harmonic generation predictions of MEDUSA.

REFERENCES

[1] G. Neil *et al*., Nucl. Instrum. Meth. A557 (2006) 9.

[2] H.P. Freund, S.G. Biedron, and S.V. Milton, IEEE J. Quantum Electron. 36 (2000) 275.

[3] H.P. Freund, Phys. Rev. ST-AB 8 (2005) 110701.

[4] S.V. Benson *et al*., Nucl. Instrum. Meth. A407 (1998) 401.

[5] P.A. Sprangle, A. Ting, and C.M. Tang, Phys. Rev. A 36 (1987) 2773.

[6] D.W. Small, R.K. Wong, W.B. Colson, and R.L. Armistead, Nucl. Instrum. Meth. A393, 262 (1997).

GENERATION AND CHARACTERIZATION OF THE MICROBUNCHED BEAMS IN THE RANGE FROM 0.3 TO 500 FEMTOSECONDS

V. E. Yakimenko, M. Babzien, K. P. Kusche, Brookhaven National Lab., Upton, NY 11973, U.S.A,
X. Ding, University of Southern California, CA 90089, U.S.A,
E. Kallos, P. Muggli UCLA, Los Angeles, CA 90095, U.S.A,
W. D. Kimura, STI Optronics, Inc., Bellevue, WA 98004, U.S.A,
F. Zhou, Stanford Linear Accelerator Center, Stanford, CA 94025, U.S.A.

Abstract

The recent results include formation and measurement of the micro bunch structures of the different time scales. Double beam structure produced and characterized at 100 fs – 0.5 ps range using beam splitting during compression in the magnetic chicane – "dog leg" arrangement. Arbitrary number of 10-50 femtoseconds micro bunches are sliced out of 5 ps long beam using wire mesh. CSR interferometer is used for detailed characterization of the beams in the two techniques above. 0.3 fs bunches are produced by IFEL and characterized by spectral measurements of the multiple harmonics. Presentation covers experimental results at Brookhaven Accelerator Test Facility.

INTRODUCTION

Three distinct experimental methods are discussed in this paper in the following 3 chapters. The first one discusses measurements of micro bunched beams generated with CO2 laser in the IFEL wiggler. Comparison of the coherent transition radiation CTR power in multiple harmonic leads to much more precise information about micro bunch length. The second part of the paper discuses generation of micro bunched beams that are not seeded with laser. Wire mesh targets were shaping the beam in the dispersive region and converting correlation between energy and time into current time modulation. Tunable spacing is the result of this technique. We used an interferometer to characterize these beams. The last chapter of this paper discusses controllable beam break up into two beam structure. The two beam formation happens during its compression in the magnetic chicane – dog-leg combination. Effects of the space charge and CTR are very important and stabilize the process contrarily to initial expectations. We used interferometer and plasma wakefield capillary to characterize two 100 fs bunches formed in this process.

CHARACTERIZATION OF SUBMICRON MICROBUNCHES PRODUCED BY IFEL WITH CTR IN MULTIPLE HARMONICS

We collect the coherent transition radiation (CTR) emitted when the microbunches traverse two 1μm thin titanium metal foils in order to diagnose the quality of the microbunching of the IFEL modulated electron beam. CTR is emitted because the electric fields of the electrons in the beam displace violently the free electrons in the metal surfaces, which in turn radiate due to the acceleration they suffer.

The first metal foil is placed perpendicularly to the beam direction of propagation and serves the purpose of blocking the CO2 radiation previously used at the IFEL interaction that could interfere with the CTR signal. The second foil is placed at 45° with respect to the direction of propagation and emits radiation out of the beamline. The sum of the radiation emitted from both foils is collected.

The spectrum of the CTR radiation contains information about the geometry of the electron beam. The on axis spectrum is proportional to the amplitude squared of the Fourier transform of the beam and shown on figure 1.

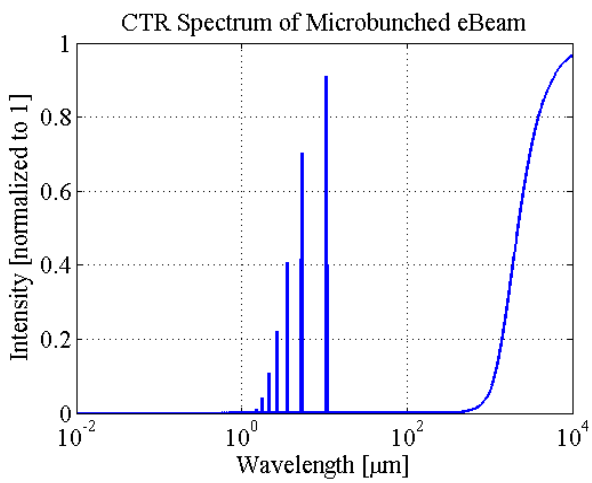

Figure 1. The spectrum of the CTR emitted when the microbunched electron beam passes through a metal foil.

The geometry of the electron beam is uniquely mapped into its CTR spectrum. The low frequency (long wavelength) radiation on the right corresponds to the envelope of the beam. In other wavelengths the radiation in general adds out of phase except at the harmonics of the separation wavelength λ_0=10.6μm between the microbunches.

Finally and most importantly, the amplitudes of these harmonics are modulated by the Fourier transform of each microbunch. The existence of radiation at each harmonic is a strong indication for the periodicity of the microbunch train. Also, the energy radiated at each harmonic depends

on the shape of each microbunch, hence it provides a direct way of estimating its width, which is assumed to be Gaussian in this case.

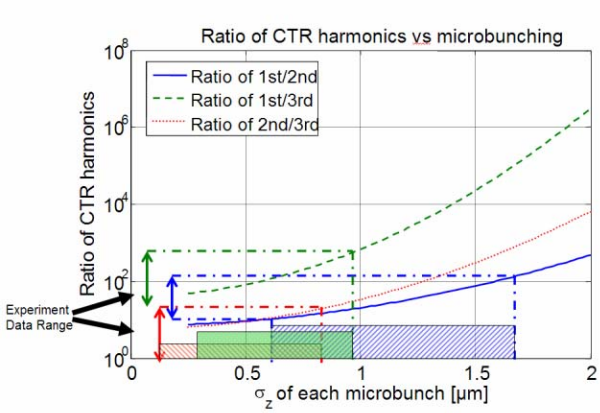

Figure 2. The ratios of the energies radiated at each of the harmonics as a function of microbunch width. The 3 data sets agree at the region around σ_z=0.7μm .

In order to collect the CTR, a cold detector sensitive between 3μm-20μm wavelengths is used. Furthermore, narrow Gaussian bandpass filters with roughly 5% FWHM transmission bandwidth were used to isolate the radiation of the first, second and third harmonic, in successive measurements. After recording about 100 events at a roughly constant IFEL laser pulse energy (within a factor of 2) at all three harmonics, we calculated the three possible ratios of the harmonics signals. The data range for each ratio is shown on the vertical axis on figure 2.

Using prediction for small angles and after accounting for the response of the detector and the filters calibrated with the black body source, we calculated the expected theoretical ratio between the energy radiated under each of the harmonics as a function of the microbunches' widths. These three predicted ratios also are plotted in figure 2. It shows that the measured rations indicate a width of σ_z=0.7μm for each microbunch. Although the microbunch width was inferred using CTR [1] and staged laser accelerator [2] before, this is its first direct measurement that also utilizes information from different harmonics.

In order to confirm the 10.6μm separation between the microbunches the IFEL laser was tuned at 10.2μm, while still using the same narrow 10.6μm filter to detect the CTR. In that case the signal recorded was at least 100 times less than when the IFEL was driven at 10.6μm and very close to the noise level of the detector, thus confirming the periodicity of the bunching at the laser's wavelength only.

TUNABLE MICROBUNCH TRAIN

The microbunched beam described above offers stable, well defined by spacing the laser. It is a disadvantage if the laser in not easily available in the range that is needed. We attempted to use a periodic wire mask installed at the dispersive region of the beam transport to generate microbunches with the spacing that is determined by the target period. The idea is very simple: a beam is chirped in the linac and therefore energy-time correlation is introduced. The target is installed in the location where dispersion is large while betatron size in the plane of the dispersion is smaller then target period. This effectively creates time-current modulation. We use 125-500μm diameter wire to make targets. Low emittance 50 MeV beam is effectively scattered by this wire. The photograph of the taget is shown on figure 3.

Figure 3. Photograph of the wire target for adjustable microbunch beam generation.

One can clearly see modulation in of current vs energy on the electron beam energy spectrometer. It is even possible to see unintentional defect of the target "double wire" approximately in the middle of the beam.

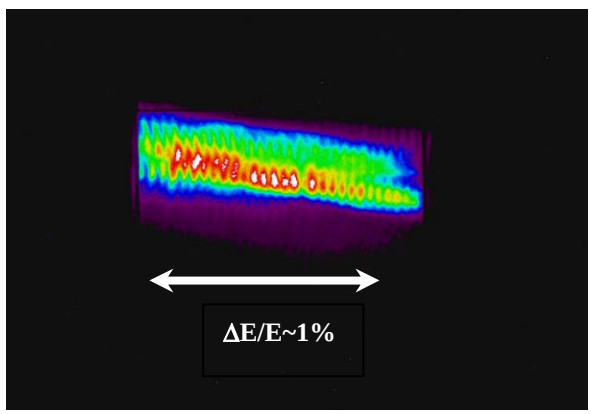

Figure 4. Image from the beam energy spectrometer. It shows 15 microbunches stretched over ~1% energy chirp induced on the beam.

The translation of the microbunch spacing from target period naturally depends on the chirp and dispersion value at the target location. We operated with a set of parameters where it is adjustable 10: target with 250 μm period will generate microbunches spaced by 25 μm. We use a pair of installed before target sextupole magnets to linearize or chirp the spacing between micro bunches. High energy slit opening that controls energy spread envelope of the beam can be used to select arbitrary number of microbunches. The demagnification can be

adjusted by change of dispersion, beam chirp or target rotation.

CTR interferometer [4] was used to measure modulation in time. Our attempt to measure individual microbunches with the period of ~25-30 μm did not produce the expected result due to cutoff of the window transmission around 30 μm. The signal strength on the detector increased considerably for the modulated beam. The interference showed expected envelope of the beam Interference curve was triangular that translates to the "square' beam envelope. (Tails of the beam were cat by high energy slip.)

We detected individual bunches with correct periodicity after switching to the 1mm target and retuning transport line for 1:5 demagnification. Interferogram is shown on figure 5.

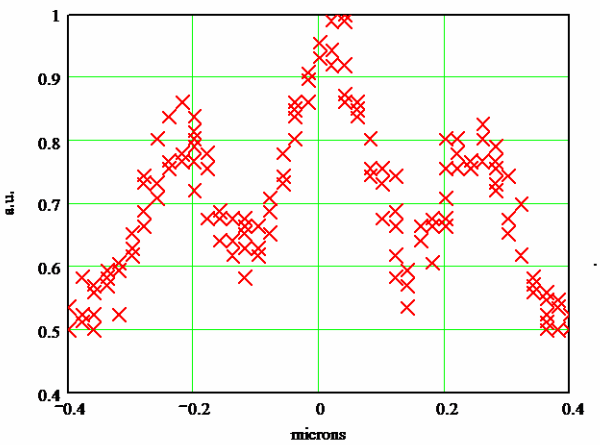

Figure 5. Interferogram of the microbunched beam generated with the periodic wire target.

SUBPICOSECOND DOUBLE ELECTRON BUNCH GENERATION

As part of these efforts towards improving beam for various experiments related to advanced accelerator research, a chicane, designed and built by UCLA [1], was installed on the linac downstream of the RF accelerating structures. The chicane was designed to provide approximately 30 times compression of the incoming electron bunch. Figure 6 is a diagram of the chicane.

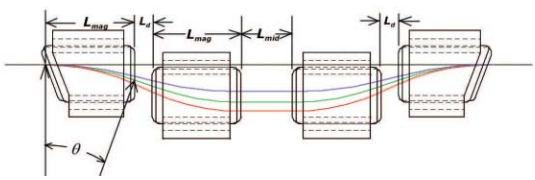

Figure 6. Diagram of ATF chicane.

It was discovered that when compressing the electron bunch from the linac that the beam breaks up into two distinct bunches with subpicosecond compressed bunch lengths. It does this in a consistent and reliable manner. Unlike most of other facilities that are utilizing a chicane for pulse compression, the ATF does not have a subsequent RF acceleration section downstream of the chicane, which can be used to compensate for residual energy chirp on the electron beam (e-beam) exiting the chicane. Not being able to use a downstream acceleration section was one reason the double-bunch formation process was possible.

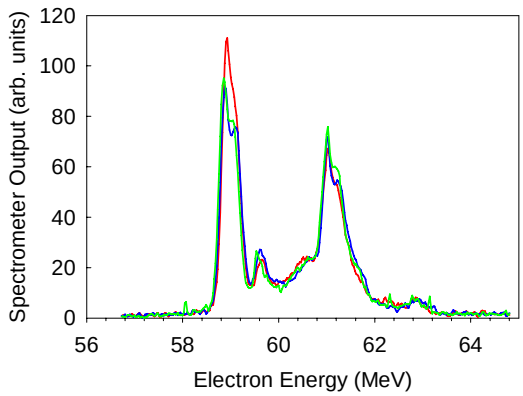

Figure 7. Energy spectrums of double-bunch e-beam. Three spectrums taken many minutes apart demonstrating stability of the double-bunch formation process

Figure 7 shows energy spectrums of the double-bunch beam. It shows two bunches separated in energy by 1.8 MeV. It is an overlay of three shots taken many minutes apart. The good reproducibility of the spectrums indicates the energy distribution and positions are very stable.

A coherent transition radiation (CTR) interferometer was used to characterize the compressed e-beam. The CTR emission is in the THz range. An autocorrelation of the CTR signal is obtained by scanning the translation mirror shown in Figure 8

Analysis of this autocorrelation signal yields information about the e-beam bunch characteristics [4].

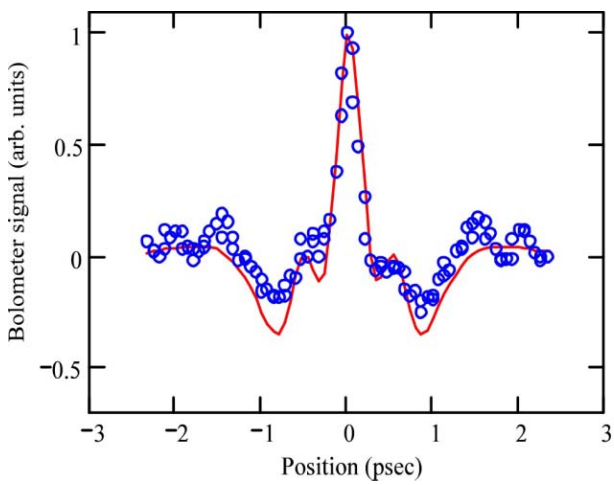

Figure 8: Example of raw data from CTR interferometer (circles) and the curve fits to the data (solid line) calculated from the autocorrelation integral [2]. "Bumps" around +- 0.5 ps indicate double bunch spacing.

For a single bunch, the curve fit of the autocorrelation integral with the data requires selecting values for the bunch length and the cut-off frequency of the detection

system, where we have assumed a Gaussian bunch shape. In particular, the width of the central peak of the autocorrelation signal is primarily affected by the bunch length. The shape of the curve on either side of the peak is mostly affected by the cut-off frequency.

For a double e-beam bunch, there are five free parameters in the autocorrelation integral. We were able to characterize each bunch individually using CTR and beam charge monitor. Single bunch data was obtained by using the high-energy slit located downstream of the chicane to block one of the bunches (either the low-E or high-E bunch). Individual bunch data for each bunch of the double bunches permits reducing the number of free parameters to one, i.e., the time delay between the two bunches. For the example shown in Figure 8, the single-bunch CTR data indicates the lengths of the two bunches is 144 and 90 fs, the cut-off frequency is 1.7 THz, and the second bunch has 60% of the charge in the first bunch. Hence, for the curve fit shown in Figure 8, we find the time delay between the bunches is 500 fs.

Results of simulations with Elegant [5] confirmed our hypothesis that double beam structure is cased by the combination of nonlinear energy chirp and different sign of compression in the chicane and dog leg. Self induced beam wakes narrowed energy spread in the beam and let to complete separation.

ACKNOWLEDGMENTS

The authors wish to thank Samer Banna and ATF staff for contributions to the experiments. This work was supported by the U.S. Department of Energy, Grant Nos. DE-FG02-04ER41294, DE-AC02-98CH10886, DE-FG03-92ER40695, and DE-FG02-92ER40745

REFERENCES

[1] Liu, Y. et al., Phys. Rev. Lett. 80, 4418–4421 (1998).
[2] Kimura, W. D., et al., Phys. Rev. Lett. 92, 054801 (2004).
[3] R. B. Agustsson, UCLA, M.S. thesis, 2004.
[4] A. Murokh, et al., Nucl. Inst. Meth. Phys. Res., A 410, 452 (1998).
[5] M. Borland, “User’s Manual for elegant,” available on-line at http://www.aps.anl.gov/asd/oag/manuals/elegantver14.1/elegant.html.

DESIGN OF A LONG WAVELENGTH FEL FOR EXPERIMENTS UNDER HIGH MAGNETIC FIELDS

Wim J. van der Zande#, Th. Rasing, J.C. Maan, A.P.M. Kentgens and F.J.M. Harren,
Institute for Molecules and Materials, Radboud University Nijmegen, PO Box 9010, 6500 GL Nijmegen, The Netherlands.

Abstract

At the University of Nijmegen, a novel collaboration has been established that combines a number of spectroscopic laboratories. These laboratories form a centre for advanced spectroscopy and constitute the spectroscopic department of the (Research) Institute for Molecules and Materials combining physical and chemical techniques. As part of the spectroscopic centre, a long-wavelength far-infrared free electron laser (FIR-FEL) operating between 100 μm/3 THz and 1.5 mm/200 GHz will be designed and constucted in the coming years. The FIR-light should facilitate new experiments in the existing high field magnet laboratory (HFML), a large European Rereach Infrastructure and in the NMR pavillion equipped with NMR instrumentation operating up to 800 MHz, especially for dynamic nuclear polarization technology.

THE NIJMEGEN CENTRE FOR ADVANCED SPECTROSCOPY

The Insitute of Molecules and Materials at the University of Nijmegen houses a number of spectroscopic laboratories. These laboratories combine laser spectroscopy in the European Trace Gas Facility [1], scanning probe technology, employing various forms of scanning tunneling and atomic force microscopic techniques [2], nucelar magnetic resonance (NMR) laboratory [3] and the high field magnet laboratory (HFML) [4]. Existing collaborations between the various laboratories have resulted in experimetns ranging from a 1.277 GHz NMR spectrometer built in a 30 Tesla Bittter magnet to NMR on a chip employing force microscopy to detect the radiofrequency absorption, and experiments exploiting diamagnetism to neutralize gravity in near-zero-gravity experiments inside strong magnetic fields.

In respons to a call from the Netherlands Government named the National Programme for Investments in Large Scale Facilities [5], we have proposed to strengthen existing facilities and to develop two novel instuments, a 45 Tesla Hybrid magnet and a Free Electron Laser operating in the far infrared (FIR).

The frequency window between the microwave region on the low photon-energy side and the infrared radiation on the high photon-energy side is called Far Infrared or THz regime. This energy regime knows many applications and radiation sources with different characteristics are rapidly developed. We believe that at present the most powerful and versatile THz radiation source is a free electron laser. We have proposed the construction of a THz-FEL optimized for the demands of advanced material research in combination with high magnetic fields and for advanced studies of molecular and macromolecular systems. The design aims at generating light between 100 μm and 1.5 mm with a spectral bandwidth of $\Delta\lambda/\lambda<510^{-5}$ while maintaining intensities of the order of 100 Watt during pulses of minimum duration 10 μs and maintaining the possibility of pump-probe experiments at a 10 to 30 picoseconds time resolution. The science driver that resulted in the success of our proposal has been the ambition to bring material research a significant step forward by performing saturation experiments and pulse-echo experiments in magnetic fields above 30 Tesla. In these fields, the relatively high-energy excitations reduce the interference of thermal effects while studying material properties. The total proposal encompassing a 40-45 Tesla hybrid magnet, the FEL and received about 26 M€ (excluding building costs, including some exploitation funds). As the FEL will be a part of an operational large scale facility, and as experience in free electron lasers is still small in Nijmegen, some design specifications will be made conservatively.

SCIENCE DRIVERS AND EXPERIMENTAL LIMITATIONS.

The science call carried the intention to fortify in the Netherlands the number of large scale facilities. It was realized that the Netherlands could not play a sufficiently large role as host country for important international facilities and international researchers. In many other countries the relative number of facilities was found to be significantly larger. In our proposal, we express the ambition that the University of Nijmegen may host many scientific guests using scanning probe techniques, the laser laboratory, and the high field magnets (using the THz radiation source), NMR or the FEL in its own right as versatile spectroscopic light source. The specifications defined above have been formed in collaboration with the FOM Institute Rijnhuizen, which hosts FELIX (free electron laser for infrared experiments). The FELIX staff will not only provide a lot of experience and advice but also forms an example for the management of a highly successful FEL facility. The spectral range chosen for the proposed FIR-FEL complements that of FELIX

#w.vanderzande@science.ru.nl

purposefully to optimize the collaboration between the two facilities.

An ideal laser source is easily tuneable in the THz regime, has a flexible pulse structure allowing pump-probe experiments, as well as bandwidth limited in the case of long macro-pulses, and is (quasi-) continuous with an average power of about 1 kWatt. Although the physics does not pose fundamental restrictions, the relative inefficiency of the FEL principle, without energy recovery, and more importantly, technological limitations in the creation of high intensity, relativistic electron beams requires choices optimizing specific aspects.

.

Science Drivers

In the following three of the science drivers are identified. An important group of experiments study the spectroscopy and dynamics in solid state materials by observing pulse-echo's following electron spin excitations or cyclotron resonances in magnetic fields. Depending on the effective mass of the electron, FIR-radiation near 1 THz is required in a magnetic field around 35 T. Saturation of these transitions in the form of excitation by a $\pi/2$ pulse within about 100 ns requires powers of about 100 Watt with a bandwidth of $\Delta\lambda/\lambda \approx 2\ 10^{-5}$. Pulse-echo experiments further require the possibility to shape pulses and delay pulses. Atypical experiment requires three of even more of these pulses within a few μs separated at arbitrary time delays ranging from tens of nanoseconds to one microsecond. Hence, we require laser pulses with about 10 μs duration that can be transformed by fast mirrors into the requested pulse train.

A second group of experiments is the use of FIR radiation to saturate electron spin transitions within an NMR instrument. By exploiting the coupling between the electron spin with nearby nuclear spin, the saturation of the electron spin population may be transferred to the nuclear spin. This process is called dynamic nuclear polarization (DNP). Although in principle DNP can enhance the sensitivity of NMR by a factor of more than 10^4, technological and system specific hurdles are enormous for a realization with a wide scope of applications. For DNP, the need for a high absolute duty cycle for FIR radiation may establish the largest obstacle for FEL technology to be optimally applicable.

In the first two examples, large magnetic fields play an important role. A third science driver makes optimal use of the flexibility to change the wavelength of a FEL continuously. A research program is anticipated on molecular spectroscopy of bio-organic molecules, biomemetics (analogues of bio molecules), and smart organic molecules often inspired on biological systems. Characterization of the THz response may not only provide spectroscopic information on the structure of these molecules but also on slow intra- and intermolecular motions related to their functionality.

Technological Choices.

The anticipated design for the FIR-FEL is based on experiments performed with the FELIX instrument in The Netherlands. FELIX is a short-pulse Free-Electron Laser operating in the IR from 5 to 250 μm. The spectral width of the output ranges from 0.5 to 7% depending on the frequency. The overall duty cycle is small with a repetition rate up to 10 macro-pulses per second of a maximum duration of 10 μs each. Each individual macro-pulse consists of up to a few thousand micro-pulses each consisting of tens of optical cycles, implying duration of a few picoseconds for each micro-pulse.

In terms of the macro-pulse structure, the duty cycle of FELIX is about $5\ 10^{-5}$ with an average output power of about 1 Watt, implying an average power of 20 kWatt during the macro-pulse. The maximum power in the picoseconds micro-pulses is another three orders higher. From here, we will describe the design for the Nijmegen FIR-FEL. The pulse structure will be similar to the one of FELIX and has the form of a low repetition rate 10 – 15 μs macro pulse structure. The macro pulse will consist of micro pulses with a fixed repetition rate in the range from 1 to 3 GHz. The special property that we aim for is that *all micropulses have a very well defined phase relation.* It is of interest to note that a narrow bandwidth using this mechanism has been one of the original design ambitions of FELIX. Oepts and Colson [6] presented the initial ideas of phase locking otherwise independent micropulses. Also Madey and coworkers started around this time [7,8]. Initial measurements at FELIX were performed by Bakker, Oepts van der Meer and co-workers [9,10], followed by Weits, Oepts and coworkers [11,12]. This research resulted in an experimental scheme to create a pulse train of phase locked light pulses. These authors observed significant phase stability between the micropulses and drew favourable conclusions regarding the bandwidth that may be achieved using external filtering using interferometers.

It is required to have a large number of optical pulses circulating simultaneously in the normally very large FEL cavity (more than 40 pulses in a cavity with an effective length of about 10 meter). As the optical pulses are generated from electron pulses moving at nearly the speed of light, an extra (optical) system has to couple the optical phases in this train of light pulses. An interferometer inside the cavity ensures that photons from a single electron bunch will affect the coherence of the light generated from many electron bunches injected later. The resulting pulse train of coherent and phase coupled micropulses constitutes a frequency comb with narrow FIR lines spaced with the repetition rate of the electron pulses (by the 1 to 3 GHz rf frequency) . These narrow lines have a width that is determined by the quality of the interferometer and by the magnitude of the interpulse phase-coherence. Each line in the frequency comb further consists of one or more longitudinal modes of the large FEL laser cavity, separated by 0.001 cm^{-1} for a 10 m

cavity. To achieve really a single longitudinal frequency output, filtering of one interferometer mode outside of the laser cavity is required. This filtering reduces the average power of the macro pulse by factor of at least 50 depending on the quality of the filtering process.

At FELIX experiments have been performed at a fixed wavelength near λ=69 μm, achieving a spectral resolution of $2\ 10^{-5}$ using a Fox-Smith type interferometer. Other groups have simulated and employed Michelson type interferometers in the FEL cavity for the same purpose. [9,10] The above specifications have resulted in the expectation that a dedicated design for a FIR-FEL could provide near single mode lasing at the average power of 100 Watt during a macro pulse even when starting with a short pulse FEL instrument. It is realized that it will require a careful design to establish continuous tuning in such a FEL as the timing structure of the RF electron accelerator system and the RF frequency generates strongly preferred absolute frequencies.

DISCUSSION

Many of the specifications related to the science drivers discussed above suggest designing a quasi CW-FEL such as the high quality UCSB FIR FEL operating at the University of Santa Barbara. This long-wavelength output of the FIR-FEL in Santa Barbara combines many of the characteristics required for the experiments planned at high magnetic fields. In fact, the power output of a CW–FEL can be of the order of 1 – 6 kWatt during the macro pulse clearly exceeding the expectations of a pulsed frequency comb FIR FEL as suggested above. The ambition of the Israeli FEL project to improve on the UCSB FEL design such that an *average* power of kWatt may become feasible implying a near CW operation with very high duty cycle while maintaining a large wavelength range seems to bring very difficult experiments such as DNP in NMR experiments more feasible.

At this moment, the extra possibilities to use a pulsed FEL for strongly non-linear experiments employing the very high micro pulse peak powers and to use the FEL for time resolved experiments with 10- 30 picoseconds time-resolution has resulted in the decision to study the possibilities of a pulsed frequency comb type FIR-FEL. The planning of the project involves in the upcoming 18 months design studies and detailed planning of the construction phase of the FEL. Lasing and the opening of a user facility along the lines of the present very successful FELIX facility are foreseen in about five and a half years from now.

ACKNOWLEDGMENTS.

WJvdZ wants to express his gratitude to Dick Oepts, Lex van der Meer and the rest of the staff at the FOM Institute for Plasma physics for the many discussions and support while preparing the proposal and in preparing the design phase of the proposed FEL.

REFERENCES

[1] http://www.ru.nl/tracegasfacility/
[2] http://www.ru.nl/nanolab/
[3] http://www.ru.nl/physchem/solid_state_nmr/
[4] http://www.hfml.kun.nl/
[5] //nwo.nl/nwohome.nsf/pages/NWOP_6GFARR_Eng
[6] D. Oepts and W.B. Colson, IEEE J. of Quantum Electron., 26 (1990) 723
[7] E.B. Szarmes, E.D. Madden, and J.M. Madey, J. Opt Soc. Am. B, 13 (1996) 452
[8] E.B. Szarmes and J.M. Madey, IEEE J. of Quantum Electron., 29 (1993) 452
[9] D. Oepts, A.F.G. van der Meer, R.J.Bakker, and P.W. Amersfoort, Phys. Rev. Letters, 70 (1993) 3255
[10] D. Oepts, R.J.Bakker, D.A. Jaroszynski, A.F.G. van der Meer, and P.W. Amersfoort, Nucl. Instr. And Meth., A331 (1993) 42
[11] H.H. Weits, A.F.G. van der Meer, D. Oepts, and Meisong Ding, Nucl. Instr. And Meth., A393 (1997) 61
[12] H.H. Weits, Thesis, Technical University Eindhoven, 1998

THE ROSSENDORF IR-FEL ELBE

P. Michel, H. Buettig, F. Gabriel, M. Helm, U. Lehnert, Ch. Schneider, R. Schurig, W. Seidel, D. Stehr, J. Teichert, S. Winnerl, R. Wuensch
Forschungszentrum Rossendorf, Germany.

Abstract

The radiation source ELBE is the central research facility in the Forschungszentrum Rossendorf. The machine is based on a 40 MeV superconducting RF Linac which can be operated up to 1 mA in cw mode. After commissioning the Bremsstrahlung and the X-ray facilities in 2002 and 2003, respectively, and the first lasing of the mid-IR FEL (3-22 µm) in 2004 about 7000 hours user beamtime have been provided. At present a second FEL for long IR waves (20-150 µm) using a partial waveguide is under commissioning. First lasing was demonstrated on August 21-st, 2006. Besides in-house users particularly the IR beam is available to external users in the FELBE (FEL@ELBE) program which is a part of the EU funded integrated activity on synchrotron and free electron laser science. In this contribution the fundamental features of the ELBE IR FEL's and the operational experiences which were collected during two years of FEL user operation are described. Future projects like the combination of the new High Magnetic Field lab with the ELBE-IR beams will open up unique experimental possibilities.

INTRODUCTION

In the Forschungszentrum Rossendorf in Dresden, Germany, the superconducting electron accelerator ELBE (Electron Linac with high Brilliance and low Emittance) has come into user operation in 2002. ELBE accelerates electrons to energies up to 40 MeV with an average beam current of 1 mA in quasi continuous wave (cw) mode. The electron linac [1] serves as a driver to generate several kinds of secondary radiation and particle beams, which are FEL-Infrared Radiation for a very large field of applications reaching from semiconductor physics to biology, MeV Bremsstrahlung for nuclear (astro) physics, monochromatic hard-X-ray channelling radiation for radiobiological experiments, and in near future also neutrons and positrons for studies in nuclear reactor science and materials research. The kind and characteristics of the produced secondary beams at ELBE are in accordance with the scientific profile and the experimental requirements of the Forschungszentrum Rossendorf. For a layout of the ELBE building see Fig. 1.

ELECTRON LINAC

A driver for these different kinds of secondary radiation must be characterized by a high average beam current and a small transverse and longitudinal emittance. For this reason only a superconducting high frequency accelerator was taken into consideration. Low energy electron bunches are produced in a grid-pulsed thermionic gun operating at 250 keV DC voltage. It delivers pulses with a bunch charge up to 77 pC at 13 MHz repetition rate and about 450 ps length. The transverse emittance in this case is about 10 mm mrad caused by the electric-field deformation close to the grid [2]. To generate beams with smaller emittance values the grid can be pulsed with 260 MHz at drastically reduced bunch charge. In combination with phase space cutting using apertures, emittance values below 2 mm mrad can be achieved in this regime. For reduced average power, macro bunching is possible as well, yielding 100 µs or longer macro pulses at a < 25 Hz repetition rate. Pulse compression down to 10 ps which is necessary for injection into the 1.3 GHz RF accelerator is done by a two-stage RF bunch compressor operating at 260 MHz and 1.3 GHz, respectively.

The two main accelerator stages are based on two 9-cell RF cavities which were developed for the TESLA project at DESY [3] and are kept at 2 K using superfluid helium delivered by a commercial helium liquefier (Linde). The cavities are individually driven by 10 kW CPI klystron amplifiers. The RF couplers consist of a double-window arrangement and a door-knob shaped adapter for RF transmission from rectangular waveguides to co-axial cavity coupler antenna. The vacuum windows are rectangular plastic windows at room-temperature level and circular ceramic windows cooled by liquid nitrogen. The maximum acceleration field gradients of the cavities exceed 10 MV/m. In practice only 9-9.5 MV/m are accomplished limited by cavity heat loading and field emission. Taking into account that the total acceleration energy is reduced by nearly two MeV due to the capture of low-beta electrons in the first accelerator stage, the maximum total energy is about 36 MeV in practice. To achieve higher acceleration field the RF can be pulsed up to a duty cycle of 1:2. Maximum energy of about 50 MeV can be obtained at a duty cycle of 1:10. A magnetic bunch compressor with adjustable R_{56} < 500 mm is located between the acceleration modules and serves, together with the RF phase of the accelerator cavities, to modify the longitudinal phase space configuration. The electron beam parameters at ELBE will be considerably improved by replacing the thermionic DC gun by a superconducting RF photo gun [4] which is planned for 2007.

FREE ELECTRON LASERS

To cover the required wavelength range two FELs are required. The calculated ranges for both FELs are shown

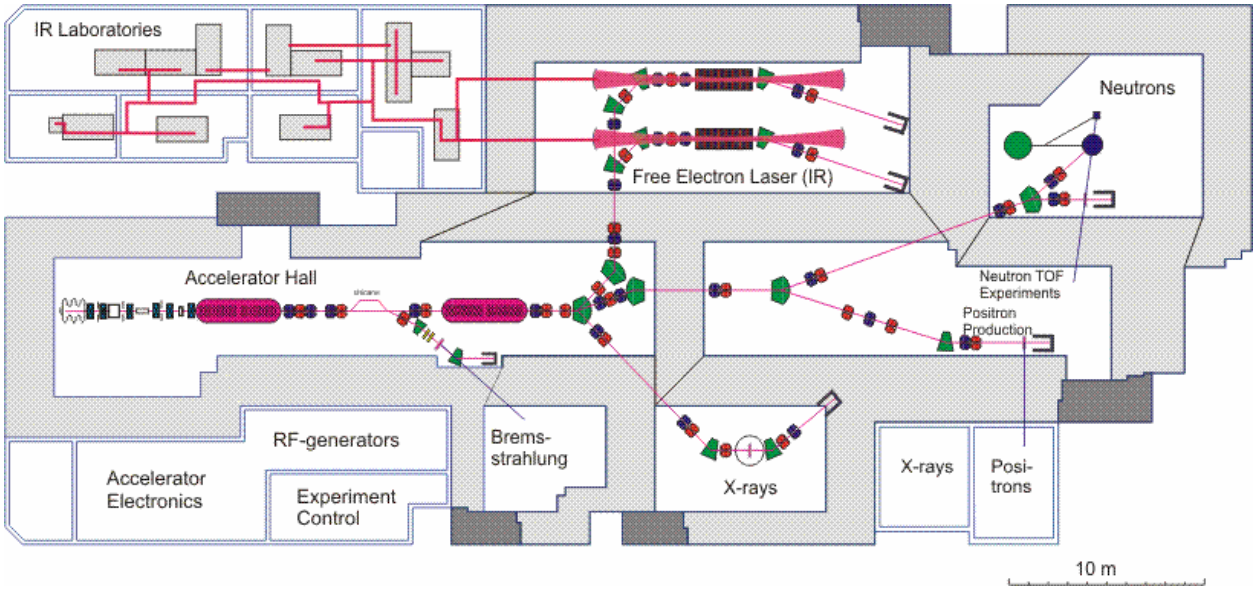

Figure 1: Layout of the Radiation Source ELBE

in Fig. 2. The U27 FEL consists of two 34-pole sections with individually adjustable gaps. The undulator period is 27.3 mm and the magnet material is NdFeB (hybrid type). The distance between the two sections is adjustable for phase matching. The gaps can be varied independently from 13.8 mm to 21 mm corresponding to K_{rms}= 0.7 to 0.3. To optimize the extraction ratio over the whole wavelength range mirrors with different outcoupling hole sizes (1.5, 2, 3, and 4 mm in diameter) are used. The mirrors are made of gold coated copper.

The U100 FEL for the far infrared range is based on a SmCo hybrid undulator which consists of 38 magnet periods each 100 mm long. The K_{rms} can be adjusted from

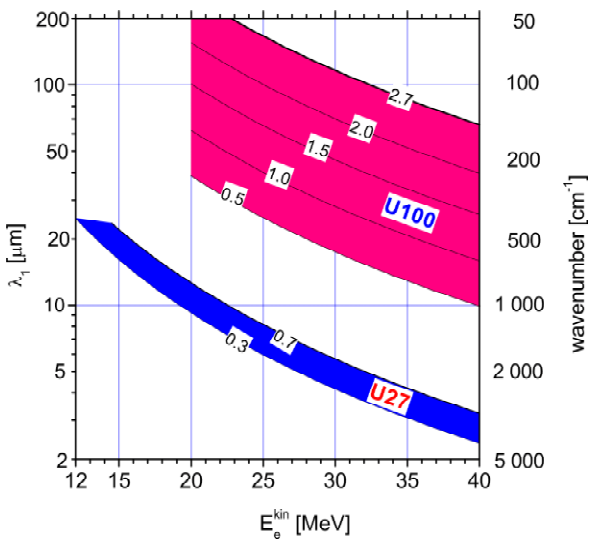

Fig.2: Wavelength ranges of the U27 and the U100 FELs at ELBE as a function of the electron kinetic energy calculated for the indicated values of the undulator parameter K_{rms}.

0.3 to 2.7 which corresponds to gaps of 85 to 24 mm. It is also equipped with interchangeable outcoupling mirrors (hole diameter 2, 4.5 and 7 mm). To obtain high enough magnetic fields in the undulator the gap and consequently the optical mode has to be sufficiently small. To fulfill this requirement the U100 FEL is equipped with a partial parallel-plate waveguide 10 mm wide. The horizontal size is wide enough to allow free propagation. The waveguide spans from the undulator entrance to the downstream mirror. In the remaining part of the optical cavity the optical mode propagates freely. Mirrors are toroidal on the free propagation side (6.33 m and 3.61 m curvature) and cylindrical (6.33 m curvature) on the waveguide side. They are also made of copper with gold coating.

OPTICAL USER LABS

Experiments are performed in the IR user labs, that are shown in the upper left corner of the sketch of Fig. 1. A lot of ancillary equipment is provided, most importantly a number of table-top optical sources like femtosecond Ti:sapphire lasers and a ps Nd:YAG laser which can be synchronized with the FEL to better than a picosecond. The labs are specially equipped for imaging of thin films on surfaces by polarization-modulation IR reflection-absorption spectroscopy and time resolved femtosecond (pump-probe) experiments. Scattering scanning-near-field optical microscopy (SNOM) has been performed as well, There is one user lab with permission for handling of radioactive substances which allows IR spectroscopy on radioactive samples.

The IR beams coming from U27 or U100 both enter a common beam path at the diagnostic station shown in Fig. 3. Most of its components are designed for remotely controlled operation. A scraper mirror is used to outcouple a certain fraction of the main beam for

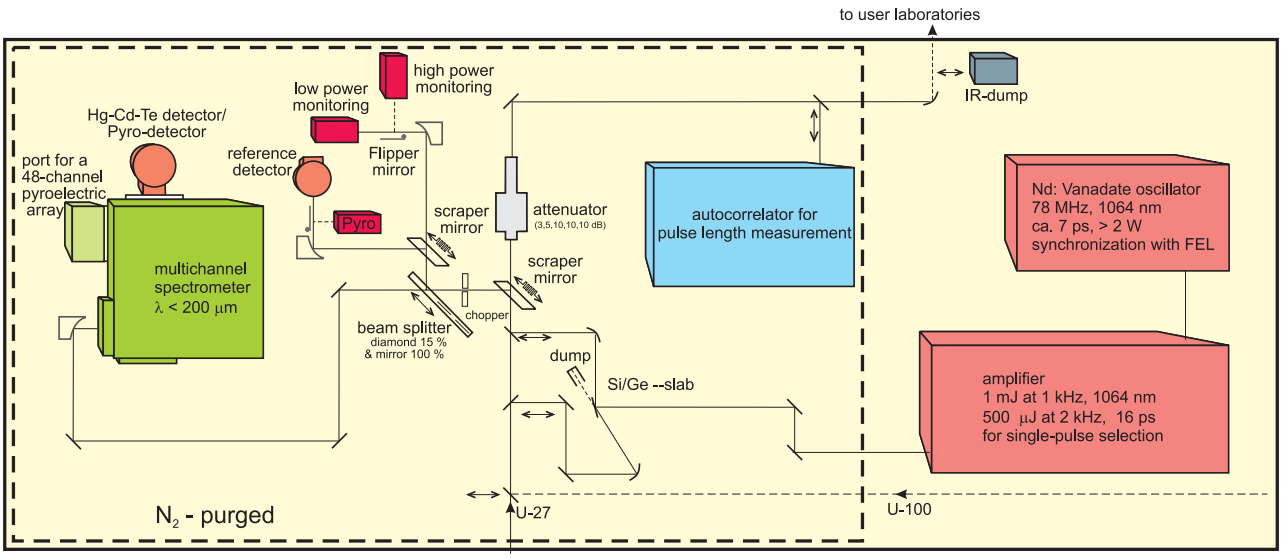

Fig 3. Layout of the diagnostic station for the IR beam.

diagnostic purposes. It can be directed either to an MCT detector which is used to monitor the start up of the laser and its temporal structure and which also acts as a reference detector for experiments or to one out of two power meters. Several MCT detectors are available with preamplifier bandwidth ranging up to 20 MHz enabling us to detect individual micro pulses. For very long wavelengths or measurements with extremely high sensitivity a Ge-Ga detector can be set up. Via a beam splitter part of the diagnostic beam can be sent through a wide-range spectrometer. To cope with CW operation of the FEL a chopper is included in the diagnostic beam path which is synchronized to the macro pulse in pulsed-mode operation. The main beam path to the user laboratories first contains a remotely controlled attenuator. A non-collinear background-free autocorrelator can be used to characterize the optical pulse duration. For experiments requiring lower repetition rates than the 13 MHz round-trip time of the optical resonators a semiconductor plasma switch driven by a Nd:YAG laser amplifier at 1 kHz rate can be used as pulse picker. The optical beamline to the user laboratories is designed for less that 15% transmission loss between 3 and 150 µm wavelength. The typical horizontal polarization is conserved but can be switched if necessary.

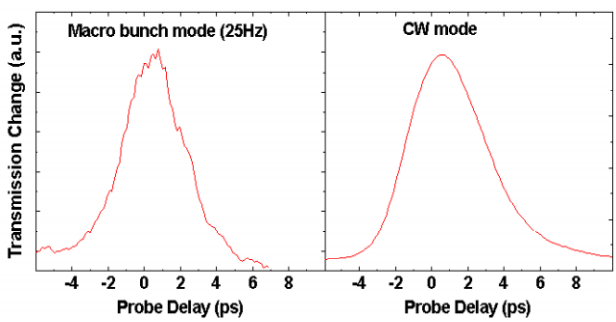

Fig 4. Transient transmission change measured with the pump-probe technique in accelerator macro pulsed mode (left) and in cw mode (right). Both pulses (15.8 µm) are generated by the FEL.

Proposals for FEL experiments are evaluated and selected in a peer-review system. Under the name FELBE the facility is a member of the EC funded “Integrating Activity on Synchrotron and Free Electron Laser Science (IA-SFS)” which comprises most synchrotron and FEL facilities in Europe and provides financial support to users from the EC and associated states. Up to now 12 experiments have been running at the ELBE FEL facility.

OPERATIONAL EXPERIENCES

First lasing of the U27 FEL was achieved in May 2004 [5]. Immediately after commissioning routine user operation was started. Up to now more than 1300 hours for user FEL experiments were delivered. The availability of the machine in 2006 has been higher than 90 %. The following parameters are achieved in practice: Laser radiation from 3.4 to 22 µm was generated. The outcoupled beam power depends strongly on the wavelength range. Low average power (<5 W) was observed in the ranges shorter than 5 and longer than 13 µm. In the range in between up to 25 W power could be extracted. In the region above 20 µm the outcoupled power is smaller than 1 W and finding stable conditions for lasing is difficult due to the high diffraction and aperture losses in the undulator vacuum chamber. The IR pulse duration can be varied by detuning the optical cavity. At 11 µm, which was an often required wavelength for user experiments, it could be adjusted from 0.9 to 3.4 ps. It could be shown by comparing autocorrelation traces with optical spectra that the pulses are bandwidth limited. By many of the FEL users high average power implying cw operation is required. Apart

from the higher measuring rate and the associated better signal to noise ratio a clearly higher stability of the laser at cw operation was observed. Reasons for this observation are the continuous loading of the superconducting RF cavities and the continuous laser operation. Fluctuations due to build up of the laser into saturation can be avoided. Fig. 3 demonstrates the improved quality of the experimental data in cw mode. It shows a typical time resolved transmission traces measured by the pump-probe-technique in macro pulse mode (left) and cw mode (right). The measurements were done in the framework of an experiment to study electron dynamics in superlattices [6].

OUTLOOK

First lasing of the U100 FEL was demonstrated on August, 21-st, a few days before the FEL2006 conference. Now the actually available wavelength range and the parameters of the IR beam have to be determined. Then the extended wavelength range will immediately be made available to the user experiments.

In the near future the beams of the two FELs will be delivered into the new High Magnetic Field Lab Dresden (HLD) [7] which was built recently in immediate vicinity to the ELBE building. The HLD will provide magnetic-field pulses in the 60-100 Tesla range with 1000-10 ms pulse duration, thus opening the way for many new spectroscopic investigations, in particular in solid state and semiconductor physics. For these investigations also time resolved experiments are envisaged. The challenge here is to obtain a complete time-delay scan during the time of one magnetic field pulse. Recently we have demonstrated the measurement of an FEL interferometric autocorrelation trace within 25 ms [8]. In general, no synchronization of the FEL with magnetic field pulses is needed, since the FEL runs continuously at 13 MHz in cw mode which means that about 10^5 FEL pulses overlap with one 10 ms-magnetic field pulse. This should provide excellent measurement conditions.

ACKNOWLEDGEMENT

The authors thank Todd Smith from HEPL Stanford University and A.F.G. van der Meer from FELIX Nieuwegein for her useful help and advice. Furthermore we thank the engineering stuff of the Forschungszentrum Rossendorf for the successful cooperation.

REFERENCES

[1] F.Gabriel et al., NIM B 161-163 (2000), 1143-1147.
[2] J. Teichert et al., Proceedings of the 6th International Computational Accelerator Physics Conference, Darmstadt, Germany, 2000.
[3] TESLA Test Facility Linac – Design Report (Ed. D.A. Edwards), DESY print TESLA 95-01.
[4] J.Teichert et al., Proceedings of the 2005 FEL Conference, p. 534-537, Stanford, USA.
[5] P.Michel et al., Proceedings of the 2004 FEL Conference, p. 8-18, Trieste, Italy.
[6] D. Stehr et al., Appl. Phys. Lett. **88** 151108 (2006)
[7] http://www.fz-rossendorf.de/HLD
[8] H. Schneider et al., Appl. Phys. Lett. **89** (2006), in print.

STATUS OF THE NOVOSIBIRSK HIGH POWER TERAHERTZ FEL*

N.A. Vinokurov#, N.G. Gavrilov B.A. Knyazev, E.I. Kolobanov, V.V. Kotenkov, V.V. Kubarev, G.N. Kulipanov, A.N. Matveenko, L.E. Medvedev, S.V. Miginsky, L.A. Mironenko, A.D. Oreshkov, V.K. Ovchar, V.M. Popik, T.V. Salikova, M.A. Scheglov, S.S. Serednyakov, O.A. Shevchenko, A.N. Skrinsky, V.G. Tcheskidov, Budker INP, Novosibirsk, Russia.

Abstract

The first stage of Novosibirsk high power free electron laser (FEL) was commissioned in 2003. It is based on the normal conducting CW energy recovery linac (ERL). Now the FEL provides electromagnetic radiation in the wavelength range 120 - 230 micron. The maximum average power is 400 W. The minimum measured linewidth is 0.3%, which is close to the Fourier-transform limit. Four user stations are in operation now. Manufacturing of the second stage of the FEL (based on the four-turn ERL) is in progress.

INTRODUCTION

A new source of terahertz radiation was commissioned recently in Novosibirsk. [1]. It is CW FEL based on an accelerator–recuperator, or an energy recovery linac (ERL). It differs from other ERL-based FELs [2, 3] in the low frequency non-superconducting RF cavities and longer wavelength operation range. Full-scale Novosibirsk free electron laser is to be based on the four-orbit 40 MeV electron accelerator-recuperator (see Fig. 1). It is to generate radiation in the range from 5 micrometer to 0.24 mm [4, 5].

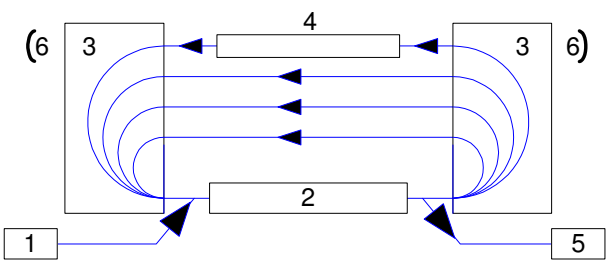

Figure 1: Scheme of the accelerator-recuperator based FEL. 1 - injector, 2 - accelerating RF structure, 3 - 180-degree bends, 4 – undulator, 5 – beam dump, 6 – mirrors of the optical resonator.

ACCELERATOR-RECUPERATOR

The first stage of the machine contains a full-scale RF system, but has only one orbit. Layout of the accelerator–recuperator is shown in Fig. 2. The 2 MeV electron beam from an injector passes through the accelerating structure, acquiring the 12 MeV energy, and comes to the FEL, installed in the straight section. After interaction with radiation in the FEL the beam passes once more through the accelerating structure, returning the power, and comes to the beam dump at the injection energy. Main parameters of the accelerator are listed in Table 1.

Table 1: Accelerator parameters (first stage)

RF frequency, MHz	180
Number of RF cavities	16
Amplitude of accelerating voltage at one cavity, MV	0.7
Injection energy, MeV	2
Final electron energy, MeV	12
Maximum bunch repetition rate, MHz	22.5
Maximum average current, mA	20
Beam emitance, mm·mrad	2
Final electron energy spread, FWHM, %	0.2
Final electron bunch length, ns	0.1
Final peak electron current, A	10

The electron source is the 300 keV DC gun with gridded cathode. Maximum charge per bunch is 1.7 nC.

FEL

The FEL is installed in a long straight section of a single-orbit accelerator-recuperator. It consists of two undulators, a magnetic buncher, and optical resonator. Both electromagnetic planar undulators are identical. The length of an undulator is 4 m, period is 120 mm, the gap is 80 mm, and deflection parameter K is up to 1.2. The buncher is simply a three-pole electromagnetic wiggler. It is necessary to optimize the relative phasing of undulators and is used now at low longitudinal dispersion $N_d < 1$.

Both laser resonator mirrors are spherical, 15 m curvature radius, made of the gold-plated copper, and water-cooled [6]. In the center of each mirror there is a hole. It serves for mirror alignment (using the He-Ne laser beam) and output of small amount of radiation. The distance between mirrors is 26.6 m. The forward mirror has the hole with the diameter 3.5 mm, and the rear one - with the diameter 8 mm (See Fig.3). The calculated transparency of the mirror with the 8-mm hole, at the wavelength 150 micron, is 1.5%. At this wavelength the measured round-trip loss are near 7%. The output radiation passes through two windows, which separated the FEL and accelerator vacuum from the atmosphere. After the forward mirror the additional iris and the normal-incidence quartz window are installed. After the rear one there is a diamond window, tilted at the Brewster angle.

* The work was partially supported by SB RAS grant N174/06 and by grant №2.1.1.3846 of Russian Ministry of Science and Education.
# vinokurov@inp.nsk.su

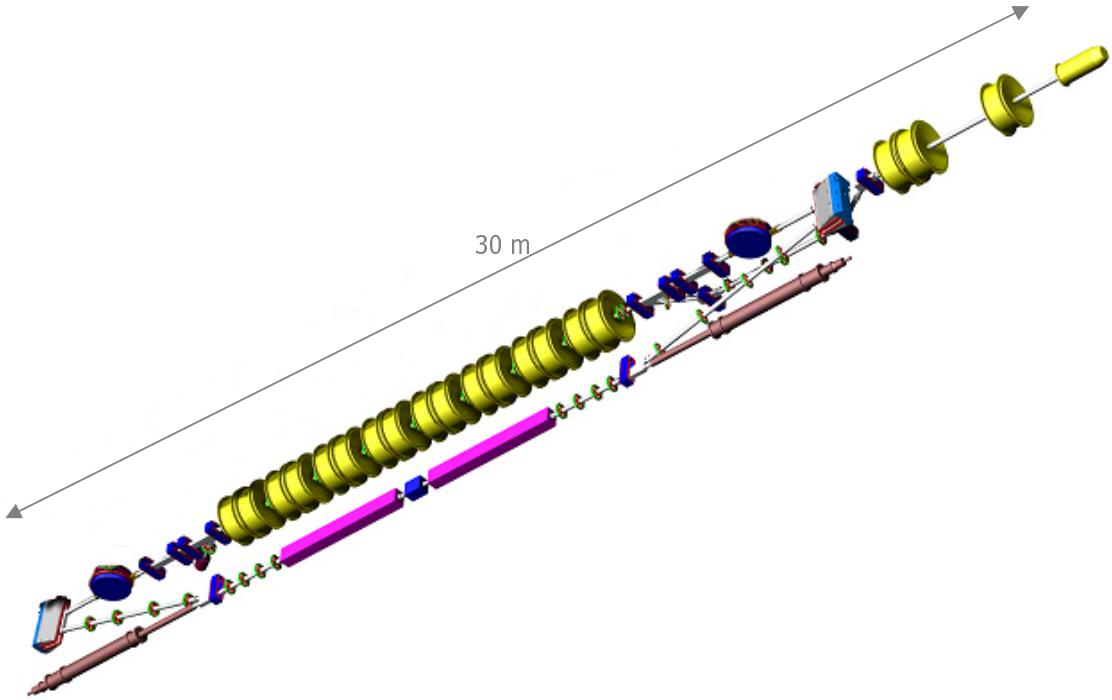

Figure 2: Scheme of the first stage of the Novosibirsk terahertz FEL. The loop lies in the vertical.

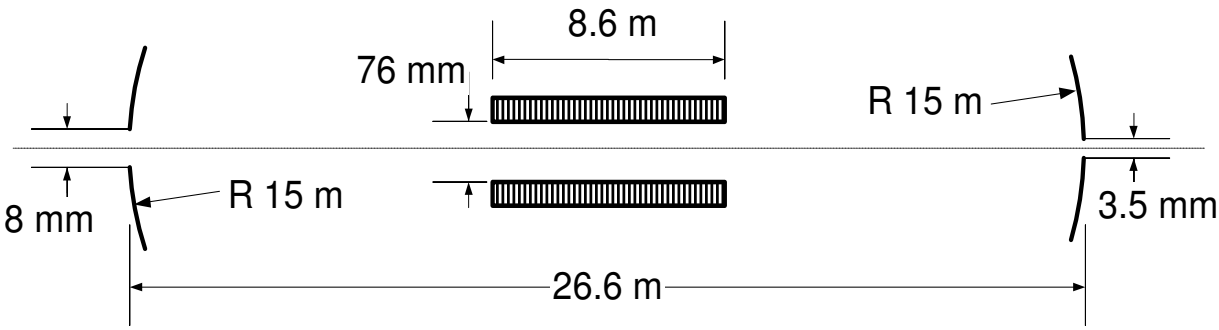

Figure 3: Scheme of the optical resonator.

RADIATION STUDY

The first measurements of radiation parameters were reported before [1].

Instead of the fine tuning of the optical resonator length we tuned the RF frequency. The tuning curve is shown in Fig. 4. The preliminary simulation results [7] demonstrated a reasonable agreement with measured data. The experimental curve is wider, which may be explained by the shortening of the optical resonator due to mirror heating.

The average radiation power, passed through the hole at the rear mirror, was about 400 W. Taking into account the 7% loss, one get approximately 2 kW of power, extracted from the electron beam. The electron beam power was 200 kW. Therefore an electron efficiency is about 1%. The radiation parameters are listed in Table 2.

Table 2: The radiation parameters

Wavelength, mm	0.12...0.23
Minimum relative linewidth, FWHM	0.003
Pulse length, FWHM, ns	0.05
Peak power, MW	1
Repetition rate, MHz	11.2
Maximum average power, kW	0.4

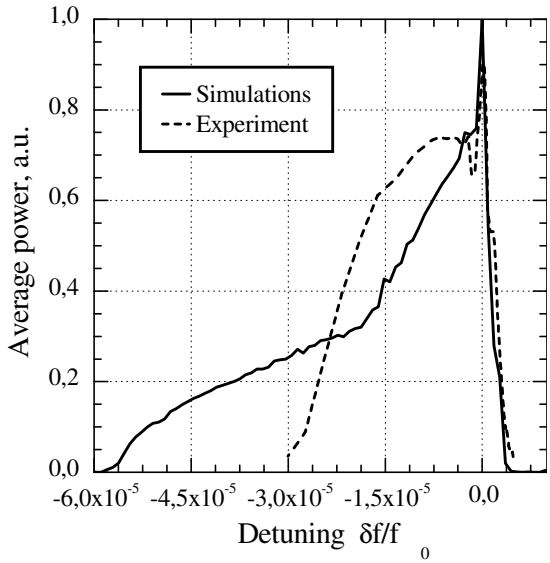

Figure 4: Dependence of the average power on the RF frequency detuning.

BEAMLINE AND USER STATIONS

To transmit the radiation from the rear mirror hole to user stations, the beamline from the accelerator hall to the user hall was built. As the diffractional angular divergence $1.22 \cdot \lambda/D = 0.03$ (for 200 micron) is high, the spherical mirror is used to transform the radiation beam to almost parallel one. The incidence angle is only 7 degrees, therefore astigmatism is negligible (see Fig. 5).

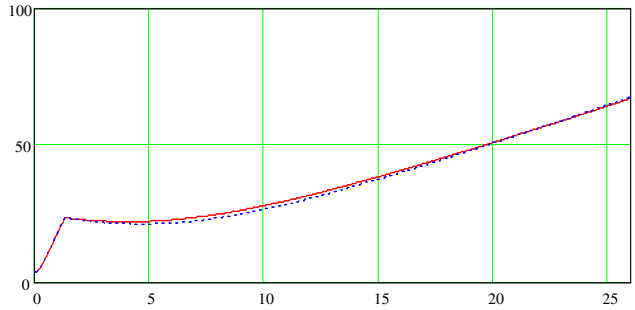

Figure 5: Calculated size of equivalent Gaussian beam (mm) vs. distance along the beamline (m).

Other 5 mirrors are flat. The beamline is filled by dry nitrogen. It is separated from the accelerator vacuum by the diamond window, and from the air by the polyethylene window. After installation of nitrogen dryer we obtained almost complete transparency of the beamline.

Now radiation may be delivered to 5 stations. Two of them are used for measurement of radiation spectrum, and other three – for users. In particular, the terahertz ablation of DNA and other biologically relevant molecules was performed [8]. It was shown, that transfer from surface occurred without molecular destruction.

FURTHER DEVELOPMENTS

We plan to increase further the output power. The electron gun upgrade for the increase of the average

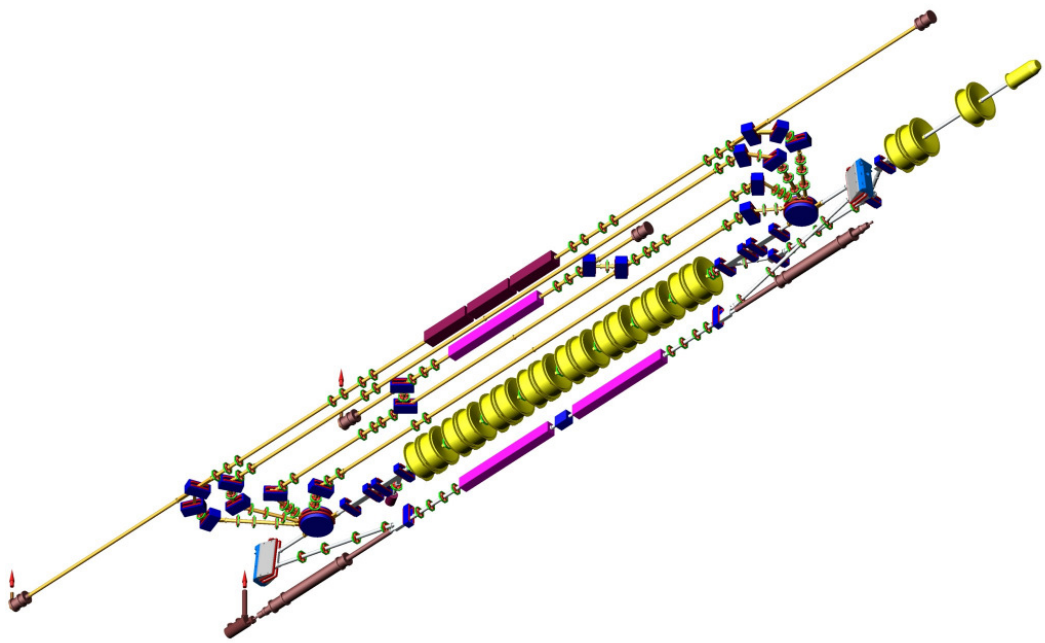

Figure 6: Scheme of the second stage of the Novosibirsk terahertz FEL. The terahertz FEL orbit lies in the vertical plain. Other four orbits lie in the horizontal one.

current up to 0.1 A is in progress.

The design and manufacturing of the full-scale four-turn ERL is underway. An artistic view of the machine is shown in Fig. 6. The existing orbit with the terahertz FEL lies in the vertical plane. The new four turns are in the horizontal one. One FEL is installed at the fourth orbit (40 MeV energy), and the second one at the bypass of the second orbit (20 MeV energy).

REFERENCES

[1] E. A. Antokhin et al. NIM A528 (2004) p.15-18.
[2] G.R. Neil et al. Phys. Rev. Lett. 84 (2000), p. 662.
[3] E.J. Minehara. NIM A483, p. 8, 2002.
[4] N.G. Gavrilov et al. IEEE J. Quantum Electron., QE-27, p. 2626, 1991.
[5] V.P.Bolotin et al. Proc. of FEL-2000, Durham, USA, p. II-37 (2000).
[6] Kubarev V.V., Persov B.Z., Vinokurov N.A., Davidov A.V. NIM A528 (2004), No. ½, p. 199-202.
[7] O.A. Shevchenko, A.V. Kuzmin, N.A. Vinokurov. NIM A543 (2005), No. 1, p. 114-117.
[8] A. K. Petrov et al., Russian Dokl. Acad. Nauk, v. 404 (2005), No. 5, p. 1 – 3.

FEL ACTIVITIES IN INDIA

S. Krishnagopal*, B. Biswas, S. Chouksey, S. K. Gupta, U. Kale, A. Kumar, V. Kumar, S. Lal, P. Mehta, P. Nerpagar, K. K. Pant, RRCAT, Indore, India.

Abstract

We are building a Compact Ultrafast TErahertz Free-Electron Laser (CUTE-FEL), designed to lase from 50 – 100 μm. The FEL will be driven by a 10-15 MeV electron beam from a Plane-Wave Transformer (PWT) linac. The undulator is a 5 cm period, 2.5 m long PPM planar undulator. We present details of the FEL design and the present status of activities. We also present very preliminary plans for a short-wavelength SASE FEL in India.

INTRODUCTION

FEL activity in India is presently restricted to the Raja Ramanna Centre for Advanced Technology, Indore, where a terahertz FEL is under construction. Earlier, however, there was some activity at Pune University, where a 26 mm period, 39 cm long pure permanent magnet undulator was built and characterized [1]. At the Institute for Plasma Research, Ahmedabad, there was interest in FELs for plasma heating and diagnostics. A 50 period electromagnet undulator was developed, a 300 keV sheet electron beam from a Tesla transformer was transmitted through this undulator, and spontaneous emission was observed [2].

In this paper we focus on ongoing activities at RRCAT, and present briefly our plans for the future.

THE CUTE-FEL PROJECT

The terahertz is a relatively unexplored part of the electromagnetic spectrum, and there is presently substantial interest in terahertz sources. For an FEL the terahertz is attractive because the long wavelength allows for higher gain, and reduces the requirements on the beam current and quality. A THz FEL is therefore a good green-field FEL project.

The Compact Ultrafast TErahertz FEL (CUTE-FEL) project aims to lase between 50-100 μm. The layout of the beamline is shown in Figure 1. The main parameters of the FEL are given in Table 1.

The electron source is a thermionic electron gun, that will provide 90 kV, 1 nC, 1 ns (FWHM) electron pulses at 36.62 MHz. The design normalized rms beam emittance is 5π mm-mrad, and the rms energy spread will be better than 1%. This gun is under procurement. In the meantime we continue experiments with a 40 kV, 2 μs, triode gun that was built by another group in RRCAT [3].

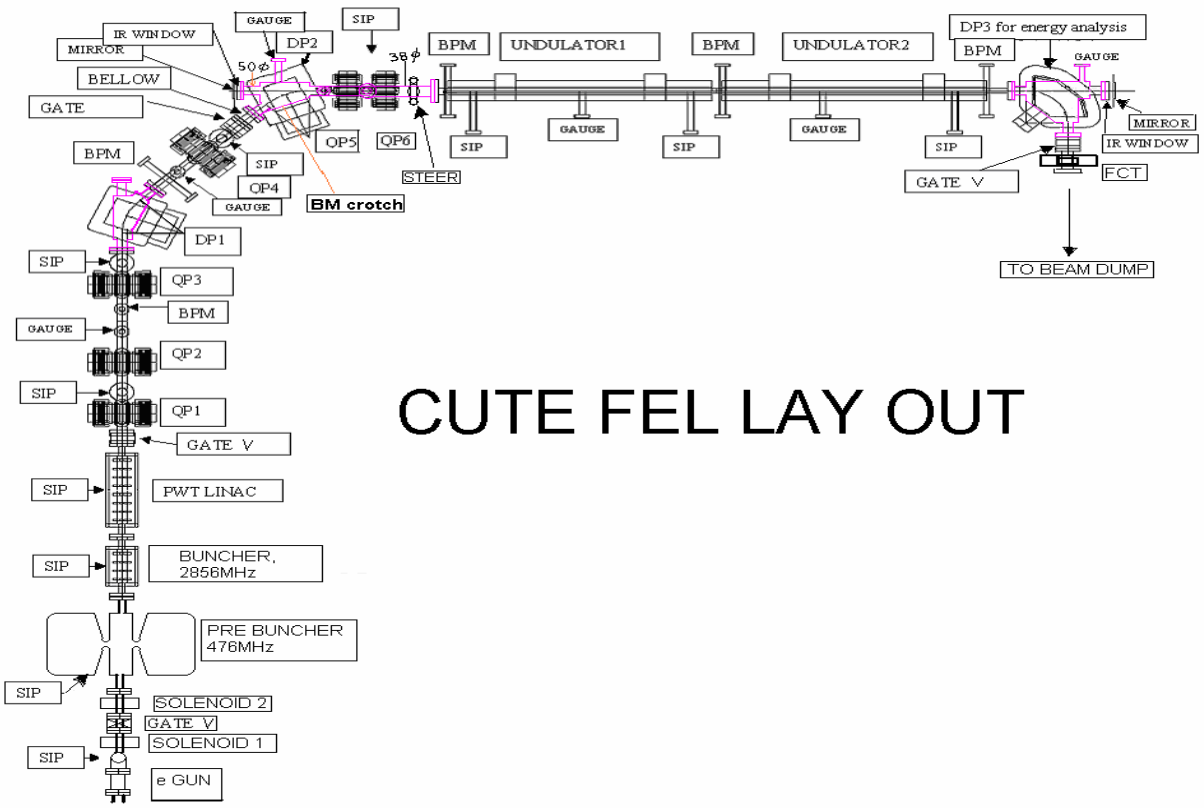

Figure 1: Beam-transport line for the CUTE-FEL.

*skrishna@cat.ernet.in

The electrons from the gun will be bunched in a 476 MHz pre-buncher, which has been designed by us and is presently being fabricated. The design is a standard re-entrant pillbox cavity, and will compress the beam by a factor of around 18.

The buncher at 2856 MHz will be a 4-cell Plane Wave Transformer (PWT) structure, and the linac itself will comprise up to two 8-cell structures to go to a maximum energy of 15 MeV. More details on the PWT structure, which we have developed ourselves, are given in a later section.

Table 1: Main parameters of the CUTE-FEL

Parameter	**Value**	**Unit**
Energy	10-15	MeV
Peak current	20	A
Micro-pulse	20 @ 36.62	ps @ MHz
Macro-pulse	8 @ 10	μs @ Hz
Und. period	5	cm
Und. length	2.5	m
Und. param.	0.8	
Wavelength	50-100	μm

The undulator is a standard Halbach configuration, planar PPM undulator, using NdFeB magnets. It has a period of 5 cm and a total length of 2.5 m. We have performed detailed design simulations using the code TDAOSC [4] AND GENESIS 1.3 [5]. In order to make the FEL compact, we have tried to keep the optical cavity as short as possible – it is only 4.1 m long. The resonator is near-concentric, to provide good mode stability.

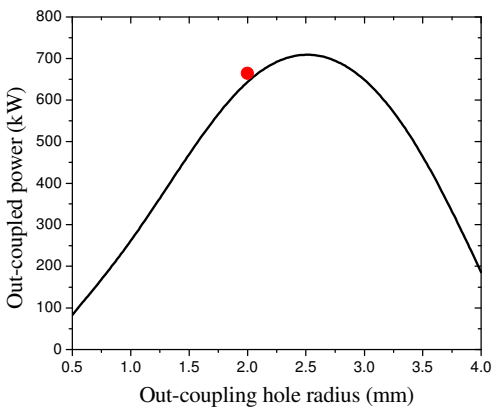

Figure 2: Optimisation curve for the size of the out-coupling hole.

Radiation is out-coupled through a hole at the centre of one of the gold-plated copper mirrors. The optimal hole radius, to maximize the out-coupled power while maintaining a good mode profile, was determined to be 2 mm (see Fig. 2). For our design we get a peak out-coupled power of around 0.5 MW. The small-signal gain is 88%, while the round-trip loss is 15%.

Figure 3 shows the variation of the FEL beam size down the undulator. At the entrance and exit of the undulator the maximum 1/e beam radius is around 5 mm. Note that the matched rms vertical beam size of the electron beam within the undulator is 0.8 mm.

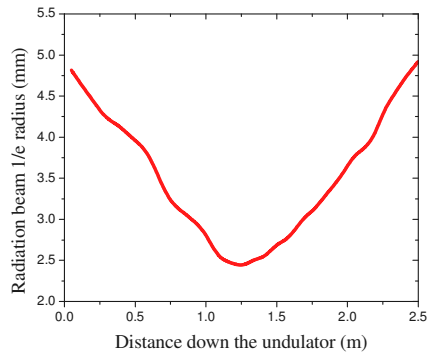

Figure 3: Size of the radiation beam as a function of distance down the undulator.

UNDULATOR

The 5 cm period, 2.5 m long PPM undulator has been constructed [6] in two equal segments of 25 periods each (Fig. 4). The undulator gap can be varied from 20-100 mm. The magnets are made of NdFeB, each 12.5 x 12.5 x 50 mm^3 in size. Individual magnets were characterized, and their arrangement in the undulator determined using a global optimisation (simulated annealing) algorithm. Field measurement of the assembled undulator segments was done using a three-axis Hall probe (Senis GmbH), with a spatial resolution of 0.1 mm.

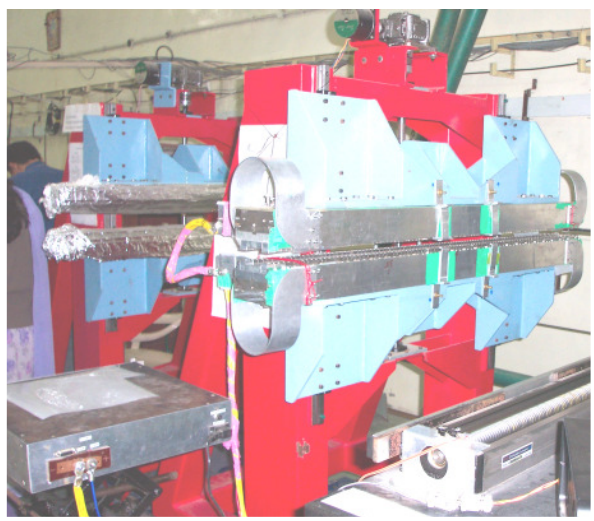

Figure 4: A view of the two undulator segments, each of length 1.25 m.

A summary of the measurements is given in Table 2. It can be seen that almost all the parameters are within the design specification. Our initial measurements showed that the beam trajectory through U25.2 had a degree of drift. To correct this we built a corrector coil that gives a

small, 0.77 G, vertical field. With this correction the trajectory straightens out to within acceptable limits (Fig. 5). Further improvements can be done by shimming the magnets.

Table 2: Design and measured parameters of the two undulator segments

Parameter	Design value	U25.1 measured	U25.2 measured
Error in peak field	< 1%	0.9%	0.7%
Error in period	< 100 μm	82 μm	85 μm
rms phase-shake	< 5°	2°	2°
Beam wander	< 1	1.14	0.33

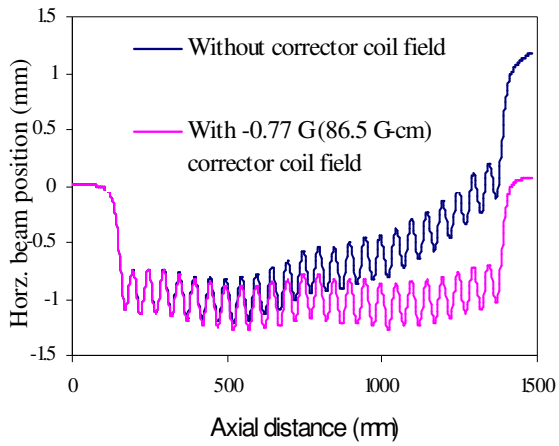

Figure 5: Electron beam trajectory through the undulator, with and without the corrector coil.

PWT LINAC

A major challenge has been the indigenous development of the linear accelerator technology. We also chose to build a rather unconventional structure – the plane wave transformer (PWT) linac [6]. This is a much more open structure, with strong coupling between the cells – and consequently with reduced fabrication tolerances. The only PWT linac working in the world is at UCLA [7], where it is routinely used, mainly for FEL applications.

After building a number of prototypes and ascending a steep learning curve, we now have a four-cell, 21 cm long structure, PWT3 (Fig. 6) that has been fabricated to the required tolerances (30 μm) and surface finish (0.2 μm CLA), which can hold UHV ($1x10^{-8}$ torr), resonates at the desired frequency of 2856 MHz, and has a loaded Q of 8,000.

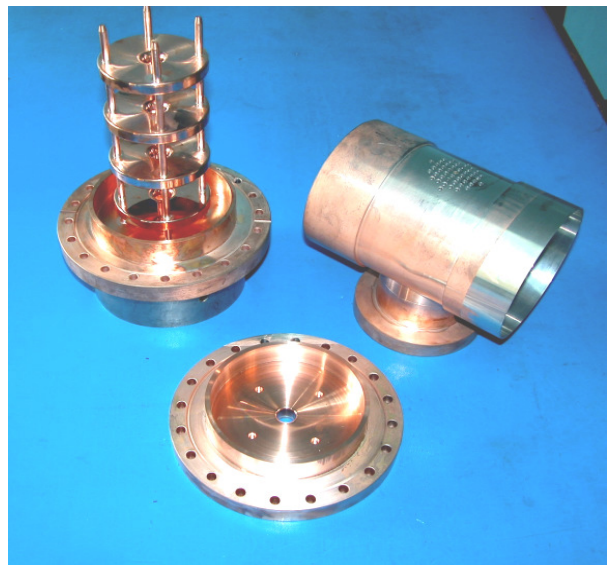

Figure 6: Components of the 4-cell PWT linac structure.

We have injected beam from a 40 kV thermionic electron gun into this structure, and have accelerated it to an energy of 3.5 MeV, corresponding to an accelerating gradient of around 25 MV/m. We also have ready a second 4-cell structure, PWT4, and are presently in the midst of fabricating an 8-cell PWT structure.

S-BAND PHOTOINJECTOR

Independent of the CUTE-FEL project, we have also been developing an S-band photoinjector, keeping in mind the requirements of short-wavelength FELs [8]. Our gun is based on the standard BNL/SLAC/UCLA Gun 4 design. We have performed extensive electromagnetic and beam dynamics design simulations using SUPERFISH, GDFIDL and PARMELA. We have also studied the injection of beam from the gun into a PWT linac structure.

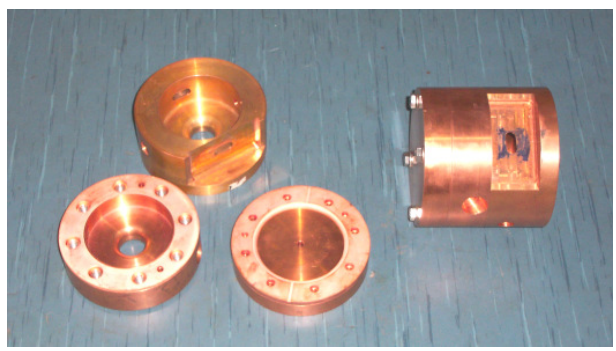

Figure 7: Components of the ETP Cu prototypes of the photocathode RF gun.

We have built a number of prototypes, of ETP and OFE copper, to qualify machining and brazing issues (Fig. 7). We have also built a number of aluminium prototypes for cold tests and for tuning the gun. We have developed a two-step tuning procedure to get the desired gun parameters – resonant frequency of the π-mode at 2856

MHz, β = 1 and field balance of unity, directly, without empirical tuning of the gun during cold-tests (Fig. 8). We have now given an order to an Indian vendor for fabricating four photocathode guns.

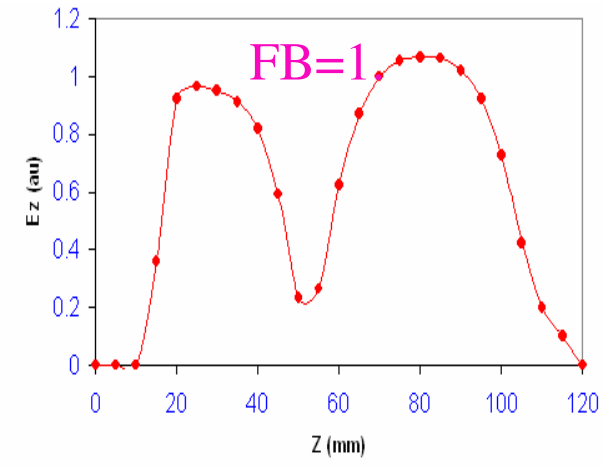

Figure 8: Bead-pull of a tuned Al prototype photocathode gun.

FUTURE PLANS

While we are presently focused on getting the CUTE-FEL lasing, some thought is also being given to future FEL activities in the country.

Table 3: Preliminary proposal of a 3-stage roadmap for the FEL programme in India

	Stage I	**Stage II**	**Stage III**
Wavelength (nm)	1,000	10	0.1
Energy (GeV)	0.1	1	10
Norm. emitt. (mm-mrad)	5	3	1
Undulator period (mm)	50	30	30
Undulator length (m)	5	30	100
Undulator param. 'K'	1	1.5	3
Peak current (A)	0.1	2	4
Pulse structure (fs @ Hz)	1,500 @ 50	150 @ 50	75 @ ??
Accel. Tech.	Norm. cond.	Norm. cond.	???

A joint Indo-French Workshop on FELs, was held in Goa, India, in March 2006. The consensus that emerged from this Workshop, especially from the Indian users who participated, was that a phased approach towards short-wavelength FELs, perhaps ultimately culminating in an XFEL, was highly desirable. To this end a preliminary three-stage roadmap has been proposed, summarized in Table 3.

There is already substantial interest amongst the user community in the country, particularly in materials science, for an IR-FEL facility (Stage I of the proposed roadmap). Another user workshop is planned to be held later this year.

CONCLUSIONS

A terahertz FEL, the CUTE-FEL, is in an advanced stage of construction at RRCAT. We have developed a PWT linac injector for the FEL, and have accelerated beam to 3.5 MeV in a 4-cell structure. We have built a 5 cm period, 2.5 m long PPM undulator. We are also in the final stages of development of an S-band photoinjector. Based on this foundation, and on interest shown by the user community, we expect a rapid expansion in the FEL activities in India in the coming years, starting with an IR-FEL facility, and perhaps continuing towards an XFEL in the future.

ACKNOWLEDGEMENTS

We thank Dr. R. V. Nandedkar and Dr. V. C. Sahni for their constant support and encouragement. We also thank a large number of colleagues, too numerous to be listed, for their support and contribution to the CUTE-FEL project.

REFERENCES

[1] V. B. Asgekar et al., Jap J Appl Phys, **37**, 3563, (1998).

[2] A. V. Ravi Kumar at al., IEEE Trans. Plasma Sci. **26**, 556 (1998).

[3] S. Mahadevan et al., Nucl. Instr. And Method **A**, **496**, 26 (2003).

[4] S. Krishnagopal et al., Nucl. Instr. And Meth. **A 318**, 661 (1992).

[5] http://pbpl.physics.ucla.edu/~reiche/index.html

[6] B. Biswas et al., InPAC'05, Kolkata, March 2005, p. 89.

[7] A. Kumar, K. K. Pant, S. Krishnagopal, Phys. Rev. ST Accel. Beams, **5**, 00033501 (2002).

[8] R. Zhang, Ph. D. Dissertation, UCLA, 1997.

[9] A. Kumar, K. K. Pant, S. Krishnagopal, Phys. Rev. ST Accel. Beams, **5**, 103501 (2002).